EUROPEAN ORGANIZATION FOR NUCLEAR RESEARCH
STANFORD LINEAR ACCELERATOR CENTER

CERN-PH-EP/2005-041
SLAC-R-774
hep-ex/0509008
7 September 2005

Precision Electroweak Measurements on the Z Resonance

The ALEPH, DELPHI, L3, OPAL, SLD Collaborations,[1]
the LEP Electroweak Working Group,[2]
the SLD Electroweak and Heavy Flavour Groups

Accepted for publication in *Physics Reports*

[1] See Appendix A for the lists of authors.
[2] Web access at `http://www.cern.ch/LEPEWWG`

Abstract

We report on the final electroweak measurements performed with data taken at the Z resonance by the experiments operating at the electron-positron colliders SLC and LEP. The data consist of 17 million Z decays accumulated by the ALEPH, DELPHI, L3 and OPAL experiments at LEP, and 600 thousand Z decays by the SLD experiment using a polarised beam at SLC. The measurements include cross-sections, forward-backward asymmetries and polarised asymmetries. The mass and width of the Z boson, m_{Z} and Γ_{Z}, and its couplings to fermions, for example the ρ parameter and the effective electroweak mixing angle for leptons, are precisely measured:

$$\begin{aligned} m_{\mathrm{Z}} &= 91.1875 \pm 0.0021 \text{ GeV} \\ \Gamma_{\mathrm{Z}} &= 2.4952 \pm 0.0023 \text{ GeV} \\ \rho_{\ell} &= 1.0050 \pm 0.0010 \\ \sin^2\theta_{\mathrm{eff}}^{\mathrm{lept}} &= 0.23153 \pm 0.00016 \,. \end{aligned}$$

The number of light neutrino species is determined to be 2.9840 ± 0.0082, in agreement with the three observed generations of fundamental fermions.

The results are compared to the predictions of the Standard Model. At the Z-pole, electroweak radiative corrections beyond the running of the QED and QCD coupling constants are observed with a significance of five standard deviations, and in agreement with the Standard Model. Of the many Z-pole measurements, the forward-backward asymmetry in b-quark production shows the largest difference with respect to its Standard Model expectation, at the level of 2.8 standard deviations.

Through radiative corrections evaluated in the framework of the Standard Model, the Z-pole data are also used to predict the mass of the top quark, $m_{\mathrm{t}} = 173^{+13}_{-10}$ GeV, and the mass of the W boson, $m_{\mathrm{W}} = 80.363 \pm 0.032$ GeV. These indirect constraints are compared to the direct measurements, providing a stringent test of the Standard Model. Using in addition the direct measurements of m_{t} and m_{W}, the mass of the as yet unobserved Standard Model Higgs boson is predicted with a relative uncertainty of about 50% and found to be less than 285 GeV at 95% confidence level.

Keywords: Electron-positron physics, electroweak interactions, decays of heavy intermediate gauge bosons, fermion-antifermion production, precision measurements at the Z resonance, tests of the Standard Model, radiative corrections, effective coupling constants, neutral weak current, Z boson, W boson, top quark, Higgs boson.

PACS: 12.15.-y, 13.38.-b, 13.66.-a, 14.60.-z, 14.65.-q, 14.70.-e, 14.80.-j.

Acknowledgements

We would like to thank the CERN accelerator divisions for the efficient operation of the LEP accelerator, the precise information on the absolute energy scale and their close cooperation with the four experiments. The SLD collaboration would like to thank the SLAC accelerator department for the efficient operation of the SLC accelerator. We would also like to thank members of the CDF, DØ, NuTeV and E-158 Collaborations for making results available to us and for useful discussions concerning their combination. Finally, the results and their interpretation within the Standard Model would not have been possible without the close collaboration of many theorists.

Contents

1 Introduction **14**
- 1.1 LEP and SLC Data . . . 14
  - 1.1.1 LEP . . . 16
  - 1.1.2 SLC . . . 19
- 1.2 LEP/SLC Detectors . . . 21
- 1.3 Basic Measurements . . . 23
- 1.4 Standard Model Relations . . . 26
- 1.5 The Process $e^+e^- \to f\bar{f}$ . . . 30
  - 1.5.1 Cross-Sections and Partial Widths . . . 31
  - 1.5.2 Invisible Width and Number of Neutrinos . . . 35
  - 1.5.3 Asymmetry and Polarisation . . . 35
  - 1.5.4 Relating Theory and Experiment . . . 39
- 1.6 Interpretation and Impact of the Results . . . 41

2 The Z Lineshape and the Leptonic Forward-Backward Asymmetries **45**
- 2.1 Introduction . . . 45
- 2.2 Measurements of Total Cross-Sections and Forward-Backward Asymmetries . . . 47
  - 2.2.1 Event Selection . . . 47
  - 2.2.2 Cross-Section Measurements . . . 49
  - 2.2.3 Measurements of the Lepton Forward-Backward Asymmetries . . . 52
  - 2.2.4 Experimental Systematic Errors . . . 54
  - 2.2.5 Energy Calibration . . . 55
- 2.3 Experimental Results . . . 60
- 2.4 Common Uncertainties . . . 64
  - 2.4.1 Energy Calibration Uncertainties . . . 65
  - 2.4.2 Uncertainties Related to the t-Channel . . . 65
  - 2.4.3 Luminosity Uncertainties . . . 66
  - 2.4.4 Theory Uncertainties . . . 67
- 2.5 Combination of Results . . . 69
  - 2.5.1 Multiple Z-Mass Fits . . . 70
  - 2.5.2 Shifts for Halved Experimental Errors . . . 70
  - 2.5.3 Influence of the γ–Z Interference Term . . . 72
  - 2.5.4 Direct Standard Model Fits to Cross-Sections and Asymmetries . . . 73
- 2.6 Combined Results . . . 74

3 Measurement of Left-Right and Lepton Asymmetries at the SLC **77**
3.1 Left-Right Asymmetry Measurements . . . 77
3.1.1 Electron Polarisation at the SLC . . . 78
3.1.2 Polarimetry at the SLC . . . 78
3.1.3 Energy Spectrometry . . . 85
3.1.4 Event Selection . . . 86
3.1.5 Control of Systematic Effects . . . 87
3.1.6 Results . . . 89
3.2 Lepton Asymmetry Measurements . . . 93
3.2.1 Analysis Method . . . 93
3.2.2 Systematic Errors . . . 95
3.2.3 Results . . . 96
3.3 Combined Results . . . 97

4 The Tau Polarisation Measurements **98**
4.1 Introduction . . . 98
4.2 Experimental Methods . . . 99
4.3 Systematic Errors . . . 109
4.3.1 Decay-Independent Systematic Uncertainties . . . 110
4.3.2 Decay-Dependent Systematic Uncertainties . . . 111
4.4 Results . . . 114

5 Results from b and c Quarks **118**
5.1 Introduction . . . 118
5.2 Heavy Flavour Tagging Methods . . . 119
5.2.1 Lifetime Tagging . . . 120
5.2.2 Combined Lifetime Tag . . . 122
5.2.3 Lepton Tagging . . . 125
5.2.4 D-Meson Tags . . . 126
5.3 Partial Width Measurements . . . 130
5.3.1 R_{b} Measurements . . . 131
5.3.2 R_{c} Measurements . . . 132
5.4 Asymmetry Measurements . . . 134
5.4.1 Lepton and D-Meson Measurements . . . 137
5.4.2 Jet and Vertex Charge . . . 137
5.4.3 Kaons . . . 139
5.4.4 Asymmetry Measurements used in the Combination . . . 139
5.5 Auxiliary Measurements . . . 140
5.6 External Inputs to the Heavy Flavour Combination . . . 140
5.6.1 Fragmentation of Heavy Quarks . . . 141
5.6.2 Heavy Quarks from Gluon Splitting . . . 143
5.6.3 Multiplicities in Heavy Flavour Decays . . . 143
5.6.4 Heavy Flavour Lifetimes . . . 144
5.6.5 Charmed Hadron Decays to Exclusive Final States . . . 145
5.6.6 Heavy Flavour Leptonic Decays . . . 145
5.6.7 Hemisphere Correlations in Double-Tag Methods . . . 147
5.6.8 Light Quark Background in Lifetime Tagged Samples . . . 148
5.7 Corrections to the Electroweak Observables . . . 149

5.7.1 Corrections to R_b and R_c . . . 149
5.7.2 QCD Corrections to the Forward-Backward Asymmetries . . . 149
5.7.3 Other Corrections to the Asymmetries . . . 150
5.8 Combination Procedure . . . 151
5.9 Results . . . 153

6 Inclusive Hadronic Charge Asymmetry 164
6.1 Asymmetry of Flavour-Inclusive Hadronic Events . . . 164
6.2 Systematic Uncertainties . . . 166
6.3 Combination Procedure . . . 167
6.4 Combined Results and Discussion . . . 167

7 Z Boson Properties and Effective Couplings 170
7.1 Summary of Z-Pole Results . . . 170
7.1.1 Overview . . . 170
7.2 Z-Boson Decay Widths and Branching Fractions . . . 172
7.2.1 Z-Boson Decay Parameters . . . 172
7.2.2 Invisible Width and Number of Light Neutrino Species . . . 172
7.3 Effective Couplings of the Neutral Weak Current . . . 175
7.3.1 The Asymmetry Parameters $\mathcal{A}_f$ . . . 176
7.3.2 The Effective Coupling Constants . . . 179
7.3.3 The ρ_f Parameters and the Effective Electroweak Mixing Angles . . . 184
7.3.4 The Leptonic Effective Electroweak Mixing Angle . . . 184
7.3.5 Discussion . . . 188
7.4 Sensitivity to Radiative Corrections Beyond QED . . . 189

8 Constraints on the Standard Model 192
8.1 Parameters of the Standard Model . . . 192
8.2 Hadronic Vacuum Polarisation . . . 194
8.3 Additional Measurements . . . 195
8.3.1 Mass of the Top Quark . . . 195
8.3.2 Mass and Width of the W Boson . . . 195
8.3.3 Measurements at Low Momentum Transfer . . . 196
8.4 Parametric and Theoretical Uncertainties . . . 197
8.4.1 Parameter Dependence . . . 197
8.4.2 Theoretical Uncertainties . . . 201
8.5 Analysis Procedure . . . 208
8.5.1 Treatment of Systematic Uncertainties . . . 209
8.6 Standard Model Analyses . . . 209
8.6.1 Z-Pole Results . . . 209
8.6.2 The Mass of the Top Quark and of the W Boson . . . 211
8.6.3 The Mass of the Higgs Boson . . . 213
8.7 Discussion . . . 218

9 Summary and Conclusions 224

A Author Lists **226**
A.1 The ALEPH Collaboration . . . 227
A.2 The DELPHI Collaboration . . . 231
A.3 The L3 Collaboration . . . 236
A.4 The OPAL Collaboration . . . 240
A.5 The SLD Collaboration . . . 245

B Heavy-Flavour Fit including Off-Peak Asymmetries **247**

C The Measurements used in the Heavy Flavour Averages **249**

D Limits on Non-Standard Z Decays **263**

E Tests of Electroweak Radiative Corrections **265**
E.1 Parametrisations . . . 265
E.2 Results . . . 266

F Results using Light Flavour Hadronic Events **270**
F.1 Asymmetry Measurements . . . 270
F.2 Partial Width Measurements . . . 274
F.3 Comparison with Standard Model Expectations . . . 276
F.4 Z Boson Properties and Effective Couplings . . . 276
F.4.1 Z-Boson Decay Widths and Branching Fractions . . . 277
F.4.2 Effective Couplings of the Neutral Weak Current . . . 278

G Standard Model Predictions **281**

List of Figures

1.1 The lowest-order s-channel Feynman diagrams for $e^+e^- \to f\overline{f}$. 15
1.2 The hadronic cross-section as a function of energy. 15
1.3 The LEP storage ring 17
1.4 The SLC linear collider 19
1.5 Longitudinal polarisation at SLC 20
1.6 A typical LEP/SLC detector. 22
1.7 Event display pictures of $q\overline{q}$, e^+e^-, $\mu^+\mu^-$ and $\tau^+\tau^-$ 24
1.8 Side view of $Z \to b\overline{b}$ 25
1.9 Higher-order corrections to the gauge boson propagators 27
1.10 Vertex corrections to the process $e^+e^- \to b\overline{b}$. 28
1.11 QED corrections to fermion-pair production 32
1.12 The hadronic cross-section and muon forward-backward asymmetry *vs.* $\sqrt{s}$ . . . 33
1.13 Number of neutrinos 36
1.14 $\mathcal{A}_f$ as a function of $\sin^2\theta^f_{\rm eff}$ 40
1.15 The 1987 status of $g_{V\ell}$ and $g_{A\ell}$. 43
1.16 Predictions and measurements of m_t. 44

2.1 Separation of final states 48
2.2 Luminosity measurement 50
2.3 Hadronic cross-section measurements 53
2.4 t-channel contribution to e^+e^- final states 54
2.5 $\mu^+\mu^-$ differential cross-section 55
2.6 Width of the depolarising spin resonance 57
2.7 Energy from model *vs.* depolarisation calibrations 58
2.8 Beam energy variations around the LEP ring 59
2.9 Measurements of of m_Z,Γ_Z, $\sigma^0_{\rm had}$, R^0_ℓ and $A^{0,\ell}_{\rm FB}$ 63
2.10 Multiple m_Z fits 71
2.11 R^0_ℓ vs. $A^{0,\ell}_{\rm FB}$ 76

3.1 The SLC Compton polarimeter setup 81
3.2 Compton scattering asymmetry as a function of channel position 82
3.3 The linearity of a polarimeter channel 83
3.4 Comparison between the SLD photon and electron polarimeter results 84
3.5 The SLC extraction-line energy spectrometer 85
3.6 History of the SLD $A^0_{\rm LR}$ measurements. 92
3.7 Polarisation dependent angular distributions for leptons 94

4.1 Decay configurations for two τ helicity states 100
4.2 Distributions of polarisation sensitive kinematic variables 102

4.3 OPAL τ polarisation: $\tau \to \pi\nu$ momentum spectrum . . . 105
4.4 ALEPH τ polarisation: $\tau \to \rho\nu$ optimal variable spectrum . . . 106
4.5 L3 τ polarisation: $\tau \to$ e $\nu\bar{\nu}$ energy spectrum . . . 107
4.6 DELPHI τ polarisation: $\tau \to \mu\nu\bar{\nu}$ momentum spectrum . . . 108
4.7 Measured τ polarisation *vs.* $\cos\theta_\tau$ for all LEP experiments . . . 115
4.8 Comparison of τ polarisation measurements of $\mathcal{A}_\tau$ and $\mathcal{A}_\mathrm{e}$ . . . 117

5.1 Impact parameter significance from DELPHI for data and simulation. . . . 122
5.2 Impact parameter b-tag from L3. . . . 123
5.3 Decay length significance and neural network tagging variable for OPAL. . . . 124
5.4 Reconstructed vertex mass from SLD for data and simulation. . . . 125
5.5 Muon momentum and transverse momentum spectra obtained by L3 . . . 126
5.6 $\mathrm{D}^{*\pm}$ momentum spectra from OPAL . . . 127
5.7 $\mathrm{D}^0 \to \mathrm{K}^-\pi^+$, $\mathrm{D}^+ \to \mathrm{K}^-\pi^+\pi^+$, $\mathrm{D_s} \to \mathrm{K}^+\mathrm{K}^-\pi^+$ and $\Lambda_\mathrm{c}^+ \to \mathrm{pK}^-\pi^+$ mass spectra . 128
5.8 Mass difference $m(\pi^+\mathrm{D}^0) - \mathrm{m}(\mathrm{D}^0)$ spectrum from OPAL in different channels. . 129
5.9 p_t^2 spectrum of the slow pion opposite a high energy D-meson. . . . 130
5.10 $\cos\theta$ distribution from the ALEPH b-asymmetry measurement with leptons . . . 136
5.11 Reconstructed $\cos\theta$ distributions from the SLD vertex charge $\mathcal{A}_\mathrm{b}$ analysis. . . . 136
5.12 Charge separation of the ALEPH neural net tag . . . 139
5.13 R_b^0 and R_c^0 measurements used in the heavy flavour combination. . . . 155
5.14 $A_\mathrm{FB}^{0,\,\mathrm{b}}$ and $A_\mathrm{FB}^{0,\,\mathrm{c}}$ measurements used in the heavy flavour combination. . . . 156
5.15 $\mathcal{A}_\mathrm{b}$ and $\mathcal{A}_\mathrm{c}$ measurements used in the heavy flavour combination. . . . 157
5.16 Energy dependence of A_FB^b and A_FB^c. . . . 158
5.17 Contours in the $\mathcal{A}_\mathrm{c}$-$\mathcal{A}_\mathrm{b}$ plane from the Z-pole data . . . 162
5.18 Contours in the $A_\mathrm{FB}^{0,\,\mathrm{c}}$-$A_\mathrm{FB}^{0,\,\mathrm{b}}$ and R_c^0-R_b^0 planes from the Z-pole data . . . 163

6.1 The Q_+ and Q_- distributions obtained from Monte Carlo simulation by L3 . . . 166
6.2 Results on $\sin^2\theta_\mathrm{eff}^\mathrm{lept}$ from $Q_\mathrm{FB}^\mathrm{had}$ measurements . . . 169

7.1 Top and Higgs sensitivity of Γ_inv . . . 175
7.2 Comparison of the asymmetry parameters $\mathcal{A}_\mathrm{f}$ . . . 178
7.3 Comparison of the effective coupling constants for leptons . . . 181
7.4 Comparison of the effective coupling constants for heavy quarks . . . 183
7.5 Comparison of ρ_f and the effective electroweak mixing angle $\sin^2\theta_\mathrm{eff}^\mathrm{f}$ . . . 185
7.6 Comparison of the effective electroweak mixing angle $\sin^2\theta_\mathrm{eff}^\mathrm{lept}$ . . . 187
7.7 Contour curve in the $(\rho_\ell, \sin^2\theta_\mathrm{eff}^\mathrm{lept})$ plane . . . 190
7.8 Top sensitivity of R_b^0 . . . 191

8.1 Top-quark mass sensitivity . . . 199
8.2 Higgs-boson mass sensitivity . . . 200
8.3 Constraints on m_t and m_H from measurements of R_b^0, $\Gamma_{\ell\ell}$, $\sin^2\theta_\mathrm{eff}^\mathrm{lept}$ and m_W . . . 202
8.4 Higgs sensitivity of Γ_Z, σ_had^0, R_ℓ^0, $A_\mathrm{FB}^{0,\,\ell}$ and $\sin^2\theta_\mathrm{eff}^\mathrm{lept}(Q_\mathrm{FB}^\mathrm{had})$ . . . 203
8.5 Higgs sensitivity of $\mathcal{A}_\ell(A_\mathrm{FB}^{0,\,\ell})$, $\mathcal{A}_\ell(P_\tau)$, $\mathcal{A}_\ell$(SLD), $A_\mathrm{FB}^{0,\,\mathrm{b}}$ and $A_\mathrm{FB}^{0,\,\mathrm{c}}$ . . . 204
8.6 Higgs sensitivity of R_b^0, R_c^0, $\mathcal{A}_\mathrm{b}$, $\mathcal{A}_\mathrm{c}$ and $\sin^2\theta_\mathrm{eff}^\mathrm{lept}(Q_\mathrm{FB}^\mathrm{had})$ . . . 205
8.7 Higgs sensitivity of m_W, Γ_W, $\sin^2\theta_\mathrm{W}$, $\sin^2\theta_{\overline{\mathrm{MS}}}(m_\mathrm{Z})$ and Q_W . . . 206
8.8 Comparison of results on the mass of the top quark . . . 212
8.9 Comparison of results on the mass of the W boson . . . 212
8.10 Comparison of top-quark and W-boson mass determinations . . . 214

8.11 Constraints on the Higgs-boson mass from m_{t} and m_{W} . . . 215
8.12 Constraints on the Higgs-boson mass from $\Delta\alpha^{(5)}_{\mathrm{had}}(m^2_{\mathrm{Z}})$ . . . 216
8.13 The "blue-band" plot $\Delta\chi^2(m_{\mathrm{H}})$ . . . 217
8.14 Measurements and pulls . . . 220
8.15 Higgs-boson mass constraints . . . 221

E.1 Results on ϵ parameters . . . 268
E.2 Results on STU parameters . . . 269

F.1 Performance of the DELPHI RICH . . . 271
F.2 SLD measurement of $\mathcal{A}_{\mathrm{s}}$ . . . 273
F.3 Comparison of the effective coupling constants . . . 280

List of Tables

1.1 LEP beam energies and integrated luminosities . . . 17
1.2 Recorded event statistics for LEP . . . 18
1.3 The weak-isospin structure of the fermions in the SM. . . . 26

2.1 Selection efficiencies and backgrounds . . . 51
2.2 Experimental systematic errors . . . 56
2.3 Summary of errors on the centre-of-mass energy . . . 60
2.4 Nine parameter results . . . 61
2.5 Five parameter results . . . 64
2.6 Common energy errors for nine-parameter fits . . . 65
2.7 Common $t, s-t$ uncertainties . . . 66
2.8 TOPAZ0-ZFITTER differences . . . 68
2.9 QED-related common errors . . . 69
2.10 Covariance matrix of combined lineshape and asymmetry measurements . . . 70
2.11 Shifts in central values with halved experimental errors . . . 72
2.12 Direct SM fits . . . 74
2.13 Combined results . . . 75

3.1 Systematic uncertainties in the A_{LR} measurement for 1997/98 . . . 86
3.2 SLD Z event counts and corrections . . . 90
3.3 Summary of the SLD A_{LR} measurements . . . 91
3.4 Properties of the SLD $\mathrm{e^+e^-} \to \ell^+\ell^-$ event selections . . . 95
3.5 Summary of uncertainties for the 1997-1998 SLD $\mathrm{e^+e^-} \to \ell^+\ell^-$ data . . . 96
3.6 Results on the leptonic asymmetry parameters $\mathcal{A}_\ell$ from SLD . . . 96

4.1 Tau polarisation decay channel sensitivity . . . 103
4.2 Common systematic errors in τ polarisation measurements . . . 112
4.3 LEP results for $\mathcal{A}_\tau$ and $\mathcal{A}_{\mathrm{e}}$ . . . 116
4.4 Tau polarisation error correlation matrix for $\mathcal{A}_\tau$ and $\mathcal{A}_{\mathrm{e}}$ . . . 116

5.1 Vertex detector characteristics and experimental resolutions. . . . 121
5.2 b-Tagging performance of the different experiments. . . . 125
5.3 Correlation between the lepton charge and the quark charge at decay time. . . . 137
5.4 The most important external parameters used in the heavy flavour analyses . . . 142
5.5 Topological rates for the different charm-meson species. . . . 144
5.6 Error sources for the QCD corrections to the forward-backward asymmetries. . . . 150
5.7 Corrections to be applied to the quark asymmetries. . . . 151
5.8 The measurements of R^0_{b}. . . . 154
5.9 The forward-backward asymmetry results from the 18-parameter fit . . . 154

5.10 The results of the 14-parameter fit to the LEP/SLD heavy flavour data 159
5.11 The correlation matrix for the set of the 14 heavy flavour parameters. 160
5.12 Dominant error sources for the heavy-flavour electroweak parameters 161

6.1 $\sin^2\theta^{\rm lept}_{\rm eff}$ from inclusive hadronic charge asymmetry 168

7.1 Partial Z widths 173
7.2 Z branching fractions 174
7.3 Comparison of the leptonic asymmetry parameters $\mathcal{A}_\ell$ 177
7.4 Results on the leptonic asymmetry parameters $\mathcal{A}_\ell$ 177
7.5 Determination of the quark asymmetry parameters $\mathcal{A}_{\rm q}$ 177
7.6 Results on the asymmetry parameters $\mathcal{A}_{\rm f}$ 177
7.7 Results on the effective coupling constants for leptons 180
7.8 Results on the effective coupling constants for leptons 180
7.9 Results on the effective coupling constants 182
7.10 Results on $\rho_{\rm f}$ and $\sin^2\theta^{\rm f}_{\rm eff}$ for leptons 186
7.11 Results on $\rho_{\rm f}$ and $\sin^2\theta^{\rm f}_{\rm eff}$ 186

8.1 Theoretical Uncertainties 198
8.2 Results for SM input parameters from Z-pole measurements 210
8.3 Results for SM input parameters 216
8.4 Overview of results 219
8.5 Overview of predictions 223

B.1 The correlation matrix for the set of the 18 heavy flavour parameters. 248

C.1 The measurements of $R^0_{\rm b}$. 250
C.2 The measurements of $R^0_{\rm c}$. 251
C.3 The measurements of $A^{\rm b\overline{b}}_{\rm FB}(-2)$. 252
C.4 The measurements of $A^{\rm c\overline{c}}_{\rm FB}(-2)$. 253
C.5 The measurements of $A^{\rm b\overline{b}}_{\rm FB}({\rm pk})$. 254
C.6 The measurements of $A^{\rm c\overline{c}}_{\rm FB}({\rm pk})$. 255
C.7 The measurements of $A^{\rm b\overline{b}}_{\rm FB}(+2)$. 256
C.8 The measurements of $A^{\rm c\overline{c}}_{\rm FB}(+2)$. 257
C.9 The measurements of $\mathcal{A}_{\rm b}$. 258
C.10 The measurements of $\mathcal{A}_{\rm c}$. 258
C.11 The measurements of $B({\rm b}\to\ell^-)$. 259
C.12 The measurements of $B({\rm b}\to{\rm c}\to\ell^+)$. 259
C.13 The measurements of $B({\rm c}\to\ell^+)$. 259
C.14 The measurements of $\overline{\chi}$. 260
C.15 The measurements of $P({\rm c}\to{\rm D}^{*+}\to\pi^+{\rm D}^0)$. 260
C.16 The measurements of $R_{\rm c}f({\rm D}^+)$. 260
C.17 The measurements of $R_{\rm c}f({\rm D_s})$. 261
C.18 The measurements of $R_{\rm c}f({\rm c_{baryon}})$. 261
C.19 The measurements of $R_{\rm c}f({\rm D}^0)$. 261
C.20 The measurements of $R_{\rm c}P({\rm c}\to{\rm D}^{*+}\to\pi^+{\rm D}^0)$. 262

D.1 Limits on non-SM widths and branching fractions 264

E.1 Results on all ϵ parameters . . . 267
E.2 Results on the three Z-pole $STU\gamma_b$ parameters . . . 267

F.1 Comparison of direct photon analyses . . . 275
F.2 Partial Z widths . . . 277
F.3 Z branching fractions . . . 277
F.4 Results on the asymmetry parameter $\mathcal{A}_{\mathrm{q}}$ for light quarks . . . 279
F.5 Results on the effective coupling constants for light quarks . . . 279
F.6 Results on ρ_{q} and $\sin^2\theta^{\mathrm{q}}_{\mathrm{eff}}$ for light quarks . . . 279

G.1 SM predictions for pseudo-observables . . . 281
G.2 SM predictions for pseudo-observables . . . 282
G.3 SM predictions for pseudo-observables . . . 283
G.4 SM predictions for pseudo-observables . . . 284
G.5 SM predictions for pseudo-observables . . . 285
G.6 SM predictions for pseudo-observables . . . 286
G.7 SM predictions for pseudo-observables . . . 287

Chapter 1

Introduction

With the observation of neutral current interactions in neutrino-nucleon scattering in 1973 [1] and the discovery of the W and Z bosons in $p\overline{p}$ collisions ten years later [2,3], these key features of the Standard Model [4] (SM) of electroweak interactions were well established experimentally. The LEP and SLC accelerators were then designed during the 1980s to produce copious numbers of Z bosons via e^+e^- annihilation, allowing detailed studies of the properties of the Z boson to be performed in a very clean environment.

The data accumulated by LEP and SLC in the 1990s are used to determine the Z boson parameters with high precision: its mass, its partial and total widths, and its couplings to fermion pairs. These results are compared to the predictions of the SM and found to be in agreement. From these measurements, the number of generations of fermions with a light neutrino is determined. Moreover, for the first time, the experimental precision is sufficient to probe the predictions of the SM at the loop level, demonstrating not only that it is a good model at low energies but that as a quantum field theory it gives an adequate description of experimental observations up to much higher scales. The significant constraints which the data impose on the size of higher order electroweak radiative corrections allow the effects of particles not produced at LEP and SLC, most notably the top quark and the Higgs boson, to be investigated.

1.1 LEP and SLC Data

The process under study is $e^+e^- \to f\overline{f}$, which proceeds in lowest order via photon and Z boson exchange, as shown in Figure 1.1. Here the fermion f is a quark, charged lepton or neutrino. All known fermions except the top quark are light enough to be pair produced in Z decays. The LEP [5] and SLC [6] e^+e^- accelerators were designed to operate at centre-of-mass energies of approximately 91 GeV, close to the mass of the Z boson.[1] Figure 1.2 illustrates two prominent features of the hadronic cross-section as a function of the centre-of-mass energy. The first is the $1/s$ fall-off, due to virtual photon exchange, corresponding to the left-hand diagram in Figure 1.1, which leads to the peak at low energies. The second is the peak at 91 GeV, due to Z exchange, which corresponds to the right-hand diagram of Figure 1.1, and allows LEP and SLC to function as "Z factories".

The LEP accelerator operated from 1989 to 2000, and until 1995, the running was dedicated to the Z boson region. From 1996 to 2000, the centre-of-mass energy was increased to 161 GeV

[1] In this report $\hbar = c = 1$.

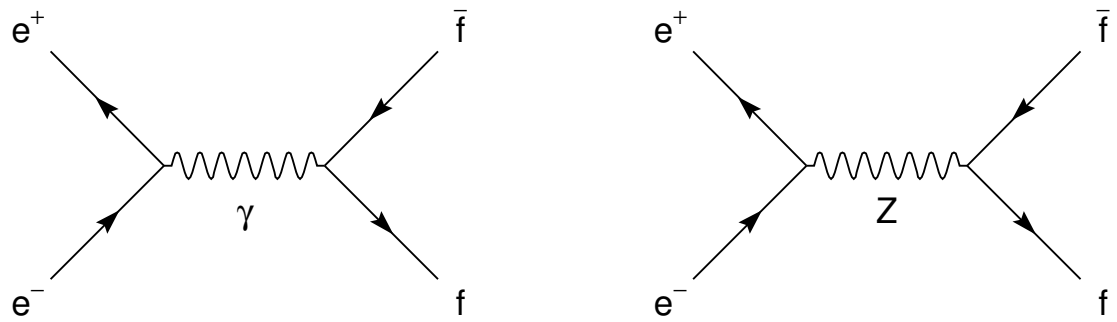

Figure 1.1: The lowest-order s-channel Feynman diagrams for $e^+e^- \to f\bar{f}$. For e^+e^- final states, the photon and the Z boson can also be exchanged via the t-channel. The contribution of Higgs boson exchange diagrams is negligible.

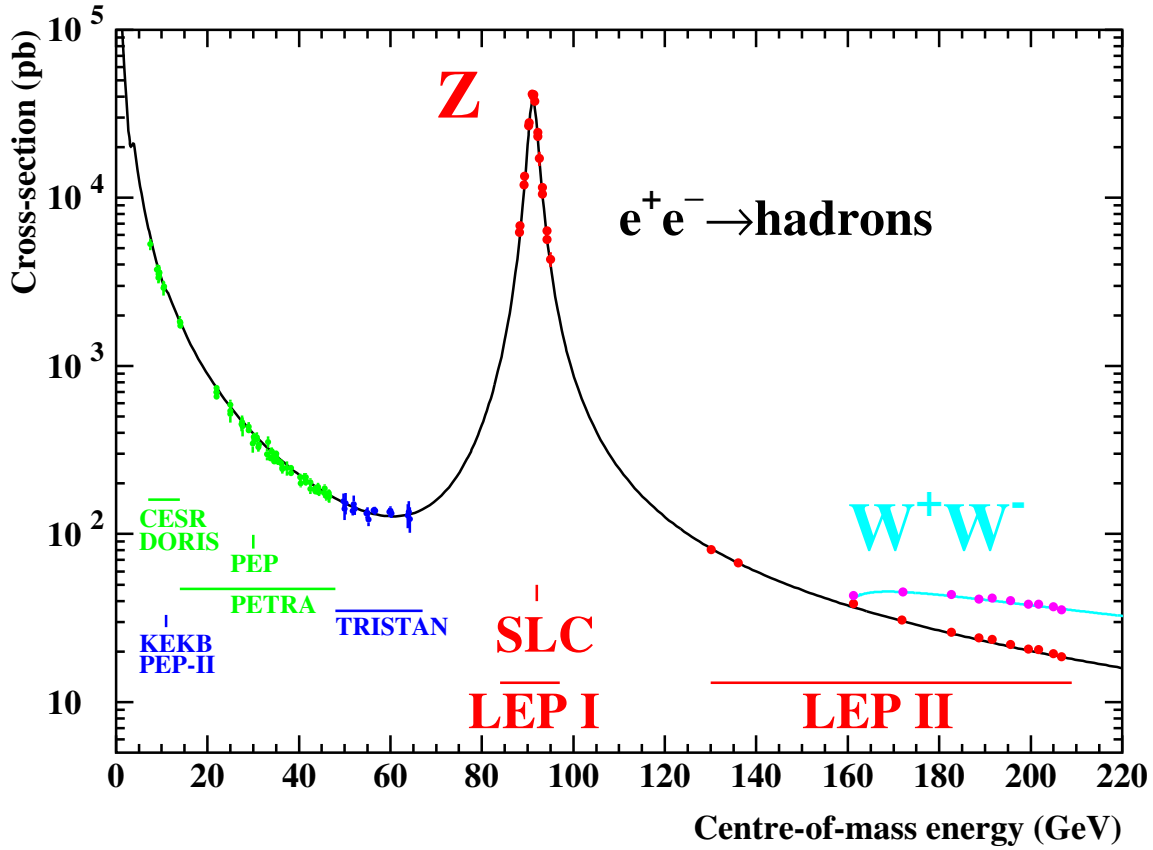

Figure 1.2: The hadronic cross-section as a function of centre-of-mass energy. The solid line is the prediction of the SM, and the points are the experimental measurements. Also indicated are the energy ranges of various e^+e^- accelerators. The cross-sections have been corrected for the effects of photon radiation.

and ultimately to 209 GeV allowing the production of pairs of W bosons, $e^+e^- \to W^+W^-$, as indicated in Figure 1.2. Although some results from this later running will be used in this report, the bulk of the data stems from the Z period. When needed, the Z period will be denoted "LEP-I", and the period beginning in 1996 "LEP-II". During the seven years of running at LEP-I, the four experiments ALEPH [7], DELPHI [8], L3 [9] and OPAL [10] collected approximately 17 million Z decays in total, distributed over seven centre-of-mass energy points within plus or minus 3 GeV of the Z pole.

The SLC accelerator started running in 1989 and the Mark-II collaboration published the first observations of Z production in e^+e^- collisions [11]. However, it was not until 1992 that longitudinal polarisation of the SLC electron beam was established. By then the SLD detector [12, 13] had replaced Mark-II. From 1992 until 1998, when the accelerator was shut down, SLD accumulated approximately 600 thousand Z decays. Although the data set is much smaller than that of LEP, the presence of longitudinal polarisation allows complementary and competitive measurements of the Z couplings. Other properties of the accelerator have been used to improve further the statistical power of the data. For example, the extremely small luminous volume of the interaction point improves the resolution in the measurement of the lifetimes of heavy flavour hadrons, which are used to select b- and c-quark events.

1.1.1 LEP

LEP [5] was an electron-positron collider ring with a circumference of approximately 27 km, making it the largest particle accelerator in the world. The collider layout included eight straight sections, with collisions between electron and positron bunches allowed to take place in four of them. The four interaction regions were each instrumented with a multipurpose detector: L3, ALEPH, OPAL and DELPHI, as indicated in Figure 1.3.

In the summer of 1989 the first Z bosons were produced at LEP and observed by the four experiments. Over the following years the operation of the machine and its performance were steadily improved. At the end of LEP data taking around the Z resonance in autumn 1995 the peak luminosity had reached $2 \times 10^{31}\mathrm{cm}^{-2}\mathrm{s}^{-1}$, above its design value of $1.6 \times 10^{31}\mathrm{cm}^{-2}\mathrm{s}^{-1}$. At this luminosity, approximately 1000 Z bosons were recorded every hour by each of the four experiments, making LEP a true Z factory. Table 1.1 summarises the data taking periods, the approximate centre-of-mass energies and the delivered integrated luminosities.

The data collected in 1989 constitute only a very small subset of the total statistics and are of lower quality, and therefore these have not been used in the final analyses. In the years 1990 and 1991 "energy scans" were performed at seven different centre-of-mass energies around the peak of the Z resonance, placed about one GeV apart. In 1992 and 1994 there were high-statistics runs only at the peak energy. In 1993 and 1995 data taking took place at three centre-of-mass energies, about 1.8 GeV below and above the peak and at the peak. The accumulated event statistics amount to about 17 million Z decays recorded by the four experiments. A detailed break-down is given in Table 1.2.

Originally four bunches of electrons and four bunches of positrons circulated in the ring, leading to a collision rate of 45 kHz. The luminosity was increased in later years by using eight equally spaced bunches, or alternatively four trains of bunches with a spacing of order a hundred meters between bunches in a train. Electrons and positrons were accelerated to about 20 GeV in the PS and SPS accelerators, then injected and accumulated in bunches in the LEP ring. When the desired bunch currents were achieved, the beams were accelerated and only then brought into collision at the interaction regions at the nominal centre-of-mass

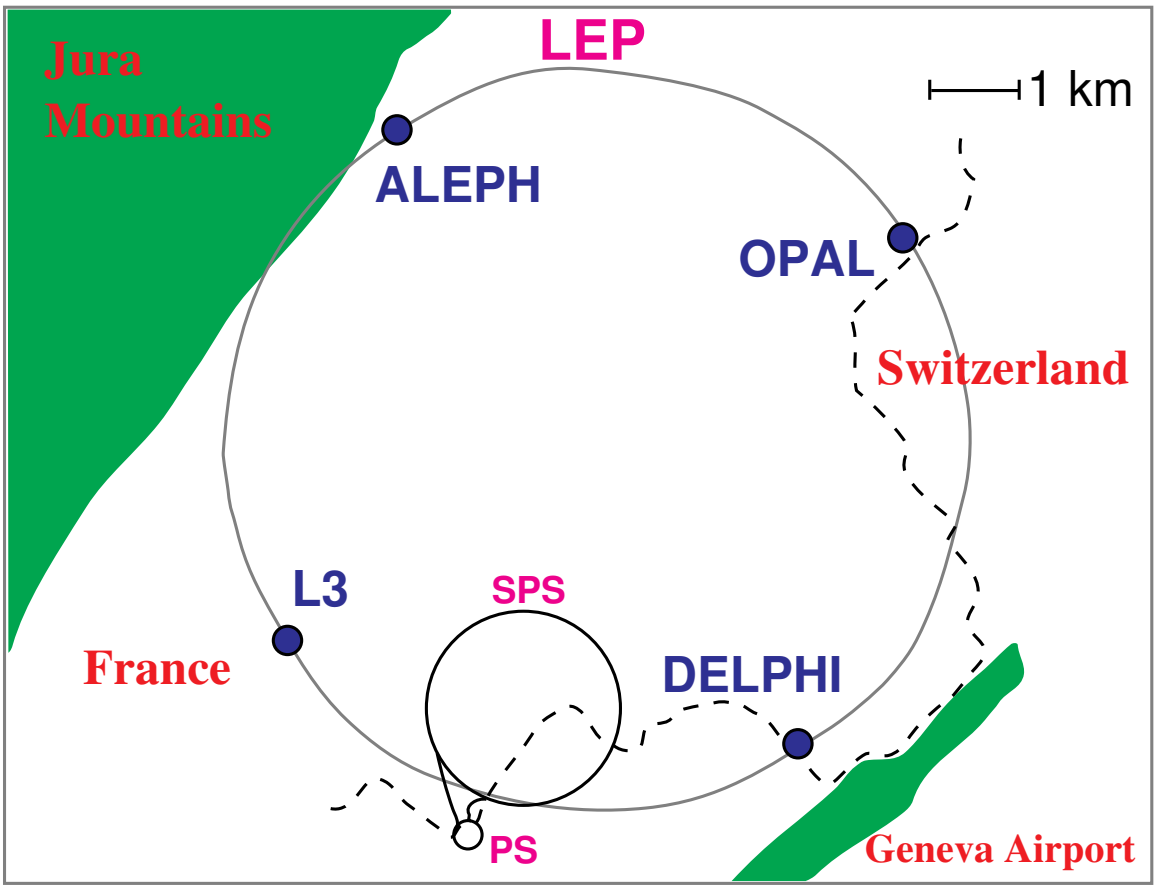

Figure 1.3: The LEP storage ring, showing the locations of the four experiments, and the PS and SPS accelerators used to pre-accelerate the electron and positron bunches.

Year	Centre-of-mass energy range [GeV]	Integrated luminosity [pb^{-1}]
1989	88.2 – 94.2	1.7
1990	88.2 – 94.2	8.6
1991	88.5 – 93.7	18.9
1992	91.3	28.6
1993	89.4, 91.2, 93.0	40.0
1994	91.2	64.5
1995	89.4, 91.3, 93.0	39.8

Table 1.1: Approximate centre-of-mass energies and integrated luminosities delivered per LEP experiment. In 1990 and 1991, a total of about 7 pb^{-1} was taken at off-peak energies, and 20 pb^{-1} per year in 1993 and in 1995. The total luminosity used by the experiments in the analyses was smaller by 10–15% due to data taking inefficiencies and data quality cuts.

Number of Events										
	$Z \to q\overline{q}$					$Z \to \ell^+\ell^-$				
Year	A	D	L	O	LEP	A	D	L	O	LEP
1990/91	433	357	416	454	1660	53	36	39	58	186
1992	633	697	678	733	2741	77	70	59	88	294
1993	630	682	646	649	2607	78	75	64	79	296
1994	1640	1310	1359	1601	5910	202	137	127	191	657
1995	735	659	526	659	2579	90	66	54	81	291
Total	4071	3705	3625	4096	15497	500	384	343	497	1724

Table 1.2: The $q\overline{q}$ and $\ell^+\ell^-$ event statistics, in units of 10^3, used for Z analyses by the experiments ALEPH (A), DELPHI (D), L3 (L) and OPAL (O).

energy for that "fill". A fill would continue for up to about 10 hours before the remaining beams were dumped and the machine refilled. The main bending field was provided by 3280 concrete-loaded dipole magnets, with hundreds of quadrupoles and sextupoles for focusing and correcting the beams in the arcs and in the straight sections. For LEP-I running, the typical energy loss per turn of 125 MeV was compensated by a radio-frequency accelerating system comprised of copper cavities installed in just two of the straight sections, to either side of L3 and OPAL.

Much effort was dedicated to the determination of the energy of the colliding beams. A precision of about 2 MeV in the centre-of-mass energy was achieved, corresponding to a relative uncertainty of about $2 \cdot 10^{-5}$ on the absolute energy scale. This level of accuracy was vital for the precision of the measurements of the mass and width of the Z, as described in Chapter 2. In particular the off-peak energies in the 1993 and 1995 scans were carefully calibrated employing the technique of resonant depolarisation of the transversely polarised beams [14,15]. In order to minimise the effects of any long-term instabilities during the energy scans, the centre-of-mass energy was changed for every new fill of the machine. As a result, the data samples taken above and below the resonance are well balanced within each year, and the data at each energy are spread evenly in time. The data recorded within a year around one centre-of-mass energy were combined to give one measurement at this "energy point".

The build-up of transverse polarisation due to the emission of synchrotron radiation [16] was achieved with specially smoothed beam trajectories. Measurements with resonant depolarisation were therefore only made outside normal data taking, and typically at the ends of fills. Numerous potential causes of shifts in the centre-of-mass energy were investigated, and some unexpected sources identified. These include the effects of earth tides generated by the moon and sun, and local geological deformations following heavy rainfall or changes in the level of Lake Geneva. While the beam orbit length was constrained by the RF accelerating system, the focusing quadrupoles were fixed to the earth and moved with respect to the beam, changing the effective total bending magnetic field and the beam energy by 10 MeV over several hours. Leakage currents from electric trains operating in the vicinity provoked a gradual change in the bending field of the main dipoles, directly affecting the beam energy. The collision energy at each interaction point also depended for example on the exact configuration of the RF accelerating system. All these effects are large compared to the less than 2 MeV systematic uncertainty on the centre-of-mass energy eventually achieved through careful monitoring of the running conditions and modelling of the beam energy.

1.1.2 SLC

The SLC [6] was the first e^+e^- linear collider. As such, its mode of operation was significantly different from that of LEP. It used the SLAC linear accelerator to accelerate alternate bunches of electrons and positrons, a set of two damping rings to reduce the size and energy spread of the electron and positron bunches, and two separate arcs to guide the bunches to a single interaction region, as shown in Figure 1.4. The repetition rate was 120 Hz, compared to either 45 kHz or 90 kHz, depending on the mode, for LEP.

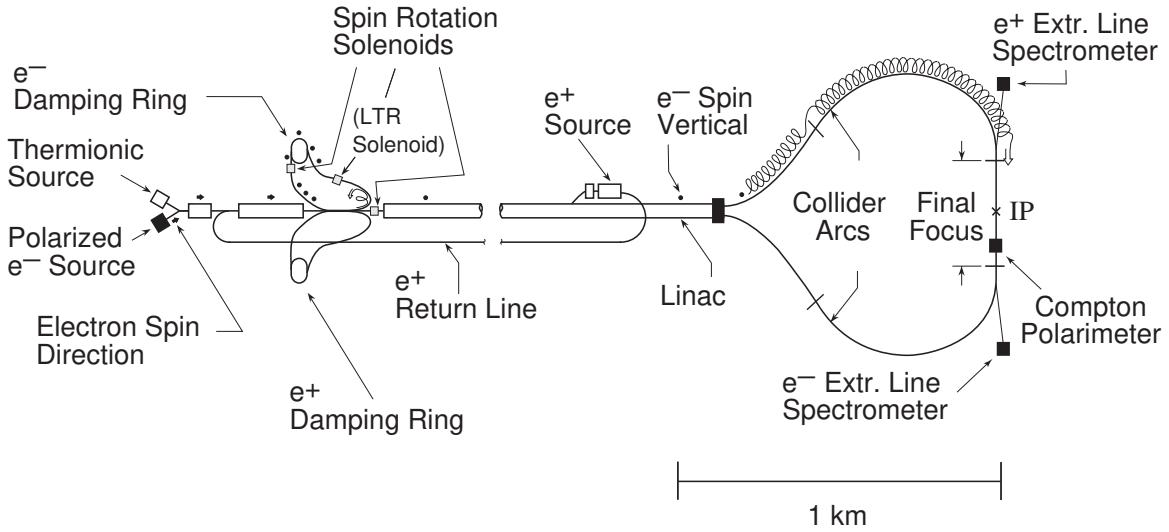

Figure 1.4: The SLC linear collider complex, showing the electron source, the damping rings, the positron source, the 3 km long linac and arcs and the final focus. The helix and arrow superimposed on the upper arc schematically indicate the electron spin precession which occurs during transport.

The standard operating cycle began with the production of two closely spaced electron bunches, the first of which was longitudinally polarised. These bunches were accelerated part way down the linac before being stored in the electron damping rings at 1.2 GeV. In the linac-to-ring (LTR) transfer line, the longitudinal polarisation was rotated first into a horizontal transverse orientation, and then, using a spin rotator magnet, into a vertical orientation perpendicular to the plane of the damping ring. After damping, the two bunches were extracted and accelerated in the linac. At 30 GeV, the second bunch was diverted to a target, where positrons were created. The positrons were captured, accelerated to 200 MeV and sent back to the beginning of the linac, where they were then stored in the positron damping ring. The positron bunch was then extracted just before the next two electron bunches, and accelerated. The remaining positron and electron bunches were accelerated to the final energy of ≈ 46.5 GeV and then transported in the arcs to the final focus and interaction point. Approximately 1 GeV was lost in the arcs due to synchrotron radiation, so the centre-of-mass energy of the e^+e^- collisions was at the peak of the Z resonance. The electron spins were manipulated during transport in the arcs, so that the electrons arrived at the interaction point with longitudinal polarisation.

The era of high-precision measurements at SLC started in 1992 with the first longitudinally polarised beams. The polarisation was achieved by shining circularly polarised laser light on a

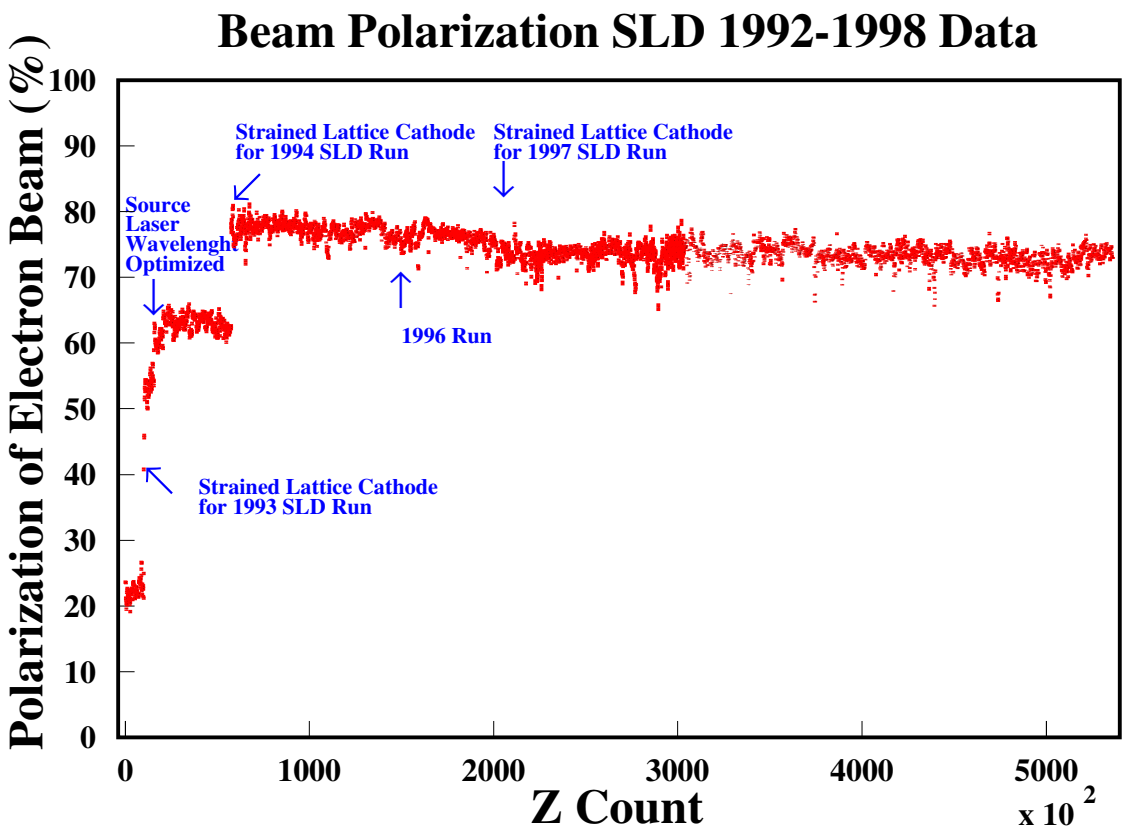

Figure 1.5: The amount of longitudinal electron polarisation as a function of the number of recorded Z decays at SLD.

gallium arsenide photo-cathode at the electron source. At that time, the electron polarisation was only 22%. Shortly thereafter, "strained lattice" photocathodes were introduced, and the electron polarisation increased significantly, as shown in Figure 1.5. Almost 60% of the data were collected in the last two years of SLC running, from 1997 to 1998, with the second to last week of running producing more than 20000 Z bosons. Much work was invested in the SLC machine to maintain the electron polarisation at a very high value throughout the production, damping, acceleration and transfer through the arcs. In addition, to avoid as much as possible any correlations in the SLC machine or SLD detector, the electron helicity was randomly changed on a pulse-to-pulse basis by changing the circular polarisation of the laser.

The polarised beam physics programme at the SLC required additional instrumentation beyond the main SLD detector, most notably, precision polarimetry. At the onset of the programme, it was hoped that the Compton-scattering polarimeter installed near the beam interaction point (IP) would reach a relative precision of 1%. In fact, an ultimate precision of 0.5% was achieved, which ensured that polarimetry systematics were never the leading contributor to the uncertainty of even the highest precision SLD measurements. This device employed a high-power circularly-polarised laser which was brought into nearly head-on collision with the electron beam downstream from the IP. Compton scattered electrons were deflected by dipole magnets and detected in a threshold Cherenkov counter, providing a beam polarisation measurement with good statistical precision every few minutes. Over the course of SLC operation, significant time was expended in a number of polarimetry cross-checks which served to ensure

confidence in the final polarimeter results. These took the form of additional polarimeter detectors used at the IP and elsewhere in the SLC (the more widely used but less precise Møller scattering polarimeters), and specialized short-term accelerator experiments designed to test polarised beam transport and to reveal, and mitigate, unanticipated systematic effects.

Secondary in importance compared to the polarimeter, but essential to the precision electroweak measurements, were two energy spectrometers installed in the extraction lines for the electron and positron beams. These instruments employed precisely calibrated analyzing bend magnets, and were needed to accurately determine the centre-of-mass collision energy. The expected precision of this measurement was about 20 MeV. In 1998 SLD performed a scan of the Z resonance, which allowed recalibration of the SLC energy scale to the precise value of m_{Z} determined at LEP. Further details of the SLC operation, in particular concerning polarisation, are given in Chapter 3.

1.2 LEP/SLC Detectors

The designs of the LEP and SLC detectors are quite similar, although the details vary significantly among them. As an example, the OPAL detector is shown in Figure 1.6. The five detectors all use the coordinate conventions indicated in this figure. The polar angle θ is measured with respect to the electron beam, which travels in the direction of the z-axis. The azimuthal angle ϕ is measured in the x-y plane. Starting radially from the interaction point, there is first a vertex detector, followed by a gas drift chamber to measure the parameters of charged particle tracks. Typically all tracks with transverse momenta greater than $\sim 200\mathrm{MeV}$ resulting from each Z decay could be reconstructed in three dimensions with high efficiency. The momentum resolution provided by the tracking chamber was also sufficient to determine the sign of a single charged particle carrying the full beam momentum.

Surrounding the tracking system is a calorimeter system, usually divided into two sections. The first section is designed to measure the position and energy of electromagnetic showers from photons, including those from π^0 decay, and electrons. The electromagnetic calorimeter is followed by a hadronic calorimeter to measure the energy of hadronic particles. Finally, an outer tracking system designed to measure the parameters of penetrating particles (muons) completes the system.

The central part of the detector (at least the tracking chamber) is immersed in a solenoidal magnetic field to allow the measurement of the momentum of charged particles. In addition, particle identification systems may be installed, including $\mathrm{d}E/\mathrm{d}x$ ionisation loss measurements in the central chamber, time-of-flight, and ring-imaging Cherenkov detectors. These measurements can be used to determine the velocity of particles; coupled with the momentum, they yield the particle masses.

Special detectors extending to polar angles of $\sim 25\mathrm{mrad}$ with respect to the beam axis detect small-angle Bhabha scattering events. The rate of these events was used for the luminosity determinations, as the small-angle Bhabha process is due almost entirely to QED, and the cross-section can be calculated precisely. All the LEP experiments replaced their first-generation luminosity detectors, which had systematic uncertainties around the percent level, by high-precision devices capable of pushing systematic errors on the acceptance of small-angle Bhabha scattering events below one per-mille.

Each LEP experiment also upgraded its original vertex detector with multi-layer silicon devices, which significantly improved the ability to measure impact parameters and to identify secondary vertices with a resolution of approximately 300 μm. As the typical B-hadron pro-

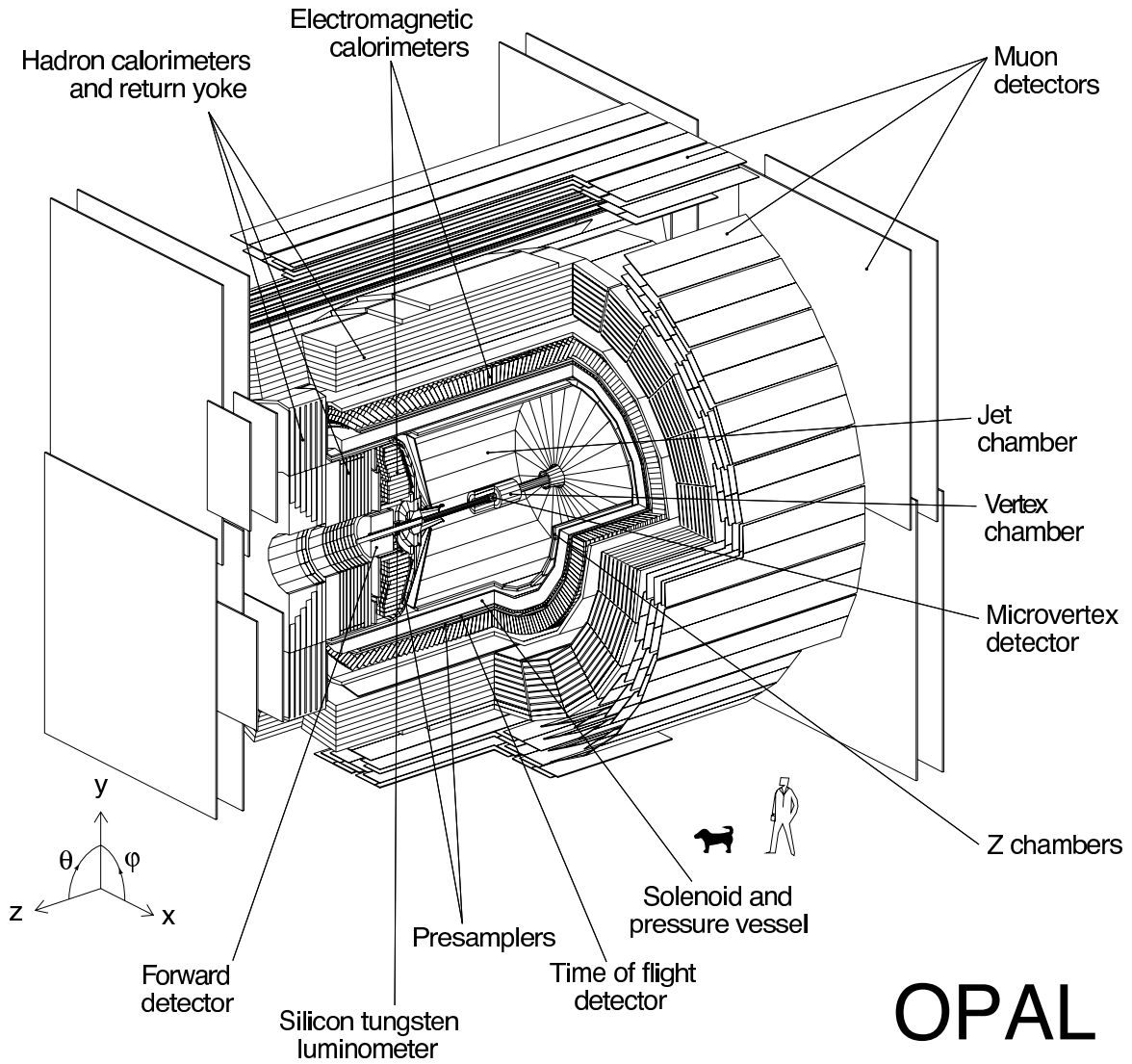

Figure 1.6: A cut-away view of the OPAL detector, as an example LEP/SLC detector. The z-axis points along the direction of the electron beam.

duced in Z decays will move about 3 mm from the primary vertex before decaying, the use of these detectors allowed the selection of a heavy quark sample with high purity. The typical beam spot size was 150 μm $\times$ 5 μm for LEP and 1.5 μm $\times$ 0.7 μm for SLC, in the bending and non-bending planes, respectively.

The smaller dimensions of the SLC beams and their low repetition rate allowed SLD to place slow but very high-resolution CCD arrays at a smaller radius than the micro-strip devices used at LEP. Both features resulted in SLD's superior vertex reconstruction.

As a consequence of the improvements to the detectors and also in the understanding of the beam energy at LEP-I, and the production of high beam polarisation at SLC, statistical and systematic errors are much smaller for the later years of data taking, which hence dominate the precision achieved on the Z parameters.

All five detectors had almost complete solid angle coverage; the only holes being at polar angles below the coverage of the luminosity detectors. Thus, most events were fully contained in the active elements of the detectors, allowing straight-forward identification. A few typical Z

decays, as seen in the detectors, are shown in Figure 1.7. As can be seen, the events at LEP and SLC were extremely clean, with practically no detector activity unrelated to the products of the annihilation event, allowing high-efficiency and high-purity selections to be made. Shown in Figure 1.8 is a side view of an SLD event interpreted as the decay of a Z into $\mathrm{b\overline{b}}$. The displaced vertex from the decay of a B hadron is clearly visible.

1.3 Basic Measurements

As suggested by the event pictures, the decays of the Z to charged leptons and to quarks are distinguished relatively easily, and in addition some specific quark flavours can be identified. Total cross-sections for a given process are determined by counting selected events, N_{sel}, subtracting the expected background, N_{bg}, and normalising by the selection efficiency (including acceptance), ϵ_{sel}, and the luminosity, $\mathcal{L}$:

$$\sigma \;=\; \frac{N_{\mathrm{sel}} - N_{\mathrm{bg}}}{\epsilon_{\mathrm{sel}}\mathcal{L}}\,. \tag{1.1}$$

The expected background and the selection efficiencies are determined using Monte Carlo event generators (for example [17, 18, 19, 20, 21, 22, 23]). The generated events are typically passed through a program that simulates the detector response, using packages such as GEANT [24], and then processed by the same reconstruction program as used for the data.

The cross-sections as a function of centre-of-mass energy around the Z pole yield the Z mass, m_{Z}, and total width, Γ_{Z}, together with a pole cross-section. The ratios of cross-sections for different processes give the partial widths and information about the relative strengths of the Z couplings to different final-state fermions.

The Z couples with a mixture of vector and axial-vector couplings. This results in measurable asymmetries in the angular distributions of the final-state fermions, the dependence of Z production on the helicities of the colliding electrons and positrons, and the polarisation of the produced particles.

One of the simplest such asymmetries to measure is the number of forward events, N_{F}, minus the number of backward events, N_{B}, divided by the total number of produced events:

$$A_{\mathrm{FB}} \;=\; \frac{N_{\mathrm{F}} - N_{\mathrm{B}}}{N_{\mathrm{F}} + N_{\mathrm{B}}}, \tag{1.2}$$

where "forward" means that the produced fermion (as opposed to anti-fermion) is in the hemisphere defined by the direction of the electron beam (polar scattering angle $\theta < \pi/2$). For example, the tagged jet with four tracks all emerging from a common secondary vertex in Figure 1.8 is in the forward part of the detector. If it is determined that this jet was generated by the decay of a primary b-quark rather than $\overline{\mathrm{b}}$-quark (see Section 5.2), it would be classified as a forward event.

The simple expression in terms of the numbers of forward and backward events given in Equation 1.2 is only valid for full 4π acceptance. The forward-backward asymmetries are therefore usually derived from fits to the differential distribution of events as a function of the polar angle of the outgoing fermion with respect to the incoming electron beam, see Section 1.5.

This is the usual type of asymmetry measured at LEP. Further asymmetries, defined in Section 1.5.3, can be measured if information is available about the helicities of the incom-

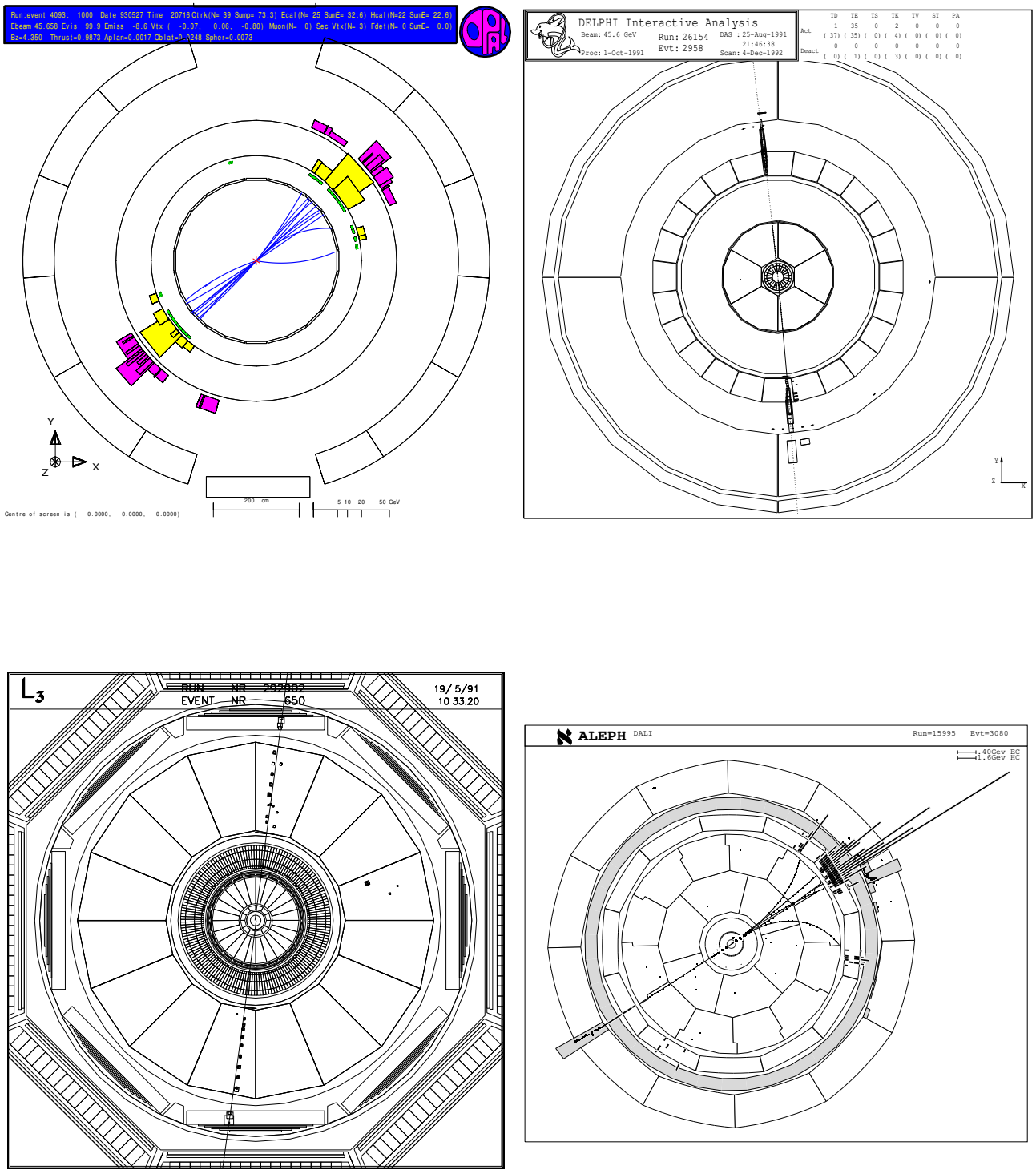

Figure 1.7: Pictures of $q\overline{q}$, e^+e^-, $\mu^+\mu^-$ and $\tau^+\tau^-$ final states, visualised with the event displays of the OPAL, DELPHI, L3 and ALEPH collaborations, respectively. In all views, the electron-positron beam axis is perpendicular to the plane of the page. The stability of the electron and the long lifetime of the muon allow these fundamental Z decays to be directly observed, while the low-multiplicity products of τ decays are confined to well-isolated cones. Hadronic Z decays result in higher-multiplicity jets of particles produced in the QCD cascades initiated by the initial $q\overline{q}$ pair.

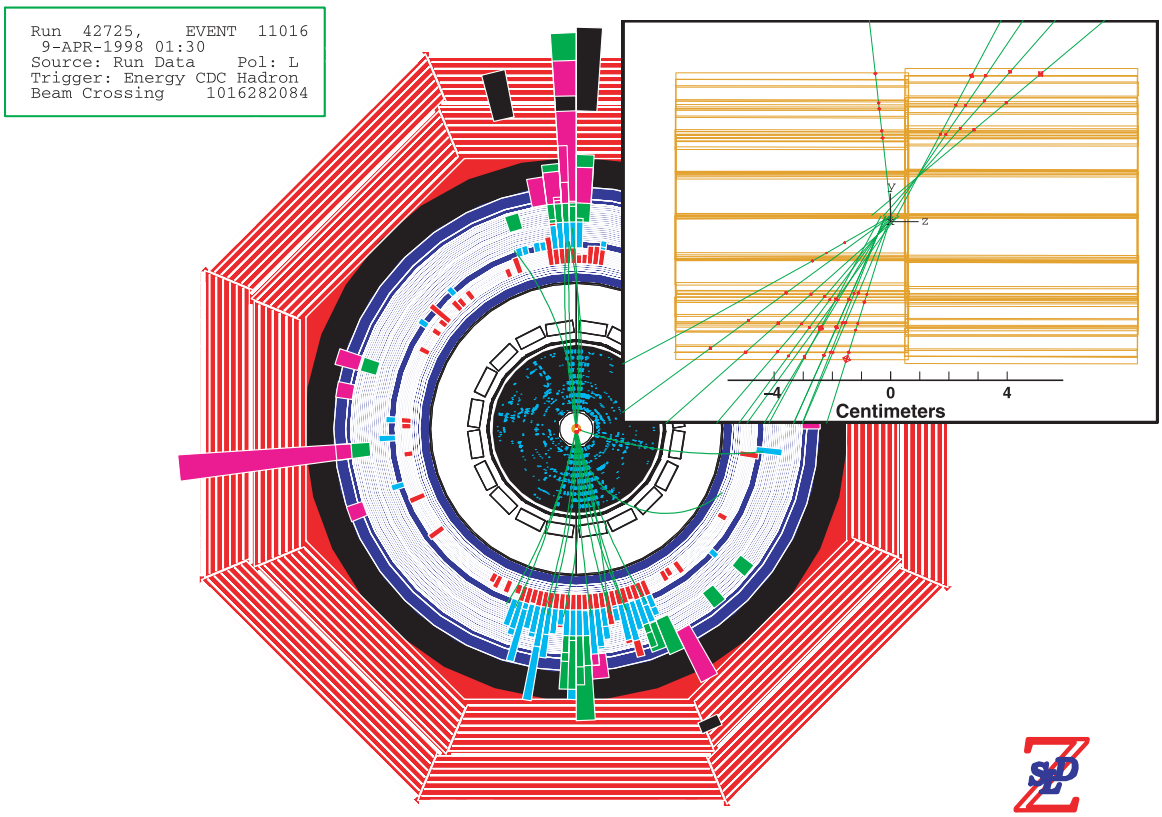

Figure 1.8: Front view of an event classified as $Z \to b\bar{b}$. The displaced secondary vertex is visible in the expanded side view (r-z view) of the beam interaction point.

ing or outgoing particles. In particular, the polarised electron beam at the SLC allowed the measurement of the left-right asymmetry:

$$A_{LR} = \frac{N_L - N_R}{N_L + N_R} \frac{1}{\langle \mathcal{P}_e \rangle}, \tag{1.3}$$

where, irrespective of the final state, N_L is the number of Z bosons produced for left-handed electron bunches, N_R is the corresponding number for right-handed bunches and $\langle \mathcal{P}_e \rangle$ is the magnitude of luminosity-weighted electron polarisation. This expression assumes that the luminosity and the magnitude of the beam polarisation are helicity-symmetric (see Chapter 3). One attractive feature of the A_{LR} measurement is the fact that it depends only on knowing the beam polarisation, and not the acceptance of the detector.

When the Z decays to a pair of τ leptons, their polarisation asymmetry is determined through the distribution of their decay products, which are visible in the detectors.

The relationships between the cross-sections and asymmetries and the Z couplings to fermions will be discussed further in Section 1.5 after examining the underlying theory and its implications for the process $e^+e^- \to f\bar{f}$.

Family			T	T_3	Q
$\begin{pmatrix} \nu_{\rm e} \\ {\rm e} \end{pmatrix}_L$	$\begin{pmatrix} \nu_\mu \\ \mu \end{pmatrix}_L$	$\begin{pmatrix} \nu_\tau \\ \tau \end{pmatrix}_L$	1/2	+1/2	0
				−1/2	−1
$\nu_{{\rm e}R}$	$\nu_{\mu R}$	$\nu_{\tau R}$	0	0	0
${\rm e}_R$	μ_R	τ_R	0	0	−1
$\begin{pmatrix} {\rm u} \\ {\rm d} \end{pmatrix}_L$	$\begin{pmatrix} {\rm c} \\ {\rm s} \end{pmatrix}_L$	$\begin{pmatrix} {\rm t} \\ {\rm b} \end{pmatrix}_L$	1/2	+1/2	+2/3
				−1/2	−1/3
${\rm u}_R$	${\rm c}_R$	${\rm t}_R$	0	0	+2/3
${\rm d}_R$	${\rm s}_R$	${\rm b}_R$	0	0	−1/3

Table 1.3: The weak-isospin structure of the fermions in the SM. "L" and "R" stand for left-handed and right-handed fermions, T and T_3 are the total weak-isospin and its third component, and Q is the electric charge. Note that the results presented in this report are insensitive to, and independent of, any small ($<$ MeV) neutrino masses.

1.4 Standard Model Relations

In the SM at tree level, the relationship between the weak and electromagnetic couplings is given by

$$G_{\rm F} \;=\; \frac{\pi\alpha}{\sqrt{2} m_{\rm W}^2 \sin^2\theta_{\rm W}^{\rm tree}}, \tag{1.4}$$

where $G_{\rm F}$ is the Fermi constant determined in muon decay, α is the electromagnetic fine-structure constant, $m_{\rm W}$ is the W boson mass, and $\sin^2\theta_{\rm W}^{\rm tree}$ is the electroweak mixing angle. In addition, the relationship between the neutral and charged weak couplings is fixed by the ratio of the W and Z boson masses:

$$\rho_0 \;=\; \frac{m_{\rm W}^2}{m_{\rm Z}^2 \cos^2\theta_{\rm W}^{\rm tree}}. \tag{1.5}$$

The ρ_0 parameter [25] is determined by the Higgs structure of the theory; in the Minimal Standard Model containing only Higgs doublets, $\rho_0 = 1$.

The fermions are arranged in weak-isospin doublets for left-handed particles and weak-isospin singlets for right-handed particles, as shown in Table 1.3. The interaction of the Z boson with fermions depends on charge, Q, and the third component of weak-isospin, T_3, and is given by the left- and right-handed couplings:

$$g_{\rm L}^{\rm tree} \;=\; \sqrt{\rho_0}\,(T_3^{\rm f} - Q_{\rm f}\sin^2\theta_{\rm W}^{\rm tree}) \tag{1.6}$$

$$g_{\rm R}^{\rm tree} \;=\; -\sqrt{\rho_0}\,Q_{\rm f}\sin^2\theta_{\rm W}^{\rm tree}\,, \tag{1.7}$$

or, equivalently in terms of vector and axial-vector couplings:

$$g_{\rm V}^{\rm tree} \;\equiv\; g_{\rm L}^{\rm tree} + g_{\rm R}^{\rm tree} \;=\; \sqrt{\rho_0}\,(T_3^{\rm f} - 2Q_{\rm f}\sin^2\theta_{\rm W}^{\rm tree}) \tag{1.8}$$

$$g_{\rm A}^{\rm tree} \;\equiv\; g_{\rm L}^{\rm tree} - g_{\rm R}^{\rm tree} \;=\; \sqrt{\rho_0}\,T_3^{\rm f}\,. \tag{1.9}$$

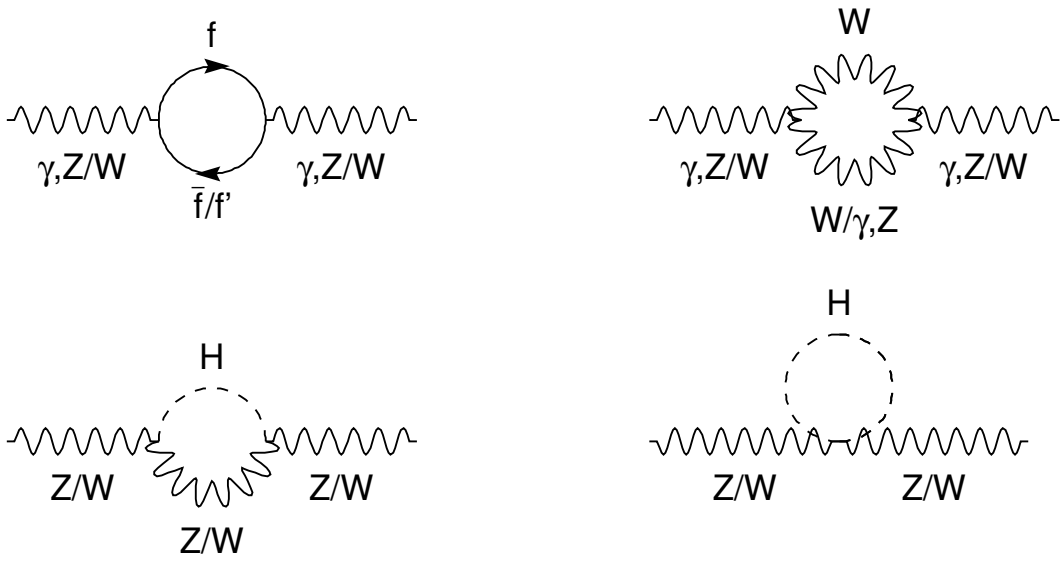

Figure 1.9: Higher-order corrections to the gauge boson propagators due to boson and fermion loops.

These tree-level quantities are modified by radiative corrections to the propagators and vertices such as those shown in Figures 1.9 and 1.10. When these corrections are renormalized in the "on-shell" scheme [26], which we adopt here, the form of Equation 1.5 is maintained, and taken to define the on-shell electroweak mixing angle, $\theta_{\rm W}$, to all orders, in terms of the vector boson pole masses:

$$\rho_0 \;=\; \frac{m_{\rm W}^2}{m_{\rm Z}^2 \cos^2\theta_{\rm W}}. \tag{1.10}$$

In the following, $\rho_0 = 1$ is assumed.

The bulk of the electroweak corrections [25] to the couplings at the Z-pole is absorbed into complex form factors, $\mathcal{R}_{\rm f}$ for the overall scale and $\mathcal{K}_{\rm f}$ for the on-shell electroweak mixing angle, resulting in complex effective couplings:

$$\mathcal{G}_{\rm Vf} \;=\; \sqrt{\mathcal{R}_{\rm f}}\,(T_3^{\rm f} - 2Q_{\rm f}\mathcal{K}_{\rm f}\sin^2\theta_{\rm W}) \tag{1.11}$$

$$\mathcal{G}_{\rm Af} \;=\; \sqrt{\mathcal{R}_{\rm f}}\,T_3^{\rm f}\,. \tag{1.12}$$

In terms of the real parts of the complex form factors,

$$\rho_{\rm f} \;\equiv\; \Re(\mathcal{R}_{\rm f}) \;=\; 1 + \Delta\rho_{\rm se} + \Delta\rho_{\rm f} \tag{1.13}$$

$$\kappa_{\rm f} \;\equiv\; \Re(\mathcal{K}_{\rm f}) \;=\; 1 + \Delta\kappa_{\rm se} + \Delta\kappa_{\rm f}\,, \tag{1.14}$$

the effective electroweak mixing angle and the real effective couplings are defined as:

$$\sin^2\theta_{\rm eff}^{\rm f} \;\equiv\; \kappa_{\rm f}\sin^2\theta_{\rm W} \tag{1.15}$$

$$g_{\rm Vf} \;\equiv\; \sqrt{\rho_{\rm f}}\,(T_3^{\rm f} - 2Q_{\rm f}\sin^2\theta_{\rm eff}^{\rm f}) \tag{1.16}$$

$$g_{\rm Af} \;\equiv\; \sqrt{\rho_{\rm f}}\,T_3^{\rm f}\,, \tag{1.17}$$

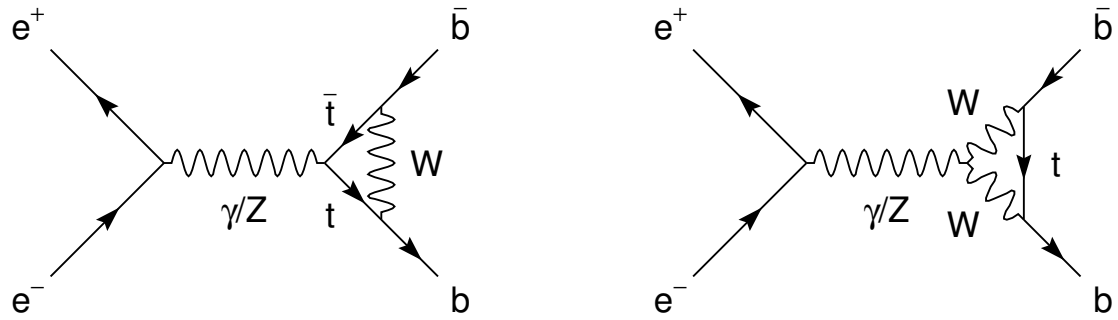

Figure 1.10: Vertex corrections to the process $e^+e^- \to b\overline{b}$.

so that:

$$\frac{g_{\mathrm{Vf}}}{g_{\mathrm{Af}}} \;=\; \Re\left(\frac{\mathcal{G}_{\mathrm{Vf}}}{\mathcal{G}_{\mathrm{Af}}}\right) \;=\; 1 - 4|Q_{\mathrm{f}}|\sin^2\theta^{\mathrm{f}}_{\mathrm{eff}}\,. \tag{1.18}$$

The quantities $\Delta\rho_{\mathrm{se}}$ and $\Delta\kappa_{\mathrm{se}}$ are universal corrections arising from the propagator self-energies, while $\Delta\rho_{\mathrm{f}}$ and $\Delta\kappa_{\mathrm{f}}$ are flavour-specific vertex corrections. For simplicity we ignore the small imaginary components of these corrections in most of the following discussion. The leading order terms in $\Delta\rho_{\mathrm{se}}$ and $\Delta\kappa_{\mathrm{se}}$ for $m_{\mathrm{H}} \gg m_{\mathrm{W}}$ are [27]:

$$\Delta\rho_{\mathrm{se}} \;=\; \frac{3G_{\mathrm{F}}m_{\mathrm{W}}^2}{8\sqrt{2}\pi^2}\left[\frac{m_{\mathrm{t}}^2}{m_{\mathrm{W}}^2} - \frac{\sin^2\theta_{\mathrm{W}}}{\cos^2\theta_{\mathrm{W}}}\left(\ln\frac{m_{\mathrm{H}}^2}{m_{\mathrm{W}}^2} - \frac{5}{6}\right) + \cdots\right] \tag{1.19}$$

$$\Delta\kappa_{\mathrm{se}} \;=\; \frac{3G_{\mathrm{F}}m_{\mathrm{W}}^2}{8\sqrt{2}\pi^2}\left[\frac{m_{\mathrm{t}}^2}{m_{\mathrm{W}}^2}\frac{\cos^2\theta_{\mathrm{W}}}{\sin^2\theta_{\mathrm{W}}} - \frac{10}{9}\left(\ln\frac{m_{\mathrm{H}}^2}{m_{\mathrm{W}}^2} - \frac{5}{6}\right) + \cdots\right] \tag{1.20}$$

For $m_{\mathrm{H}} \ll m_{\mathrm{W}}$, the Higgs terms are modified, for example:

$$\Delta\rho_{\mathrm{se}} \;=\; \frac{3G_{\mathrm{F}}m_{\mathrm{W}}^2}{8\sqrt{2}\pi^2}\left[\frac{m_{\mathrm{t}}^2}{m_{\mathrm{W}}^2} + \frac{2}{3}\frac{m_{\mathrm{Z}}^2}{m_{\mathrm{W}}^2}\ln\frac{m_{\mathrm{H}}^2}{m_{\mathrm{Z}}^2} - \frac{7\pi}{3}\frac{m_{\mathrm{H}}m_{\mathrm{Z}}}{m_{\mathrm{W}}^2} + \cdots\right] \tag{1.21}$$

where only internal Higgs loops are considered. Note the change of sign in the slope of the Higgs correction for low m_{H} seen in Equation 1.21 compared to Equation 1.19, which is due to contributions from the derivative of the Z self-energy with respect to momentum transfer [28]. Existence of the process $e^+e^- \to Z^*H$ (Higgsstrahlung) would tend to reduce the m_{H} dependence in Equation 1.21 [29]. The radiative corrections have a quadratic dependence on the top quark mass and a weaker logarithmic dependence on the Higgs boson mass. The flavour dependence is very small for all fermions, except for the b-quark, where the effects of the diagrams shown in Figure 1.10 are significant, due to the large mass splitting between the bottom and top quarks and the size of the diagonal CKM matrix element $|V_{\mathrm{tb}}| \simeq 1$, resulting in a significant additional contribution for $b\overline{b}$ production [28] (The effects of the off-diagonal CKM matrix elements are here negligible.):

$$\Delta\kappa_{\mathrm{b}} \;=\; \frac{G_{\mathrm{F}}m_{\mathrm{t}}^2}{4\sqrt{2}\pi^2} + \cdots\,, \tag{1.22}$$

$$\Delta\rho_{\mathrm{b}} \;=\; -2\Delta\kappa_{\mathrm{b}} + \cdots\,. \tag{1.23}$$

By interpreting the Z-pole measurements in terms of these corrections, the top quark mass can be determined indirectly, and compared to the direct measurements. The Z-pole measurements, even when taken alone, have sufficient power to separate the Higgs and top corrections

to some extent, and thus provide independent indications of both $m_{\rm t}$, and, less sensitively, $m_{\rm H}$. The constraint on $m_{\rm H}$ becomes more precise when additional results, in particular the direct measurement of $m_{\rm t}$, are also considered (see Section 8.6.2).

The classic "ρ parameter" [25], which describes the ratio of the neutral to charged current couplings in neutrino interactions at low momentum transfer, is also modified by radiative corrections:

$$\rho \;=\; 1 + \Delta\rho\,. \tag{1.24}$$

Although ρ displays a similar $m_{\rm t}$-dependence to that of $\rho_{\rm f}$, its $m_{\rm H}$-dependence specifically lacks the change in sign at low $m_{\rm H}$ which is evident in Equation 1.21.

The form of the fundamental SM relation derived from Equations 1.4 and 1.10 is preserved in the presence of radiative corrections for both low momentum transfer, and at the Z-pole [27]:

$$\cos^2\theta_{\rm W}\sin^2\theta_{\rm W} \;=\; \frac{\pi\alpha(0)}{\sqrt{2}m_{\rm Z}^2 G_{\rm F}}\frac{1}{1-\Delta r} \tag{1.25}$$

$$\cos^2\theta^{\rm f}_{\rm eff}\sin^2\theta^{\rm f}_{\rm eff} \;=\; \frac{\pi\alpha(0)}{\sqrt{2}m_{\rm Z}^2 G_{\rm F}}\frac{1}{1-\Delta r^{\rm f}}, \tag{1.26}$$

where Δr and $\Delta r^{\rm f}$ are given by:

$$\Delta r \;=\; \Delta\alpha + \Delta r_{\rm w} \tag{1.27}$$

$$\Delta r^{\rm f} \;=\; \Delta\alpha + \Delta r^{\rm f}_{\rm w}. \tag{1.28}$$

The $\Delta\alpha$ term arises from the running of the electromagnetic coupling due to fermion loops in the photon propagator, and is usually divided into three categories: from leptonic loops, top quark loops and light quark (u/d/s/c/b) loops:

$$\Delta\alpha(s) \;=\; \Delta\alpha_{{\rm e}\mu\tau}(s) + \Delta\alpha_{\rm top}(s) + \Delta\alpha^{(5)}_{\rm had}(s). \tag{1.29}$$

The terms $\Delta\alpha_{{\rm e}\mu\tau}(s)$ and $\Delta\alpha_{\rm top}(s)$ can be precisely calculated, whereas the term $\Delta\alpha^{(5)}_{\rm had}(s)$ is best determined by analysing low-energy $\rm e^+e^-$ data using a dispersion relation (see Section 8.2). These effects are absorbed into α as:

$$\alpha(s) \;=\; \frac{\alpha(0)}{1-\Delta\alpha(s)}. \tag{1.30}$$

At LEP/SLC energies, α is increased from the zero q^2 limit of 1/137.036 to 1/128.945.

The weak part of the corrections contains $\Delta\rho$ (see Equation 1.24) plus a remainder [27]:

$$\Delta r_{\rm w} \;=\; -\frac{\cos^2\theta_{\rm W}}{\sin^2\theta_{\rm W}}\Delta\rho + \cdots \tag{1.31}$$

$$\Delta r^{\rm f}_{\rm w} \;=\; -\Delta\rho + \cdots. \tag{1.32}$$

It should be noted that since $G_{\rm F}$ and $m_{\rm Z}$ are better determined than $m_{\rm W}$, Equations 1.10 and 1.25 are often used to eliminate direct dependence on $m_{\rm W}$ [27]:

$$m_{\rm W}^2 \;=\; \frac{m_{\rm Z}^2}{2}\left(1+\sqrt{1-4\frac{\pi\alpha}{\sqrt{2}G_{\rm F}m_{\rm Z}^2}\frac{1}{1-\Delta r}}\right). \tag{1.33}$$

This substitution introduces further significant $m_{\rm t}$ and $m_{\rm H}$ dependencies through Δr. For example, in Equation 1.15 $\sin^2\theta^{\rm lept}_{\rm eff}$ receives radiative corrections both from $\Delta\kappa_{\rm se}$ directly, and

from $\Delta r_{\rm w}$ implicitly through $\sin^2\theta_{\rm W}$, as can be seen in Equation 1.26. Here the implicit correction is of opposite sign, and in fact dominates the direct correction, so that the $m_{\rm t}$ and $m_{\rm H}$ dependences of $\sin^2\theta^{\rm lept}_{\rm eff}$ are opposite in sign from the dependences of $\Delta\kappa_{\rm se}$ described in Equation 1.20.

The discussion of radiative corrections given here is leading order only. The actual calculations used in fits (*e.g.*, Chapters 7 and 8) are performed to higher order, using the programs TOPAZ0 [30] and ZFITTER [31]. The interested reader is encouraged to consult the authoritative discussion in Reference 32.

1.5 The Process $e^+e^- \to f\bar{f}$

The differential cross-sections for fermion pair production (see Figure 1.1) around the Z resonance can be cast into a Born-type structure using the complex-valued effective coupling constants given in the previous section. Effects from photon vacuum polarisation are taken into account by the running electromagnetic coupling constant (Equation 1.30), which also acquires a small imaginary piece. Neglecting initial and final state photon radiation, final state gluon radiation and fermion masses, the electroweak kernel cross-section for unpolarised beams can thus be written as the sum of three contributions, from s-channel γ and Z exchange and from their interference [32],

$$
\begin{aligned}
&\frac{2s}{\pi}\frac{1}{N_c^{\rm f}}\frac{d\sigma_{\rm ew}}{d\cos\theta}(e^+e^- \to f\bar{f}) \;=\\
&\underbrace{|\alpha(s)Q_{\rm f}|^2\,(1+\cos^2\theta)}_{\sigma^\gamma}\\
&\underbrace{-8\Re\left\{\alpha^*(s)Q_{\rm f}\chi(s)\left[\mathcal{G}_{\rm Ve}\mathcal{G}_{\rm Vf}(1+\cos^2\theta)+2\mathcal{G}_{\rm Ae}\mathcal{G}_{\rm Af}\cos\theta\right]\right\}}_{\gamma\text{–Z interference}} \qquad (1.34)\\
&\underbrace{\begin{array}{c}+16|\chi(s)|^2\left[(|\mathcal{G}_{\rm Ve}|^2+|\mathcal{G}_{\rm Ae}|^2)(|\mathcal{G}_{\rm Vf}|^2+|\mathcal{G}_{\rm Af}|^2)(1+\cos^2\theta)\right.\\ \left.+8\Re\left\{\mathcal{G}_{\rm Ve}{\mathcal{G}_{\rm Ae}}^*\right\}\Re\left\{\mathcal{G}_{\rm Vf}{\mathcal{G}_{\rm Af}}^*\right\}\cos\theta\right]\end{array}}_{\sigma^{\rm Z}}
\end{aligned}
$$

with:

$$
\chi(s) \;=\; \frac{G_{\rm F}m_{\rm Z}^2}{8\pi\sqrt{2}}\frac{s}{s-m_{\rm Z}^2+is\Gamma_{\rm Z}/m_{\rm Z}}\,, \qquad (1.35)
$$

where θ is the scattering angle of the out-going fermion with respect to the direction of the e^-. The colour factor $N_c^{\rm f}$ is one for leptons (f=ν_e, ν_μ, ν_τ, e, μ, τ) and three for quarks (f=d, u, s, c, b), and $\chi(s)$ is the propagator term with a Breit-Wigner denominator with an s-dependent width.

If the couplings are left free to depart from their SM values, the above expression allows the resonance properties of the Z to be parametrised in a very model-independent manner. Essentially the only assumptions imposed by Equation 1.34 are that the Z possesses vector and axial-vector couplings to fermions, has spin 1, and interferes with the photon. Certain SM assumptions are nevertheless employed when extracting and interpreting the couplings; these are discussed in Sections 1.5.4 and 2.5.3.

The $1+\cos^2\theta$ terms in the above formula contribute to the total cross-section, whereas the terms multiplying $\cos\theta$ contribute only to the forward-backward asymmetries for an experimental acceptance symmetric in $\cos\theta$. In the region of the Z peak, the total cross-section is completely dominated by Z exchange. The γ–Z interference determines the energy dependence of the forward-backward asymmetries and dominates them at off-peak energies, but its leading contribution, from the real parts of the couplings, vanishes at $\sqrt{s} = m_{\mathrm{Z}}$.

In Bhabha scattering, $\mathrm{e^+e^-} \to \mathrm{e^+e^-}$, the t-channel diagrams also contribute to the cross-sections, with a very dominant photon contribution at large $\cos\theta$, *i.e.*, in the forward direction. This contribution, and its interference with the s-channel, add to the pure s-channel cross-section for $\mathrm{e^+e^-} \to \mathrm{e^+e^-}$ (see Section 2.4.2 for details).

The definition of the mass and width with an s-dependent width term in the Breit-Wigner denominator is suggested [33] by phase-space and the structure of the electroweak radiative corrections within the SM. It is different from another commonly used definition, the real part of the complex pole [34], where the propagator term takes the form $\chi(s) \propto s/(s-\overline{m}_{\mathrm{Z}}{}^2+i\overline{m}_{\mathrm{Z}}\overline{\Gamma}_{\mathrm{Z}})$. However, under the transformations $\overline{m}_{\mathrm{Z}} = m_{\mathrm{Z}}/\sqrt{1+\Gamma_{\mathrm{Z}}^2/m_{\mathrm{Z}}^2}$ and $\overline{\Gamma}_{\mathrm{Z}} = \Gamma_{\mathrm{Z}}/\sqrt{1+\Gamma_{\mathrm{Z}}^2/m_{\mathrm{Z}}^2}$, and adjusting the scales of Z exchange and γ/Z interference, the two formulations lead to exactly equivalent resonance shapes, $\sigma(s)$.

Photon radiation (Figure 1.11) from the initial and final states, and their interference, are conveniently treated by convoluting the electroweak kernel cross-section, $\sigma_{\mathrm{ew}}(s)$, with a QED radiator, $H_{\mathrm{QED}}^{\mathrm{tot}}$,

$$\sigma(s) \;=\; \int_{4m_{\mathrm{f}}^2/s}^{1} dz\, H_{\mathrm{QED}}^{\mathrm{tot}}(z,s)\sigma_{\mathrm{ew}}(zs). \tag{1.36}$$

The difference between the forward and backward cross-sections entering into the determination of the forward-backward asymmetries, $\sigma_{\mathrm{F}} - \sigma_{\mathrm{B}}$, is treated in the same way using a radiator function $H_{\mathrm{QED}}^{\mathrm{FB}}$. These QED corrections are calculated to third order, and their effects on the cross-sections and asymmetries are shown in Figure 1.12. At the peak the QED deconvoluted cross-section is 36% larger than the measured one, and the peak position is shifted downwards by about 100 MeV. At and below the peak A_{FB}^{μ} and A_{FB}^{τ} are offset by an amount about equal to their deconvoluted value of 0.017. The estimated precision of these important corrections is discussed in Section 2.4.4. It is important to realize that these QED corrections are essentially independent of the electroweak corrections discussed in Section 1.4, and therefore allow the parameters of Equation 1.34 to be extracted from the data in a model-independent manner.

1.5.1 Cross-Sections and Partial Widths

The partial Z decay widths are defined inclusively, *i.e.*, they contain QED and QCD [35] final state corrections and contributions from the imaginary and non-factorisable parts [36] of the effective couplings,

$$\Gamma_{\mathrm{f\bar{f}}} \;=\; N_c^{\mathrm{f}}\frac{G_{\mathrm{F}}m_{\mathrm{Z}}^3}{6\sqrt{2}\pi}\left(|\mathcal{G}_{\mathrm{Af}}|^2R_{\mathrm{Af}} + |\mathcal{G}_{\mathrm{Vf}}|^2R_{\mathrm{Vf}}\right) + \Delta_{\mathrm{ew/QCD}}. \tag{1.37}$$

The primary reason to define the partial widths including final state corrections and the contribution of the complex non-factorisable terms of the couplings is that the partial widths defined in this way add up straightforwardly to yield the total width of the Z boson. The radiator factors R_{Vf} and R_{Af} take into account final state QED and QCD corrections as well as non-zero fermion masses; $\Delta_{\mathrm{ew/QCD}}$ accounts for small contributions from non-factorisable

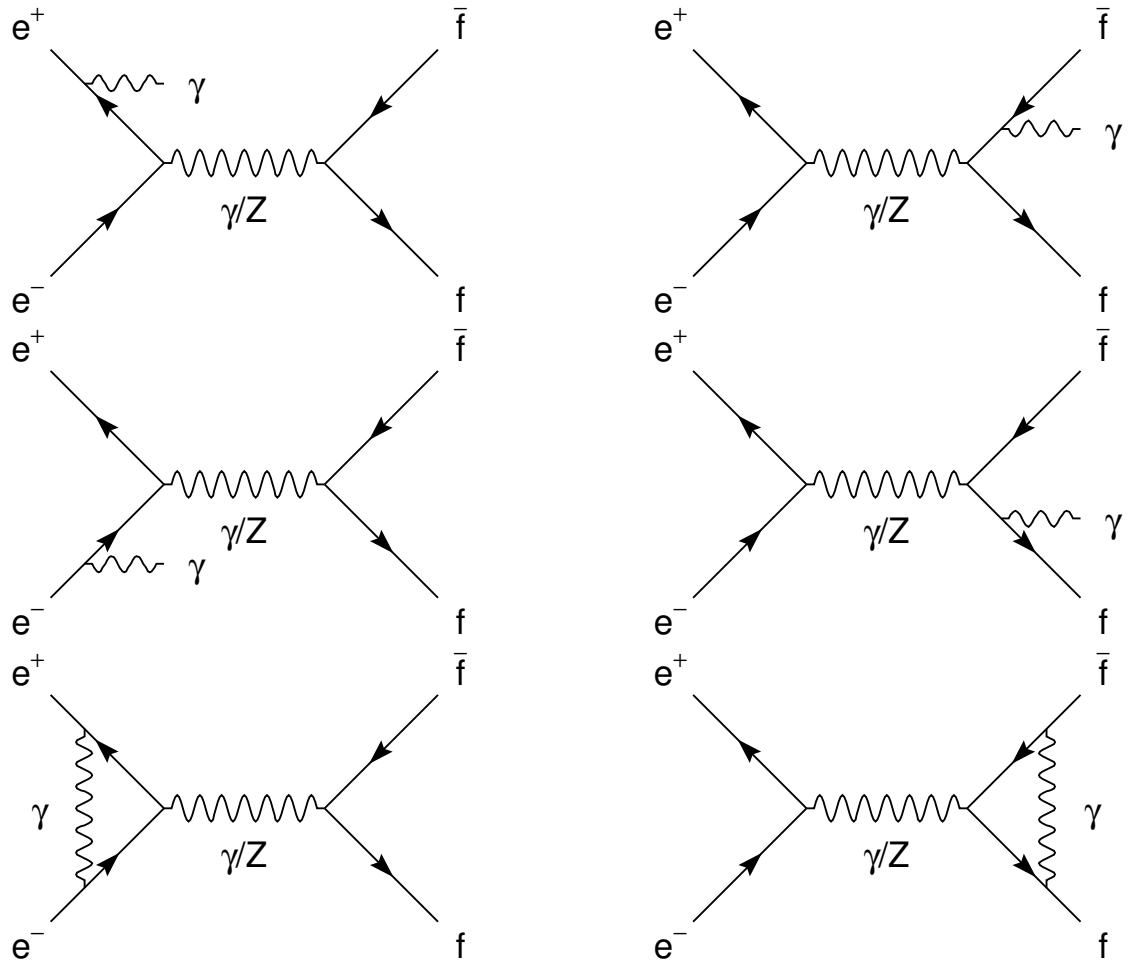

Figure 1.11: Some of the lowest order QED corrections to fermion-pair production. Together with photonic box diagrams, which give much smaller contributions, these form a gauge-invariant sub-set included in the radiator functions $H_{\rm QED}$. Weak boxes are added explicitly to the kernel cross-section [32].

electroweak/QCD corrections. The inclusion of the complex parts of the couplings in the definition of the leptonic width, $\Gamma_{\ell\ell}$, leads to changes of 0.15 per-mille corresponding to only 15% of the LEP-combined experimental error on $\Gamma_{\ell\ell}$. The QCD corrections only affect final states containing quarks. To first order in $\alpha_{\rm S}$ for massless quarks, the QCD corrections are flavour independent and the same for vector and axial-vector contributions:

$$R_{\rm A,QCD} \;=\; R_{\rm V,QCD} = R_{\rm QCD} = 1 + \frac{\alpha_{\rm S}(m_{\rm Z}^2)}{\pi} + \cdots . \tag{1.38}$$

The hadronic partial width therefore depends strongly on $\alpha_{\rm S}$. The final state QED correction is formally similar, but much smaller due to the smaller size of the electromagnetic coupling:

$$R_{\rm A,QED} \;=\; R_{\rm V,QED} = R_{\rm QED} = 1 + \frac{3}{4}Q_{\rm f}^2\frac{\alpha(m_{\rm Z}^2)}{\pi} + \cdots . \tag{1.39}$$

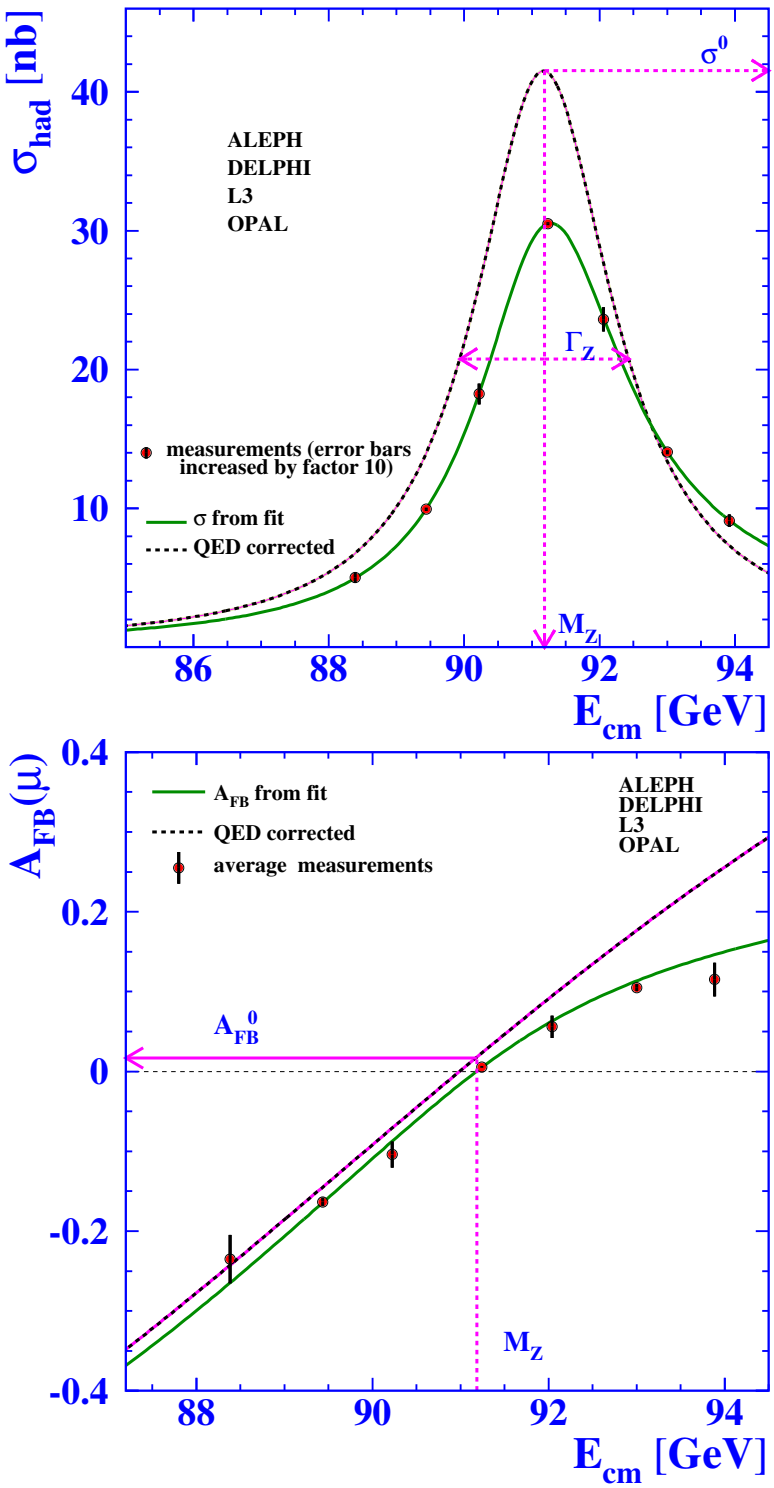

Figure 1.12: Average over measurements of the hadronic cross-sections (top) and of the muon forward-backward asymmetry (bottom) by the four experiments, as a function of centre-of-mass energy. The full line represents the results of model-independent fits to the measurements, as outlined in Section 1.5. Correcting for QED photonic effects yields the dashed curves, which define the Z parameters described in the text.

The total cross-section arising from the $\cos\theta$-symmetric Z production term can also be written in terms of the partial decay widths of the initial and final states, Γ_{ee} and $\Gamma_{f\bar{f}}$,

$$\sigma_{f\bar{f}}^{Z} = \sigma_{f\bar{f}}^{peak} \frac{s\Gamma_Z^2}{(s-m_Z^2)^2 + s^2\Gamma_Z^2/m_Z^2}, \tag{1.40}$$

where

$$\sigma_{f\bar{f}}^{peak} = \frac{1}{R_{QED}} \sigma_{f\bar{f}}^{0} \tag{1.41}$$

and

$$\sigma_{f\bar{f}}^{0} = \frac{12\pi}{m_Z^2} \frac{\Gamma_{ee}\Gamma_{f\bar{f}}}{\Gamma_Z^2}. \tag{1.42}$$

The term $1/R_{QED}$ removes the final state QED correction included in the definition of Γ_{ee}.

The overall hadronic cross-section is parametrised in terms of the hadronic width given by the sum over all quark final states,

$$\Gamma_{had} = \sum_{q \neq t} \Gamma_{q\bar{q}}. \tag{1.43}$$

The invisible width from Z decays to neutrinos, $\Gamma_{inv} = N_\nu \Gamma_{\nu\bar{\nu}}$, where N_ν is the number of light neutrino species, is determined from the measurements of the decay widths to all visible final states and the total width,

$$\Gamma_Z = \Gamma_{ee} + \Gamma_{\mu\mu} + \Gamma_{\tau\tau} + \Gamma_{had} + \Gamma_{inv}. \tag{1.44}$$

Because the measured cross-sections depend on products of the partial widths and also on the total width, the widths constitute a highly correlated parameter set. In order to reduce correlations among the fit parameters, an experimentally-motivated set of six parameters is used to describe the total hadronic and leptonic cross-sections around the Z peak. These are

- the mass of the Z, m_Z;
- the Z total width, Γ_Z;
- the "hadronic pole cross-section",

$$\sigma_{had}^{0} \equiv \frac{12\pi}{m_Z^2} \frac{\Gamma_{ee}\Gamma_{had}}{\Gamma_Z^2}; \tag{1.45}$$

- the three ratios

$$R_e^0 \equiv \Gamma_{had}/\Gamma_{ee}, \; R_\mu^0 \equiv \Gamma_{had}/\Gamma_{\mu\mu} \;\text{ and }\; R_\tau^0 \equiv \Gamma_{had}/\Gamma_{\tau\tau}. \tag{1.46}$$

  If lepton universality is assumed, the last three ratios reduce to a single parameter:

$$R_\ell^0 \equiv \Gamma_{had}/\Gamma_{\ell\ell}, \tag{1.47}$$

  where $\Gamma_{\ell\ell}$ is the partial width of the Z into one massless charged lepton flavour. (Due to the mass of the tau lepton, even with the assumption of lepton universality, $\Gamma_{\tau\tau}$ differs from $\Gamma_{\ell\ell}$ by about $\delta_\tau = -0.23\%$.)

For those hadronic final states where the primary quarks can be identified, the following ratios are defined:

$$R^0_{\mathrm{q}} \equiv \Gamma_{\mathrm{q\overline{q}}}/\Gamma_{\mathrm{had}},\ e.g.\ R^0_{\mathrm{b}} = \Gamma_{\mathrm{b\overline{b}}}/\Gamma_{\mathrm{had}}. \tag{1.48}$$

Experimentally, these ratios have traditionally been treated independently of the above set, as described in Chapter 5 and Appendix F.

The leading contribution from γ–Z interference is proportional to the product of the vector couplings of the initial and final states and vanishes at $\sqrt{s} = m_{\mathrm{Z}}$, but becomes noticeable at off-peak energies and therefore affects the measurement of the Z mass. Because an experimental determination of all quark couplings is not possible, the γ–Z interference term in the hadronic final state is fixed to its predicted SM value in the analysis. The implications of this are discussed in Section 2.5.3.

The six parameters describing the leptonic and total hadronic cross-sections around the Z peak are determined exclusively from the measurements of the four LEP collaborations, due to the large event statistics available and the precise determination of the LEP collision energy. In the measurement of R^0_{b} and R^0_{c}, however, the greater purity and significantly higher efficiency which SLD achieved in identifying heavy quarks offset the statistical advantage of LEP, and yield results with comparable, and in some cases better, precision.

1.5.2 Invisible Width and Number of Neutrinos

If the Z had no invisible width, all partial widths could be determined without knowledge of the absolute scale of the cross-sections. Not surprisingly, therefore, the measurement of Γ_{inv} is particularly sensitive to the cross-section scale. Assuming lepton universality, and defining $R^0_{\mathrm{inv}} = \Gamma_{\mathrm{inv}}/\Gamma_{\ell\ell}$, Equations 1.44 and 1.45 can be combined to yield

$$R^0_{\mathrm{inv}} = \left(\frac{12\pi R^0_\ell}{\sigma^0_{\mathrm{had}} m^2_{\mathrm{Z}}}\right)^{\frac{1}{2}} - R^0_\ell - (3+\delta_\tau)\,, \tag{1.49}$$

where the dependence on the absolute cross-section scale is explicit.

Assuming that the only invisible Z decays are to neutrinos coupling according to SM expectations, the number of light neutrino generations, N_ν, can then be determined by comparing the measured R^0_{inv} with the SM prediction for $\Gamma_{\nu\overline{\nu}}/\Gamma_{\ell\ell}$:

$$R^0_{\mathrm{inv}} = N_\nu \left(\frac{\Gamma_{\nu\overline{\nu}}}{\Gamma_{\ell\ell}}\right)_{\mathrm{SM}}. \tag{1.50}$$

The strong dependence of the hadronic peak cross-section on N_ν is illustrated in Figure 1.13. The precision ultimately achieved in these measurements allows tight limits to be placed on the possible contribution of any invisible Z decays originating from sources other than the three known light neutrino species.

1.5.3 Asymmetry and Polarisation

Additional observables are introduced to describe the $\cos\theta$ dependent terms in Equation 1.34 as well as effects related to the helicities of the fermions in either the initial or final state. These observables quantify the parity violation of the neutral current, and therefore differentiate the vector- and axial-vector couplings of the Z. Their measurement determines $\sin^2\theta^{\mathrm{f}}_{\mathrm{eff}}$.

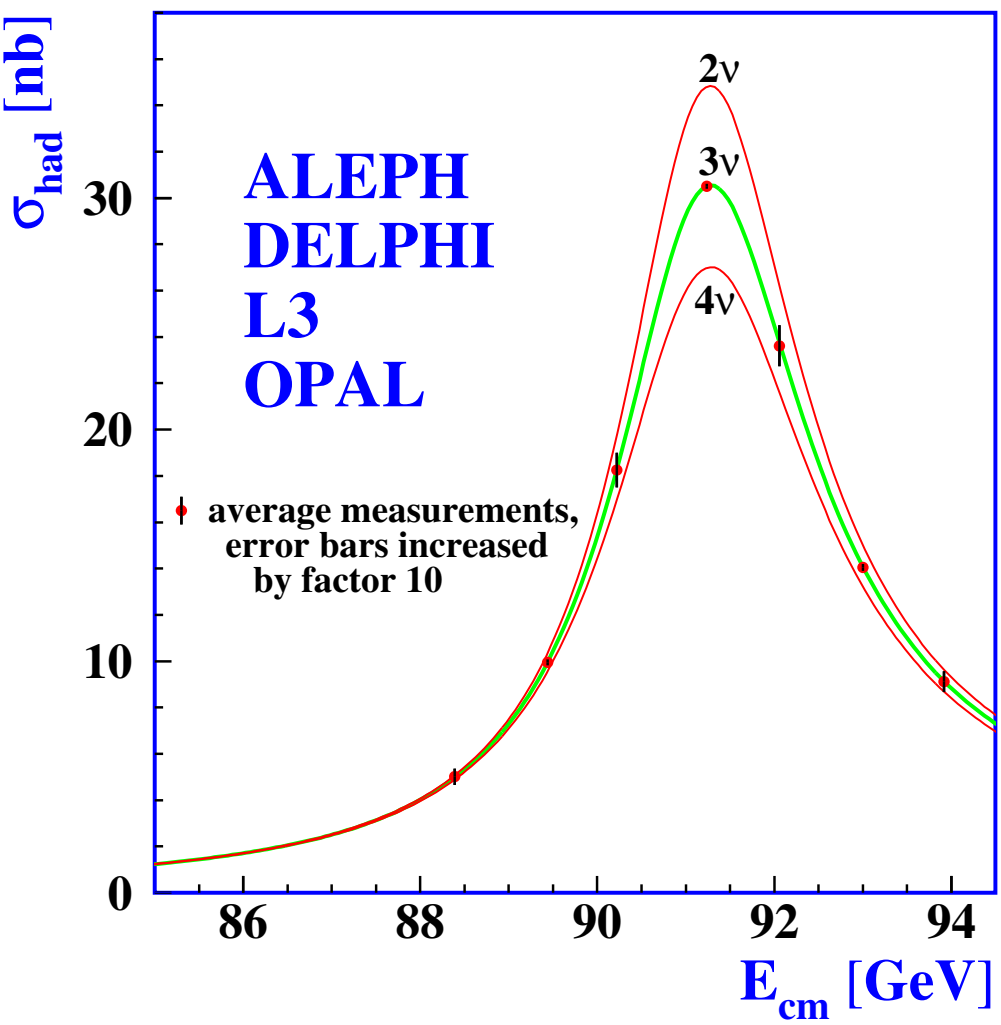

Figure 1.13: Measurements of the hadron production cross-section around the Z resonance. The curves indicate the predicted cross-section for two, three and four neutrino species with SM couplings and negligible mass.

Since the right- and left-handed couplings of the Z to fermions are unequal, Z bosons can be expected to exhibit a net polarisation along the beam axis even when the colliding electrons and positrons which produce them are unpolarised. Similarly, when such a polarised Z decays, parity non-conservation implies not only that the resulting fermions will have net helicity, but that their angular distribution will also be forward-backward asymmetric.

When measuring the properties of the Z boson, the energy-dependent interference between the Z and the purely vector coupling of the photon must also be taken into account. This interference leads to an additional asymmetry component which changes sign across the Z-pole.

Considering the Z exchange diagrams and real couplings only,[2] to simplify the discussion,

[2] As in the previous section, the effects of radiative corrections, and mass effects, including the imaginary parts of couplings, are taken into account in the analysis. They, as well as the small differences between helicity and chirality, are neglected here to allow a clearer view of the helicity structure. It is likewise assumed that the magnitude of the beam polarisation is equal in the two helicity states.

the differential cross-sections specific to each initial- and final-state fermion helicity are:

$$\frac{\mathrm{d}\sigma_{\mathrm{Ll}}}{\mathrm{d}\cos\theta} \propto g^2_{\mathrm{Le}} g^2_{\mathrm{Lf}} (1+\cos\theta)^2 \tag{1.51}$$

$$\frac{\mathrm{d}\sigma_{\mathrm{Rr}}}{\mathrm{d}\cos\theta} \propto g^2_{\mathrm{Re}} g^2_{\mathrm{Rf}} (1+\cos\theta)^2 \tag{1.52}$$

$$\frac{\mathrm{d}\sigma_{\mathrm{Lr}}}{\mathrm{d}\cos\theta} \propto g^2_{\mathrm{Le}} g^2_{\mathrm{Rf}} (1-\cos\theta)^2 \tag{1.53}$$

$$\frac{\mathrm{d}\sigma_{\mathrm{Rl}}}{\mathrm{d}\cos\theta} \propto g^2_{\mathrm{Re}} g^2_{\mathrm{Lf}} (1-\cos\theta)^2. \tag{1.54}$$

Here the upper-case subscript of the cross-section defines the helicity of the initial-state electron, while the lower-case defines the helicity of the final-state fermion. Note that the designations "+" and "−" are sometimes used in place of "r" and "l", particularly when discussing τ polarisation. Due to the point-like nature of the couplings and the negligible masses of the fermions involved, the helicity of the anti-fermion is opposite that of the fermion at each vertex.

From these basic expressions the Born level differential cross-section for Z exchange only, summed over final-state helicities, assuming an unpolarised positron beam but allowing polarisation of the electron beam, is:

$$\frac{\mathrm{d}\sigma_{\mathrm{f\bar{f}}}}{\mathrm{d}\cos\theta} = \frac{3}{8}\sigma^{\mathrm{tot}}_{\mathrm{f\bar{f}}} \left[(1-\mathcal{P}_{\mathrm{e}}\mathcal{A}_{\mathrm{e}})(1+\cos^2\theta) + 2(\mathcal{A}_{\mathrm{e}}-\mathcal{P}_{\mathrm{e}})\mathcal{A}_{\mathrm{f}}\cos\theta \right] . \tag{1.55}$$

The electron beam polarisation, $\mathcal{P}_{\mathrm{e}}$, is taken as positive for right-handed beam helicity, negative for left. The dependence on the fermion couplings has been incorporated into convenient asymmetry parameters, $\mathcal{A}_{\mathrm{f}}$:

$$\mathcal{A}_{\mathrm{f}} = \frac{g^2_{\mathrm{Lf}} - g^2_{\mathrm{Rf}}}{g^2_{\mathrm{Lf}} + g^2_{\mathrm{Rf}}} = \frac{2 g_{\mathrm{Vf}} g_{\mathrm{Af}}}{g^2_{\mathrm{Vf}} + g^2_{\mathrm{Af}}} = 2\frac{g_{\mathrm{Vf}}/g_{\mathrm{Af}}}{1+(g_{\mathrm{Vf}}/g_{\mathrm{Af}})^2} . \tag{1.56}$$

As the third form makes clear, the asymmetry parameters depend only on the ratio of the couplings, and within the SM bear a one-to-one relation with $\sin^2\theta^{\mathrm{f}}_{\mathrm{eff}}$.

Although the asymmetry analyses typically utilise maximum likelihood fits to the expected angular distributions, the simple form of Equation 1.55 also allows the coefficients of the $\cos\theta$ and $(1+\cos^2\theta)$ terms to be determined in terms of the integral cross-sections over the forward or backward hemispheres. Naturally, at SLC, the two helicity states of the polarised electron beam also need to be distinguished.

Designating the integrals over the forward and backward hemispheres with subscripts F and B and the cross-sections for right and left electron helicities with subscripts R and L, three basic asymmetries can be measured:

$$A_{\mathrm{FB}} = \frac{\sigma_{\mathrm{F}} - \sigma_{\mathrm{B}}}{\sigma_{\mathrm{F}} + \sigma_{\mathrm{B}}} \tag{1.57}$$

$$A_{\mathrm{LR}} = \frac{\sigma_{\mathrm{L}} - \sigma_{\mathrm{R}}}{\sigma_{\mathrm{L}} + \sigma_{\mathrm{R}}} \frac{1}{\langle|\mathcal{P}_{\mathrm{e}}|\rangle} \tag{1.58}$$

$$A_{\mathrm{LRFB}} = \frac{(\sigma_{\mathrm{F}} - \sigma_{\mathrm{B}})_{\mathrm{L}} - (\sigma_{\mathrm{F}} - \sigma_{\mathrm{B}})_{\mathrm{R}}}{(\sigma_{\mathrm{F}} + \sigma_{\mathrm{B}})_{\mathrm{L}} + (\sigma_{\mathrm{F}} + \sigma_{\mathrm{B}})_{\mathrm{R}}} \frac{1}{\langle|\mathcal{P}_{\mathrm{e}}|\rangle} . \tag{1.59}$$

Inspection of Equation 1.55 shows that the forward-backward asymmetry, A_{FB}, picks out the coefficient $\mathcal{A}_{\mathrm{e}}\mathcal{A}_{\mathrm{f}}$ in the $\cos\theta$ term, the left-right asymmetry, A_{LR}, picks out the coefficient $\mathcal{A}_{\mathrm{e}}$ in the $(1+\cos^2\theta)$ term, and the left-right forward-backward asymmetry [37], A_{LRFB}, picks out the coefficient $\mathcal{A}_{\mathrm{f}}$ in the $\cos\theta$ term.

The polarisation of a final-state fermion is the difference between the cross-sections for right- and left-handed final-state helicities divided by their sum:

$$\mathcal{P}_{\mathrm{f}} \;=\; \frac{\mathrm{d}(\sigma_{\mathrm{r}}-\sigma_{\mathrm{l}})}{\mathrm{d}\cos\theta} \Bigg/ \frac{\mathrm{d}(\sigma_{\mathrm{r}}+\sigma_{\mathrm{l}})}{\mathrm{d}\cos\theta} \;. \tag{1.60}$$

At Born level the numerator and denominator can be derived from the helicity-specific cross-sections of Equations 1.51 to 1.54:

$$\frac{\mathrm{d}(\sigma_{\mathrm{r}}-\sigma_{\mathrm{l}})}{\mathrm{d}\cos\theta} \;=\; -\frac{3}{8}\sigma_{\mathrm{f\overline{f}}}^{\mathrm{tot}}\left[\mathcal{A}_{\mathrm{f}}(1+\cos^2\theta)+2\mathcal{A}_{\mathrm{e}}\cos\theta\right] \tag{1.61}$$

$$\frac{\mathrm{d}(\sigma_{\mathrm{r}}+\sigma_{\mathrm{l}})}{\mathrm{d}\cos\theta} \;=\; \frac{3}{8}\sigma_{\mathrm{f\overline{f}}}^{\mathrm{tot}}\left[(1+\cos^2\theta)+2\mathcal{A}_{\mathrm{e}}\mathcal{A}_{\mathrm{f}}\cos\theta\right] \;. \tag{1.62}$$

Here we assume Z exchange only, and unpolarised beams. The average final-state fermion polarisation, $\langle\mathcal{P}_{\mathrm{f}}\rangle$, as well as the forward-backward polarisation asymmetry, $A_{\mathrm{FB}}^{\mathrm{pol}}$, can be found in terms of the helicity cross-sections integrated over the forward and backward hemispheres:

$$\langle\mathcal{P}_{\mathrm{f}}\rangle \;=\; \frac{\sigma_{\mathrm{r}}-\sigma_{\mathrm{l}}}{\sigma_{\mathrm{r}}+\sigma_{\mathrm{l}}} \tag{1.63}$$

$$A_{\mathrm{FB}}^{\mathrm{pol}} \;=\; \frac{(\sigma_{\mathrm{r}}-\sigma_{\mathrm{l}})_{\mathrm{F}}-(\sigma_{\mathrm{r}}-\sigma_{\mathrm{l}})_{\mathrm{B}}}{(\sigma_{\mathrm{r}}+\sigma_{\mathrm{l}})_{\mathrm{F}}+(\sigma_{\mathrm{r}}+\sigma_{\mathrm{l}})_{\mathrm{B}}} \,. \tag{1.64}$$

Again, examination of Equations 1.61 and 1.62 shows that $\langle\mathcal{P}_{\mathrm{f}}\rangle$ picks out the coefficient $\mathcal{A}_{\mathrm{f}}$ in the $(1+\cos^2\theta)$ term and $A_{\mathrm{FB}}^{\mathrm{pol}}$ picks out the coefficient $\mathcal{A}_{\mathrm{e}}$ in the $\cos\theta$ term.

The net polarisation of a final-state fermion as a function of $\cos\theta$ is simply the ratio of Equations 1.61 and 1.62:

$$\mathcal{P}_{\mathrm{f}}(\cos\theta) \;=\; -\,\frac{\mathcal{A}_{\mathrm{f}}(1+\cos^2\theta)+2\mathcal{A}_{\mathrm{e}}\cos\theta}{(1+\cos^2\theta)+2\mathcal{A}_{\mathrm{f}}\mathcal{A}_{\mathrm{e}}\cos\theta} \,. \tag{1.65}$$

Since the polarisation of the final-state fermion can only be measured in the case of the τ-lepton, which decays in a parity violating manner within the detectors, these quantities are measured only for the final state $\tau^+\tau^-$. As in the case of the other asymmetries, a maximum-likelihood fit to Equation 1.65 is used in the actual τ polarisation analyses to extract both $\langle\mathcal{P}_\tau\rangle$ and $A_{\mathrm{FB}}^{\mathrm{pol}}$, rather than using the simpler integral expressions of Equations 1.63 and 1.64.

The measured asymmetries and polarisations are corrected for radiative effects, γ exchange and γ–Z interference to yield "pole" quantities designated with a superscript 0. In the case where the final state is $\mathrm{e^+e^-}$, important corrections for t-channel scattering must also be taken into account. QED corrections [38] to A_{FB}^{ℓ} are as large as the value of the asymmetry itself, and must be understood precisely (see Section 2.4.4). Off-peak, the contributions from γ–Z interference to the forward-backward asymmetries become even larger. The corrections to A_{LR}, A_{LRFB}, $\langle\mathcal{P}_\tau\rangle$ and $A_{\mathrm{FB}}^{\mathrm{pol}}$ are relatively small.

At LEP the forward-backward asymmetries, $A_{\mathrm{FB}}^{0,\mathrm{e}}$, $A_{\mathrm{FB}}^{0,\mu}$, $A_{\mathrm{FB}}^{0,\tau}$ and $A_{\mathrm{FB}}^{0,\mathrm{q}}$ are measured for final states $\mathrm{e^+e^-}$, $\mu^+\mu^-$, $\tau^+\tau^-$ and $\mathrm{q\overline{q}}$. Tagging methods for b- and c-quarks allow $\mathrm{q\overline{q}}$ forward-backward asymmetries for these flavours to be measured precisely. All four LEP experiments measure $\mathcal{P}_\tau$.

SLD measures the asymmetries involving initial-state polarisation. The left-right asymmetry, A_{LR}^0, is independent of the final state, and the measurement is dominated by $\mathrm{e^+e^-}\to\mathrm{q\overline{q}}$. Despite the smaller event sample available to SLD, the measurement of A_{LR}^0 provided the single most precise determination of the initial state coupling (Z to electron). SLD also measures

$A^0_{\rm LRFB}$ for each of the final states e^+e^-, $\mu^+\mu^-$, $\tau^+\tau^-$ and $q\overline{q}$, where q includes not only b- and c-quarks, but also s-quarks.

In contrast to the partial widths, which are defined using the full complex couplings in order to ensure that the sum over all partial widths equals the total width, the pole asymmetries are defined purely in terms of the real parts of the effective Z couplings, and bear particularly direct relationships to the relevant asymmetry parameters:

$$A^{0,\,\rm f}_{\rm FB} = \frac{3}{4}\mathcal{A}_{\rm e}\mathcal{A}_{\rm f} \tag{1.66}$$

$$A^0_{\rm LR} = \mathcal{A}_{\rm e} \tag{1.67}$$

$$A^0_{\rm LRFB} = \frac{3}{4}\mathcal{A}_{\rm f} \tag{1.68}$$

$$\langle \mathcal{P}^0_\tau \rangle = -\,\mathcal{A}_\tau \tag{1.69}$$

$$A^{\rm pol,0}_{\rm FB} = -\frac{3}{4}\mathcal{A}_{\rm e}\,. \tag{1.70}$$

The negative sign of the quantities involving the polarisation is simply a consequence of defining the polarisation of a right-handed fermion as positive in a world in which left-handed couplings dominate. It should be noted that although the pole asymmetries are defined in terms of only the real parts of the couplings, the complex parts are taken into account when correcting the measurements to yield pole quantities.

Using the measurements of $\mathcal{A}_{\rm e}$, the parameters $\mathcal{A}_\mu$, $\mathcal{A}_\tau$, $\mathcal{A}_{\rm b}$ and $\mathcal{A}_{\rm c}$ can also be inferred from forward-backward asymmetry measurements at LEP via Equation 1.66. Thus, the LEP and SLC results form a complementary and practically complete set of $\mathcal{A}_{\rm f}$ measurements.

When the couplings conform to the SM structure, then

$$\frac{g_{\rm Vf}}{g_{\rm Af}} = 1 - \frac{2Q_{\rm f}}{T^{\rm f}_3}\sin^2\theta^{\rm f}_{\rm eff} = 1 - 4|Q_{\rm f}|\sin^2\theta^{\rm f}_{\rm eff}\,, \tag{1.71}$$

and the expected variation of $\mathcal{A}_{\rm f}$ with $\sin^2\theta^{\rm f}_{\rm eff}$ is shown in Figure 1.14. Due to the proximity of $\sin^2\theta^{\rm f}_{\rm eff}$ to 1/4, $\mathcal{A}_\ell$ and the leptonic forward-backward asymmetries at $\sqrt{s} = m_{\rm Z}$ are small, but very sensitive to $\sin^2\theta^{\rm f}_{\rm eff}$. Compared with the leptons, the coupling parameters of the quarks in the SM are determined more by their charge and weak isospin assignments than by the value of $\sin^2\theta^{\rm f}_{\rm eff}$. For down-type quarks, as can be seen from Figure 1.14, the relative sensitivity of $\mathcal{A}_{\rm q}$ to changes in $\sin^2\theta^{\rm q}_{\rm eff}$ is a factor of almost 100 less than it is for $\mathcal{A}_\ell$. It is therefore of particular interest to compare the relatively static SM prediction for $\mathcal{A}_{\rm q}$ with measurement. On the other hand, if the SM prediction for $\mathcal{A}_{\rm q}$ is assumed to be valid, the observed forward-backward asymmetries for quarks provide a sensitive measurement of $\sin^2\theta^{\rm lept}_{\rm eff}$ via Equation 1.66.

1.5.4 Relating Theory and Experiment

The parameters introduced in the preceding subsections, which describe the main features of all measurements around the Z resonance, are not "realistic observables" like the underlying measurements themselves, but are defined quantities with significant theoretical corrections. Therefore they are commonly named pseudo-observables. Where necessary, the pseudo-observables are denoted by a superscript 0; for example, $\sigma_{\rm had}$ is the measured hadronic cross-section, whereas $\sigma^0_{\rm had}$ is the pole cross-section derived from the measurements. Similarly, $R_{\rm b}$ is the measured

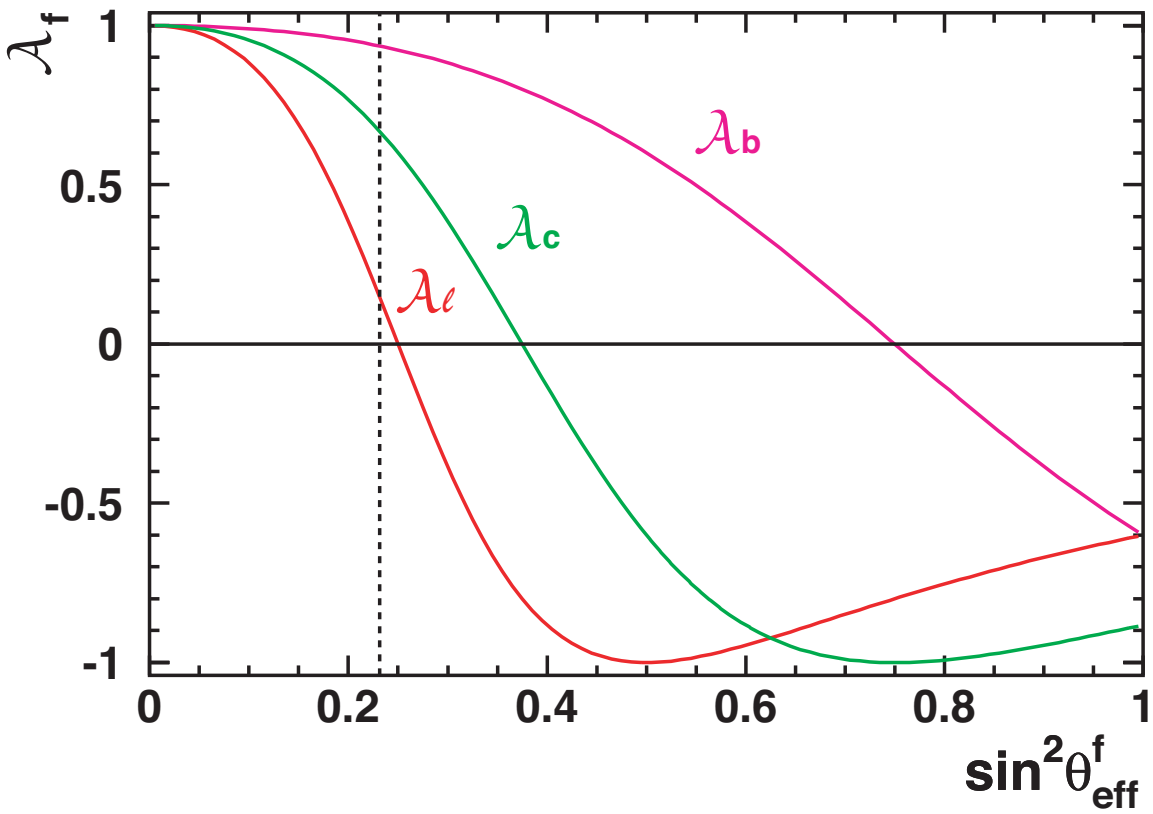

Figure 1.14: In the SM the variation of $\mathcal{A}_{\rm f}$ with $\sin^2\theta^{\rm f}_{\rm eff}$ is controlled by the charge and weak isospin assignment of the fermion species concerned. The measured values of $\sin^2\theta^{\rm f}_{\rm eff}$ are near the vertical line. In this region, $\mathcal{A}_\ell$ depends strongly on $\sin^2\theta^{\rm lept}_{\rm eff}$, while $\mathcal{A}_{\rm b}$ depends much more weakly on $\sin^2\theta^{\rm b}_{\rm eff}$.

b-quark cross-section divided by the hadronic cross-section, $\sigma_{\rm b\overline{b}}/\sigma_{\rm had}$, while $R^0_{\rm b}$ is the derived ratio of Z boson partial widths, $\Gamma_{\rm b\overline{b}}/\Gamma_{\rm had}$.

In the Z lineshape analysis the true realistic observables are the experimental cross-sections and asymmetries measured in the acceptances particular to each detector. Before these can be further analysed, each collaboration applies small corrections to extrapolate them to more generic, idealized acceptances, as described in Section 2.2.2.

The programs TOPAZ0 and ZFITTER are able to calculate the cross-sections measured within these idealized acceptances, including the effects of QED radiation, as a function of the set of nine pseudo-parameters chosen to describe the observable features of the Z resonance in a model-independent manner. It is important to realize that the bulk of the radiative corrections necessary to interpret the real observables in terms of the pseudo-observables are QED effects distinct from the deeper electroweak corrections which modify the relations between the pseudo-parameters in the context of any particular model, such as the SM. Further details are discussed in Section 8.4.2.

After these QED effects which depend in a model-independent manner on the resonance properties of the Z have been accounted for, the remaining differences between the pseudo-observables and the QED deconvoluted observables at $\sqrt{s} = m_{\rm Z}$ are attributable to non-factorisable complex components, termed "remnants", of the couplings $\mathcal{G}_{\rm Af}$ and $\mathcal{G}_{\rm Vf}$ and of $\alpha(m^2_{\rm Z})$ in Equation 1.34. These effects are found to be small in the SM. For example, the calculated value of $\sigma^0_{\rm f\overline{f}}$, given in terms of the partial decay widths, agrees to better than 0.05%

for both hadrons and leptons with the QED deconvoluted cross-sections without the photon exchange contribution at $\sqrt{s} = m_{\mathrm{Z}}$. This is only a fraction of the LEP combined experimental error. The difference between $A_{\mathrm{FB}}^{0,\ell}$ and the QED deconvoluted forward-backward asymmetry at the peak is dominated by a contribution of 0.0015 from the imaginary part of $\alpha(m_{\mathrm{Z}}^2)$, which accounts, via the optical theorem, for the decay of a massive photon to fermion pairs. The remaining electroweak contribution in the SM to be treated explicitly is -0.0005, again smaller than the LEP combined error on $A_{\mathrm{FB}}^{0,\ell}$.

It is therefore important to treat these complex parts correctly, but the measurements have no sensitivity to SM parameters entering through these components: the effects on the remnants are much smaller than the experimental uncertainties.

Since one of the main goals of the Z-pole analysis is to test theory with experimental results, considerable effort has been expended to make the extraction of the pseudo-observables describing the Z resonance as model-independent as possible, so that the meanings of "theory" and "experiment" remain distinct. Since the pseudo-observables do depend slightly on SM assumptions, as explained above, a more precise definition of what we mean by "model-independence" is that our analysis is valid in any scenario in which the predicted remnants remain small. The very small uncertainties arising from ambiguities in the theoretical definition of the pseudo-observables are discussed in Section 2.4.4, and quantified in Table 2.8.

In the same spirit, the contribution of the 4-fermion process $\mathrm{e^+e^-} \to \mathrm{Z} \to \mathrm{Z^*H} \to \mathrm{f\bar{f}H}$ entering the fermion-pair samples used for analysis should be negligible. The limit of $m_{\mathrm{H}} > 114.4$ GeV [39] established by the direct search for the Higgs boson at LEP-II ensures that this is in fact the case. Only when hypothetical Higgs masses well below the experimental limit are considered in the course of exploring the full parameter-space of the SM must allowances be made for the treatment of such ZH contributions [29], both in the experimental analyses and in the theoretical calculations.

1.6 Interpretation and Impact of the Results

This paper aims to be an authoritative compendium of the properties of the Z boson derived from precise electroweak measurements performed at LEP-I and SLC. These properties, based on χ^2 combinations [40] of the results of five experiments described in detail in this paper, are largely independent of any model, and represent a comprehensive distillation of our current knowledge of the Z pole.

Since these observed properties are found to be in good agreement with expectations of the SM, we leave theoretical speculations which go beyond the SM context to others. We first focus on comparing the Z-pole data with the most fundamental SM expectations (lepton universality, consistency between the various manifestations of $\sin^2\theta_{\mathrm{W}}$, etc.).

We then assume the validity of the SM, and perform fits which respect all the interrelationships among the measurable quantities which it imposes. These fits find optimum values of the SM parameters, and determine whether these parameters can adequately describe the entire set of measurements simultaneously. At first we restrict the set of measurements to the Z-pole results presented here, and later extend the analysis to a larger set of relevant electroweak results, including the direct measurements of the top quark and W boson masses. This expanded set of measurements yield the narrowest constraints on the mass of the only particle of the SM not yet observed: the Higgs boson.

The LEP/SLC era represents a decade of extraordinary progress in our experimental knowledge of electroweak phenomena. It is the goal of the remainder of this paper to demonstrate

in detail how the LEP/SLD measurements confront the theory of the SM much more precisely than previous experiments. The mass of the Z is now one of the most precisely known electroweak parameters, and will long serve as an important reference for future investigations. The strong constraint on the number of light neutrinos, implying that there are only three "conventional" generations of particles, is of particular significance for astrophysics and cosmology. An illustration of the improved knowledge of the properties of the Z, in addition to the precise measurements of its mass, width and pole production cross-section, is shown in Figure 1.15, comparing the $g_{\mathrm{V}\ell}$ and $g_{\mathrm{A}\ell}$ measurements before and after the LEP and SLC programmes. The small dot in the 1987 plot shows the true scale of the circle enclosing the 2002 inset.

The good agreement between the top quark mass measured directly at the Tevatron and the predicted mass determined indirectly within the SM framework on the basis of measurements at the Z-pole, shown in Figure 1.16, is a convincing illustration of the validity of SM radiative corrections and stands as a triumph of the electroweak SM.

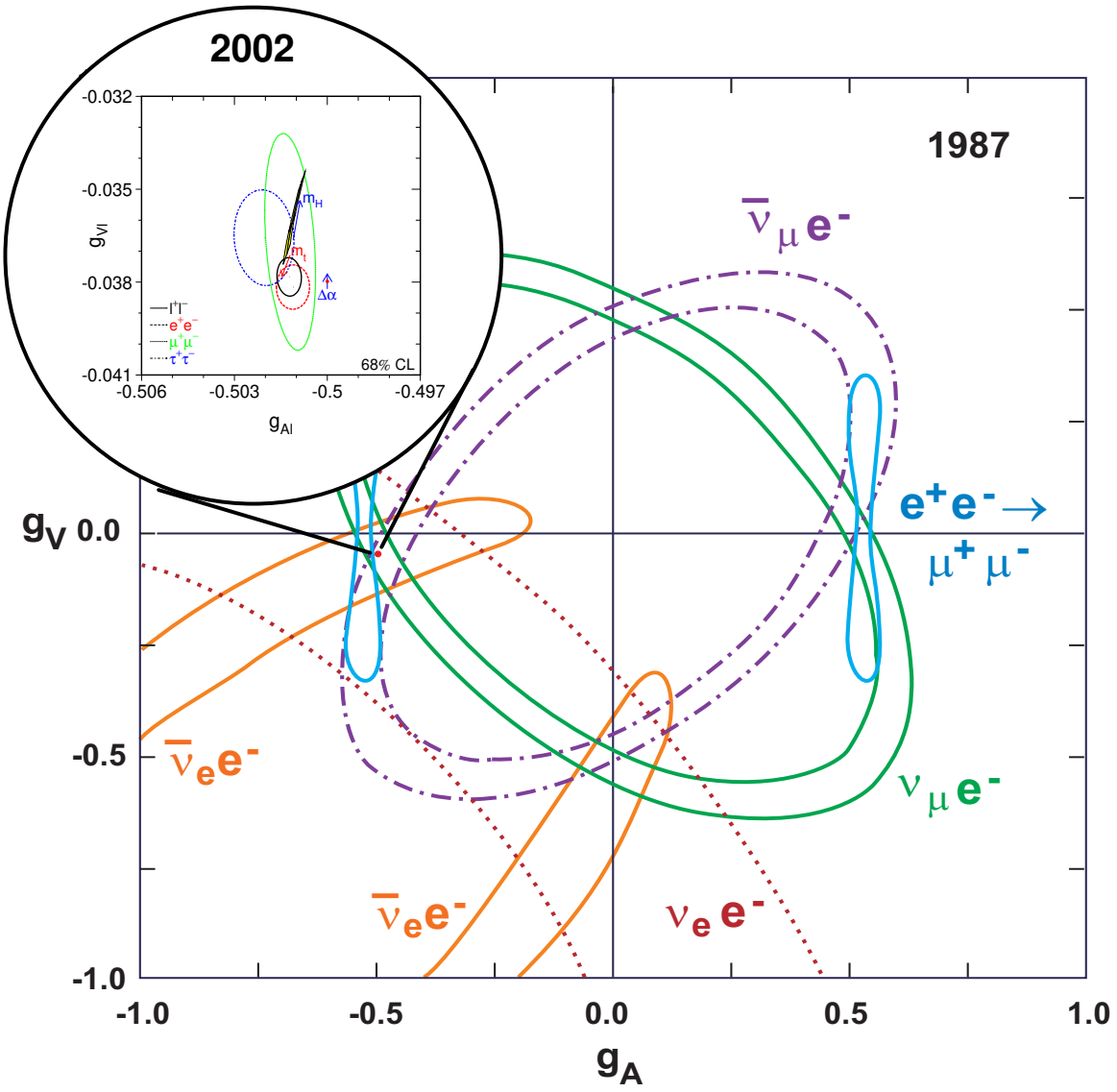

Figure 1.15: The neutrino scattering and e^+e^- annihilation data available in 1987 constrained the values of $g_{V\ell}$ and $g_{A\ell}$ to lie within broad bands, whose intersections helped establish the validity of the SM and were consistent with the hypothesis of lepton universality. The inset shows the results of the LEP/SLD measurements at a scale expanded by a factor of 65 (see Figure 7.3). The flavour-specific measurements demonstrate the universal nature of the lepton couplings unambiguously on a scale of approximately 0.001.

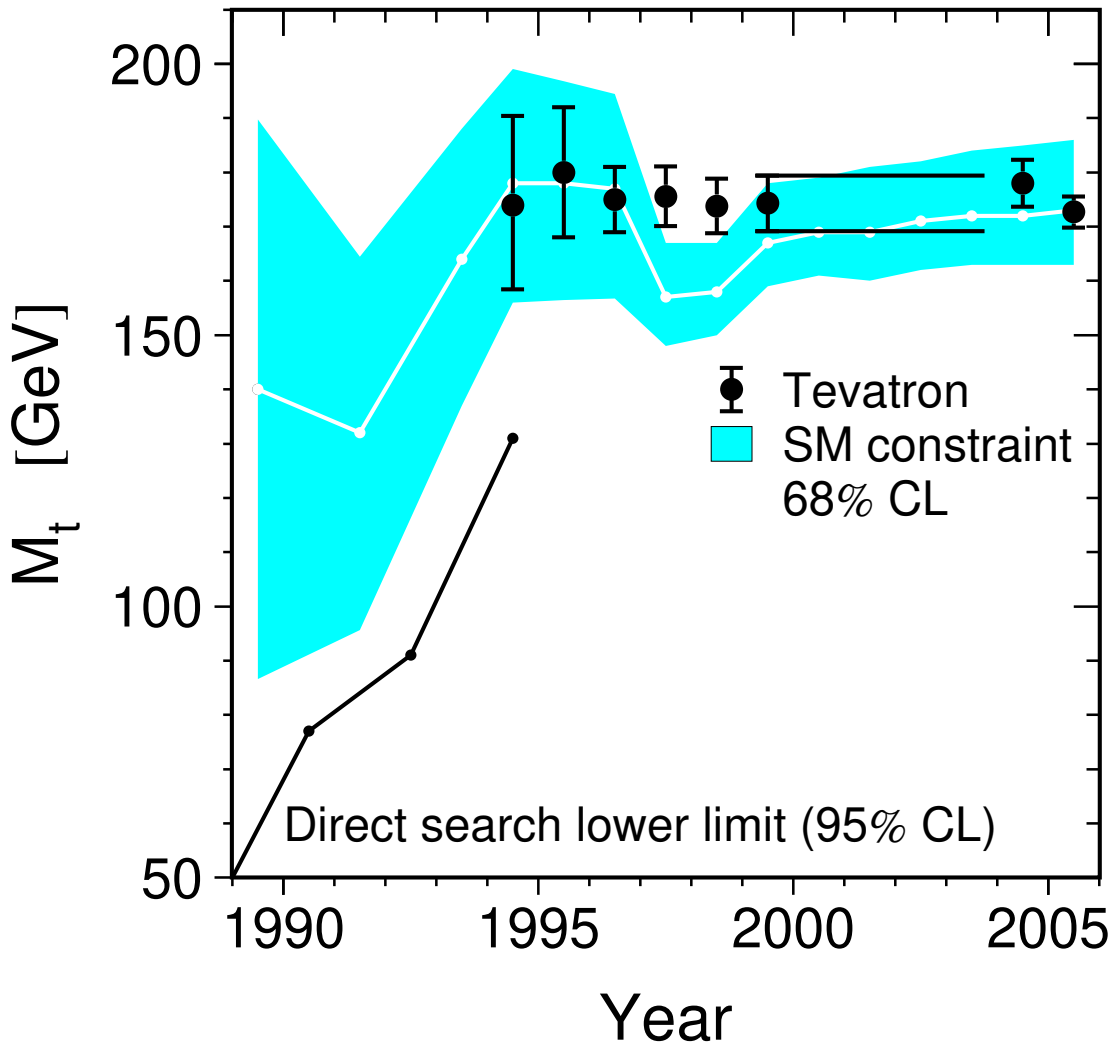

Figure 1.16: Comparison of direct and indirect determinations of the mass of the top quark, m_t, as a function of time. The shaded area denotes the indirect determination of m_t at 68% confidence level derived from the analysis of radiative corrections within the framework of the SM using precision electroweak measurements. The dots with error bars at 68% confidence level denote the direct measurements of m_t performed by the Tevatron experiments CDF and DØ. Also shown is the 95% confidence level lower limit on m_t from the direct searches before the discovery of the top quark. Predictions and measurements agree well.

Chapter 2

The Z Lineshape and the Leptonic Forward-Backward Asymmetries

2.1 Introduction

The measurements described in this chapter are designed to determine the essential parameters of the Z resonance, its mass, its width, its branching fractions, and the angular distribution of its decay products. Specifically, the nine parameters m_{Z}, Γ_{Z}, σ^0_{had} as well as R^0_ℓ and $A^{0,\ell}_{\mathrm{FB}}$ for each of the three charged lepton species, as defined in Section 1.5.1, provide a complete (hadron-inclusive) description of the Z resonance. The mass of the Z is a central parameter of the Standard Model (SM). Because of the LEP programme, m_{Z} is now measured with a relative precision of $2.3 \cdot 10^{-5}$, and thus represents one of the most precisely known parameters of the SM. Together with the Fermi constant G_{F}, known to a precision of $0.9 \cdot 10^{-5}$, both G_{F} and m_{Z} currently act as two fixed points of the SM, around which all other quantities are forced to find their place.

The role of the total width Γ_{Z} is of similar importance. As can be seen from Equation 1.37, the width of the Z to each of its decay channels is proportional to the fundamental Z-fermion couplings. The total width Γ_{Z} is in fact the only Z-pole observable in the experimentally motivated nine-parameter set from which the absolute scale of the couplings can be determined: Since Γ_{Z} is large compared to the energy spread of the colliding beams at LEP, it does not manifest itself in terms of the apparent peak cross-section[1], as is the case for a narrow resonance like the J/Ψ, but in terms of the measurable width of the lineshape as the beam energy is scanned across the resonance. In order to determine Γ_{Z}, off-peak data are thus needed in addition to peak data, as is the case for the measurement of m_{Z}. The beam energies of this off-peak running were carefully tuned to optimise the precision of the measurement, and focused on a small set of centre-of-mass energies within ± 3 GeV around $\sqrt{s} = m_{\mathrm{Z}}$. Even after all four experiments have been combined, the dominant error in Γ_{Z} is statistical, rather than systematic.

Since the Z is expected to decay only to fermion pairs, the number of partial decay widths to be determined is small. The decision to treat all Z decays to quarks as a single inclusive hadronic decay channel in the lineshape analysis further limits the number of partial widths to a very manageable number. Since some of the very properties of the hadronic decays which make the identity of the primary quarks difficult to determine also make the experimental acceptance quark-flavour independent, the attraction of a precise inclusive hadronic analysis is

[1] The peak cross-sections would in fact remain constant if the couplings to all final states increased or decreased proportionally, see Equation 1.42.

obvious. Separation of the primary quarks and the determination of their couplings is therefore left to the specialised analyses described in Chapter 5 and Appendix F, employing dedicated flavour and charge tagging techniques. The expected approximate branching fractions of the Z are 70 %, 20 % and 10 % to hadrons, neutrinos and charged leptons, respectively. The statistical dominance of the hadronic decays makes them decisive in determining the fundamental parameters m_{Z} and Γ_{Z}.

Due to the tight linkage between pole cross-sections, branching ratios and partial widths implied by Equation 1.42 and the constraint that the sum of all partial widths should equal the total width, the parameters Γ_{Z}, σ^0_{had} and the three hadron/lepton species ratios, $R^0_\ell = \Gamma_{\mathrm{had}}/\Gamma_{\ell\ell}$, were chosen as a less-correlated representation of the complete set of five partial widths. Although Z decays to neutrinos escape direct detection, and are therefore referred to as "invisible decays", the corresponding Z decay width can be derived from the other parameters, according to the relation described in Equation 1.49. Therefore the observed peak cross-sections depend strongly on the number of existing neutrino generations, as already shown in Figure 1.13. The precision ultimately achieved in the determination of the number of neutrinos thus hinges on a precise absolute cross-section measurement, requiring a precise determination of the integrated luminosity and an accurate calculation of QED radiative corrections.

The spin-1 nature of the Z is well substantiated by the observed $1 + \cos^2\theta$ angular distribution of its decay products. The $\cos\theta$ terms of the angular decay distributions, varying as a function of energy due to γ–Z interference, determine the three leptonic pole forward-backward asymmetries, $A^{0,\ell}_{\mathrm{FB}}$. The violation of parity conservation in Z production and decay, which is most precisely quantified by the analyses of Chapters 3 to 5, is evident from the non-zero values of these three measured leptonic pole forward-backward asymmetries.

The full LEP-I data set relevant to this analysis consists of about 200 measurements from each experiment of hadronic and leptonic cross-sections and of leptonic forward-backward asymmetries at different centre-of-mass energies. Although this complete set of basic measurements carries all available experimental information on the Z resonance parameters, the construction of the overall error matrix describing all the inter-experiment correlations is too complex a task in practice. Instead, each experiment has independently extracted the agreed-upon set of nine pseudo-observables discussed above in single multi-parameter fits to all their measurements of cross-sections and forward-backward asymmetries. The electroweak libraries used for this extraction are TOPAZ0 [30] and ZFITTER [31], which include QED and QCD corrections necessary to extract the pseudo-parameters in a model-independent manner as well as those electroweak corrections according to the SM which can only be described by the imaginary parts of the Z couplings, as discussed in Section 1.5.4.

The main task of the analysis undertaken here is to combine the resulting four sets of pseudo-observables with an appropriate treatment of common errors and especially the recognition that re-weighting of particular datasets will occur when the balance of statistical and systematic errors changes under the act of combination. Much of this work involves novel techniques which were specially developed for this analysis.

After a brief description of the key features of the experimental analyses (Section 2.2) and the presentation of the individual results (Section 2.3), the main emphasis in the following sections is given to the hitherto unpublished aspects of the combination procedure, namely the errors common to all experiments (Section 2.4) and the combination procedure (Section 2.5). Essential cross-checks of the general validity of the combination procedure are also discussed in this section, which is followed by the presentation of the combined results. Re-parametrisations in terms of partial widths and branching fractions will be given later (see Section 7.2).

2.2 Measurements of Total Cross-Sections and Forward-Backward Asymmetries

The main features of the event selection procedures for measurements of the total hadronic and leptonic cross-sections and of the leptonic forward-backward asymmetries are briefly described below. Detailed descriptions of the individual experimental analyses are given in the References [41, 42, 43, 44].

2.2.1 Event Selection

The event selection for $q\overline{q}$, e^+e^-, $\mu^+\mu^-$ and $\tau^+\tau^-$ final states in each of the experiments is aimed at high selection efficiencies within the largest possible acceptance in order to keep corrections small.

The design of the detectors and the cleanliness of the LEP beams allowed the experiments to trigger on hadronic and leptonic Z decays with high redundancy and essentially 100% efficiency. The selections are as open as possible to events with initial and final state radiation in order to benefit from cancellations between real and virtual particle emission. Good discrimination of $q\overline{q}$ from $\ell^+\ell^-$ final states is mandatory for the analyses, and excellent separation of e^+e^-, $\mu^+\mu^-$ and $\tau^+\tau^-$ permits checks of the universality of the Z couplings to the different lepton species to be carried out. Machine-induced backgrounds at LEP-I were small, and the only significant source of background from e^+e^- processes comes from two-photon reactions. The accumulated event statistics are given in Table 1.2, and event pictures of each of the final states are shown in Figure 1.7 in Chapter 1.

The principles used to separate leptonic and hadronic events and to distinguish two-photon reactions are illustrated in Figure 2.1. A peak from e^+e^- and $\mu^+\mu^-$ events at high momenta and low multiplicities is clearly separated from the background of two-photon reactions at relatively low multiplicities and momenta. The intermediate momentum region at low multiplicities is populated by $\tau^+\tau^-$ events. The separation of electrons and muons is achieved using also the information from the electromagnetic and hadron calorimeters and from the muon chambers. Hadronic events populate the high multiplicity region at energies below the centre-of-mass energy, since neutral particles in the jets are not measured in the central detector.

In somewhat more detail, hadronic events in the detectors are characterised by a large number of particles arising from the hadronisation process of the originally produced quark pair. This leads to high track multiplicities in the central detectors and high cluster multiplicities in the electromagnetic and hadron calorimeters. For $Z \to q\overline{q}$ events, the deposited energy is balanced along the beam line, which is generally not the case for hadronic events produced in two-photon reactions. In addition, two-photon collision events have an almost constant production cross-section around the Z resonance. It is thus possible to estimate the fraction of two-photon reactions directly from the data by studying the energy dependence of two event samples, one with an enriched contribution of two-photon reactions and another with tight selection cuts for genuine $Z \to q\overline{q}$ events, which show a resonant behaviour. Background from $\tau^+\tau^-$ events is subtracted using Monte Carlo simulation.

Lepton pairs are selected by requiring low track and cluster multiplicities. Electrons are characterised by energy deposits in the electromagnetic calorimeters that match well the measured momenta in the tracking detectors. Muons exhibit only minimum ionising energy deposits in the electromagnetic and hadron calorimeters and produce signals in the outer muon chambers. Tau leptons decay before reaching any detector component. Their visible decay

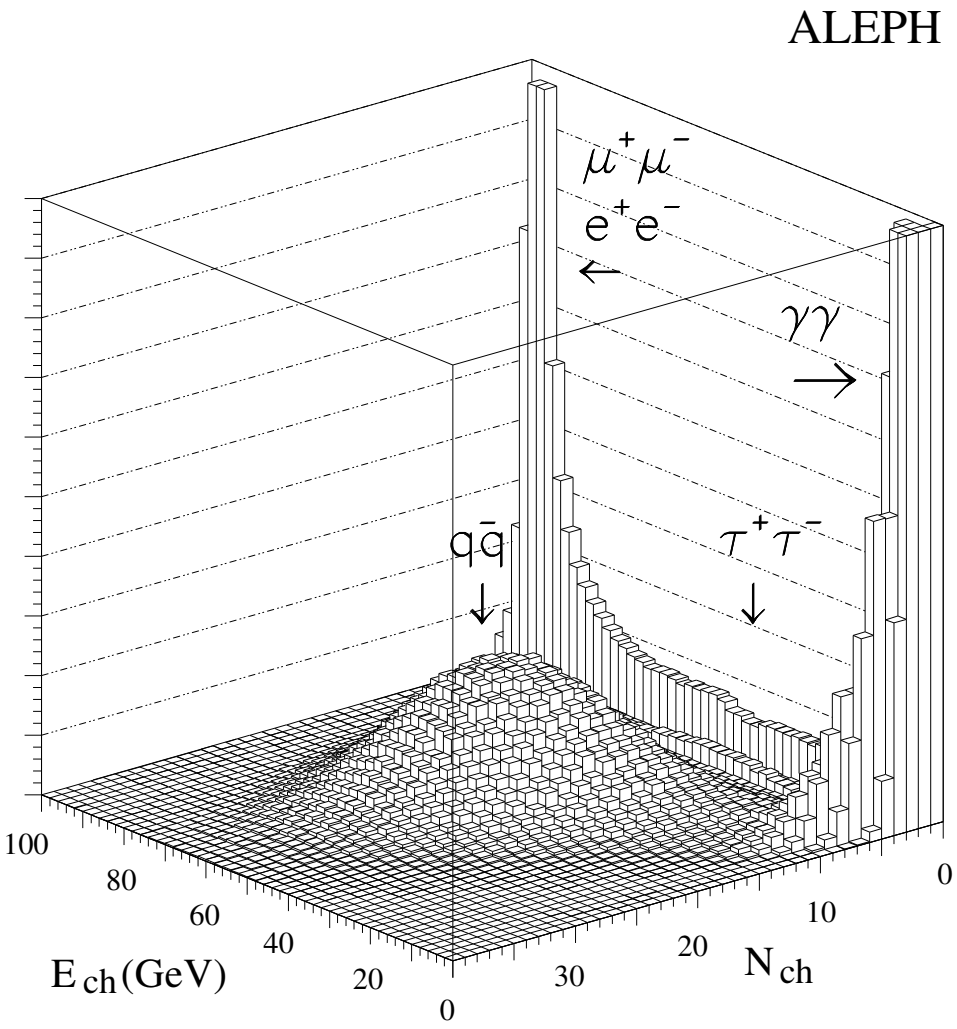

Figure 2.1: Experimental separation of the final states using only two variables, the sum of the track momenta, E_{ch}, and the track multiplicity, N_{ch}, in the central detector of the ALEPH experiment.

products are either a single electron, muon or hadron, or a collimated jet consisting of three or five charged hadrons and a few neutral hadrons; in addition energy is missing due to the undetectable neutrinos. $\tau^+\tau^-$ events are therefore selected by requiring the total energy and momentum sums to be below the centre-of-mass energy to discriminate against $Z \to e^+e^-$ and $Z \to \mu^+\mu^-$, and to be above a minimum energy to reject lepton pairs arising from two-photon reactions. The direction of flight of the τ is approximated by the momentum sum of the visible decay products. Leptonic events with photons or fermion pairs radiated from the initial- or final-state leptons are contained in the signal definition. Initial-state pairs typically remain in the beam pipe and are therefore experimentally indistinguishable from initial state photon radiation. The classification of final states with radiated fermion pairs, *i.e.* of four-fermion events, into one of the three lepton categories is made by choosing the lepton pair with the highest invariant mass.

The experiments use very detailed detector simulations [24, 45] to understand the selection efficiencies. Owing to the high redundancy of the detectors, cross-checks and corrections

using the actual data are possible by comparing event samples identified with different selection criteria. Various Monte Carlo generators are interfaced to the detector simulations and are used to describe the kinematics of the physics reactions of interest: $q\overline{q}$ production with gluon radiation including phenomenological modelling of the non-perturbative hadronisation process [17, 18, 19], production of $\mu^+\mu^-$ and $\tau^+\tau^-$ final states [20, 21], e^+e^- final states including the t-channel contribution [22, 46, 47, 48], and finally e^+e^- scattering in the forward direction [23], which is dominated by t-channel photon exchange and serves as the normalisation reaction in determining the luminosity of the colliding e^+e^- beams. The effects of fermion pair radiation in the final-state are studied using four-fermion event generators [49, 50].

The Monte Carlo generators are used to apply corrections at the edges of the experimental acceptance, and for small extrapolations of the measured cross-sections and forward-backward asymmetries from the true experimental cuts to sets of simple cuts that can be handled at the fitting stage. In the case of $q\overline{q}$ final states, this ideal acceptance is defined by the single requirement $s' > 0.01\,s$, where $\sqrt{s'}$ is the effective centre-of-mass energy after initial-state photon radiation. The idealised acceptances chosen for each lepton decay channel vary among the experiments and are specified in Table 2.1 below. The results quoted for the e^+e^- final state either include contributions originating from t-channel diagrams, or the t and s-t interference effects are explicitly subtracted, allowing the same treatment of e^+e^- and $\mu^+\mu^-$ or $\tau^+\tau^-$ final states in the fits for the Z parameters.

2.2.2 Cross-Section Measurements

The total cross-section, $\sigma_{\rm tot}$, is determined from the number of selected events in a final state, $N_{\rm sel}$, the number of expected background events, $N_{\rm bg}$, the selection efficiency including acceptance, $\epsilon_{\rm sel}$, and the integrated luminosity, $\mathcal{L}$, according to $\sigma_{\rm tot} = (N_{\rm sel} - N_{\rm bg})/(\epsilon_{\rm sel}\mathcal{L})$.

Measurement of Luminosity

The luminosity of the beams is measured [51] from the process of small-angle Bhabha scattering. Further information is available in the lineshape publications [41, 42, 43, 44]. Events with forward-going electrons are recorded concurrently with all other processes, thus ensuring that they correctly reflect any data-taking inefficiencies arising from readout deadtimes and detector downtimes. Furthermore, the statistical precision of this process is high, matching well even the high statistics of hadronic events at the Z resonance. The luminosity measurement requires the detection of back-to-back energy deposits by electrons and positrons close to the beam direction. Their positions and energies are measured by calorimeters placed at small angles with respect to the beam line, typically covering a range in polar angle from 25 mrad to 60 mrad. Depending on the experiment, the accepted cross-section in the luminosity devices is at least twice as large as the hadronic on-peak cross-section, and therefore the statistical errors arising from the luminosity determination are small. The typical experimental signature of luminosity events is shown in Figure 2.2. The main experimental systematic error arises from the definition of the geometrical acceptance for this process. Since the angular distribution is steeply falling with increasing scattering angle ($\propto \theta^{-3}$), the precise definition of the inner radius of the acceptance region is most critical. Background arises from random coincidences between the calorimeters at the two sides and is largely beam-induced. The integrated luminosity is given by the ratio of the number of observed small-angle e^+e^- events and the calculated cross-section for this process within the detector acceptance. The Bhabha cross-section at small scattering angles

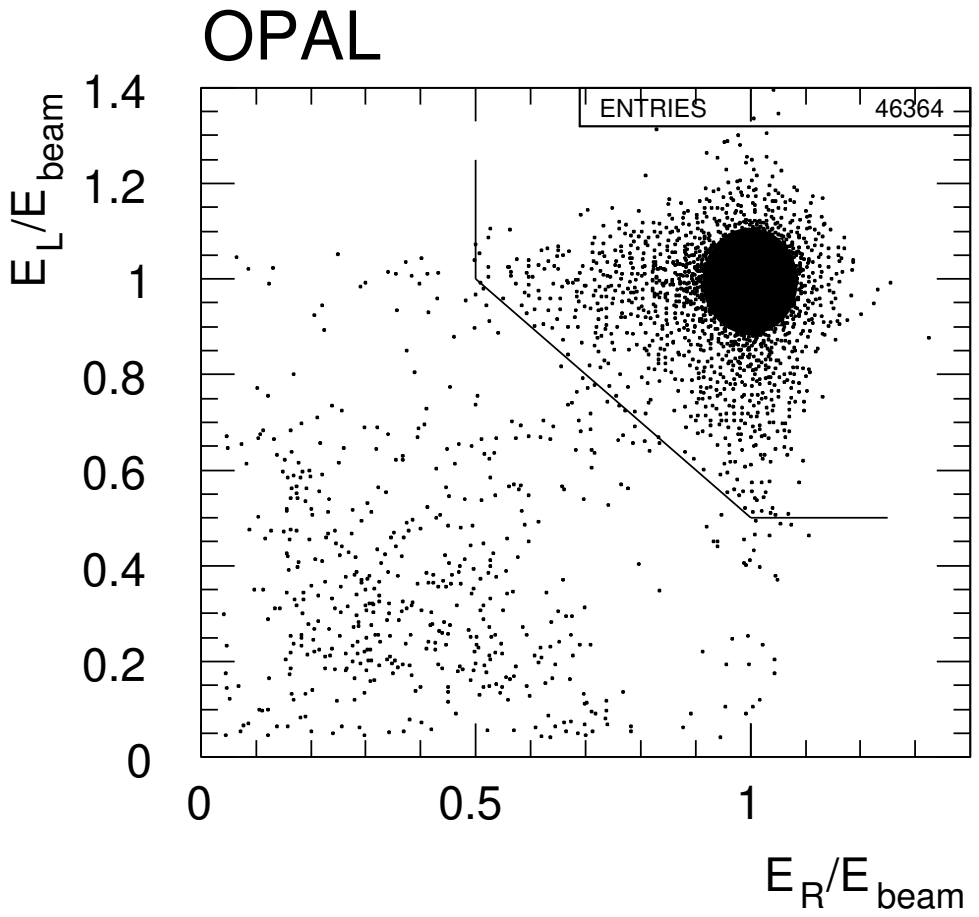

Figure 2.2: Fraction of the beam energy observed in the left and right luminosity calorimeters of the OPAL experiment, after all cuts except the one on the deposited energies. The lines indicate the acceptance region for the signal events. Initial state photon radiation leads to tails towards lower deposited energies. Background events from accidental coincidences populate the low-energy regions in both calorimeters.

is dominated by the well-known QED process of t–channel scattering, but nonetheless calculational uncertainties give rise to an important theoretical error of about 0.5 per-mille affecting all experiments coherently, as is discussed in Section 2.4.3. Typical experimental systematic errors on the luminosity are well below 1 per-mille.

Event Selection Efficiency and Background Levels

In the hadronic channel the selection efficiencies within the acceptance are high, typically above 99 %. Backgrounds are dominated by $Z \to \tau^+\tau^-$ and non-resonant $q\overline{q}$ production from two-photon reactions. At the peak of the resonance these together contribute at a level of a few per-mille. Backgrounds in the lepton selections are typically around 1 % for e^+e^- and $\mu^+\mu^-$ and slightly larger for $\tau^+\tau^-$ final states. The dominant background in e^+e^- and $\mu^+\mu^-$ final states arises from $\tau^+\tau^-$ events, a contribution which cancels when the total leptonic cross-section is measured. Backgrounds other than $\tau^+\tau^-$ in the e^+e^- and $\mu^+\mu^-$ channels are of order 0.1 %. Backgrounds in $\tau^+\tau^-$ events are larger, 2–3 %, and arise from low-multiplicity hadronic events, from two-photon reactions and from e^+e^- and $\mu^+\mu^-$ events with small measured lepton

momenta, which may result either from undetected radiated photons or from measurement errors.

An overview of the selection efficiencies within the acceptance and of the background levels is presented in Table 2.1. The acceptances quoted in the table are ideal ones suitable as input to the electroweak program libraries used for fitting, while the actual set of experimental cuts is more complicated. Monte Carlo event generators and detailed detector simulations in combination with corrections derived from studies of the actual data are used to transform the true experimental acceptances to the ideal ones. As is shown in the table, the selection efficiencies are high, above 95 % in e^+e^- and $\mu^+\mu^-$ and 70–90 % in $\tau^+\tau^-$ final states.

	ALEPH	DELPHI	L3	OPAL
$q\overline{q}$ final state				
acceptance	$s'/s > 0.01$	$s'/s > 0.01$	$s'/s > 0.01$	$s'/s > 0.01$
efficiency [%]	99.1	94.8	99.3	99.5
background [%]	0.7	0.5	0.3	0.3
e^+e^- final state				
acceptance	$-0.9 < \cos\theta < 0.7$ $s' > 4m_\tau^2$	$\lvert\cos\theta\rvert < 0.72$ $\eta < 10°$	$\lvert\cos\theta\rvert < 0.72$ $\eta < 25°$	$\lvert\cos\theta\rvert < 0.7$ $\eta < 10°$
efficiency [%]	97.4	97.0	98.0	99.0
background [%]	1.0	1.1	1.1	0.3
$\mu^+\mu^-$ final state				
acceptance	$\lvert\cos\theta\rvert < 0.9$ $s' > 4m_\tau^2$	$\lvert\cos\theta\rvert < 0.94$ $\eta < 20°$	$\lvert\cos\theta\rvert < 0.8$ $\eta < 90°$	$\lvert\cos\theta\rvert < 0.95$ $m_{f\overline{f}}^2/s > 0.01$
efficiency [%]	98.2	95.0	92.8	97.9
background [%]	0.2	1.2	1.5	1.0
$\tau^+\tau^-$ final state				
acceptance	$\lvert\cos\theta\rvert < 0.9$ $s' > 4m_\tau^2$	$0.035 < \lvert\cos\theta\rvert < 0.94$ $s' > 4m_\tau^2$	$\lvert\cos\theta\rvert < 0.92$ $\eta < 10°$	$\lvert\cos\theta\rvert < 0.9$ $m_{f\overline{f}}^2/s > 0.01$
efficiency [%]	92.1	72.0	70.9	86.2
background [%]	1.7	3.1	2.3	2.7

Table 2.1: Ideal acceptances, selection efficiencies* and background contribution at the peak of the resonance (1994 data).
*The lepton selection efficiencies given by the experiments were in some cases quoted with respect to full acceptance in $\cos\theta$; for the purpose of comparison, they were corrected to the fiducial cuts in $\cos\theta$ actually used in the analyses, assuming a shape of the differential cross-section according to $(1 + \cos^2\theta)$.

The idealised acceptances are defined by the scattering angle, θ, of the negatively charged lepton in the laboratory frame, and also require a cut-off for initial-state photon radiation. The latter may either be given by a cut on the acollinearity of the two final-state leptons, η, or by an explicit cut on the invariant mass of the final-state leptons, $m_{f\overline{f}}$; alternatively, the effective centre-of-mass energy after initial-state photon radiation, $\sqrt{s'}$, may be used. The experimental efficiencies for low values of $m_{f\overline{f}}$ or s' are small. Despite the differing definitions, the efficiencies given in the table can nevertheless be directly compared, because the acceptance difference

between the wider definition, $s'/s > 4m_\tau^2$, and a tight definition using an acollinearity cut at $\eta < 10^\circ$ is only 2 %.

Total Cross-Section

The total cross-section for the production of each final state is obtained from the efficiency and background-corrected numbers of selected events normalised to the luminosity. Data taken at the same energy point and within the same year are combined into a single cross-section measurement at the average energy. As an example, the measurements of the hadronic cross-section around the three principal energies are shown in Figure 2.3. Because the hadron statistics are almost ten times larger than the lepton statistics, these measurements dominate the determination of the mass and the width of the Z.

The energy dependence of the hadronic cross-section (the "lineshape") is shown in the upper plot of Figure 1.12 in Section 1.5. The energy dependence of the muon and tau cross-section is nearly identical in shape to the hadronic one. In e^+e^- final states however, diagrams involving photon exchange in the t-channel and their interference with the s-channel diagrams also contribute. The different contributions are shown as a function of centre-of-mass energy in the left-hand plot of Figure 2.4.

2.2.3 Measurements of the Lepton Forward-Backward Asymmetries

The forward-backward asymmetry, $A_{\rm FB}$, is defined by the numbers of events, $N_{\rm F}$ and $N_{\rm B}$, in which the final state lepton goes forward ($\cos\theta_{\ell^-} > 0$) or backward ($\cos\theta_{\ell^-} < 0$) with respect to the direction of the incoming electron, $A_{\rm FB} = (N_{\rm F} - N_{\rm B})/(N_{\rm F} + N_{\rm B})$. This definition of $A_{\rm FB}$ depends implicitly on the acceptance cuts applied on the production polar angle, $\cos\theta$, of the leptons. The measurements of $A_{\rm FB}(\ell^+\ell^-)$ require the determination of $\cos\theta$ and the separation of leptons and anti-leptons based on their electric charges, which are determined from the curvature of the tracks in the magnetic fields of the central detectors. For $\mu^+\mu^-$ and $\tau^+\tau^-$ final states, $A_{\rm FB}$ is actually determined from un-binned maximum-likelihood fits to the differential cross-section distributions of the form $\mathrm{d}\sigma/\mathrm{d}\cos\theta \propto 1 + \cos^2\theta + 8/3 \cdot A_{\rm FB}\cos\theta$. This procedure makes better use of the available information and hence leads to slightly smaller statistical errors. Determined this way the $A_{\rm FB}$ measurements are insensitive to any distortions of the detection efficiency as long as these are not at the same time asymmetric in charge and asymmetric in $\cos\theta$. Examples of the measured angular distributions for the e^+e^- and $\mu^+\mu^-$ final states are shown in Figure 2.5.

The shape of the differential cross-section in the electron final state is more complex due to contributions from the t-channel and the s-t-interference, which lead to a large number of events in which the electron is scattered in the forward direction. A maximum-likelihood fit to obtain $A_{\rm FB}(e^+e^-)$ may be performed after subtracting the t and s-t contributions, but usually the asymmetry is determined from the efficiency-corrected numbers of events with forward and backward-going electrons.

The energy dependence of the forward-backward asymmetry in the $\mu^+\mu^-$ final state is shown in the lower plot of Figure 1.12 above. The forward-backward asymmetry as a function of centre-of-mass energy in the e^+e^- final state including the t and the s-t contributions is illustrated in the right-hand plot of Figure 2.4.

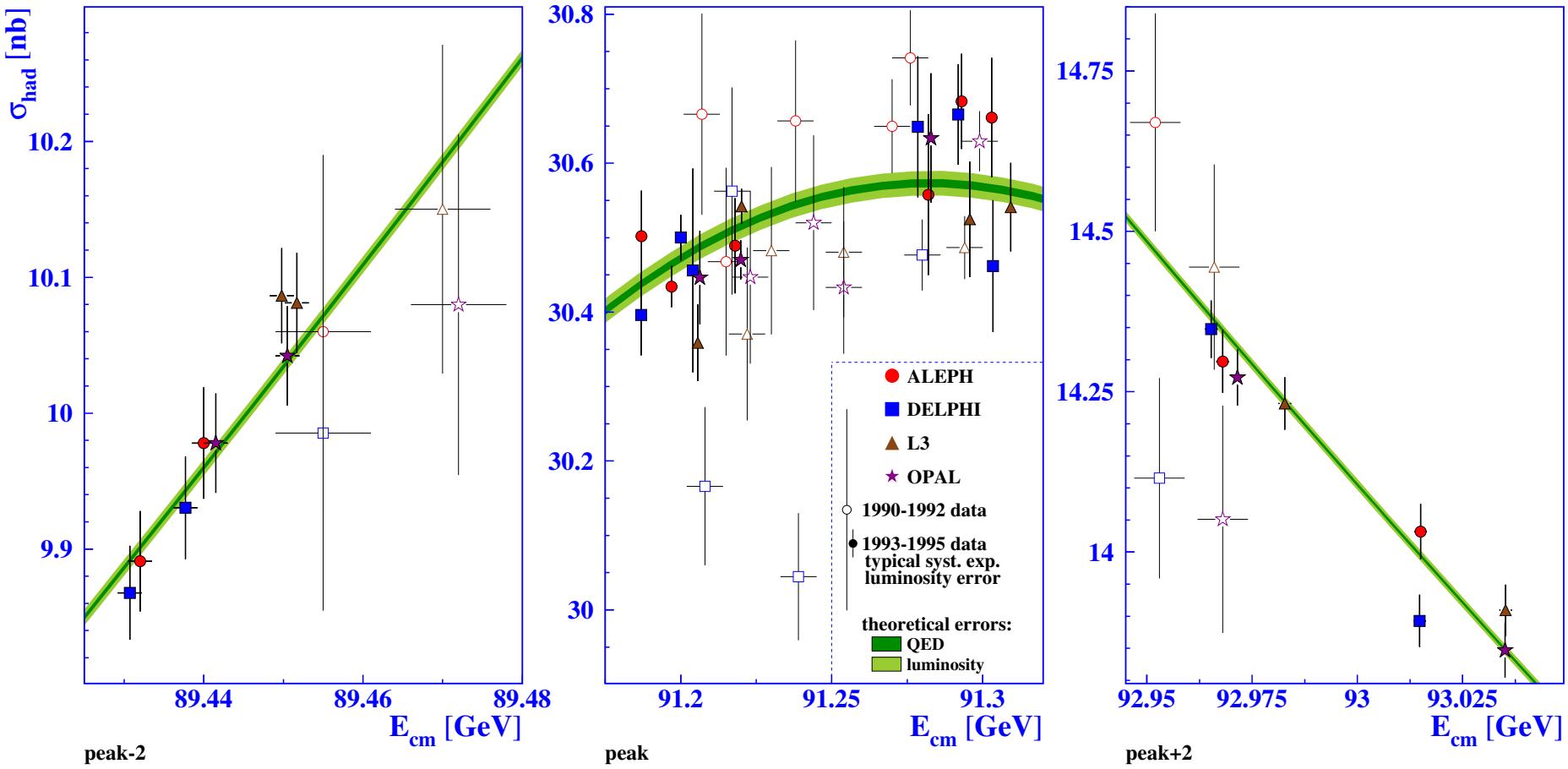

Figure 2.3: Measurements by the four experiments of the hadronic cross-sections around the three principal energies. The vertical error bars show the statistical errors only. The open symbols represent the early measurements with typically much larger systematic errors than the later ones, shown as full symbols. Typical experimental systematic errors on the determination of the luminosity are indicated in the legend; these are almost fully correlated within each experiment, but uncorrelated among the experiments. The horizontal error bars show the uncertainties in LEP centre-of-mass energy, where the errors for the period 1993–1995 are smaller than the symbol size in some cases. The centres of the bands represent the cross-section parametrisation in terms of the combined pseudo-observables of the four experiments. The width of the bands represents the linear superposition of the two most important common theoretical errors from initial-state photon radiation and from the calculations of the small-angle Bhabha cross-section.

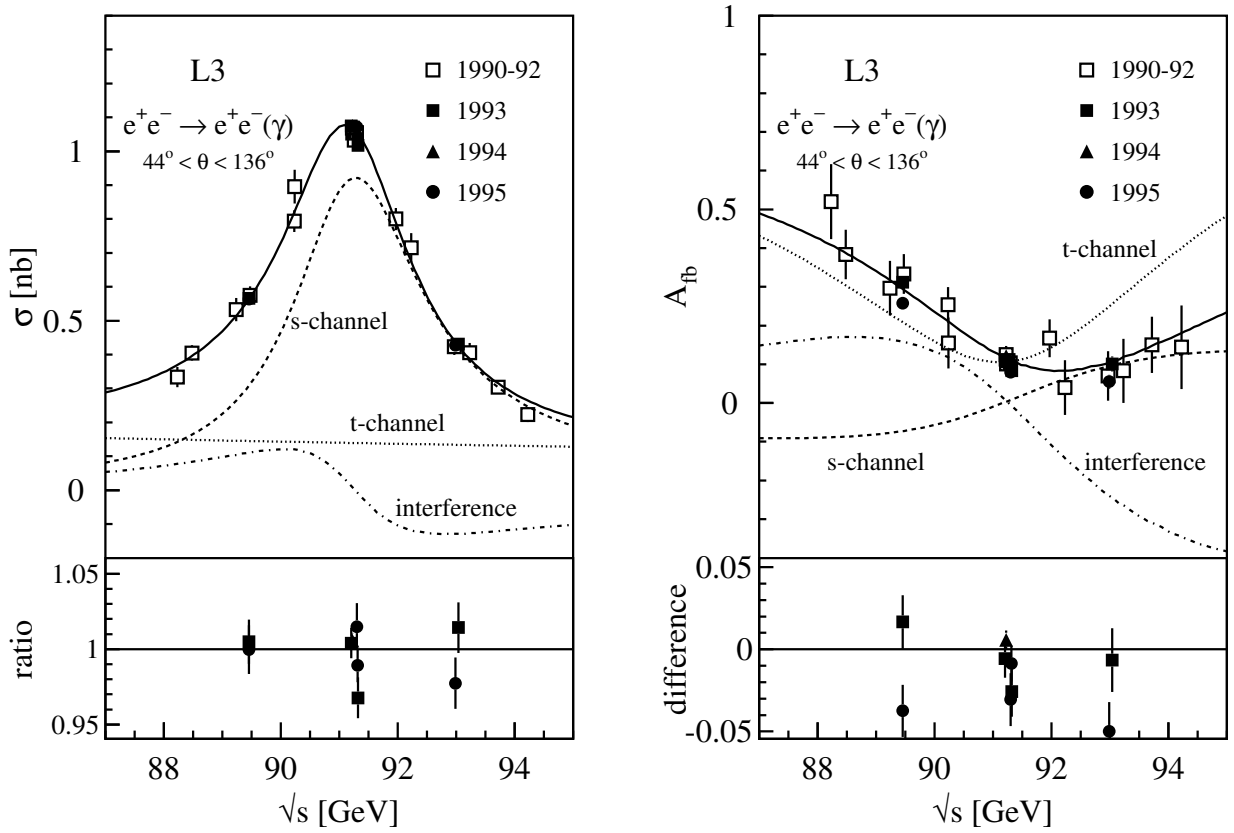

Figure 2.4: The energy dependence and the contributions from the s and t-channel diagrams and from the s-t interference for observables in the e^+e^- channel. Shown are the total cross-section (left) and the difference between the forward and backward cross-sections after normalisation to the total cross-section (right). The data points measured by the L3 collaboration refer to an angular acceptance of $|\cos\theta| < 0.72$, an acollinearity $\eta < 25^\circ$ and a minimum energy of $E_{e^\pm}$>1 GeV. The lines represent the model-independent fit to all L3 data.

2.2.4 Experimental Systematic Errors

In general, the systematic errors arising from the selection procedures are small and so the accumulated statistics can be fully exploited. Furthermore, the purely experimental errors arising from the limited understanding of detector acceptances are uncorrelated among the experiments. An overview of the experimental systematic errors is given in Table 2.2. Statistical errors per experiment on the cross-sections are only around 0.5 per-mille in the hadronic channel and around 2.5 per-mille in each of the three lepton channels. Statistical errors from the number of small-angle Bhabha events affect all channels in a correlated way, but even on-peak they are smaller than those in the hadronic channel by at least a factor of $\sqrt{2}$. Experimental systematic errors on the forward-backward asymmetries are between two and five times smaller than the statistical errors. Errors common to all experiments may arise from the use of common Monte Carlo generators and detector simulation programs. However, each experiment used its own tuning procedures for the QCD parameters determining the simulation of the hadronisation process; furthermore, the physical acceptances of the detectors, the event selection procedures as well as the quantities used to define the acceptances after all cuts vary among the experiments,

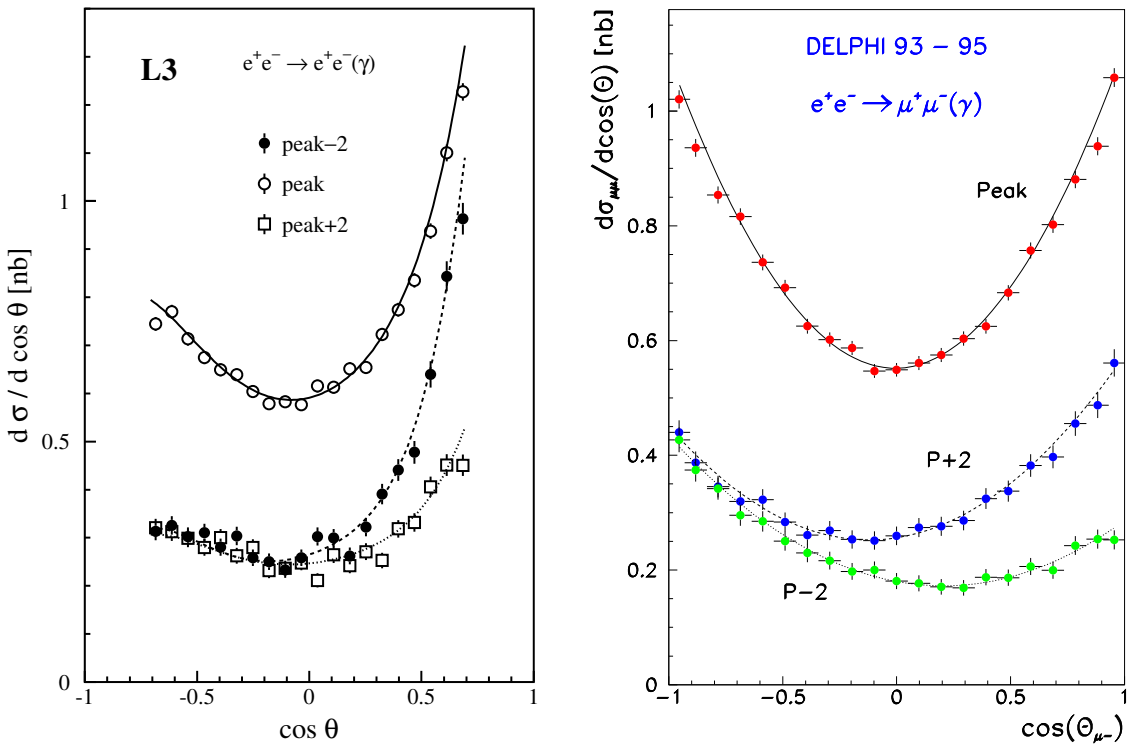

Figure 2.5: Distribution of the production polar angle, $\cos\theta$, for e^+e^- and $\mu^+\mu^-$ events at the three principal energies during the years 1993–1995, measured in the L3 (left) and DELPHI (right) detectors, respectively. The curves show the SM prediction from ALIBABA [52] for e^+e^- and a fit to the data for $\mu^+\mu^-$ assuming the parabolic form of the differential cross-section given in the text.

and therefore the related common errors are small and were neglected in the combination procedure.

Errors arising from limitations in theoretical precision, such as the calculation of the small-angle Bhabha cross-section, the t-channel contribution in the e^+e^- final state or pure QED corrections to the cross-section, are common to all experiments. They are discussed in detail in Section 2.4.

2.2.5 Energy Calibration

Precise knowledge of the centre-of-mass energy is essential for the determination of the mass and width of the Z resonance. The uncertainty in the absolute energy scale, *i. e.* uncertainties correlated between the energy points, directly affect the determination of the Z mass, whereas the Z width is only influenced by the error in the difference in energy between energy points. The determination of the mass and width are completely dominated by the high-statistics scans taken at the off-peak points approximately ±2 GeV away from the resonance in 1993 and 1995, and the errors due to energy calibration are therefore given by

$$\begin{aligned} \Delta m_{\mathrm{Z}} &\approx \tfrac{1}{2}\cdot\Delta(E_{+2}+E_{-2}) \text{ and} \\ \Delta\Gamma_{\mathrm{Z}} &\approx \tfrac{\Gamma_{\mathrm{Z}}}{E_{+2}-E_{-2}}\Delta(E_{+2}-E_{-2})\,. \end{aligned} \tag{2.1}$$

	ALEPH			DELPHI		
	1993	1994	1995	1993	1994	1995
$\mathcal{L}^{\rm exp}$	0.067%	0.073%	0.080%	0.24%	0.09%	0.09%
$\sigma_{\rm had}$	0.069%	0.072%	0.073%	0.10%	0.11%	0.10%
$\sigma_{\rm e}$	0.15%	0.13%	0.15%	0.46%	0.52%	0.52%
σ_{μ}	0.11%	0.09%	0.11%	0.28%	0.26%	0.28%
σ_{τ}	0.26%	0.18%	0.25%	0.60%	0.60%	0.60%
$A^{\rm e}_{\rm FB}$	0.0006	0.0006	0.0006	0.0026	0.0021	0.0020
$A^{\mu}_{\rm FB}$	0.0005	0.0005	0.0005	0.0009	0.0005	0.0010
$A^{\tau}_{\rm FB}$	0.0009	0.0007	0.0009	0.0020	0.0020	0.0020

	L3			OPAL		
	1993	1994	1995	1993	1994	1995
$\mathcal{L}^{\rm exp}$	0.086%	0.064%	0.068%	0.033%	0.033%	0.034%
$\sigma_{\rm had}$	0.042%	0.041%	0.042%	0.073%	0.073%	0.085%
$\sigma_{\rm e}$	0.24%	0.17%	0.28%	0.17%	0.14%	0.16%
σ_{μ}	0.32%	0.31%	0.40%	0.16%	0.10%	0.12%
σ_{τ}	0.68%	0.65%	0.76%	0.49%	0.42%	0.48%
$A^{\rm e}_{\rm FB}$	0.0025	0.0025	0.0025	0.001	0.001	0.001
$A^{\mu}_{\rm FB}$	0.0008	0.0008	0.0015	0.0007	0.0004	0.0009
$A^{\tau}_{\rm FB}$	0.0032	0.0032	0.0032	0.0012	0.0012	0.0012

Table 2.2: Experimental systematic errors for the analyses at the Z peak. The errors are relative for the cross-sections and absolute for the forward-backward asymmetries. None of the common errors discussed in Section 2.4 are included here.

The average momentum of particles circulating in a storage ring is proportional to the magnetic bending field integrated over the path of the particles. The very accurate determination of the average energy of the beams in LEP was based on the technique of resonant spin depolarisation [53, 54], which became available in 1991, after transverse polarisation of the electron beam in LEP had first been observed in 1990 [55] with a Compton polarimeter [56]. Transverse polarisation of single or separated beams due to the Sokolov-Ternov mechanism [16] was observed in LEP after careful adjustment of the beam orbit in order to avoid any static depolarising resonances. The same magnetic bending field seen by the particles along their path leads to precession of the average spin vector of the polarised bunches. The beam energy is therefore proportional to the number of spin precessions per turn, the "spin tune", ν. The spin precession frequency is measured by observing the depolarisation which occurs when an artificial spin resonance is excited with the help of a weak oscillating radial magnetic field. This method offers a very high precision, as good as ± 0.2 MeV, on the beam energy at the time of the measurement. The resolution of the method is illustrated in Figure 2.6, which shows the observed drop in polarisation as a function of the oscillations per turn of the depolarising magnetic field, corresponding to the fractional spin tune of the beam particles.

Measurements with resonant depolarisation were only possible outside normal data taking, typically at the end of fills. About 40% of the recorded off-peak luminosity in the 1993 scan and about 70% in the 1995 scan was taken during fills with at least one such precise calibration of the beam energy. Other techniques had to be employed to extrapolate these calibrations

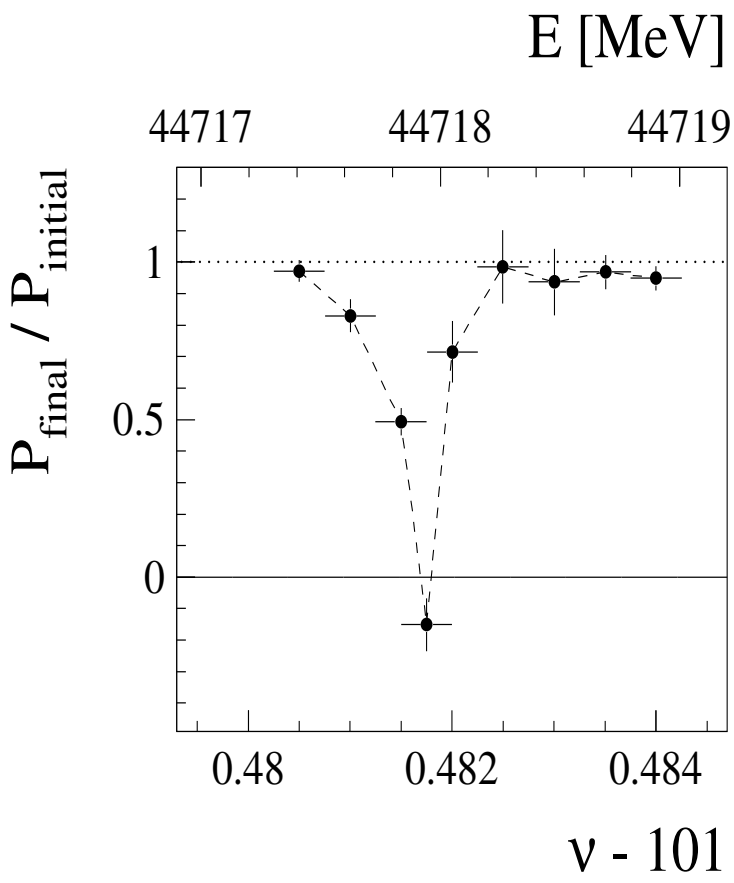

Figure 2.6: Measurement of the width of the artificially excited spin resonance which is used for the energy calibration of LEP (from Reference 54). The drop in the observed polarisation level is shown as a function of the "fractional spin tune", *i. e.* the spin tune ν minus its integer part of 101.

back to earlier times in a fill and to those fills where no calibrations by resonant depolarisation could be made. This required precise knowledge of the values and time evolution of numerous parameters and careful modelling of their impact on the beam energy [14, 15].

For particles on central orbit the magnetic bending field is given by the field produced by the bending dipoles and corrector magnets and by small contributions from the Earth's magnetic field and from remnant fields in the beam pipe. In addition, magnetic fields originating from leakage DC currents produced by trains in the Geneva area had to be taken into account. The magnetic field of the dipoles was initially measured with a single nuclear magnetic resonance probe ("NMR") installed only in a reference dipole on the surface. In 1995, two NMR probes were installed in two of the tunnel dipoles, which measured the magnetic field directly above the beam pipe.

Contributions from the quadrupoles and sextupoles must also be considered if the beam particles do not pass, on average, through the centres of these magnets, i.e. if the particles oscillate around non-central orbits. Because the ultra-relativistic electrons and positrons circulate synchronously with the frequency of the accelerating radio frequency cavities with a speed which is constant to a very high level of precision, the path length per revolution remains constant. Movements of the LEP equipment, caused by geological deformations of the LEP tunnel,

therefore brought the beam orbit away from the central position, where the beam particles now sensed the extra magnetic fields of the quadrupoles. As a consequence, the bending field became different, and the particle energies changed accordingly through changes of their phases relative to the radio frequency clock. Among the identified origins of such movements of the LEP equipment relative to the beam orbit were tidal effects from the Sun and the Moon, the water level in Lake Geneva and rainfall in the Jura Mountains. These could all be tracked by frequent and precise measurements of the beam orbit position inside the LEP beam pipe. An energy model was developed that was able to predict the beam energy at any given time. The quality of this model and remaining uncertainties can be estimated by comparing the energy predicted by the model with the precise energy determinations by resonant depolarisation, as is shown in Figure 2.7.

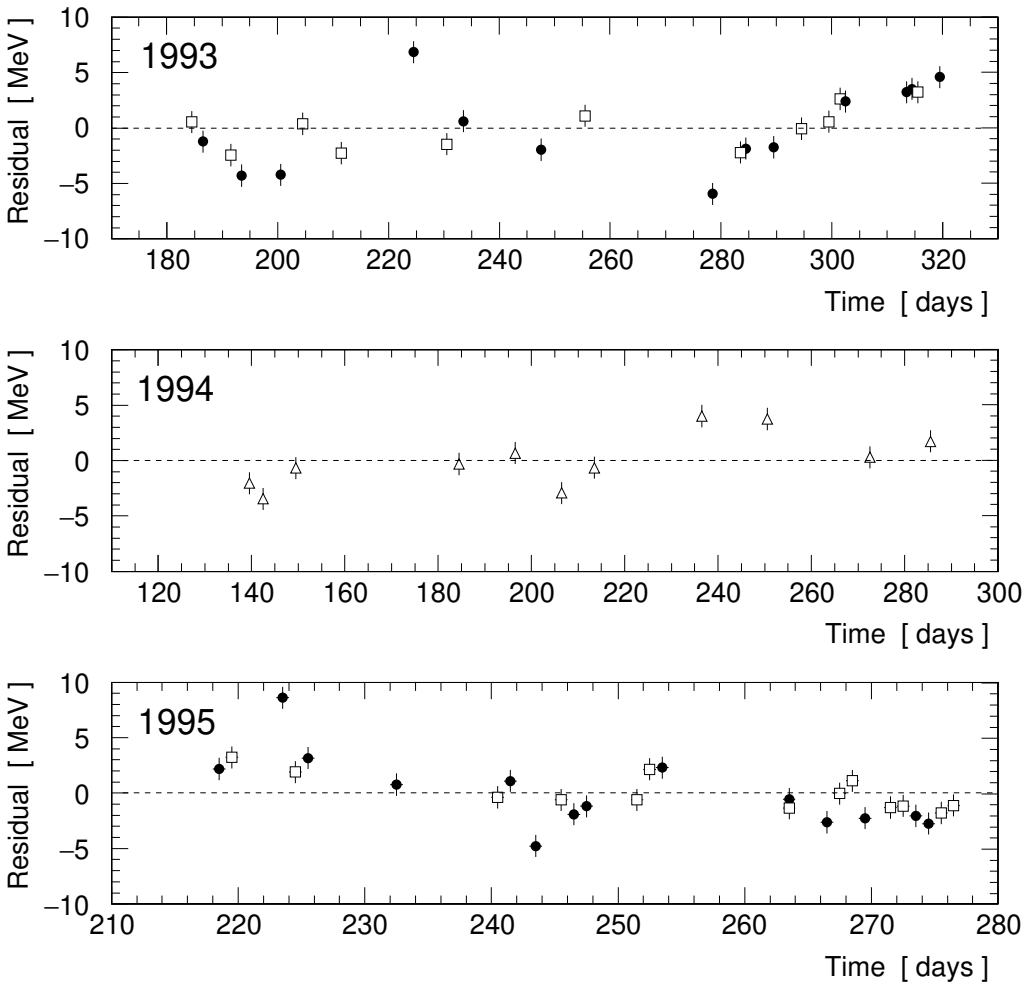

Figure 2.7: Difference between centre-of-mass energies measured by resonant depolarisation and from the energy model (from Reference 15). The black circles are for peak-2, the open triangles for peak energies and the open squares are for peak+2 energy points. The error bars have a size of ± 1 MeV.

In order to obtain the energy of the particles colliding at an interaction point ("IP"), additional effects have to be considered. Figure 2.8 shows the variations of the beam energy of electrons and positrons as they travel round the ring and the large energy corrections at the interaction points. Precise knowledge of all relevant parameters of the radio frequency system

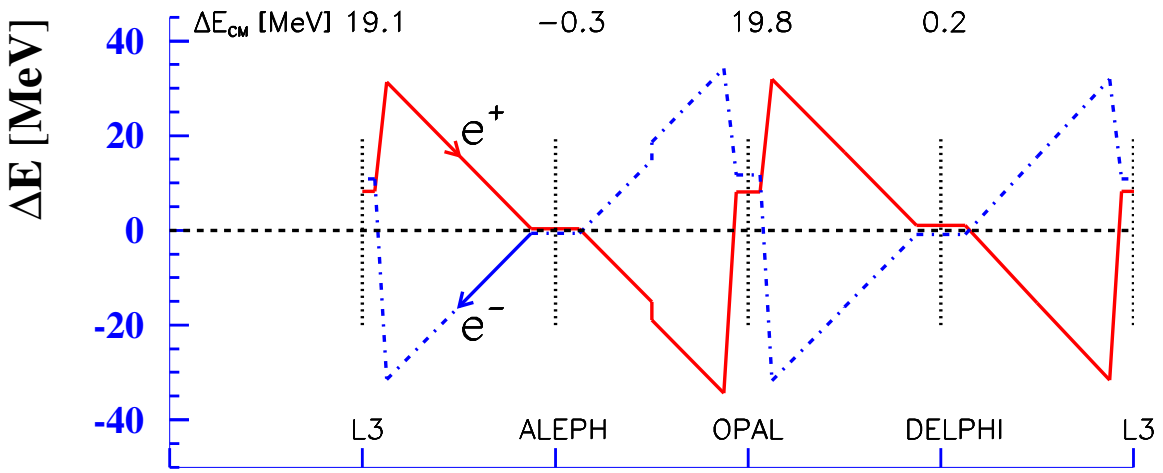

Figure 2.8: Typical variations of the beam energy around the LEP ring during the 1993 run. Energy losses from synchrotron radiation in the arcs, and in wiggler magnets between the ALEPH and OPAL IPs, are compensated by acceleration in the radio frequency cavities mounted in the straight sections on both sides of L3 and OPAL. The detailed modelling results in significant corrections on the centre-of-mass energy at the IPs between acceleration sections, as indicated by the numbers on the top.

at any time is mandatory for the reliable calculation of these corrections in a detailed 'RF model'. Frequent measurements of the synchrotron tune and of beam orbit positions as well as measurements of the position of the collision vertex performed by the experiments and comparisons of these measurements with predictions from the RF model were essential to ensure the internal consistency of all the input parameters and to keep systematic errors small. If the bunches in a collider do not precisely collide head-on at an IP, a possible energy-dependence of the distribution of particle positions in a bunch, so-called "dispersion effects", may lead to shifts in the average collision energy. Due to the operation of LEP in bunch train mode in 1995, unlike-sign dispersion of the colliding electron and positron bunches in the vertical direction was present, which would have led to significant energy displacements of about 2 MeV for collision offsets of one μm between the bunches. Such collision offsets therefore had to be minimised during data-taking, which was achieved by small vertical movements of the beams and adjusting them such that the luminosity was maximised.

For each experiment a value of the beam energy was provided every 15 minutes. Errors on the centre-of-mass energy are largely dominated by the uncertainties in the energy model mentioned above. A summary of the typical size of the main effects and of their contributions to the error is shown in Table 2.3.

The energy errors vary slightly among the interaction points, mainly due to different configurations of the radio frequency cavities. The energy errors for different experiments and data taking periods have large common parts, and therefore the use of a full correlation matrix is necessary. Assuming that all experiments contribute with the same weight allows all the LEP energy errors to be conveniently summarised in a single error matrix, common to all interaction points, as given in Reference 15.

The energy of individual beam particles is usually not at the mean value considered above, but oscillates around the mean energy. Therefore observables are not measured at a sharp energy, E^0_{cm}, but instead their values are averaged over a range in energies $E^0_{cm} \pm \delta E_{cm}$. With the assumption of a Gaussian shape of the energy distribution, the total cross-sections, $\sigma(E_{cm})$,

Origin of correction	Correction to E_{CM} Size [MeV]	Error [MeV]	Error on m_Z [MeV]	Γ_Z [MeV]
Energy measurement by resonant depolarisation		0.5	0.4	0.5
Mean fill energy, from uncalibrated fills		[0.5–5.0]	0.5	0.8
Dipole field changes	up to 20	[1.3–3.3]	1.7	0.6
Tidal deformations	±10	[0.0–0.3]	0.0	0.1
e^+ energy difference	<0.3	0.3	0.2	0.1
Bending field from horizontal correctors	[0–2]	[0.0–0.5]	0.2	0.1
IP dependent RF corrections	[0–20]	[0.5–0.7]	0.4	0.2
Dispersion at IPs	0.5	[0.4–0.7]	0.2	0.1

Table 2.3: Breakdown of effects on the centre-of-mass energy, for illustrative purposes only. The last two columns give the approximate contribution of each effect to the error on m_Z and Γ_Z. The full evaluation of the energy errors used values specific to each year and energy, and also took into account their correlations. (See Reference 15 for a complete discussion.)

receive a correction proportional to δE_{cm}^2 and the second derivative of $\sigma(E_{cm})$ with respect to E_{cm}. At LEP-I, typical values of the centre-of-mass energy spread were around 50 MeV. The effects of the correction lead to an increase of the cross-section at the peak of the Z resonance by 0.16% and a decrease of the width by about 5 MeV. The beam energy spread is affected by the operation of wiggler magnets used to optimise the luminosity. It is also related through some machine parameters to the length of the luminous region at the interaction points, which was precisely measured by the experiments and thus allowed a permanent monitoring of the beam energy spread. Bunch length measurements also served as a cross-check in evaluating the uncertainties on the energy spread from the uncertainties in numerous machine and beam parameters. Uncertainties on the centre-of-mass energy spread were around ±1 MeV in 1993–1995, and constitute an almost negligible source of error common to all experiments.

Changes in the mean beam energy due to changes of machine parameters have an effect similar to the natural beam energy spread. Data taking periods with a very similar centre-of-mass energy were combined into a single energy point in the experimental analyses by performing a luminosity-weighted average. The additional energy spread resulting from this grouping was only around 10 MeV, which is added in quadrature to the natural beam energy spread of the accelerator.

Uncertainties from the energy calibration as described in this subsection and corrections for the beam energy spread were taken into account by all experiments in the fits from which the Z parameters were extracted; the related common uncertainties are discussed in Section 2.4.1.

2.3 Experimental Results

The common set of pseudo-observables used for the parametrisation of the differential cross-section, as described in the introductory chapter, was extracted by each experiment independently from the largely model-independent fits to their measured cross-sections and forward-backward asymmetries [41, 42, 43, 44]. The results presented here deviate slightly from those published by the experiments in order to facilitate the combination procedure. The four dedicated sets of fit results for the combination are summarised in Table 2.4.

		Correlations								
		m_{Z}	Γ_{Z}	σ^0_{had}	R^0_{e}	R^0_{μ}	R^0_{τ}	$A^{0,\mathrm{e}}_{\mathrm{FB}}$	$A^{0,\mu}_{\mathrm{FB}}$	$A^{0,\tau}_{\mathrm{FB}}$
χ^2/dof = 169/176					ALEPH					
m_{Z} [GeV]	91.1891 ± 0.0031	1.000								
Γ_{Z} [GeV]	2.4959 ± 0.0043	0.038	1.000							
σ^0_{had} [nb]	41.558 ± 0.057	−0.091	−0.383	1.000						
R^0_{e}	20.690 ± 0.075	0.102	0.004	0.134	1.000					
R^0_{μ}	20.801 ± 0.056	−0.003	0.012	0.167	0.083	1.000				
R^0_{τ}	20.708 ± 0.062	−0.003	0.004	0.152	0.067	0.093	1.000			
$A^{0,\mathrm{e}}_{\mathrm{FB}}$	0.0184 ± 0.0034	−0.047	0.000	−0.003	−0.388	0.000	0.000	1.000		
$A^{0,\mu}_{\mathrm{FB}}$	0.0172 ± 0.0024	0.072	0.002	0.002	0.019	0.013	0.000	−0.008	1.000	
$A^{0,\tau}_{\mathrm{FB}}$	0.0170 ± 0.0028	0.061	0.002	0.002	0.017	0.000	0.011	−0.007	0.016	1.000
χ^2/dof = 177/168					DELPHI					
m_{Z} [GeV]	91.1864 ± 0.0028	1.000								
Γ_{Z} [GeV]	2.4876 ± 0.0041	0.047	1.000							
σ^0_{had} [nb]	41.578 ± 0.069	−0.070	−0.270	1.000						
R^0_{e}	20.88 ± 0.12	0.063	0.000	0.120	1.000					
R^0_{μ}	20.650 ± 0.076	−0.003	−0.007	0.191	0.054	1.000				
R^0_{τ}	20.84 ± 0.13	0.001	−0.001	0.113	0.033	0.051	1.000			
$A^{0,\mathrm{e}}_{\mathrm{FB}}$	0.0171 ± 0.0049	0.057	0.001	−0.006	−0.106	0.000	−0.001	1.000		
$A^{0,\mu}_{\mathrm{FB}}$	0.0165 ± 0.0025	0.064	0.006	−0.002	0.025	0.008	0.000	−0.016	1.000	
$A^{0,\tau}_{\mathrm{FB}}$	0.0241 ± 0.0037	0.043	0.003	−0.002	0.015	0.000	0.012	−0.015	0.014	1.000
χ^2/dof = 158/166					L3					
m_{Z} [GeV]	91.1897 ± 0.0030	1.000								
Γ_{Z} [GeV]	2.5025 ± 0.0041	0.065	1.000							
σ^0_{had} [nb]	41.535 ± 0.054	0.009	−0.343	1.000						
R^0_{e}	20.815 ± 0.089	0.108	−0.007	0.075	1.000					
R^0_{μ}	20.861 ± 0.097	−0.001	0.002	0.077	0.030	1.000				
R^0_{τ}	20.79 ± 0.13	0.002	0.005	0.053	0.024	0.020	1.000			
$A^{0,\mathrm{e}}_{\mathrm{FB}}$	0.0107 ± 0.0058	−0.045	0.055	−0.006	−0.146	−0.001	−0.003	1.000		
$A^{0,\mu}_{\mathrm{FB}}$	0.0188 ± 0.0033	0.052	0.004	0.005	0.017	0.005	0.000	0.011	1.000	
$A^{0,\tau}_{\mathrm{FB}}$	0.0260 ± 0.0047	0.034	0.004	0.003	0.012	0.000	0.007	−0.008	0.006	1.000
χ^2/dof = 155/194					OPAL					
m_{Z} [GeV]	91.1858 ± 0.0030	1.000								
Γ_{Z} [GeV]	2.4948 ± 0.0041	0.049	1.000							
σ^0_{had} [nb]	41.501 ± 0.055	0.031	−0.352	1.000						
R^0_{e}	20.901 ± 0.084	0.108	0.011	0.155	1.000					
R^0_{μ}	20.811 ± 0.058	0.001	0.020	0.222	0.093	1.000				
R^0_{τ}	20.832 ± 0.091	0.001	0.013	0.137	0.039	0.051	1.000			
$A^{0,\mathrm{e}}_{\mathrm{FB}}$	0.0089 ± 0.0045	−0.053	−0.005	0.011	−0.222	−0.001	0.005	1.000		
$A^{0,\mu}_{\mathrm{FB}}$	0.0159 ± 0.0023	0.077	−0.002	0.011	0.031	0.018	0.004	−0.012	1.000	
$A^{0,\tau}_{\mathrm{FB}}$	0.0145 ± 0.0030	0.059	−0.003	0.003	0.015	−0.010	0.007	−0.010	0.013	1.000

Table 2.4: Individual results on Z parameters and their correlation coefficients from the four experiments. Systematic errors are included here except those summarised in Table 2.9.

All fits are based on versions 6.23 of ZFITTER and 4.4 of TOPAZ0. The published ALEPH results were derived using version 6.10 of ZFITTER, which did not yet contain the improved treatment of fermion pairs radiated from the initial state [57]. For the combination presented here, the ALEPH measurements were re-analysed using version 6.23 of ZFITTER, leading to small changes at the level of a few tenths of MeV in m_{Z} and Γ_{Z}.

While the individual publications were based on the experiment-specific energy error matrices, the combined energy error matrix described above [15] was used in the fits for the input to the combination. This makes a small difference at the level of 0.1 MeV on m_{Z} and Γ_{Z} and their errors for L3 only, where uncertainties arising from the modelling of the radio frequency cavities are largest.

The calculated s-t interference in the Bhabha final state has a small dependence on the assumed value of the Z mass. Although this is practically negligible for a single experiment, a consistent treatment becomes important for the combination. Despite some different choices in the publications of the individual analyses, all experiments evaluated the t,s-t channel correction at their own value of m_{Z} for the results presented here. The resulting interdependencies between the Z mass and the parameters from the Bhabha final state are explicitly included in the error correlation coefficients between m_{Z} and R^0_{e} or $A^{0,\mathrm{e}}_{\mathrm{FB}}$.

The LEP experiments agreed to use a standard set of parameters for the calculation of the SM remnants (see Section 1.5.4) in the theory programs. The important parameters are the Z mass, $m_{\mathrm{Z}} = 91.187$ GeV, the Fermi constant, $G_{\mathrm{F}} = 1.16637 \cdot 10^{-5}$ GeV^{-2}, the electromagnetic coupling constant, $\alpha(m^2_{\mathrm{Z}}) = 1/128.886$,[2] the strong coupling constant, $\alpha_s(m^2_{\mathrm{Z}}) = 0.119$, the top quark mass, $m_{\mathrm{t}} = 175$ GeV, and finally the Higgs mass, $m_{\mathrm{H}} = 150$ GeV. The dependence of the fit results arising from uncertainties in these parameters is negligible except for m_{H}, as discussed in Section 2.4.4.

All experiments also provided fits to their measured cross-sections and asymmetries with lepton universality imposed, *i. e.* R^0_{e}, R^0_{μ} and R^0_{τ} are replaced by R^0_{ℓ}, and $A^{0,\mathrm{e}}_{\mathrm{FB}}$, $A^{0,\mu}_{\mathrm{FB}}$ and $A^{0,\tau}_{\mathrm{FB}}$ are replaced by $A^{0,\ell}_{\mathrm{FB}}$ in the model-independent parametrisation of the differential cross-section. Here R^0_{ℓ} is not a simple average over the three lepton species, but refers to Z decays into pairs of a single massless charged lepton species. The individual experimental results and the correlation matrices are given in Table 2.5. A graphical overview of the results is given in Figure 2.9; the averages are those discussed in Section 2.5 below.

Compared with the nine-parameter results of Table 2.4, there is a noticeable change in m_{Z} of a few tenths of MeV in all experiments. This is a consequence of the dependence of the t-channel correction on m_{Z}, as discussed in Section 2.4.2. When R^0_{e} and $A^{0,\mathrm{e}}_{\mathrm{FB}}$ are replaced by the leptonic quantities R^0_{ℓ} and $A^{0,\ell}_{\mathrm{FB}}$, their correlation with the Z mass leads to a shift, which is driven by the (statistical) difference between R^0_{e} and R^0_{ℓ} and $A^{0,\mathrm{e}}_{\mathrm{FB}}$ and $A^{0,\ell}_{\mathrm{FB}}$. Similarly, replacing R^0_{e} and $A^{0,\mathrm{e}}_{\mathrm{FB}}$ from the values of a single experiment by the LEP average introduces a shift in m_{Z} in the presence of these particular correlation coefficients. Such a shift should be smaller when averaged over the four experiments, and indeed this is observed with the average of the shifts being only -0.2 MeV.

[2] This corresponds to a value of the correction due to hadronic vacuum polarisation of $\Delta\alpha^{(5)}_{\mathrm{had}} = 0.02804 \pm 0.00065$ [58]. Note that a more precise value of $\Delta\alpha^{(5)}_{\mathrm{had}} = 0.02758 \pm 0.00035$ [59] became available after these analyses had been finalised.

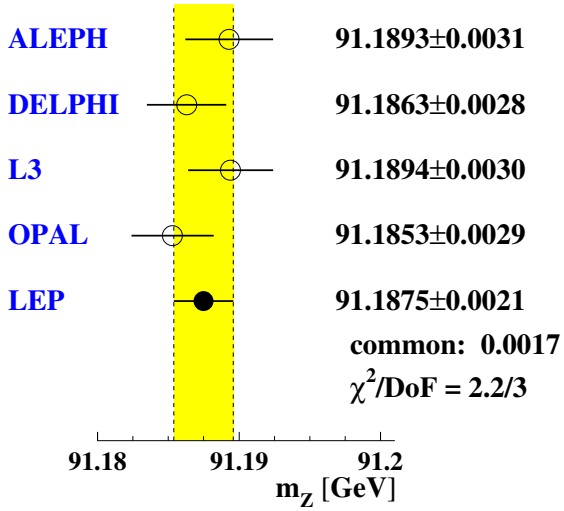

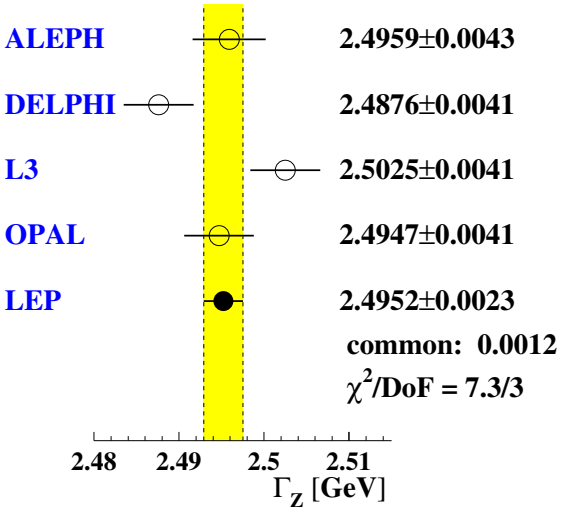

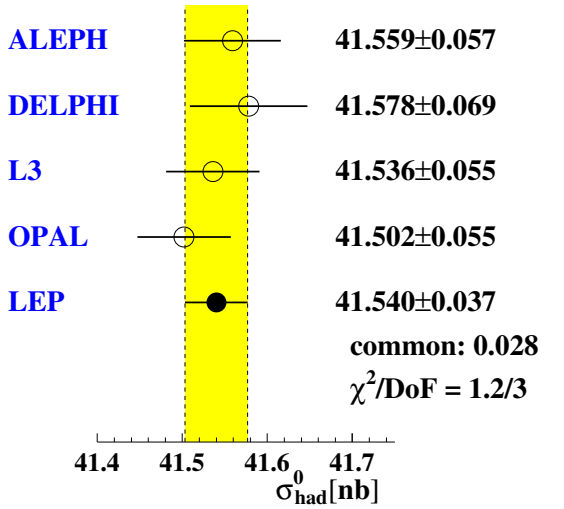

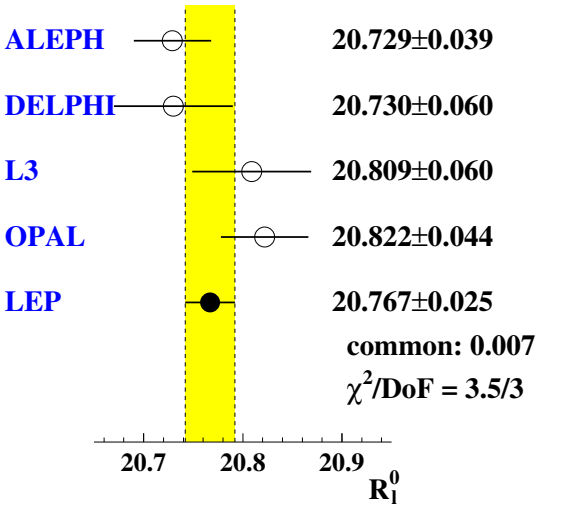

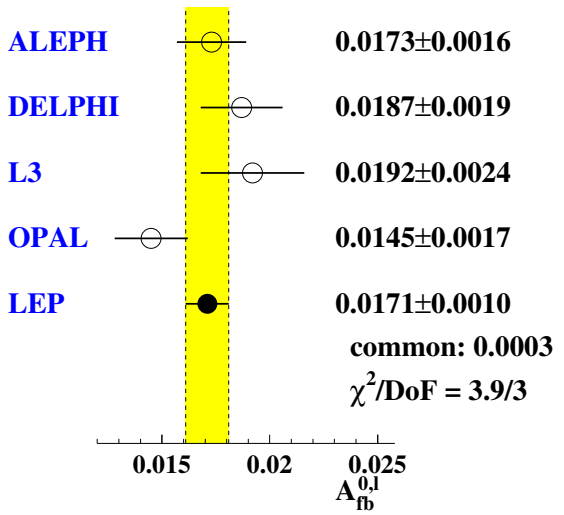

Figure 2.9: Measurements of m_{Z}, Γ_{Z}, σ^0_{had}, R^0_ℓ and $A^{0,\ell}_{\mathrm{FB}}$. The averages indicated were obtained using the common errors and combination method discussed in the text. The values of χ^2 per degree of freedom were calculated considering error correlations between measurements of the same parameter, but not error correlations between different parameters.

		Correlations				
		$m_{\rm Z}$	$\Gamma_{\rm Z}$	$\sigma^0_{\rm had}$	R^0_ℓ	$A^{0,\ell}_{\rm FB}$
χ^2/dof = 172/180		ALEPH				
$m_{\rm Z}$ [GeV]	91.1893 ± 0.0031	1.000				
$\Gamma_{\rm Z}$ [GeV]	2.4959 ± 0.0043	0.038	1.000			
$\sigma^0_{\rm had}$ [nb]	41.559 ± 0.057	−0.092	−0.383	1.000		
R^0_ℓ	20.729 ± 0.039	0.033	0.011	0.246	1.000	
$A^{0,\ell}_{\rm FB}$	0.0173 ± 0.0016	0.071	0.002	0.001	−0.076	1.000
χ^2/dof = 183/172		DELPHI				
$m_{\rm Z}$ [GeV]	91.1863 ± 0.0028	1.000				
$\Gamma_{\rm Z}$ [GeV]	2.4876 ± 0.0041	0.046	1.000			
$\sigma^0_{\rm had}$ [nb]	41.578 ± 0.069	−0.070	−0.270	1.000		
R^0_ℓ	20.730 ± 0.060	0.028	−0.006	0.242	1.000	
$A^{0,\ell}_{\rm FB}$	0.0187 ± 0.0019	0.095	0.006	−0.005	0.000	1.000
χ^2/dof = 163/170		L3				
$m_{\rm Z}$ [GeV]	91.1894 ± 0.0030	1.000				
$\Gamma_{\rm Z}$ [GeV]	2.5025 ± 0.0041	0.068	1.000			
$\sigma^0_{\rm had}$ [nb]	41.536 ± 0.055	0.014	−0.348	1.000		
R^0_ℓ	20.809 ± 0.060	0.067	0.020	0.111	1.000	
$A^{0,\ell}_{\rm FB}$	0.0192 ± 0.0024	0.041	0.020	0.005	−0.024	1.000
χ^2/dof = 158/198		OPAL				
$m_{\rm Z}$ [GeV]	91.1853 ± 0.0029	1.000				
$\Gamma_{\rm Z}$ [GeV]	2.4947 ± 0.0041	0.051	1.000			
$\sigma^0_{\rm had}$ [nb]	41.502 ± 0.055	0.030	−0.352	1.000		
R^0_ℓ	20.822 ± 0.044	0.043	0.024	0.290	1.000	
$A^{0,\ell}_{\rm FB}$	0.0145 ± 0.0017	0.075	−0.005	0.013	−0.017	1.000

Table 2.5: Results on Z parameters and error correlation matrices from the four experiments, with lepton universality imposed. Systematic errors are included here except those summarised in Table 2.9.

2.4 Common Uncertainties

Important common errors among the results from all LEP experiments arise from several sources. These include the calibration of the beam energy, the theoretical error on the calculation of the small-angle Bhabha cross-section used as the normalisation reaction, the theoretical uncertainties in the t-channel and s-t interference contribution to the differential large-angle Bhabha cross-section, the theoretical uncertainties in the calculations of QED radiative effects and, finally, from small uncertainties in the parametrisation of the electroweak cross-section near the Z resonance in terms of the standard set of pseudo-observables. These common errors are quantified below and are used in the combination.

For the purpose of combining the experimental results at the parameter level, the common sources of error on each individual cross-section or asymmetry measurement need to be transformed into errors on the extracted pseudo-observables. A popular method to measure the contribution of an error component of an input quantity on a fit parameter is to set the input error to zero and repeat the fit. However, this will also lead to shifts in central values if the

omitted error component is large. Such shifts indicate that the internal weighting of inputs has changed, and the estimated error contribution may be wrong. A better method therefore is to examine the changes in the error matrices resulting from special fits with only slightly modified input errors. The contribution of each input error component to the full covariance matrix of the fit parameters can then be determined under the constraint of maintaining the weights at their actual values. This method will be used and illustrated more clearly in the following sections.

2.4.1 Energy Calibration Uncertainties

The first step in the determination of common energy related uncertainties on the pseudo-observables is for each experiment to scale the energy errors by factors of $1\pm\epsilon$, while maintaining the experimental errors fixed. Typical values of ϵ used are between 5 % and 20 %. Performing the standard fits to the cross-section and asymmetry measurements with these scaled errors generates two pseudo-observable covariance matrices, $V_\pm$, from which the covariance matrix due to energy errors, V_E, can be separated from the other errors, $V_{\rm exp}$, using the relation $(V_\pm) = (1\pm\epsilon)^2(V_E)+(V_{\rm exp})$. The validity of this procedure was verified using a data set restricted to the hadronic cross-section measurements of the years 1993–1995, which were combined both at the cross-section level and at the parameter level.

The estimated energy errors differ only slightly depending on which experimental data set is used to derive them. Combinations may be attempted based on each of them, or on the average. For all such choices the central values and errors of each of the averaged parameters agree to well within 5 % of the error. It is therefore most appropriate to take the average of the error estimates over the experiments as the common energy errors, which are shown in Table 2.6.

	$m_{\rm Z}$	$\Gamma_{\rm Z}$	$\sigma^0_{\rm had}$	$R^0_{\rm e}$
$m_{\rm Z}$ [GeV]	0.0017			
$\Gamma_{\rm Z}$ [GeV]	−0.0006	0.0012		
$\sigma^0_{\rm had}$ [nb]	−0.0018	−0.0027	0.011	
$R^0_{\rm e}$	0.0017	−0.0014	0.0073	0.013

	$A^{0,\rm e}_{\rm FB}$	$A^{0,\mu}_{\rm FB}$	$A^{0,\tau}_{\rm FB}$
$A^{0,\rm e}_{\rm FB}$	0.0004		
$A^{0,\mu}_{\rm FB}$	−0.0003	0.0003	
$A^{0,\tau}_{\rm FB}$	−0.0003	0.0003	0.0003

Table 2.6: Common energy errors for nine-parameter fits. Values are given as the signed square root of the covariance matrix elements; elements above the diagonal have been omitted for simplicity. The anti-correlation between electron and muon or tau asymmetries arises from the different energy dependence of the electron asymmetry due to the t-channel contribution.

2.4.2 Uncertainties Related to the t-Channel

The t channel and s-t interference contributions are calculated in the SM using the programs ALIBABA [52] and TOPAZ0 [30]. The theoretical uncertainty on the t-channel correction is discussed in detail in Reference 60. The size of the uncertainty is typically 1.1 pb for the forward cross-section and 0.3 pb for the backward cross-section and depends slightly on the acceptance cuts [61]. All collaborations incorporate the theory uncertainty as an additional error on the electron pair cross-section and asymmetry. In order to evaluate the common error due to the t, s-t theory error, each collaboration performed two fits, with and without the theory error,

and the quadratic differences of the covariance matrix elements for $R_{\rm e}^0$ and $A_{\rm FB}^{0,\rm e}$ are taken as an estimate of the common error. The unknown error correlation between energy points below and above the peak is included in the error estimates by adding in quadrature the observed shifts in mean values of $R_{\rm e}^0$ and $A_{\rm FB}^{0,\rm e}$ when varying this correlation between -1 and $+1$. The t, s-t related errors estimated by individual experiments are all very similar, and therefore the average is taken as the common error matrix, as shown in Table 2.7.

	$R_{\rm e}^0$	$A_{\rm FB}^{0,\rm e}$
$R_{\rm e}^0$	0.024	
$A_{\rm FB}^{0,\rm e}$	-0.0054	0.0014

Table 2.7: Common uncertainties arising from the t channel and s-t interference contribution to the $\rm e^+e^-$ final states, given as the signed square root of the covariance matrix elements.

The s-t interference contribution to the t-channel correction in Bhabha final states depends on the value of the Z mass. For the purpose of this combination, all experiments parametrise the t and s-t contributions as a function of $m_{\rm Z}$. This allows the t, s-t correction to follow the determination of $m_{\rm Z}$ in the fits, which results in correlations between $m_{\rm Z}$ and $R_{\rm e}^0$ or $A_{\rm FB}^{0,\rm e}$. Typical changes of the correlation coefficients amount to about $+10\,\%$ for the correlation $m_{\rm Z}$–$R_{\rm e}^0$ and $-10\,\%$ for $m_{\rm Z}$–$A_{\rm FB}^{0,\rm e}$. The presence of these correlations induces changes in $R_{\rm e}^0$ and $A_{\rm FB}^{0,\rm e}$ when $m_{\rm Z}$ takes its average value in the combination of the four experiments.

2.4.3 Luminosity Uncertainties

The four collaborations use similar techniques to measure the luminosity of their data samples by counting the number of small-angle Bhabha-scattered electrons. The experimental details of the four measurements are sufficiently different that no correlations are considered to exist in the experimental component of the luminosity errors. All four collaborations, however, use BHLUMI 4.04 [23], the best available Monte Carlo generator for small-angle Bhabha scattering, to calculate the accepted cross-section of their luminosity counters. Therefore significant correlations exist in the errors assigned to the scale of the measured cross-sections due to the uncertainty in this common theoretical calculation.

The total theoretical uncertainty, including an estimate large enough to cover the entire contribution from light fermion pair production, which is not included in BHLUMI, is $0.061\,\%$ [62]. The contribution of light pairs has been calculated [63], and explicit inclusion of this effect allowed OPAL to reduce the theoretical uncertainty to $0.054\,\%$. This $0.054\,\%$ error is taken to be fully correlated with the errors of the other three experiments, which among themselves share a mutual correlated error of $0.061\,\%$.

These errors affect almost exclusively the hadronic pole cross-section, and contribute about half its total error after combination. The common luminosity error also introduces a small contribution to the covariance matrix element between $\Gamma_{\rm Z}$ and $\sigma_{\rm had}^0$. This correlation was neglected in the common error tables given above, as it had no noticeable effect on the combined result.

2.4.4 Theory Uncertainties

An additional class of common theoretical errors arises from the approximations and special choices made in the fitting codes. These comprise contributions from QED radiative corrections, including initial-state pair radiation, and the parametrisation of the differential cross-section around the Z resonance in terms of pseudo-observables defined precisely at the peak and for pure Z exchange only. In order to estimate the uncertainties from the parametrisation of the electroweak cross-sections near the Z resonance the two most advanced calculational tools, TOPAZ0 [30] and ZFITTER [31] were compared. In addition, there are "parametric uncertainties" arising from parameters of the SM that are needed to fix the SM remnants.

QED Uncertainties

The effects of initial state radiation (ISR) are more than two orders of magnitude larger than the experimental precision, which is below the per-mille level in the case of the hadronic cross-section. The radiation of fermion pairs (ISPP), although much smaller than ISR in absolute effect, exhibits a larger uncertainty. Therefore these corrections play a central role in the extraction of the pseudo-observables from the measured cross-sections and asymmetries.

The most up-to-date evaluations of photonic corrections to the measurements are complete in $\mathcal{O}(\alpha^2)$ and for the total cross-sections also include the leading contributions up to $\mathcal{O}(\alpha^3)$. Two different schemes are available to estimate the remaining uncertainties:

1. KF: $\mathcal{O}(\alpha^2)$ calculations [64] including the exponentiation scheme of Kuraev-Fadin [65] with $\mathcal{O}(\alpha^3)$ [66].[3]

2. YFS: the 2$^{\text{nd}}$ order inclusive exponentiation scheme of References 68 and 67, based on the YFS approach [69]. Third order terms are also known and have only a small effect [70].

Differences between these schemes, which are both implemented in TOPAZ0, ZFITTER and MIZA [71], and uncertainties due to missing higher order corrections [70], amount to at most ± 0.1 MeV on m_{Z} and Γ_{Z}, and $\pm 0.01\,\%$ on σ^0_{had}.

The influence of the interference between initial and final state radiation on the extracted parameters has also been studied [72], and uncertainties on m_{Z} of at most ± 0.1 MeV from this source are expected for experimental measurements which accept events down to small values of s', the effective squared centre-of-mass energy after photon radiation from the initial state. The methods for the extrapolation of the leptonic s-channel cross-sections to full angular acceptance and from large to small s' differ among the experiments and therefore the resulting uncertainties are believed to be largely uncorrelated.

Although contributing only 1 % of the ISR correction, the radiation of fermion pairs from the initial state dominates the QED related uncertainties. Starting from the full second order pair radiator [64, 73], a simultaneous exponentiation scheme for radiated photons and pairs was proposed in Reference 74. A third-order pair radiator was calculated [57] and compared with the other existing schemes, which are all available in ZFITTER since version 6.23. Independent implementations of some schemes exist in TOPAZ0 and in MIZA. The largest uncertainty arises from the sub-sub-leading terms of the third order and from the approximate treatment of hadronic pairs. The maximum differences are 0.3 MeV on m_{Z}, 0.2 MeV on Γ_{Z} and 0.015 % on σ^0_{had}.

[3] Third-order terms for the KF scheme had also been calculated previously [67].

In summary, comparing the different options for photonic and fermion-pair radiation leads to error estimates of ± 0.3 MeV on m_{Z} and ± 0.2 MeV on Γ_{Z}. The observed differences in σ^0_{had} are slightly smaller than the error estimate of $\pm 0.02\,\%$ in Reference 70, which is therefore taken as the error for the QED-related uncertainties.

Choice of Parametrisation of Lineshape and Asymmetries

In a very detailed comparison [75] of TOPAZ0 and ZFITTER, cross-sections and asymmetries from SM calculations and from differing choices in the model-independent parametrisation were considered. Uncertainties on the fitted pseudo-observables may be expected to arise from these choices in parametrisation of the electroweak cross-sections near the Z resonance. To evaluate such differences, cross-sections and forward-backward asymmetries were calculated with TOPAZ0 and these results fitted with ZFITTER. Errors were assigned to the calculated cross-sections and forward-backward asymmetries which reflect the integrated luminosity taken at each energy, thus ensuring that each energy point entered with the appropriate weight.

The dominant part of the small differences between the two codes results from details of the implementation of the cross-section parametrisation in terms of the pseudo-observables. This is particularly visible for the off-peak points, where the assignment of higher-order corrections to the Z resonance or to the SM remnants is not in all cases unambiguous. The size of the differences also depends on the particular values of the pseudo-observables, since these do not necessarily respect the exact SM relations. Slightly different choices are made in the two codes if the SM relations between the pseudo-observables are not fulfilled. Finally, variations of factorisation schemes and other options in the electroweak calculations may affect the fit results through the SM remnants, but were found to have a negligible effect.

In Table 2.8 differences between TOPAZ0 and ZFITTER are shown, which are taken as systematic uncertainties. They were evaluated around the set of pseudo-observables representing the average of the four experiments; cross-sections and asymmetries were calculated for full acceptance with only a cut on $s' > 0.01\,s$. The only non-negligible systematic error of this kind is that on R^0_ℓ, which amounts to 15 % of the combined error.

Δm_{Z} [GeV]	$\Delta\Gamma_{\mathrm{Z}}$ [GeV]	$\Delta\sigma^0_{\mathrm{had}}$ [nb]	ΔR^0_ℓ	$\Delta A^{0,\ell}_{\mathrm{FB}}$
0.0001	0.0001	0.001	0.004	0.0001

Table 2.8: Differences in fit results obtained with TOPAZ0 and ZFITTER, taken as part of the common systematic errors.

Putting all sources together, the overall theoretical errors as listed in Table 2.9 are obtained, and these are used as common errors in the combination.

Parametric Uncertainties

Through the SM remnants the fit results depend slightly on the values of some SM parameters. Varying these within their present experimental errors, or between 100 GeV and 1000 GeV in case of the Higgs boson mass, leads to observable effects only on the Z mass, which is affected through the γ–Z interference term. The dominant dependence is on m_{H}, followed by $\alpha^{(5)}_{\mathrm{had}}(m^2_{\mathrm{Z}})$.

	m_{Z}	Γ_{Z}	σ^0_{had}	R^0_{e}	R^0_{μ}	R^0_{τ}	$A^{0,\mathrm{e}}_{\mathrm{FB}}$	$A^{0,\mu}_{\mathrm{FB}}$	$A^{0,\tau}_{\mathrm{FB}}$
m_{Z}[GeV]	0.0003								
Γ_{Z}[GeV]		0.0002							
σ^0_{had}[nb]			0.008						
R^0_{e}				0.004					
R^0_{μ}				0.004	0.004				
R^0_{τ}				0.004	0.004	0.004			
$A^{0,\mathrm{e}}_{\mathrm{FB}}$							0.0001		
$A^{0,\mu}_{\mathrm{FB}}$							0.0001	0.0001	
$A^{0,\tau}_{\mathrm{FB}}$							0.0001	0.0001	0.0001

Table 2.9: Common theoretical errors due to photon and fermion-pair radiation and the choice of model-independent parametrisation, given as the signed square root of the covariance matrix elements.

The effect on m_{Z} from a variation of $\Delta\alpha^{(5)}_{\mathrm{had}}(m^2_{\mathrm{Z}})$ by its error of ± 0.00065 is ± 0.05 MeV, which is negligibly small compared to the systematic error on m_{Z} arising from other QED-related uncertainties (see Table 2.9). The change in m_{Z} due to m_{H} amounts to $+0.23$ MeV per unit change in $\log_{10}(m_{\mathrm{H}}/\mathrm{GeV})$. Note that this is small compared to the total error on m_{Z} of ± 2.1 MeV and is not considered as an error, but rather as a correction to be applied if and when a SM Higgs boson is found and its mass measured. The consequences of a completely model-independent treatment of the γ–Z interference in the hadronic channel are discussed in Section 2.5.3.

2.5 Combination of Results

The combination of results on the Z parameters is based on the four sets of nine parameters m_{Z}, Γ_{Z}, σ^0_{had}, R^0_{e}, R^0_{μ}, R^0_{τ}, $A^{0,\mathrm{e}}_{\mathrm{FB}}$, $A^{0,\mu}_{\mathrm{FB}}$ and $A^{0,\tau}_{\mathrm{FB}}$ and the common errors given in the previous chapter.

For this purpose it is necessary to construct the full $(4\times 9)\times(4\times 9)$ covariance matrix of the errors. The four on-diagonal 9×9 matrices consist of the four error matrices specified by each experiment (Table 2.4). The 9×9 common error matrices build the off-diagonal elements.

A symbolic representation of the full error matrix is shown in Table 2.10. Each table element represents a 9×9 matrix; $(\mathcal{C}_{exp})$ for exp = A, D, L and O are the covariance matrices of the experiments (see Table 2.4), and $(\mathcal{C}_c) = (\mathcal{C}_E) + (\mathcal{C}_{\mathcal{L}}) + (\mathcal{C}_t) + (\mathcal{C}_{\mathrm{QED,th}})$ is the matrix of common errors. $(\mathcal{C}_E)$ (Table 2.6) is the error matrix due to LEP energy uncertainties, $(\mathcal{C}_{\mathcal{L}})$ (Section 2.4.3) arises from the theoretical error on the small-angle Bhabha cross-section calculations, $\mathcal{C}_t$ (Table 2.7) contains the errors from the t-channel treatment in the $\mathrm{e^+e^-}$ final state, and $(\mathcal{C}_{\mathrm{QED,th}})$ contains the errors from initial state photon and fermion pair radiation and from the model-independent parametrisation (Table 2.9). Since the latter errors were not included in the experimental error matrices, they were also added to the block matrices in the diagonal of Table 2.10.

The combined parameter set and its covariance matrix are obtained from a χ^2 minimisation, with

$$\chi^2 \;=\; (\mathbf{X}-\mathbf{X_m})^T(\mathcal{C})^{-1}(\mathbf{X}-\mathbf{X_m}); \tag{2.2}$$

$(\mathcal{C})$	ALEPH	DELPHI	L3	OPAL
A	$(\mathcal{C}_A) + (\mathcal{C}_{\rm QED,th})$			
D	(C_c)	$(\mathcal{C}_D) + (\mathcal{C}_{\rm QED,th})$		
L	(C_c)	(C_c)	$(\mathcal{C}_L) + (\mathcal{C}_{\rm QED,th})$	
O	(C_c)	(C_c)	(C_c)	$(\mathcal{C}_O) + (\mathcal{C}_{\rm QED,th})$

Table 2.10: Symbolic representation of the covariance matrix, $(\mathcal{C})$, used to combine the lineshape and asymmetry results of the four experiments. The components of the matrix are explained in the text.

$(\mathbf{X} - \mathbf{X_m})$ is the vector of residuals of the combined parameter set to the individual results.

Some checks of the combination procedure outlined above are described in the following subsections, and the combined results are given in the tables of Section 2.6.

2.5.1 Multiple Z-Mass Fits

In 1993 and 1995, the two years when LEP performed precision energy scans to measure the Z lineshape, the experimental errors are very comparable, but the LEP energy was appreciably better understood in 1995 than in 1993. For a single experiment the errors are not dominated by those from the energy. This changes if the combined data set is considered, since then energy errors are comparable in size to the combined experimental errors. In determining the optimum value of $m_{\rm Z}$ in a statistical sense, therefore, more weight should be given to the 1995 data for four experiments combined than is given to the 1995 data in the independent determinations. To quantify this issue the measurements of each experiment were fit to determine independent values of $m_{\rm Z}$ for the three periods 1990–1992, 1993–1994 and 1995. In this "eleven-parameter fit", each of the three mass values $m_{\rm Z}^{90-92}$, $m_{\rm Z}^{93-94}$ and $m_{\rm Z}^{95}$ has its specific energy error reflecting the different systematic errors on the absolute energy scale of LEP. The combination of these four sets of 11 parameters was carried out and thus the relative importance of energy-related and independent experimental errors on the mass values is properly treated.

When the three values of $m_{\rm Z}$ are condensed into one, the effects of the time dependence of the precision in the energy calibration are taken into account. The difference of -0.2 MeV from the $m_{\rm Z}$ value from the nine-parameter fits corresponds to 10 % of the combined error. All other parameters are identical to their values from the nine-parameter fit to within less than 5 % of the combined error. This result justifies using the standard combination based on the nine parameters.

The averages over the four experiments of the three values $m_{\rm Z}^{90-92}$, $m_{\rm Z}^{93-94}$ and $m_{\rm Z}^{95}$ also provide a cross-check on the consistency of the energy calibration, which dominates the errors on $m_{\rm Z}$ in each of the periods considered. The mass values for the three different periods and the correlated and uncorrelated parts of their errors are shown in Figure 2.10. The differences amount to $|m_{\rm Z}^{90-92} - m_{\rm Z}^{93-94}| = 31\,\%$, $|m_{\rm Z}^{90-92} - m_{\rm Z}^{95}| = 56\,\%$ and $|m_{\rm Z}^{93-94} - m_{\rm Z}^{95}| = 43\,\%$ of the uncorrelated errors, *i. e.* the three Z mass values are consistent.

2.5.2 Shifts for Halved Experimental Errors

When the average over the experiments is performed at the level of the pseudo-observables, information on the individual contribution of particular data points to the average is lost. Thus, if the average were to be performed over the data points themselves, the relative importance

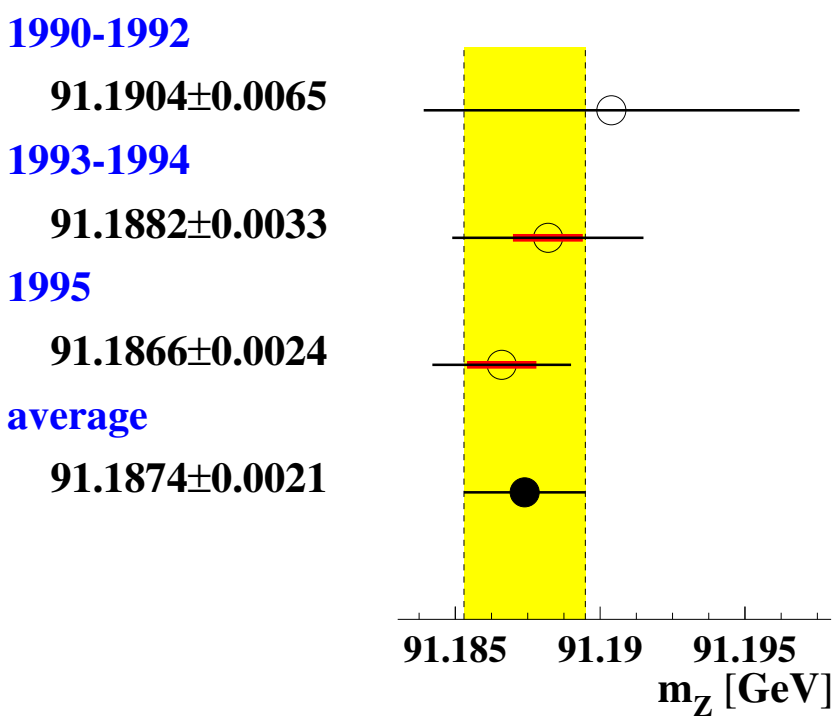

Figure 2.10: m_{Z} in GeV for three different periods of data taking, before 1993, 1993–1994 and 1995. The second, smaller error bar represents the correlated error component of 1.2 MeV between m_{Z}^{93-94} and m_{Z}^{95}. The value of m_{Z}^{90-92} is essentially uncorrelated with the other two.

of independent experimental errors and the common errors would be expected to change. The examples of m_{Z} and the importance of the t-channel errors for R_{ℓ}^{0}, as discussed in the previous subsections, provide good illustrations of such effects.

While m_{Z} is properly treated by the eleven-parameter fits, other pseudo-observables may suffer from similar shifts due to weight changes. A generic "combined" experiment can be simulated by halving the independent experimental errors in each experiment. The observed shifts in central values resulting from fits to the measurements with errors modified in such a way can be used as a monitoring tool. The average of these shifts over the four LEP experiments serves to estimate the differences between an average at the parameter level compared to an average at the level of the raw measurements. Of course, this simple procedure assumes that all measurements from individual experiments enter into the average with the same weight. As a test of the validity of this technique, it was demonstrated that averaging the shifts in m_{Z} which each experiment observed when halving its experimental errors also reproduced the shift seen in a full combined fit to the four sets of hadronic cross-section measurements. The observed shifts are small for each of the nine pseudo-observables, as is summarised in Table 2.11. The shift downwards in m_{Z} of 0.3 MeV corresponds to the slightly smaller shift of 0.2 MeV already seen in the multiple-m_{Z} fits.

The average changes in m_{Z}, $\sigma_{\mathrm{had}}^{0}$, R_{e}^{0}, $A_{\mathrm{FB}}^{0,\mu}$ and $A_{\mathrm{FB}}^{0,\tau}$ amount to about 10 % of the combined errors, in all other cases they are even smaller. This is an estimate of the magnitude of the changes in the final results that would arise from a combination of the four experiments at the cross-section level rather than the averaging at the parameter level. Given the smallness of the

	A	D	L	O	Average	% of error
m_{Z} [GeV]	−0.0006	0.0000	−0.0004	−0.0001	−0.00028	13
Γ_{Z} [GeV]	−0.0002	+0.0001	−0.0004	0.0000	−0.00013	5
σ^0_{had} [nb]	+0.006	0.000	+0.008	+0.0036	+0.0037	10
R^0_{e}	+0.004	+0.017	0.000	+0.004	+0.0063	13
R^0_{μ}	0.000	0.000	0.000	+0.001	0.0000	0
R^0_{τ}	0.000	0.000	−0.001	+0.002	+0.0003	1
$A^{0,\mathrm{e}}_{\mathrm{FB}}$	−0.0001	−0.0003	0.0000	−0.0000	−0.00011	5
$A^{0,\mu}_{\mathrm{FB}}$	+0.0002	+0.0003	0.0000	+0.0001	+0.00014	11
$A^{0,\tau}_{\mathrm{FB}}$	+0.0002	+0.0003	0.0000	+0.0001	+0.00015	9

Table 2.11: Shifts in central values of the fitted pseudo-observables seen when halving the independent experimental errors, for individual experiments and the average.

observed effects it is obvious that the parameter-level average is adequate.

2.5.3 Influence of the γ–Z Interference Term

In the nine-parameter analyses discussed here, the γ–Z interference terms in the differential cross-sections for leptons are expressed using the effective coupling constants and the electric charges of the electron and the final state fermion (see Equation 1.34). This dependence can be exploited in the fits to fix the interference terms in leptonic final states, although the actual experimental procedures are slightly different in detail, as described in the original publications [41,42,43,44]. For the inclusive hadronic final state, however, the γ–Z interference term must be fixed to the SM value. Fits with a free interference term are possible in the S-matrix scheme [76]. The OPAL collaboration also studied a similar approach based on an extension of the standard parameter set [44]. In the S-matrix approach the interference terms are considered as free and independent parameters. The hadronic interference term is described by the parameter $j^{\mathrm{had}}_{\mathrm{tot}}$, given in the SM by

$$j^{\mathrm{had}}_{\mathrm{tot}} = \frac{G_{\mathrm{F}} m_{\mathrm{Z}}^2}{\sqrt{2}\pi\alpha(m_{\mathrm{Z}}^2)} Q_{\mathrm{e}}\, g_{\mathrm{Ve}} \cdot 3 \sum_{\mathrm{q}\neq\mathrm{t}} Q_{\mathrm{q}}\, g_{\mathrm{Vq}}\,. \tag{2.3}$$

Note that the running of α as well as final state QED and QCD corrections are also included in the definition of the S-matrix parameters. The SM value of $j^{\mathrm{had}}_{\mathrm{tot}}$ is 0.21 ± 0.01.

The dependence of the nine parameters on possible variations of the hadronic γ–Z interference term away from the SM value is studied by considering a set of ten parameters consisting of the standard nine parameters extended by the parameter $j^{\mathrm{had}}_{\mathrm{tot}}$ from the S-matrix approach. The extra free parameter $j^{\mathrm{had}}_{\mathrm{tot}}$ is strongly anti-correlated with m_{Z}, resulting in errors on m_{Z} enlarged by a factor of almost three, as is observed in the existing S-matrix analyses of LEP-I data [77].

The dependence of m_{Z} on $j^{\mathrm{had}}_{\mathrm{tot}}$ is given by:

$$\frac{\mathrm{d}m_{\mathrm{Z}}}{\mathrm{d}j^{\mathrm{had}}_{\mathrm{tot}}} \;=\; -1.6 \text{ MeV}/0.1\,. \tag{2.4}$$

The changes in all other parameters are below 20 % of their combined error for a change in $j^{\mathrm{had}}_{\mathrm{tot}}$ of 0.1 .

Improved experimental constraints on the hadronic interference term are obtained by including measurements of the hadronic total cross-section at centre-of-mass energies further away from the Z pole than just the off-peak energies at LEP-I. Including the measurements of the TRISTAN collaborations at KEK, TOPAZ [78] and VENUS [79], at $\sqrt{(}s) = 58$ GeV, the error on $j_{\rm tot}^{\rm had}$ is about ± 0.1, while its central value is in good agreement with the SM expectation. Measurements at centre-of-mass energies above the Z resonance at LEP-II [80, 81, 82, 83] also provide constraints on $j_{\rm tot}^{\rm had}$, and in addition test modifications to the interference terms arising from the possible existence of a heavy Z$'$ boson.

The available experimental constraints on $j_{\rm tot}^{\rm had}$ thus lead to uncertainties on $m_{\rm Z}$, independent of SM assumptions in the hadronic channel, which are already smaller than its error. No additional error is assigned to the standard nine-parameter results from effects which might arise from a non-SM behaviour of the γ–Z interference.

2.5.4 Direct Standard Model Fits to Cross-Sections and Asymmetries

Since an important use of the combined results presented here is to test the validity of the SM and to determine its parameters, it is crucial to verify that the parameter set chosen for the combination represents the four sets of experimental measurements with no significant loss in precision. When the set of pseudo-observables is used in the framework of the SM, the role of $m_{\rm Z}$ changes from an independent parameter to that of a Lagrangian parameter of the theory, intimately linked with other quantities. This imposes additional constraints which can be expected to shift the value of $m_{\rm Z}$.

To check whether the nine parameters adequately describe the reaction to these constraints, each collaboration provided results from direct SM fits to their cross-section and asymmetry data. The comparison of these results with those obtained from SM fits using the set of pseudo-observables as input is shown in Table 2.12. $m_{\rm H}$ and α_s were free parameters in these fits, while the additional inputs $m_{\rm t} = 174.3 \pm 5.1$ GeV [84] and $\Delta\alpha_{\rm had}^{(5)} = 0.02804 \pm 0.00065$ [58] (corresponding to $1/\alpha(m_{\rm Z}^2) = 128.886 \pm 0.090$) provided external constraints.

Significant shifts in $m_{\rm Z}$ of up to 20 % of its error are observed in some experiments, which however cancel out to almost zero in the average over the four experiments. One anticipated source of these shifts has already been mentioned: the Z couplings defining the γ–Z interference term depend on $m_{\rm H}$, which is allowed to move freely in the first fit, but is fixed to 150 GeV for the extraction of the pseudo-observables. The approximate values of $m_{\rm H}$ preferred by the SM fit to the cross-sections and asymmetries are indicated in the second part of the table. Using the dependence of $m_{\rm Z}$ on the value of $m_{\rm H}$ given in Section 2.4.4, the differences in $m_{\rm Z}$ can be corrected to a common value of the Higgs mass of $m_{\rm Z} = 150$ GeV, as is shown in the last line of Table 2.12. The results indicate that the expected $m_{\rm Z}$ dependence on $m_{\rm H}$ is not the dominant mechanism responsible for the differences. Since the two procedures compared here represent different estimators for $m_{\rm Z}$, such differences may be expected due to fluctuations of the measurements around the exact SM expectations.

It was verified that the two procedures lead to identical results if applied to pseudo-data calculated according to the SM. If the origin of the shifts is due to fluctuations of the measurements within errors, a reduction of the shifts with increased statistical precision is expected to occur, which is indeed what is observed when averaging over the four experiments. The net average difference in $m_{\rm Z}$ directly from the realistic observables or through the intermediary of the pseudo-observables is less than 0.1 MeV. Shifts in the other SM parameters, in the individ-

	A	D	L	O	Average	% of error
χ^2/dof	174/180	184/172	168/170	161/198		
$\Delta m_{\rm Z}$ [MeV]	-0.7	$+0.5$	0.0	$+0.1$	-0.03	1
$\Delta m_{\rm t}$ [GeV]	0.0	0.0	0.0	0.0	0.0	<2
$\Delta \log_{10}(m_{\rm H}/{\rm GeV})$	-0.01	$+0.04$	$+0.02$	$+0.04$	$+0.02$	4
$\Delta\alpha_s$	0.0000	-0.0002	$+0.0002$	$+0.0002$	$+0.0001$	4
$\Delta(\Delta\alpha^{(5)}_{\rm had})$	$+0.00002$	-0.00004	0.00000	-0.00004	-0.00002	2
fit value of $m_{\rm H}$ [GeV]	40.	10.	35.	390.		
$\Delta m_{\rm Z}$ [MeV] corr. to 150 GeV $m_{\rm H}$	-0.6	$+0.7$	$+0.1$	0.0	$+0.05$	2

Table 2.12: Shifts in SM parameters, when fit directly to the cross-sections and forward-backward asymmetries compared to when fit to the nine-parameter results. The numbers in the last line of the table give the shifts in $m_{\rm Z}$ if the results from the first line are corrected to a common value of the Higgs mass of 150 GeV.

ual data sets as well as in the average, are all well under 5 % of the errors, and therefore also negligible.

The conclusion of this study is that SM parameters extracted from the pseudo-observables are almost identical to the ones that would be obtained from the combined cross-sections and asymmetries. Within the SM the combined set of pseudo-observables provides a description of the measurements of the Z parameters that is equivalent to the full set of cross-sections and asymmetries. This is also true for any theory beyond the SM which leads to corrections that are absorbed in the pseudo-observables. An exception to this are those theories which lead to significant modifications of the γ–Z interference term, like theories with additional Z′-bosons. (See the discussion in Section 2.5.3.)

2.6 Combined Results

The full result of the combination of the four sets of nine pseudo-observables including the experimental and common error matrices is given in Table 2.13. The central values and errors on the combined results are presented graphically and compared with the corresponding input values of the four experiments in Figure 2.9. The parametric uncertainties due to the residual dependence on the choice of SM parameters used to calculate the remnants are not included. The only significant such uncertainty concerns the value of the Higgs boson mass, which is taken to be 150 GeV and is relevant only for the value of $m_{\rm Z}$. The value of $m_{\rm Z}$ changes by $+0.23$ MeV per unit change in $\log_{10}(m_{\rm H}/{\rm GeV})$, as was discussed in Section 2.4.4.

The value of χ^2 per degree of freedom of the combination of the nine-parameter results is 32.6/27 and corresponds to a probability of 21 % to find a value of χ^2 which is larger than the one actually observed. The correlation matrix of the combined result shows significant correlations of $\sigma^0_{\rm had}$ with $\Gamma_{\rm Z}$ and $R^0_{\rm e}$, R^0_μ and R^0_τ, and between $R^0_{\rm e}$ and $A^{0,\,{\rm e}}_{\rm FB}$.

A comparison of the leptonic quantities $R^0_{\rm e}$, R^0_μ and R^0_τ, and of $A^{0,\,{\rm e}}_{\rm FB}$, $A^{0,\,\mu}_{\rm FB}$ and $A^{0,\,\tau}_{\rm FB}$ shows that they agree within errors. Note that R^0_τ is expected to be larger by 0.23 % because of τ

Without lepton universality		Correlations								
χ^2/dof = 32.6/27		m_Z	Γ_Z	σ^0_{had}	R^0_e	R^0_μ	R^0_τ	$A^{0,e}_{FB}$	$A^{0,\mu}_{FB}$	$A^{0,\tau}_{FB}$
m_Z [GeV]	91.1876± 0.0021	1.000								
Γ_Z [GeV]	2.4952 ± 0.0023	−0.024	1.000							
σ^0_{had} [nb]	41.541 ± 0.037	−0.044	−0.297	1.000						
R^0_e	20.804 ± 0.050	0.078	−0.011	0.105	1.000					
R^0_μ	20.785 ± 0.033	0.000	0.008	0.131	0.069	1.000				
R^0_τ	20.764 ± 0.045	0.002	0.006	0.092	0.046	0.069	1.000			
$A^{0,e}_{FB}$	0.0145 ± 0.0025	−0.014	0.007	0.001	−0.371	0.001	0.003	1.000		
$A^{0,\mu}_{FB}$	0.0169 ± 0.0013	0.046	0.002	0.003	0.020	0.012	0.001	−0.024	1.000	
$A^{0,\tau}_{FB}$	0.0188 ± 0.0017	0.035	0.001	0.002	0.013	−0.003	0.009	−0.020	0.046	1.000

With lepton universality		Correlations				
χ^2/dof = 36.5/31		m_Z	Γ_Z	σ^0_{had}	R^0_ℓ	$A^{0,\ell}_{FB}$
m_Z [GeV]	91.1875± 0.0021	1.000				
Γ_Z [GeV]	2.4952 ± 0.0023	−0.023	1.000			
σ^0_{had} [nb]	41.540 ± 0.037	−0.045	−0.297	1.000		
R^0_ℓ	20.767 ± 0.025	0.033	0.004	0.183	1.000	
$A^{0,\ell}_{FB}$	0.0171 ± 0.0010	0.055	0.003	0.006	−0.056	1.000

Table 2.13: Combined results for the Z parameters of the four sets of nine pseudo-observables from Table 2.4. The errors include all common errors except the parametric uncertainty on m_Z due to the choice of m_H.

mass effects. Figure 2.11 shows the corresponding 68 % confidence level contours in the R^0_ℓ–$A^{0,\ell}_{FB}$ plane.

Imposing the additional requirement of lepton universality in the nine-parameter combination leads to the results shown in the second part of Table 2.13.[4] Note that R^0_ℓ is defined for massless leptons. The value of χ^2/dof of 36.5/31 for the combination of the four sets of nine pseudo-observables into the five parameters of Table 2.13 corresponds to a χ^2 probability of 23 %. The central ellipse in Figure 2.11 shows the 68 %-CL contour for the combined values of R^0_ℓ and $A^{0,\ell}_{FB}$ determined from all three lepton species.

While the errors on most of the pseudo-observables are dominated by independent experimental or statistical errors, the combined errors on m_Z and σ^0_{had} have large contributions from a single, common systematic error. The dominant contribution to the error in m_Z arises from the uncertainty in the calibration of the energy of the beams in LEP, and amounts to ±1.7 MeV. The uncertainty on σ^0_{had} arising from the theoretical error on the small-angle Bhabha cross-section amounts to ±0.025 nb, the total contribution of common systematic errors is ±0.028 nb. The systematic error on Γ_Z, ±1.2 MeV, is dominated by the uncertainty of the beam energy. Common systematics on R^0_ℓ amount to ±0.007 and contribute ±0.0003 to $A^{0,\ell}_{FB}$.

[4] Performing the average at the level of the five-parameter results leads to slightly different values for R^0_ℓ due to weight shifts originating from the common t-channel error on R^0_e, which is not treated properly in this case.

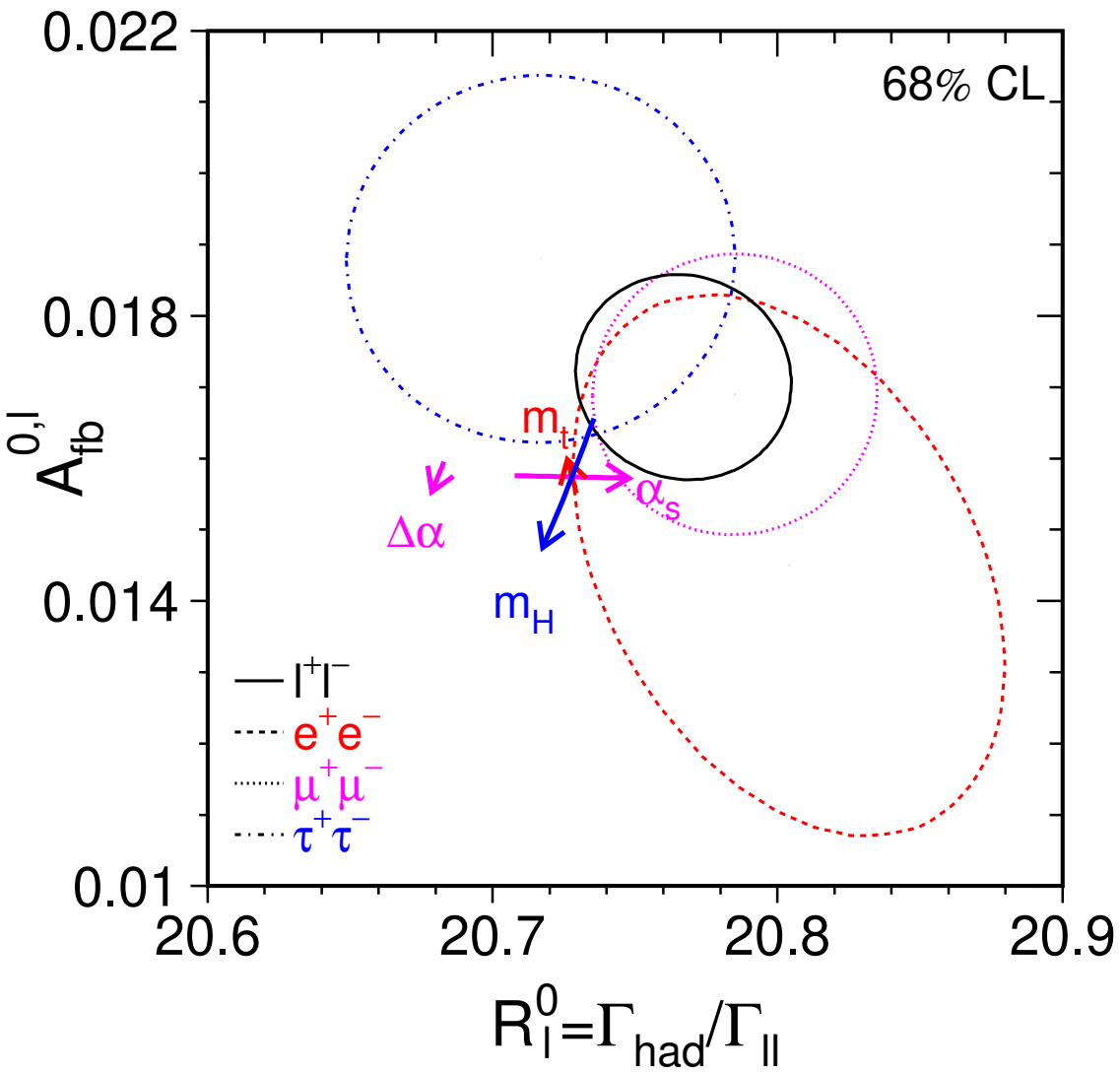

Figure 2.11: Contour lines (68 % CL) in the R_ℓ^0–$A_{\rm FB}^{0,\ell}$ plane for $\rm e^+e^-$, $\mu^+\mu^-$ and $\tau^+\tau^-$ final states and for all leptons combined. For better comparison the results for the τ lepton are corrected to correspond to the massless case. The SM prediction for $m_{\rm Z} = 91.1875$ GeV, $m_{\rm t} = 178.0$ GeV, $m_{\rm H} = 300$ GeV, and $\alpha_{\rm S}(m_{\rm Z}^2) = 0.118$ is also shown as the intersection of the lines with arrows, which correspond to the variation of the SM prediction when $m_{\rm t}$, $m_{\rm H}$ and $\alpha_{\rm S}(m_{\rm Z}^2)$ are varied in the intervals $m_{\rm t} = 178.0 \pm 4.3$ GeV, $m_{\rm H} = 300^{+700}_{-186}$ GeV, and $\alpha_{\rm S}(m_{\rm Z}^2) = 0.118 \pm 0.003$, respectively. The arrow showing the small dependence on the hadronic vacuum polarisation $\Delta\alpha_{\rm had}^{(5)}(m_{\rm Z}^2) = 0.02758 \pm 0.00035$ is displaced for clarity. The arrows point in the direction of increasing values of these parameters.

Chapter 3

Measurement of Left-Right and Lepton Asymmetries at the SLC

3.1 Left-Right Asymmetry Measurements

The measurement of the left-right cross-section asymmetry, $A_{\rm LR}$, by SLD [85] at the SLC provides a determination of the asymmetry parameter $\mathcal{A}_{\rm e}$, which is presently the most precise single measurement of this quantity, with the smallest systematic error. In addition, $A_{\rm LR}$, along with the tau polarisation measurements, is the observable most sensitive to the effective weak mixing angle among the asymmetries, with $\delta A_{\rm LR} \approx 8\delta \sin^2\theta^{\rm lept}_{\rm eff}$.

In principle the analysis is straightforward: one counts the numbers of Z bosons produced by left and right longitudinally polarised electron bunches, $N_{\rm L}$ and $N_{\rm R}$, forms the asymmetry, and then divides by the luminosity-weighted e^- beam polarisation magnitude $\langle\mathcal{P}_{\rm e}\rangle$ - the e^+ beam is not polarised (see Equation 1.58) :

$$A_{\rm LR} = \frac{N_{\rm L} - N_{\rm R}}{N_{\rm L} + N_{\rm R}} \frac{1}{\langle\mathcal{P}_{\rm e}\rangle}. \tag{3.1}$$

The measurement requires no detailed final-state event identification: e^+e^- final-state events are removed since they contain non-resonant t-channel contributions, as are all other backgrounds not due to Z decay. It is also insensitive to all acceptance and efficiency effects. In order to relate $A_{\rm LR}$ at a particular value of $E_{\rm cm}$ to a determination of the effective weak mixing angle, the result is converted into a "Z-pole" value by the application of an approximately 2.0% relative correction for initial-state radiation and γ–Z interference, $\Delta A_{\rm LR}$ [31],

$$A_{\rm LR} + \Delta A_{\rm LR} = A^0_{\rm LR} \equiv \mathcal{A}_{\rm e}. \tag{3.2}$$

The calculation of this correction requires a good measurement of the luminosity-weighted average centre-of-mass collision energy $E_{\rm cm}$. The $\Delta A_{\rm LR}$ correction is small compared to the analogous QED corrections for the leptonic forward-backward asymmetry measurements, while similar in size to those required for the tau polarization and bottom quark asymmetries. There is no need for QCD corrections for the measurement of $A_{\rm LR}$.

For the data of 1997 and 1998, the small total relative systematic error of 0.65% is dominated by the 0.50% relative systematic error in the determination of the luminosity-weighted average e^- polarisation, with the second largest error, 0.39%, arising from uncertainties in the determination of the luminosity-weighted average centre-of-mass energy. A number of much smaller contributions to the systematic error is discussed below. The relative statistical error on

$A_{\rm LR}$ from all data is about 1.3%. In what follows, some of the details of the $A_{\rm LR}$ measurement are described and some historical context for the $A_{\rm LR}$ programme at SLC/SLD from 1992 until 1998 is provided.

3.1.1 Electron Polarisation at the SLC

In Section 1.1.2, the operation of the SLC is briefly outlined, and Figure 1.4 provides a schematic of the machine. The SLC produced longitudinally polarised electrons by illuminating a GaAs photocathode with circularly polarised light produced by a Ti-Sapphire laser. Following the advent of high polarisation "strained lattice" GaAs photocathodes in 1994 [86], where mechanical strain induced in a 0.1μm GaAs layer lifts an angular momentum degeneracy in the valence band of the material, the average electron polarisation at the e^+e^- interaction point (IP) was in the range 73% to 77%, only slightly lower than the value produced at the source, see Figure 1.5. The corresponding polarisation results were about 22% in 1992 using an unstrained "bulk" GaAs cathode, and 63% in 1993 using a 0.3μm strained-layer cathode design. The electron helicity was chosen randomly pulse-to-pulse at the machine repetition rate of 120 Hz by controlling the circular polarisation of the source laser.

The electron spin orientation was longitudinal at the source and remained longitudinal until it was transported to the damping ring (DR). In this linac-to-ring (LTR) transport line, the electron spins precessed horizontally due to the dipole bending magnets, where the spin precession angle is given in terms of the anomalous magnetic moment: $\theta_{\rm precession} = (\frac{g-2}{2})\frac{E}{m}\theta_{\rm bend}$. By design, the bend angle $\theta_{\rm bend}$ resulted in transverse spin orientation at the entrance to the LTR spin rotator magnet. This superconducting solenoid magnet was used to rotate the polarisation about the beam direction into the vertical orientation for storage in the DR. This was necessary as any horizontal spin components precessed rapidly and were completely dissipated during the 8.3 msec (1/120 seconds) storage time due to energy spread in the bunch. The polarised electron bunches could be stored in one of two possible configurations by the reversal of the LTR spin rotator solenoid magnet. These reversals, typically done at three month intervals, were useful for identifying and minimising the small ($\mathcal{O}(10^{-4})$) polarisation asymmetries produced at the source.

The electron spin was vertical in the linac and had to be reoriented for maximal longitudinal polarisation at the IP. Spin manipulation was possible during transport through the electron arc by employing two large vertical betatron oscillations in the beam orbit ("spin bumps"). As the betatron phase advance closely matched the spin precession, 1080 and 1085 degrees, respectively, in each of the 23 bending-magnet assemblies ("achromats") used in the arc, the electron arc operated close to a spin-tune resonance, and hence an iterative spin bump procedure was effective in optimising IP polarization [87]. As a result, excepting for the 1992 running, the two additional SLC spin rotator solenoids located downstream of the damping ring were not necessary for spin orientation and were used only in a series of specialised polarisation experiments.

3.1.2 Polarimetry at the SLC

The SLD collaboration monitored the longitudinal polarization of the electron beam with a Compton scattering polarimeter. The Compton polarimeter detected beam electrons that had been scattered by photons from a circularly polarised laser. The scattered electrons were momentum analysed by magnets and swept into a multi-channel detector. The choice of a

Compton-scattering polarimeter was dictated by the requirements that the device be operated continually while beams were in collision and that uncertainties in the physics of the scattering process not be a limiting factor in the systematic error. Both of these requirements are troublesome issues for Møller scattering instruments due to their magnetic alloy targets. In addition, the pulse-to-pulse controllability of the laser polarisation sign, as well as its high polarisation value of 99.9%, are additional advantages of a Compton polarimeter relative to other options.

In Compton scattering of longitudinally polarised electrons from circularly polarised photons, the differential cross-section in terms of the normalised scattered photon energy fraction x is given by:

$$\frac{\mathrm{d}\sigma}{\mathrm{d}x} = \frac{\mathrm{d}\sigma_0}{\mathrm{d}x}[1 - \mathcal{P}_\gamma \mathcal{P}_\mathrm{e} A(x)], \tag{3.3}$$

where $\mathrm{d}\sigma_0/\mathrm{d}x$ is the unpolarised differential cross-section, $\mathcal{P}_{\gamma,\mathrm{e}}$ are the photon and electron polarisations, and $A(x)$ is the Compton asymmetry function. The asymmetry arises due to the difference between spin parallel and spin anti-parallel cross-sections, $\sigma(j = 3/2) > \sigma(j = 1/2)$. Both the asymmetry function and differential cross-section are well known theoretically [88]. The unpolarized cross-section is a relatively slowly varying function of the energy of the scattered electron or photon. At the SLC, typical laser/electron-beam luminosities led to about 1000 Compton scatters per laser pulse. The asymmetry function changes sign (corresponding to going from forward to backward photon scattering in the electron rest frame), and reaches extreme values at the kinematic endpoints, corresponding to full forward or back scattering. In the SLD polarimeter, scattered electrons of minimum energy and maximum deflection in the spectrometer exhibited the maximum asymmetry.

In a polarimeter, the Compton-scattered photons or electrons are detected, and the requisite instrumental effects are incorporated into an energy dependent detector response function. The normalised weighting of $A(x)$ with $\mathrm{d}\sigma_0/\mathrm{d}x$ and the response function $R(x)$, all functions of the fractional energy x, is known as the "analysing power" a:

$$a = \frac{\int A(x)R(x)\frac{\mathrm{d}\sigma_0}{\mathrm{d}x}\mathrm{d}x}{\int R(x)\frac{\mathrm{d}\sigma_0}{\mathrm{d}x}\mathrm{d}x}, \tag{3.4}$$

where the integration is over the relevant acceptance in x. For a multichannel detector, as was used by the SLD, a_i and $R_i(x)$ are defined for the ith channel. For example, in the case of the Cherenkov detector discussed below, the response function for a given detector channel quantified the Cherenkov light produced by an incident electron as a function of the range of x or equivalently, the transverse position in the spectrometer bending plane, corresponding to the acceptance of that channel.

As mentioned above, the laser/electron-beam luminosities for the SLD polarimeter led to a large number of Compton scatters per laser pulse. All of the channels of the polarimeter detector were hit on virtually every laser pulse, and for every pulse, each channel integrated the response to many Compton scattered electrons as well as backgrounds. Linearity of response was therefore an essential detector requirement. The Compton scattering asymmetry in the SLD polarimeter was formed from the time averaged detector channel responses, typically taken over a few minutes, for each of the four possible electron-photon helicity combinations.

For the i^{th} detector channel, the two spin aligned configurations were combined to give $\langle N\rangle^i_{3/2}$, while the two spin opposed configurations yielded $\langle N\rangle^i_{1/2}$. The SLC operated at 120 Hz and the polarimeter laser fired every 7th beam crossing,[1] so that the six intervening "laser-

[1] The laser firing sequence was automatically shifted by one beam crossing at regular intervals to avoid undesirable synchronisation with periodic effects in the SLC.

off" beam crossings were used to monitor the polarimeter background responses $\langle N\rangle^i_{off}$. The measured asymmetry is

$$A^i \;=\; \frac{\langle N\rangle^i_{3/2} - \langle N\rangle^i_{1/2}}{\langle N\rangle^i_{3/2} + \langle N\rangle^i_{1/2} - 2\langle N\rangle^i_{off}}. \tag{3.5}$$

The set of A^i are corrected for small effects due to electronics noise and detector non-linearity, as described below, and the result can then be related to the known analysing powers a^i and laser polarization as:

$$A^i_C \;=\; \mathcal{P}_\gamma \mathcal{P}_{\rm e} a^i, \tag{3.6}$$

which can be solved for $\mathcal{P}_{\rm e}$.

Figure 3.1 illustrates the essential features of the polarimeter setup: Frequency doubled Nd:YAG laser pulses were circularly polarised by a linear polariser and a Pockels cell pair. The laser beam was transported to the SLC beamline by four sets of phase-compensating mirror pairs and into the vacuum chamber through a reduced-strain quartz window. About 30 meters downstream from the IP, the laser beam was brought into nearly head-on collisions with the outgoing electron beam at the Compton Interaction Point (CIP), and then left the beampipe through a second window to an analysis station. The pair of Pockels cells on the optical bench allowed for full control of elliptical polarisation and was used to automatically scan the laser beam polarisation at regular intervals in order to monitor, and maximise, laser polarisation at the CIP. This procedure significantly improved the magnitude of the laser circular polarisation, and the precision of its determination [89]. In colliding a $\sim$ 45 GeV electron beam with visible light, the scattered photons are very strongly boosted along the electron beam direction and are essentially collinear with the Compton-scattered electrons.[2] Downstream from the CIP, a pair of bend magnets swept out the off-energy Compton-scattered electrons, which passed through a thin window and out of the beamline vacuum into a nine-channel transversely segmented gas Cherenkov detector, each channel covering 1 cm. By detecting the Compton-scattered electrons with a Cherenkov device whose threshold was about 11 MeV, the copious soft backgrounds originating from the beam-beam interactions and from synchrotron radiation, were dramatically reduced.

The minimum energy 17.4 GeV electrons, corresponding to full backscattering, generally fell into the 7th channel (see Figure 3.2). At this point in the electron spectrum, known as the "Compton edge", the polarisation asymmetry function reached its maximum value of 0.748. A number of effects, including electron scattering and showering in the detector and in the detector vicinity, signal response in the detector, and beam steering and focusing, tend to slightly smear the asymmetry function. Small deviations from the theoretical Compton energy dependent asymmetry function, of order 1% near the Compton edge, were determined by modelling the detector response functions for each of the nine channels. An EGS4 simulation was used for this calculation, which included a detailed Monte Carlo of the detector geometry and relevant beamline elements, the Cherenkov light generation and transport, and the magnetic spectrometer [90,91]. The detector was mounted on a movable platform and the Compton edge was scanned across several channels at regular intervals in order to constrain the individual channel gains, monitor the location of the Compton edge and to experimentally constrain the detector/spectrometer simulation. For each edge scan, a multi-parameter fit to the channel

[2] Compton-scattered photons with energies in the range from the kinematically allowed maximum of 28 GeV down to 1 GeV are contained within an angle of about 100 μrad with respect to the electron beam direction.

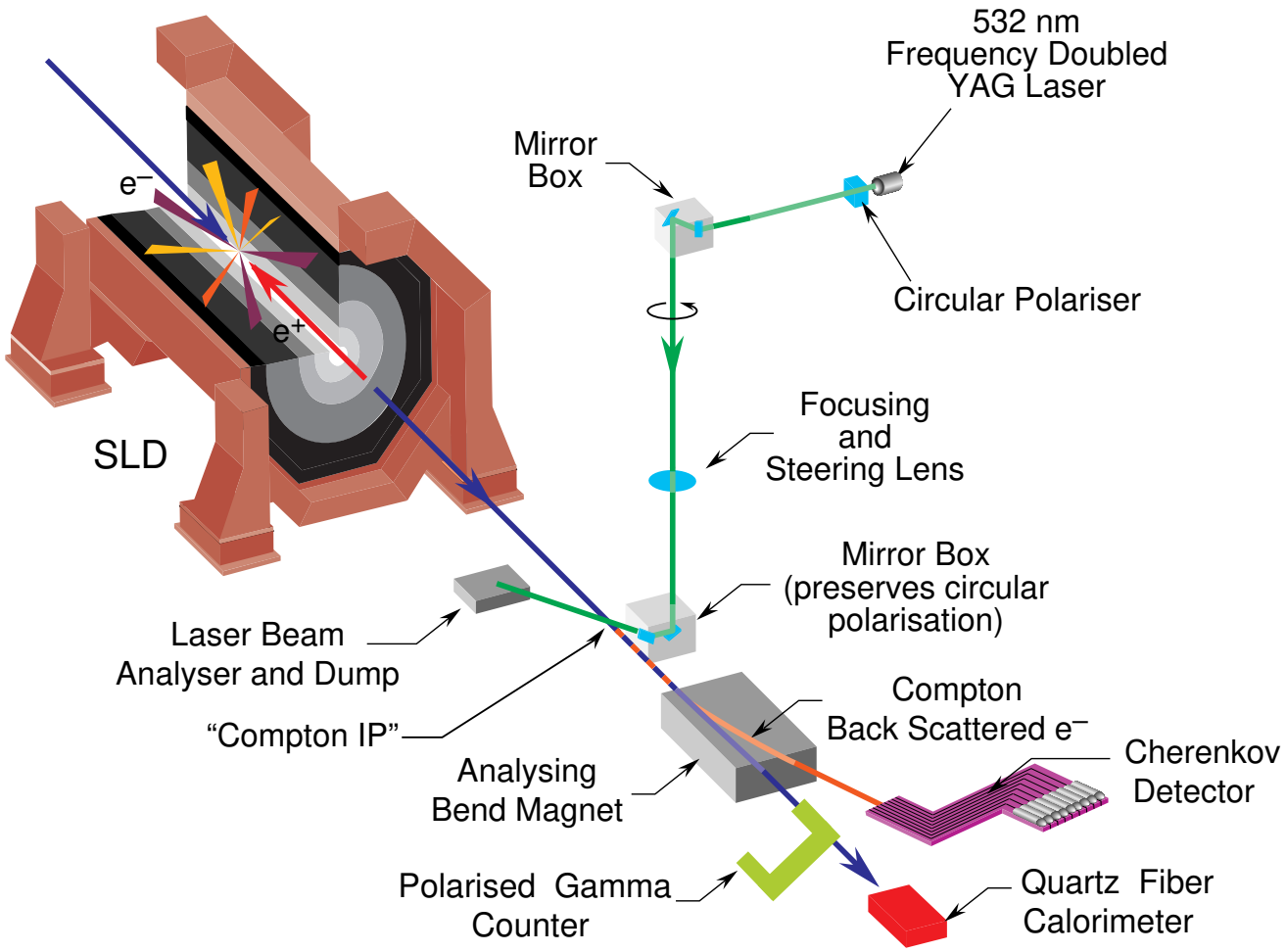

Figure 3.1: A conceptual diagram of the SLD Compton Polarimeter. The laser beam, consisting of 532 nm wavelength 8 ns pulses produced at 17 Hz and a peak power of typically 25 MW, were circularly polarised and transported into collision with the electron beam at a crossing angle of 10 mrad approximately 30 meters from the IP. Following the laser/electron-beam collision, the electrons and Compton-scattered photons, which are strongly boosted along the electron beam direction, continue downstream until analysing bend magnets deflect the Compton-scattered electrons into a transversely-segmented Cherenkov detector. The photons continue undeflected and are detected by a gamma counter (PGC) and a calorimeter (QFC) which are used to cross-check the polarimeter calibration.

scan data for the 16 scan positions was performed to determine the beam position, the relative channel gains of a set of outer channels (usually, channels 5-8), a normalization (luminosity) at each platform position, and the polarisation product $\mathcal{P}_\gamma \mathcal{P}_e$. From these fits, the reliability of the simulation was tested. For example, the main cause of the small deviations from ideal response functions arose due to showering in a lead pre-radiator in front of the detector that had been installed to optimize signal to noise. The resulting smearing of the acceptance of each channel was shown to be well modeled when compared with the edge-scan data. Additional cross-checks tracked the stability of the analysing powers during time periods between edge scans (for example, the ratios between selected channel asymmetries were monitored). Representative data showing the corrected Compton asymmetry as well as the magnitude of the correction, as a function of position and scattered electron energy, is shown in Figure 3.2. There is good agreement between the corrected asymmetry and the data in each channel.

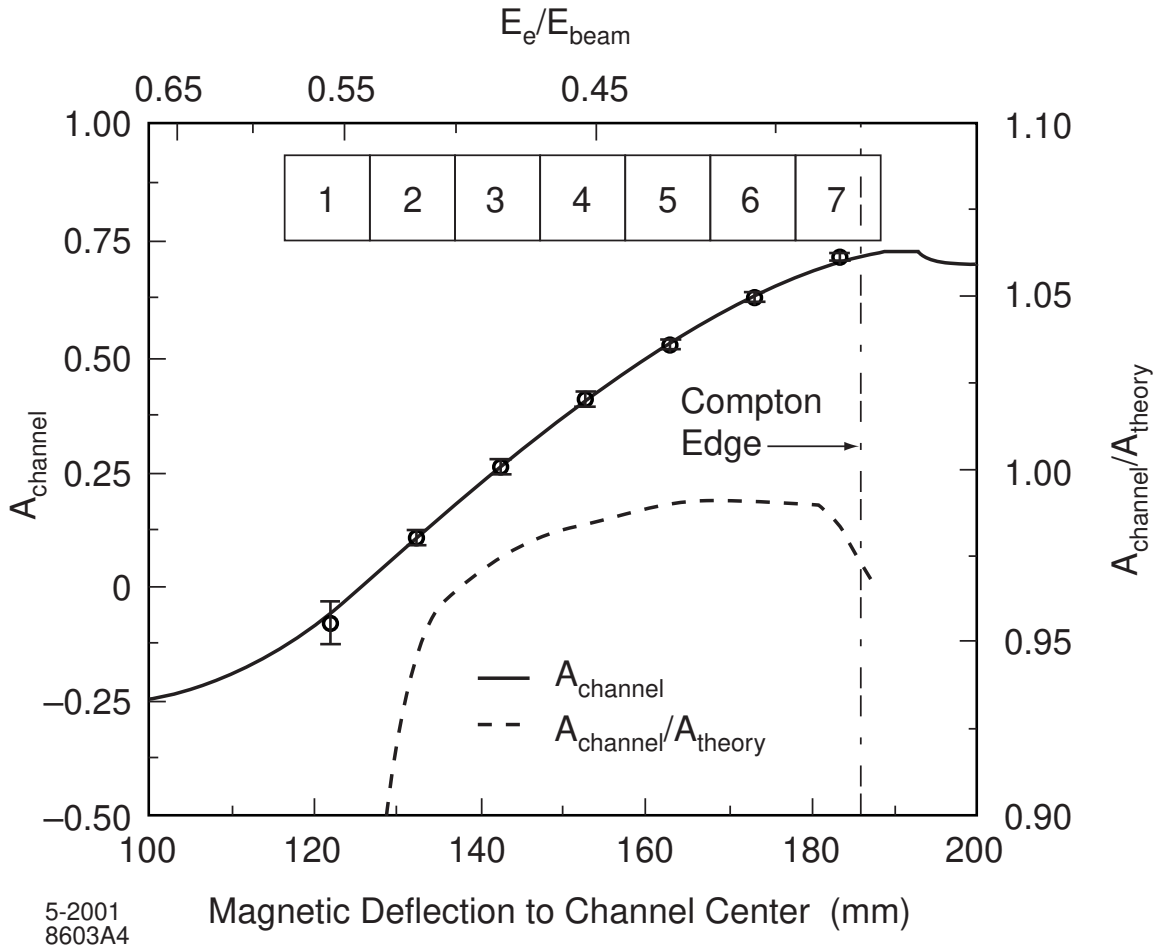

Figure 3.2: Compton scattering asymmetry as a function of channel position. The deflection of the electron beam in the spectrometer is shown on the horizontal axis as the distance in mm from the centre of the detector channels, each 1 cm wide, to the path of a hypothetical infinite momentum electron beam. The inset shows the seven inner detector channels, sized to match the horizontal scale. The per channel asymmetry data is plotted as open circles, and the corrected asymmetry function is the solid curve. The relative size of the correction to the theoretical QED calculation is indicated by the dashed curve and the right-side vertical scale.

Detector effects such as non-linearity in the electronics and/or the photomultiplier tubes, and electronic noise, mainly due to pickup from the laser Q-switch used to produce the short high peak power laser pulse, are measured from the data. Firstly, the highly variable e^+e^- collision-related backgrounds in the polarimeter, as well as the varying CIP luminosity, produced signals over a wide dynamic range in each channel, which allowed for an effective linearity measurement, as shown in Figure 3.3.

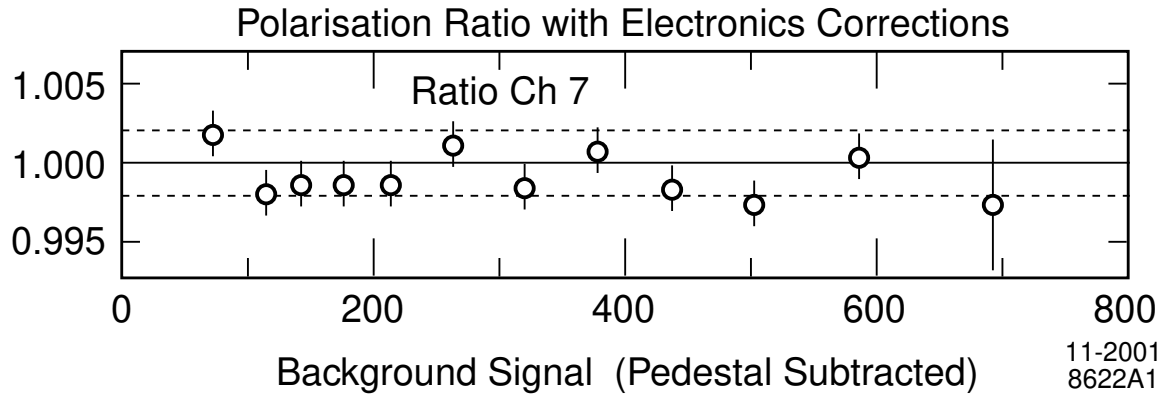

Figure 3.3: The linearity of channel 7 is shown for a wide range of detector background levels (expressed here in pedestal subtracted ADC counts). Plotted on the vertical axis is the fully corrected polarisation result, normalised to the "zero background" case. The result here is seen to be constant to within 0.2% over the full range. Running conditions varied widely, but on average were a total response of 500 counts, including 300 counts of signal.

The "zero-backgrounds" condition was determined from polarisation measurements taken when the positron beam was absent, as backgrounds were dominated by beam-beam interaction effects. Secondly, the electronic pickup effects were conveniently studied using the occasional machine cycles without either the electron or positron beams. A number of offline electronics tests and specialised test procedures during running, for example, photomultiplier tube voltage scans, were also useful in establishing the size of systematic uncertainties.

Starting in 1996, two additional polarimeter detectors [92, 93] that were sensitive to the Compton-scattered photons and which were operated in the absence of positron beam, were used to verify the precision polarimeter calibration. These two devices were of different design, one was a threshold-gas Cherenkov detector and the other was a quartz-fiber calorimeter, with different systematic errors, and had in common with the primary electron polarimeter only the instrumental errors due to the polarised laser. The cross-check provided by these photon detectors was used to establish a calibration uncertainty of 0.4%, as shown in Figure 3.4. The systematic errors due to polarimetry are summarised in Table 3.1. During the period 1992-1998, this total fractional systematic error decreased from 2.7% to its final value of 0.50%, with the most significant reductions coming from greatly improved understanding of the laser polarisation and Cherenkov detector nonlinearities. The final systematic error is dominated by the analysing power calibration uncertainty discussed above.

The polarimeter result was corrected for higher order QED and accelerator-related effects by a total of $(-0.22 \pm 0.15)\%$ for 1997-1998 data. The higher order QED offset was small and determined to be -0.1% [94]. The primary accelerator-related effect arose from energy-to-polarisation correlations and energy-to-luminosity correlations that, together with the finite energy spread in the beam, caused the average beam polarisation measured by the Compton

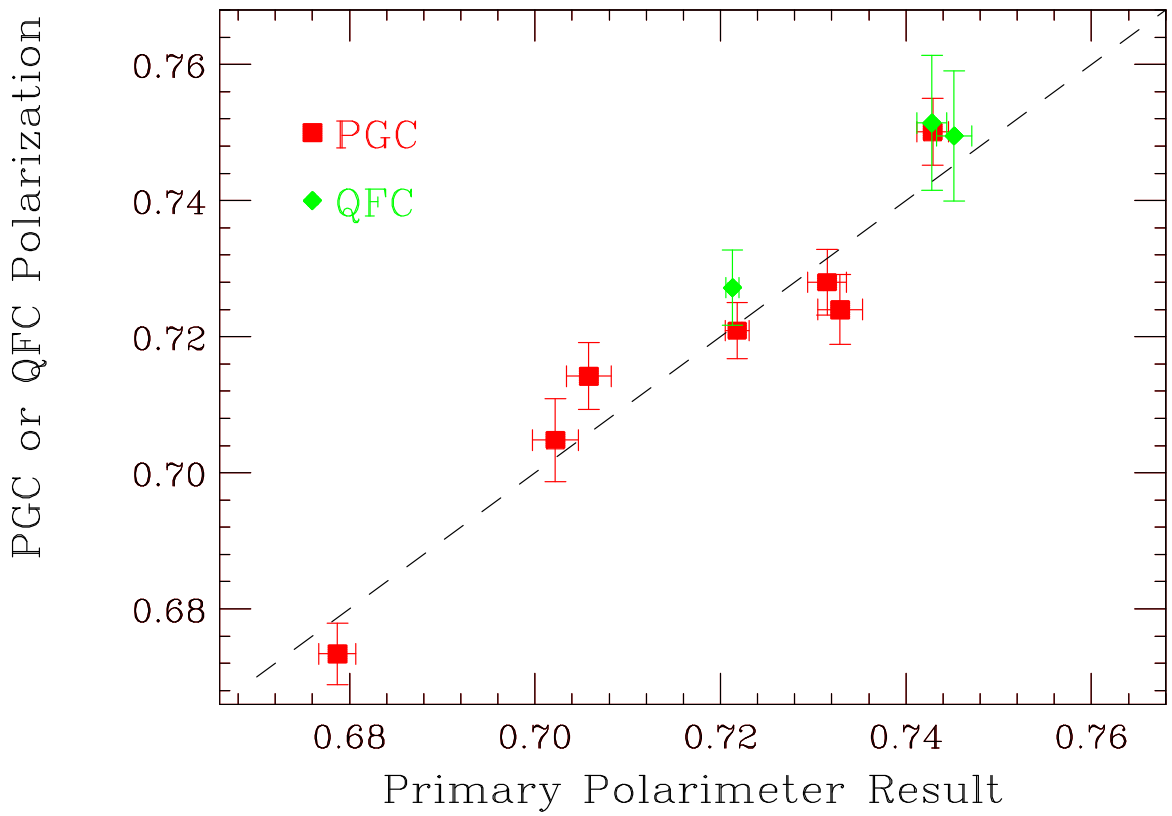

Figure 3.4: The polarised gamma counter (PGC) and quartz fiber calorimeter (QFC) photon detector polarisation results (vertical axis) compared to the primary electron detector polarimeter measurements (horizontal axis).

Polarimeter to differ slightly from the luminosity-weighted average beam polarisation at the IP. When first observed in 1993, this *chromaticity* correction and its associated error was $(1.1 \pm 1.7)\%$. In 1994-1998 a number of changes in the operation of the SLC and in monitoring procedures, such as smaller and better determined beam energy spread and polarisation energy dependence, reduced the size of this effect and its uncertainty to below 0.2%. An effect of comparable magnitude arose due to the small precession of the electron spin in the final focusing elements between the IP and the polarimeter. The contribution of collisional depolarisation was determined to be negligible, as expected, by comparing polarimeter data taken with and without beams in collision. All effects combined yielded a correction with the uncertainty given in Table 3.1.

The luminosity-weighted average polarisation $\langle \mathcal{P}_e \rangle$ for each run was estimated from measurements of $\mathcal{P}_e$ made when Z events were recorded:

$$\langle \mathcal{P}_e \rangle \;=\; (1+\xi) \cdot \frac{1}{N_Z} \sum_{i=1}^{N_Z} \mathcal{P}_i \,, \tag{3.7}$$

where N_Z is the total number of Z events, $\mathcal{P}_i$ is the polarisation measurement associated in time with the i^{th} event, and ξ is the small total correction described in the previous paragraph. The polarimeter was operated continually, where for typical background conditions about three minutes were required to achieve a relative statistical precision of order 1% for each polarisation measurement.

The fully corrected luminosity weighted average polarisations corresponding to each of the SLD runs are given in Table 3.3. The evolution of GaAs photo-cathode performance is evident in 1993 and again in 1994-1995. Changes in the achieved polarisation in later years mainly reflect variations in photo-cathode manufacture.

3.1.3 Energy Spectrometry

The SLC employed a pair of energy spectrometers located in the electron and positron extraction lines (Figure 1.4). The beam deflection by a precision dipole magnet was detected and measured using the separation between synchrotron radiation swathes emitted by the beam in deflector magnets, oriented perpendicular to the bending plane and located before and after the bend, see Figure 3.5.

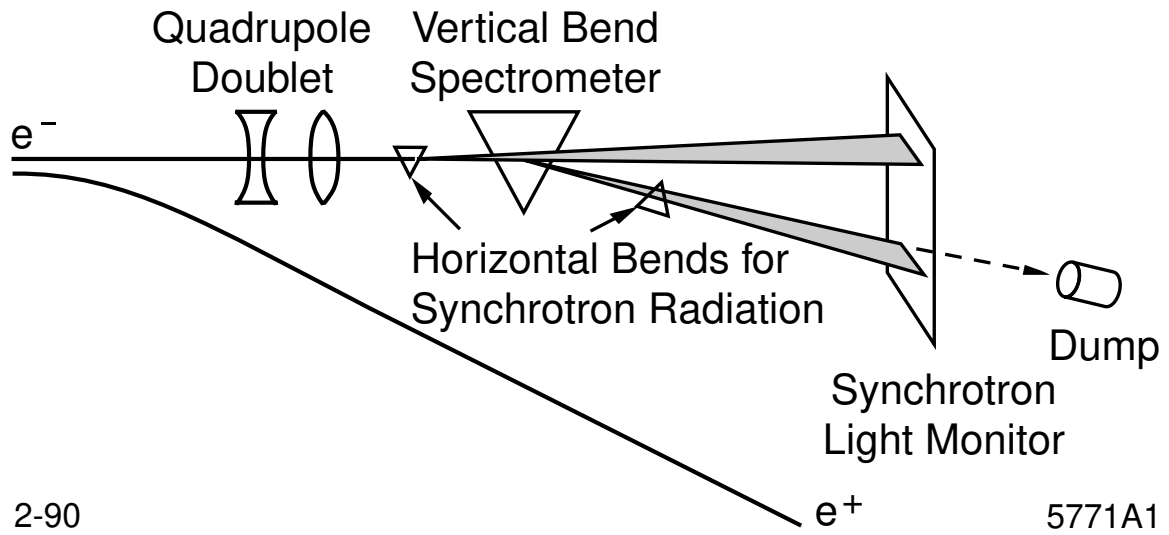

Figure 3.5: The energy spectrometer for electrons (a similar device is used on the positron side) uses a precision bend magnet and synchrotron-radiation-producing deflector magnets before and after the bend, in order to determine the beam bend angle.

These devices were first operated in their final configuration in 1989 by the Mark II experiment, and the calibration of the two precision spectrometer magnets was performed in 1988 [95]. Their expected precision was about ± 20 MeV on the measured centre-of-mass collision energy $E_{\rm cm}$. The importance of these devices to the $A_{\rm LR}$ measurement is quantified by the approximate rule of thumb that an 80 MeV uncertainty in $E_{\rm cm}$ corresponds to a 1% error on the Z-pole asymmetry $A^0_{\rm LR}$. For this reason, in 1998 a Z peak scan was performed in order to calibrate the spectrometers to the LEP measurement of the Z mass. The scan used two optimised off-peak points at $+0.88$ GeV and -0.93 GeV, and approximately 9 000 on-peak Z equivalents of luminosity (300 nb^{-1}) to reach a statistical precision on the peak position of 20 MeV. The results of a complete analysis of systematic effects determined an offset of -46 MeV and a total $E_{\rm cm}$ uncertainty of 29 MeV, the latter corresponding to a 0.39% uncertainty on $A^0_{\rm LR}$, as shown in Table 3.1 [96]. The measured offset appeared to be correlated with energy spectrometer backgrounds during the high luminosity operation of the SLC in 1997-1998, and a correction was applied to only this run (which constituted about 70% of the data).

Uncertainty	$\delta\mathcal{P}_e/\mathcal{P}_e$ [%]	$\delta A_{LR}/A_{LR}$ [%]	$\delta A^0_{LR}/A^0_{LR}$ [%]
Laser polarisation	0.10		
Detector linearity	0.20		
Analysing power calibration	0.40		
Electronic noise	0.20		
Total polarimeter uncertainty	0.50	0.50	
Chromaticity and IP corrections		0.15	
Corrections in Equation 3.8		0.07	
A_{LR} Systematic uncertainty		0.52	0.52
Electroweak interference correction			0.39
A^0_{LR} Systematic uncertainty			0.64

Table 3.1: Systematic uncertainties that affect the A_{LR} measurement for 1997/98. The uncertainty on the electroweak interference correction is caused by the uncertainty on the SLC energy scale.

3.1.4 Event Selection

A simple calorimetric event selection in the Liquid Argon Calorimeter (LAC), supplemented by track multiplicity and topology requirements in the Central Drift Chamber (CDC), were used to select hadronic Z decays. For each event candidate, energy clusters were reconstructed in the LAC. Selected events were required to contain at least 22 GeV of energy observed in the clusters and to have a normalised energy imbalance of less than 0.6.[3] The left-right asymmetry associated with final-state e^+e^- events is expected to be diluted by the t-channel photon exchange subprocess. Therefore, we excluded e^+e^- final states by requiring that each event candidate contain at least 4 selected CDC tracks, with at least 2 tracks in each hemisphere, defined with respect to the beam axis, or at least 4 tracks in either hemisphere. This track topology requirement excludes Bhabha events which contain a reconstructed gamma conversion.

Aside from t-channel effects in e^+e^- production, A_{LR} is independent of the final-state fermion flavour, and hence tau and muon pairs are not a background. However, the event selection was optimised for hadronic events. Tau and muon pairs were almost completely removed,[4] but were instead included in the complementary analysis described in section 3.2. Small backgrounds in the A_{LR} data sample were due to residual e^+e^- final-state events, and to two-photon events, beam-related noise, and cosmic rays. For the data collected from 1996 to 1998, the total background contamination was estimated to be $< 0.05\%$ for a hadronic event selection efficiency of $(91\pm1)\%$. For a discussion of event selection used in the earlier A_{LR} analyses, see reference [97] and reference [98] for the 1992 and 1993 datasets, respectively.

[3] The energy imbalance is defined as a normalised vector sum of the energy clusters as follows, $E_{imb} = |\sum \vec{E}_{cluster}|/\sum |E_{cluster}|$.

[4] Tau pairs constituted $(0.3 \pm 0.1)\%$ of the sample, while muon pair events deposited little energy in the calorimeter and were completely removed by the cuts.

3.1.5 Control of Systematic Effects

The $A_{\rm LR}$ measurement is remarkably resistant to detector dependent systematic effects and Monte Carlo modelling uncertainties. By far the dominant systematic effects arise from polarimetry and from the determination of the collision energy, rather than from any details of the analysis or the operation of the SLD. The simple expression given in Equation 3.1 applies to the ideal case in the absence of systematic effects, and as such it is a good approximation to better than a relative 0.2%.

Nevertheless, systematic left-right asymmetries in luminosity, polarisation, beam energy, and acceptance, as well as background and positron polarisation effects, can be incorporated into an extended expression for the cross-section asymmetry. Note that while the random helicity of the delivered electron bunches is exactly 50% right-handed, it is in principle possible that the magnitude of the luminosity is not equal for the two helicities. In addition, the individual polarisation measurements of Equation 3.7 average over many beam crossings and over any systematic left-right polarisation difference, and hence additional information is needed to make the required correction. One finds the measured asymmetry $A_{\rm m}$ is related to $A_{\rm LR}$ by the following expression which incorporates a number of small correction terms in lowest-order approximation,

$$\begin{aligned} A_{\rm LR} &= \frac{A_{\rm m}}{\langle\mathcal{P}_{\rm e}\rangle} + \frac{1}{\langle\mathcal{P}_{\rm e}\rangle}\Big[f_{\rm bkg}(A_{\rm m} - A_{\rm bkg}) - A_{\mathcal{L}} + A_{\rm m}^2 A_{\mathcal{P}} \\ &\qquad - E_{\rm cm}\frac{\sigma'(E_{\rm cm})}{\sigma(E_{\rm cm})}A_E - A_\varepsilon + \langle\mathcal{P}_{\rm e}\rangle\mathcal{P}_{\rm p}\Big]\,, \end{aligned} \tag{3.8}$$

where $\langle\mathcal{P}_{\rm e}\rangle$ is the mean luminosity-weighted polarisation; $f_{\rm bkg}$ is the background fraction; $\sigma(E)$ is the unpolarised Z boson cross-section at energy E; $\sigma'(E)$ is the derivative of the cross-section with respect to E; $A_{\rm bkg}$, $A_{\mathcal{L}}$, $A_{\mathcal{P}}$, A_E, and A_ε are the left-right asymmetries[5] of the residual background, the integrated luminosity, the beam polarisation, the centre-of-mass energy, and the product of detector acceptance and efficiency, respectively; and $\mathcal{P}_{\rm p}$ is any longitudinal positron polarisation of constant helicity. Since the colliding electron and positron bunches were produced on different machine cycles and since the electron helicity of each cycle was chosen randomly, any positron helicity arising from the polarisation of their parent electrons was uncorrelated with electron helicity at the IP. The net effect of positron polarisation from this process vanishes rigorously. However, positron polarisation of constant helicity would affect the measurement.

The close ties between this measurement and the SLC accelerator complex are evident from numerous accelerator-based experiments dedicated to the SLD physics programme, for which the energy-calibrating Z-peak scan is one example. Other examples include:

- *Communication of the* e^- *bunch helicity from the polarised source was verified (1992-1993).* Although the electron bunch polarisation state was transmitted via reliable and redundant paths to the SLD detector/polarimeter complex, the SLD electroweak group proposed a series of independent tests of the synchronisation of this data and the SLD event data. In one such test, the laser optics at the SLC polarised source were temporarily modified by the addition of a polariser and quarter-wave plate so that photo-cathode illumination was nulled for one of the two circular polarisation states. The positron beam

[5] The left-right asymmetry for a quantity Q is defined as $A_Q \equiv (Q_{\rm L} - Q_{\rm R})/(Q_{\rm L} + Q_{\rm R})$ where the subscripts L and R refer to the left- and right-handed beams, respectively.

was turned off, and the electron beam was delivered to the IP. Beam-related background in the SLD liquid-argon calorimeter (LAC) was detected, but only for the non-extinct pulses. By this means, the expected correlation between helicity and the presence of beam, and hence the LAC data stream, was verified [99]. In addition, the helicity sequence generated at the source was pseudo-random and deterministic, and pulse patterns received at the SLD could be verified.

- *Moderate precision Møller and Mott polarimeters confirmed the high precision Compton polarimeter result to* $\sim 3\%$ *(1993-1995).* Møller polarimeters located at the end of the SLAC linac and in the SLC electron extraction line were used to cross-check the Compton polarimeter. The perils of employing a less reliable method to test a precision device were apparent when large corrections for atomic electron momentum effects in the Møller target were discovered [100], after which, good agreement was obtained. In addition, a less direct comparison was provided by Mott polarimeter bench tests of the GaAs photo-cathodes [101].

- *SLC arc spin transport was extensively studied (1993-1998), and was frequently monitored and adjusted.* A series of experiments was done that studied the beam polarisation reported by the Compton polarimeter as a function of beam energy, beam energy spread and beam trajectory in the SLC arcs. Two spin rotators (in the linac, and in the ring-to-linac return line) were scanned in order to determine the IP polarisation maximum. An important result of these experiments was the discovery that the SLC arcs operate near a spin tune resonance, leading to the advent of spin manipulation via "spin bumps" in the SLC arcs mentioned earlier. This procedure eliminated the need for the two spin rotators and allowed the spin chromaticity ($\mathrm{d}\mathcal{P}/\mathrm{d}E$) to be minimised, reducing the resulting polarisation correction from $> 1\%$ in 1993 to $< 0.2\%$ by 1995. In subsequent years the spin transport properties of the SLC arcs were monitored at regular intervals.

- *Positron polarisation was experimentally constrained.* In 1998, a dedicated experiment was performed in order to directly test the expectation that unintended polarisation of the positron beam was negligible ; the positron beam was delivered to a Møller polarimeter in the SLAC End Station A (ESA). Experimental control was assured by first delivering the polarised electron beam, and then an unpolarised electron beam (sourced from SLAC's thermionic electron gun), to the ESA, confirming polarimeter operation. In addition, the spin rotator magnet located in the Linac was reversed halfway through the positron beam running, reversing the sense of polarisation at the Møller target and reducing systematic error. The final result verified that positron polarisation was consistent with zero (-0.02 ± 0.07)% [102].

The asymmetries in luminosity, polarisation, and beam energy, approximately 10^{-4}, 10^{-3} and 10^{-7}, respectively, were all continually monitored using a small-angle radiative Bhabha counter located $\approx$ 40m from the IP, beamstrahlung monitors, beam current monitors, the Compton polarimeter, and energy spectrometer data. The long-term average values of all asymmetries of this type were reduced by the roughly tri-monthly reversal of the transverse polarisation sense in the electron damping ring referred to in Section 3.1.1. The dominant cause of the observed asymmetries was the small current asymmetry produced at the SLC polarised source. This effect arose because of the source photo-cathode sensitivity to linearly polarised light, together with residual linear polarisation in the source laser light that was correlated with

the light helicity. This effect was minimised by a polarisation control and intensity feedback system starting in 1993, and was generally maintained at below 10^{-4}.

The value of $A_{\rm LR}$ is unaffected by decay-mode-dependent variations in detector acceptance and efficiency provided, for the simple case of Z decay to a fermion pair, that the efficiency for detecting a fermion at some polar angle is equal to the efficiency for detecting an antifermion at the same polar angle. In hadronic Z decays, the fermions in question are the initial quark-antiquark pair, which materialise as multi-particle jets. These facts, and the high degree of polar symmetry in the SLD detector, render A_ε completely negligible. Finally, $\mathcal{P}_{\rm p}$ was experimentally demonstrated to be consistent with zero to a precision of 7×10^{-4} as described above. Calculations based on polarisation buildup in the positron damping ring suggested a much smaller number, $\mathcal{P}_{\rm p} < \mathcal{O}(10^{-5})$. Hence, no correction for $\mathcal{P}_{\rm p}$ was applied to the data.

The systematic effects discussed in this section are summarised in Table 3.2. The corrections for backgrounds and accelerator asymmetries, and the associated uncertainties, were much smaller than the leading systematic errors due to polarimetry and energy uncertainties, as can be seen by comparing the penultimate three rows of Table 3.2.

3.1.6 Results

The run-by-run $A_{\rm LR}$ results are shown in Table 3.3. The $E_{\rm cm}$ dependent radiative correction, and its uncertainty, is evident in the difference between $A_{\rm LR}$ and $A^0_{\rm LR}$. These five results show a χ^2 of 7.44 for 4 degrees of freedom, corresponding to a probability of 11.4% (Figure 3.6). The $\sin^2\theta^{\rm lept}_{\rm eff}$ results derive from the equivalence $A^0_{\rm LR} \equiv \mathcal{A}_{\rm e}$, which along with Equations 1.56 and 1.71 provide that

$$A^0_{\rm LR} \;=\; \frac{2(1-4\sin^2\theta^{\rm lept}_{\rm eff})}{1+(1-4\sin^2\theta^{\rm lept}_{\rm eff})^2}. \tag{3.9}$$

The average for the complete SLD data sample is:

$$A^0_{\rm LR} \;=\; 0.1514 \pm 0.0022 \tag{3.10}$$

or equivalently:

$$\sin^2\theta^{\rm lept}_{\rm eff} \;=\; 0.23097 \pm 0.00027\,. \tag{3.11}$$

Small correlated systematic effects due to polarimetry are accounted for in forming this average. The estimated systematic uncertainties for these results are ± 0.0011 and ± 0.00013, respectively.

Source	**1992**	**1993**	**1994-95**	**1996**	**1997-98**
N_{L}	5,226	27,225	52,179	29,016	183,335
N_{R}	4,998	22,167	41,465	22,857	148,259
A_{m}	0.0223 $\pm$0.0099	0.1024 $\pm$0.0045	0.1144 $\pm$0.0032	0.1187 $\pm$0.0044	0.1058 $\pm$0.0017
f_{bkg} (%)	1.4 $\pm$1.4	0.25 $\pm$0.10	0.11 $\pm$0.08	0.029 $\pm$0.021	0.042 $\pm$0.032
A_{bkg}		0.031 $\pm$0.010	0.055 $\pm$0.021	0.033 $\pm$0.026	0.023 $\pm$0.022
$A_{\mathcal{L}}$ (10^{-4})	1.8 $\pm$ 4.2	0.38 $\pm$ 0.50	-1.9 $\pm$ 0.3	$+0.03$ $\pm$ 0.50	-1.3 $\pm$ 0.7
$A_{\mathcal{P}}$ (10^{-4})	-29	-33 $\pm$ 1	$+24$ $\pm$ 10	$+29$ $\pm$ 43	$+28$ $\pm$ 69
A_E (10^{-4})		0.0044 $\pm$0.0001	0.0092 $\pm$0.0002	-0.0001 $\pm$0.0035	$+0.0028$ $\pm$0.0014
$E_{\mathrm{cm}}\frac{\sigma'(E_{\mathrm{cm}})}{\sigma(E_{\mathrm{cm}})}$		-1.9	0.0 $\pm$ 2.5	2.0 $\pm$ 3.0	4.3 $\pm$ 2.9
A_{ε}	0	0	0	0	0
$\mathcal{P}_{\mathrm{p}}$ (10^{-4})	< 0.16	< 0.16	< 0.16	< 0.16	-2 $\pm$ 7
Total correction, $\Delta A_{\mathrm{LR}}/A_{\mathrm{LR}}$, (%)	*+ 2.2* *± 2.3*	+ 0.10 ± 0.08	+ 0.2 ± 0.06	+0.02 ± 0.05	+0.16 ± 0.07
$\delta\mathcal{P}_{\mathrm{e}}/\mathcal{P}_{\mathrm{e}}$ (%)	2.7	1.7	0.67	0.52	0.52
Electroweak interference correction [relative (%)]	*− 2.4* *± 1.4*	+ 1.7 ± 0.3	+ 1.8 ± 0.3	+ 2.2 ± 0.4	+ 2.5 ± 0.39
Total systematic error [relative (%)]	3.9	1.7	0.75	0.63	0.64

Table 3.2: Z event counts and corrections (see Equation 3.8) for all SLD run periods. Also shown are the total polarimetry errors (including chromaticity and IP effects), the relative errors due to the electroweak interference correction needed for the conversion of A_{LR} to A^0_{LR}, and the total systematic errors. Note that due to low statistics a number of effects were ignored for the 1992 data and no corrections were applied (given here in italics). Also, the total systematic error reported in 1992 (3.6%) ignored the uncertainty due to the electroweak correction.

	$\langle \mathcal{P}_e \rangle$	A_{LR}	A^0_{LR}	$\sin^2\theta^{lept}_{eff}$
1992	0.244 ± 0.006	0.100 $\pm 0.044 \pm 0.004$	0.100 $\pm 0.044 \pm 0.004$	0.2378 $\pm 0.0056 \pm 0.0005$
1993	0.630 ± 0.011	0.1628 $\pm 0.0071 \pm 0.0028$	0.1656 $\pm 0.0071 \pm 0.0028$	0.2292 $\pm 0.0009 \pm 0.0004$
1994/95	0.7723 ± 0.0052	0.1485 $\pm 0.0042 \pm 0.0010$	0.1512 $\pm 0.0042 \pm 0.0011$	0.23100 $\pm 0.00054 \pm 0.00014$
1996	0.7616 ± 0.0040	0.1559 $\pm 0.0057 \pm 0.0008$	0.1593 $\pm 0.0057 \pm 0.0010$	0.22996 $\pm 0.00073 \pm 0.00013$
1997/98	0.7292 ± 0.0038	0.1454 $\pm 0.0024 \pm 0.0008$	0.1491 $\pm 0.0024 \pm 0.0010$	0.23126 $\pm 0.00030 \pm 0.00012$
All combined			0.1514 $\pm 0.0019 \pm 0.0011$	0.23097 $\pm 0.00024 \pm 0.00013$

Table 3.3: Summary of the SLD A_{LR} measurements for all runs. Listed are the luminosity-weighted mean electron polarisation ($\langle \mathcal{P}_e \rangle$), the measured A_{LR}, its value corrected to the Z-pole (A^0_{LR}) and $\sin^2\theta^{lept}_{eff}$. For $\langle \mathcal{P}_e \rangle$ the total error shown is dominantly systematic. For the other quantities, the errors are the statistical and systematic components respectively. The final combined result accounts for correlated uncertainties.

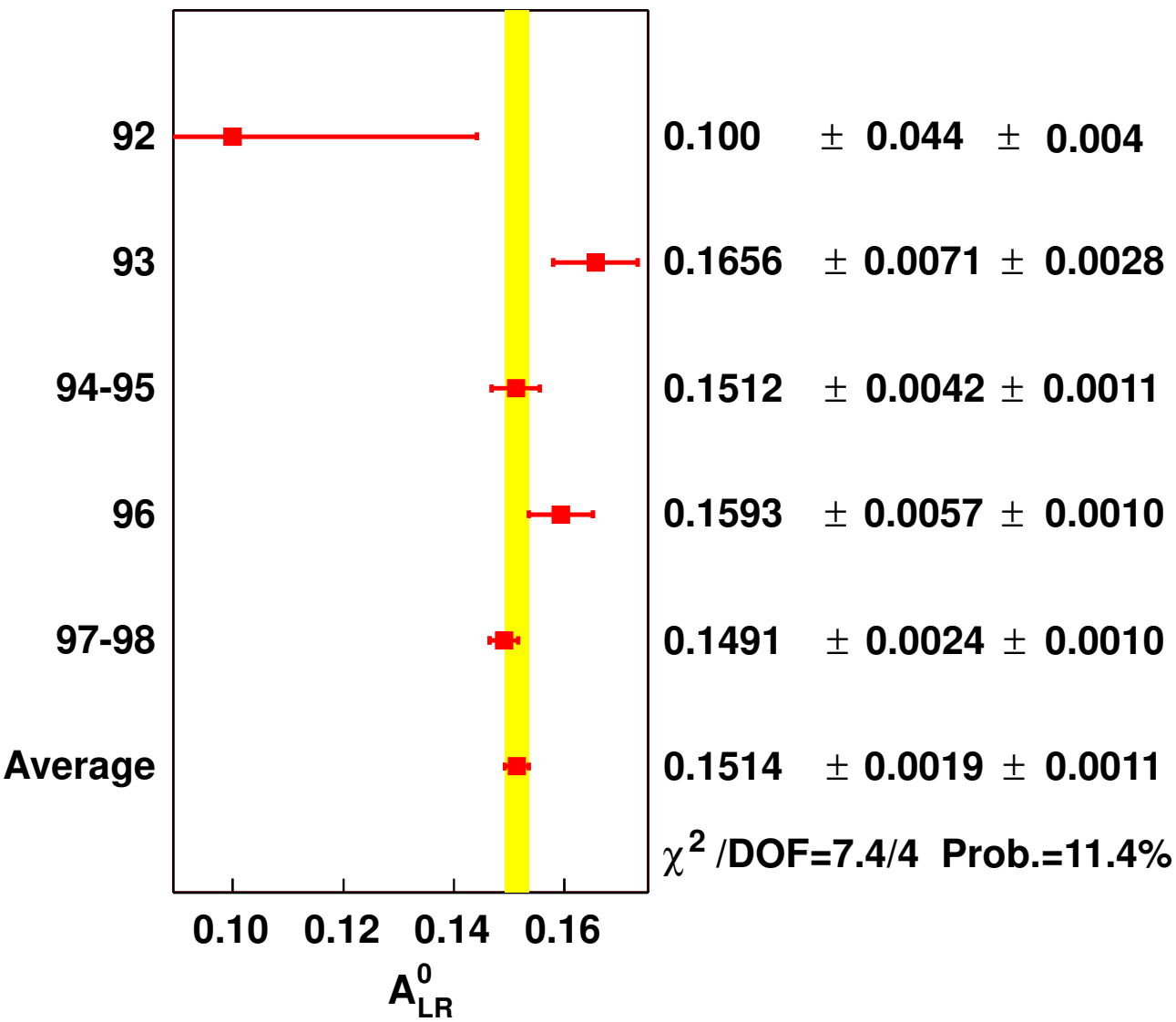

Figure 3.6: A compilation of the published SLD $A_{\rm LR}^0$ results, ordered by year. The final average is formed including correlations in systematic errors.

3.2 Lepton Asymmetry Measurements

The SLD collaboration determined the individual lepton asymmetry parameters using lepton final-state events [103, 104]. Electron polarisation allows one to determine the final-state asymmetry parameter $\mathcal{A}_\ell$ for lepton ℓ in a single measurement using the left-right forward-backward asymmetry, $A_{\rm LRFB}^{0,\ell} = \frac{3}{4}|\mathcal{P}_{\rm e}|\mathcal{A}_\ell$. An advantage of polarisation is that with $\mathcal{P}_{\rm e} = 75\%$, the left-right forward-backward asymmetries yield a statistical precision equivalent to measurements of the unpolarised forward-backward asymmetry using a 25 times larger event sample.

If lepton universality is assumed, the results for all three lepton flavours can be combined to yield a determination of $\sin^2\theta_{\rm eff}^{\rm lept}$, which in turn can be combined with the more precise result from $A_{\rm LR}$. The event sample used for $A_{\rm LR}$ is almost purely hadronic as there is only a very small, $(0.3 \pm 0.1)\%$, admixture of tau pair events - hence the left-right asymmetry of the lepton events was a statistically independent measurement. While the lepton final-state analysis described in what follows is more sophisticated than an $A_{\rm LR}$-style counting measurement, essentially all the information on $\sin^2\theta_{\rm eff}^{\rm lept}$ is obtained from the left-right asymmetry of these events. The inclusion of the distributions in polar angle that are essential for the extraction of the final-state asymmetries improves the resulting precision on $\sin^2\theta_{\rm eff}^{\rm lept}$, but only to ± 0.00076 compared to about ± 0.00078 obtained from a simple left-right event count.

The differential cross-section for the pure Z amplitude $\mathrm{e^+e^-} \to \mathrm{Z} \to \mathrm{f\bar{f}}$ is factorized as follows:

$$\begin{aligned} \frac{d}{dx}\sigma_{\rm Z}(x, s, \mathcal{P}_{\rm e}; \mathcal{A}_{\rm e}, \mathcal{A}_\ell) &\equiv f_{\rm Z}(s)\Omega_{\rm Z}(x, \mathcal{P}_{\rm e}; \mathcal{A}_{\rm e}, \mathcal{A}_\ell) \\ &= f_{\rm Z}(s)\left[(1 - \mathcal{P}_{\rm e}\mathcal{A}_{\rm e})(1 + x^2) + (\mathcal{A}_{\rm e} - \mathcal{P}_{\rm e})\mathcal{A}_\ell 2x\right], \end{aligned} \tag{3.12}$$

where $f_{\rm Z}$ isolates dependence on s, the squared centre-of-mass energy, and $\Omega_{\rm Z}$ contains the dependence on $x = \cos\theta$, which gives the direction of the outgoing lepton ℓ^- with respect to the electron-beam direction. For a complete description of lepton pair production, photon exchange terms and, if the final-state leptons are electrons, t-channel contributions have to be taken into account, as we describe below.

3.2.1 Analysis Method

Figure 3.7 shows the $\cos\theta$ distributions for $\mathrm{e^+e^-}$, $\mu^+\mu^-$, and $\tau^+\tau^-$ candidates for the 1997-1998 data. Leptonic final-state events are identified, and Table 3.4 summarises the selection efficiencies, backgrounds and numbers of selected candidates for $\mathrm{e^+e^-}$, $\mu^+\mu^-$, and $\tau^+\tau^-$ final states. The pre-1997 results are similar but have smaller acceptance $|\cos\theta| \leq 0.8$, reflecting the improved acceptance of an upgraded vertex detector used for the newer data, which allowed for efficient track finding up to $|\cos\theta| = 0.9$. The SLD event totals, including all data, are 22 254, 16 844 and 16 084 for the electron-, muon- and tau-pair final states respectively.

An event-by-event maximum likelihood fit is used to incorporate the contributions of all the terms in the cross-section and to include the effect of initial-state radiation. There are three likelihood functions for individual lepton final states. All three lepton final states contribute to the measurement of $\mathcal{A}_{\rm e}$, while $\mu^+\mu^-$ and $\tau^+\tau^-$ final states are used to determine $\mathcal{A}_\mu$ and $\mathcal{A}_\tau$ respectively.

The likelihood function for muon- and tau-pair final states is defined as follows:

$$\mathcal{L}(x, s, \mathcal{P}_{\rm e}; \mathcal{A}_{\rm e}, \mathcal{A}_\ell) = \int \mathrm{d}s' H(s, s') \left\{ \frac{\mathrm{d}}{\mathrm{d}x}\sigma_{\rm Z}(x, s', \mathcal{P}_{\rm e}; \mathcal{A}_{\rm e}, \mathcal{A}_\ell) \right.$$

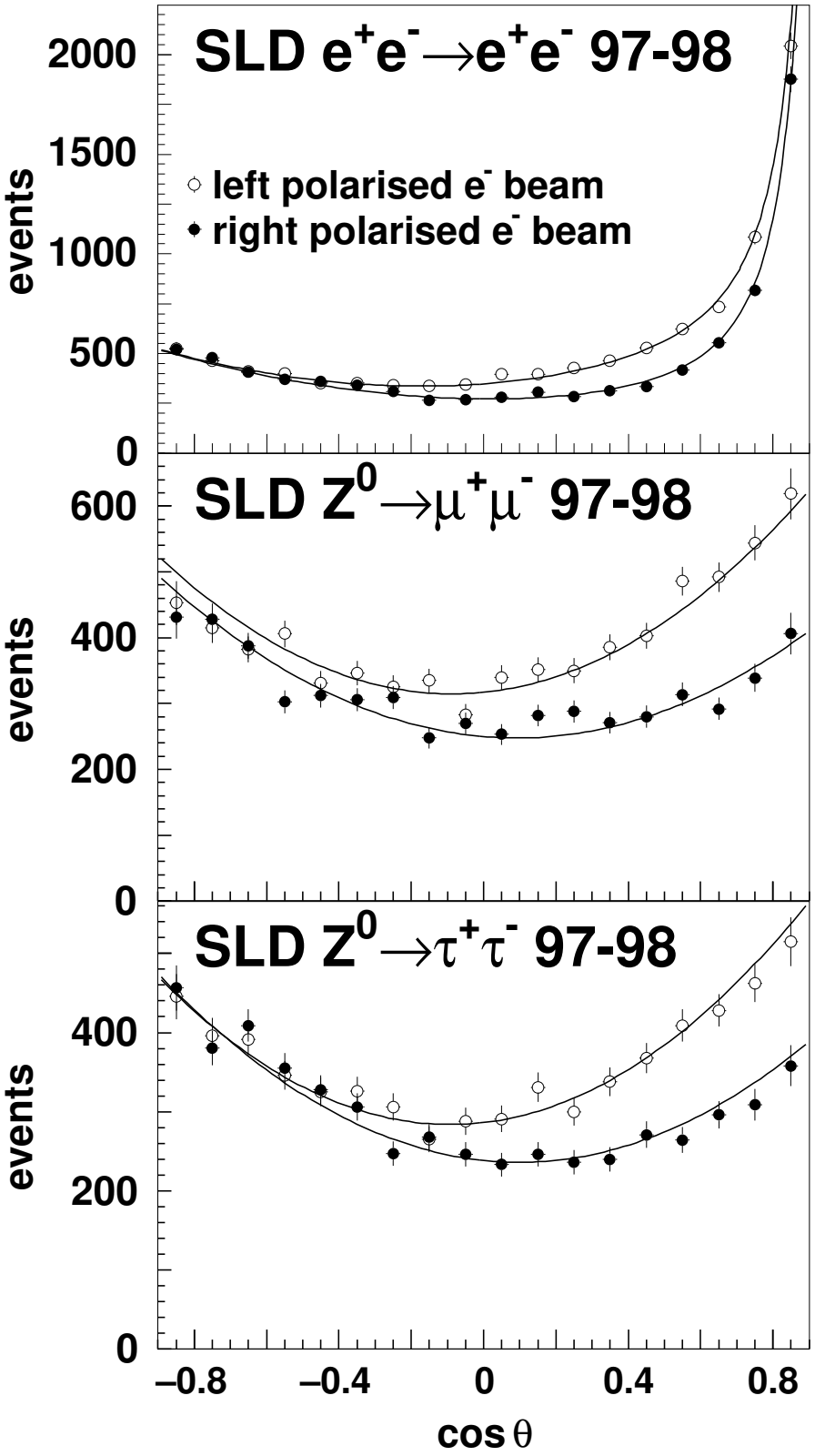

Figure 3.7: Polar-angle distributions for Z decays to e, μ and τ pairs for the 1997-1998 SLD run. The solid line represents the fit, while the points with error bars show the data in bins of 0.1 in $\cos\theta_{\rm thrust}$. For $|\cos\theta_{\rm thrust}| > 0.7$, the data are corrected for a decrease in the detection efficiency with increasing $|\cos\theta_{\rm thrust}|$. Note that the polarization independence at $\cos\theta = -1$ implied by Equation 3.12, for the case of lepton universality, is apparent.

Event Sample	Background Fraction [%]	Efficiency in $\lvert\cos\theta\rvert < 0.9$ [%]	Selected Events
$e^+e^- \to e^+e^-$	$\tau^+\tau^-$: 0.7	75	15675
$e^+e^- \to \mu^+\mu^-$	$\tau^+\tau^-$: 0.2	77	11431
$e^+e^- \to \tau^+\tau^-$	e^+e^-: $\mu^+\mu^-$: $\gamma\gamma$: had: 0.9 2.9 0.9 0.6	70	10841

Table 3.4: Summary of event selections, efficiency, and purity for $e^+e^- \to \ell^+\ell^-$ for the 1997-1998 SLD data

$$+\frac{\mathrm{d}}{\mathrm{d}x}\sigma_{Z\gamma}(x,s',\mathcal{P}_e;\mathcal{A}_e,\mathcal{A}_\ell)+\frac{\mathrm{d}}{\mathrm{d}x}\sigma_\gamma(x,s')\Big\}\,, \tag{3.13}$$

where $\mathcal{A}_e$ and $\mathcal{A}_\ell$ ($=\mathcal{A}_\mu$ or $\mathcal{A}_\tau$) are free parameters and $H(s,s')$ is a radiator function. The integration over s' was done with the program MIZA [71] to take into account the initial-state radiation. The spread in the beam energy had a negligible effect. $(\mathrm{d}\sigma_Z/\mathrm{d}x)(...)$, $(\mathrm{d}\sigma_\gamma/\mathrm{d}x)(...)$, and $(\mathrm{d}\sigma_{Z\gamma}/\mathrm{d}x)(...)$ are the tree-level differential cross-sections for Z exchange, photon exchange, and their interference. The integration was performed before the fit to obtain the coefficients $\bar{f}_Z$, $\bar{f}_{Z\gamma}$, and $\bar{f}_\gamma$, resulting in the likelihood function for muon- and tau-pair final states :

$$\mathcal{L}(x,s,\mathcal{P}_e;\mathcal{A}_e,\mathcal{A}_\ell) \;=\; \bar{f}_Z(s)\Omega_Z(x,\mathcal{P}_e;\mathcal{A}_e,\mathcal{A}_\ell)+\bar{f}_{Z\gamma}(s)\Omega_{Z\gamma}(x,\mathcal{P}_e;\mathcal{A}_e,\mathcal{A}_\ell)+\bar{f}_\gamma(s)\Omega_\gamma(x)\,, \tag{3.14}$$

where the differential cross-sections have been factorized in analogy with Equation 3.12. These coefficients gave the relative sizes of the three terms at the SLC centre-of-mass energy, e.g., $\sqrt{s} = 91.237 \pm 0.029$ GeV for the 1997-1998 run.

The e^+e^- final state includes both s-channel and t-channel Z and photon exchanges which yields four amplitudes and ten cross-section terms. All ten terms are energy-dependent. A maximum likelihood function for e^+e^- final states was defined by modifying Equations 3.13 and 3.14 to include all ten terms. The integration over s' was performed with DMIBA [105] to obtain the coefficients for the relative size of the ten terms.

3.2.2 Systematic Errors

Systematic uncertainties are summarised in Table 3.5, from which it is clear that this measurement is entirely statistics dominated. The errors for the 1997-98 dataset, which dominates the sample, are shown.

The uncertainty on the beam polarisation is correlated among all the measurements and corresponds to an uncertainty on $\mathcal{A}_\ell$ of ± 0.0008. The uncertainty in the amount of background and its effect on the fitted parameters are taken into account. The background contaminations have been derived from detailed Monte Carlo simulations as well as from studying the effect of cuts in background-rich samples of real data.

The radiative corrections and their systematic errors are estimated using MIZA [71] and DMIBA [105]. The uncertainty in the asymmetry parameters due to a $\pm 1\sigma$ variation of $\sqrt{s}$, the dominant systematic effect for radiative corrections, is of the order 10^{-4}, except for the $\mathcal{A}_e$ determination from e^+e^- final states for which it is of order 10^{-3}.

The dominant systematic error in the tau analysis results from the V-A structure of tau decay, which introduces a selection bias in the analysis. For example, if both taus decay to

Observable	$\mathcal{A}_e$	$\mathcal{A}_e$	$\mathcal{A}_e$	$\mathcal{A}_\mu$	$\mathcal{A}_\tau$
Channel $e^+e^- \to$	e^+e^-	$\mu^+\mu^-$	$\tau^+\tau^-$	$\mu^+\mu^-$	$\tau^+\tau^-$
Uncertainty	$[10^{-4}]$	$[10^{-4}]$	$[10^{-4}]$	$[10^{-4}]$	$[10^{-4}]$
Statistics	110	130	130	180	180
Polarisation	8	8	8	8	8
Backgrounds	5	–	13	–	14
Radiative Correction	23	2	2	3	2
V-A	–	–	–	–	18
Charge Confusion	–	–	–	7	11
Detector asymmetry	–	–	–	–	4
Nonuniform efficiency	2	–	–	–	–

Table 3.5: Summary of statistical and systematic uncertainties, in units of 10^{-4}, for the 1997-1998 SLD $e^+e^- \to \ell^+\ell^-$ data.

$\pi\nu$, helicity conservation requires that both pions generally have lower momentum for a left-handed τ^- and right-handed τ^+ and higher momentum otherwise. This effect, which biases the reconstructed event mass, is large at the SLD because the high beam polarisation induces a very high and asymmetric tau polarisation as a function of polar angle. The value of $\mathcal{A}_e$ extracted from $\tau^+\tau^-$ final states is not affected since the overall relative efficiencies for left-handed beam and right-handed beam events are not changed significantly, only the polar angle dependence of the efficiencies is changed.

3.2.3 Results

Results for all SLD runs are combined while accounting for small effects due to correlations entering through the systematic uncertainties in polarisation and average SLD centre-of-mass energy. From purely leptonic final states, one obtains $\mathcal{A}_e = 0.1544 \pm 0.0060$. This $\mathcal{A}_e$ result is combined with the left-right asymmetry measurement in the final tabulation of SLD leptonic asymmetry results which is reported in Table 3.6.

Parameter	Average	Correlations		
		$\mathcal{A}_e$	$\mathcal{A}_\mu$	$\mathcal{A}_\tau$
$\mathcal{A}_e$	0.1516±0.0021	1.000		
$\mathcal{A}_\mu$	0.142±0.015	0.038	1.000	
$\mathcal{A}_\tau$	0.136±0.015	0.033	0.007	1.000

Table 3.6: Results on the leptonic asymmetry parameters $\mathcal{A}_\ell$ not assuming neutral-current lepton universality obtained at SLD. The result on $\mathcal{A}_e$ includes the result on $A^0_{\rm LR}$.

3.3 Combined Results

These results are consistent with lepton universality and hence can be combined into $\mathcal{A}_\ell$, which in the context of the Standard Model is simply related to the electroweak mixing angle. Assuming lepton universality and accounting for correlated uncertainties, the combined result is:

$$\mathcal{A}_\ell = 0.1513 \pm 0.0021, \tag{3.15}$$

where the total error includes the systematic error of ± 0.0011. This measurement is equivalent to a determination of:

$$\sin^2 \theta_{\rm eff}^{\rm lept} = 0.23098 \pm 0.00026, \tag{3.16}$$

where the total error includes the systematic error of ± 0.00013.

Chapter 4

The Tau Polarisation Measurements

4.1 Introduction

Parity violation in the weak neutral current results in a non-zero longitudinal polarisation of fermion pairs produced in the reaction $e^+e^- \to f\bar{f}$, with the τ lepton being the only fundamental final-state fermion whose polarisation is experimentally accessible at LEP [106]. The τ polarisation, $\mathcal{P}_\tau$, is given by

$$\mathcal{P}_\tau \equiv (\sigma_+ - \sigma_-)/(\sigma_+ + \sigma_-)\,, \tag{4.1}$$

where σ_+ represents the cross-section for producing positive helicity τ^- leptons and σ_- those of negative helicity. The $g_{\rm L}$ and $g_{\rm R}$ neutral current couplings, introduced in Equations 1.6 and 1.7, quantify the strength of the interaction between the Z and the chiral states of the fermions. A subtle, but conceptually important, point is that the polarisation measurements involve the fermion helicity states, as opposed to their chiral states. The $(1 \pm \gamma_5)/2$ operators project out states of a definite chirality: $(1 - \gamma_5)/2$ projects out the left-handed chiral fermion (and right-handed anti-fermion) states and $(1 + \gamma_5)/2$ the right-handed chiral fermion (and left-handed anti-fermion) states. In contrast, helicity is the projection of the spin onto the direction of the fermion momentum: if the spin and momentum are oppositely aligned, the helicity is negative whereas if the spin and momentum are aligned, the helicity is positive. In the extreme relativistic limit, $(1 - \gamma_5)/2$ projects out negative helicity states and $(1 + \gamma_5)/2$ positive helicity states. The left-handed chiral fermion (and right-handed anti-fermion) states become indistinguishable from the measured negative helicity states and the right-handed chiral fermion (and left-handed anti-fermion) states from the positive helicity states. Consequently, at LEP, where the τ leptons are produced with highly relativistic energies, $\mathcal{P}_\tau$ provides a direct measurement of the chiral asymmetries of the neutral current. By convention, $\mathcal{P}_\tau \equiv \mathcal{P}_{\tau^-}$ and since, to a very good approximation, the τ^- and τ^+ have opposite helicities at LEP, $\mathcal{P}_{\tau^-} = -\mathcal{P}_{\tau^+}$.

For pure Z exchange in the interaction of the unpolarised e^+e^- beams at LEP, the dependence of $\mathcal{P}_\tau$ on θ_{τ^-}, the angle between the τ^- momentum and e^- beam, can be described by a simple relation expressed in terms of the two neutral current asymmetry parameters, $\mathcal{A}_\tau$ and $\mathcal{A}_{\rm e}$, and the forward-backward asymmetry of the τ, $A^\tau_{\rm FB}$:

$$\mathcal{P}_\tau(\cos\theta_{\tau^-}) = -\frac{\mathcal{A}_\tau(1+\cos^2\theta_{\tau^-}) + 2\mathcal{A}_{\rm e}\cos\theta_{\tau^-}}{(1+\cos^2\theta_{\tau^-}) + \frac{8}{3}A^\tau_{\rm FB}\cos\theta_{\tau^-}}. \tag{4.2}$$

The τ polarisation measurements allow for the determination of $\mathcal{A}_\tau$ and $\mathcal{A}_{\rm e}$ and are largely insensitive to $A^\tau_{\rm FB}$.

The four LEP experiments use kinematic distributions of the observable τ decay products, and the V−A nature of the charged weak current decays, to measure the polarisation as a function of $\cos\theta_{\tau^-}$ in data collected during the 1990-95 Z running period. Because the actual reaction does not only contain the pure Z propagator but also includes contributions from the photon propagator, γ–Z interference, and other photonic radiative corrections, the parameters obtained using Equation 4.2 are approximations to $\mathcal{A}_\tau$ and $\mathcal{A}_e$. In order to distinguish between these pure Z parameters and those which include the small non-Z effects, the measured parameters are denoted as $\langle\mathcal{P}_\tau\rangle$ and $A_{\rm FB}^{\rm pol}$ in the literature. $\langle\mathcal{P}_\tau\rangle$ is the average τ polarisation over all production angles and $A_{\rm FB}^{\rm pol}$ is the forward-backward polarisation asymmetry. If one had only pure Z exchange, these would be trivially related to the neutral current asymmetry parameters: $\langle\mathcal{P}_\tau\rangle = -\mathcal{A}_\tau$ and $A_{\rm FB}^{\rm pol} = -\frac{3}{4}\mathcal{A}_e$. ZFITTER [31] is used to convert from $\langle\mathcal{P}_\tau\rangle$ and $A_{\rm FB}^{\rm pol}$ to $\mathcal{A}_\tau$ and $\mathcal{A}_e$, respectively, by correcting for the contributions of the photon propagator, γ–Z interference and electromagnetic radiative corrections for initial state and final state radiation. These corrections have a $\sqrt{s}$ dependence which arises from the non-Z contributions to $\langle\mathcal{P}_\tau\rangle$ and $A_{\rm FB}^{\rm pol}$. This latter feature is important since the off-peak data are included in the event samples for all experiments. Ultimately, all LEP collaborations express their τ polarisation measurements in terms of $\mathcal{A}_\tau$ and $\mathcal{A}_e$.

It is important to remark that this method of measuring $\mathcal{P}_\tau(\cos\theta_{\tau^-})$ yields nearly independent determinations of $\mathcal{A}_\tau$ and $\mathcal{A}_e$. Consequently, the τ polarisation measurements provide not only a determination of $\sin^2\theta_{\rm eff}^{\rm lept}$ but also test the hypothesis of the universality of the couplings of the Z to the electron and τ lepton.

A general overview describing the experimental methods for measuring the τ polarisation at LEP is contained in Section 4.2. This is followed in Section 4.3 by a discussion of the dominant systematic uncertainties relevant to these measurements. The results for $\mathcal{A}_\tau$ and $\mathcal{A}_e$ from each of the four LEP experiments are presented in Section 4.4 as well as the combined results with and without the assumption of lepton universality. The treatment of correlations between the measurements in the combined results is also discussed in that section.

4.2 Experimental Methods

The polarisation measurements rely on the dependence of kinematic distributions of the observed τ decay products on the helicity of the parent τ lepton. Because the helicity of the parent cannot be determined on an event-by-event basis, the polarisation measurement is performed by fitting the observed kinematic spectrum of a particular decay mode to a linear combination of the positive and negative helicity spectra associated with that mode.

For the simplest case, that of the two-body decay of a τ lepton to a spin-zero π meson and ν_τ, $\tau \to \pi\nu_\tau$, the maximum sensitivity is provided by the energy spectrum of the π in the laboratory frame. The pure V−A charged weak current decay of the τ together with angular momentum conservation produces a π with momentum preferentially aligned with the helicity of the τ as depicted in Figure 4.1. In the laboratory frame this means that a π^- produced from the decay of a positive-helicity τ^- will, on average, be more energetic than a π^- produced from the decay of a negative-helicity τ^-.[1] In the helicity rest frame of the τ,[2] the differential decay

[1] For τ^+ decays the current is V+A and the opposite kinematic relations hold. However, because the τ^- and τ^+ are produced with opposite helicities, for a given $\mathcal{P}_\tau$ the decay distributions are the same.

[2] The τ rest frame whose z-axis is aligned with the τ momentum as measured in the laboratory frame.

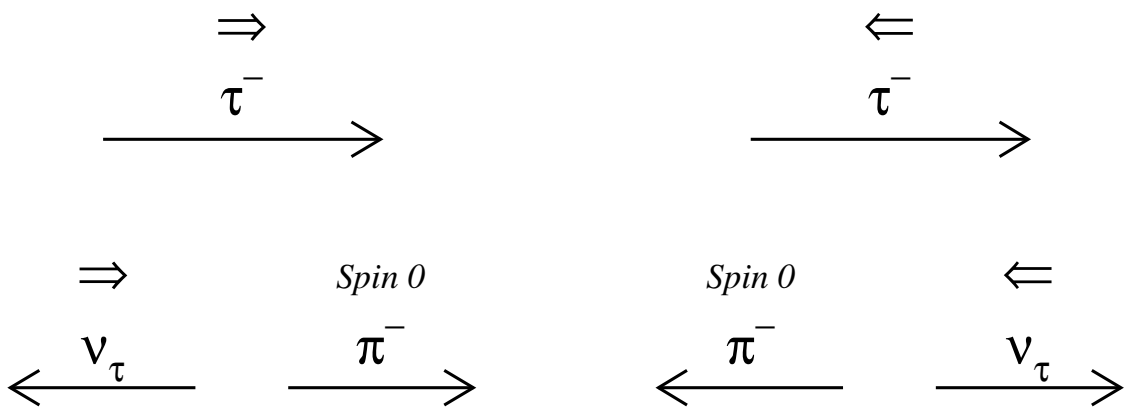

Figure 4.1: Decay configurations for two τ helicity states for the decay $\tau^- \to \pi^-\nu_\tau$. The positive helicity configuration is on the left and the negative configuration is on the right. For each particle, the long arrow depicts the momentum direction while the short double arrow that of the spin. The lower pair of figures is depicted in the helicity rest frame of the parent τ.

width is

$$\frac{1}{\Gamma}\frac{d\Gamma}{d\cos\theta_\pi} \;=\; \frac{1}{2}\left(1+\mathcal{P}_\tau\cos\theta_\pi\right)\,, \tag{4.3}$$

where θ_π is the polar angle of π momentum in the τ helicity rest frame and $\mathcal{P}_\tau$ is the net polarisation for an ensemble of τ leptons. This expression, when boosted into the lab frame, gives a differential decay width of

$$\frac{1}{\Gamma}\frac{d\Gamma}{dx_\pi} \;=\; 1+\mathcal{P}_\tau(2x_\pi-1)\,, \tag{4.4}$$

where $x_\pi = E_\pi/E_\tau$ is the pion energy in the lab frame scaled by the maximum energy available and terms of order $(m_\pi/m_\tau)^2$ have been neglected. This is depicted in Figure 4.2a for both helicity states.

More complex is the $\tau \to \rho\nu$ decay. The charged ρ is a vector meson with a 770 MeV mass which decays promptly via $\rho \to \pi\pi^0$. Having spin-1, the ρ itself is polarised with either helicity λ_ρ=0 or λ_ρ=$\pm$1 for each τ helicity configuration. The cases where the ρ is polarised with λ_ρ=0 are equivalent to the $\tau \to \pi\nu$ configurations, but the λ_ρ=$\pm$1 polarised cases produce the opposite angular distribution.

The differential widths for $\tau \to \rho\nu$ are given by [107]

$$\frac{1}{\Gamma}\frac{d\Gamma^{\lambda_\rho=0}}{d\cos\theta^*} \;=\; \frac{m_\tau^2/2}{m_\tau^2+2m_\rho^2}\left(1+\mathcal{P}_\tau\cos\theta^*\right) \tag{4.5}$$

$$\frac{1}{\Gamma}\frac{d\Gamma^{\lambda_\rho=\pm1}}{d\cos\theta^*} \;=\; \frac{m_\rho^2}{m_\tau^2+2m_\rho^2}\left(1-\mathcal{P}_\tau\cos\theta^*\right) \tag{4.6}$$

where θ^* is the angle between the ρ momentum in the τ rest frame and the direction of the τ in the laboratory frame. The latter case effectively diminishes the sensitivity to $\mathcal{P}_\tau$ when only the θ^* angle is used, or, equivalently, in the laboratory frame when only the ρ energy is used.

Much of this sensitivity, however, may be recovered by using information from the ρ decay products by, in effect, spin-analysing the ρ. The kinematic variable that provides this information is the angle, ψ, between the charged pion momentum in the ρ rest frame and the ρ flight direction in the laboratory frame. The two variables can be combined to form a single variable without loss of polarisation sensitivity [108]. This 'optimal variable', ω_ρ, is given by

$$\omega_\rho \;=\; \frac{\mathrm{W}_+(\theta^*,\psi) - \mathrm{W}_-(\theta^*,\psi)}{\mathrm{W}_+(\theta^*,\psi) + \mathrm{W}_-(\theta^*,\psi)}, \tag{4.7}$$

where $\mathrm{W}_{+(-)}$ is proportional to the differential decay width for positive (negative) helicity τ leptons, as a function of θ^* and ψ. The distributions of ω_ρ, for both positive and negative helicity τ decays, are shown in Figure 4.2b.

As with the $\tau \to \rho\nu$ decay, the $\tau \to \mathrm{a_1}\nu$ channel exhibits significantly reduced polarisation sensitivity when only the $\mathrm{a_1}$ energy is measured in the laboratory frame. The $\mathrm{a_1}$ is an axial-vector meson with mass and width of approximately 1230 MeV and 500 MeV, respectively, and decays to $\pi^-\pi^-\pi^+$ or $\pi^-\pi^0\pi^0$ with nearly equal probability. There are again two possible spin configurations where much of the sensitivity can be regained through a spin analysis of the $\mathrm{a_1}$ decay. In this case six variables are used which include: the angle θ^* between the $\mathrm{a_1}$ momentum in the τ rest frame and the τ laboratory flight direction; the angle ψ in the rest frame of the $\mathrm{a_1}$ between the vector perpendicular to the $\mathrm{a_1}$ decay plane and the $\mathrm{a_1}$ laboratory flight direction; the angle γ in the $\mathrm{a_1}$ rest frame between the unlike-sign pion momentum and the $\mathrm{a_1}$ laboratory flight direction projected into the $\mathrm{a_1}$ decay plane;[3] the 3π-invariant mass; and the two unlike-sign pion mass combinations present in the decays. In complete analogy with the $\tau \to \rho\nu$, the polarisation information from these six variables is fully contained in a single optimal variable, $\omega_{\mathrm{a_1}}$ [108]. The $\omega_{\mathrm{a_1}}$ distributions for both positive and negative helicity τ decays are plotted in Figure 4.2c.

For the leptonic channels, $\tau \to \mathrm{e}\nu\overline{\nu}$ and $\tau \to \mu\nu\overline{\nu}$, the situation is less favourable: all three final state particles carry off angular momentum, but only one of the particles is measured. This causes a substantial unrecoverable reduction in sensitivity relative to the $\tau \to \pi\nu$ channel. For these decays the variable is the scaled energy of the charged decay product: $x_\ell = E_\ell/E_\tau$ for $\ell = \mathrm{e}, \mu$. The decay distributions of the two leptonic channels are almost identical. Ignoring the masses of the daughter leptons, the differential decay width is [109]:

$$\frac{1}{\Gamma}\frac{d\Gamma}{dx_\ell} \;=\; \frac{1}{3}\left[(5 - 9x_\ell^2 + 4x_\ell^3) + \mathcal{P}_\tau(1 - 9x_\ell^2 + 8x_\ell^3)\right]. \tag{4.8}$$

Shown in Figure 4.2d are the distributions for both positive and negative helicity $\tau \to \mu\nu\overline{\nu}$ decays where the decrease in sensitivity is apparent. It should also be noted that, in contrast to the $\tau \to \pi\nu$ channel, the positive helicity case now produces a charged particle with lower energy on average than the negative helicity case.

Each LEP experiment measures $\mathcal{P}_\tau$ using the five τ decay modes $\mathrm{e}\nu\overline{\nu}$, $\mu\nu\overline{\nu}$, $\pi\nu$, $\rho\nu$ and $a_1\nu$ [110, 111, 112, 113] comprising approximately 80% of τ decays.[4] As just demonstrated, the five decay modes do not all have the same sensitivity to the τ polarisation. The maximum sensitivity for each decay mode, defined as $\frac{1}{\sqrt{N}\sigma}$ where σ is the statistical error on the polarisation measurement using N events for $\mathcal{P}_\tau$=0, is given in Table 4.1. It assumes that all the available

[3] The 'unlike-sign pion' is defined as the π^+ in the $\pi^-\pi^-\pi^+$ decay and the π^- in the $\pi^-\pi^0\pi^0$ decay.

[4] As no experiment discriminates between charged pions and kaons, the $\tau \to \pi\nu$ channel also includes $\tau \to \mathrm{K}\nu$ decays and the $\tau \to \rho\nu$ channel also includes $\tau \to \mathrm{K}\pi^0\nu$ decays. Negligible sensitivity is lost by combining these modes.

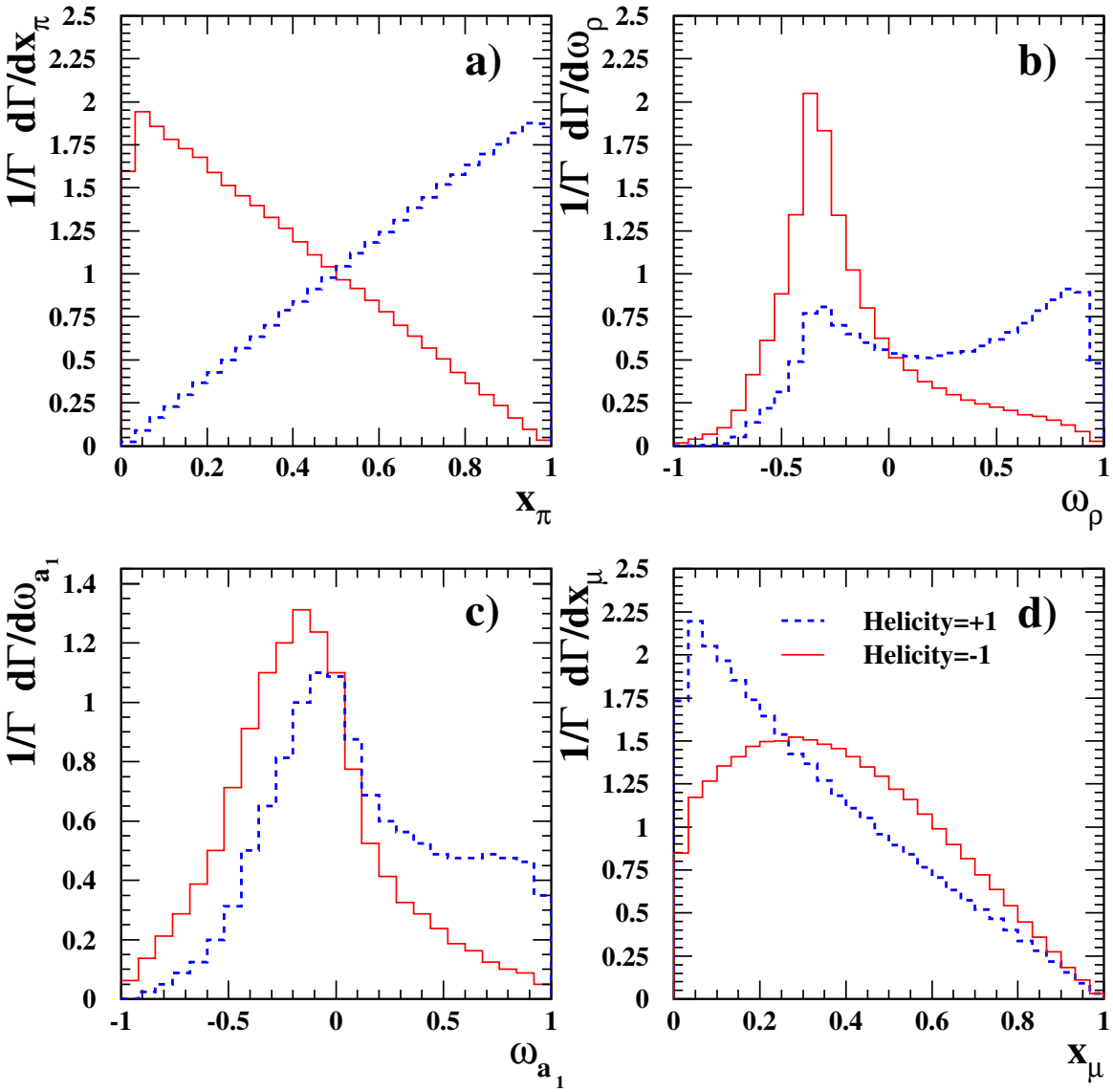

Figure 4.2: Monte Carlo simulated distributions of polarisation sensitive kinematic variables defined in the text for (a) $\tau \to \pi\nu$, (b) $\tau \to \rho\nu$, (c)$\tau \to \mathrm{a}_1\nu$ and (d) $\tau \to \mu\nu\overline{\nu}$ decays for positive and negative helicity τ leptons excluding the effects of selection and detector response.

	$\tau \to \rho\nu$	$\tau \to \pi\nu$	$\tau \to \mathrm{e}\nu\overline{\nu}$	$\tau \to \mu\nu\overline{\nu}$	$\tau \to \mathrm{a}_1\nu$ $\mathrm{a}_1 \to \pi^{\pm}\pi^{+}\pi^{-}$
Branching fraction	0.25	0.12	0.18	0.17	0.09
Maximum sensitivity:					
no 3D τ direction	0.49	0.58	0.22	0.22	0.45
with 3D τ direction	0.58	0.58	0.27	0.27	0.58
Normalised ideal weight:					
no 3D τ direction	0.44	0.30	0.06	0.06	0.13
with 3D τ direction	0.47	0.22	0.07	0.07	0.17

Table 4.1: The branching fractions, maximum sensitivity [108] and normalised ideal weight for the five decay modes listed. The ideal weight is calculated as the product of the branching fraction and the square of the maximum sensitivity. Presented in the last two lines of the table is the ideal weight for each channel divided by the sum of the ideal weights of the five channels.

information in the decay is used with full efficiency both for the case when the three-dimensional τ direction information is not used and for the case when it is used. The additional information provided by the τ direction is an azimuthal angle of the decay of the hadronic system in the τ rest frame [108]. When included in the decay distributions of spin-1 hadronic channels with even modest precision an improvement in the sensitivity is achieved. A measure of the weight with which a given decay mode ideally contributes to the overall measurement of the polarisation is given by that decay mode's sensitivity squared multiplied by its branching fraction. Normalised ideal weights, which are calculated assuming maximum sensitivity and perfect identification efficiency and purity, for each decay mode, are also given in Table 4.1. As can be seen, the $\tau \to \rho\nu$ and $\tau \to \pi\nu$ channels are expected to dominate the combined polarisation measurement, especially if information from the τ direction is not used. The actual sensitivity achieved by each experiment for its selected event sample is degraded because of inefficiencies in the process of selecting a sample of decays, by the presence of background in the sample and, to a lesser extent, by resolution effects. Much of the background from cross-contamination from other τ decay channels, however, retains some polarisation information which is exploited by the fitting procedure.

In all analyses, a value of $\mathcal{P}_\tau$ is extracted from the data by fitting linear combinations of positive and negative helicity distributions in kinematic variables appropriate to each τ decay channel to the data, where the two distributions are obtained from Monte Carlo simulation. As discussed above, in the $\tau \to \mu\nu\overline{\nu}$, $\tau \to \mathrm{e}\nu\overline{\nu}$ and $\tau \to \pi\nu$ channels, the energy of the charged particle from the τ decay divided by the beam energy is the appropriate kinematic variable while for the $\tau \to \rho\nu$ and $\tau \to \mathrm{a}_1\nu$ channels, the appropriate optimal variable, ω, is employed. Using Monte Carlo distributions in the fitting procedure allows for simple inclusion of detector effects and their correlations, efficiencies and backgrounds. Any polarisation dependence in the backgrounds from other τ decays are automatically incorporated into these analyses. The systematic errors associated with the detector then amount to uncertainties in how well the detector response is modelled by the Monte Carlo simulation, whereas the errors associated with uncertainties in the underlying physics content in the distributions arise from uncertainties in the Monte Carlo generators of the signal and backgrounds. The spin correlations between the

two τ-leptons produced in a Z decay are treated differently in the different experiments and are discussed below.

All four LEP experiments analyse the five exclusive channels listed in Table 4.1 [110, 112, 111, 113]. In addition to those, ALEPH, DELPHI and L3 include the $\tau \to \pi 2\pi^0 \nu$ mode in their exclusive channel $\tau \to \mathrm{a}_1 \nu$ analyses. ALEPH also uses information from the τ direction for the hadronic decays, as discussed in [108]. The addition of the τ direction information ideally increases the sensitivity of the $\tau \to \mathrm{a}_1 \nu$ and $\tau \to \rho \nu$ channels by the amounts indicated in Table 4.1. Examples of the different kinematic distributions from the different experiments are shown in Figures 4.3 to 4.6.

To their exclusive channel analyses, ALEPH [110], DELPHI [111] and L3 [112] add an inclusive hadronic decay analysis in which the single charged track (one-prong) hadronic decay modes are collectively analysed. This approach yields a high overall efficiency for these modes by sacrificing the optimal sensitivity characterising the analysis of high purity channels. For DELPHI and L3 the correlations between the polarisation measurements from their inclusive hadronic analysis and measurements using separately identified single-track hadronic channels are small enough that significant improvements are achieved when both results are combined. In the case of ALEPH, however, the exclusive reconstruction efficiencies are high enough to produce strong correlations between the exclusive and inclusive measurements, and little is gained from the inclusive analysis.

The OPAL [113] $\mathcal{A}_\tau$ and $\mathcal{A}_\mathrm{e}$ results are based entirely on an analysis in which all five exclusive channels listed in Table 4.1 are combined in a global binned maximum likelihood analysis. A single fit to all distributions in the kinematic observables of all decay modes and $\cos\theta_{\tau^-}$ yields $\langle \mathcal{P}_\tau \rangle$ and $A_\mathrm{FB}^\mathrm{pol}$. When both τ^+ and τ^- decays of a given event are identified, the event is analysed as a whole. This global analysis approach fully accounts for the intrinsic correlation between the helicities of the τ^+ and τ^- produced in the same Z decay, an effect which is accounted for by the other experiments by applying a correction to the statistical errors of the fit results. In such a global analysis, the evaluation of the systematic errors automatically incorporates all correlations between the systematic uncertainties in the different channels. For the channel-by-channel analyses of ALEPH, L3 and DELPHI, the correlation in the systematic errors between channels are taken into account in the combination.

DELPHI [111] augments their exclusive five channel and inclusive one-prong analysis with a separate neural network analysis of its 1993-1995 one-prong data set. The neural network is used to classify all one-prong decays as either $\tau \to \rho \nu$, $\tau \to \pi \nu$, $\tau \to \mathrm{e} \nu \overline{\nu}$, $\tau \to \mu \nu \overline{\nu}$ or $\tau \to \pi 2\pi^0 \nu$. A simultaneous fit for $\mathcal{P}_\tau$ as a function of $\cos\theta_{\tau^-}$ is performed with $\mathcal{A}_\tau$ and $\mathcal{A}_\mathrm{e}$ determined from a separate fit to the $\mathcal{P}_\tau(\cos\theta_{\tau^-})$ functional form as described below. As with OPAL's global analysis, the channel-to-channel correlated systematic errors are automatically evaluated in this analysis.

ALEPH [110] and L3 [112] complement their analyses of the kinematic distributions of the different decay modes, by including information from event acollinearity to measure the τ polarisation. Although of modest polarisation sensitivity, this information has the advantage of being sensitive to detector-related systematic errors that are different from those associated with the measurements of spectra.

In order to extract $\mathcal{A}_\tau$ and $\mathcal{A}_\mathrm{e}$ from their data, ALEPH, DELPHI and L3 measure the polarisation as a function of $\cos\theta_{\tau^-}$ and then perform a separate fit for the two parameters using the theoretical expectation of the dependence. The results quoted by OPAL [113], which depend on a single maximum likelihood fit, do not explicitly use measurements of the polarisation as a function of $\cos\theta_{\tau^-}$, although such fits are performed as cross-checks and for graphical

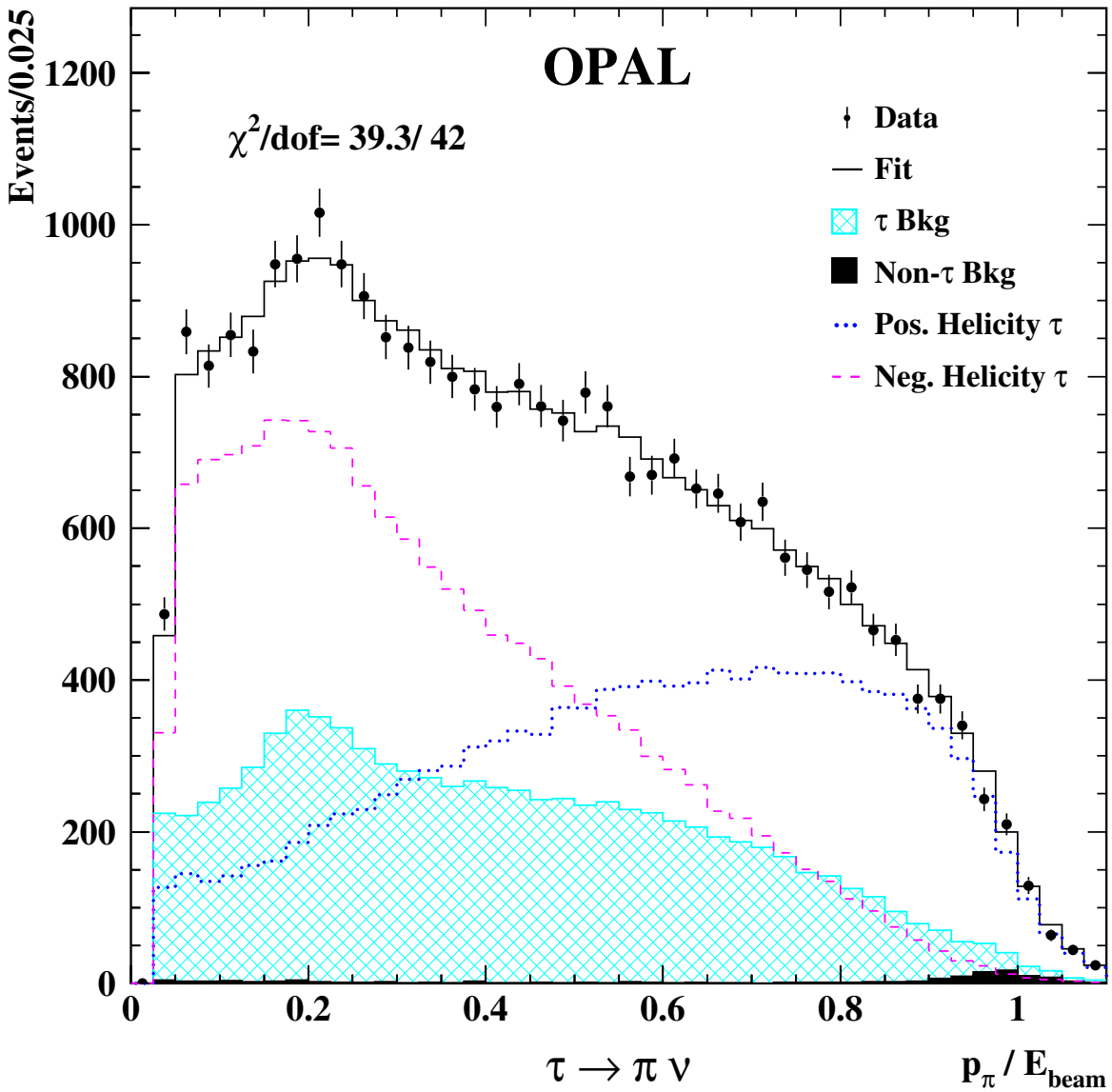

Figure 4.3: The measured distributions in the polarisation-sensitive variable for the $\tau \to \pi\nu$ decays in the OPAL experiment. The variable is the ratio of the measured charged hadron momentum to the beam energy, which is an approximation of $x_\pi = E_\pi/E_\tau$. The data, shown by points with error bars, are integrated over the whole $\cos\theta_{\tau^-}$ range. Overlaying this distribution are Monte Carlo distributions for the positive (dotted line) and negative (dashed line) helicity τ leptons and for their sum including background, assuming a value for $\langle\mathcal{P}_\tau\rangle$ equal to the fitted polarisation. The hatched histogram represents the Monte Carlo expectations of contributions from cross-contamination from other τ decays and the dark shaded histogram the background from non-τ sources. The level of agreement between the data and Monte Carlo distributions is quantified by quoting the χ^2 and the number of degrees of freedom.

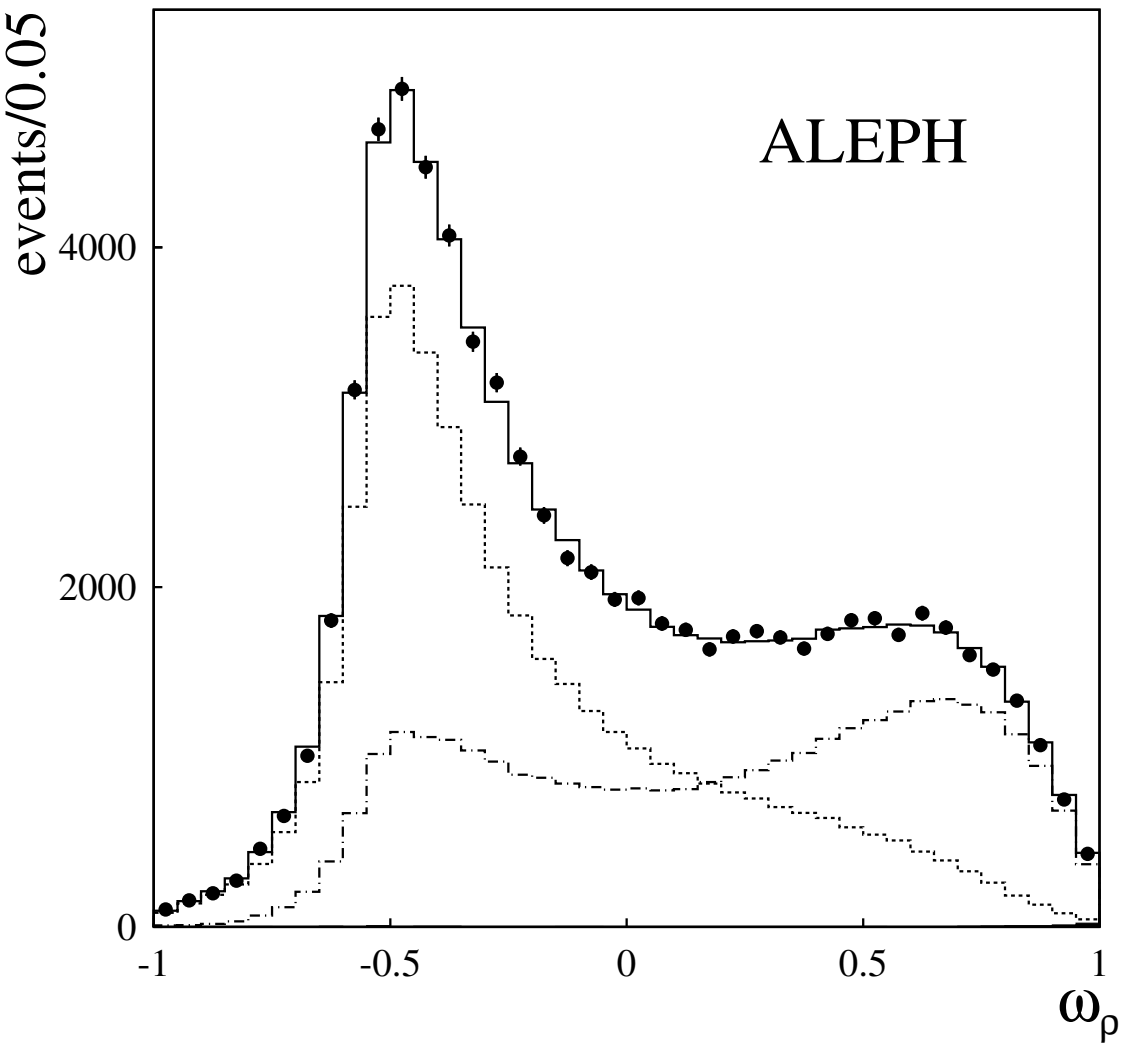

Figure 4.4: The measured spectrum of the polarisation-sensitive variable ω_ρ, described in the text, for the $\tau \to \rho\nu$ decays in the ALEPH experiment. The dashed and dashed-dotted lines correspond to the contributions of negative and positive helicity τ's, respectively. The small shaded area near ω=1 is the non-τ background contribution.

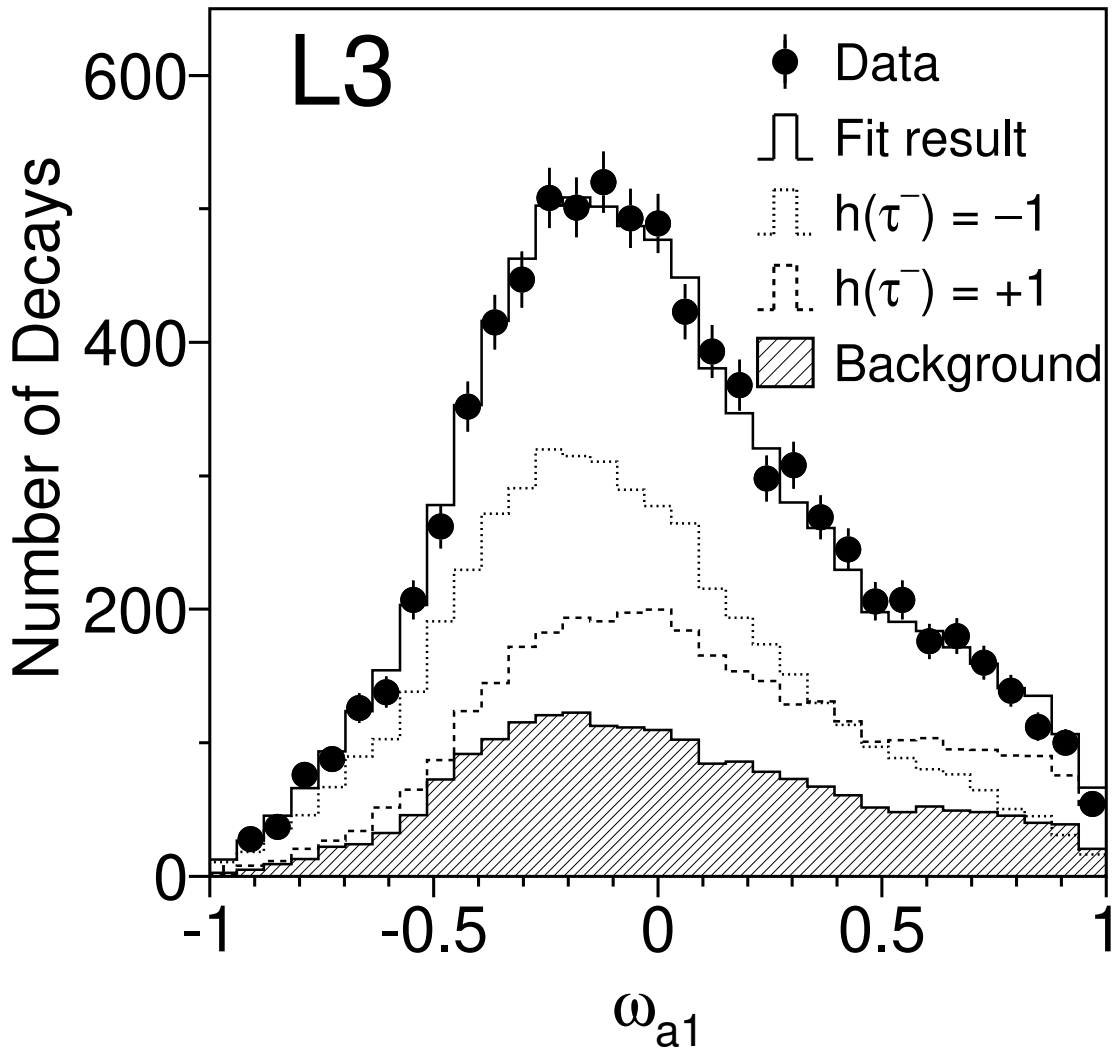

Figure 4.5: The measured spectrum of the polarisation-sensitive variable ω_{a_1}, described in the text, for the $\tau \to a_1 \nu$ decays in the L3 experiment. The distributions for both $a_1^- \to \pi^-\pi^+\pi^-$ and $a_1^- \to \pi^-\pi^0\pi^0$ decays are combined in this figure. The two helicity components and the background are shown separately.

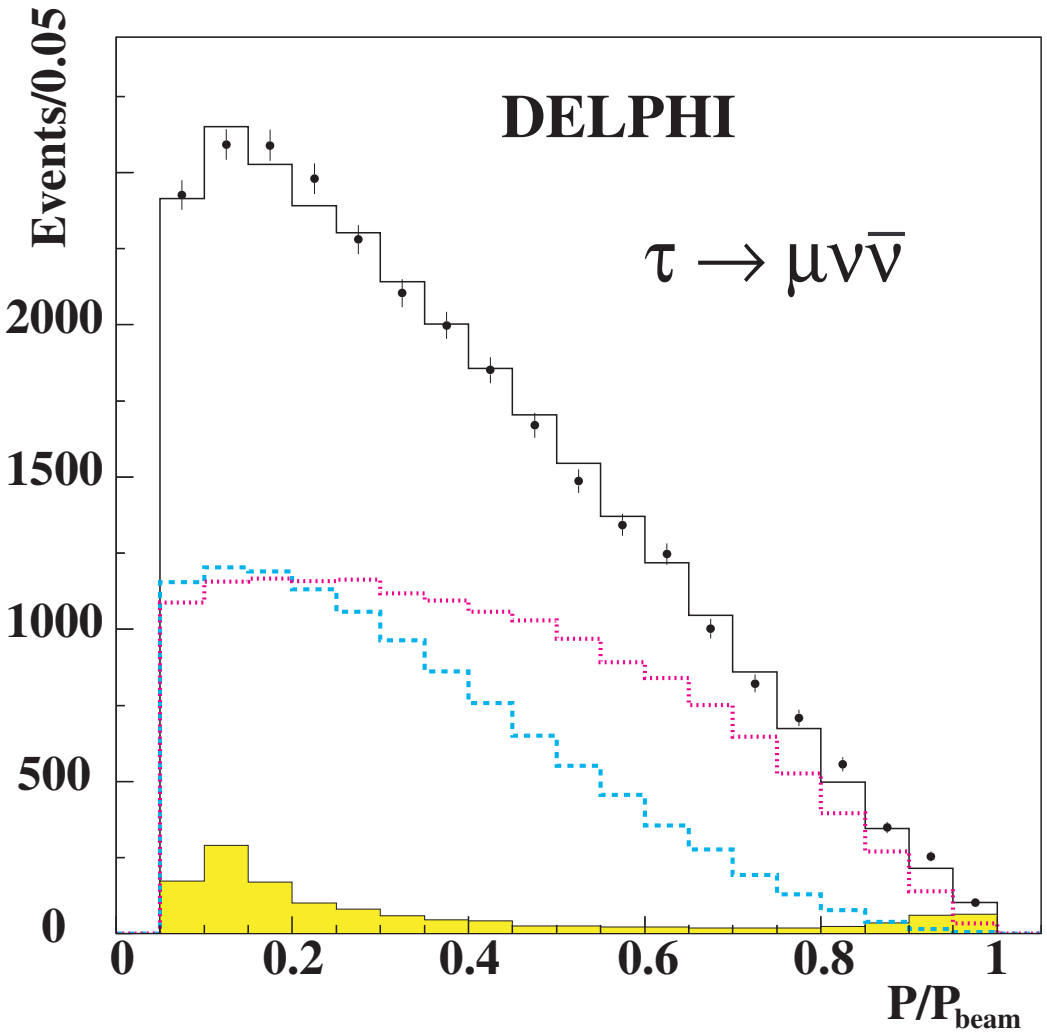

Figure 4.6: The measured spectrum of the polarisation-sensitive variable for the $\tau \to \mu\nu\bar{\nu}$ decays in the DELPHI experiment. The variable is the ratio of the measured muon momentum to the beam energy, which is an approximation of $x_\mu = E_\mu/E_\tau$. The data are compared to the results of the polarisation fit. The points with error bars are data and the solid line is simulated data for the fitted values of $\mathcal{A}_\tau$ and $\mathcal{A}_\mathrm{e}$. The shaded area is background and the dashed and dotted lines correspond to the positive and negative helicity contributions respectively.

presentation. ALEPH, L3 and OPAL use Equation 4.2 in their fits but treat $A_{\rm FB}^{\tau}$ differently as discussed in Section 4.3. Small corrections for the effects of initial state radiation, the photon propagator and γ–Z interference, and the fact that not all data are collected at the peak of the Z resonance are incorporated into the quoted values of $\mathcal{A}_\tau$ and $\mathcal{A}_{\rm e}$. These corrections, of $\mathcal{O}(0.005)$, are calculated using ZFITTER [31]. DELPHI incorporates these corrections directly into the fit they perform by using ZFITTER to predict $\mathcal{P}_\tau(\cos\theta_{\tau^-})$, averaged over the luminosity-weighted centre-of-mass energies, as a function of $\mathcal{A}_\tau$ and $\mathcal{A}_{\rm e}$. This automatically includes the QED and weak effects as a function of $\cos\theta_{\tau^-}$, rather than as a separate correction as in the approach taken by the other three LEP experiments.

Although the size of the event samples used by the four experiments are roughly equal, smaller errors on the asymmetries are obtained by ALEPH (see Table 4.3). This is largely associated with the higher angular granularity of the ALEPH electromagnetic calorimeter. The τ 'jets' produced in hadronic τ decays are tightly collimated at LEP energies which results in a substantial overlap of the energy deposited in the calorimeter by different particles. A calorimeter with a higher granularity is better able to identify the individual photons from π^0 decay and therefore provides greater discrimination between hadronic decay channels of the τ. This results in improved signal-to-noise thereby providing greater polarisation sensitivity and smaller systematic errors.

The LEP combination is made using the overall results of $\mathcal{A}_\tau$ and $\mathcal{A}_{\rm e}$ from each experiment, rather than by first combining the results for each decay mode. Correlations between decay channels are dominated by detector-specific systematic errors which are most reliably taken into account by the individual experiments as discussed in Section 4.3. The combinations of the eight measurements, four each of $\mathcal{A}_\tau$ and $\mathcal{A}_{\rm e}$, take into account all other correlations and are presented in the following sections.

4.3 Systematic Errors

As will be shown in Section 4.4, the combined statistical errors on $\mathcal{A}_\tau$ and $\mathcal{A}_{\rm e}$ are 0.0035 and 0.0048, respectively. Systematic errors on these parameters which are less than 0.0003 will not alter the combined errors when two significant figures are quoted. Therefore, such systematic errors are considered to be negligible. The one exception is the systematic error associated with ZFITTER, which contributes ± 0.0002 to all measurements of $\mathcal{A}_\tau$ and $\mathcal{A}_{\rm e}$.

The systematic errors on $\mathcal{A}_{\rm e}$ are considerably smaller than those on $\mathcal{A}_\tau$ because, for the most part, the systematic effects are symmetric in $q \times \cos\theta$ and consequently cancel in $\mathcal{A}_{\rm e}$ but not in $\mathcal{A}_\tau$.[5] This includes large cancellations of the Monte Carlo statistical errors which arise by using the same Monte Carlo samples in reflected $\cos\theta$ bins. Different approaches to evaluating the degree of cancellation of the $\mathcal{A}_{\rm e}$ systematic errors are adopted by the four experiments and are detailed in References 110, 111, 112, 113.

There are two broad categories of systematic error in these measurements: those associated with the uncertainty of the underlying physics assumptions and their treatment, and those associated with the modelling of the detector. The systematic errors in the latter category

[5] Here, q is the charge of a τ lepton whose decay is analysed and contributes to the measurements of $\mathcal{A}_\tau$ and $\mathcal{A}_{\rm e}$. Systematic differences in the responses of different $\cos\theta$ regions of a detector generate systematic errors in $\mathcal{A}_\tau$, but to contribute to $\mathcal{A}_{\rm e}$ there must be uncontrolled differences in the response of the detector to positively and negatively charged particles in the same $\cos\theta$ region of a detector. As detector responses are approximately charge-symmetric for particles passing through the same region of a detector, there are smaller systematic uncertainties associated with quantities that are symmetric in $q \times \cos\theta$.

depend on the details of each of the individual detectors. Together with Monte Carlo statistical errors, these detector modelling errors tend to dominate the systematic uncertainties. Although three of the four experiments depend on the same detector simulation software, GEANT [24], the designs of the four detectors are sufficiently different that these detector related errors are uncorrelated between experiments. However, these uncertainties can be strongly correlated between measurements from different decay channels performed with the same detector. For example, the uncertainty in the momentum scale for one of the detectors is independent of that in the other three detectors, but the momentum scale error is correlated between the $\mathcal{P}_\tau$ measurements from different decay modes made with the same detector. Because each of the experiments takes these correlations into account when quoting a systematic error on the measurements of $\mathcal{A}_\tau$ and $\mathcal{A}_\mathrm{e}$ using all channels, only the global results from each of the four experiments can be reliably combined to give a LEP average.

Turning now to the uncertainty of the treatment of the physics of τ production and decay, there are a number of systematic uncertainties in this category that are common to all four experiments. One set of these uncertainties affects all decay modes in the same way while others are different for each τ decay mode. The origins of some of the common uncertainties are the common software tools that are used to describe the production and decay of the τ [20] and the major backgrounds [20, 47, 17, 114, 115, 116]; and the tools [31] used to interpret the data in terms of the Standard Model. Another source of common errors arises from a reliance on the same physics input used in the analyses of the four experiments, such as the branching fractions of τ decay modes.

4.3.1 Decay-Independent Systematic Uncertainties

In the category of systematic uncertainty that affects all τ decay modes, the following have been identified as potential sources of error common to all experiments:

Electromagnetic radiative corrections

Initial state radiation from the e^+ and e^- and final state radiation from the τ^+ and τ^- influence the measurement in two ways. The first relates to the fact that the experiments measure $\langle\mathcal{P}_\tau\rangle$ and $A_\mathrm{FB}^\mathrm{pol}$ integrated over $\sqrt{s'}$, $\sqrt{s'}$ being the centre-of-mass energy of the τ-pair system excluding initial state radiation. This effect is included in the ZFITTER correction discussed below. The second influence relates to changes to the kinematic distributions caused by initial and final state radiation and potential $\sqrt{s'}$ biases introduced in the selection procedure. In this case, the four experiments rely on the KORALZ Monte Carlo event generator to take these effects into account. This radiation is calculated to $\mathcal{O}(\alpha^2)$ and includes exclusive exponentiation in both initial and final state radiation. Although interference between the initial and final state radiation is not included in the generator when producing the simulated events, such effects have negligible impact on the $\mathcal{P}_\tau$ measurements. Because of its precision, the treatment of initial and final state radiation, although common to all experiments, introduces no significant contribution to the systematic error.

Energy dependence of the τ polarisation

The ZFITTER treatment of $\sqrt{s}$ dependence of $\mathcal{P}_\tau$, including the effects of initial state radiation, and of photon propagator and γ–Z interference amounts to the application of the SM interpretation of $\langle\mathcal{P}_\tau\rangle$ and $A_\mathrm{FB}^\mathrm{pol}$ in terms of $\mathcal{A}_\tau$ and $\mathcal{A}_\mathrm{e}$. Although the experiments introduce this

interpretation at different stages of their analyses, it effectively involves applying corrections of $\mathcal{O}(0.005)$ to both $\langle\mathcal{P}_\tau\rangle$ and $A_{\rm FB}^{\rm pol}$. For data at the peak of the Z resonance, the photon propagator and γ–Z interference introduce the dominant component of the correction, having a value of approximately +0.005 for both $|\langle\mathcal{P}_\tau\rangle|$ and $\frac{4}{3}|A_{\rm FB}^{\rm pol}|$. Because relatively little data is collected off the peak and because the corrections below the peak are of opposite sign to those above the peak, the impact of the $\sqrt{s}$ dependence is small, contributing $\mathcal{O}(+0.0003)$ to the corrections. Initial state radiation changes the relative contribution of the pure Z exchange and introduces a small distortion to the $\mathcal{P}_\tau(\cos\theta_{\tau^-})$ relationship of Equation 4.2. The actual value of this component of the correction depends on the details of the individual experiment. However, the uncertainty on the total correction is significantly smaller than the correction itself as given by variations of the unknown parameters in the model. The variation of the Higgs mass alters this correction by ± 0.0002 and is used to estimate this uncertainty. Since all experiments rely on ZFITTER for this treatment, the error is common across experiments as well as to $\mathcal{A}_\tau$ and $\mathcal{A}_{\rm e}$.

Mass effects

Born level mass terms lead to helicity flip configurations. At the $\mathcal{O}(10^{-3})$ level, the τ^- and τ^+ will have the same instead of opposite helicities. Although this effect cannot be seen in the quoted measurements at this level of precision, it is included in the KORALZ treatment nonetheless.

The value of $A_{\rm FB}^\tau$ used in the fit

The different experiments treat this differently. ALEPH and DELPHI use the SM values of $A_{\rm FB}^\tau$ with appropriate $\sqrt{s}$ dependence. OPAL uses its measured values of $A_{\rm FB}^\tau$ for τ-pairs at the different values of $\sqrt{s}$. L3 assumes the relation $A_{\rm FB}^\tau = \frac{3}{4}\mathcal{A}_{\rm e}\mathcal{A}_\tau$ in the denominator of Equation 4.2. Since $A_{\rm FB}^\tau$ enters into the analysis as a small number in the denominator, its uncertainty introduces a correspondingly small systematic error for each experiment. Although the SM assumptions regarding $A_{\rm FB}^\tau$ by ALEPH and DELPHI imply that some correlation exists from this source between the measurements of these two experiments, it is negligible and consequently ignored in the combined LEP results. The OPAL treatment introduces a small correlation between the τ-polarisation measurement and the OPAL $A_{\rm FB}^\tau$ measurement. Varying the value of $A_{\rm FB}^\tau$ by 0.001, however, introduces negligible changes to the $\mathcal{A}_\tau$ and $\mathcal{A}_{\rm e}$ measurements.

Summary

In conclusion, all of these effects are theoretically well defined and have been calculated to more than adequate precision for the measurements at hand. Of these, only the ZFITTER error of ± 0.0002 is included as a common error in the LEP combination, see Table 4.2.

4.3.2 Decay-Dependent Systematic Uncertainties

Concerning the category of uncertainty that affects each τ decay mode separately, the following sources of potentially common systematic error have been identified:

	ALEPH		DELPHI		L3		OPAL	
	$\delta\mathcal{A}_\tau$	$\delta\mathcal{A}_\mathrm{e}$	$\delta\mathcal{A}_\tau$	$\delta\mathcal{A}_\mathrm{e}$	$\delta\mathcal{A}_\tau$	$\delta\mathcal{A}_\mathrm{e}$	$\delta\mathcal{A}_\tau$	$\delta\mathcal{A}_\mathrm{e}$
ZFITTER	0.0002	0.0002	0.0002	0.0002	0.0002	0.0002	0.0002	0.0002
τ branching fractions	0.0003	0.0000	0.0016	0.0000	0.0007	0.0012	0.0011	0.0003
two-photon bg	0.0000	0.0000	0.0005	0.0000	0.0007	0.0000	0.0000	0.0000
had. decay model	0.0012	0.0008	0.0010	0.0000	0.0010	0.0001	0.0025	0.0005

Table 4.2: The magnitude of the major common systematic errors on $\mathcal{A}_\tau$ and $\mathcal{A}_\mathrm{e}$ by category for each of the LEP experiments.

Branching fractions of the τ decay modes

These arise since the purity for selecting any particular decay mode for polarisation analysis is not unity. All experiments use the world average values of the branching fractions as determined by the Particle Data Group [117, 118], along with the quoted errors. Consequently, the components of the systematic error which are associated with uncertainties in the branching fractions are correlated between experiments. These errors are taken into account in the combined error, and are shown in Table 4.2 for the combined error on $\mathcal{A}_\tau$ and $\mathcal{A}_\mathrm{e}$ for each of the experiments.

Radiative corrections for τ leptonic decays

The radiation in the decays $\tau \to \mathrm{e}\nu\overline{\nu}$ and $\tau \to \mu\nu\overline{\nu}$ are treated exactly to $\mathcal{O}(\alpha)$ in KORALZ and negligible contributions to the systematic error are introduced by this treatment.

Bhabha background

OPAL uses the BHWIDE Monte Carlo generator [47] to describe this background while DELPHI uses the BABAMC [22] and UNIBAB [48] in addition to BHWIDE. ALEPH primarily uses UNIBAB but also uses BABAMC as an auxiliary generator. L3 uses the BHAGENE3 [46] generator. The use of common generators by some of the experiments potentially introduces a common systematic error. However, in the case of experiments where there is very little $\mathrm{e^+e^-} \to \mathrm{e^+e^-}$ background, the errors are negligible. It should be noted that much of the uncertainty associated with this is detector-specific, and in fact has been found to constitute a negligible common systematic error.

Two-photon background

The background from two-photon collision processes can be problematic since the two-photon Monte Carlo generators used by the experiments do not include initial state radiation, although these QED radiative effects are expected to be small. The potential danger is that the measured event transverse momentum (p_T), a quantity which discriminates between τ-pair events, which have large p_T, and two-photon events which have small p_T, is sensitive to initial state radiation. Consequently, low energy events, which can have a high $\mathcal{P}_\tau$ analysing power, do not have perfectly modelled backgrounds. This is common to all experiments, but the sensitivity of a given experiment to the effect depends on the effectiveness with which two-photon events are

identified and removed from the sample. These errors are taken into account in the combined error with the contributions from each experiment shown in Table 4.2 but do not represent a significant correlation because some experiments make corrections to this background based on control samples in their own data.

Modelling of hadronic decays

Model dependent uncertainties in the a_1 decay mode have been evaluated by all experiments. These uncertainties arise both in the analysis of the $\tau \to a_1\nu$ channel itself and in the analysis of channels where backgrounds from the a_1 can be significant, such as the $\tau \to \rho\nu$. These errors can be common to all experiments, but will vary in sensitivity depending on the purity of the samples and details of the analysis. The KORALZ [119] Monte Carlo simulation of the $\tau \to \pi \geq 3\pi^0\nu_\tau$ and $\tau \to 3\pi^\pm \geq 2\pi^0\nu_\tau$ decays, which are backgrounds to some of the $\mathcal{P}_\tau$ analysing channels, also have model dependencies with a corresponding uncertainty. Consequently, each experiment estimates how much these deficiencies affect their $\mathcal{P}_\tau$ measurements and, because they depend on the channel selection purity, there is variation in the magnitude of these effects between experiments.

Another aspect of hadronic decay modelling is the treatment of radiative corrections for τ hadronic final states. Unlike radiation from leptons, there is no precise formalism for handling these corrections. The KORALZ generator uses an $\mathcal{O}(\alpha)$ correction in the leading logarithmic approximation as implemented in the PHOTOS software package [120]. In the $\tau \to \pi\nu$ channel, this radiation affects the polarisation at the 0.01 level absolute, while for $\tau \to \rho\nu$ the effects are less than half that. Theoretical work [121, 122] indicates that the treatment of radiation in the decay $\tau \to \pi\nu\gamma$ is valid to the 5% level of the decay rate. Consequently, the uncertainties in the decay radiation treatment contribute at the 0.0005 level to the systematic error of the $\tau \to \pi\nu$ measurement of $\mathcal{A}_\tau$, and much less than that to the error on the combined measurements. Unfortunately, no analogous theoretical studies have been performed for the $\tau \to \rho\nu\gamma$ decay. Following reference [120], the error on the treatment of the radiation is approximately $1/\ln(m_\tau/m_\rho)$ of the magnitude of the effect of the radiation on the measurement of $\mathcal{P}_\tau$. This results in an error of no more than 0.001 on $\mathcal{A}_\tau$ and a negligible error on $\mathcal{A}_e$. The equivalent radiation effects for the other hadronic decay modes introduce a negligible contribution to the combined systematic error. These hadronic modelling errors are summarised in Table 4.2 and are found to contribute a small effect to the measurements over all channels.

Modelling of multihadronic background

The modelling uncertainty of the multihadronic background introduces negligible errors in all channels but the $\tau \to a_1\nu$. However, because the background itself is small and the weight of the $\tau \to a_1\nu$ measurement is not high, this is a negligible contribution to the error on $\mathcal{P}_\tau$ from all channels.

Modelling of muon-pair background

The modelling of μ-pair background has a negligible error. Any uncertainty arising from μ-pair events is evaluated as a detector-related systematic error.

4.4 Results

Figure 4.7 shows the measured values of $\mathcal{P}_\tau$ as a function of $\cos\theta_{\tau^-}$ for all four LEP experiments. The curves overlaying the figure depict Equation 4.2 for the combined results with and without assuming lepton universality. It is interesting to remark that if lepton universality is assumed, $\mathcal{P}_\tau$ is forced to be zero at $\cos\theta_{\tau^-} = -1$, regardless of the actual values of the SM couplings. From Figure 4.7 it is evident that the data are indeed consistent with $\mathcal{P}_\tau$=0 at $\cos\theta_{\tau^-} = -1$.

The results for $\mathcal{A}_\tau$ and $\mathcal{A}_\mathrm{e}$ obtained by the four LEP collaborations [110, 111, 112, 113] are shown in Table 4.3. The measurements from all experiments are consistent with each other and are combined to give values of $\mathcal{A}_\tau$ and $\mathcal{A}_\mathrm{e}$ from a fit which includes the effects of correlated errors. The combined results are included in Table 4.3 and are also summarised in Figure 4.8.

There are small ($\leq 5\%$) statistical and, in some cases, systematic correlations between $\mathcal{A}_\tau$ and $\mathcal{A}_\mathrm{e}$ performed by a single experiment. There are also systematic correlations between the different experimental values as discussed in the previous section. Therefore a single fit to all of the data using the complete 8×8 error correlation matrix, given in Table 4.4, is used to obtain the LEP combined values of these two parameters.

We take the ±0.0002 ZFITTER errors to be fully correlated between $\mathcal{A}_\tau$ and $\mathcal{A}_\mathrm{e}$. Other systematic errors listed in Table 4.2 are taken to be fully correlated between either $\mathcal{A}_\tau$ or $\mathcal{A}_\mathrm{e}$ measurements. These are used to calculate the inter-experiment off-diagonal elements of the error correlation matrix. The correlated errors between $\mathcal{A}_\tau$ and $\mathcal{A}_\mathrm{e}$ for a given experiment as quoted by the experiment are also included in the error correlation matrix.

The fitted values for $\mathcal{A}_\tau$ and $\mathcal{A}_\mathrm{e}$ with no assumption of lepton universality are:

$$\mathcal{A}_\tau = 0.1439 \pm 0.0043 \tag{4.9}$$

$$\mathcal{A}_\mathrm{e} = 0.1498 \pm 0.0049\,, \tag{4.10}$$

where the χ^2 is 3.9 for six degrees of freedom and the correlation is +0.012. These asymmetries are consistent with each other, in agreement with lepton universality. Assuming e-τ universality, the values for $\mathcal{A}_\tau$ and $\mathcal{A}_\mathrm{e}$ can be combined in a fit with a single lepton asymmetry parameter which yields a result of:

$$\mathcal{A}_\ell = 0.1465 \pm 0.0033\,, \tag{4.11}$$

where the total error contains the systematic error of 0.0015. The χ^2 is 0.8 for one degree of freedom, considering this to be a combination of $\mathcal{A}_\tau$ and $\mathcal{A}_\mathrm{e}$. If one considers the eight measurements contributing to $\mathcal{A}_\ell$, the χ^2 is 4.7 for seven degrees of freedom. This value of $\mathcal{A}_\ell$ corresponds to a value of:

$$\sin^2\theta^{\mathrm{lept}}_{\mathrm{eff}} = 0.23159 \pm 0.00041\,. \tag{4.12}$$

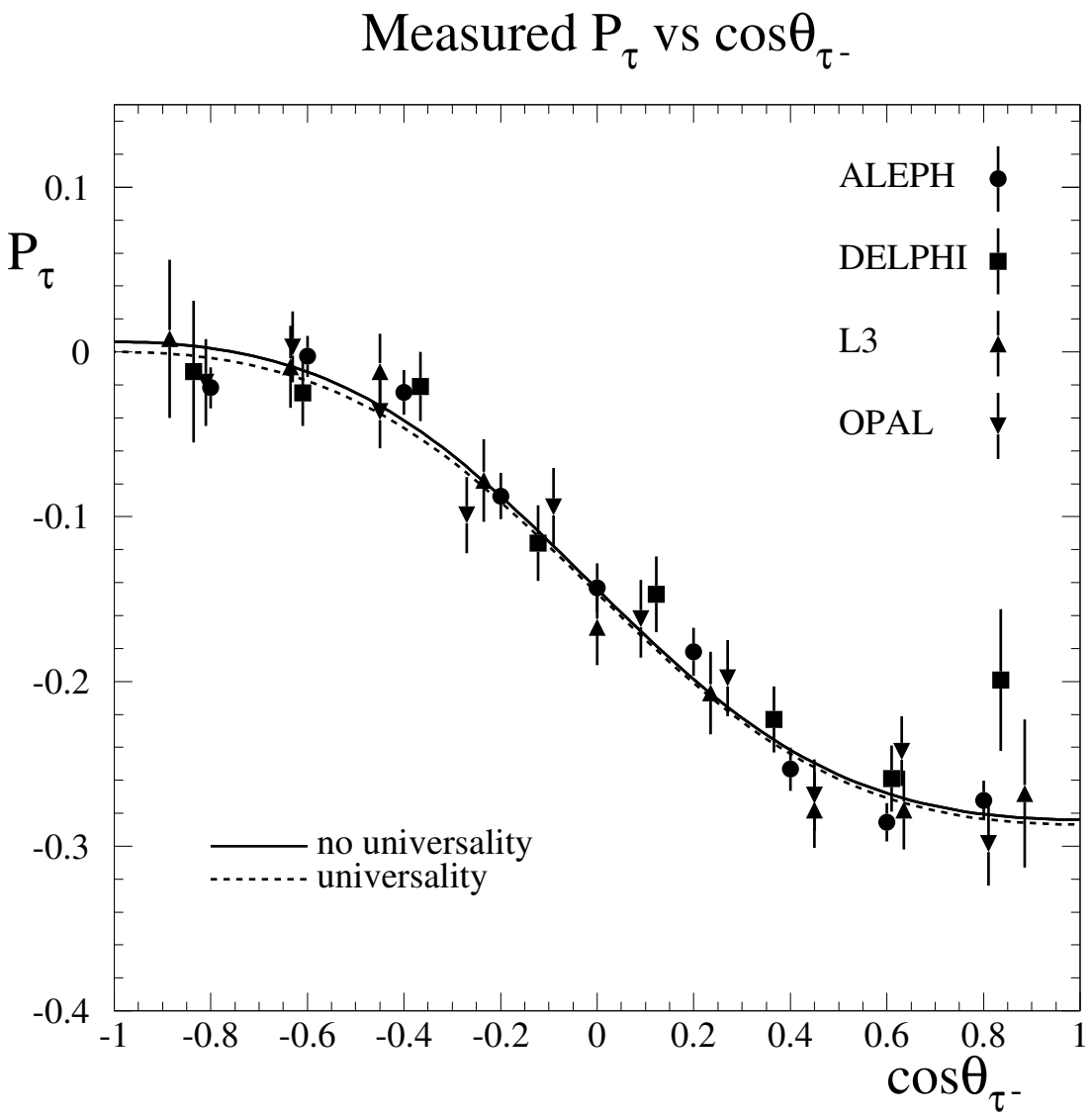

Figure 4.7: The values of $\mathcal{P}_\tau$ as a function of $\cos\theta_{\tau^-}$ as measured by each of the LEP experiments. Only the statistical errors are shown. The values are not corrected for radiation, interference or pure photon exchange. The solid curve overlays Equation 4.2 for the LEP values of $\mathcal{A}_\tau$ and $\mathcal{A}_e$. The dashed curve overlays Equation 4.2 under the assumption of lepton universality for the LEP value of $\mathcal{A}_\ell$.

Experiment	$\mathcal{A}_\tau$	$\mathcal{A}_\mathrm{e}$
ALEPH	$0.1451 \pm 0.0052 \pm 0.0029$	$0.1504 \pm 0.0068 \pm 0.0008$
DELPHI	$0.1359 \pm 0.0079 \pm 0.0055$	$0.1382 \pm 0.0116 \pm 0.0005$
L3	$0.1476 \pm 0.0088 \pm 0.0062$	$0.1678 \pm 0.0127 \pm 0.0030$
OPAL	$0.1456 \pm 0.0076 \pm 0.0057$	$0.1454 \pm 0.0108 \pm 0.0036$
LEP	$0.1439 \pm 0.0035 \pm 0.0026$	$0.1498 \pm 0.0048 \pm 0.0009$

Table 4.3: LEP results for $\mathcal{A}_\tau$ and $\mathcal{A}_\mathrm{e}$. The first error is statistical and the second systematic.

	$\mathcal{A}_\tau$(A)	$\mathcal{A}_\tau$(D)	$\mathcal{A}_\tau$(L)	$\mathcal{A}_\tau$(O)	$\mathcal{A}_\mathrm{e}$(A)	$\mathcal{A}_\mathrm{e}$(D)	$\mathcal{A}_\mathrm{e}$(L)	$\mathcal{A}_\mathrm{e}$(O)
$\mathcal{A}_\tau$(A)	1.000							
$\mathcal{A}_\tau$(D)	0.029	1.000						
$\mathcal{A}_\tau$(L)	0.022	0.024	1.000					
$\mathcal{A}_\tau$(O)	0.059	0.047	0.032	1.000				
$\mathcal{A}_\mathrm{e}$(A)	-0.002	0.000	0.000	0.000	1.000			
$\mathcal{A}_\mathrm{e}$(D)	0.000	0.025	0.000	0.000	0.000	1.000		
$\mathcal{A}_\mathrm{e}$(L)	0.000	0.000	0.032	0.000	0.001	0.000	1.000	
$\mathcal{A}_\mathrm{e}$(O)	0.000	0.000	0.000	0.025	0.005	0.000	0.002	1.000

Table 4.4: Error correlation matrix for the total error of the eight measurements, used for the combination of the LEP results for $\mathcal{A}_\tau$ and $\mathcal{A}_\mathrm{e}$. The order is: $\mathcal{A}_\tau$ for ALEPH, DELPHI, L3 and OPAL; followed by $\mathcal{A}_\mathrm{e}$ for ALEPH, DELPHI, L3 and OPAL.

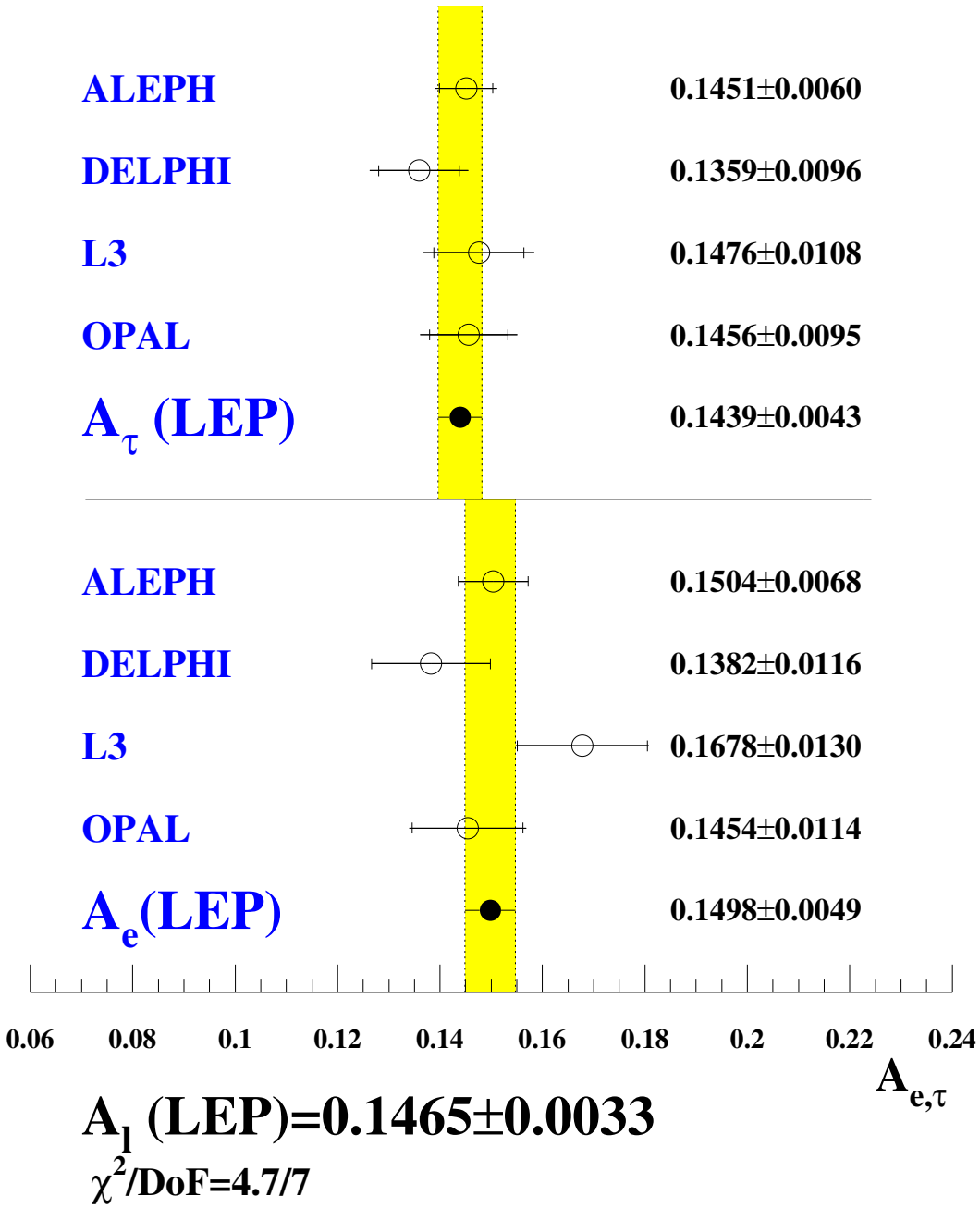

Figure 4.8: Measurements of $\mathcal{A}_\tau$ and $\mathcal{A}_\mathrm{e}$ from the four LEP experiments. The error bars indicate the quadrature sum of the statistical and systematic errors. The magnitude of the statistical error alone is indicated by the small tick marks on each error bar. The value of $\mathcal{A}_\ell$ and the χ^2 of the fit assuming lepton universality are also quoted.

Chapter 5

Results from b and c Quarks

5.1 Introduction

Heavy flavours can be identified with high efficiency and purity at LEP and SLD, allowing precise electroweak measurements. As already explained in Chapter 1, the b and c partial widths, normalised to the total hadronic width of the Z: R^0_{b}, R^0_{c}, the forward-backward asymmetries with unpolarised beams: $A^{\mathrm{b\overline{b}}}_{\mathrm{FB}}$, $A^{\mathrm{c\overline{c}}}_{\mathrm{FB}}$, and, with polarised beams, the left-right-forward-backward asymmetries: $A^{\mathrm{b\overline{b}}}_{\mathrm{LRFB}}$, $A^{\mathrm{c\overline{c}}}_{\mathrm{LRFB}}$, can be measured. These measurements probe the fundamental charge and weak-isospin structure of the Standard Model (SM) couplings for quarks and, in case of $A^{\mathrm{b\overline{b}}}_{\mathrm{FB}}$ and $A^{\mathrm{c\overline{c}}}_{\mathrm{FB}}$ for the initial state leptons. The ratio R^0_{b} is of special interest since it probes corrections to the $\mathrm{Zb\overline{b}}$ vertex which are sensitive to new physics, for example from a super-symmetric Higgs sector. As illustrated in Figure 1.14, the SM predictions for the quark asymmetry parameters, $\mathcal{A}_{\mathrm{q}}$ are essentially fixed points in the model, insensitive even to variations in $\sin^2\theta^{\mathrm{q}}_{\mathrm{eff}}$. If $\mathcal{A}_{\mathrm{q}}$ agrees with the SM prediction this fact makes the $A^{\mathrm{q\overline{q}}}_{\mathrm{FB}}$ measurements sensitive probes of the initial-state $\mathrm{Ze^+e^-}$-couplings, resulting in one of the most precise measurements of $\sin^2\theta^{\mathrm{lept}}_{\mathrm{eff}}$. Even considering departures from the SM, predictions for $\mathcal{A}_{\mathrm{q}}$ are basically invariant in any model where new physics appears only in loops, making $A^{\mathrm{q\overline{q}}}_{\mathrm{LRFB}} = 3/4\mathcal{A}_{\mathrm{q}}$ a good experimental test for new Born-level physics like Z-Z′ mixing. Due to the inferior tagging possibilities for light quarks, as discussed in Appendix F, electroweak tests of similar precision are not possible for u, d or s quarks.

The LEP experiments and SLD measure these quantities with a variety of methods. Since all the measurements make some assumptions about the fragmentation of b- and c-quarks and decays of hadrons containing these heavy quarks, there are many sources of systematic correlations between them. In addition, different observables are sometimes measured simultaneously, giving rise to statistical correlations between the results. For these reasons a simple average of the different results is not sufficient. A more sophisticated procedure is needed as described below.

To derive consistent averages the experiments have agreed on a common set of input parameters and associated uncertainties. These parameters are described in Section 5.6. They consist of the electroweak parameters of interest plus some auxiliary parameters that are included in the combination for technical reasons. These auxiliary parameters from LEP and SLD are either measured together with some of the electroweak quantities or they share systematic uncertainties with them. To treat the dependences of these parameters on the electroweak parameters correctly they are included in the electroweak heavy flavour fit. The fit parameters in the electroweak heavy flavour fit thus are:

- the Z partial decay widths to b- and c-quarks normalised to the Z hadronic width: $R^0_{\rm b}$, $R^0_{\rm c}$,
- the b- and c-quark forward-backward asymmetries: $A^{\rm b,c}_{\rm FB}(\sqrt{s})$, either at three different centre-of-mass energies around the Z-peak or with all asymmetries transported to the peak,
- the b- and c-quark asymmetry parameters: $\mathcal{A}_{\rm b}$, $\mathcal{A}_{\rm c}$ measured from the left-right-forward-backward asymmetries at SLD,
- the $\rm B^0\overline{B^0}$ effective mixing parameter $\overline{\chi}$, which is the probability that a semileptonically decaying b-quark has been produced as an anti-b-quark,
- the prompt and cascade semileptonic branching fraction of the b-hadrons $B(\rm b \to \ell^-)$[1] and $B(\rm b \to c \to \ell^+)$ and the prompt semileptonic branching fraction of the c-hadrons $B(\rm c \to \ell^+)$.
- the fraction of charm hemispheres fragmenting into a specified weakly-decaying charmed hadron: $f(\rm D^+)$, $f(\rm D_s)$, $f(\rm c_{baryon})$,[2]
- the probability that a c-quark fragments into a $\rm D^{*+}$ that decays into $\rm D^0\pi^+$: $P(\rm c \to D^{*+}) \times B(\rm D^{*+} \to \pi^+ D^0)$, denoted $P(\rm c \to D^{*+} \to \pi^+ D^0)$ in the following.

The input parameters used in the combination are either the fit parameters themselves or simple combinations of them that make a correct error treatment easier.

The methods of tagging heavy flavours at LEP and SLD are described in Section 5.2. The different measurements of the electroweak and auxiliary parameters used in the heavy flavour combinations are outlined in Sections 5.3 to 5.5. Section 5.6 describes the agreed common external parameters. In Section 5.7 the corrections to the electroweak parameters due to physics effects such as QED and QCD corrections are described, and the combination procedure is explained in Section 5.8. Finally the results are summarised in Section 5.9.

5.2 Heavy Flavour Tagging Methods

In principle, the rate measurements $R_{\rm q} = \sigma_{\rm q}/\sigma_{\rm had}$ only require a selection of the quark flavour q from hadronic events with an identification algorithm, usually referred to as a tag, that has efficiencies and purities that are known to high precision. The asymmetry measurements require in addition that a distinction between quark and antiquark is made, with a known charge-tagging efficiency. Cancellations in the asymmetry definition make these measurements largely independent of the flavour tagging efficiency, apart from background corrections.

At LEP and SLD three basic methods are used for flavour tagging. In the first method the finite path traversed by the hadron containing the heavy quark during its long lifetime is utilised. Due to the somewhat longer lifetime and the larger mass these methods are especially efficient for b-quarks. They tag only the flavour of the quarks. To obtain the quark charge additional methods have to be used.

The second and historically oldest method is to tag prompt leptons. b- and c-quarks can decay semileptonically and, because of the higher b-mass, the two quark species can be separated by the transverse momentum of the lepton with respect to the jet axis. For direct decays

[1] Unless otherwise stated, charge conjugate modes are always included.

[2] The quantity $f(\rm D^0)$ is calculated from the constraint $f(\rm D^0) + f(\rm D^+) + f(\rm D_s) + f(\rm c_{baryon}) = 1$.

the sign of the quark charge is equal to that of the lepton, so that leptons tag simultaneously the quark flavour and charge.

The third method is the reconstruction of charmed hadrons. Most charmed hadrons have low multiplicity decay modes with relatively high branching fractions so that they can be used for flavour tagging. Since most charmed hadron decays are not charge symmetric they can also be used for quark charge tagging. Charmed hadrons tag charm quarks and, via the decay $b \to c$, b-quarks. Properties of the fragmentation or lifetime tags have thus to be used to separate the two.

5.2.1 Lifetime Tagging

Lifetime tagging represents the most efficient and pure way of selecting b-hadrons from hadronic Z decays. The two principal techniques are based on the reconstruction of secondary vertices and on the measurement of the large impact parameter of the b-hadron decay products. Since the average b lifetime is about 1.6 ps and the b-hadrons are produced with a mean energy of 32 GeV at the Z peak, they travel for about 3 mm before decaying. Their mean charged multiplicity is $\sim$5 (see Section 5.6.3). The silicon vertex detectors of the LEP experiments and SLD have a resolution for the secondary vertex position about one order of magnitude smaller than the mean decay length.

Since the b-hadron decay vertex is separated from the e^+e^--interaction point, some of the tracks originating from the decay will appear to miss the reconstructed primary vertex. The impact parameter is defined as the distance of closest approach of the reconstructed track to the interaction point. It is given by

$$\delta = \gamma\beta c\tau \sin\psi \,, \tag{5.1}$$

where τ is the particle proper decay time and ψ is the angle between the secondary particle and the b-hadron flight direction in the lab frame.

For a high momentum track, $\sin\psi$ is proportional to $1/\beta\gamma$, and the average impact parameter is then proportional to the average lifetime τ: $\delta \propto c\tau$, independent of the b-hadron energy. Since at LEP the b-hadron momentum is high, the uncertainty on the b-hadron momentum distribution, i.e. the b-fragmentation function, has only a small effect on the impact parameter distribution. The impact parameter of the b-hadrons is about 300 μm, to be compared with the experimental resolution of 20 to 70 μm, depending on the track momentum. ALEPH, L3, and SLD compute the impact parameter in 3D space, while DELPHI and OPAL compute the impact parameter separately in the two projections $R\phi$ and Rz. The two projections are then treated as two separate variables.

The precise determination of the Z decay point, the so called primary vertex, is required in lifetime b-tagging techniques. It is determined separately for each hadronic event using the location of the e^+e^- interaction region (the beam spot) as a constraint. At LEP the width along the horizontal x-axis varies with time but is typically 100 to 150 μm. The width along the vertical y-axis is around 5 μm, which is below the detector resolution, and the longitudinal length along the z-axis is about 1 cm. Since the beam spot width in z is much larger than the detector resolution, the exact position and width in this direction does not influence the tagging efficiencies. At SLC the beam spot is only a few microns wide in the transverse ($R\phi$) plane, giving an almost point-like primary vertex resolution. Only the vertex position along the z-axis needs to be reconstructed event by event.

The event primary vertex is determined by a fit to all tracks after having excluded tracks classified to originate from decays of long lived particles or hadronic interaction products. The

	ALEPH	DELPHI	L3	OPAL	SLD
Number of layers	2	3	2	2	3
Radius of layers (cm)	6.5/11.3	6.3/9/11	6.2/7.7	6.1/7.5	2.7-4.8
$R\phi$ imp. par. res. (μm)	25*	20	30	16	8
z imp. par. res. (μm)		30	100	35	10
Primary vertex res. $x \times y \times z$ (μm)	$58 \times 10 \times 60$	$60 \times 10 \times 70$	$77 \times 10 \times 100$	$80 \times 12 \times 85$	$4 \times 4 \times 17$

Table 5.1: Vertex detector characteristics and experimental resolutions: the impact parameter resolution is given for 45 GeV muons and the vertex resolution is given for $b\bar{b}$-events when including the beam spot information.
* for ALEPH the 3D impact parameter resolution is given.

precision of the reconstructed primary vertex position depends on the algorithm used, on the geometry of the silicon vertex detectors and on the size of the beam spot. The parameters of the various vertex detectors and the relevant resolution for a lifetime b-tag are summarised for the LEP and SLC experiments in Table 5.1.

A lifetime sign is assigned to each track impact parameter. This is positive if the extrapolated track is consistent with a secondary vertex which lies on the same side of the primary vertex as the track itself, otherwise it is negative. Due to the finite resolution of the detector, the relevant quantity for the identification of the b-quark is the impact parameter significance S, defined as the lifetime-signed impact parameter divided by its error. In Figure 5.1 the projection in the $R\phi$ plane of the lifetime-signed impact parameter significance distribution is shown for tracks coming from the different quark flavours. Decay tracks of a K^0_s and Λ are removed, so that the distribution of the light quark reflects the resolution of the apparatus (DELPHI in this case).

A good description of S in the simulation is crucial for a reliable estimate of the tagging efficiencies. Negative significance values arise mainly from primary-vertex-tracks, which have no lifetime information and show the effects of finite resolution. This allows a calibration of the tag from the negative side of the significance distribution. Even for tracks coming from the primary vertex the distribution of S is expected to be non-Gaussian. This is caused by pattern recognition mistakes, non-Gaussian tails of multiple scattering and elastic hadronic interactions. It has been verified by simulation that these tails are symmetric for primary tracks.

A simple b-tag can use the number of tracks with a large positive significance. A better estimator is constructed by combining all the positive track significances: first the negative part of the significance distribution is fitted to a functional form that defines the resolution of the detector, then for each track the integral of this function from negative infinity to the S of the track is computed giving the probability that the track originates from the primary vertex, which by construction is flat from zero to one. The probability that all tracks in a jet, hemisphere or event, come from the primary vertex is calculated by combining the probabilities for all tracks in that jet, hemisphere or event [123]. By construction it is flat if all tracks originate from the primary vertex. The probability for a group of tracks from an u, d or s event is then flat between zero and one. The probability for a group of tracks from a b-quark event, however, is peaked at zero.

Figure 5.2 shows the distribution of the L3 b-tagging variable D which is the negative

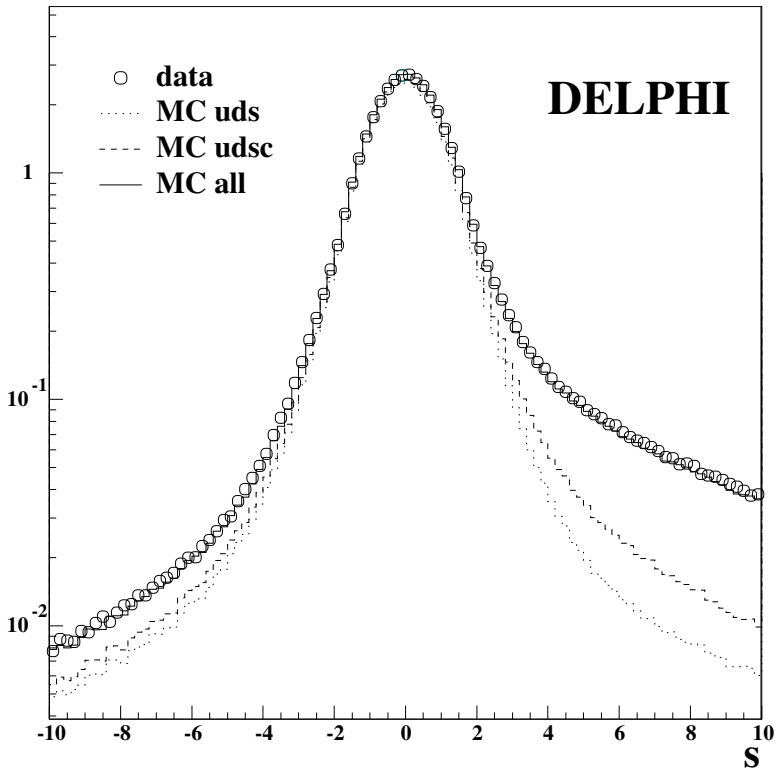

Figure 5.1: Impact parameter significance from DELPHI for data and simulation. The contributions of the different quark flavours are shown separately. The normalisation is arbitrary.

logarithm of the hemisphere impact parameter probability. It can be seen that at large values of D high tag purities can be achieved with impact parameters only.

An alternative lifetime-based tag uses the reconstruction of secondary vertices. OPAL fits all well-reconstructed high momentum tracks in a jet to a single secondary vertex, then progressively removes those which do not fit well. The decay length significance L/σ_L (the reconstructed distance between the primary and secondary vertices divided by its error) is used as the b-tagging variable, signed depending on whether the secondary vertex is reconstructed in front of or behind the primary vertex (see Figure 5.3). This allows the background from light quark events with $L/\sigma_L > 0$ to be estimated using the number of events with $L/\sigma_L < 0$.

The extremely precise SLD vertex detector and small stable SLC beam spot allow a different approach to secondary vertex finding, based on representing tracks as Gaussian 'probability tubes' [126]. Spatial overlaps between the probability tubes give regions of high probability density corresponding to candidate vertices, to which tracks are finally attached. This algorithm finds at least one secondary vertex in 73% (29%) of the hemispheres in $b\overline{b}$ ($c\overline{c}$) events. Among the b hemispheres that have at least one secondary vertex, two or more secondary vertices are found in 30% of them mostly coming from the decay of the secondary charmed hadron.

5.2.2 Combined Lifetime Tag

The pure lifetime tags have an intrinsic limitation because D-mesons have a lifetime comparable to B-mesons. However this can be overcome if additional information is used. Since B-mesons are much heavier than D-mesons, the most obvious variable is the invariant mass of the particles

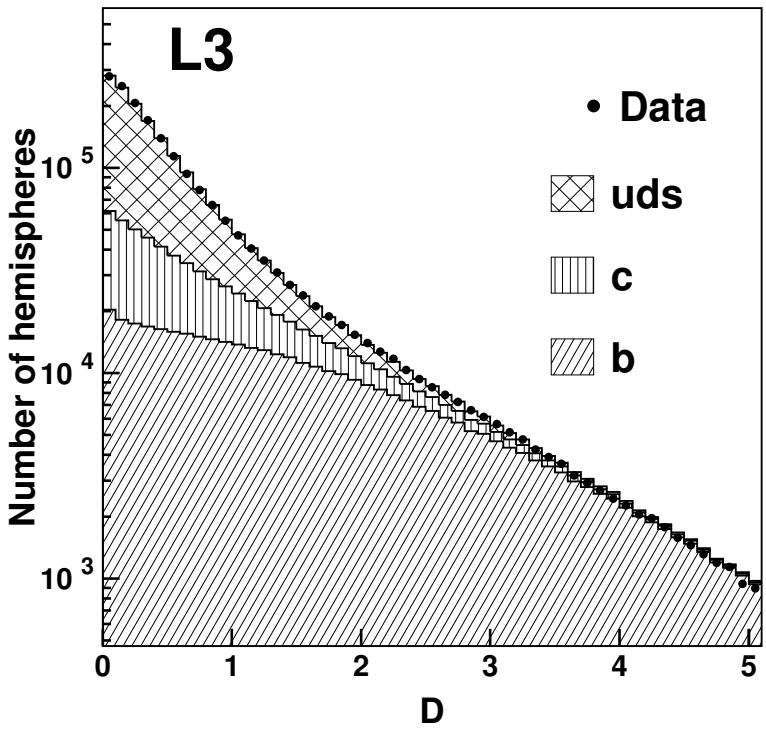

Figure 5.2: Impact parameter b-tag from L3 [124]. D is the negative logarithm of the hemisphere impact parameter probability.

fitted to the secondary vertex. In SLD this mass is used as a b-tag with an additional correction for the neutral decay products of the B. From the flight direction of the B, calculated from the primary and the B-decay vertex, and the momentum vector of the charged decay products of the B, fitted to the secondary vertex, the transverse momentum, p_t, of the sum of the neutral decay products can be calculated. Adding a massless pseudo-particle with momentum p_t to the secondary vertex gives an improved lower limit for the mass of the decaying particle.

In Figure 5.4 the p_t-corrected mass of the secondary vertex is shown for b events and for the uds and c background. The high efficiency for assigning the correct tracks to the decay vertex results in a very high b-tagging purity of 98% for 53% efficiency, simply by requiring the p_t-corrected mass to be above the D-meson mass. A further improvement of the performance is obtained with the introduction of a neural network to optimise the track to vertex association and a second neural network to improve the c-b separation by using the vertex decay length, multiplicity and momentum in addition to the p_t-corrected vertex mass. With this improved tag the b-tagging efficiency increases to 62% with the same purity [126].

The LEP beam spot is much larger in the x and y directions than that of SLC, the resolution of the SLD CCD-detectors are about a factor two better than the ones of the microstrips used at LEP, and the innermost silicon layers of the LEP vertex detectors have to be at approximately twice the innermost radius of the SLD vertex detector, as indicated in Table 5.1. This limits the b-tagging performance of the LEP detectors and motivates development of tags that combine additional information together with the impact parameter or decay length information.

DELPHI utilises a likelihood technique combining 4 variables: the probability that the tracks in the jet come from the primary vertex (see Section 5.2.1), the mass of the reconstructed secondary vertex, the energy of the charged tracks belonging to the secondary vertex and their

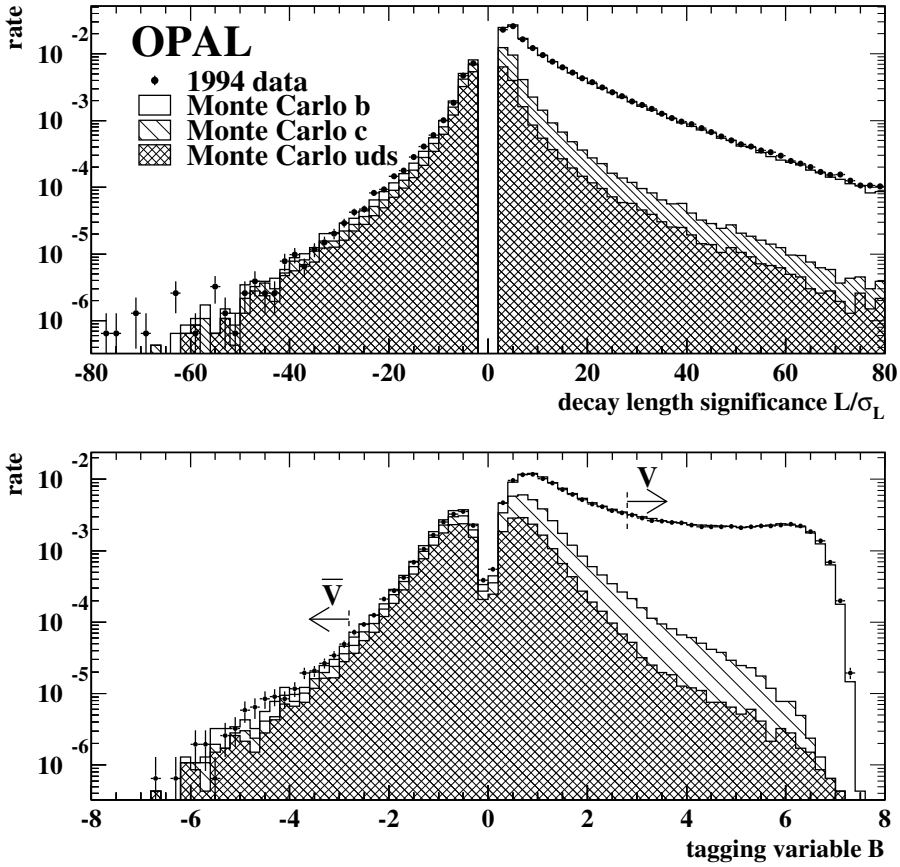

Figure 5.3: Decay length significance L/σ_L (top) and neural network tagging variable (bottom) for the OPAL secondary vertex based b-tag [125]. The gaps around zero significance are due to neural network preselection cuts removing jets with no significant secondary vertex. v and $\bar{v}$ are the cut values used in the R_b analysis.

rapidity [127, 128]. Combining track properties with the information from the reconstructed secondary vertices makes the tag more robust against detector resolution effects. A considerable improvement is obtained if the direction defined by the primary and secondary vertex is used as the b-hadron direction, instead of the jet axis.

ALEPH uses a linear combination of two lifetime-related variables [129]. The first is the probability that the tracks from each hemisphere come from the primary vertex (as defined in Section 5.2.1). The second variable is correlated with the mass of the hadron produced. In each jet the tracks are combined in order of decreasing inconsistency with the primary vertex until their mass exceeds 1.8 GeV. The mass-sensitive variable is defined as the impact parameter probability of the last track added.

L3 identifies b-hemispheres using the impact parameter tag only [124].

OPAL uses a vertex tag based on a neural network combining five variables [125]. The first four are derived from the reconstructed secondary vertex: the decay length significance L/σ_L, the decay length L, the number of tracks in the secondary vertex and a variable that measures the stability of the vertex against mismeasured tracks. The fifth variable exploits the high mass of b-hadrons. For each track in the jet, the relative probabilities that it came from the primary and secondary vertex are calculated, using impact parameter and kinematic information. As in the ALEPH tag, these tracks are then combined in decreasing order of secondary vertex

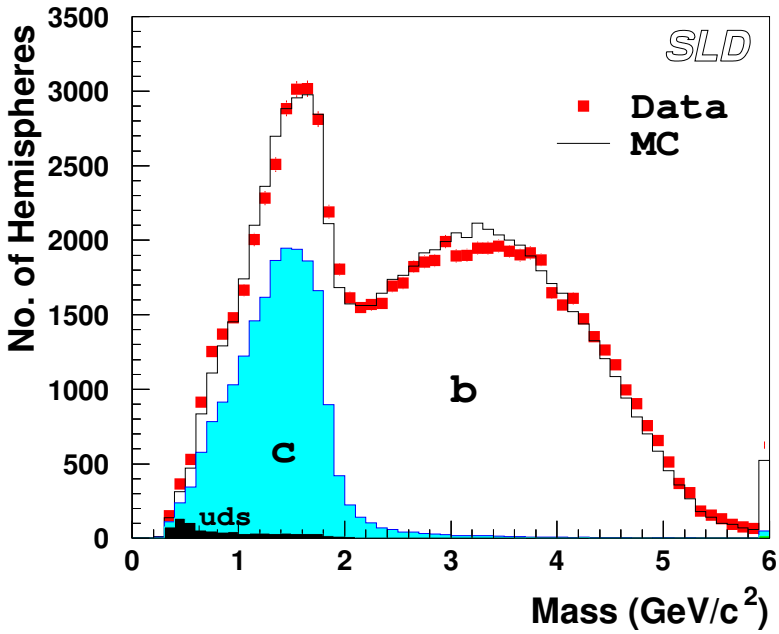

Figure 5.4: Reconstructed vertex mass from SLD for data and simulation.

	ALEPH	DELPHI	L3	OPAL	SLD
b Purity [%]	97.8	98.6	84.3	96.7	98.3
b Efficiency [%]	22.7	29.6	23.7	25.5	61.8

Table 5.2: b-Tagging performance of the different experiments at the cut where the R_b analyses are performed. The lifetime tagging is combined with other information (see text). The OPAL tag is an OR of a secondary vertex and a lepton tag.

probability until the charm-hadron mass is exceeded, and the secondary vertex probability of the last track added is used as input to the main neural network. The neural network output is signed according to the sign of L, preserving the 'folding' symmetry of the simple L/σ_L tag and allowing the light quark background to be subtracted (see Figure 5.3).

The b-tag performance of SLD and the LEP experiments at the purity/efficiency working point used for the R_b analysis are shown in Table 5.2.

5.2.3 Lepton Tagging

The semileptonic decays of heavy quarks provide a clean signature that was the basis of the first methods used to identify the flavour composition of jets. Due to the hard fragmentation and the large mass of b hadrons leptons from b-decays are characterised by large total and transverse momenta. Leptons from c-decays also have high momentum, but a significantly smaller transverse momentum. The dominant semileptonic decay modes are $\mathrm{b} \to \ell^-$, $\mathrm{c} \to \ell^+$ and the cascade decay $\mathrm{b} \to \mathrm{c} \to \ell^+$. The transverse momentum, p_t, of the decay lepton with respect to the decaying hadron direction is limited to half the hadron mass. The direction of the jet containing the lepton, which experimentally serves as the reference for measuring p_t provides a good approximation of the hadron direction. Since b-quarks have a harder fragmentation

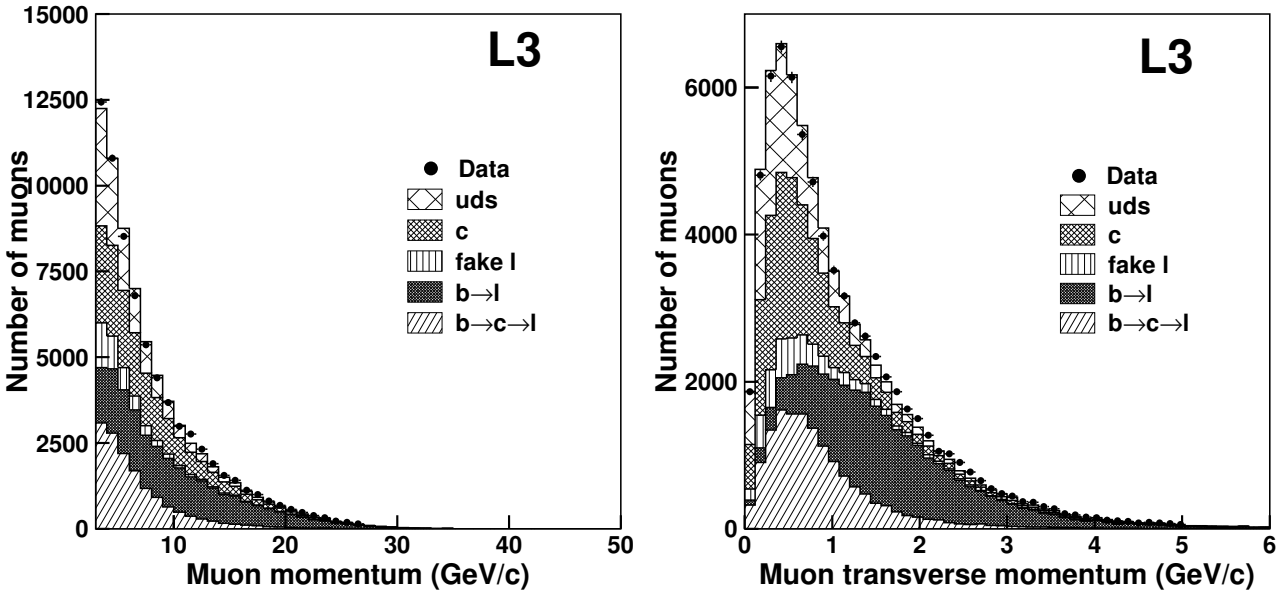

Figure 5.5: Muon momentum and transverse momentum spectra obtained by L3, together with expectations from simulation for the contributions from the various sources.

spectrum than c-quarks, additional separation power is given by the lepton momentum. Figure 5.5 shows the muon p and p_t spectrum from L3 compared to the simulation of the different sources. $b \to \ell$ can be separated cleanly with a simple cut on p_t. However the other sources overlap strongly and can only be separated from each other on a statistical basis. At SLD the good resolution of their vertex detector can also be used to separate $b \to \ell^-$ and $b \to c \to \ell^+$.

The charge of the lepton from a b- or c-decay is correlated to the charge of the decaying quark. Therefore in the asymmetry measurements the lepton tag can be used simultaneously to tag the quark flavour and to distinguish between the quark and the antiquark. b- and c-quarks decay semileptonically into either electrons or muons with approximately equal branching fractions of about 10%. While the lepton always carries the sign of the parent quark charge, the possibility exists to confuse $c \to \ell^+$ and $\overline{b} \to \ell^+$. Due to the fermion / anti-fermion flip in the case of c- but not b-quarks, and because the sign of the two quark asymmetries is the same, this leads to a large sensitivity of the asymmetry measurements with leptons to the sample composition. Apart from these three main sources, there are also some other sources with different charge correlations, mainly $b \to \overline{c} \to \ell^-$, $b \to \tau^- \to \ell^-$ and $b \to (J/\psi, \psi') \to \ell\ell$. In addition there are misidentified hadrons and electrons from photon conversion.

As a b flavour tag the lepton tag is not competitive with the lifetime tag. As one can see from Figure 5.5 only the $b \to \ell^-$ decay allows a tag with sufficient purity and efficiency about 20%. Even from this efficiency roughly half is lost due to the lepton tag efficiency and a necessary p_t cut. However due to the simultaneous b-charge tag the lepton tag provides precise asymmetry measurements.

5.2.4 D-Meson Tags

Since charmed hadrons are only rarely produced during light quark fragmentation, their presence tags c-quarks coming either from the primary Z-decay or from decay products of a b-quark. Charmed hadrons from a primary c-quark have on average a higher momentum than those from

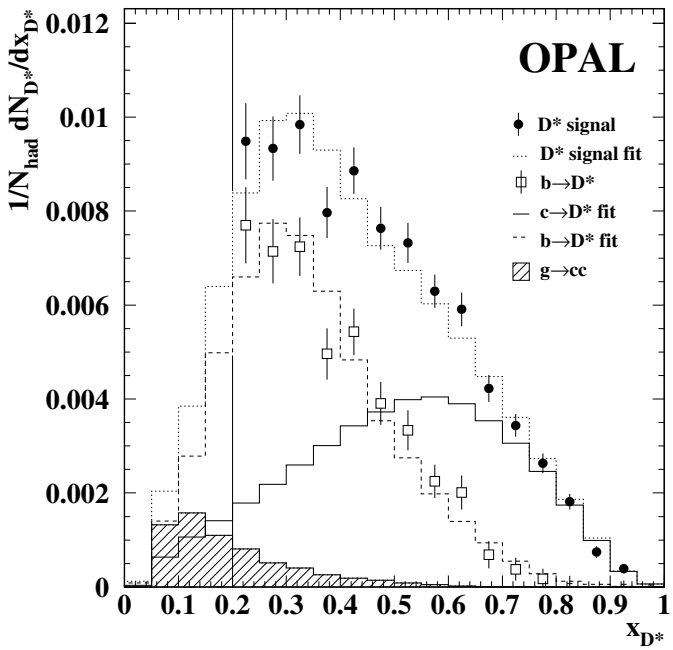

Figure 5.6: $D^{*\pm}$ momentum spectrum for all events and for $b\overline{b}$ and $c\overline{c}$ events from OPAL normalised to the beam energy after subtraction of combinatorial background [130].

a b-decay (see Figure 5.6). In addition, the decay length of the reconstructed hadron or lifetime tagging on the whole event can be used to separate the two sources.

At LEP and SLD the weakly-decaying charmed hadrons D^0, D^+, D_s and Λ_c^+ can be reconstructed in particular exclusive final states (see Figure 5.7). The charm tagging efficiency is limited by the low branching fractions for these decay modes, which are typically only a few percent. The decay $D^{*+} \to \pi^+ D^0$ can be reconstructed particularly cleanly, due to the small mass difference $\Delta m = m_{D^{*+}} - m_{D^0}$, which leads to a characteristic narrow peak with little background, as shown in Figure 5.8. Because of the good resolution, even D^0 decays which are not fully reconstructed, such as $D^0 \to \ell\nu X$ or $D^0 \to K^-\pi^+\pi^0$, where the π^0 is not seen, can be used.

The decay $D^{*+} \to \pi^+ D^0$ can also be tagged inclusively without specifically recognising any of the decay products of the D^0. The small mass difference between the D^{*+} and D^0 and the low mass of the pion result in a very low pion momentum in the D^{*+} rest-frame. Therefore in the laboratory frame the pion closely follows the D^{*+} direction and has a very low transverse momentum, p_t, with respect to the jet direction. As shown in Figure 5.9, the number of D^{*+} in a sample can thus be measured from the excess in the p_t^2 spectrum at very low values. Because of the large background, this tag is typically used to count c-quarks on a statistical basis in conjunction with other tags.

The flavour of D-mesons also measures the flavour of the original quark. In $c\overline{c}$-events the primary quark is directly contained in the D-meson, while in $b\overline{b}$-events the c-quark comes from the decay chain $b \to c$. The decay $b \to \bar{c}$ (via $b \to cW^-, W^- \to \bar{c}s$) is suppressed, so that the quark flavour tag using D-mesons is almost always correct, in contrast to the lepton tag, where the $b \to \ell^-$ and $b \to c \to \ell^+$ decays have to be separated. Another advantage of a D-meson tag is that it separates directly the quark from the antiquark and not positively from negatively charged quarks as in the lepton case, so that the sensitivity of the asymmetry measurements to the sample composition is significantly reduced. Since the absolute efficiency cancels in

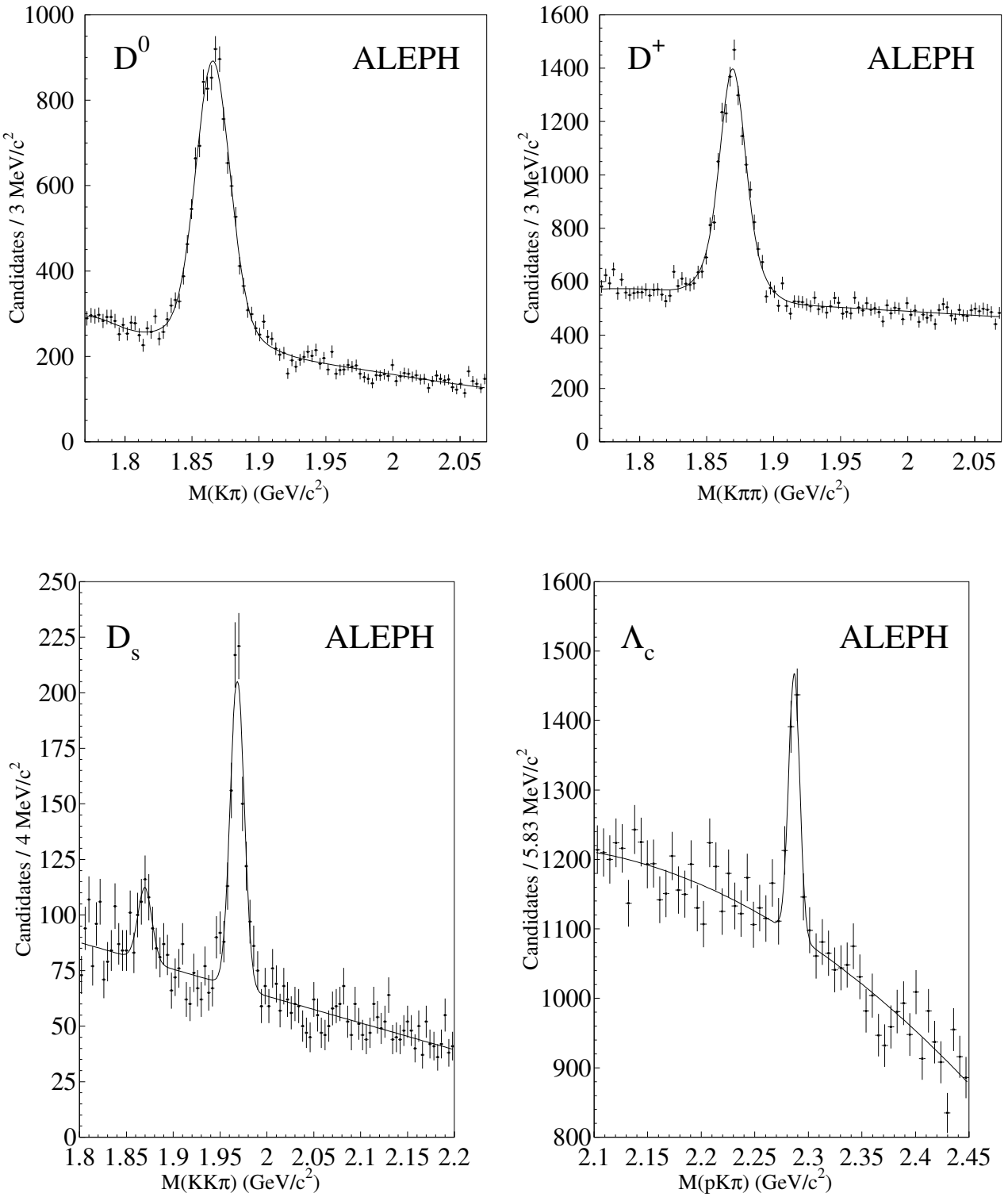

Figure 5.7: Mass spectra for $D^0 \to K^-\pi^+$, $D^+ \to K^-\pi^+\pi^+$, $D_s \to K^+K^-\pi^+$ and $\Lambda_c^+ \to pK^-\pi^+$ obtained by ALEPH [131].

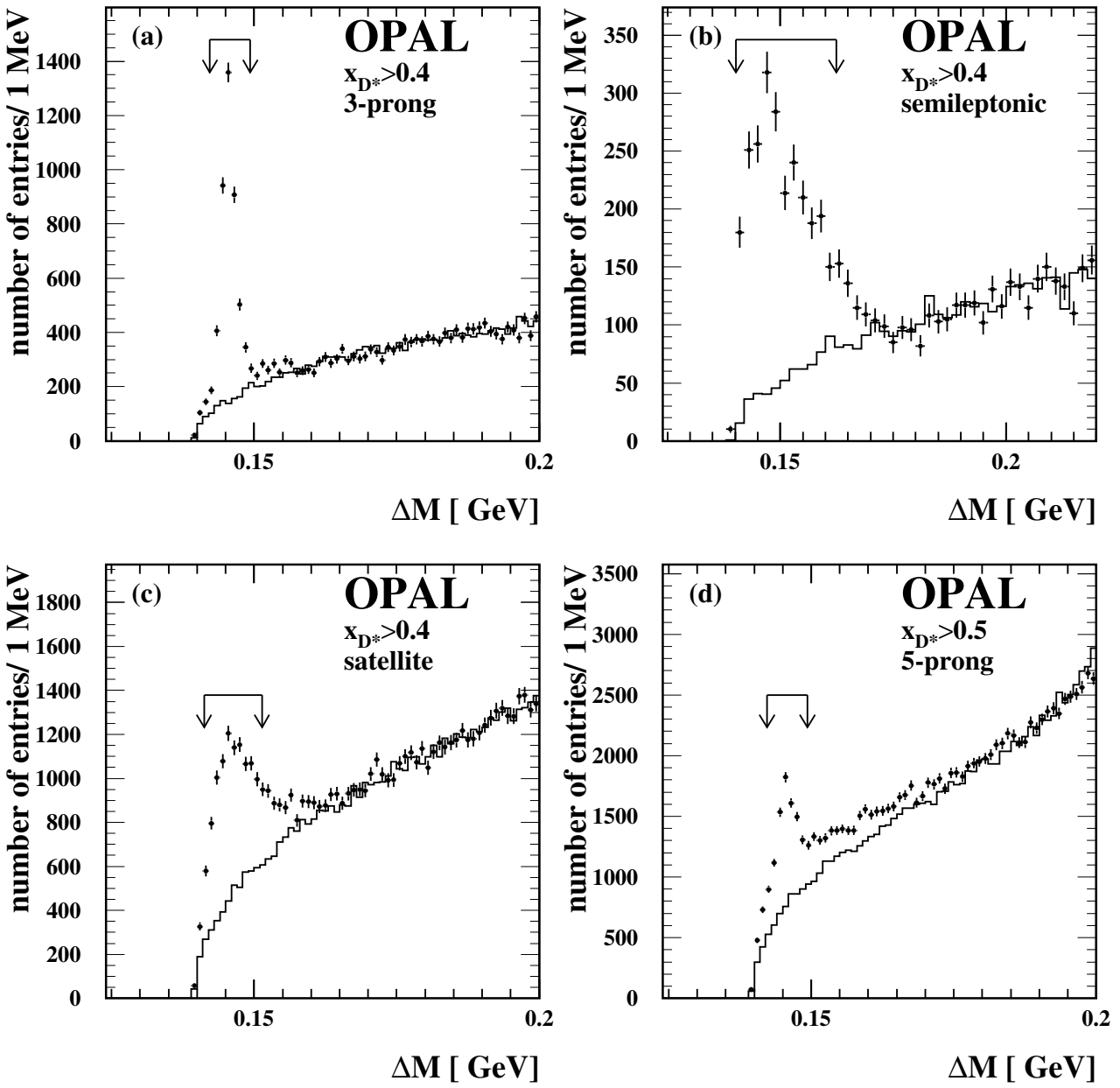

Figure 5.8: Mass difference spectrum $m(\pi^+ D^0) - m(D^0)$ from OPAL in different channels [130]. In a) and d) the D^0 is fully reconstructed in the decay modes $D^0 \to K^-\pi^+$ and $D^0 \to K^-\pi^+\pi^+\pi^-$ In c) the decay mode $D^0 \to K^-\pi^+\pi^0$ is used, where the π^0 is not reconstructed. This $K^-\pi^+$ mass peak is enhanced due to the large polarisation of the intermediate ρ^+ produced in the $D^0 \to K^-\rho^+ \to K^-\pi^+\pi^0$ decay. In b) the D^0 is partially reconstructed in the semileptonic decay mode. The points with the error bars are the measured data. The solid histogram is the background estimated from measured data by a hemisphere mixing technique.

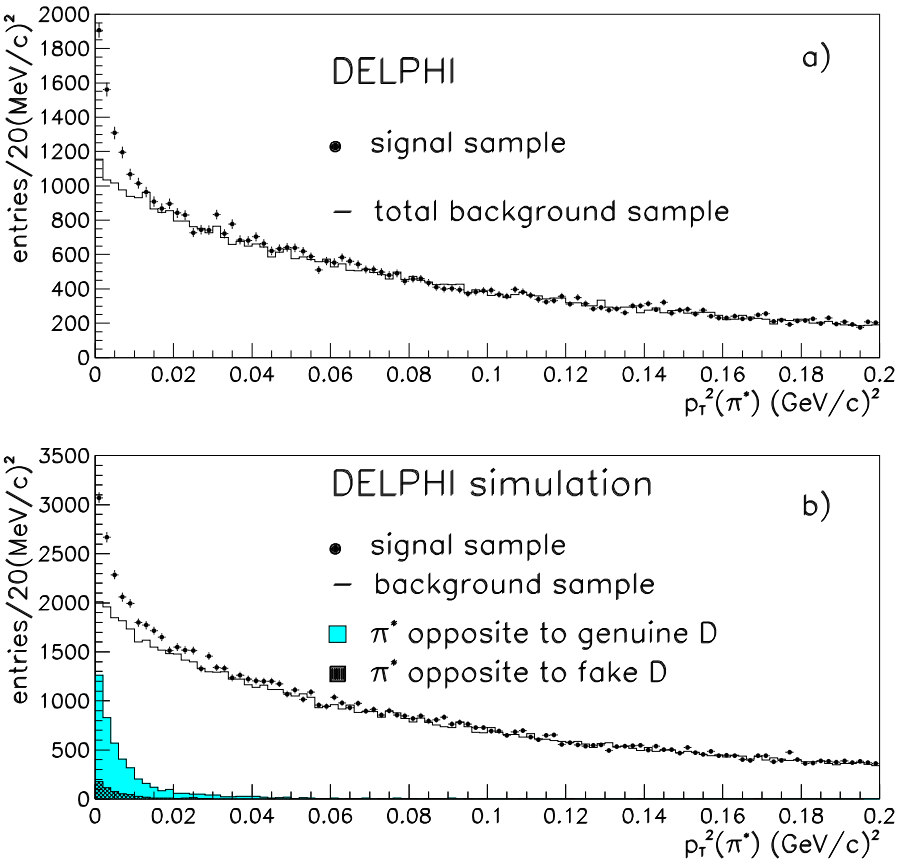

Figure 5.9: p_t^2 spectrum of the slow pion opposite a high energy D-meson candidate [132]. The points show pions with charge opposite that of the charm quark in the D-meson, while the histogram shows those with the same charge. The data is shown in a) and the simulation in b), with the signal component indicated separately.

the asymmetries many different states can be used. Because of the low background, however, the most sensitive decay is $D^{*+} \to \pi^+ D^0$ with $D^0 \to K^-\pi^+$. Asymmetry measurements with D-mesons contribute with a significant weight to $A_{FB}^{c\bar{c}}$ while they contribute only little to $A_{FB}^{b\bar{b}}$.

5.3 Partial Width Measurements

In principle, the partial width measurements only require counting the fraction of hadronic events tagged as a particular flavour, and knowing the efficiency and purity of the tag to a high precision. This "single-tag" approach has been adopted in some of the R_c measurements.

The single-tag approach is highly sensitive to knowledge of the tagging efficiency, which in any case is best extracted from the data itself. So-called double-tag methods have been developed which provide a simultaneous determination of the tagging efficiency and quark rate through comparison of the probabilities that one or both of the two hemispheres in each event is tagged. Since the statistical precision of these methods varies as the tagging efficiency squared, they are most useful when this efficiency is high.

A summary of all individual measurements of R_b and R_c, used in the combination is given in Tables C.1 and C.2 of Appendix C.

5.3.1 R_{b} Measurements

The Double-tag Method

All precise measurements of R_{b} are primarily based on counting events with either one or both hemispheres tagged. The fraction of hemispheres which are b-tagged, f_s, and the fraction of events where both hemispheres are b-tagged, f_d, are given by:

$$\begin{aligned} f_s &= \varepsilon_{\mathrm{b}} R_{\mathrm{b}} + \varepsilon_{\mathrm{c}} R_{\mathrm{c}} + \varepsilon_{\mathrm{uds}}(1 - R_{\mathrm{b}} - R_{\mathrm{c}}) \\ f_d &= \varepsilon_{\mathrm{b}}^{(d)} R_{\mathrm{b}} + \varepsilon_{\mathrm{c}}^{(d)} R_{\mathrm{c}} + \varepsilon_{\mathrm{uds}}^{(d)}(1 - R_{\mathrm{b}} - R_{\mathrm{c}})\,, \end{aligned} \tag{5.2}$$

where ε_{f} is the hemisphere tagging efficiency for flavour f. The double-tagging efficiency $\varepsilon_{\mathrm{f}}^{(d)}$ can be written as

$$\varepsilon_{\mathrm{f}}^{(d)} = (1 + \mathcal{C}_{\mathrm{f}})\varepsilon_{\mathrm{f}}^2 \tag{5.3}$$

where the correction factor $\mathcal{C}_{\mathrm{f}} \neq 0$ accounts for the fact that the two hemispheres in an event are slightly correlated. For the high purity b-tags used in the analyses $\mathcal{C}_{\mathrm{c}}$ and $\mathcal{C}_{\mathrm{uds}}$ can be safely neglected. Neglecting all hemisphere correlations and background one has $R_{\mathrm{b}} = f_s^2/f_d$, independent of the b-tagging efficiency ε_{b} which then does not need to be determined from simulation. In reality, corrections dependent on the background efficiencies ε_{c}, $\varepsilon_{\mathrm{uds}}$ and hemisphere correlations $\mathcal{C}_{\mathrm{b}}$ must be applied and these have to be determined from Monte Carlo. The uncertainties on these parameters are included in the systematic errors. The effect of an uncertainty $\Delta\varepsilon_x$ from a background source x is approximately given by $\Delta R_{\mathrm{b}} = 2\Delta\varepsilon_x/\varepsilon_{\mathrm{b}} R_x$ and for an uncertainty on the correlation by $\Delta R_{\mathrm{b}} = \Delta\mathcal{C}_{\mathrm{b}} R_{\mathrm{b}}$. The statistical uncertainty is dominated by the double tag statistics so that the number of events needed to achieve the same statistical precision is proportional to $1/\varepsilon_{\mathrm{b}}^2$. A large b-tag efficiency also reduces the sensitivity to the uncertainty on hemisphere correlations since it usually results in less dependence on parameters like the b-hadron momentum. Therefore it is essential to develop a high efficiency and high purity b-tag to enable the double tag scheme to achieve the necessary statistical and systematic precision. Details about the hemisphere correlations are explained in Section 5.6.7.

OPAL [125] and SLD [133] measure R_{b} with the double-tag technique, OPAL with a logical OR of secondary vertex and lepton tags and SLD with only their neural network improved vertex mass tag explained in Section 5.2.2.

The Multi-tag Method

In the double-tag method, hemispheres are tagged simply as b or non-b. This leads to two equations and six unknowns, R_{b}, R_{c}, ε_{b}, ε_{c}, $\varepsilon_{\mathrm{uds}}$ and $\mathcal{C}_{\mathrm{b}}$. Three of them (ε_{c}, $\varepsilon_{\mathrm{uds}}$ and $\mathcal{C}_{\mathrm{b}}$) are taken from simulation and R_{c} is fixed. The R_{c}-dependence is then accounted for in the systematic error of the experimental publications and in the combination procedure described in Section 5.8. The method can be extended by adding more tags, *e.g.*, additional b-tags with lower purity, or charm and light flavour tags [134]. The tags are made exclusive, such that each hemisphere is counted as tagged by only one tag method, and the untagged hemispheres are counted as an extra 'null' tag.

With T separate hemisphere tags, there are then $T(T+1)/2$ double tag fractions f_d^{ij} $(i, j = 1 \ldots T)$, given (analogously with Equations 5.2) by:

$$f_d^{ij} = \varepsilon_{\mathrm{b}}^i \varepsilon_{\mathrm{b}}^j (1 + \mathcal{C}_{\mathrm{b}}^{ij}) R_{\mathrm{b}} + \varepsilon_{\mathrm{c}}^i \varepsilon_{\mathrm{c}}^j (1 + \mathcal{C}_{\mathrm{c}}^{ij}) R_{\mathrm{c}} + \varepsilon_{\mathrm{uds}}^i \varepsilon_{\mathrm{uds}}^j (1 + \mathcal{C}_{\mathrm{uds}}^{ij})(1 - R_{\mathrm{b}} - R_{\mathrm{c}})\,, \tag{5.4}$$

where $\varepsilon_{\rm f}^i$ is the hemisphere tagging efficiency for flavour f with tag i, and $\mathcal{C}_{\rm f}^{ij}$ is the hemisphere correlation coefficient for tagging an event of flavour f with tag i in one hemisphere and j in the other. The single tag rates do not give additional information in this case, since they can be written as sums over the appropriate double tag fractions.

With T tags and F event types, there are $F(T-1)$ unknown efficiencies $\varepsilon_{\rm q}^j$ (since the T efficiencies for each flavour must add up to one) and $F-1$ unknown partial width ratios R_f. If all the correlation coefficients $\mathcal{C}_{\rm f}^{ij}$ are taken from simulation, that leaves $F(T-1)+(F-1) = TF-1$ unknowns to be determined from $T(T+1)/2-1$ independent double tag rates, f_d^{ij}. With $F=3$ event types (b, c, uds), the minimum number of tags for an over-constrained system is six.

ALEPH [129, 135] and DELPHI [127] both use this multi-tag method for measuring $R_{\rm b}$. The six tags used are: three b-tags with different purities, a charm tag, a light quark tag and the "untagged" hemispheres. However, even with these six tags, the solution for all efficiencies and partial widths is still not well determined. This problem is solved by exploiting the very high purity of the high-purity b-tag, taking the small background efficiencies for charm and light quark events from Monte Carlo, as in the simple double-tag analysis. $R_{\rm c}$ is also fixed in the analysis to its SM value and the dependence on the assumed $R_{\rm c}$ is taken into account in the combination.

Since the auxiliary b-tags contribute to the measurement, the statistical error of a multi-tag analysis is smaller than a double-tag analysis using the same high purity b-tag alone. The charm and light quark tags also allow the data to constrain the backgrounds in the additional b-tags. The systematic error due to the backgrounds in the high purity b-tag stays the same as in the double tag method. It can be reduced by changing the working point of the high purity b-tag towards higher purity, thus sacrificing some of the gain in statistical error. Many additional hemisphere correlations have to be estimated from Monte Carlo, but the impact of the most important, between two hemispheres tagged with the high purity b-tag, is reduced. The total systematic uncertainty from hemisphere correlations is therefore almost unchanged.

L3 [124] also use a multi-tag analysis for $R_{\rm b}$, but with only two tags, based on lifetime and leptons, and determine the background efficiencies for both tags from simulation. The b-tagging efficiency for the lepton tag is used to provide a measurement of the semileptonic branching fraction $B(\mathrm{b} \to \ell^-)$.

5.3.2 $R_{\rm c}$ Measurements

For $R_{\rm c}$ the situation is more complicated than for $R_{\rm b}$. Especially at LEP, the c-tags are less efficient and less pure than the b-tags. To obtain the optimal $R_{\rm c}$ precision under these circumstances a variety of methods are employed.

Double Tag Measurements

In the normal double tag analyses the statistical error is determined by the size of the double tagged sample, which is proportional to the square of the tagging efficiency. Thus only SLD is able to present a high-precision $R_{\rm c}$ measurement with the normal double tagging technique [133]. The charm tag is based on the same neural network used for the b tag. An output value of the network greater than 0.75 is considered a b tag and a value below 0.3 a charm tag. In addition, two intermediate tags are introduced covering intervals from 0.3 to 0.5 and 0.5 to 0.75. The charm tag has an efficiency of 18% at a purity of 85%. The tag has a very low uds-background, which can be estimated with sufficient precision from simulation. The b

background is relatively high, but can be measured accurately in hemispheres opposite a high-purity b-tag. R_c is extracted from a simultaneous fit to the count rates of the 4 different tags. The b and charm efficiencies are fitted from data.

ALEPH also presents a double tag measurement of R_{c} using fully reconstructed D-mesons. Due to the small branching fractions, however, the efficiency is low and the statistical error relatively large [136].

Inclusive/Exclusive Double Tags

At LEP more precise results can be obtained with the inclusive/exclusive double-tag method. In the first step $R_{\mathrm{c}}P(\mathrm{c} \to \mathrm{D}^{*+} \to \pi^{+}\mathrm{D}^{0})$ is measured from a sample of exclusively reconstructed D^{*+} (the 'exclusive tag'). In the second step $P(\mathrm{c} \to \mathrm{D}^{*+} \to \pi^{+}\mathrm{D}^{0})$ is obtained using an inclusive D^{*+} tag where only the charged pion from the D^{*+} decay is identified (see Section 5.2.4). A fit is made to the π^{-} p_t spectrum in hemispheres tagged as containing a charm quark using a high energy D^{*+} reconstructed in the other hemisphere of the event. The uds background in this tagged charm sample is estimated from the sidebands in the mass spectra of the high energy D^{*+}, and the b-background is measured using lifetime tags and the D^{*+} momentum distribution. The fragmentation background under the low p_t pion D^{*+} signal can be estimated by exploiting the charge correlation between the pion and the D^{*} in the opposite hemisphere. Genuine signal pions have the opposite charge to that of the D^{*}, while background pions can have either charge (see Figure 5.9).

In this method the reconstruction efficiency for the D^{0} and the relevant decay branching fraction (normally $\mathrm{D}^{0} \to \mathrm{K}^{-}\pi^{+}$) still need to be known from simulation or external measurements. However the probability that a c-quark fragments into a D^{*+}, which is hard to calculate, is measured from the data. ALEPH [136], DELPHI [132, 137] and OPAL [130] present such inclusive/exclusive double tag measurements. DELPHI and OPAL give both R_{c} and $P(\mathrm{c} \to \mathrm{D}^{*+} \to \pi^{+}\mathrm{D}^{0})$ as results while ALEPH does the unfolding internally and presents only R_{c}.

Charm Counting

Another method for measuring R_{c} is known as charm counting. All charm quarks finally end up in a weakly-decaying charmed hadron. The production rate of a single charmed hadron $\mathrm{D_i}$ is proportional to $R_{\mathrm{c}}f(\mathrm{D_i})$, where $f(\mathrm{D_i})$ is the fraction of charm quarks that eventually produce a $\mathrm{D_i}$. However if all weakly-decaying charmed hadrons can be reconstructed, the constraint $\sum_{\mathrm{i}} f(\mathrm{D_i}) = 1$ can be exploited and R_{c} can be measured without the unknown fragmentation probabilities $f(\mathrm{D_i})$. In practice D^{0}, D^{+}, $\mathrm{D_s}$ and Λ_{c}^{+} are reconstructed and small corrections for unmeasured strange charmed baryons have to be applied [131]:

$$f(\mathrm{c_{baryon}}) \;=\; (1.15 \pm 0.05) f(\Lambda_{\mathrm{c}}^{+})\,. \tag{5.5}$$

R_{c} is then obtained using the constraint

$$f(\mathrm{D}^{0}) + f(\mathrm{D}^{+}) + f(\mathrm{D_s}) + f(\mathrm{c_{baryon}}) \;=\; 1\,. \tag{5.6}$$

A priori there is the same amount of charmed hadrons coming from primary c-quarks and from b-decays. The b component can, however be efficiently separated using lifetime tags and the momentum of the reconstructed charmed hadrons. The efficiency to reconstruct a given decay channel has to be taken from simulation. As a by-product these measurements

obtain the production rates of the weakly-decaying charmed hadrons $f(\mathrm{D_i})$, which are needed to calculate the charm tagging efficiency of the lifetime b-tags. ALEPH [131], DELPHI [137] and OPAL [138] present charm counting R_c analyses. The method is however limited by the knowledge of branching fractions to the decay modes used in calculating the reconstruction efficiency, especially for the $\mathrm{D_s}$ and the Λ_c^+.

Lepton Tag

ALEPH also measures R_c with leptons [136]. They measure the lepton total and transverse momentum spectrum and subtract the contribution from b decays. This is determined from the lepton spectra measured in b events tagged in the opposite hemisphere by a lifetime-based b-tag. The result is proportional to $R_\mathrm{c}B(\mathrm{c}\to\ell^+)$, where $B(\mathrm{c}\to\ell^+)$ is measured by DELPHI [132] and OPAL [139] in charm events tagged in the opposite hemisphere by a high energy D^{*+}.

5.4 Asymmetry Measurements

The forward backward asymmetry for a quark flavour q is defined as

$$A_\mathrm{FB}^{\mathrm{q\overline{q}}} \;=\; \frac{\sigma_\mathrm{F}^\mathrm{q}-\sigma_\mathrm{B}^\mathrm{q}}{\sigma_\mathrm{F}^\mathrm{q}+\sigma_\mathrm{B}^\mathrm{q}}\,, \tag{5.7}$$

where the cross-sections are integrated over the full forward (F) and backward (B) hemisphere. "Forward" means that the quark, rather than the antiquark, is produced at positive $\cos\theta$. The differential cross-section with respect to the scattering angle is, on Born level, given by

$$\frac{d\sigma^\mathrm{q}}{d\cos\theta} \;=\; \sigma_\mathrm{tot}^\mathrm{q}\left[\frac{3}{8}\left(1+\cos^2\theta\right)+A_\mathrm{FB}^{\mathrm{q\overline{q}}}\cos\theta\right]\,. \tag{5.8}$$

This dependence can be used to correct for a non-uniform efficiency or can be fitted directly to the data. The asymmetry at a quark production angle θ can be written as

$$A_\mathrm{FB}^{\mathrm{q\overline{q}}}(\cos\theta) \;=\; \frac{8}{3}A_\mathrm{FB}^{\mathrm{q\overline{q}}}\frac{\cos\theta}{1+\cos^2\theta} \;=\; \mathcal{A}_\mathrm{e}\mathcal{A}_\mathrm{q}\frac{2\cos\theta}{1+\cos^2\theta}\,. \tag{5.9}$$

Most experimental analyses measure $A_\mathrm{FB}^{\mathrm{q\overline{q}}}(\cos\theta)$ and then use Equation 5.9 to fit $A_\mathrm{FB}^{\mathrm{q\overline{q}}}$. This is statistically slightly more powerful than simple event counting. The exact angular form is slightly modified by QCD and mass effects. This is corrected for by simulation. A more detailed description of these effects can be found in [140]. The quark asymmetries share a similar freedom from systematic detector effects as is enjoyed by the lepton asymmetries. Neither a detector asymmetry in $\cos\theta$ nor charge alone is sufficient to disturb the measurement. Both must simultaneously be present, and be correlated.

Mass effects are formally of order m_q^2/s as a relative correction to the asymmetry. Especially for b-quarks they are additionally suppressed by an accidental cancellation of the mass effect in the numerator and denominator [38]. The very small residual mass effects are included in the asymmetry corrections explained in section 5.7.3.

With the availability of beam polarisation, as in the case of the SLD experiment, the forward-backward-left-right asymmetry can be formed as

$$A_\mathrm{LRFB}^{\mathrm{q\overline{q}}} \;=\; \frac{1}{|\mathcal{P}_\mathrm{e}|}\frac{(\sigma_\mathrm{F}-\sigma_\mathrm{B})_\mathrm{L}-(\sigma_\mathrm{F}-\sigma_\mathrm{B})_\mathrm{R}}{(\sigma_\mathrm{F}+\sigma_\mathrm{B})_\mathrm{L}+(\sigma_\mathrm{F}+\sigma_\mathrm{B})_\mathrm{R}}\,, \tag{5.10}$$

where L,R denote the cross-sections with left- and right-handed electron beams and $\mathcal{P}_e$ is the beam polarisation. The more general Born level differential cross-section with polarised electron beam is given by

$$\frac{d\sigma^q}{d\cos\theta} = \frac{3}{8}\sigma^q_{tot}\left[(1-\mathcal{P}_e\mathcal{A}_e)(1+\cos^2\theta)+2(\mathcal{A}_e-\mathcal{P}_e)\mathcal{A}_q\cos\theta\right] \quad (5.11)$$

where the electron beam polarisation $\mathcal{P}_e$ is positive for right-handed beam. The asymmetry $A^{q\overline{q}}_{LRFB}$ as a function of polar angle can therefore be expressed as

$$A^{q\overline{q}}_{LRFB}(\cos\theta) = |\mathcal{P}_e|\mathcal{A}_q\frac{2\cos\theta}{1+\cos^2\theta}\,. \quad (5.12)$$

Comparing Equations 5.12 and 5.9, it can be seen that $A^{q\overline{q}}_{FB}$ measures the product of $\mathcal{A}_e\mathcal{A}_q$ while $A^{q\overline{q}}_{LRFB}$ measures $\mathcal{A}_q$ directly. $A^{q\overline{q}}_{LRFB}$ also gives a significant statistical advantage for sensitivity to $\mathcal{A}_q$ compared to $A^{q\overline{q}}_{FB}$ by a factor of $(|\mathcal{P}_e|/\mathcal{A}_e)^2 \sim 25$, given a highly polarised electron beam with $|\mathcal{P}_e| \sim 75\%$. The analysis procedure for $A^{q\overline{q}}_{LRFB}$ is otherwise similar to $A^{q\overline{q}}_{FB}$. As for $A^{q\overline{q}}_{FB}$ the total tagging efficiencies and the luminosity cancel in the calculation of $A^{q\overline{q}}_{LRFB}$, although one needs to ensure there is no luminosity asymmetry between the two beam polarisation states by monitoring low angle Bhabhas. The actual analyses at SLD use a maximum likelihood fit to the differential cross sections (Equation 5.11) in order to extract $\mathcal{A}_q$. This procedure is equivalent to $A^{q\overline{q}}_{LRFB}$ (Equation 5.12) at first order, although with slightly improved statistical precision on $\mathcal{A}_q$ and a very small dependence on $\mathcal{A}_e$.

As a first step of both asymmetry analyses, the thrust axis of the event is used to define the quark direction θ, signed by the charge tagging methods described in the following. The thrust axis is stable against infrared and collinear divergences, so that it can be calculated in perturbative QCD and it is relatively insensitive to fragmentation effects.

In order to measure a quark asymmetry two ingredients are needed. The quark flavour needs to be tagged and the quark has to be distinguished from the antiquark. For the flavour tagging the methods described in Sections 5.2.1 to 5.2.4 can be used. For the charge tagging essentially five methods have been used, relying on leptons, D-mesons, jet-charge, vertex-charge and kaons. Some analyses also combine the information from the different methods.

In every $A^{q\overline{q}}_{FB}$ analysis the measured asymmetry is given by

$$A^{meas}_{FB} = \sum_q (2\omega_q - 1)\eta_q A^{q\overline{q}}_{FB}\,, \quad (5.13)$$

where η_q is the fraction of $q\overline{q}$ events in the sample, ω_q is the probability to tag the quark charge correctly and the sum is taken over all quark flavours. It should be noted that the tagging methods often tag the quark charge and not the flavour, so that in these cases $(2\omega_q - 1)$ is close to -1 for charm if it is constructed to be positive for b-quarks. Similar flavour composition and quark charge tag factors also apply to corresponding equation for $A^{q\overline{q}}_{LRFB}$ analyses.

As an example, Figure 5.10 shows the reconstructed $\cos\theta$ distribution from the ALEPH $A^{b\overline{b}}_{FB}$ and $A^{c\overline{c}}_{FB}$ measurement with leptons. The asymmetry of about 10% for $A^{b\overline{b}}_{FB}$ and 6% for $A^{c\overline{c}}_{FB}$ can clearly be seen. An example of the event angular distributions for the SLD vertex charge $A^{q\overline{q}}_{LRFB}$ analysis is shown in Figure 5.11. The much larger forward-backward asymmetry is a result of the highly polarised electron beam. The slightly larger number of events in the left-handed sample is due to the cross-section asymmetry A_{LR}. The change of asymmetry sign between the left-handed and right-handed samples, and the slightly steeper asymmetry in the left-handed sample can be understood from the proportionality to $(\mathcal{A}_e - \mathcal{P}_e)$ in Equation 5.11, dominated by the large $\mathcal{P}_e$.

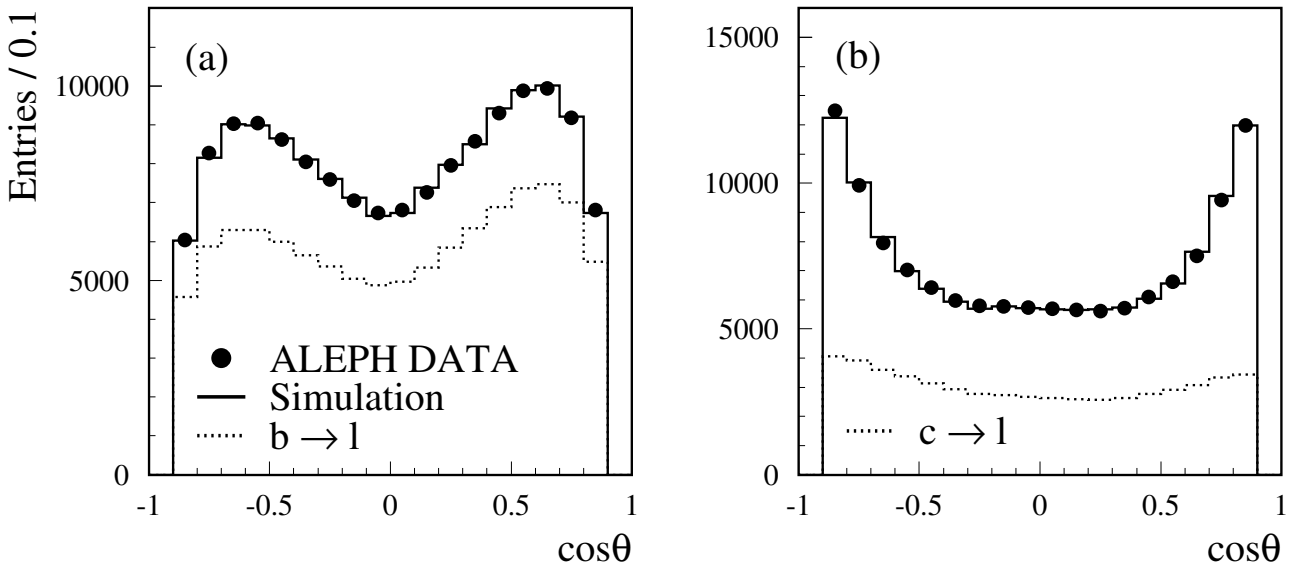

Figure 5.10: Reconstructed $\cos\theta$ distribution from the ALEPH asymmetry measurements with leptons for a) the b-enriched and b) the c-enriched sample [141]. The full histogram shows the expected raw angular distribution in the simulation. The dashed histogram show the signal component.

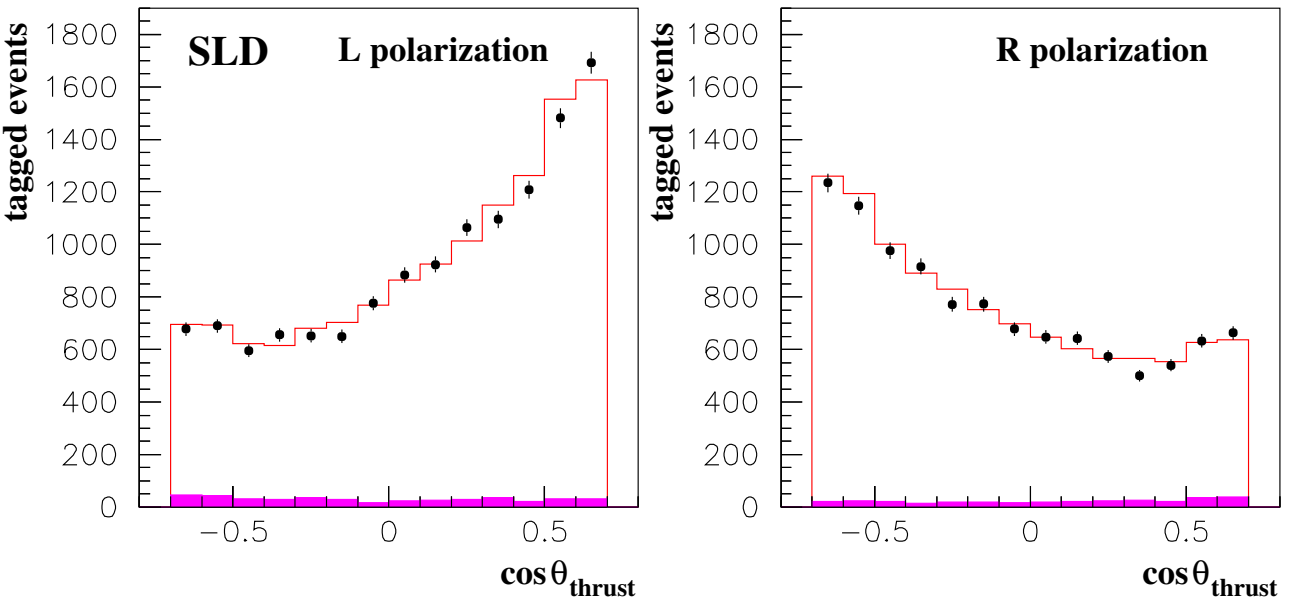

Figure 5.11: Reconstructed $\cos\theta$ distributions from the SLD vertex charge $\mathcal{A}_b$ analysis for events with left-handed and right-handed electron beam polarisations. The shaded region corresponds to udsc background in the sample estimated from Monte Carlo.

Lepton source	charge correlation	fraction for $p_t > 1.25$GeV
$b \to \ell^-$, $b \to \overline{c} \to \ell^-$	1	0.795
$b \to c \to \ell^+$	-1	0.046
$c \to \ell^+$	1	0.048
background	weak	0.111

Table 5.3: Correlation between the lepton charge and the quark charge at decay time. The sample composition for $p_t > 1.25\,\mathrm{GeV}$ in the ALEPH lepton sample is also shown.

5.4.1 Lepton and D-Meson Measurements

As described in Sections 5.2.3 and 5.2.4 the identification of leptons and D-mesons simultaneously provide flavour and charge tagging. A simple cut on the lepton transverse momentum provides good enhancement of $b \to \ell$, as seen in Figure 5.5. Table 5.3 provides an example of sample compositions for the ALEPH lepton sample with a transverse momentum cut of $p_t > 1.25\,\mathrm{GeV}$ together with the correlation between the lepton charge and decaying quark charge. The quark charge at production is however the relevant quantity for the asymmetry determination, requiring correction for the effects of $B^0\overline{B^0}$ mixing via the integrated mixing parameter $\overline{\chi}$.

To enhance the sensitivity of lepton-based analyses to $A_{\mathrm{FB}}^{c\overline{c}}$, the experiments use additional information like lifetime tagging, jet charge in the opposite hemisphere or hadronic information from the lepton jet. Tagging D-mesons also provides a relatively pure charm sample after a momentum cut and additional b-tagging requirements are used to enhance the sensitivity to $A_{\mathrm{FB}}^{b\overline{b}}$.

In both cases the sample composition is usually taken from simulation. For the lepton tag analyses the uncertainties on the sample composition due to the modelling of the semileptonic decays are generally rather large. Therefore, in addition to the asymmetries, the experiments measure the $B^0\overline{B^0}$ effective mixing parameter $\overline{\chi}$, the prompt and cascade semileptonic branching fraction of b-hadrons $B(b \to \ell^-)$ and $B(b \to c \to \ell^+)$ and the prompt semileptonic branching fraction of c-hadrons $B(c \to \ell^+)$. If the same analysis cuts are used in both cases, these auxiliary measurements serve as an effective parametrisation of the lepton spectrum, greatly reducing the modelling errors.

In the case of the D-meson analyses the fragmentation function for D-mesons from b- and c-quarks is measured from data. However, there is only one important source of D-mesons per quark flavour, and the correlation between the quark flavour and the D-meson flavour is the same for b- and c-quarks, so that the sign of the D-meson asymmetry for the two quark species is the same. For these reasons the sensitivity to the sample composition is much smaller than in the lepton case.

5.4.2 Jet and Vertex Charge

The average charge of all particles in a jet, or jet charge, retains some information on the original quark charge. Usually the jet charge is defined as:

$$Q_h \;=\; \frac{\sum_i q_i p_{\parallel i}^{\kappa}}{\sum_i p_{\parallel i}^{\kappa}}\,, \tag{5.14}$$

where the sum runs over all charged particles in a hemisphere with charge q_i and longitudinal momentum with respect to the thrust axis $p_{\parallel i}$, and κ is a tunable parameter with typical values between 0.3 and 1.

For B- and D-mesons the meson charge is correlated with the flavour of the b- or c-quark. If all charged particles of a jet can be uniquely assigned to the primary or the decay vertex, the charge sum of the decay vertex, if non-zero, uniquely tags the quark charge. At SLD the $\mathcal{A}_{\mathrm{b}}$ measurement with vertex charge is the most precise measurement of this quantity. At LEP the vertex charge has also been used in conjunction with other tags, however the impact parameter resolutions at LEP limit the efficiencies in comparison with SLD.

For both charge tagging methods, it is difficult to estimate the charge tagging efficiency from simulation due to uncertainties from fragmentation and B-decays. However, the efficiency can be obtained reliably from data using double tags. In a cut based analysis, defining ω_q as the efficiency to tag the quark charge correctly in a pure sample of q-quarks, the fraction of same sign double tags in the sample of all double tags is given by

$$f_{SS} \;=\; 2\omega_q(1-\omega_q)\,, \tag{5.15}$$

apart from small corrections due to hemisphere correlations. Equation 5.15 can then be used to obtain ω_q. Corrections for background and hemisphere correlations are obtained from simulation.

Since the charge tagging efficiency for the jet charge is rather modest, a statistical method to extract the asymmetry is usually used. With $Q_{\mathrm{F/B}}$ being the jet charge of the forward/backward hemisphere and $Q_{\mathrm{q/\overline{q}}}$ the jet charge of the quark/antiquark hemisphere, one has

$$\begin{aligned} \langle Q_{\mathrm{FB}} \rangle &= \langle Q_{\mathrm{F}} - Q_{\mathrm{B}} \rangle \\ &= \delta_{\mathrm{q}} A_{\mathrm{FB}}^{\mathrm{q\overline{q}}} \\ \delta_{\mathrm{q}} &= \langle Q_{\mathrm{q}} - Q_{\bar{\mathrm{q}}} \rangle\,, \end{aligned} \tag{5.16}$$

for a pure sample of $\mathrm{q\overline{q}}$-events. The "charge separation" δ_{q} can be measured from data using:[3]

$$\left(\frac{\delta_{\mathrm{q}}}{2}\right)^2 \;=\; \frac{\langle Q_{\mathrm{F}} \cdot Q_{\mathrm{B}} \rangle + \rho_{\mathrm{q\overline{q}}}\sigma(Q)^2 + \mu(Q)^2}{1+\rho_{\mathrm{q\overline{q}}}}, \tag{5.17}$$

where $\mu(Q)$ is the mean value of Q for all hemispheres and $\sigma(Q)$ is its variance. $\mu(Q)$ is slightly positive due to an excess of positive particles in secondary hadronic interactions. The hemisphere correlations, $\rho_{\mathrm{q\overline{q}}}$, arise from charge conservation, hard gluon radiation and some other small effects and have to be taken from simulation.

The analyses select a relatively pure sample of $\mathrm{b\overline{b}}$ events using lifetime tagging techniques. Light quark background is always subtracted using Monte Carlo simulation. The charge separation for charm is either taken from Monte Carlo or determined by performing the analysis in bins of different b-purities and fitting δ_{b} and δ_{c} from the data. It should be noted that dilution due to $\mathrm{B^0\overline{B^0}}$-mixing is completely absorbed into the measured δ_{b}. Effects from gluon radiation are also included to a large extent, so that only small QCD corrections have to be applied.

The above formalism can be generalised to any variable sensitive to the quark charge, including the combination of several different charge tagging techniques. As an example Figure 5.12 shows the charge tagging from ALEPH, which combines jet charge, vertex charge and charged kaon information using a neural net to reach almost perfect tagging at high Q_{FB} values.

[3] The exact formulae used by the experiments vary slightly, however the general formalism is identical.

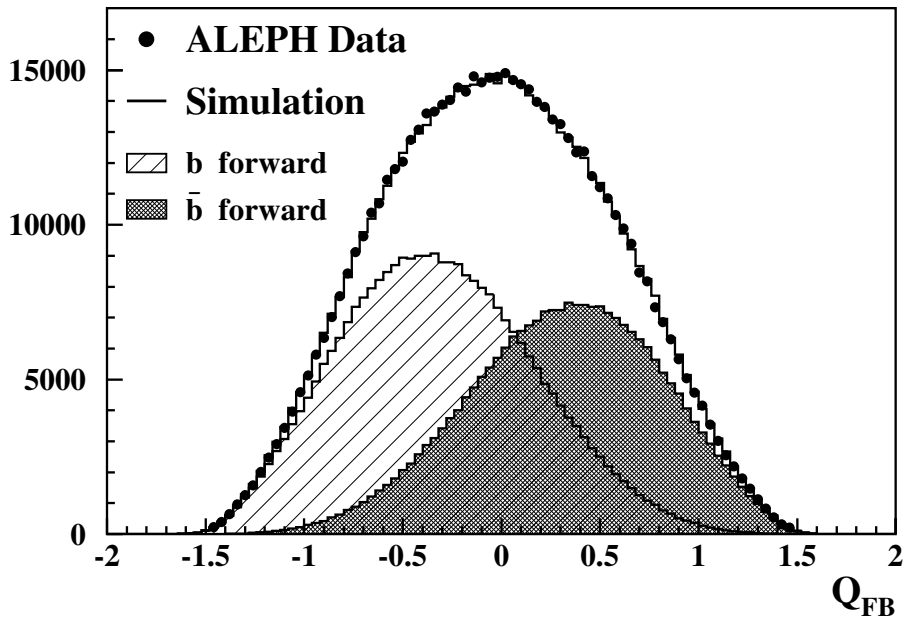

Figure 5.12: Charge separation of the ALEPH neural net tag using jet charge, vertex charge and charged kaons [142]. The asymmetry reflects $A_{\rm FB}^{\rm b\overline{b}}$ diluted by the non-perfect charge tagging.

5.4.3 Kaons

Charged kaons from b- and c-decays are also sensitive to the quark flavour, via the decay chains $\rm b \to c \to s$ and $\rm c \to s$. Only kaons with large impact parameters are used, to suppress those produced in the fragmentation process. As with other methods, the charge tagging efficiency is measured using the double tag technique.

In the SLD measurements of the asymmetries using kaons, only identified kaons coming from a secondary vertex are used. The kaon tag is in fact not used in the $\mathcal{A}_{\rm b}$ measurement for the bulk of the data from 1996–1998, since the vertex charge tag dominates hemispheres with a charged b hadron, while the neutral B mixing significantly limits the additional contribution from the kaon tag in the remaining hemispheres. On the other hand, the kaon tag has a good correct quark charge tag probability of 86% for a charm hemisphere which is comparable to the 91% achieved by the vertex charge tag in the $\mathcal{A}_{\rm c}$ analysis. They are therefore combined as a joint tag and the joint correct tag efficiency is calibrated from the data for the SLD $\mathcal{A}_{\rm c}$ measurement.

5.4.4 Asymmetry Measurements used in the Combination

The forward-backward asymmetry measurements included in the average are:

- Measurements of $A_{\rm FB}^{\rm b\overline{b}}$ and $A_{\rm FB}^{\rm c\overline{c}}$ using leptons from ALEPH [141], DELPHI [143], L3 [144] and OPAL [145]: L3 measures $A_{\rm FB}^{\rm b\overline{b}}$ only from a sample of high p_t leptons. ALEPH, DELPHI and OPAL measure $A_{\rm FB}^{\rm b\overline{b}}$ and $A_{\rm FB}^{\rm c\overline{c}}$ using leptons combined with lifetime tagging and some additional information. ALEPH adds properties of hadrons in the events and information from the missing energy due to escaping neutrinos. OPAL also uses hadronic properties while DELPHI includes the jet charge of the hemisphere opposite the lepton.

- Measurements of $A_{\rm FB}^{\rm b\overline{b}}$ based on lifetime tagged events with a jet charge measurement using the weight method (see Equation 5.16) from ALEPH [142], L3 [146] and OPAL [147]. ALEPH and OPAL combine their jet charge with additional information like vertex charge and kaons. The DELPHI analysis of $A_{\rm FB}^{\rm b\overline{b}}$, also combining jet charge, vertex charge, kaons and some other variables sensitive to the b-quark charge in a neural net [148], is based on a cut on the charge estimator.

- Analyses with D-mesons from ALEPH [149], DELPHI [150] and OPAL [151]: ALEPH measures $A_{\rm FB}^{\rm c\overline{c}}$ only from a sample of high momentum D-mesons. DELPHI and OPAL measure $A_{\rm FB}^{\rm b\overline{b}}$ and $A_{\rm FB}^{\rm c\overline{c}}$ by fitting the momentum spectrum of the D-mesons and including lifetime information.

The left-right-forward-backward asymmetry measurements from SLD are directly quoted in terms of $\mathcal{A}_{\rm b}$ and $\mathcal{A}_{\rm c}$. The following results are included:

- Measurements of $\mathcal{A}_{\rm b}$ and $\mathcal{A}_{\rm c}$ using leptons [152];

- A measurement of $\mathcal{A}_{\rm c}$ using D-mesons [153];

- A measurement of $\mathcal{A}_{\rm b}$ using jet charge [154];

- A measurement of $\mathcal{A}_{\rm b}$ using vertex charge [155];

- A measurement of $\mathcal{A}_{\rm b}$ using kaons [156];

- A measurement of $\mathcal{A}_{\rm c}$ using vertex charge and kaons [155].

All these measurements are listed in detail in Appendix C.

5.5 Auxiliary Measurements

The measurements of the charmed hadron fractions $P(\rm c \to D^{*+} \to \pi^+ D^0)$, $f(\rm D^+)$, $f(\rm D_s)$ and $f(\rm c_{baryon})$ are included in the $R_{\rm c}$ analyses and are described there.

ALEPH [157,141], DELPHI [158], L3 [159,124,144] and OPAL [160,145] measure $B(\rm b \to \ell^-)$, $B(\rm b \to c \to \ell^+)$ and $\overline{\chi}$ or a subset from a sample of leptons opposite a b-tagged hemisphere and from a double lepton sample. DELPHI [132] and OPAL [139] measure $B(\rm c \to \ell^+)$ from a sample opposite a high energy $\rm D^{*\pm}$. All the auxiliary measurements used in the combination are listed in Appendix C.

5.6 External Inputs to the Heavy Flavour Combination

All the measurements contributing to the heavy flavour combination require some input from simulated events. Quantities derived from the simulation are affected by uncertainties related to the modelling of the detector response, as well as by the limited knowledge of the physics processes that are simulated. These latter sources are common to all experiments, and they have to be treated as correlated when averaging individual results. Furthermore, in order to produce consistent averages, the external physics parameters or models used in the simulation must be the same for all analyses in all experiments.

The choice of the external physics parameters and models relevant for electroweak heavy flavour analyses is discussed below. Whenever possible measurements at LEP/SLD or at lower energies are used to constrain the models used in the simulations. The uncertainties on the fitted partial widths and asymmetries due to the knowledge of the external parameters can be seen from Table 5.12. If a parameter does not appear in Table 5.12 the error is negligible either because the parameter is relatively unimportant or because it is known very precisely.

In many cases the world averages of the Particle Data Group are used. They are consistently taken from the 1998 edition of the RPP [117]. It has been checked that updates published in the 2004 edition [84] do not change any of the results. Table 5.4 summarises the important external parameters used. Details of their choice are explained in the remainder of this section

5.6.1 Fragmentation of Heavy Quarks

The process of hadron production is modelled as the convolution of a perturbative part (hard gluon radiation), and a non-perturbative part, called fragmentation, described with phenomenological models.

In the JETSET [17] simulation the fragmentation model by Peterson *et al.* [161] is used, which describes the process in terms of the variable $z = (E + p_\parallel)_{\mathrm{hadron}}/(E + p_\parallel)_{\mathrm{quark}}$, where $p_\parallel$ is the momentum component in the direction of the fragmenting quark. The model contains one free parameter, ε_{Q}, which is tuned to reproduce a given value of the mean energy of the heavy hadrons produced. Such tuning depends on the cut-off used for the transition between the perturbative and the non-perturbative part, therefore ε_{Q} can not be given an absolute meaning. The energy spectrum is more conveniently described in terms of the variable x_Q, defined as the energy of the weakly-decaying hadron containing the heavy quark Q normalised to the beam energy.

The analyses quoted in Reference [162,163,164,165,166], provide values for the mean energy of weakly-decaying b hadrons, which are averaged to obtain:

$$\langle x_E \rangle_{\mathrm{b}} \;=\; 0.702 \pm 0.008 \tag{5.18}$$

where the error includes the uncertainty due to the modelling of the fragmentation function. This uncertainty is estimated by using the functional forms proposed by Collins and Spiller [167], and by Kartvelishvili *et al.* [168] as alternatives to Peterson *et al.* [161] when extracting $\langle x_E \rangle_{\mathrm{b}}$. Only analyses which are close to the heavy flavour analyses, especially with leptons, are used in the average. This ensures a consistent treatment of B-fragmentation leading to some error cancellations.

The energy of charmed hadrons is measured in analyses which make use of lepton tags or inclusive reconstruction of $\mathrm{D}^0/\mathrm{D}^+$-mesons [163, 138], and in analyses with full reconstruction of D^{*+}-mesons [169, 170, 171]. The former have a larger dependence on the modelling of the spectrum, while the latter need an additional correction to obtain the energy of the weakly-decaying hadron. In all cases the contribution from charmed hadrons produced by hard gluons splitting to heavy quarks is removed. The average energy of weakly-decaying charmed hadrons is found to be

$$\langle x_E \rangle_{\mathrm{c}} \;=\; 0.484 \pm 0.008 \tag{5.19}$$

which again includes the estimated uncertainty from the modelling of the spectrum.

Error Source	Used Range
$\langle x_E \rangle_{\mathrm{b}}$	0.702 ± 0.008
$\langle x_E \rangle_{\mathrm{c}}$	0.484 ± 0.008
Choice of b fragmentation function	See sec. 5.6.1
Choice of c fragmentation function	See sec. 5.6.1
$B(\mathrm{b} \to \overline{\mathrm{c}} \to \ell^-)$	$(1.62\,^{+0.44}_{-0.36})\%$
$B(\mathrm{b} \to \tau^- \to \ell^-)$	$(0.419 \pm 0.055)\%$
$B(\mathrm{b} \to (J/\psi, \psi') \to \ell\ell)$	$(0.072 \pm 0.006)\%$
Semilept. model $\mathrm{b} \to \ell^-$	ACCMM $(^{+\mathrm{ISGW}}_{-\mathrm{ISGW}**})$ (sec. 5.6.6)
Semilept. model $\mathrm{c} \to \ell^+$	ACCMM1 $(^{+\mathrm{ACCMM2}}_{-\mathrm{ACCMM3}})$ (sec. 5.6.6)
$\mathrm{B} \to \mathrm{D}$ model	Peterson $\epsilon = 0.42 \pm 0.07$
D^0 lifetime	0.415 ± 0.004 ps
D^+ lifetime	1.057 ± 0.015 ps
$\mathrm{D_s}$ lifetime	0.467 ± 0.017 ps
Λ_{c}^+ lifetime	0.206 ± 0.012 ps
B lifetime	1.576 ± 0.016 ps
$B(\mathrm{D}^0 \to \mathrm{K}^-\pi^+)$	0.0385 ± 0.0009
$B(\mathrm{D}^+ \to \mathrm{K}^-\pi^+\pi^+)$	0.090 ± 0.006
$B(\mathrm{D_s}^+ \to \phi\pi^+)$	0.036 ± 0.009
$\frac{B(\mathrm{D_s}^+ \to \overline{\mathrm{K}}^{*0}\mathrm{K}^+)}{B(\mathrm{D_s}^+ \to \phi\pi^+)}$	0.92 ± 0.09
$B(\Lambda_{\mathrm{c}} \to \mathrm{pK}^-\pi^+)$	0.050 ± 0.013
B charged decay multiplicity	4.955 ± 0.062
D charged decay multiplicity	See sec. 5.6.3
D neutral decay multiplicity	See sec. 5.6.3
$\mathrm{g} \to \mathrm{c}\overline{\mathrm{c}}$ per multi-hadron	$(2.96 \pm 0.38)\%$
$\mathrm{g} \to \mathrm{b}\overline{\mathrm{b}}$ per multi-hadron	$(0.254 \pm 0.051)\%$
Rate of long-lived light hadrons	Tuned JETSET$\pm$10% (sec. 5.6.8)
Light quark fragmentation	See sec. 5.6.8
QCD hemisphere correlations	See sec. 5.6.7

Table 5.4: The most important external parameters used in the heavy flavour analyses

5.6.2 Heavy Quarks from Gluon Splitting

Gluons can occasionally split to heavy quark pairs. In several analyses these contributions need to be subtracted. In particular the uncertainty on the rate of gluons splitting to $\mathrm{b\overline{b}}$ pairs is the single largest contribution to the systematic error on the R_b world average.

The rates $g_{\mathrm{c\overline{c}}}$ and $g_{\mathrm{b\overline{b}}}$ are defined as the number of hadronic Z decays containing a gluon splitting to a $\mathrm{c\overline{c}}$ or $\mathrm{b\overline{b}}$ pair, normalised to the total number of hadronic Z decays.

Measurements of $g_{\mathrm{b\overline{b}}}$ [172] rely on an inclusive lifetime-based tag applied to the jets reconstructed in the event, while measurements of $g_{\mathrm{c\overline{c}}}$ [131, 173, 174] make use of exclusive D^* reconstruction, final states containing leptons, or are based on the combination of event shape variables.

Averaging published results yields:

$$\begin{aligned} g_{\mathrm{c\overline{c}}} &= 0.0296 \pm 0.0038\,, \\ g_{\mathrm{b\overline{b}}} &= 0.00254 \pm 0.00051\,, \end{aligned} \tag{5.20}$$

with only a very small correlation between the two values [175].

5.6.3 Multiplicities in Heavy Flavour Decays

Many analyses make use of inclusive b tagging methods which exploit the long lifetimes of b hadrons. The discrimination is based on the presence, in a jet, or a hemisphere, or the whole event, of charged tracks with significant impact parameter from the primary vertex of the events. Therefore the tagging efficiency is directly affected by the number of charged tracks produced in the long-lived hadron decay.

In R_b measurements the tag is applied to hemispheres, and the b efficiency is measured directly in the data from the fraction of events with both hemispheres tagged. The b charged multiplicity only enters, as a simulation uncertainty, through the hemisphere correlation. Measurements of the average b charged multiplicity performed at LEP are used. Results from lower energy experiments cannot be used because of the different b-hadron mixture.

However, the charm selection efficiency is taken from the simulation, at least for the samples with highest purity. It is therefore crucial to propagate correctly the uncertainty due to the decay charged multiplicities of the various charmed hadrons. This is done separately for each hadron species due to the significant differences in lifetimes.

The charm selection efficiency also depends on the number of neutral particles accompanying the charged particles in a given topological decay channel. The size of this effect depends on how invariant mass cuts are implemented and might vary substantially in different analyses. The uncertainty is evaluated varying the K^0 and π^0 production rates in charmed hadron decays.

Average Charged Multiplicity in b Hadron Decays

Inclusive measurements of the mean b-hadron charged multiplicity at LEP [176] are combined to obtain:

$$\langle n_b^{ch} \rangle = 4.955 \pm 0.062\,. \tag{5.21}$$

Particles coming from the decay of $\mathrm{B}^{\star\star}$ or other possible excited b states are excluded; the result is also corrected to exclude charged particles originating from the decay of K^0 and Λ.

Charged Multiplicities of c Hadron Decays

Inclusive topological branching fractions have been measured for D^0, D^+ and D_s [177]. For each species, each channel is varied within its uncertainty, except for the channel with the highest rate, which is used to compensate the variation. The resulting errors are combined using the corresponding correlation coefficients. The values f_i of the branching fractions for the decays into i charged particles, the corresponding errors σ_i and correlation coefficients C_{ij} are given in Table 5.5. For charm baryons, for which no measurements are available, an uncertainty of ± 0.5 in the overall charged decay multiplicity was used.

D meson	Topological Decays			
D^0	$f_0 = 0.054$ $\sigma_0 = 0.011$ $C_{04} = 0.07$	$f_2 = 0.634$	$f_4 = 0.293$ $\sigma_4 = 0.023$ $C_{46} = -0.46$	$f_6 = 0.019$ $\sigma_6 = 0.009$ $C_{06} = 0$
D^+	$f_1 = 0.384$ $\sigma_1 = 0.023$ $C_{15} = -0.33$	$f_3 = 0.541$	$f_5 = 0.075$ $\sigma_5 = 0.015$	
D_s	$f_1 = 0.37$ $\sigma_1 = 0.10$ $C_{15} = -0.02$	$f_3 = 0.42$	$f_5 = 0.21$ $\sigma_5 = 0.11$	

Table 5.5: Topological rates for the different charm-meson species, with estimated errors and correlation coefficients. The subscripts indicate the number of charged particles produced.

Neutral Particle Production in c Hadron Decays

The procedure to estimate the residual dependence of the lifetime tag efficiency on the average rate of neutral particles produced in charm decays is tailored, case by case, on the specific properties of the tag and based on the measurements available [117]. Although the procedures differ somewhat between experiments, the resulting estimated uncertainties are taken as fully correlated.

5.6.4 Heavy Flavour Lifetimes

The lifetimes of heavy hadrons are relevant to many analyses, in particular all those which make use of lifetime-based b tagging methods. As for the charged multiplicity, in the case of the R_b analyses charm lifetimes enter directly in the estimate of the charm contamination in high purity samples, whereas b hadron lifetimes only affect the estimate of the hemisphere correlations.

Average b Hadron Lifetime

The average lifetime of b hadrons is taken [117] to be

$$\tau_b \;=\; 1.576 \pm 0.016 \text{ ps} \;, \tag{5.22}$$

which is obtained from analyses of fully inclusive b final states. The lifetime difference between b species has in general little impact in all analyses. It is considered as a source of uncertainty in the $R_{\rm b}$ analyses either by using the individual lifetimes [117] or by enlarging the error to 0.05 ps.

Lifetimes of c Hadrons

The lifetimes of the different c hadron species are considered as individual sources of uncertainties. The values and errors [117] are:

$$\begin{aligned} \tau(\mathrm{D}^0) &= 0.415 \pm 0.004 \text{ ps} , \\ \tau(\mathrm{D}^+) &= 1.057 \pm 0.015 \text{ ps} , \\ \tau(\mathrm{D_s}) &= 0.467 \pm 0.017 \text{ ps} , \\ \tau(\Lambda_c^+) &= 0.206 \pm 0.012 \text{ ps} . \end{aligned} \tag{5.23}$$

5.6.5 Charmed Hadron Decays to Exclusive Final States

Charm counting measurements determine the production rates of individual c-hadron species by tagging exclusive final states, using the branching fraction for the appropriate decay mode as input. The values and errors used are [117, 178]:

$$\begin{aligned} B(\mathrm{D}^0 \to \mathrm{K}^-\pi^+) &= 0.0385 \pm 0.0009 , \\ B(\mathrm{D}^+ \to \mathrm{K}^-\pi^+\pi^+) &= 0.090 \pm 0.006 , \\ B(\mathrm{D_s^+} \to \phi\pi^+) &= 0.036 \pm 0.009 , \\ \frac{B(\mathrm{D_s^+} \to \overline{\mathrm{K}}^{\star 0}\mathrm{K}^+)}{B(\mathrm{D_s^+} \to \phi\pi^+)} &= 0.92 \pm 0.09 , \\ B(\Lambda_\mathrm{c} \to \mathrm{pK}^-\pi^+) &= 0.050 \pm 0.013 . \end{aligned} \tag{5.24}$$

5.6.6 Heavy Flavour Leptonic Decays

Many analyses rely on semileptonic final states in order to tag the presence of heavy hadrons and possibly their charge. Assessing the performance of such tags involves estimating the rates of the different sources of lepton candidates in hadronic events, and modelling the kinematics of the leptons produced in the decay of heavy hadrons.

The rates for the major sources (direct decays, $\mathrm{b} \to \ell^-$ and $\mathrm{c} \to \ell^+$, cascade b decays, $\mathrm{b} \to \mathrm{c} \to \ell^+$) are measured at LEP, and included as fitted parameters. The modelling of the decay kinematics is a common source of systematic uncertainty. The rates for the other sources are taken from external measurements.

Modelling of Direct Semileptonic b Decays

For the semileptonic decays of B^0 and B^+ mesons the CLEO collaboration has compared decay models to their data and measured the free parameters of the models. Based on the CLEO fits [179], the LEP experiments quote results for three different models.

- The model proposed by Altarelli *et al.* [180] is an extension of the free quark model which attempts to account for non-perturbative effects kinematically. The two free parameters of the model, the Fermi momentum of the constituent quarks inside the heavy meson

and the mass of the final quark, are determined from CLEO data to be $p_{\rm F} = 298$ MeV, $m_c = 1673$ MeV.

- The form-factor model proposed by Isgur *et al.* [181], with the model prediction that 11% of semileptonic B meson decays result in an L=1 charm meson, D**.
- The same model with the rate of D** mesons increased to 32%, as preferred by the CLEO data [179, 181].

The model of Altarelli *et al.* is used to derive the central values of the analyses, while the two others, which give respectively harder and softer lepton spectra, are used to give an estimate of the associated uncertainty.

Reweighting functions are constructed to adjust the lepton spectrum of semileptonic B^0 and B^+ decays in the LEP Monte Carlo samples to the three models based on CLEO data. For use in Z decays, the same reweighting functions have been assumed to be valid for the B_s meson and b baryons. This would be correct in the simplest spectator model, and is thought more generally to be adequate for the B_s. The baryon contribution is only about 10%, and no additional systematic error is assigned.

Modelling of Direct Semileptonic c Decays

The measurements of DELCO [182] and MARK III [183] for D^0 and D^+ semileptonic decays have been combined and parametrised using the model of Altarelli *et al.* as a convenient functional form. The D boost and the experimental resolution are taken into account in the fit to the data. Based on this fit [184], the model parameters are fixed to $p_{\rm F} = 467$ MeV, $m_s = 1$ MeV and they are varied to $p_{\rm F} = 353$ MeV, $m_s = 1$ MeV and $p_{\rm F} = 467$ MeV, $m_s = 153$ MeV to derive an estimate of the associated uncertainty. The reweighting functions derived from D^0 and D^+ decays are assumed to be valid for all charm hadrons.

Modelling of Cascade Semileptonic b Decays

For the cascade decays, $b \to c \to \ell^+$, the three models used for $c \to \ell^+$ decays are combined with the measured $B \to D$ spectrum from CLEO [185] to generate three models for the lepton momentum spectrum in the rest frame of the b hadron. The CLEO $B \to D$ decay spectrum can be conveniently modelled by a Peterson function [161] with free parameter $\varepsilon = 0.42 \pm 0.07$. The effect of this $B \to D$ model uncertainty on the $b \to c \to \ell^+$ spectrum is negligible compared to the uncertainty from the $c \to \ell^+$ models.

Rate of $b \to \overline{c} \to \ell^-$ Transitions

Several quantities related to the rate of leptons from c hadrons produced from the "upper vertex" in b-hadron decays[4] have been measured. An estimate of this rate is therefore possible, based upon experimental results.

The inclusive and flavour-specific $B \to D, X$ and $B \to \Lambda_c^+, X$ rates measured at CLEO [186], which are sensitive to the sum $(B \to c) + (B \to \overline{c})$, are combined with the $B \to D\overline{D}(X)$ rates measured in ALEPH [187] to extract the probabilities of producing the different c-hadrons from the upper vertex in b decays. These are combined with the c-hadron semileptonic branching fractions to obtain a value for the $B(b \to \overline{c} \to \ell^-)$.

[4] The term "upper vertex" is used in the literature for the decay of the virtual W from the b-quark decay.

The estimate obtained is

$$B(\mathrm{b} \to \overline{\mathrm{c}} \to \ell^-) \;=\; 0.0162\,^{+0.0044}_{-0.0036}\,. \tag{5.25}$$

Other Semileptonic Decays

The rate for $\mathrm{b} \to \tau^- \to \ell^-$ decays is derived from existing measurements of $B(\mathrm{b} \to \tau)$ [188] combined with the τ leptonic branching fraction [117]. The procedure yields:

$$B(\mathrm{b} \to \tau^- \to \ell^-) \;=\; 0.00419 \pm 0.00055\,. \tag{5.26}$$

The rate for $\mathrm{b} \to (J\!/\!\psi, \psi') \to \ell\ell$ decays is calculated from the production rate of $J\!/\!\psi$ and ψ' in $\mathrm{Z} \to \mathrm{b\overline{b}}$ decays, and the $J\!/\!\psi$ and ψ' leptonic branching fractions [117], yielding

$$B(\mathrm{b} \to (J\!/\!\psi, \psi') \to \ell\ell) \;=\; 0.00072 \pm 0.00006\,. \tag{5.27}$$

5.6.7 Hemisphere Correlations in Double-Tag Methods

In analyses where a b-tagging algorithm is applied in one hemisphere, the tagging efficiency can be measured from the data by comparing the fraction of hemispheres that are tagged and the fraction of events with both hemispheres tagged. However, the correlation between the tagging efficiencies in the two hemispheres, defined in Equation 5.3, must then be estimated from simulation. This is particularly crucial for the precise R_b double tag measurements.

There are basically three physics sources for such a correlation:

- detector inhomogeneities,
- the use of a common primary vertex,
- kinematic correlations, mainly due to gluon radiation.

Detector effects are easily controllable from the data by measuring the tagging rate as a function of the jet direction and then calculating the correlation from this rate assuming that the quarks in an event are back-to-back. This error source is of statistical nature and uncorrelated between the experiments.

The second of these sources is relatively small for algorithms based on the reconstruction of the b decay length, since this is dominated by the uncertainty on the position of the secondary vertex. However, it is a major issue for tags based on track impact parameters, and it is particularly difficult to control since it heavily influences the other sources. Therefore in the R_b analyses the primary vertex is generally reconstructed independently in the two hemispheres, rendering this source of correlation negligible.

The kinematic correlations are correlated between the experiments. They mainly arise from the fact that the tagging efficiency depends on the b hadron momentum and that a gluon emitted at a large angle reduces the energy of both quarks.

If the efficiency is proportional to the b hadron momentum, the efficiency correlation is directly given by the momentum correlation. Analytic $\mathcal{O}(\alpha_\mathrm{S})$ QCD calculations predict effects of about 1.4 % [189] for the correlation between the two b-quark momenta. At the parton level, fragmentation models agree at the 0.2 % level with this number. At the hadron level HERWIG [18] gives a correlation up to 0.8 % larger than JETSET or ARIADNE.

Since the proportionality between the B momentum and the tagging efficiency is only approximate, in practice the experiments have derived test quantities that are sensitive to the

kinematical correlations and the systematic uncertainties are derived from data/Monte Carlo comparisons. These methods are described in detail in the experimental papers. As an example the momentum of the fastest jet, assuming a three-jet topology, can be calculated and the tagging rate for the hemisphere containing this jet and for the opposite hemisphere are measured. Although these errors have a large statistical component, they are conservatively taken as fully correlated between the experiments.

Events where the radiated gluon is so hard that the two b hadrons are in the same hemisphere are particularly relevant for the estimate of the correlation. The rate of such events (about 1 % of all $Z \to b\overline{b}$ events) is varied by $30 - 40$ %, motivated by a comparison of matrix element and parton shower models, and by studies of the modelling of events with two b-tags in the same hemisphere.

Furthermore, the hemisphere correlation also depends on b hadron production and decay properties. Such a dependence is a small second order effect for analyses which reconstruct the primary vertex independently in the two hemispheres, but can be substantial if a common primary vertex is used, due to the inclusion of tracks which actually come from b hadrons in the primary vertex determination. The sources of uncertainty considered are:

- average charged track multiplicity in b-hadron decay,
- b fragmentation,
- b hadron lifetimes,

and the errors are evaluated according to the prescription in this section.

5.6.8 Light Quark Background in Lifetime Tagged Samples

The amount of light quark background in lifetime-tagged samples is mainly determined by the rate of long-lived light hadrons, namely K_s^0 and Λ, produced in the fragmentation. This is only a significant source of uncertainty for the precise R_b measurements. In the case of forward-backward asymmetry measurements, details of light quark fragmentation are relevant in the extraction of the asymmetry from the measured charge flow.

Rate of Long-Lived Light Hadrons

All experiments have measured the rates of long-lived light hadrons and tuned their fragmentation model accordingly. Variations of 10 % around the central value are used to estimate the uncertainty.

Fragmentation of Light Quarks

The JETSET model contains many free parameters, several of which influence the charge flow predictions. These parameters have been tuned individually by the experiments and it is not possible to define a common procedure to evaluate the errors due to light quark fragmentation. Fortunately these errors turn out to be relatively small, and they are assumed to be fully correlated even if the procedures to evaluate them vary between the experiments.

5.7 Corrections to the Electroweak Observables

5.7.1 Corrections to R_b and R_c

Small corrections have to be applied to the raw experimental measurements. The R_b and R_c analyses measure the ratio of production cross-sections $R_q = \sigma_{q\bar{q}}/\sigma_{had}$. To obtain the ratios of partial widths $R_q^0 = \Gamma_{q\bar{q}}/\Gamma_{had}$, small corrections for photon exchange and γ–Z interference have to be applied. These corrections are typically $+0.0002$ for R_b and -0.0002 for R_c, and are applied by the experiments before the combination as their size depends slightly on the invariant mass cutoff of the $q\bar{q}$-system imposed in the analysis.

5.7.2 QCD Corrections to the Forward-Backward Asymmetries

Due to QCD effects the measured forward-backward asymmetries do not correspond to the underlying quark asymmetries on the electroweak level. The dominant corrections are due to radiation of gluons from the final state quarks. The QCD corrections do not depend on the beam polarisation and are thus identical for the unpolarised forward-backward asymmetry and the left-right-forward-backward asymmetries. All statements on $A_{FB}^{q\overline{q}}$ in this section equally apply to $A_{LRFB}^{q\overline{q}}$.

Theoretical calculations use either the quark direction or the thrust direction to compute the asymmetry. In case the thrust direction is used, the thrust axis is signed by the projection of the quark direction on this axis. Since the reconstructed thrust axis is generally used as the heavy quark direction estimator in experimental measurements, calculations based on the thrust axis are considered.

The effect on the asymmetry at the scale $\mu^2 = m_Z^2$ is parametrised as [140]:

$$\begin{aligned} \left(A_{FB}^{q\overline{q}}\right)_{meas} &= (1 - C_{QCD}) \left(A_{FB}^{q\overline{q}}\right)_{no\,QCD} \\ &= \left(1 - \frac{\alpha_s(m_Z^2)}{\pi} c_1 - \left(\frac{\alpha_s(m_Z^2)}{\pi}\right)^2 c_2\right) \left(A_{FB}^{q\overline{q}}\right)_{no\,QCD} . \end{aligned} \tag{5.28}$$

The first-order corrections are known including mass effects [190]. Taking the thrust axis as the direction and using the pole mass, they are $c_1 = 0.77$ for $A_{FB}^{b\overline{b}}$ and $c_1 = 0.86$ for $A_{FB}^{c\overline{c}}$.

The second-order corrections have been recalculated in [191] and [192] and both calculations agree well if the quark direction is used. However only the latter contains also the case where the thrust axis is used as a reference so that this one is used to correct the LEP and SLD measurements. The two calculations disagree with previous results [190], however there is a general consensus that the newer ones, which are in agreement amongst each other, should be trusted. The calculation of [192] is strictly massless and also neglects the corrections from triangle diagrams involving top quarks, given in [190]. Corrections arising from diagrams which lead to two-parton final states are the largest, and they can be added to the results of [192], as they apply in the same way to calculations based either on the thrust or the quark direction.

The second order coefficients used are $c_2 = 5.93$ for $A_{FB}^{b\overline{b}}$ and $c_2 = 8.5$ for $A_{FB}^{c\overline{c}}$. The final QCD correction coefficients, including further corrections due to fragmentation effects and using the thrust axis as reference direction ($C_{QCD}^{had,T}$), are $C_{QCD}^{had,T} = 0.0354 \pm 0.0063$ for $A_{FB}^{b\overline{b}}$ and $C_{QCD}^{had,T} = 0.0413 \pm 0.0063$ for $A_{FB}^{c\overline{c}}$. The breakdown of the errors is given in Table 5.6.

The procedure to implement QCD corrections in the experimental analyses is non-trivial. It is described in detail in [140] and briefly summarised in the following.

Error on $C_{\mathrm{QCD}}^{\mathrm{had,T}}$		$\mathrm{b\overline{b}}$	$\mathrm{c\overline{c}}$
Higher orders	[192]	0.0025	0.0046
Mass effects	[140]	0.0015	0.0008
Higher order mass	[192]	0.005	0.002
$\alpha_s = 0.119 \pm 0.003$		0.0012	0.0015
Hadronisation	[140]	0.0023	0.0035
Total		0.0063	0.0063

Table 5.6: Error sources for the QCD corrections to the forward-backward asymmetries.

The corrections provided by theoretical calculations are not directly applicable to experimental measurements for two main reasons. First, the thrust axis used in theoretical calculations is defined using partons in second order QCD, where the axis is signed by the projection of the b-quark on the thrust axis; a further smearing is caused by the hadronisation of partons into hadrons. This effect, about ten times smaller than the correction itself, is taken from the simulation using the JETSET model, and its full size is taken as an additional uncertainty. Second, and much more important, the experimental selection and analysis method can introduce a bias in the topology of the events used, or intrinsically correct for the effects. This analysis bias is calculated using the full detector simulation with JETSET for event-generation, where it has been verified that JETSET reproduces the analytical calculations very well for full acceptance. It turns out that analyses based on semileptonic decays typically need half of the full correction. In the jet charge analyses the QCD corrections are partly included in the measured charge separation and partly in the hemisphere correlations which are corrected for internally. The remaining corrections are very small. The experimental asymmetries are then corrected by a factor $1/(1 - C_{\mathrm{QCD}}^{\mathrm{had,T}} \cdot b)$ where b is the bias factor calculated with the simulation.

Because of the analysis dependence of the QCD corrections all asymmetries quoted in this chapter are already corrected for QCD effects.

The uncertainty on the theoretical calculation of the corrections, as well as on the additional effect due to hadronisation, are taken as fully correlated between the different measurements. The "scaling factor" applied for each individual analysis to account for the experimental bias is instead evaluated case by case together with its associated uncertainty, and these errors are taken as uncorrelated. For the jet charge measurement, the part of the QCD correction that is included in the hemisphere correlations is also accounted for in the error estimate. This part is estimated from the dependence of the hemisphere correlations on the thrust value.

5.7.3 Other Corrections to the Asymmetries

The forward-backward asymmetries at LEP vary strongly as a function of the centre-of-mass energy because of γ–Z interference. Since the mean energies at the different points vary slightly with time (see e.g. Figure 2.3), the mean energies of the different analyses are also not completely identical. The experiments quote the mean centre-of-mass energy for each asymmetry measurement. In a first fit the asymmetries are corrected to the closest of the three energies $\sqrt{s} = 89.55\,\mathrm{GeV}(-2),\ 91.26\,\mathrm{GeV}(\mathrm{pk}),\ 92.94\,\mathrm{GeV}(+2)$ assuming the SM energy dependence.

The slope of the asymmetries depends only on the well known fermion charges and axial couplings while the asymmetry value on the Z-pole is sensitive to the effective weak mixing

angle. The first fit verifies that the energy dependence is indeed consistent with the one expected in the SM. In a second fit all asymmetries are then corrected to the peak energy (91.26 GeV) before fitting.

To obtain the pole asymmetry, $A_{\rm FB}^{0,\rm q}$, which is defined by the real parts of the Z-fermion couplings, the fitted asymmetries at the peak energy, denoted as $A_{\rm FB}^{\rm q\overline{q}}({\rm pk})$ need to be corrected further as summarised in Table 5.7. These corrections are due to the energy shift from 91.26 GeV to $m_{\rm Z}$, initial state radiation, γ exchange, γ–Z interference and imaginary parts of the couplings. A very small correction due to the nonzero value of the b quark mass is also included. All corrections are calculated using ZFITTER 6.42 [31]. Further details can be found in [193]. The uncertainties on these corrections have been estimated to be $\Delta(\delta A_{\rm FB}^{\rm b\overline{b}}) = 0.0002$ and $\Delta(\delta A_{\rm FB}^{\rm c\overline{c}}) = 0.0001$ [193]. Compared to the experimental errors on the quark asymmetries they can be safely neglected. Similar corrections have been applied to the left-right-forward-backward asymmetries. The corrections are only about one tenth of the experimental error and the asymmetries are directly presented in terms of $\mathcal{A}_{\rm b}$ and $\mathcal{A}_{\rm c}$ by SLD.

Source	$\delta A_{\rm FB}^{\rm b\overline{b}}$	$\delta A_{\rm FB}^{\rm c\overline{c}}$
$\sqrt{s} = m_{\rm Z}$	-0.0014	-0.0035
QED corrections	$+0.0039$	$+0.0107$
other	-0.0006	-0.0008
Total	$+0.0019$	$+0.0064$

Table 5.7: Corrections to be applied to the quark asymmetries as $A_{\rm FB}^{0,\rm q} = A_{\rm FB}^{\rm q\overline{q}}({\rm pk}) + \delta A_{\rm FB}$. The row labelled "other" denotes corrections due to γ exchange, γ–Z interference, quark-mass effects and imaginary parts of the couplings. The uncertainties of the corrections are negligible.

5.8 Combination Procedure

The heavy flavour results are combined [184] using a χ^2 minimisation technique. In the case of the lineshape, each experiment measures the same 5 or 9 parameters. Here, the set of measurements is different for each experiment. Nonetheless, a χ^2 minimisation can be used to find the best estimate of each of the electroweak parameters. The formulation must be sufficiently flexible to allow any number of measurements of each electroweak parameter by each experiment. The measured values of closely related auxiliary parameters, detailed in Appendix C are included in the averaging procedure. Their treatment will be explained more fully below.

In order to write down an expression for this χ^2, the average value, i.e. the best estimate of the set of electroweak parameters is denoted x^μ, where the index μ refers to the different fit parameters.

$$
\begin{aligned}
x^\mu \;=\;& R_{\rm b},\, R_{\rm c}, \\
& A_{\rm FB}^{\rm b\overline{b}}(-2),\, A_{\rm FB}^{\rm c\overline{c}}(-2),\, A_{\rm FB}^{\rm b\overline{b}}({\rm pk}),\, A_{\rm FB}^{\rm c\overline{c}}({\rm pk}),\, A_{\rm FB}^{\rm b\overline{b}}(+2),\, A_{\rm FB}^{\rm c\overline{c}}(+2), \\
& \mathcal{A}_{\rm b},\, \mathcal{A}_{\rm c}, \\
& B({\rm b}\to\ell^-),\, B({\rm b}\to{\rm c}\to\ell^+),\, B({\rm c}\to\ell^+),\, \overline{\chi}, \\
& f({\rm D}^+),\, f({\rm D_s}),\, f({\rm c_{baryon}}),\, P({\rm c}\to{\rm D}^{*+}\to\pi^+{\rm D}^0).
\end{aligned}
\tag{5.29}
$$

Note that the forward-backward asymmetries can either be averaged at three different centre-of-mass energies or be interpreted as measurements of the asymmetry at the Z-peak, $A_{\rm FB}^{\rm b\overline{b}}(\rm pk)$ and $A_{\rm FB}^{\rm c\overline{c}}(\rm pk)$, as described in Section 5.7.3.

Each experimental result is referred to as r_i and is a measurement of any of the parameters $\mu(i)$ introduced in Equation 5.29: $R_{\rm b}$ corresponds to $\mu(i) = 1$, $R_{\rm c}$ corresponds to $\mu(i) = 2$ and so on. A group of k results can be measured simultaneously in the same analysis to give: r_i, r_{i+1} ... r_{i+k-1}.

The averages are given by minimising the χ^2:

$$\chi^2 \;=\; \sum_{ij}(r_i - x^{\mu(i)})\mathcal{C}_{ij}^{-1}(r_j - x^{\mu(j)})\,. \tag{5.30}$$

Since the uncertainties on the branching fractions of some of the decay modes used in the charm counting $R_{\rm c}$ analyses are rather large, two refinements are added to the fit to correct for non-linear effects. The products $R_{\rm c}P(\rm c \to D^{*+} \to \pi^+ D^0)$, $R_{\rm c}f(\rm D^+)$, $R_{\rm c}f(\rm D^0)$, $R_{\rm c}f(\rm D_s)$ and $R_{\rm c}f(\rm c_{baryon})$ are given as experimental results r_i and are compared to the product of the relevant fit parameters in the χ^2 calculation. $f(\rm D^0)$ is calculated in this case from the other charmed hadron fractions using Equation 5.6. In addition the errors on these parameters, again mainly the branching fraction errors, are more Gaussian if they are treated as relative errors. For this reason the logarithm of the products is fitted instead of the products themselves. It has been found that only in the case of $R_{\rm c}f(\rm D_s)$ and $R_{\rm c}f(\rm c_{baryon})$ do the fit results depend on whether the logarithms or the values themselves are used. However these two measurements are completely dominated by the branching fraction error for which it is clear that the logarithmic treatment is the better one.

Almost all the complications in building the χ^2 are in calculating the $n \times n$ covariance matrix, $\mathcal{C}$, relating the $i = 1, n$ measurements. This matrix must take into account statistical and systematic correlations. Statistical correlations arise from overlap of samples within an experiment, and for groups of measurements of closely related parameters in the same fit. Some systematic errors lead only to correlations between measurements made by the same experiment, for example errors due to the modelling of track resolutions in a particular detector. Others are potentially common to all the measurements. The experiments provide their measurements in the form of input tables, which list the central values, the statistical errors, any correlations between statistical errors and a detailed breakdown of the systematic errors. This breakdown is used to calculate the systematic error contribution to the covariance matrix by assuming that any particular systematic uncertainty, for example the uncertainty due to the lifetime of the $\rm B^0$ meson, is fully correlated for all measurements [184]. This assumption is legitimate since common values and uncertainties are used for those quantities taken from external experimental measurements. All results are corrected, if necessary, to use the agreed set of external parameters. The input parameters are discussed in Section 5.6. In summary, the covariance matrix has the form:

$$\mathcal{C}_{ij} \;=\; \mathcal{C}_{ij}^{\rm stat} + \sum_k \sigma_i^k \sigma_j^k\,, \tag{5.31}$$

where $\mathcal{C}_{ij}^{\rm stat}$ is the covariance matrix of statistical errors and σ_i^k is the systematic error in measurement i, due to the source of systematic uncertainty k. Some errors, such as the error from Monte Carlo statistics, are uncorrelated for all results and therefore contribute only to the diagonal elements of $\mathcal{C}$. Others, such as those connected with lepton identification or tracking efficiency, are correlated for any measurements made by the same experiment. The

remaining errors, arising from the physics sources discussed in Section 5.6, are assumed to be fully correlated for all measurements.

It is also important to take into account that even when two electroweak parameters are not measured in the same fit, the measured value of one will depend on the value assumed for the other. For example, a measurement of R_{b} often depends on the fraction of charm contamination in the sample, and therefore on the value of R_{c} that was assumed. Let r_i be a measurement of R_{b}. The explicit first order dependence of the value of r_i, on the assumed value of R_{c}, $x^{R_{\mathrm{c}}}$, is then included as follows:

$$r_i \;=\; R_{\mathrm{b}}^{\mathrm{meas}} + a_i^{R_{\mathrm{c}}} \frac{(x^{R_{\mathrm{c}}} - R_{\mathrm{c}}^{\mathrm{used}})}{x^{R_{\mathrm{c}}}} \,. \tag{5.32}$$

Here $R_{\mathrm{b}}^{\mathrm{meas}}$ is the central value of R_{b} measured by the experiment, assuming a value for $R_{\mathrm{c}} = R_{\mathrm{c}}^{\mathrm{used}}$. The constant $a_i^{R_{\mathrm{c}}}$ is given by

$$\frac{a_i^{R_{\mathrm{c}}}}{x^{R_{\mathrm{c}}}} \;=\; \frac{\mathrm{d}r_i^{R_{\mathrm{b}}}}{\mathrm{d}x^{R_{\mathrm{c}}}} \left(x^{R_{\mathrm{c}}} = R_{\mathrm{c}}^{\mathrm{used}}\right) \,. \tag{5.33}$$

The dependence of any measurement on any of the other fitted parameters can be expressed in the same way.

The system of including measurements by input tables has proved to be very flexible. Different subsets of results can be combined together in cross-checks, to verify that the results are robust.

As an example, Table 5.8 shows the measurements of R_{b}^0 used in the fit. The line labelled "R_{b}^0(published)" shows the value published by the collaborations while in the line "R_{b}^0(input)" the values corrected for the agreed external parameters are given. The errors labelled "uncorrelated" are either internal to the analysis or to the experiment while the ones labelled "correlated" are potentially in common with other experiments. Also the dependences of the R_{b}^0 measurements on the other input parameters are given.

5.9 Results

The results used in this combination have been described in Sections 5.3, 5.4 and 5.5 and are summarised in Tables C.1 to C.20 in Appendix C. Figures 5.13 to 5.15 compare the main electroweak results of the different experiments.

In the first fit the different analyses have been combined with the asymmetries kept at the three different energies, yielding in total 18 free parameters. The results of this fit for the asymmetries are listed in Table 5.9 including their correlations. These asymmetries are only corrected for QCD effects. The full fit results including the correlation matrix is shown in Appendix B. The χ^2/dof of the fit is $48/(105-18)$. Applying the corrections explained in Section 5.7.3 to the peak asymmetry only one obtains for the pole asymmetries:[5]

$$A_{\mathrm{FB}}^{0,\mathrm{b}} \;=\; 0.1000 \pm 0.0017 \tag{5.34}$$

$$A_{\mathrm{FB}}^{0,\mathrm{c}} \;=\; 0.0699 \pm 0.0036 \,, \tag{5.35}$$

with a correlation of $+0.15$. Figure 5.16 shows the energy dependence of $A_{\mathrm{FB}}^{\mathrm{b}}$ and $A_{\mathrm{FB}}^{\mathrm{c}}$ compared to the SM prediction.

[5] To correct the peak asymmetries to the pole asymmetries only a number with negligible additional uncertainty is added, see Table 5.7. All errors and correlations thus remain unchanged.

	ALEPH	DELPHI	L3	OPAL	SLD
	92-95 [135]	92-95 [127]	94-95 [124]	92-95 [125]	93-98 [133]
R_{b}^0(published)	0.2159	0.2163	0.2174	0.2178	0.2159
R_{b}^0(input)	0.2158	0.2163	0.2173	0.2174	0.2159
Statistical	0.0009	0.0007	0.0015	0.0011	0.0009
Uncorrelated	0.0007	0.0004	0.0015	0.0009	0.0005
Correlated	0.0006	0.0004	0.0018	0.0008	0.0005
Total Systematic	0.0009	0.0005	0.0023	0.0012	0.0007
$a(R_{\mathrm{c}})$	-0.0033	-0.0041	-0.0376	-0.0122	-0.0056
$R_{\mathrm{c}}^{\mathrm{used}}$	0.1720	0.1720	0.1734	0.1720	0.17123
$a(B(\mathrm{c} \to \ell^+))$			-0.0133	-0.0067	
$B(\mathrm{c} \to \ell^+)^{\mathrm{used}}$			9.80	9.80	
$a(f(\mathrm{D}^+))$	-0.0010	-0.0010	-0.0086	-0.0029	-0.0008
$f(\mathrm{D}^+)^{\mathrm{used}}$	0.2330	0.2330	0.2330	0.2380	0.2330
$a(f(\mathrm{D_s}))$	-0.0001	0.0001	-0.0005	-0.0001	-0.0003
$f(\mathrm{D_s})^{\mathrm{used}}$	0.1020	0.1030	0.1030	0.1020	0.1020
$a(f(\Lambda_{\mathrm{c}}^+))$	0.0002	0.0003	0.0008	0.0003	-0.0002
$f(\Lambda_{\mathrm{c}}^+)^{\mathrm{used}}$	0.0650	0.0630	0.0630	0.0650	0.0650

Table 5.8: The measurements of R_{b}^0. All measurements use a lifetime tag enhanced by other features like invariant mass cuts or high p_T leptons. The lines $a(X)$ and x^{used} refer to the dependences defined in Equation 5.33. The dependence on $B(\mathrm{c} \to \ell^+)$ is only present for the measurements that use leptons in their primary b-tag.

Observable	Result	Correlations					
		$A_{\mathrm{FB}}^{\mathrm{b\bar{b}}}(-2)$	$A_{\mathrm{FB}}^{\mathrm{c\bar{c}}}(-2)$	$A_{\mathrm{FB}}^{\mathrm{b\bar{b}}}(\mathrm{pk})$	$A_{\mathrm{FB}}^{\mathrm{c\bar{c}}}(\mathrm{pk})$	$A_{\mathrm{FB}}^{\mathrm{b\bar{b}}}(+2)$	$A_{\mathrm{FB}}^{\mathrm{c\bar{c}}}(+2)$
$A_{\mathrm{FB}}^{\mathrm{b\bar{b}}}(-2)$	0.0560 ± 0.0066	1.00					
$A_{\mathrm{FB}}^{\mathrm{c\bar{c}}}(-2)$	-0.018 ± 0.013	0.13	1.00				
$A_{\mathrm{FB}}^{\mathrm{b\bar{b}}}(\mathrm{pk})$	0.0982 ± 0.0017	0.03	0.01	1.00			
$A_{\mathrm{FB}}^{\mathrm{c\bar{c}}}(\mathrm{pk})$	0.0635 ± 0.0036	0.00	0.02	0.15	1.00		
$A_{\mathrm{FB}}^{\mathrm{b\bar{b}}}(+2)$	0.1125 ± 0.0055	0.01	0.01	0.08	0.02	1.00	
$A_{\mathrm{FB}}^{\mathrm{c\bar{c}}}(+2)$	0.125 ± 0.011	0.00	0.01	0.02	0.15	0.13	1.00

Table 5.9: The forward-backward asymmetry results from the 18-parameter fit, including their correlations.

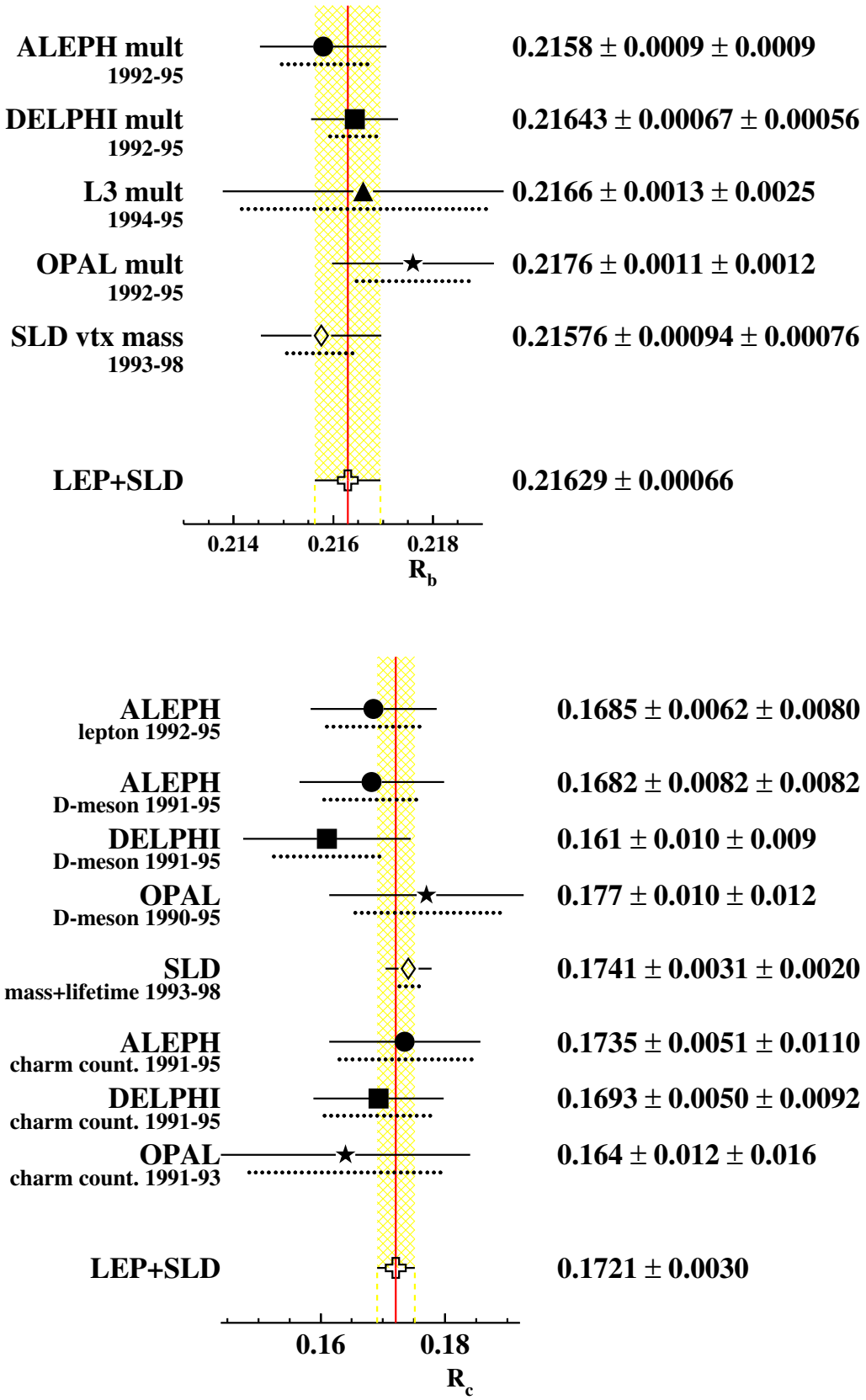

Figure 5.13: R_b^0 and R_c^0 measurements used in the heavy flavour combination, corrected for their dependence on parameters evaluated in the multi-parameter fit described in the text. The dotted lines indicate the size of the systematic error.

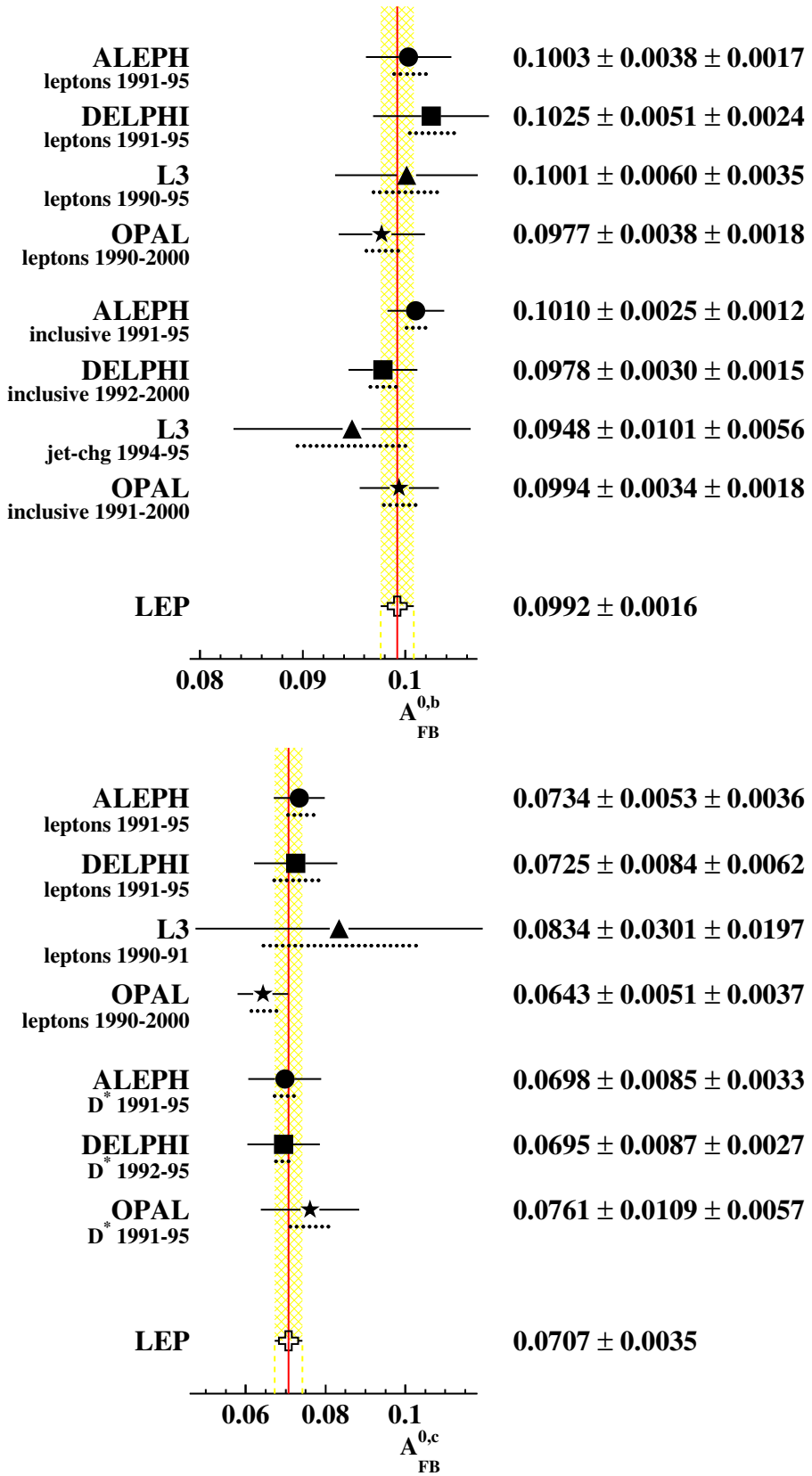

Figure 5.14: $A_{\mathrm{FB}}^{0,\mathrm{b}}$ and $A_{\mathrm{FB}}^{0,\mathrm{c}}$ measurements used in the heavy flavour combination, corrected for their dependence on parameters evaluated in the multi-parameter fit described in the text. The $A_{\mathrm{FB}}^{0,\mathrm{b}}$ measurements with D-mesons do not contribute significantly to the average and are not shown in the plots. The experimental results are derived from the ones shown in Tables C.3 to C.8 combining the different centre of mass energies. The dotted lines indicate the size of the systematic error.

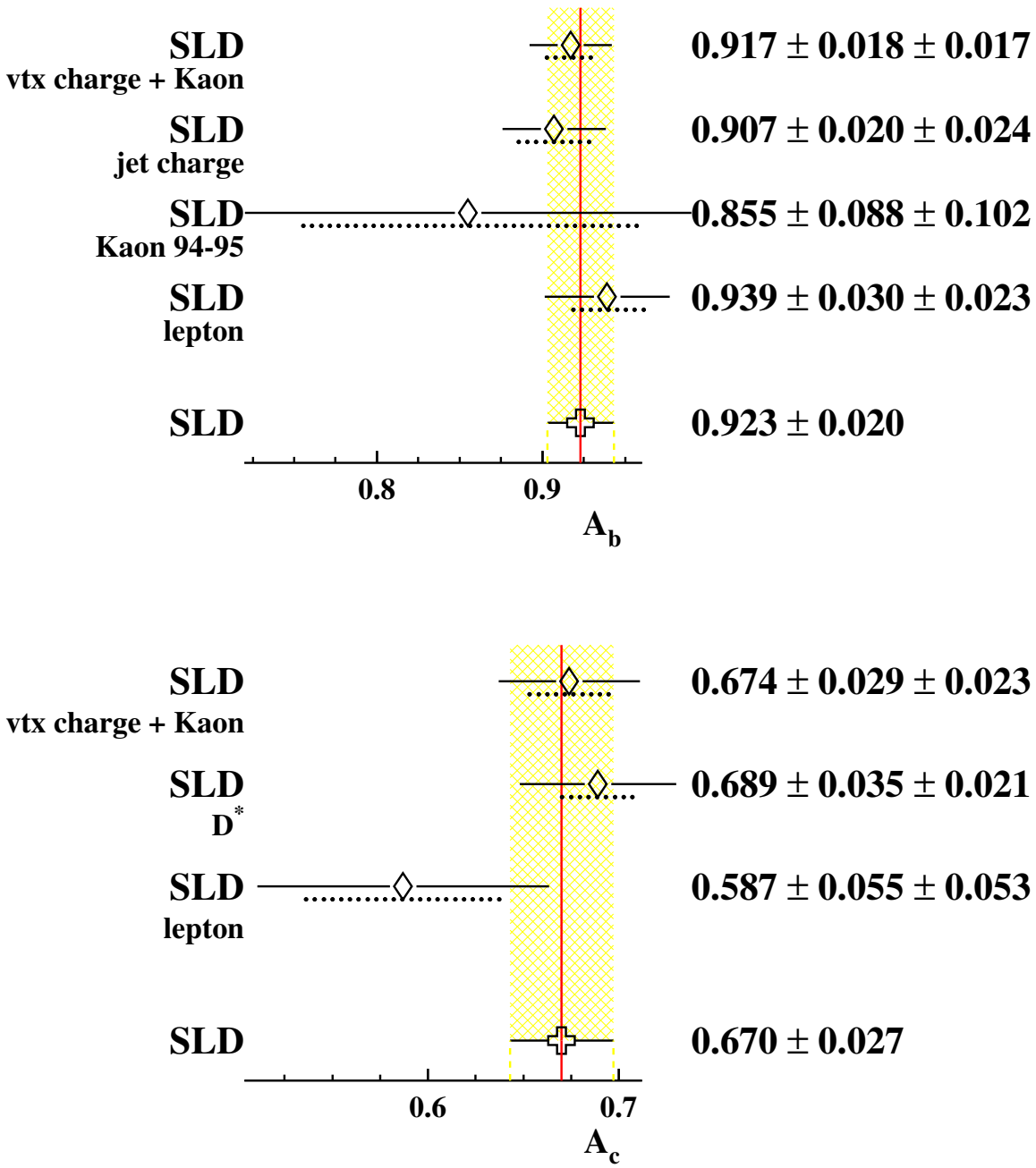

Figure 5.15: $\mathcal{A}_b$ and $\mathcal{A}_c$ measurements used in the heavy flavour combination, corrected for their dependence on parameters evaluated in the multi-parameter fit described in the text. The dotted lines indicate the size of the systematic error.

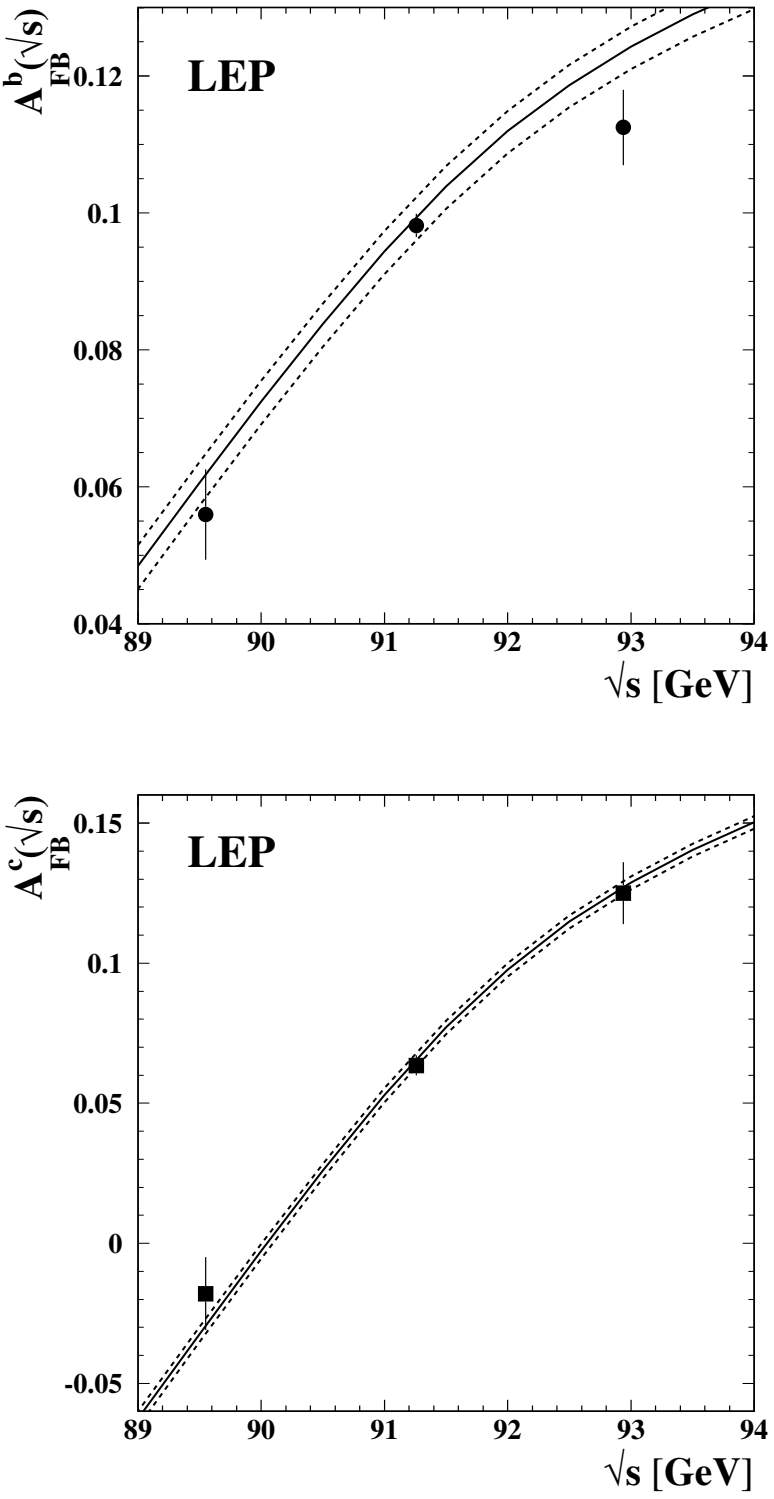

Figure 5.16: Energy dependence of $A_{\rm FB}^b$ and $A_{\rm FB}^c$. The solid line represents the SM prediction for $m_{\rm t} = 178\,\text{GeV}$, $m_{\rm H} = 300\,\text{GeV}$, the upper (lower) dashed line is the prediction for $m_{\rm H} = 100\,(1000)\,\text{GeV}$.

Since the energy dependence of the asymmetries is described by the SM prediction, in a second fit all asymmetries are corrected to the peak energy before fitting, resulting in 14 free parameters. The results of this fit are shown in Table 5.10. The χ^2/dof of the fit is $53/(105-14)$. The corresponding correlation matrix is given in Table 5.11. Note that here the values of $A_{\rm FB}^{\rm q\overline{q}}({\rm pk})$ actually found in the fit have already been corrected to pole asymmetries, as described in Section 5.7.3.[6] If the off-peak asymmetries are included in the fit the pole asymmetry $A_{\rm FB}^{0,\,{\rm b}}$ is about half a sigma below the values without these asymmetries. This is due to the somewhat low b-asymmetry at 92.94 GeV.

Observable	Result
$R_{\rm b}^0$	0.21629 ± 0.00066
$R_{\rm c}^0$	0.1721 ± 0.0030
$A_{\rm FB}^{0,\,{\rm b}}$	0.0992 ± 0.0016
$A_{\rm FB}^{0,\,{\rm c}}$	0.0707 ± 0.0035
$\mathcal{A}_{\rm b}$	0.923 ± 0.020
$\mathcal{A}_{\rm c}$	0.670 ± 0.027
$B({\rm b} \to \ell^-)$	0.1071 ± 0.0022
$B({\rm b} \to {\rm c} \to \ell^+)$	0.0801 ± 0.0018
$B({\rm c} \to \ell^+)$	0.0969 ± 0.0031
$\overline{\chi}$	0.1250 ± 0.0039
$f({\rm D}^+)$	0.235 ± 0.016
$f({\rm D_s})$	0.126 ± 0.026
$f({\rm c_{baryon}})$	0.093 ± 0.022
$P({\rm c} \to {\rm D}^{*+} \to \pi^+{\rm D}^0)$	0.1622 ± 0.0048

Table 5.10: The results of the 14-parameter fit to the LEP/SLD heavy flavour data. The correlations are listed in Table 5.11.

In all cases, the fit χ^2 is smaller than expected. As a cross check the fit has been repeated using statistical errors only, resulting in consistent central values and a χ^2/dof of $92/(105-14)$. In this case a large contribution to the χ^2 comes from $B({\rm b} \to \ell^-)$ measurements, which is sharply reduced when detector systematics are included. Subtracting the χ^2 contribution from $B({\rm b} \to \ell^-)$ measurements one gets $\chi^2/{\rm dof} = 65/(99-13)$. This shows that the low χ^2 largely comes from a statistical fluctuation. In addition many systematic errors are estimated very conservatively. Several error sources are evaluated by comparing test quantities between data and simulation. The statistical errors of these tests are taken as systematic uncertainties but no explicit correction is applied because of this test. Also in some cases fairly conservative assumptions are used for the error evaluation. Especially for the ${\rm b} \to \ell^-$ model only fairly old publications exist where the central spectrum describes the data well, but the two alternatives that are used for the error evaluation are no longer really compatible with the data. However it should be noted that especially for the quark forward backward asymmetries the systematic errors are much smaller than the statistical ones so that a possible overestimate of these errors cannot hide disagreements with other electroweak measurements.

[6] To correct the peak asymmetries to the pole asymmetries only a number with negligible additional uncertainty is added, see Table 5.7. All errors and correlations thus remain unchanged.

	$R_{\rm b}$	$R_{\rm c}$	$A_{\rm FB}^{0,\,{\rm b}}$	$A_{\rm FB}^{0,\,{\rm c}}$	$\mathcal{A}_{\rm b}$	$\mathcal{A}_{\rm c}$	$B(1)$	$B(2)$	$B(3)$	$\overline{\chi}$	$f({\rm D}^+)$	$f({\rm D_s})$	$f(c_{bar.})$	P
$R_{\rm b}$	1.00													
$R_{\rm c}$	−0.18	1.00												
$A_{\rm FB}^{0,\,{\rm b}}$	−0.10	0.04	1.00											
$A_{\rm FB}^{0,\,{\rm c}}$	0.07	−0.06	0.15	1.00										
$\mathcal{A}_{\rm b}$	−0.08	0.04	0.06	−0.02	1.00									
$\mathcal{A}_{\rm c}$	0.04	−0.06	0.01	0.04	0.11	1.00								
$B(1)$	−0.08	0.05	−0.01	0.18	−0.02	0.02	1.00							
$B(2)$	−0.03	−0.01	−0.06	−0.23	0.02	−0.04	−0.24	1.00						
$B(3)$	0.00	−0.30	0.00	−0.21	0.03	−0.02	0.01	0.10	1.00					
$\overline{\chi}$	0.00	0.02	0.11	0.08	0.06	0.00	0.29	−0.23	0.16	1.00				
$f({\rm D}^+)$	−0.15	−0.10	0.01	−0.04	0.00	0.00	0.04	0.02	0.00	0.02	1.00			
$f({\rm D_s})$	−0.03	0.13	0.00	−0.02	0.00	0.00	0.01	0.00	−0.01	−0.01	−0.40	1.00		
$f(c_{bar.})$	0.11	0.18	−0.01	0.04	0.00	0.00	−0.02	−0.01	−0.02	0.00	−0.24	−0.49	1.00	
P	0.13	−0.43	−0.02	0.04	−0.02	0.02	−0.01	0.01	0.13	0.00	0.08	−0.06	−0.14	1.00

Table 5.11: The correlation matrix for the set of the 14 heavy flavour parameters. $B(1)$, $B(2)$ and $B(3)$ denote $B({\rm b}\to\ell^-)$, $B({\rm b}\to{\rm c}\to\ell^+)$ and $B({\rm c}\to\ell^+)$ respectively, P denotes $P({\rm c}\to{\rm D}^{*+}\to\pi^+{\rm D}^0)$.

Source	R_b^0 $[10^{-3}]$	R_c^0 $[10^{-3}]$	$A_{FB}^{0,b}$ $[10^{-3}]$	$A_{FB}^{0,c}$ $[10^{-3}]$	$\mathcal{A}_b$ $[10^{-2}]$	$\mathcal{A}_c$ $[10^{-2}]$
statistics	0.44	2.4	1.5	3.0	1.5	2.2
internal systematics	0.28	1.2	0.6	1.4	1.2	1.5
QCD effects	0.18	0	0.4	0.1	0.3	0.2
$B(D \to \text{neut.})$	0.14	0.3	0	0	0	0
D decay multiplicity	0.13	0.6	0	0.2	0	0
B decay multiplicity	0.11	0.1	0	0.2	0	0
$B(D^+ \to K^-\pi^+\pi^+)$	0.09	0.2	0	0.1	0	0
$B(D_s \to \phi\pi^+)$	0.02	0.5	0	0.1	0	0
$B(\Lambda_c \to p\, K^-\pi^+)$	0.05	0.5	0	0.1	0	0
D lifetimes	0.07	0.6	0	0.2	0	0
B decays	0	0	0.1	0.4	0	0.1
decay models	0	0.1	0.1	0.5	0.1	0.1
non incl. mixing	0	0.1	0.1	0.4	0	0
gluon splitting	0.23	0.9	0.1	0.2	0.1	0.1
c fragmentation	0.11	0.3	0.1	0.1	0.1	0.1
light quarks	0.07	0.1	0	0	0	0
beam polarisation	0	0	0	0	0.5	0.3
total correlated	0.42	1.5	0.4	0.9	0.6	0.4
total error	0.66	3.0	1.6	3.5	2.0	2.7

Table 5.12: The dominant error sources for the heavy-flavour electroweak parameters from the 14-parameter fit, see text for details.

Table 5.12 summarises the dominant errors for the electroweak parameters. In all cases the two largest error sources are statistics and systematics internal to the experiments. The internal systematics consist mainly of errors due to Monte Carlo statistics, data statistics for cross-checks and the knowledge of detector resolutions and efficiencies. The error labelled "QCD effects" is due to hemisphere correlation for R_b^0 and R_c^0 (Section 5.6.7) and due to the theoretical uncertainty in the QCD corrections for the asymmetries (Section 5.7.2). For the asymmetries on average about 50 % of the QCD corrections are seen. The uncertainties due to the knowledge of the beam energy are negligible in all cases.

Amongst the non-electroweak observables the B semileptonic branching fraction is of special interest ($B(b \to \ell^-) = 0.1071 \pm 0.0022$). The largest error source for this quantity is the dependence on the semileptonic decay model $b \to \ell^-$ with

$$\Delta B(b \to \ell^-)(b \to \ell^- \text{ modelling}) = 0.0012. \tag{5.36}$$

Extensive studies have been made to understand the size of this error. Amongst the electroweak quantities, the quark asymmetries measured with leptons depend on the assumptions of the decay model while the asymmetries using other methods usually do not. The fit implicitly requires that the different methods give consistent results. This effectively constrains the decay model and thus reduces the error in $B(b \to \ell^-)$ from this source in the fit result.

To get a conservative estimate of the modelling error in $B(\mathrm{b} \to \ell^-)$ the fit has been repeated removing all asymmetry measurements. The result of this fit is

$$B(\mathrm{b} \to \ell^-) \;=\; 0.1069 \pm 0.0022 \tag{5.37}$$

with

$$\Delta B(\mathrm{b} \to \ell^-)(\mathrm{b} \to \ell^- \,\mathrm{modelling}) \;=\; 0.0013. \tag{5.38}$$

The other B-decay related observables from this fit are

$$\begin{aligned} B(\mathrm{b} \to \mathrm{c} \to \ell^+) &= 0.0802 \pm 0.0019 \\ \overline{\chi} &= 0.1259 \pm 0.0042. \end{aligned} \tag{5.39}$$

Figures 5.17 and 5.18 compare $(\mathcal{A}_\mathrm{b}, \mathcal{A}_\mathrm{c})$, $(A_{\mathrm{FB}}^{\mathrm{c\overline{c}}}, A_{\mathrm{FB}}^{\mathrm{b\overline{b}}})$ and $(R_\mathrm{b}^0, R_\mathrm{c}^0)$ with the SM prediction. Good agreement is found everywhere. However, unlike the asymmetries in lepton pair production, the quark asymmetries favour a Higgs mass of a few hundred GeV. In case of $\mathcal{A}_\mathrm{b}$-$\mathcal{A}_\mathrm{c}$ the ratio $A_{\mathrm{FB}}^{0,\mathrm{b}}/A_{\mathrm{FB}}^{0,\mathrm{c}}$ from LEP is also shown in Figure 5.17. This ratio is equal to $\mathcal{A}_\mathrm{b}/\mathcal{A}_\mathrm{c}$ and thus, unlike $A_{\mathrm{FB}}^{\mathrm{c\overline{c}}}$ and $A_{\mathrm{FB}}^{\mathrm{b\overline{b}}}$ themselves, is free from assumptions about the leptonic couplings of the Z. The data are interpreted further, together with the leptonic observables, in Chapters 7 and 8.

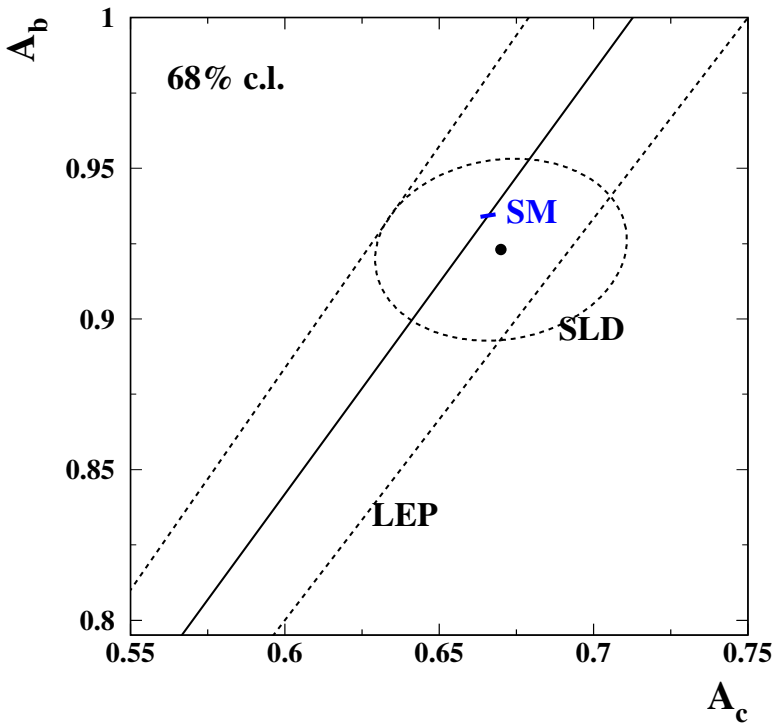

Figure 5.17: Contours in the $\mathcal{A}_\mathrm{c}$-$\mathcal{A}_\mathrm{b}$ plane and ratios of forward-backward asymmetries from the SLD and LEP, corresponding to 68 % confidence levels assuming Gaussian systematic errors. The SM prediction for $m_\mathrm{t} = 178.0 \pm 4.3\,\mathrm{GeV}$, $m_\mathrm{H} = 300^{+700}_{-186}\,\mathrm{GeV}$ and $\Delta\alpha^{(5)}_\mathrm{had}(m_\mathrm{Z}^2) = 0.02758 \pm 0.00035$ is also shown.

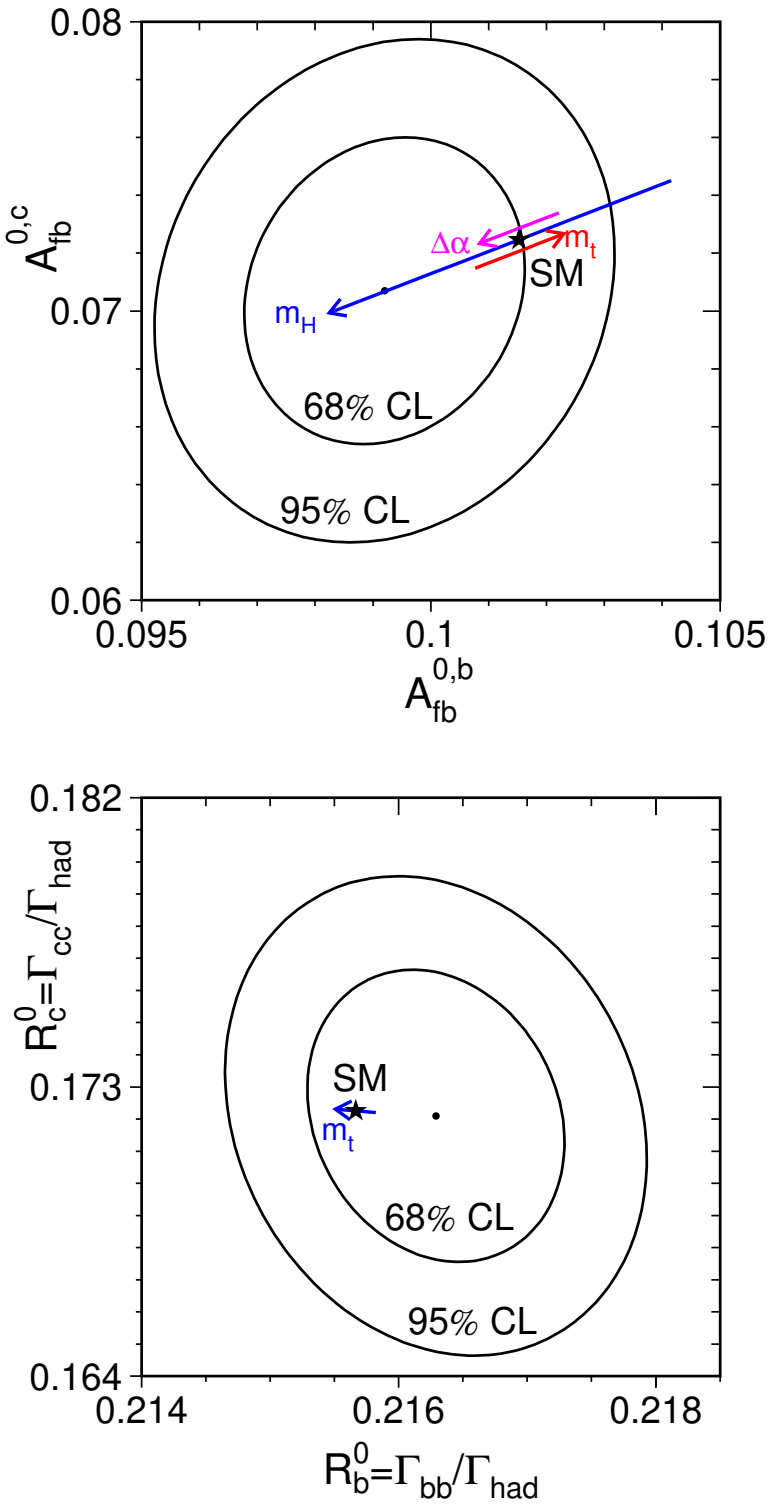

Figure 5.18: Contours in the $A_{\rm FB}^{0,\rm c}$-$A_{\rm FB}^{0,\rm b}$ and $R_{\rm c}^0$-$R_{\rm b}^0$ planes from the LEP and SLD data, corresponding to 68 % confidence levels assuming Gaussian systematic errors. The SM prediction for $m_{\rm t} = 178.0 \pm 4.3\,\mathrm{GeV}$, $m_{\rm H} = 300^{+700}_{-186}\,\mathrm{GeV}$ and $\Delta\alpha_{\rm had}^{(5)}(m_{\rm Z}^2) = 0.02758 \pm 0.00035$ is also shown.

Chapter 6

Inclusive Hadronic Charge Asymmetry

The measurement of the total hadronic partial width of the Z described in Chapter 2 makes no attempt to distinguish different quark flavours. Similarly, an inclusive forward-backward asymmetry measurement can be made using the samples of all hadronic events, taking advantage of the high statistics. This measurement is generically referred to as the $Q_{\rm FB}^{\rm had}$ measurement, since all the methods use some kind of forward-backward charge asymmetry in inclusive hadronic events. The up-type (charge 2/3) and down-type (charge $-1/3$) quarks contribute to the average forward-backward charge asymmetry with opposite sign. The average asymmetry is therefore particularly sensitive to the flavour ratios in the sample. To interpret the measurement, these ratios are usually taken from the predictions of the Standard Model (SM). Indeed, the result of the measurement is often quoted directly as a value of $\sin^2\theta_{\rm eff}^{\rm lept}$, in the context of the SM. The systematic errors are much more significant than for the high-efficiency and high-purity heavy flavour samples already discussed in Chapter 5.

Tagging methods to enhance the fraction of specific light flavour quarks (up, down or strange) have also been developed, and used to measure forward-backward asymmetries and partial widths. Further information on the partial widths of the Z to up-type and down-type quarks in hadronic Z decays has been inferred from the observed rate of direct photon production, by exploiting the fact that the probability of photon radiation from final-state quarks is proportional to the square of the quark charge. The tagged light quark and direct photon results are summarised in Appendix F, where the limited tests of the light quark couplings to the Z that they allow are also presented.

6.1 Asymmetry of Flavour-Inclusive Hadronic Events

Many of the ideas developed in Chapter 5 have been extended and applied to an inclusive sample of $\mathrm{Z} \to \mathrm{q\overline{q}}$ decays by the four LEP experiments [194, 195, 146, 196]. However, the DELPHI and OPAL publications only include data from 1990 and 1991, and the collaborations did not update the measurements with more data due to the implicit SM dependence of the technique. The details of the methods vary, but all use some variant of the jet charge, as defined in Equation 5.14. The event is divided into two hemispheres by the plane perpendicular to the thrust axis. The electron beam points into the forward hemisphere, and the jet charges are evaluated in the forward and backward hemispheres, giving $Q_{\rm F}$ and $Q_{\rm B}$. ALEPH and DELPHI then consider the observable $\langle Q_{\rm FB}\rangle \equiv \langle Q_{\rm F} - Q_{\rm B}\rangle$, the average value of the difference between the hemisphere charges. This quantity is referred to as the forward-backward charge flow. The

observable $\langle Q_{\rm FB} \rangle$ is given by:

$$\langle Q_{\rm FB} \rangle \;=\; \sum_{\rm q} R_{\rm q} A_{\rm FB}^{\rm q\overline{q}} \delta_{\rm q} C_{\rm q} \,, \tag{6.1}$$

where the sum runs over the 5 primary quark flavours, and the coefficients $C_{\rm q}$ account for the acceptance of each flavour subsample. The charge separation, $\delta_{\rm q} = \langle Q_{\rm q} - Q_{\overline{\rm q}} \rangle$, is the mean jet charge difference between the hemispheres containing quark and the anti-quark, which can equivalently be expressed in terms of the jet charges in the hemispheres containing the negatively charged parton, Q_-, and the positively charged parton, Q_+:

$$\delta_{\rm q} \;=\; s_{\rm q} \langle Q_- - Q_+ \rangle \,, \tag{6.2}$$

where $s_{\rm q} = +1$ for down-type quarks and -1 for up-type quarks. This choice of notation makes explicit the fact that the contributions to $\langle Q_{\rm FB} \rangle$ from the different quark types are of opposite sign. The main benefit of the method is that the charge separation can be evaluated from the data, as shown by Equation 5.17. The evaluation of the charge separation is discussed further below. The parameters $R_{\rm q}$ and $A_{\rm FB}^{\rm q\overline{q}}$ can be expressed in the SM as a function of the effective weak mixing angle, $\sin^2\theta_{\rm eff}^{\rm lept}$. Once the charge separations $\delta_{\rm q}$ are known, the measurement of $\langle Q_{\rm FB} \rangle$ can then be interpreted as a measurement of $\sin^2\theta_{\rm eff}^{\rm lept}$.

L3 use a very closely related approach, calling an event forward if $Q_{\rm F}$ is larger than $Q_{\rm B}$. The probability that an event is forward simply depends on the charge separation and the width of the distributions of Q_- and Q_+, with a correction for hemisphere correlations, and can be derived from data in a very similar manner to $\langle Q_{\rm FB} \rangle$. The degree of charge separation between Q_+ and Q_- is illustrated in Figure 6.1. The width of the distribution of $Q_{\rm F} + Q_{\rm B} \equiv Q_+ + Q_-$ agrees well between data and the Monte Carlo simulation.

The OPAL analysis calculates overall event weights using the three highest weight tracks per hemisphere. The overall event weight is the probability that the event is forwards. An observable average forward-backward charge asymmetry is derived in an iterative procedure, adjusting the value of $\sin^2\theta_{\rm eff}^{\rm lept}$ in the Monte Carlo simulation. The Monte Carlo modelling of the weights is controlled by comparisons with data. DELPHI also present an alternative measurement, where the value of $Q_{\rm F} - Q_{\rm B}$ is used event-by-event to decide if it is forward or backward, and an effective observable average charge asymmetry is derived.

Experimentally, the crux of the measurement is to determine the mean charge separations for each flavour. As described in Chapter 5 when discussing measurements of the forward-backward asymmetry in $\rm Z \to b\overline{b}$ events using jet charges, the mean charge separation for $\rm Z \to b\overline{b}$ events can be determined directly from the data, in a sample of b-tagged events (see Equation 5.17). In a similar way, charm tagging may be used to determine the mean charge separation in $\rm Z \to c\overline{c}$ events. However, in each case a correction must be made to account for any difference between the charge separation for tagged and untagged events of the same flavour. The reduction in systematic errors from assessing the charge separation for heavy flavours from data rather than taking it from the Monte Carlo simulation outweighs the uncertainties introduced by the correction. The charge separation in light-quark events can only be determined from Monte Carlo models. This is the largest source of systematic uncertainty in the analyses. The mean charge separation for the inclusive sample may also be determined from the data. It can be used as an additional constraint on the light-quark mean charge separations, although it is not directly applicable to the charge flow.

The only practical way to combine these analyses is at the level of the derived $\sin^2\theta_{\rm eff}^{\rm lept}$ values. The observed values of $\langle Q_{\rm FB} \rangle$ or hadronic charge asymmetries reflect the experimental

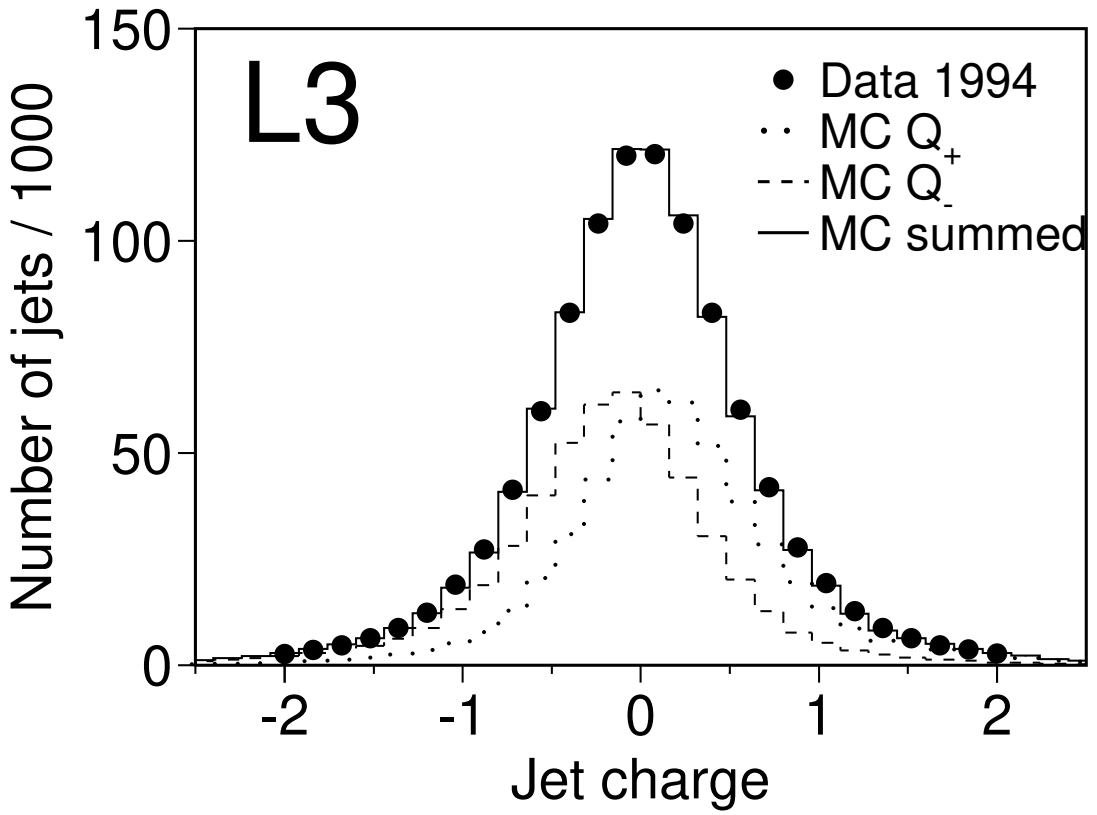

Figure 6.1: The Q_+ and Q_- distributions obtained from Monte Carlo simulation by L3. Their sum is compared to the sum of the $Q_{\rm F} + Q_{\rm B} \equiv Q_+ + Q_-$ distributions for 1994 data.

acceptance and resolution, and cannot be combined directly. It must be emphasised that because the measurements in this section are interpreted as $\sin^2\theta^{\rm lept}_{\rm eff}$ measurements entirely within the context of the SM, they must be used with care when comparing with alternative models. This is in contrast with results such as $A^{\rm b\bar{b}}_{\rm FB}$ and $R_{\rm b}$. For example, the value of $\sin^2\theta^{\rm lept}_{\rm eff}$ discussed here can only legitimately be used to test a model that does not change the relative fractions of each flavour.

6.2 Systematic Uncertainties

Due to the lack of high-purity and high-efficiency tags for specific light flavours, by far the dominant systematic uncertainties in these results arise from the model input required to describe the light quark properties. All experiments use the JETSET Monte Carlo as a reference fragmentation and hadronisation model, while the HERWIG model is used for systematic comparisons. The parameter set within JETSET is also often varied as part of the assessment of the fragmentation/hadronisation model uncertainties. However, neither the parameter set used for the central values nor the method for parameter variation is common to the experiments, with different experimental measurements being used by the experiments to constrain the model

parameters. In addition, there are typically code changes made to the Monte Carlo programs to improve the overall description in each experiment. Thus, there is far from 100% correlation between the quoted uncertainties due to fragmentation and hadronisation modelling.

The remaining significant uncertainties are all specific to a given experiment, for example due to the modelling of detector resolution, or due to the evaluation of the charge biases such as differences in the reconstruction of the tracks of positive and negative particles, or the charge-dependence of hadronic interactions in the material of the detector.

The theoretical QCD corrections applied to the forward-backward asymmetries for each flavour are potentially another common uncertainty (see Section 5.7.2). In practice, the corrections for QCD effects such as hard gluon radiation are all derived from JETSET, and are not distinguished from the overall correction for fragmentation and hadronisation effects. The theoretical QCD correction uncertainties are all much smaller than the quoted fragmentation/hadronisation uncertainties and other experimental errors, and treating them as an additional common error would have no impact on the result.

6.3 Combination Procedure

The derived values of the effective weak mixing angle, $\sin^2\theta^{\rm lept}_{\rm eff}$, are combined by first forming a full covariance matrix for the uncertainties, assuming that the errors associated with quark fragmentation and hadronisation are the only source of correlation. As explained above, these dominant systematic uncertainties are not fully correlated because they are not evaluated in the same way for each experiment. The off-diagonal terms are therefore taken to be the smaller of the two quoted fragmentation/hadronisation uncertainties for each pair of measurements (so-called "minimum-overlap" estimate). A χ^2 minimisation is then performed for the single free parameter, $\sin^2\theta^{\rm lept}_{\rm eff}$. The fit has a χ^2/dof of 0.43/3. In order to assess the sensitivity of the combined result to the assumptions made in calculating the covariance matrix, different approaches have also been considered. The resulting weights for each input result and the final combined $\sin^2\theta^{\rm lept}_{\rm eff}$ change very little when the assumptions are changed. For example, taking as the off-diagonal elements the smallest error common to all the inputs only changes the central value by 0.00007, and the uncertainty on the average by 0.00009. However, if the common systematic errors are incorrectly assumed to be fully correlated, the system is badly behaved, with some measurements getting a negative weight. This is symptomatic of an unphysical over-correlation in a set of measurements.

6.4 Combined Results and Discussion

The results from the four LEP experiments have been combined using the procedure described above. The inputs and the correlation matrix for the total errors are given in Table 6.1. The combined result is:

$$\sin^2\theta^{\rm lept}_{\rm eff} \;=\; 0.2324 \pm 0.0012\,, \tag{6.3}$$

where the total error includes a systematic component of 0.0010. The experimental results and the average are presented graphically in Figure 6.2.

The values of $\sin^2\theta^{\rm lept}_{\rm eff}$ given here for a particular experiment can be correlated with the measurement of $A^{\rm b\overline{b}}_{\rm FB}$ using the jet charge method in the same experiment and the same years' data. The correlation coefficient can be up to 25% for one experiment. However, the overall

Experiment		$\sin^2\theta^{\rm lept}_{\rm eff}$	Correlations			
ALEPH	(1990-94)	$0.2322 \pm 0.0008 \pm 0.0011$	1.00			
DELPHI	(1990-91)	$0.2345 \pm 0.0030 \pm 0.0027$	0.12	1.00		
L3	(1991-95)	$0.2327 \pm 0.0012 \pm 0.0013$	0.27	0.13	1.00	
OPAL	(1990-91)	$0.2321 \pm 0.0017 \pm 0.0029$	0.14	0.37	0.15	1.00
LEP Average		$0.2324 \pm 0.0007 \pm 0.0010$				

Table 6.1: Summary of the determination of $\sin^2\theta^{\rm lept}_{\rm eff}$ from inclusive hadronic charge asymmetries at LEP. For each experiment, the first error is statistical and the second systematic. The latter is dominated by fragmentation and hadronisation uncertainties. Also listed is the 'minimum overlap' correlation matrix for the total errors, summing statistical and systematic uncertainties in quadrature, used in the final average of $Q^{\rm had}_{\rm FB}$ results.

correlation between the average value of $\sin^2\theta^{\rm lept}_{\rm eff}$ given here and the average value of $A^{\rm b\bar{b}}_{\rm FB}$ has been estimated to be less than 4%, taking into account the additional significant contribution of lepton tag measurements to $A^{\rm b\bar{b}}_{\rm FB}$, and the fact that the DELPHI and OPAL inclusive hadronic charge asymmetry measurements only use 1990–91 data. A 4% correlation has a negligible effect when determining a global combined $\sin^2\theta^{\rm lept}_{\rm eff}$ value and in the SM fits.

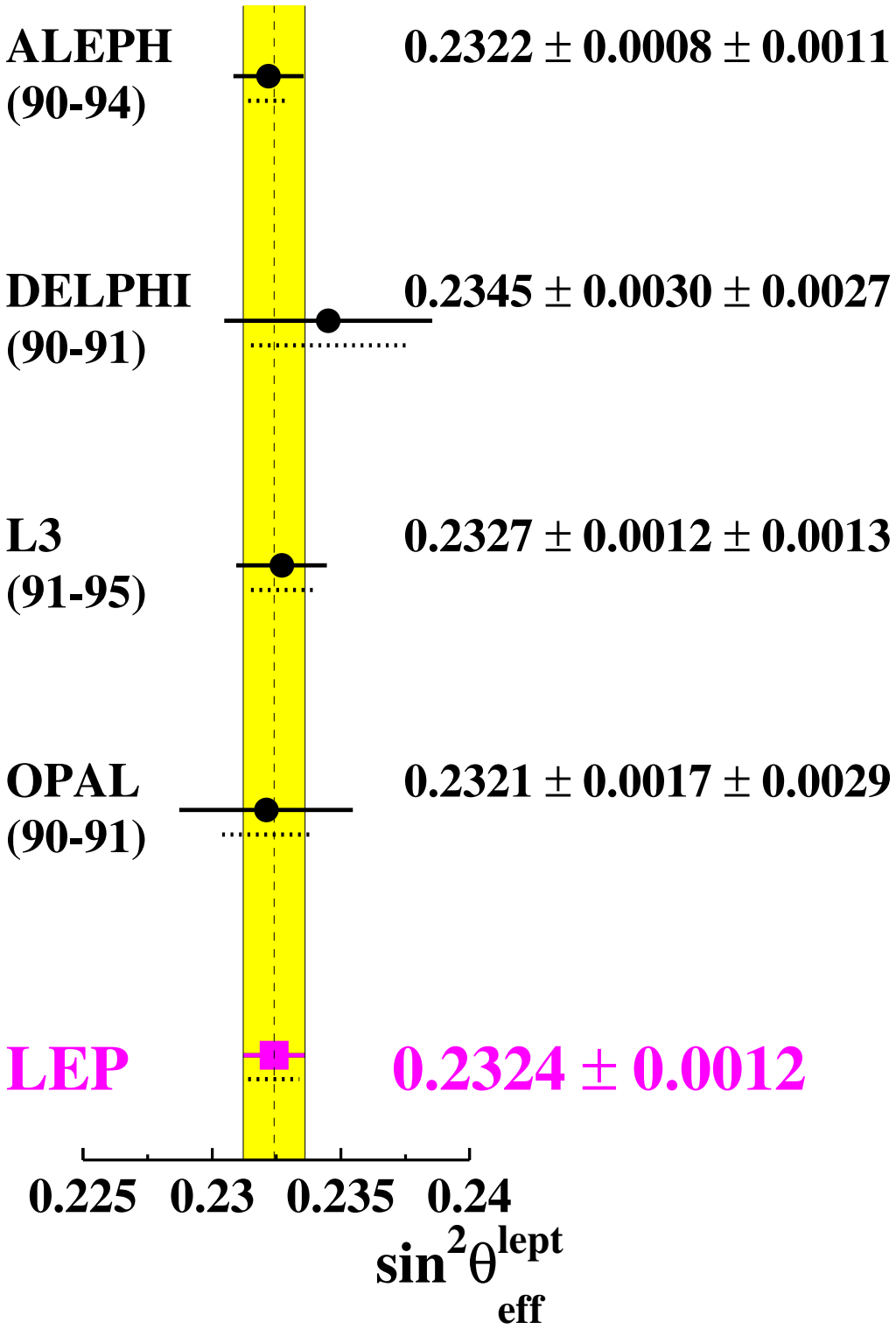

Figure 6.2: The input values and derived average of $\sin^2\theta_{\rm eff}^{\rm lept}$ from $Q_{\rm FB}^{\rm had}$ measurements. The total uncertainties are indicated by the solid lines, and the systematic contribution to the uncertainties by the dotted lines.

Chapter 7

Z Boson Properties and Effective Couplings

The final combined Z-pole results as derived from the SLD and LEP measurements, including their correlations, constitute the main result of this report. The definitions of the pseudo-observables describing the resonance properties of the heavy Z boson have been introduced in Chapter 1. The experimental measurements have been discussed in Chapters 2 to 6 and are briefly summarised again here, including an assessment of global correlated uncertainties. Based on this input, physics analyses are presented showing clearly the high precision obtained in the measurement of Z resonance parameters, and the resulting predictive power of the Z-pole measurements.

The partial decay widths and the decay branching fractions of the Z boson are presented in Section 7.2, obtained from the results of Chapters 2 and 5 using simple parameter transformations. An important aspect is the determination of the number of light neutrino species, a crucial result also in astrophysics and cosmology. The effective neutral weak current couplings, such as the asymmetry parameters and the effective coupling constants, are derived in Section 7.3 in largely model-independent analyses. Tests of lepton universality and comparisons with expectations in the framework of the Standard Model (SM) are included. In a first step towards the SM, the effective ρ_{f} parameters and the effective electroweak mixing angles $\sin^2\theta^{\mathrm{f}}_{\mathrm{eff}}$ are derived. As described in Section 7.4, the high precision of the Z-pole data allows stringent tests of radiative corrections, which are now unambiguously demonstrated to exist beyond QED. Analyses and tests within the constraining framework of the SM, such as the indirect determination of the mass of the top quark and the mass of the SM Higgs boson, are deferred to Chapter 8. Predictions of many observables within the SM framework are reported in Appendix G.

7.1 Summary of Z-Pole Results

7.1.1 Overview

The final combined Z-pole results are presented at the following locations:

- Chapter 2: Z lineshape and leptonic forward-backward asymmetries from LEP in Table 2.13;

- Chapter 3: Left-right and leptonic left-right forward-backward asymmetries from SLD in Table 3.6 and Equation 3.15;
- Chapter 4: Tau polarisation from LEP in Equations 4.9, 4.10 and 4.11;
- Chapter 5: Heavy quark flavour electroweak results from SLD and LEP in Table 5.10 and Table 5.11;
- Chapter 6: Inclusive hadronic charge asymmetry from LEP in Equation 6.3.

The interpretation of these pseudo observables describing the properties of the Z resonance is largely model independent. Based on the discussions presented in Chapter 1.5.4, the few underlying assumptions concerning the event samples selected for the measurements and the interpretation of the results are:

- Associated ZH production is negligible (implying Higgs-boson masses in excess of about 50 GeV) [39];
- Contributions from non-resonant processes such as 4-fermion production are described by the SM [197] - or are at least centre-of-mass energy independent close to the Z-pole, as discussed in Chapter 2;
- Effects of a second heavy neutral boson (Z′) are negligible [198];
- Effects of the strong interaction in heavy flavour production, namely for asymmetries needed to extract the pole asymmetries (Section 5.7.2) and for partial widths needed to extract effective coupling constants (Section 1.5.1) are correctly described by QCD;
- Electromagnetic radiative effects are described by QED to the required level of precision.

All these points are either well supported by the cited experimental results, or are believed to be well-understood theoretically.

All correlations within each group of measurements have been discussed in the previous chapters and included in the correlation matrices. The majority of these correlations concern the heavy quark flavour measurements, where most quantities have correlations exceeding 10% with four or more others, as described in Table 5.11. In addition, important correlations exist between the lineshape parameters (Γ_{Z}, σ^0_{had}) and ($A^{0,\mathrm{e}}_{\mathrm{FB}}$,$R^0_{\mathrm{e}}$), as described in Table 2.13.

Considering possible correlations between results extracted from different groups of measurements, including the SLC beam polarisation, the QCD correction for quark-pair final-state asymmetries, and the correlation between inclusive and tagged heavy-flavour asymmetries, only the uncertainty in the SLC beam polarisation creates a non-negligible effect. Thus the following additional correlation coefficients $\mathcal{C}(\mathcal{A}_\ell, \mathcal{A}_{\mathrm{q}})$ between the results on $\mathcal{A}_\ell$ (Chapter 3) and on $\mathcal{A}_{\mathrm{q}}$, (Chapter 5) arise and are taken into account:

$$\mathcal{C}(\mathcal{A}_\ell, \mathcal{A}_{\mathrm{b}}) = +0.09 \tag{7.1}$$

$$\mathcal{C}(\mathcal{A}_\ell, \mathcal{A}_{\mathrm{c}}) = +0.05\,. \tag{7.2}$$

These correlations modify values of quantities derived from the combined averages at the level of several % of the respective total uncertainty.

Even though the various sets of parameters representing the Z-pole measurements are constructed in such a way as to minimise correlations between sets and inside sets of parameters, the correlations exceed 10% in a few sets and thus need to be taken into account for any precision analysis using these final Z-pole results.

7.2 Z-Boson Decay Widths and Branching Fractions

As discussed in Chapter 2, the electroweak measurements are quoted in terms of experimentally motivated pseudo-observables defined such that correlations between them are reduced. Other, more familiar pseudo-observables describing Z-boson production and decays, such as leptonic pole cross-sections, Z-boson partial decay widths and branching fractions, are obtained through simple parameter transformations.

Assuming lepton universality, the leptonic pole cross-section $\sigma^0_{\rm lep}$, defined in analogy to the hadronic pole cross-section, is measured to be:

$$\sigma^0_{\rm lep} \equiv \frac{12\pi}{m_{\rm Z}^2}\frac{\Gamma_{\ell\ell}^2}{\Gamma_{\rm Z}^2} = \frac{\sigma^0_{\rm had}}{R^0_\ell} = 2.0003 \pm 0.0027 \text{ nb}\,, \tag{7.3}$$

in very good agreement with the SM expectation. Note that this purely leptonic quantity has a higher sensitivity to $\alpha_{\rm S}(m_{\rm Z}^2)$ than any of the hadronic Z-pole observables, as discussed in Section 8.6.

7.2.1 Z-Boson Decay Parameters

The partial Z decay widths are summarised in Table 7.1. Note that they have larger correlations than the original set of results reported in Table 2.13. If lepton universality is imposed, a more precise value of $\Gamma_{\rm had}$ is obtained, because $\Gamma_{\rm ee}$ in the relation between the hadronic pole cross-section and the partial widths is replaced by the more precise value of $\Gamma_{\ell\ell}$. The Z branching fractions, *i.e.*, the ratios between each partial decay width and the total width of the Z, are shown in Table 7.2.

In order to test lepton universality in Z decays quantitatively, the ratios of the leptonic partial widths or equivalently the ratios of the leptonic branching fractions are calculated. The results are:

$$\frac{\Gamma_{\mu\mu}}{\Gamma_{\rm ee}} = \frac{B(\mathrm{Z}\to\mu^+\mu^-)}{B(\mathrm{Z}\to\mathrm{e}^+\mathrm{e}^-)} = 1.0009 \pm 0.0028 \tag{7.4}$$

$$\frac{\Gamma_{\tau\tau}}{\Gamma_{\rm ee}} = \frac{B(\mathrm{Z}\to\tau^+\tau^-)}{B(\mathrm{Z}\to\mathrm{e}^+\mathrm{e}^-)} = 1.0019 \pm 0.0032 \tag{7.5}$$

with a correlation of +0.63. In both cases, good agreement with lepton universality is observed. Assuming lepton universality, τ mass effects are expected to decrease $\Gamma_{\tau\tau}$ and $\mathrm{B}(\mathrm{Z}\to\tau^+\tau^-)$ as quoted here by 0.23% relative to the light lepton species e and μ.

7.2.2 Invisible Width and Number of Light Neutrino Species

The invisible width, $\Gamma_{\rm inv} = \Gamma_{\rm Z} - (\Gamma_{\rm had} + \Gamma_{\rm ee} + \Gamma_{\mu\mu} + \Gamma_{\tau\tau})$, is also shown in Table 7.1. The branching fraction to invisible particles, reported in Table 7.2, is derived by constraining the sum of the inclusive hadronic, leptonic and invisible branching fractions to unity, and therefore does not constitute an independent result. The result on $\Gamma_{\rm inv}$ is compared to the SM expectation calculated as a function of $m_{\rm t}$ and $m_{\rm H}$ in Figure 7.1. It shows a small deficit of about 2.7 MeV or 1.8 standard deviations compared to the SM expectation calculated for $m_{\rm t} = 178$ GeV, mainly reflecting the observation that the hadronic pole cross-section is slightly larger than expected.

The limit on extra, non-standard contributions to the invisible width, *i.e.*, not originating from $\mathrm{Z}\to\nu\overline{\nu}$, is calculated by taking the difference between the value given in Table 7.1 and

Parameter $\Gamma_{\mathrm{f\bar{f}}}$	Average [MeV]		Correlations						
Without Lepton Universality									
			Γ_{had}	Γ_{ee}	$\Gamma_{\mu\mu}$	$\Gamma_{\tau\tau}$	$\Gamma_{\mathrm{b\bar{b}}}$	$\Gamma_{\mathrm{c\bar{c}}}$	Γ_{inv}
Γ_{had}	1745.8	$\pm$ 2.7	1.00						
Γ_{ee}	83.92	$\pm$ 0.12	-0.29	1.00					
$\Gamma_{\mu\mu}$	83.99	$\pm$ 0.18	0.66	-0.20	1.00				
$\Gamma_{\tau\tau}$	84.08	$\pm$ 0.22	0.54	-0.17	0.39	1.00			
$\Gamma_{\mathrm{b\bar{b}}}$	377.6	$\pm$ 1.3	0.45	-0.13	0.29	0.24	1.00		
$\Gamma_{\mathrm{c\bar{c}}}$	300.5	$\pm$ 5.3	0.09	-0.02	0.06	0.05	-0.12	1.00	
Γ_{inv}	497.4	$\pm$ 2.5	-0.67	0.78	-0.45	-0.40	-0.30	-0.06	1.00
With Lepton Universality									
			Γ_{had}	$\Gamma_{\ell\ell}$	$\Gamma_{\mathrm{b\bar{b}}}$	$\Gamma_{\mathrm{c\bar{c}}}$	Γ_{inv}		
Γ_{had}	1744.4	$\pm$ 2.0	1.00						
$\Gamma_{\ell\ell}$	83.985	$\pm$ 0.086	0.39	1.00					
$\Gamma_{\mathrm{b\bar{b}}}$	377.3	$\pm$ 1.2	0.35	0.13	1.00				
$\Gamma_{\mathrm{c\bar{c}}}$	300.2	$\pm$ 5.2	0.06	0.03	-0.15	1.00			
Γ_{inv}	499.0	$\pm$ 1.5	-0.29	0.49	-0.10	-0.02	1.00		

Table 7.1: Partial Z decay widths, derived from the results of Tables 2.13, 5.10 and 5.11. The width denoted as $\ell^+\ell^-$ is that of a single charged massless lepton species. The width to invisible particles is calculated as the difference of total and all other partial widths.

the SM expectation of $(\Gamma_{\mathrm{inv}})_{\mathrm{SM}} = 501.7 \pm 0.2^{+0.1}_{-0.9}$ MeV, where the first error is due to the uncertainties in the SM input parameters and the second one is due to the unknown mass of the Higgs boson, taken to be between 114 GeV and 1000 GeV with a central value of 150 GeV. This gives $\Gamma^x_{\mathrm{inv}} = -2.7^{+1.8}_{-1.5}$ MeV, or expressed as a limit, $\Delta\Gamma^x_{\mathrm{inv}} < 2.0$ MeV at 95% CL. This limit is conservatively calculated allowing only values of Γ_{inv} above the minimal value of the SM prediction for $m_{\mathrm{H}} = 1000$ GeV. In the same way, upper limits on non-standard contributions to other Z decays can be calculated and are summarized in Appendix D.

Assuming only SM particles as Z decay products, the invisible Z-decay width determines the number N_ν of light neutrinos species: $\Gamma_{\mathrm{inv}} = N_\nu \, \Gamma_{\nu\overline{\nu}}$. Since the ratio $\Gamma_{\mathrm{inv}}/\Gamma_{\ell\ell}$ is experimentally determined with higher precision than Γ_{inv}, and the SM prediction of $\Gamma_{\nu\overline{\nu}}/\Gamma_{\ell\ell}$ shows a reduced dependence on the unknown SM parameters, the number of neutrinos is derived from:

$$R^0_{\mathrm{inv}} \equiv \frac{\Gamma_{\mathrm{inv}}}{\Gamma_{\ell\ell}} = N_\nu \left(\frac{\Gamma_{\nu\overline{\nu}}}{\Gamma_{\ell\ell}}\right)_{\mathrm{SM}} . \tag{7.6}$$

Recall that in case of lepton universality, $\Gamma_{\ell\ell}$ is defined as the partial decay width for massless leptons, and the correction for the τ mass is applied explicitly in the analysis.

The SM value for the ratio of the partial widths to neutrinos and to charged leptons is 1.99125$\pm$0.00083, where the uncertainty arises from variations of the top quark mass within its experimental error, $m_{\mathrm{t}} = 178.0 \pm 4.3$ GeV, and of the Higgs mass within 100 GeV $< m_{\mathrm{H}} <$ 1000 GeV. Assuming lepton universality, the measured value of R^0_{inv} is:

$$R^0_{\mathrm{inv}} = 5.943 \pm 0.016 \, , \tag{7.7}$$

Parameter $B(\mathrm{Z} \to \mathrm{f\bar{f}})$	Average [%]	Correlations						
Without Lepton Universality								
		$\mathrm{q\bar{q}}$	$\mathrm{e^+e^-}$	$\mu^+\mu^-$	$\tau^+\tau^-$	$\mathrm{b\bar{b}}$	$\mathrm{c\bar{c}}$	inv
$\mathrm{q\bar{q}}$	69.967 ± 0.093	1.00						
$\mathrm{e^+e^-}$	3.3632 ± 0.0042	−0.76	1.00					
$\mu^+\mu^-$	3.3662 ± 0.0066	0.59	−0.50	1.00				
$\tau^+\tau^-$	3.3696 ± 0.0083	0.48	−0.40	0.33	1.00			
$\mathrm{b\bar{b}}$	15.133 ± 0.050	0.40	−0.30	0.24	0.19	1.00		
$\mathrm{c\bar{c}}$	12.04 ± 0.21	0.08	−0.06	0.05	0.04	−0.13	1.00	
inv	19.934 ± 0.098	−0.99	0.75	−0.63	−0.54	−0.40	−0.08	1.00
With Lepton Universality								
		$\mathrm{q\bar{q}}$	$\ell^+\ell^-$	$\mathrm{b\bar{b}}$	$\mathrm{c\bar{c}}$	inv		
$\mathrm{q\bar{q}}$	69.911 ± 0.057	1.00						
$\ell^+\ell^-$	3.3658 ± 0.0023	−0.29	1.00					
$\mathrm{e^+e^-}, \mu^+\mu^-, \tau^+\tau^-$	10.0899 ± 0.0068	−0.29	1.00					
$\mathrm{b\bar{b}}$	15.121 ± 0.048	0.26	−0.08	1.00				
$\mathrm{c\bar{c}}$	12.03 ± 0.21	0.05	−0.01	−0.16	1.00			
inv	20.000 ± 0.055	−0.99	0.18	−0.25	−0.05	1.00		

Table 7.2: Z branching fractions, derived from the results of Tables 2.13, 5.10 and 5.11. The branching fraction denoted as $\ell^+\ell^-$ is that of a single charged massless lepton species. The branching fraction to invisible particles is fully correlated with the sum of the branching fractions of leptonic and inclusive hadronic decays.

and the corresponding number of light neutrino species is therefore determined to be:

$$N_\nu \;=\; 2.9840 \pm 0.0082\,, \tag{7.8}$$

about 2.0 standard deviations smaller than three, driven by the observed value of Γ_{inv}. This result fixes the number of fermion families with light neutrinos to the observed three. The decomposition of the error on N_ν is given by:

$$\delta N_\nu \;\simeq\; 10.5\frac{\delta n_{\mathrm{had}}}{n_{\mathrm{had}}} \oplus 3.0\frac{\delta n_{\mathrm{lep}}}{n_{\mathrm{lep}}} \oplus 7.5\frac{\delta \mathcal{L}}{\mathcal{L}}\,, \tag{7.9}$$

where $\delta n_{\mathrm{had}}/n_{\mathrm{had}}$, $\delta n_{\mathrm{lep}}/n_{\mathrm{lep}}$ and $\delta\mathcal{L}/\mathcal{L}$ denote respectively the total errors on the number n of selected hadronic and leptonic events, and cross-section scale uncertainties from the luminosity determination, while $\oplus$ denotes addition in quadrature. The luminosity theory error of 0.061% is one of the largest contributions to the total error on the number of neutrinos, causing an error of 0.0046 on N_ν.

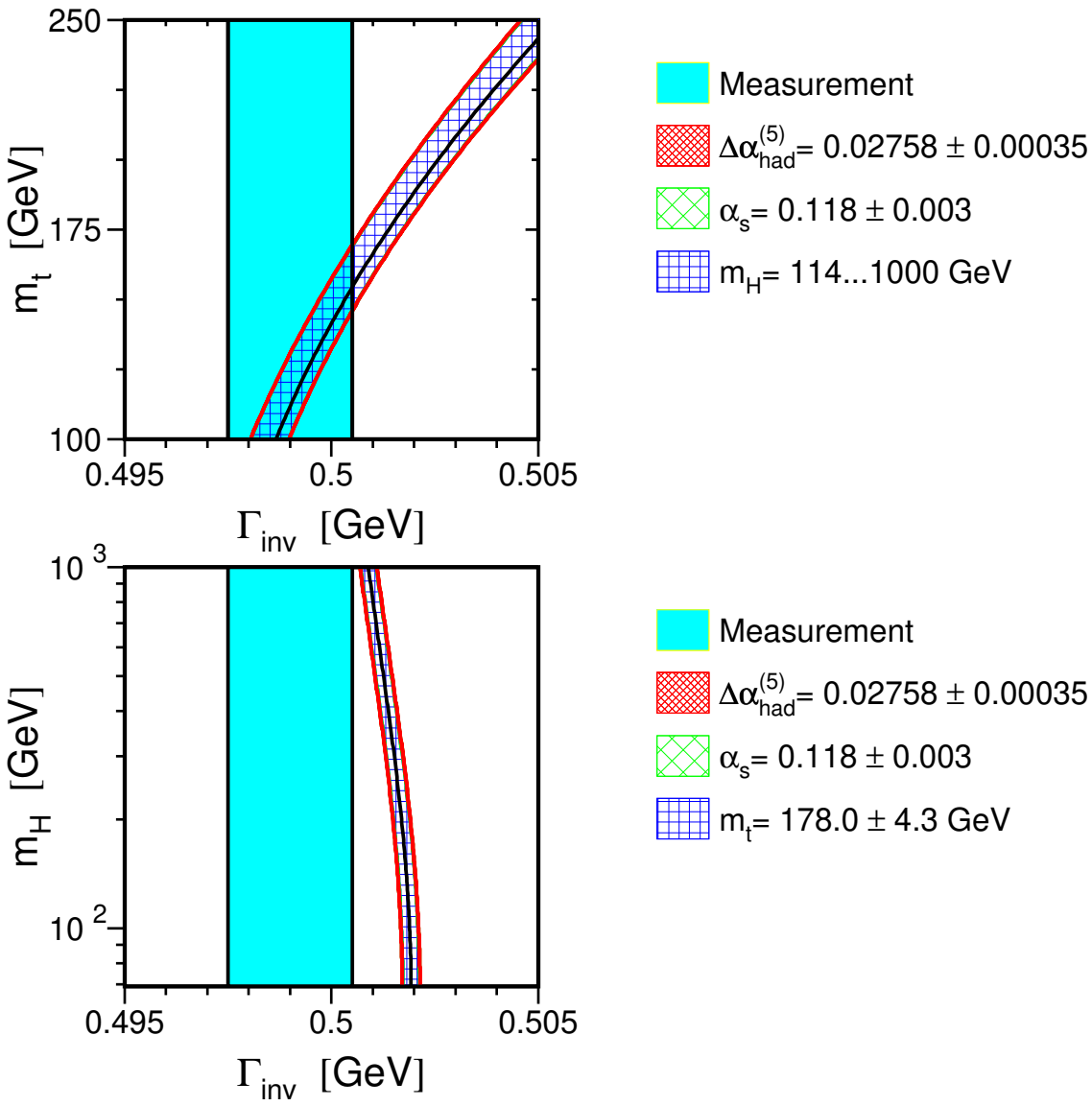

Figure 7.1: Comparison of the LEP combined result on $\Gamma_{\rm inv}$ with the SM prediction as a function of (top) the top quark mass, and (bottom) the Higgs boson mass. The measurement with its uncertainty is shown as the vertical band. The width of the SM band arises due to the uncertainties in $\Delta\alpha^{(5)}_{\rm had}(m^2_{\rm Z})$, $\alpha_{\rm S}(m^2_{\rm Z})$, $m_{\rm H}$ and $m_{\rm t}$ in the ranges indicated. The total width of the band is the linear sum of these uncertainties.

7.3 Effective Couplings of the Neutral Weak Current

The experimental measurements and results on electroweak Z-pole observables are now used to derive values for the effective couplings of the neutral weak current at the Z pole, namely: the asymmetry parameters $\mathcal{A}_{\rm f}$ in Section 7.3.1, the effective coupling constants $(g_{\rm Vf}, g_{\rm Af})$ and $(g_{\rm Rf}, g_{\rm Lf})$ in Section 7.3.2, the $\rho_{\rm f}$ parameters and the effective electroweak mixing angles $\sin^2\theta^{\rm f}_{\rm eff}$ in Section 7.3.3, and the leptonic effective electroweak mixing angle $\sin^2\theta^{\rm lept}_{\rm eff}$ in Section 7.3.4. The partial width results determine the overall scale of the effective coupling constants, while

the asymmetry results determine their ratio. The results of these largely model-independent analyses are compared to the expectations within the framework of the SM, thereby testing its validity. A concluding discussion of these analyses is given in Section 7.3.5, with special emphasis on the observation of non-QED electroweak radiative corrections in Section 7.4.

The inputs consist of the results presented in Chapter 2 to 6 and summarised in Section 7.1. The derived couplings are determined in fits to these input results, based on the simple expressions, listed in Section 1.4, of the input observables in terms of the couplings to be determined. Input observables such as m_{Z}, Γ_{Z}, σ^0_{had} or R^0_{f}, which cannot be expressed by the asymmetry parameters or the couplings to be determined, are allowed to vary in the fits as well.

For the determination of the leptonic couplings, including tests of lepton universality, the results of Chapters 2, 3 and 4 are used. For the determination of quark couplings, the results presented in Chapter 5 are included as well and lepton universality is assumed in the analysis. In the analysis for the leptonic effective electroweak mixing angle, its determination based on the hadronic charge asymmetry, Chapter 6, is also added.

In general, the results which have been obtained without imposing lepton universality are used as inputs. However, when quarks and leptons are considered in a joint analysis, the issue is no longer one of testing lepton universality, hence for leptonic pseudo-observables, the lepton universality results are used, and the correlations listed in Equations 7.1 and 7.2 are included.

7.3.1 The Asymmetry Parameters $\mathcal{A}_{\mathrm{f}}$

The polarised electron beams at SLC allow the SLD collaboration to measure the asymmetry parameters $\mathcal{A}_{\mathrm{f}}$ directly by analysing the left-right and left-right forward-backward asymmetry, $A^0_{\mathrm{LR}} = \mathcal{A}_{\mathrm{e}}$ and $A^{\mathrm{f}}_{\mathrm{LRFB}} = (3/4)\mathcal{A}_{\mathrm{f}}$. The analyses of the tau polarisation and its forward-backward asymmetry at LEP determine $\mathcal{A}_\tau$ and $\mathcal{A}_{\mathrm{e}}$ separately. The forward-backward pole asymmetries, $A^{0,\mathrm{f}}_{\mathrm{FB}} = (3/4)\mathcal{A}_{\mathrm{e}}\mathcal{A}_{\mathrm{f}}$, constrain the product of two asymmetry parameters. The measurements are performed separately for all three charged lepton species and the heavy-quark flavours b and c.

The results on the leptonic asymmetry parameters derived from various measurements which do not involve quark asymmetry parameters are reported in Table 7.3, with combined values including correlations reported in Table 7.4. The values of the asymmetry parameters obtained for the three lepton species agree well. Under the assumption of neutral-current lepton universality, the combined result is:

$$\mathcal{A}_\ell \;=\; 0.1501 \pm 0.0016\,. \tag{7.10}$$

This average has a χ^2/dof of 7.8/9, corresponding to a probability of 56%.

The analysis is now expanded to include the results on quark-pair production. The values of $\mathcal{A}_{\mathrm{q}}$ and $A^{0,\mathrm{q}}_{\mathrm{FB}}$, which have been extracted from realistic observables in Chapter 5, have been corrected for the QCD and QED effects expected in the SM and calculated with ZFITTER [31] (see Section 5.7.2). They therefore rest on the same footing as the corresponding pole quantities for leptons. As already discussed in Section 5.9 and shown in Figure 5.17, the ratio of the forward-backward pole asymmetries $A^{0,\mathrm{b}}_{\mathrm{FB}}/A^{0,\mathrm{c}}_{\mathrm{FB}} = \mathcal{A}_{\mathrm{b}}/\mathcal{A}_{\mathrm{c}}$ agrees well with the ratio of the direct measurements of the asymmetry parameters $\mathcal{A}_{\mathrm{b}}$ and $\mathcal{A}_{\mathrm{c}}$.

Numerical results on the asymmetry parameters $\mathcal{A}_{\mathrm{b}}$ and $\mathcal{A}_{\mathrm{c}}$ are compared in Table 7.5. The direct measurements of both $\mathcal{A}_{\mathrm{b}}$ and $\mathcal{A}_{\mathrm{c}}$ are seen to agree well with SM expectations. Each ratio $(4/3)A^{0,\mathrm{q}}_{\mathrm{FB}}/\mathcal{A}_\ell$ also determines $\mathcal{A}_{\mathrm{q}}$ indirectly, with a precision comparable to that of the direct measurements. Reasonable agreement between the direct measurement and the ratio is

Parameter	$A_{\rm FB}^{0,\ell}$	$A_{\rm LR}^{0}, A_{\rm LRFB}^{\ell}$	$\mathcal{P}_\tau$
$\mathcal{A}_{\rm e}$	0.139±0.012	0.1516±0.0021	0.1498±0.0049
$\mathcal{A}_\mu$	0.162±0.019	0.142±0.015	—
$\mathcal{A}_\tau$	0.180±0.023	0.136±0.015	0.1439±0.0043

Table 7.3: Comparison of the leptonic asymmetry parameters $\mathcal{A}_\ell$ using the electroweak measurements of Tables 2.13 and 3.6, and Equations 4.9 and 4.10. The results derived from $A_{\rm FB}^{0,\ell}$ are strongly correlated, with correlation coefficients of -0.75, -0.70 and $+0.55$ between eμ, eτ and $\mu\tau$, respectively.

Parameter	Average	Correlations		
		$\mathcal{A}_{\rm e}$	$\mathcal{A}_\mu$	$\mathcal{A}_\tau$
$\mathcal{A}_{\rm e}$	0.1514±0.0019	1.00		
$\mathcal{A}_\mu$	0.1456±0.0091	−0.10	1.00	
$\mathcal{A}_\tau$	0.1449±0.0040	−0.02	0.01	1.00

Table 7.4: Results on the leptonic asymmetry parameters $\mathcal{A}_\ell$ using the 14 electroweak measurements of Tables 2.13 and 3.6, and Equations 4.9 and 4.10. The combination has a χ^2/dof of 3.6/5, corresponding to a probability of 61%.

Flavour q	$\mathcal{A}_{\rm q} = \frac{4}{3}\frac{A_{\rm FB}^{0,\rm q}}{\mathcal{A}_\ell}$	Direct $\mathcal{A}_{\rm q}$	SM
b	0.881±0.017	0.923±0.020	0.935±0.001
c	0.628±0.032	0.670±0.027	0.668±0.002

Table 7.5: Determination of the quark asymmetry parameters $\mathcal{A}_{\rm q}$, based on the ratio $A_{\rm FB}^{0,\rm q}/\mathcal{A}_\ell$ and the direct measurement $A_{\rm LRFB}^{\rm q}$. Lepton universality for $\mathcal{A}_\ell$ is assumed. The correlation between $4A_{\rm FB}^{0,\rm b}/3\mathcal{A}_\ell$ and $4A_{\rm FB}^{0,\rm c}/3\mathcal{A}_\ell$ is $+0.24$, while it is $+0.11$ between the direct measurements $\mathcal{A}_{\rm b}$ and $\mathcal{A}_{\rm c}$. The expectation of $\mathcal{A}_{\rm q}$ in the SM is listed in the last column.

Parameter	Average	Correlations		
		$\mathcal{A}_\ell$	$\mathcal{A}_{\rm b}$	$\mathcal{A}_{\rm c}$
$\mathcal{A}_\ell$	0.1489±0.0015	1.00		
$\mathcal{A}_{\rm b}$	0.899±0.013	−0.42	1.00	
$\mathcal{A}_{\rm c}$	0.654±0.021	−0.10	0.15	1.00

Table 7.6: Results on the quark asymmetry parameters $\mathcal{A}_{\rm q}$ and the leptonic asymmetry parameter $\mathcal{A}_\ell$ assuming neutral-current lepton universality using the 13 electroweak measurements of Tables 2.13, 5.10 and 5.11, and Equations 3.15 and 4.11. The combination has a χ^2/dof of 4.5/4, corresponding to a probability of 34%.

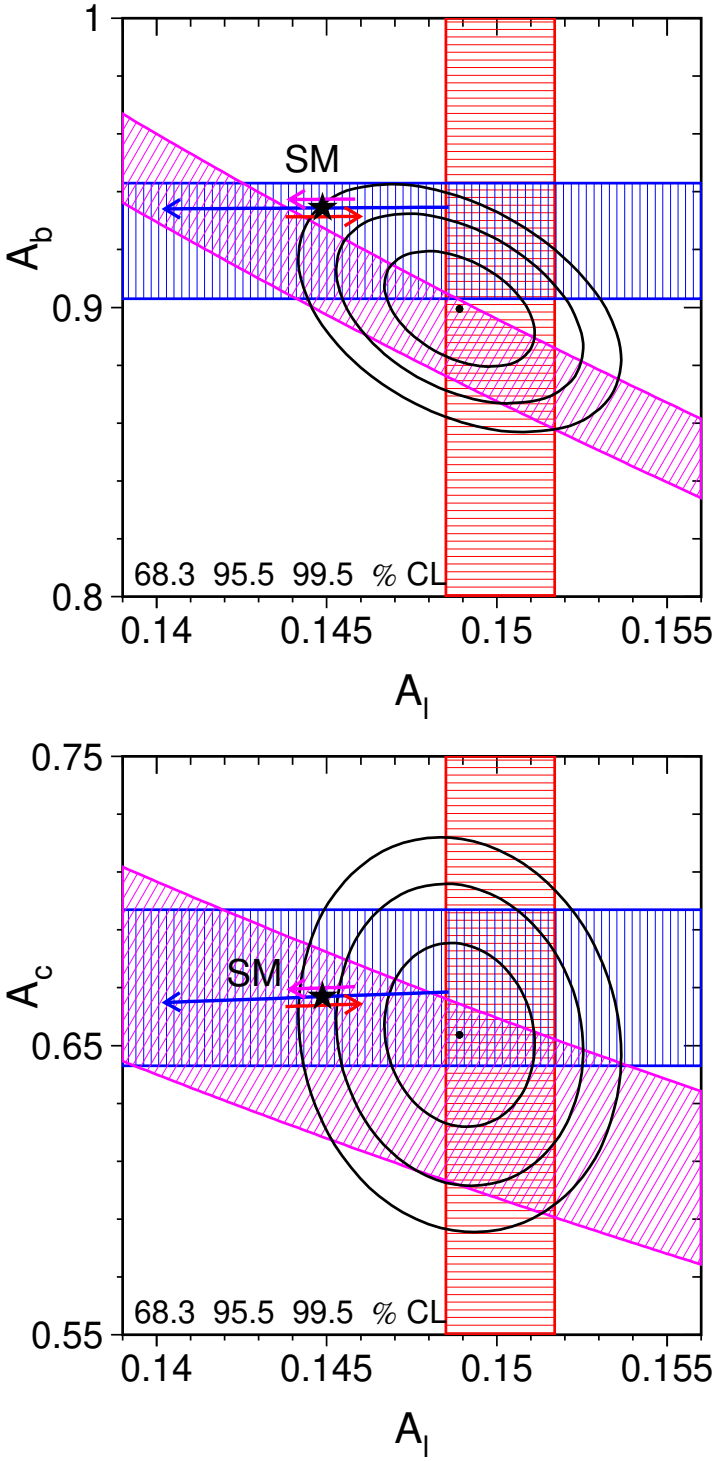

Figure 7.2: Comparison of the measurements of $\mathcal{A}_\ell$, $\mathcal{A}_\mathrm{q}$ and $A_\mathrm{FB}^{0,\mathrm{q}}$ for (top) b-quarks, and (bottom) c-quarks, assuming lepton universality. Bands of ± 1 standard deviation width in the $(\mathcal{A}_\ell, \mathcal{A}_\mathrm{q})$ plane are shown for the measurements of $\mathcal{A}_\ell$ (vertical band), $\mathcal{A}_\mathrm{q}$ (horizontal band), and $A_\mathrm{FB}^{0,\mathrm{q}} = (3/4)\mathcal{A}_\mathrm{e}\mathcal{A}_\mathrm{q}$ (diagonal band). Also shown are the 68%, 95% and 99.5% confidence level contours for the two asymmetry parameters resulting from the joint analysis (Table 7.6). The arrows pointing to the right and to the left show the variation in the SM prediction for varying $\Delta\alpha_\mathrm{had}^{(5)}(m_\mathrm{Z}^2)$ in the range 0.02758 ± 0.00035 (arrow displaced vertically upwards), m_H in the range of 300^{+700}_{-186} GeV, and m_t in the range 178.0 ± 4.3 GeV (arrow displaced vertically downwards). All arrows point in the direction of increasing values of these parameters.

observed for c quarks. In the case of b quarks, the ratio $(4/3)A_{\rm FB}^{0,\,\rm b}/\mathcal{A}_\ell$ is lower than the direct measurement of $\mathcal{A}_{\rm b}$ by 1.6 standard deviations, and lower than the SM expectation for $\mathcal{A}_{\rm b}$ by 3.2 standard deviations.

The mutual consistency of the measurements of $\mathcal{A}_{\rm q}$, $A_{\rm FB}^{0,\,\rm q} = (3/4)\mathcal{A}_{\rm e}\mathcal{A}_{\rm q}$ and $\mathcal{A}_\ell$ assuming lepton universality is shown in Figure 7.2. The results of the joint analysis of the leptonic and heavy-flavour measurements in terms of the asymmetry parameters $\mathcal{A}_{\rm f}$ are reported in Table 7.6 and shown as the error ellipses in Figure 7.2, where the constraint of lepton universality is also imposed. Since $\mathcal{A}_\ell$ and $A_{\rm FB}^{0,\,\rm b}$ are already determined with relatively small errors, the joint analysis primarily improves the determination of the b-quark asymmetry parameter $\mathcal{A}_{\rm b}$ and pulls $\mathcal{A}_\ell$ towards lower values.

As explained in connection with Figure 1.14, the hadronic asymmetry parameters, $\mathcal{A}_{\rm q}$, are very much less sensitive to SM parameters than is the case for $\mathcal{A}_\ell$. This is a consequence of the SM structure of the couplings in terms of the electric charge $Q_{\rm f}$ and of the third component of the weak isospin $T_3^{\rm f}$, see Equations 1.6 to 1.9. Particularly compared to the larger experimental uncertainties of the hadronic measurements, the SM predictions for $\mathcal{A}_{\rm q}$ have negligible dependence on SM parameters such as $m_{\rm t}$, $m_{\rm H}$ and $\alpha(m_{\rm Z}^2)$. The measured quark asymmetry parameters $\mathcal{A}_{\rm q}$ allow the SM to be tested in a manner which is insensitive to electroweak radiative corrections or the knowledge of other SM parameters.

7.3.2 The Effective Coupling Constants

The asymmetry parameters $\mathcal{A}_{\rm f}$ depend only on the ratio $g_{\rm Vf}/g_{\rm Af}$ of the effective vector and axial-vector coupling constants as shown in Equation 1.56. In contrast, the partial decay widths of the Z boson determine the sum of the squares of these two coupling constants (Equation 1.37). The expressions for both observables are invariant under the exchange $g_{\rm Vf} \leftrightarrow g_{\rm Af}$, and only the relative sign between $g_{\rm Vf}$ and $g_{\rm Af}$ is determined by $\mathcal{A}_{\rm f}$. The energy dependence of the forward backward asymmetries measured at LEP resolves the $g_{\rm Vf} \leftrightarrow g_{\rm Af}$ ambiguity, and the absolute sign of all couplings is established by the convention $g_{\rm Ae} < 0$. It is thus possible to disentangle the effective coupling constants $g_{\rm Vf}$ and $g_{\rm Af}$ by analysing both the asymmetry measurements as well as the partial Z decay widths.

For charged leptons and neutrinos, the results on $g_{\rm Vf}$ and $g_{\rm Af}$ are reported in Table 7.7. The factors $R_{\rm Af}$ and $R_{\rm Vf}$ of Equation 1.37 which are used to extract the couplings for charged leptons contain only small final-state QED corrections, $R_{\rm QED} = 1 + 3\alpha(m_{\rm Z}^2)/4\pi$, while for neutrinos $R_{\rm QED} = 1$. The term $\Delta_{\rm ew/QCD}$ vanishes for both. By attributing the entire invisible decay width of the Z to the production of neutrino pairs, the magnitude of the effective coupling of the Z boson to neutrinos can be determined. Three light neutrino families with equal effective coupling constants and $g_{\rm V\nu} \equiv g_{\rm A\nu}$ are assumed. The comparison of different charged lepton species in the $(g_{\rm V\ell}, g_{\rm A\ell})$ plane is also shown in Figure 7.3. Good agreement is observed.

The combined result under the assumption of neutral-current lepton universality is reported in Table 7.8. The neutrino coupling is smaller by about 1.8 standard deviations than the SM expectation listed in Appendix G; this is the same effect as observed above for $\Gamma_{\rm inv}$. The value of $g_{\rm A\ell}$ is different from the corresponding Born-level value of $T_3^\ell = -1/2$ by 4.7 standard deviations, indicating the presence of non-QED electroweak radiative corrections.

Including the heavy-quark measurements and assuming lepton universality, the couplings of quarks and charged leptons are reported in Table 7.9. As in the case of the leptonic couplings, final-state corrections affect the partial widths used for determining the scale of the quark couplings. Here $R_{\rm Af}$, $R_{\rm Vf}$ and $\Delta_{\rm ew/QCD}$ of Equation 1.37 include also QCD corrections, which are

Parameter	Average	Correlations						
		$g_{A\nu}$	g_{Ae}	$g_{A\mu}$	$g_{A\tau}$	g_{Ve}	$g_{V\mu}$	$g_{V\tau}$
$g_{A\nu} \equiv g_{V\nu}$	$+0.5003 \pm 0.0012$	1.00						
g_{Ae}	-0.50111 ± 0.00035	-0.75	1.00					
$g_{A\mu}$	-0.50120 ± 0.00054	0.39	-0.13	1.00				
$g_{A\tau}$	-0.50204 ± 0.00064	0.37	-0.12	0.35	1.00			
g_{Ve}	-0.03816 ± 0.00047	-0.10	0.01	-0.01	-0.03	1.00		
$g_{V\mu}$	-0.0367 ± 0.0023	0.02	0.00	-0.30	0.01	-0.10	1.00	
$g_{V\tau}$	-0.0366 ± 0.0010	0.02	-0.01	0.01	-0.07	-0.02	0.01	1.00
Parameter	Average	Correlations						
		$g_{L\nu}$	g_{Le}	$g_{L\mu}$	$g_{L\tau}$	g_{Re}	$g_{R\mu}$	$g_{R\tau}$
$g_{L\nu}$	$+0.5003 \pm 0.0012$	1.00						
g_{Le}	-0.26963 ± 0.00030	-0.52	1.00					
$g_{L\mu}$	-0.2689 ± 0.0011	0.12	-0.11	1.00				
$g_{L\tau}$	-0.26930 ± 0.00058	0.22	-0.07	0.07	1.00			
g_{Re}	$+0.23148 \pm 0.00029$	0.37	0.29	-0.07	0.01	1.00		
$g_{R\mu}$	$+0.2323 \pm 0.0013$	-0.06	-0.06	0.90	-0.03	-0.09	1.00	
$g_{R\tau}$	$+0.23274 \pm 0.00062$	-0.17	0.04	-0.04	0.44	-0.03	0.04	1.00

Table 7.7: Results on the effective coupling constants for leptons, using the 14 electroweak measurements of Tables 2.13 and 3.6, and Equations 4.9 and 4.10. The combination has a χ^2/dof of 3.6/5, corresponding to a probability of 61%.

Parameter	Average	Correlations		
		g_{ν}	$g_{A\ell}$	$g_{V\ell}$
$g_{A\nu} \equiv g_{V\nu}$	$+0.50076 \pm 0.00076$	1.00		
$g_{A\ell}$	-0.50123 ± 0.00026	-0.48	1.00	
$g_{V\ell}$	-0.03783 ± 0.00041	-0.03	-0.06	1.00
Parameter	Average	Correlations		
		$g_{L\nu}$	$g_{L\ell}$	$g_{R\ell}$
$g_{L\nu}$	$+0.50076 \pm 0.00076$	1.00		
$g_{L\ell}$	-0.26953 ± 0.00024	-0.29	1.00	
$g_{R\ell}$	$+0.23170 \pm 0.00025$	0.22	0.43	1.00

Table 7.8: Results on the effective coupling constants for leptons, using the 14 electroweak measurements of Tables 2.13 and 3.6, and Equations 4.9 and 4.10. Lepton universality is imposed. The combination has a χ^2/dof of 7.8/9, corresponding to a probability of 56%.

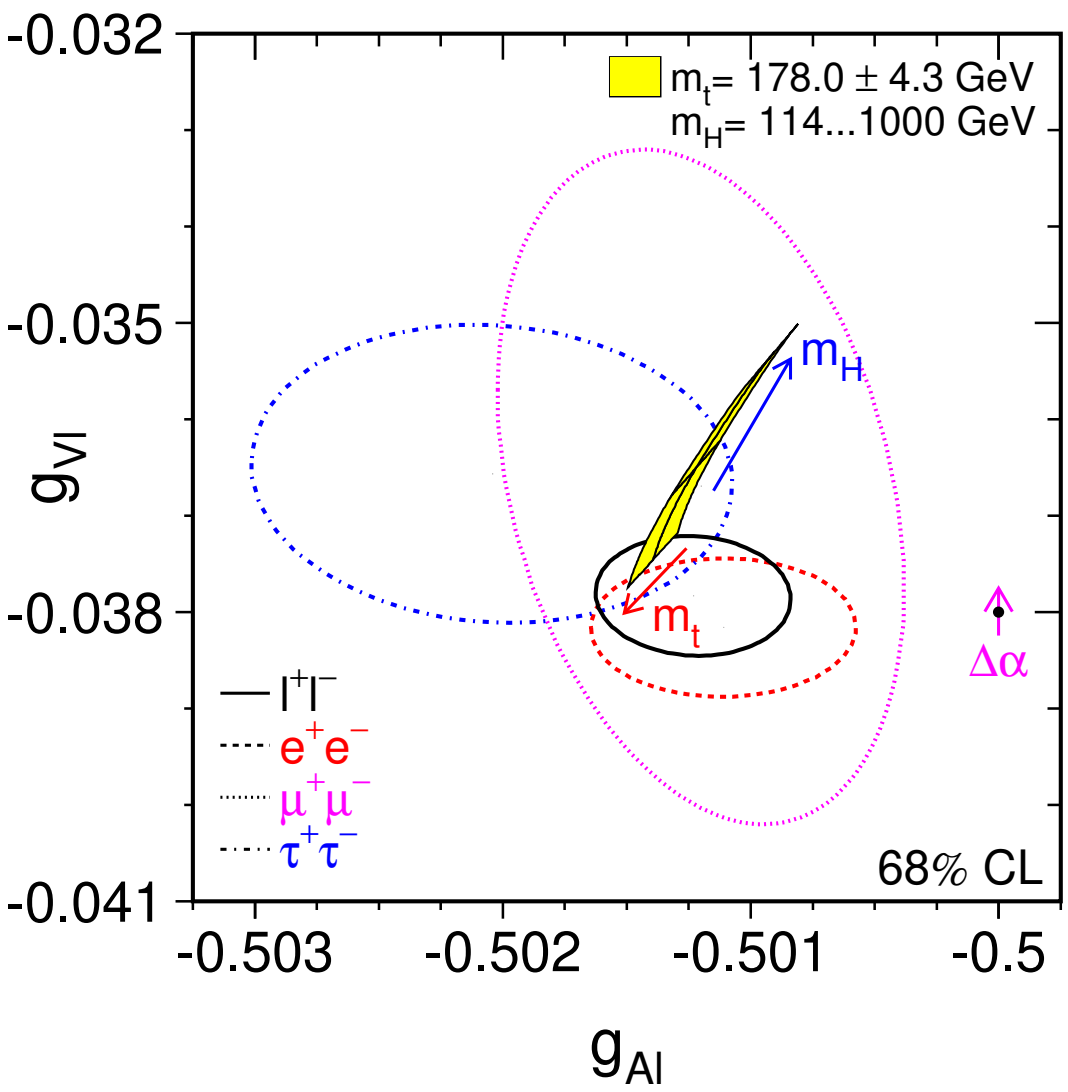

Figure 7.3: Comparison of the effective vector and axial-vector coupling constants for leptons (Tables 7.7 and 7.8). The shaded region in the lepton plot shows the predictions within the SM for $m_{\mathrm{t}} = 178.0 \pm 4.3$ GeV and $m_{\mathrm{H}} = 300^{+700}_{-186}$ GeV; varying the hadronic vacuum polarisation by $\Delta\alpha^{(5)}_{\mathrm{had}}(m^2_{\mathrm{Z}}) = 0.02758 \pm 0.00035$ yields an additional uncertainty on the SM prediction shown by the arrow labeled $\Delta\alpha$.

Parameter	Average	Correlations						
		$g_{\mathrm{A}\nu}$	$g_{\mathrm{A}\ell}$	g_{Ab}	g_{Ac}	$g_{\mathrm{V}\ell}$	g_{Vb}	g_{Vc}
$g_{\mathrm{A}\nu} \equiv g_{\mathrm{V}\nu}$	$+0.50075 \pm 0.00077$	1.00						
$g_{\mathrm{A}\ell}$	-0.50125 ± 0.00026	-0.49	1.00					
g_{Ab}	-0.5144 ± 0.0051	0.01	-0.02	1.00				
g_{Ac}	$+0.5034 \pm 0.0053$	-0.02	-0.02	0.00	1.00			
$g_{\mathrm{V}\ell}$	-0.03753 ± 0.00037	-0.04	-0.04	0.41	-0.05	1.00		
g_{Vb}	-0.3220 ± 0.0077	0.01	0.05	-0.97	0.04	-0.42	1.00	
g_{Vc}	$+0.1873 \pm 0.0070$	-0.01	-0.02	0.15	-0.35	0.10	-0.17	1.00
Parameter	Average	Correlations						
		$g_{\mathrm{L}\nu}$	$g_{\mathrm{L}\ell}$	g_{Lb}	g_{Lc}	$g_{\mathrm{R}\ell}$	g_{Rb}	g_{Rc}
$g_{\mathrm{L}\nu}$	$+0.50075 \pm 0.00077$	1.00						
$g_{\mathrm{L}\ell}$	-0.26939 ± 0.00022	-0.32	1.00					
g_{Lb}	-0.4182 ± 0.0015	0.05	-0.27	1.00				
g_{Lc}	$+0.3453 \pm 0.0036$	-0.02	0.04	-0.09	1.00			
$g_{\mathrm{R}\ell}$	$+0.23186 \pm 0.00023$	0.25	0.34	-0.37	0.07	1.00		
g_{Rb}	$+0.0962 \pm 0.0063$	0.00	-0.33	0.88	-0.14	-0.35	1.00	
g_{Rc}	-0.1580 ± 0.0051	0.00	0.08	-0.17	0.30	0.08	-0.13	1.00

Table 7.9: Results on the effective coupling constants for leptons and quarks assuming neutral-current lepton universality, using the 13 electroweak measurements of Tables 2.13, 5.10 and 5.11, and Equations 3.15 and 4.11. The combination has a χ^2/dof of 4.5/4, corresponding to a probability of 34%.

calculated according to the SM with ZFITTER [31] when extracting effective quark couplings from the partial widths. Similarly, the quoted heavy-quark asymmetries have already been corrected for final-state QCD and QED effects as expected in the SM, see Section 5.7.2. The uncertainties in the extracted quark couplings due to the uncertainty in the strong coupling constant are negligible.

The vector coupling constant for charged leptons is decreased in magnitude compared to Table 7.8 as already observed for the asymmetry parameter $\mathcal{A}_\ell$ in the previous section. For the quark flavours b and c, the results are also shown in Figure 7.4. The strong anti-correlation between the b-quark couplings arises from the tight constraint on the sum of their squares due to the measurement of R^0_{b}, which agrees with the SM prediction. The apparent deviation of the measured b-quark coupling constants from the SM expectation is a direct consequence of the combined result on $\mathcal{A}_{\mathrm{b}}$ being lower than the SM expectation as discussed in the previous section.

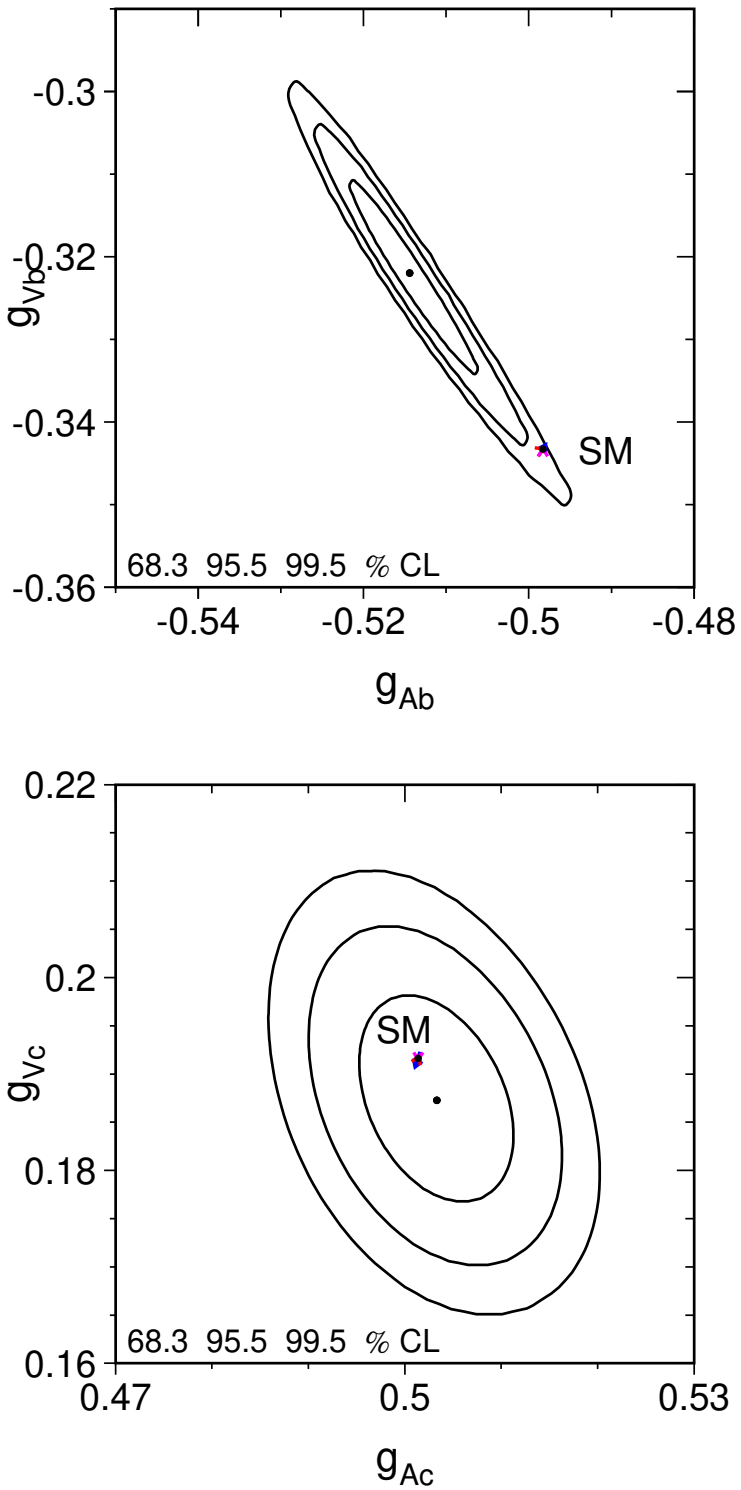

Figure 7.4: Comparison of the effective vector and axial-vector coupling constants for heavy quarks, using results on leptons and assuming lepton universality (Table 7.9). Top: b quarks; bottom: c quarks. Compared to the experimental uncertainties, the SM predictions for the heavy quarks b and c have negligible dependence on the SM input parameters.

7.3.3 The $\rho_{\rm f}$ Parameters and the Effective Electroweak Mixing Angles

The effective vector and axial-vector coupling constants obey simple relations with the ρ parameter and the effective electroweak mixing angle, given by Equations 1.16 and 1.17. For the following analyses, the electric charge $Q_{\rm f}$ and the third component of the weak isospin $T_3^{\rm f}$ are assumed to be given by the SM assignments as listed in Table 1.3. Tests of fermion universality, *i.e.*, a comparison between leptons and quarks in terms of $\rho_{\rm f}$ and $\sin^2\theta_{\rm eff}^{\rm f}$, now become possible.

Considering the leptonic measurements alone and assuming lepton universality, the combined results on $\rho_{\rm f}$ and $\sin^2\theta_{\rm eff}^{\rm lept}$ are reported in Table 7.10. As noted earlier, the neutrino coupling is smaller by about 1.8 standard deviations than the SM expectation listed in Appendix G, while for charged leptons the results are in good agreement with the SM prediction.

The results on $\rho_{\rm f}$ and the effective electroweak mixing angle for leptons and quarks are reported in Table 7.11. As before, neutral-current lepton universality is assumed. The measurement of $\sin^2\theta_{\rm eff}^{\rm lept}$ based on the hadronic charge asymmetry, Equation 6.3, is not included here as that result is derived under the assumption of quark universality. The value of ρ_ℓ is different from the corresponding Born-level value of unity by 5.0 standard deviations, again indicating the presence of non-QED electroweak radiative corrections. The strong correlation between $\rho_{\rm b}$ and $\sin^2\theta_{\rm eff}^{\rm b}$ arises, as the anti-correlation between $g_{\rm Vb}$ and $g_{\rm Ab}$ above, from the tight constraint given by the measurement of $R_{\rm b}^0 \propto g_{\rm Vb}^2 + g_{\rm Ab}^2$.

The comparison between the different fermion species is shown graphically in Figure 7.5. Within the SM, slightly different values for both $\rho_{\rm f}$ and $\sin^2\theta_{\rm eff}^{\rm f}$ are expected for different fermions due to non-universal flavour-specific electroweak radiative corrections. These specific corrections are largest for b quarks, $\rho_{\rm b} - \rho_\ell \approx -0.011$ and $\sin^2\theta_{\rm eff}^{\rm b} - \sin^2\theta_{\rm eff}^{\rm lept} \approx 0.0014$, and more than a factor of five smaller for the other quark flavours, as visible in Figure 7.5. Except for b-quarks, the non-universal flavour-specific corrections expected in the SM are small compared to the experimental errors.

Increasing the measured value of $R_{\rm b}^0$ while keeping the measured value of $A_{\rm FB}^{0,\,{\rm b}}$ fixed moves the b-quark contour parallel to the ρ-axis in the direction of increasing $\rho_{\rm b}$ values, since if $\sin^2\theta_{\rm eff}^{\rm b}$ is fixed, $R_{\rm b}^0$ is simply proportional to $\rho_{\rm b}$. Changing the measured values of $A_{\rm FB}^{0,\,{\rm b}}$, $\mathcal{A}_{\rm b}$ or $\mathcal{A}_\ell$ while keeping the measured value of $R_{\rm b}^0$ fixed moves the b-quark contour along its major axis; this is because changing $\sin^2\theta_{\rm eff}^{\rm b}$ moves both the b asymmetries and the b width, therefore $\rho_{\rm b}$ also changes in order to keep $R_{\rm b}^0$ fixed. Increasing $A_{\rm FB}^{0,\,{\rm b}}$ or $\mathcal{A}_{\rm b}$ moves the contour towards the SM expectation, with roughly equal sensitivity to a one standard deviation shift of either parameter. Decreasing $\mathcal{A}_\ell$ moves the contour in the same direction, but a one standard deviation shift in $\mathcal{A}_\ell$ has a smaller effect.

7.3.4 The Leptonic Effective Electroweak Mixing Angle

The measurements of the various asymmetries determine the effective electroweak mixing angle $\sin^2\theta_{\rm eff}^{\rm f}$ independently of $\rho_{\rm f}$, because they depend only on the ratio $g_{\rm Vf}/g_{\rm Af}$ of the effective coupling constants. As illustrated in Figure 1.14 the charge and weak isospin assignments of the quarks imply that the relative sensitivity of $\mathcal{A}_{\rm q}$ to $\sin^2\theta_{\rm eff}^{\rm q}$ is much smaller than is the case for leptons. In particular for b-quarks this sensitivity is almost a factor 100 less than it is for leptons. This is also visible in Figures 7.2 and 7.4, showing that for up-type quarks as well as down-type quarks both the asymmetry parameters $\mathcal{A}_{\rm q}$ and the effective coupling constants $g_{\rm Aq}$ and $g_{\rm Vq}$ are, on the scale of the experimental uncertainties, nearly independent of SM parameters. Therefore, the heavy quark forward-backward asymmetries $A_{\rm FB}^{0,\,{\rm q}} = (3/4)\mathcal{A}_{\rm e}\mathcal{A}_{\rm q}$ as

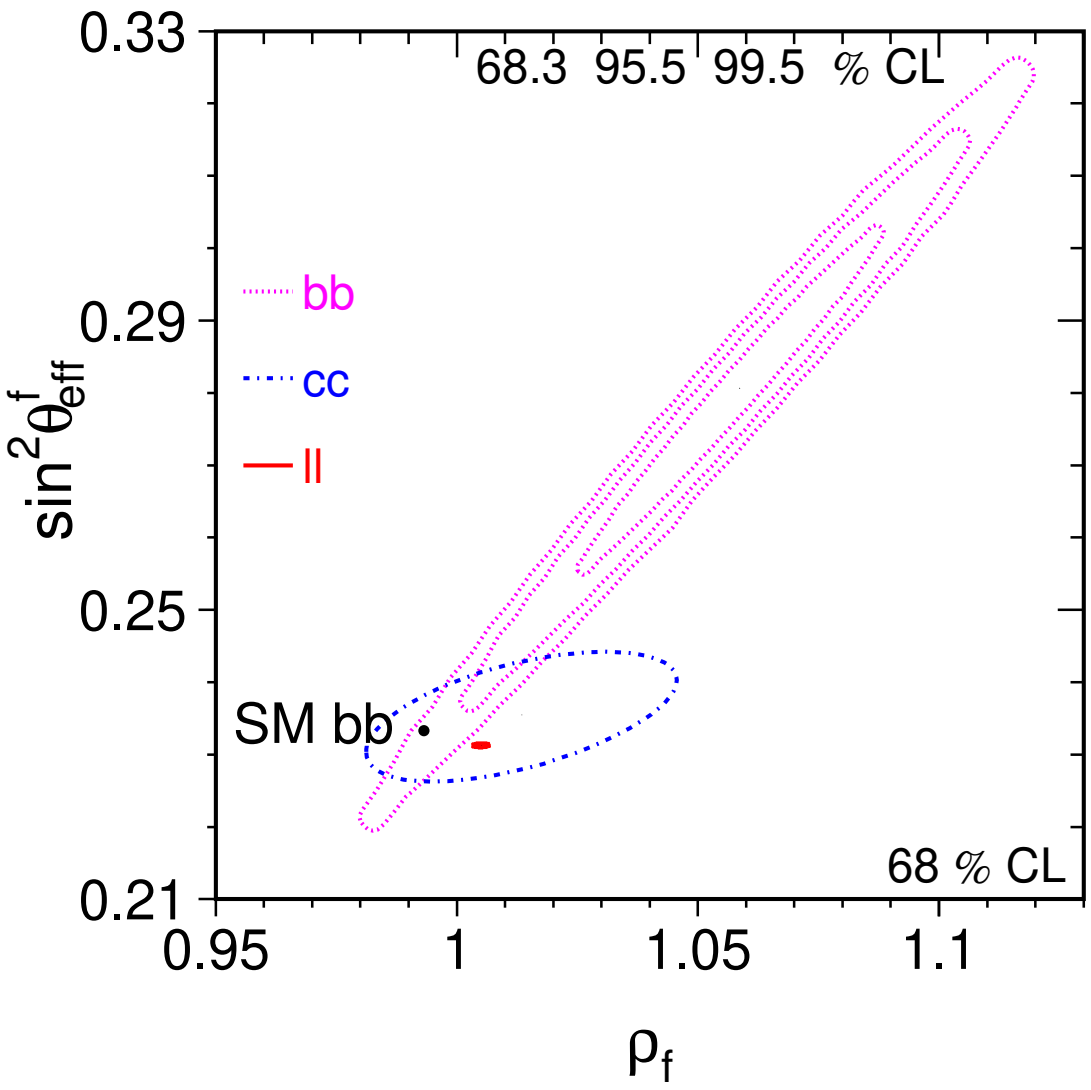

Figure 7.5: Comparison of ρ_{f} and the effective electroweak mixing angle $\sin^2\theta^{\mathrm{f}}_{\mathrm{eff}}$ for leptons, b and c quarks. The SM expectation for b quarks is shown as the dot ($\rho_{\mathrm{b}} < 1$); those of c quarks and of leptons are not drawn as they lie at the same area as the experimental contour curve for leptons ($\rho_{\ell} > 1$). Only the 68% CL contour is shown for c quarks and leptons. On the scale of this plot, variations of the SM prediction with m_{t}, m_{H} and $\Delta\alpha^{(5)}_{\mathrm{had}}(m^2_{\mathrm{Z}})$ are negligible.

Parameter	Average	Correlations		
		ρ_ν	ρ_ℓ	$\sin^2\theta^{\rm lept}_{\rm eff}$
ρ_ν	1.0030±0.0031	1.00		
ρ_ℓ	1.0049±0.0010	0.48	1.00	
$\sin^2\theta^{\rm lept}_{\rm eff}$	0.23113±0.00021	−0.01	0.11	1.00

Table 7.10: Results on $\rho_{\rm f}$ and $\sin^2\theta^{\rm f}_{\rm eff}$ for leptons, using the 14 electroweak measurements of Tables 2.13 and 3.6, and Equations 4.9 and 4.10. Lepton universality is imposed. The combination has a χ^2/dof of 7.8/9, corresponding to a probability of 56%.

Parameter	Average	Correlations						
		ρ_ν	ρ_ℓ	$\rho_{\rm b}$	$\rho_{\rm c}$	$\sin^2\theta^{\rm lept}_{\rm eff}$	$\sin^2\theta^{\rm b}_{\rm eff}$	$\sin^2\theta^{\rm c}_{\rm eff}$
ρ_ν	1.0030±0.0031	1.00						
ρ_ℓ	1.0050±0.0010	0.49	1.00					
$\rho_{\rm b}$	1.059±0.021	−0.01	−0.02	1.00				
$\rho_{\rm c}$	1.013±0.021	−0.02	0.02	0.00	1.00			
$\sin^2\theta^{\rm lept}_{\rm eff}$	0.23128±0.00019	−0.01	0.09	−0.41	−0.05	1.00		
$\sin^2\theta^{\rm b}_{\rm eff}$	0.281±0.016	0.00	−0.04	0.99	0.03	−0.42	1.00	
$\sin^2\theta^{\rm c}_{\rm eff}$	0.2355±0.0059	0.00	−0.01	0.14	0.56	−0.10	0.15	1.00

Table 7.11: Results on the $\rho_{\rm f}$ parameter and the effective electroweak mixing angle $\sin^2\theta^{\rm f}_{\rm eff}$ assuming neutral-current lepton universality, using the 13 electroweak measurements of Tables 2.13, 5.10 and 5.11, and Equations 3.15 and 4.11. The combination has a χ^2/dof of 4.5/4, corresponding to a probability of 34%.

well as the hadronic charge asymmetry $Q^{\rm had}_{\rm FB}$, are sensitive to $\sin^2\theta^{\rm lept}_{\rm eff}$ through the factor $\mathcal{A}_{\rm e}$ and rather insensitive to $\sin^2\theta^{\rm q}_{\rm eff}$. The latter fact is also evident from the $\sin^2\theta^{\rm f}_{\rm eff}$ results reported in Table 7.11, showing that the direct measurements of $\mathcal{A}_{\rm q}$ do not impose stringent constraints on $\sin^2\theta^{\rm q}_{\rm eff}$.

The resulting determinations of $\sin^2\theta^{\rm lept}_{\rm eff}$ derived from each of the six asymmetry measurements sensitive to $\sin^2\theta^{\rm lept}_{\rm eff}$ are compared in Figure 7.6. The measurements fall into two sets of three results each. In the first set, the results on $\sin^2\theta^{\rm lept}_{\rm eff}$ are derived from measurements depending on leptonic couplings only, $A^{0,\ell}_{\rm FB}$, $\mathcal{A}_\ell(P_\tau)$ and $\mathcal{A}_\ell$(SLD). In this case, only lepton universality is assumed, and no further corrections to interpret the results in terms of $\sin^2\theta^{\rm lept}_{\rm eff}$ are necessary. In the second set, consisting of $A^{0,{\rm b}}_{\rm FB}$, $A^{0,{\rm c}}_{\rm FB}$ and $Q^{\rm had}_{\rm FB}$, quark couplings are involved. In this case, the small non-universal flavour-specific electroweak corrections, making $\sin^2\theta^{\rm lept}_{\rm eff}$ different from $\sin^2\theta^{\rm q}_{\rm eff}$, are taken from the SM. The size of the applied SM flavour-specific corrections can be seen in Figure 7.5. Only the correction for b-quarks is large enough to be visible. The effect of these corrections and their uncertainties on the extracted value of $\sin^2\theta^{\rm lept}_{\rm eff}$ is, as discussed above, negligible.

The average of all six $\sin^2\theta^{\rm lept}_{\rm eff}$ determinations is:

$$\sin^2\theta^{\rm lept}_{\rm eff} \;=\; 0.23153 \pm 0.00016\,, \qquad (7.11)$$

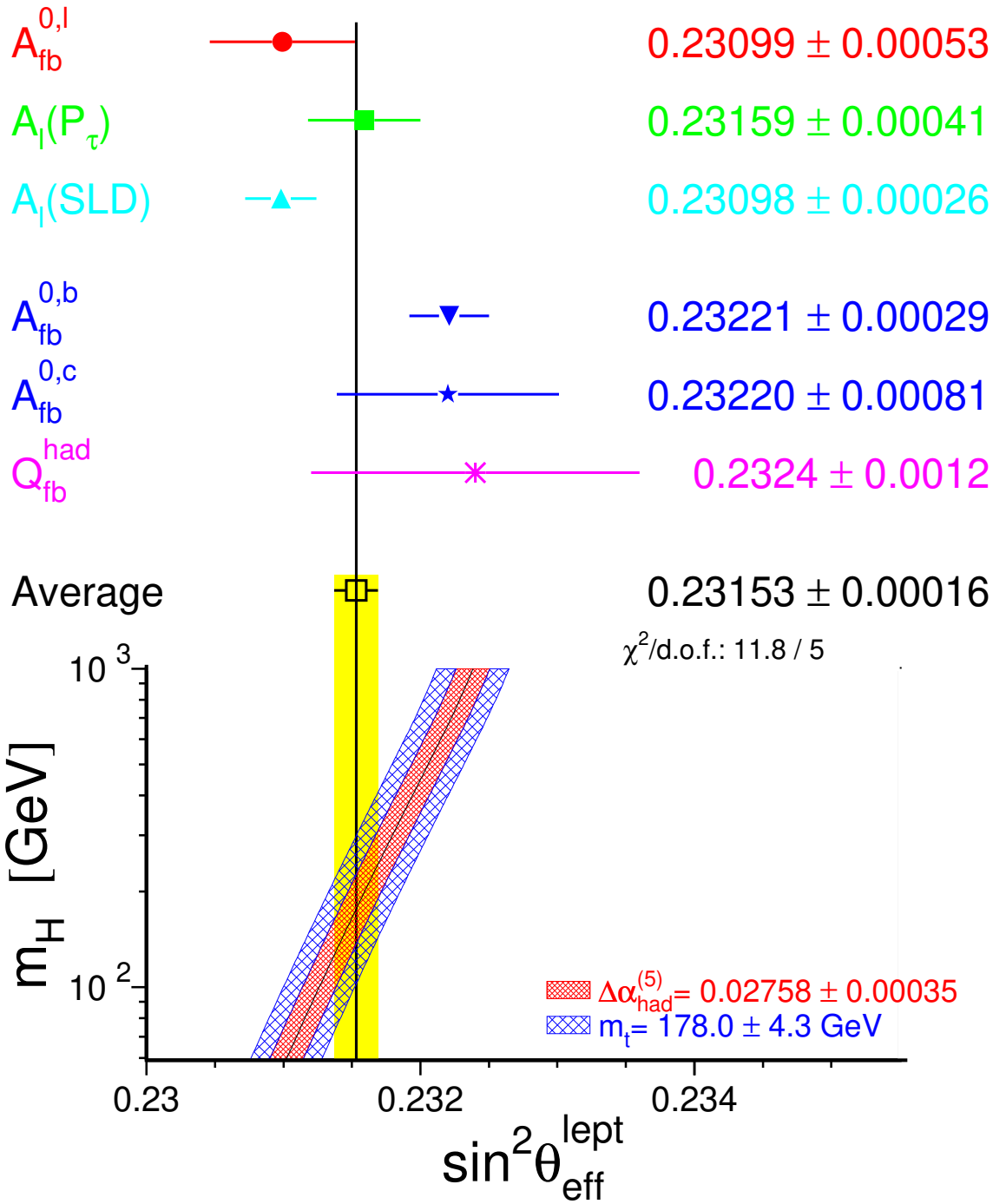

Figure 7.6: Comparison of the effective electroweak mixing angle $\sin^2\theta_{\rm eff}^{\rm lept}$ derived from measurements depending on lepton couplings only (top) and also quark couplings (bottom). Also shown is the SM prediction for $\sin^2\theta_{\rm eff}^{\rm lept}$ as a function of $m_{\rm H}$. The additional uncertainty of the SM prediction is parametric and dominated by the uncertainties in $\Delta\alpha_{\rm had}^{(5)}(m_{\rm Z}^2)$ and $m_{\rm t}$, shown as the bands. The total width of the band is the linear sum of these effects.

with a χ^2/dof of 11.8/5, corresponding to a probability of only 3.7%. This enlarged χ^2/dof is solely driven by the two most precise determinations of $\sin^2\theta_{\rm eff}^{\rm lept}$, namely those derived from the measurements of $\mathcal{A}_\ell$ by SLD, dominated by the $A_{\rm LR}^0$ result, and of $A_{\rm FB}^{0,\,\rm b}$ at LEP, which yield the largest pulls and fall on opposite sides of the $\sin^2\theta_{\rm eff}^{\rm lept}$ average. These two $\sin^2\theta_{\rm eff}^{\rm lept}$ measurements differ by 3.2 standard deviations. Thus, the sets of leptonic and hadronic measurements, yielding average values for $\sin^2\theta_{\rm eff}^{\rm lept}$ of 0.23113 ± 0.00021 (χ^2/dof = 1.6/2) and 0.23222 ± 0.00027 (χ^2/dof = 0.02/2), respectively, also differ, by 3.2 standard deviations. This is a consequence of the same effect as discussed in the previous sections: the deviation in $\mathcal{A}_{\rm b}$ as extracted from $A_{\rm FB}^{0,\,\rm b}$ discussed in Section 7.3.1 is reflected in the value of $\sin^2\theta_{\rm eff}^{\rm lept}$ extracted from $A_{\rm FB}^{0,\,\rm b}$.

7.3.5 Discussion

The unexpectedly large shifts and differences observed in the various analyses for asymmetry parameters, effective coupling constants, $\rho_{\rm f}$ and $\sin^2\theta_{\rm eff}^{\rm lept}$ all show the consequences of the same effect. It is most clearly visible in the effective couplings and $\sin^2\theta_{\rm eff}^{\rm lept}$ averages and stems from the measurements of $A_{\rm LR}^0$ and $A_{\rm FB}^{0,\,\rm b}$.

The results as shown in Figure 7.4 suggest that the effective couplings for b-quarks cause the main effect; both $g_{\rm Vb}$ and $g_{\rm Ab}$ deviate from the SM expectation at the level of two standard deviations. In terms of the left- and right-handed couplings $g_{\rm Lb}$ and $g_{\rm Rb}$, which are much better aligned with the axes of the error ellipse, only $g_{\rm Rb}$ shows a noticeable deviation from the expectation. The value of $g_{\rm Lb}$, which is essentially equivalent to $R_{\rm b}^0 \propto g_{\rm Rb}^2 + g_{\rm Lb}^2$ due to the smallness of $g_{\rm Rb}$, shows no discrepancy. The data therefore invite an economical explanation in terms of a possible deviation of the right-handed b quark coupling alone, even at Born level (see Equation 1.7), from the SM prediction. This would affect $\mathcal{A}_{\rm b}$ and $A_{\rm FB}^{0,\,\rm b}$, which both depend only on the ratio $g_{\rm Rb}/g_{\rm Lb}$, more strongly than $R_{\rm b}^0$.

From the experimental point of view, no systematic effect potentially explaining such shifts in the measurement of $A_{\rm FB}^{0,\,\rm b}$ has been identified. While the QCD corrections are significant, their uncertainties are small compared to the total errors and are taken into account, see Section 5.7.2. Within the SM, flavour specific electroweak radiative corrections as listed above and their uncertainties are much too small to explain the difference in the extracted $\sin^2\theta_{\rm eff}^{\rm lept}$ values. All known uncertainties are investigated and are taken into account in the analyses. The same holds for the $A_{\rm LR}^0$ measurement, where the most important source of systematic uncertainty, namely the determination of the beam polarization, is small and well-controlled.

Thus the shift is either a sign for new physics which invalidates the simple relations between the effective parameters assumed in this chapter, or a fluctuation in one or more of the input measurements. In the following we assume that measurement fluctuations are responsible. Furthermore, we largely continue to assume a Gaussian model for the experimental errors, despite the fact that this results in a value for $\sin^2\theta_{\rm eff}^{\rm lept}$, with small errors, which is in poor agreement with both $A_{\rm LR}^0$ and $A_{\rm FB}^{0,\,\rm b}$. As a direct consequence, the χ^2/dof in all analyses including these measurements will be inflated due to the contribution of at least 11.8 units from the six asymmetry measurements. To acknowledge the possibility that a Gaussian model may in fact poorly represent the tails of the experimental uncertainties, we also consider how subsequent analyses are affected if one or the other of the high-pull measurements in the $\sin^2\theta_{\rm eff}^{\rm lept}$ sector is excluded from consideration.

7.4 Sensitivity to Radiative Corrections Beyond QED

A fundamental question is whether the experimental Z-pole results indeed confirm the existence of electroweak radiative corrections beyond those predicted by the well known and tested theory of QED. Including only the running of α, the expectations based on Born-term expressions for the ρ parameter and the electroweak mixing angle are obtained from the equations given in Section 1.4, by setting $\Delta\rho = \Delta\kappa = \Delta r_{\rm w} = 0$. The results are:

$$\rho_0 = 1 \tag{7.12}$$

$$\sin^2\theta_0 = \frac{1}{2}\left(1 - \sqrt{1 - 4\frac{\pi\alpha(m_{\rm Z}^2)}{\sqrt{2}G_{\rm F}m_{\rm Z}^2}}\right) = 0.23098 \pm 0.00012\,, \tag{7.13}$$

where the uncertainty on $\sin^2\theta_0$ arises due to the uncertainty on $\alpha(m_{\rm Z}^2)$ mainly caused by the hadronic vacuum polarisation, see Equations 1.29, 1.30, 8.1 and 8.3. The measured values of ρ_ℓ (Table 7.11) and the effective electroweak mixing angle (Equation 7.11):

$$\rho_\ell = 1.0050 \pm 0.0010 \tag{7.14}$$

$$\sin^2\theta_{\rm eff}^{\rm lept} = 0.23153 \pm 0.00016\,, \tag{7.15}$$

differ significantly, particularly in the case of the ρ parameter, from these expectations, indicating that electroweak radiative corrections beyond QED are needed to describe the Z-pole measurements. This is also shown in Figure 7.7. Further tests of electroweak radiative corrections based on dedicated sets of parameters are presented in Appendix E.

In the case of the effective electroweak mixing angle, the uncertainty on the prediction of $\sin^2\theta_{\rm eff}^{\rm lept}$ within the SM due to the uncertainty on $\Delta\alpha_{\rm had}^{(5)}(m_{\rm Z}^2)$ is nearly as large as the accuracy of the experimental measurement of $\sin^2\theta_{\rm eff}^{\rm lept}$. This observation underlines the importance of a precise cross-section measurement of electron-positron annihilation into hadrons at low centre-of-mass energies. In contrast to $\sin^2\theta_{\rm eff}^{\rm lept}$, the SM prediction for the ρ parameter is not affected by the uncertainty in $\Delta\alpha_{\rm had}^{(5)}(m_{\rm Z}^2)$.

As discussed in Section 1.4 in connection with Figure 1.10, in the SM the $\rm b\overline{b}$ final state is subject to additional large vertex corrections which depend on the top-quark mass. These flavour-specific vertex corrections are particularly significant for the measurement of $R_{\rm b}^0$, shown in Figure 7.8 and compared to theory predictions. The measurement of $R_{\rm b}^0$ is able to discriminate between the different predictions for b-quarks versus light down-type quarks, showing that also b-specific vertex corrections are observed with high significance. The much weaker $m_{\rm t}$ dependence of $R_{\rm d}^0$, which is also shown, results mainly from b-quark contributions in the denominator of $R_{\rm d}^0 = \Gamma_{\rm d\overline{d}}/\Gamma_{\rm had}$. Due to the fact that other radiative corrections affect all quark species about equally, $R_{\rm b}^0$, as a ratio, benefits from small parametric uncertainties arising from other SM parameters, and therefore imposes a particularly direct constraint on the top-quark mass in the SM.

As will be shown in Chapter 8, also the mass of the W boson, measured at the Tevatron and at LEP-II, implies the existence of genuine electroweak radiative corrections through Δr and $\Delta r_{\rm w}$, with even higher significance. It is interesting to note that in 1987, before the advent of SLC and LEP, electroweak radiative corrections - including the large QED contributions - had been seen at the level of three standard deviations based on a variant of Δr [199], while the pure electroweak components of the corrections could not be separated. Today, it is the pure electroweak correction ρ_ℓ which is demonstrated above to deviate from unity with a significance of five standard deviations. Furthermore, using the current Z-pole results alone, the error in Δr has been reduced by a factor of about 20 compared to 1987 [199], see the next chapter.

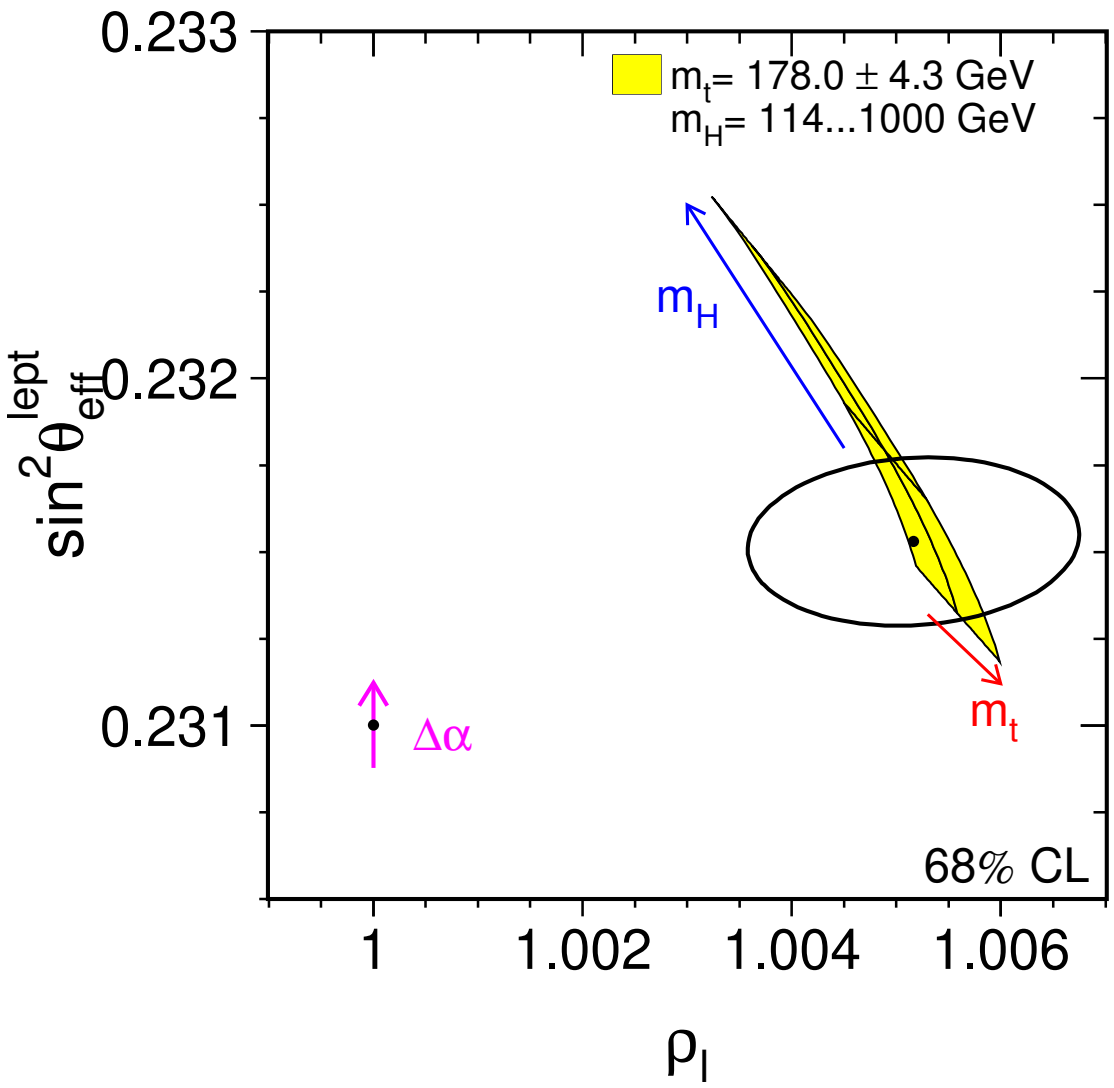

Figure 7.7: Contour curve of 68% probability in the $(\rho_\ell, \sin^2\theta^{\rm lept}_{\rm eff})$ plane. The prediction of a theory based on electroweak Born-level formulae and QED with running α is shown as the dot, with the arrow representing the uncertainty due to the hadronic vacuum polarisation $\Delta\alpha^{(5)}_{\rm had}(m^2_{\rm Z})$. The same uncertainty also affects the SM prediction, shown as the shaded region drawn for fixed $\Delta\alpha^{(5)}_{\rm had}(m^2_{\rm Z})$ while $m_{\rm t}$ and $m_{\rm H}$ are varied in the ranges indicated.

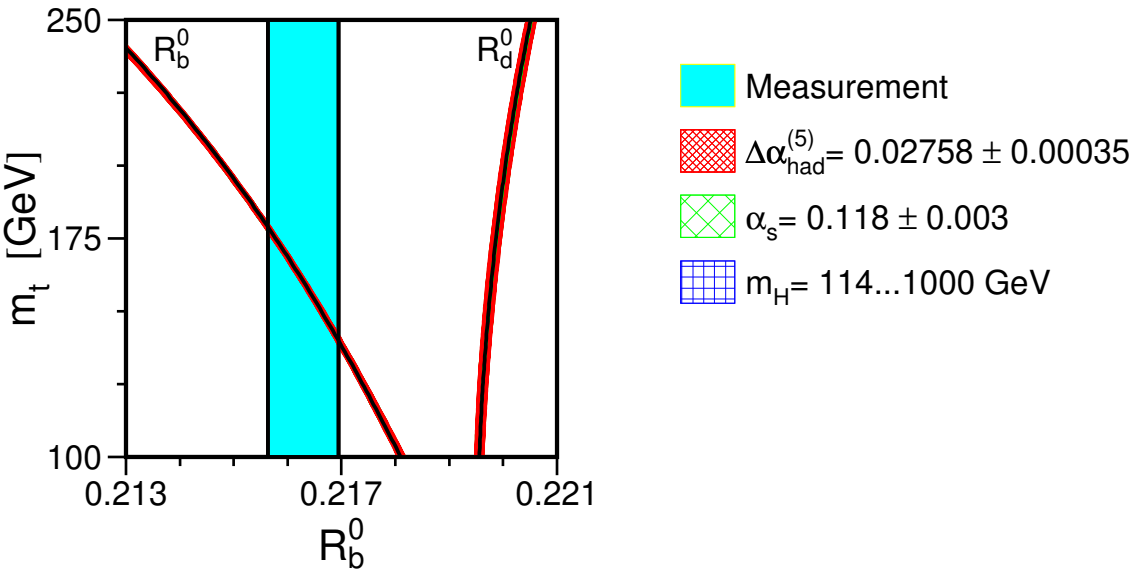

Figure 7.8: Comparison of the LEP combined measurement of R_{b}^0 with the SM prediction as a function of the mass of the top quark. The measurement with its uncertainty is shown as the vertical band. The two curves show the expectations for R_{b}^0 and R_{d}^0 as a function of m_{t}. The SM prediction for R_{d}^0 displays a markedly smaller m_{t} dependence which is also of opposite sign. The parametric uncertainties on the SM expectations due to the uncertainties in $\Delta\alpha^{(5)}_{\mathrm{had}}(m_{\mathrm{Z}}^2)$, $\alpha_{\mathrm{S}}(m_{\mathrm{Z}}^2)$ and m_{H} are shown as the width of the curves, they are negligible compared to the uncertainty of the measurement.

Chapter 8

Constraints on the Standard Model

In the previous sections, several figures have already shown comparisons between the experimental results and the expectations from the Standard Model (SM) [4]. In this chapter, the experimental results are used to constrain the input parameters of the SM. As discussed in Section 1.4, the SM prediction for each Z-pole observable depends on free parameters which are not predicted by the theory, such as the coupling constants of the various interactions and the masses of the fundamental fermions (quarks and leptons) and bosons (Z, W, and H). Consistency of the SM framework requires that all measurements are accommodated by the same values of these free SM parameters. Owing to this dependence, directly at Born level or through electroweak radiative corrections, the experimental measurements of Z-pole and other observables allow us to constrain these free parameters. Most importantly it is possible to determine the mass of the top quark precisely and also the mass of the Higgs boson, albeit with less precision.

The input parameter set chosen for SM calculations is discussed in Section 8.1. An important ingredient, the hadronic vacuum polarisation, is discussed in Section 8.2. Additional measurements from other experiments, used for comparisons, or to increase the precision of the SM constraints, are reported in Section 8.3. Parameter dependencies and theoretical uncertainties in the calculation of SM predictions for measured observables are discussed in Section 8.4. The analysis and fitting procedure used in this chapter is described in Section 8.5. The remaining sections present the results of the SM analyses: Constraints on the input parameters of the SM, in particular on the masses of the heavy particles top quark, W boson and Higgs boson are reported in Section 8.6. A concluding discussion is presented in Section 8.7. Predictions of many observables within the SM framework are reported in Appendix G.

8.1 Parameters of the Standard Model

For the electromagnetic, weak and strong interactions described by the Minimal SM, the corresponding coupling constants are not predicted, but must be inferred from measurements. Because the SM gives an integrated description of the electromagnetic and weak interactions in the form of the electroweak theory, the weak coupling is related to the electromagnetic coupling and the masses of the charged and neutral heavy gauge bosons W and Z. Therefore, just two coupling constants, those of the electromagnetic and the strong interaction, α and α_S, remain to be determined, together with the masses of the heavy gauge bosons W and Z. The mass of the electromagnetic gauge boson, the photon, is fixed at zero as required by the theory of QED.

The masses of all known fundamental fermions with the exception of the top quark are

small compared to m_{Z}, and precisely enough measured so that their influence on Z-pole observables through kinematic effects is both rather small and calculable to more than adequate precision. In the following analyses the masses of the light fermions are therefore considered fixed. In particular, the results are insensitive to small neutrino masses corresponding to current experimental limits [84].

The mass of the Z boson is precisely measured as described in Chapter 2. Although it is treated formally as a free parameter of the theory, the precision of its experimental determination is sufficient to ensure that no SM constraints can pull it appreciably, and it could just as well be taken as a fixed quantity in our analysis.

Within the SM, the mass of the W, measured directly at the Tevatron and LEP-II is related to m_{Z} and the Fermi constant G_{F} through Equation 1.33. A very precise value for the latter, $G_{\mathrm{F}} = 1.16637(1) \cdot 10^{-5}$ GeV^{-2} [84], is derived from measurements of the muon lifetime using two-loop corrections [200]. This 9 ppm precision on G_{F} greatly exceeds the relative precision with which m_{W} can be measured in the foreseeable future. Indeed, the current precision of G_{F} is so great that it is treated as a constant in the following analyses. This also motivates our substitution of G_{F} for m_{W} as an input parameter for SM calculations.[1] In addition, radiative corrections are smaller when calculated with respect to lowest-order expressions formulated in terms of G_{F}. The mass of the W boson, m_{W}, is then predicted within the SM in terms of G_{F}, m_{Z}, and the radiative correction Δr, which is a function of the other SM input parameters. Comparing this prediction with the direct measurements of m_{W} performed at the Tevatron and LEP-II yields a stringent test of the SM.

Electroweak radiative corrections such as those shown in Figure 1.9 modify the calculation of Z-pole observables. Comparisons with the measurements thus allow constraints to be placed on SM input parameters beyond those accessible directly. The top quark, with a mass of about 175 GeV, and apparently the Higgs boson, are too heavy to be produced directly in $\mathrm{e^+e^-}$ collisions at LEP-I/SLC centre-of-mass energies close to the Z pole, *i.e.*, 88 GeV $< \sqrt{s} <$ 95 GeV. Loop corrections in $\mathrm{e^+e^-}$ interactions involving virtual top quarks and Higgs bosons depend, however, on the masses of these two particles. To leading one-loop order these corrections do not depend on the species of fermion to which the Z decays, and show a dependence quadratic in the top-quark mass and logarithmic in the Higgs-boson mass, as illustrated in Equations 1.19 and 1.20. Non-leading, higher-order and fermion-specific corrections (see Equation 1.22) allow the effects from the top quark and the Higgs boson to be disentangled. The resulting indirect determination of the top-quark mass m_{t} is precise, and its comparison with the direct measurement obtained from $\mathrm{t\bar{t}}$ production in proton-antiproton collisions at the Tevatron constitutes another important test of the SM. Our determination of the Higgs mass is consistent with moderate values on the electroweak scale, and establishes a useful upper limit to guide future searches.

Loop corrections also induce a running of the electromagnetic coupling constant α with momentum transfer (or s), as described in Equation 1.30. The running of the strong coupling, $\alpha_{\mathrm{S}}(s)$, is even larger. The Z resonance is sufficiently dominant for Z-pole observables, however, that the Z-pole approximation can be taken, and the relevant coupling constants become simply $\alpha(m_{\mathrm{Z}}^2)$ and $\alpha_{\mathrm{S}}(m_{\mathrm{Z}}^2)$.

The five input parameters of the SM relevant for the calculation of Z-pole observables are therefore the coupling constants of QED and QCD at the Z pole, $\alpha(m_{\mathrm{Z}}^2)$ and $\alpha_{\mathrm{S}}(m_{\mathrm{Z}}^2)$, and the masses of the Z boson, the top quark and the Higgs boson. The measurements of

[1] Note, however, that this replacement is purely technical: none of the results would change if m_{W} rather than G_{F} were taken as an input parameter for SM calculations.

electroweak observables presented in the previous chapters are used to find optimal values for these five SM input parameters, and to test whether all the measurements can be simultaneously accommodated by this single set. Besides the mass of the Z boson, the interesting input parameters of the SM are the mass of the top quark and of course the mass of the Higgs boson. Since the electroweak sector of the SM is well understood, the hadronic Z-pole observables will give rise to one of the most precise determinations of $\alpha_{\mathrm{S}}(m_{\mathrm{Z}}^2)$. The treatment of $\alpha(m_{\mathrm{Z}}^2)$ is discussed in the following section. The programs TOPAZ0 [30] and ZFITTER [31] are used to calculate all Z-pole observables including radiative corrections in the framework of the SM and as a function of these five SM input parameters. They include the equations shown in Section 1.4, supplemented by more complicated high-order expressions for improved theoretical accuracy.

8.2 Hadronic Vacuum Polarisation

The running of the electromagnetic coupling with momentum transfer, $\alpha(0) \to \alpha(s)$, caused by fermion-pair loop insertions in the photon propagator, is customarily written as given in Equations 1.29 and 1.30:

$$\alpha(s) \;=\; \frac{\alpha(0)}{1-\Delta\alpha(s)} \;=\; \frac{\alpha(0)}{1-\Delta\alpha_{\mathrm{e}\mu\tau}(s)-\Delta\alpha_{\mathrm{top}}(s)-\Delta\alpha_{\mathrm{had}}^{(5)}(s)}\,, \tag{8.1}$$

with $\alpha(0) = 1/137.036$ [84]. The contribution of leptons is calculated diagrammatically up to third order: $\Delta\alpha_{\mathrm{e}\mu\tau}(m_{\mathrm{Z}}^2) = 0.03150$ with negligible uncertainty [201]. Since heavy particles decouple in QED, the top-quark contribution is small: $\Delta\alpha_{\mathrm{top}}(m_{\mathrm{Z}}^2) = -0.00007(1)$; it is calculated by TOPAZ0 and ZFITTER as a function of the pole mass of the top quark, m_{t}. The running electromagnetic coupling is insensitive to new particles with high masses. For light-quark loops the diagrammatic calculations are not viable as at such low energy scales perturbative QCD is not applicable. Therefore, the total contribution of the five light quark flavours to the hadronic vacuum polarisation, $\Delta\alpha_{\mathrm{had}}^{(5)}(m_{\mathrm{Z}}^2)$, is more accurately obtained through a dispersion integral over the measured hadronic cross-section in electron-positron annihilations at low centre-of-mass energies. In this case the uncertainty on $\Delta\alpha_{\mathrm{had}}^{(5)}(m_{\mathrm{Z}}^2)$ is given by the experimental uncertainties in the measured hadronic cross-section at low centre-of-mass energies, leading to [58, 202]:

$$\Delta\alpha_{\mathrm{had}}^{(5)}(m_{\mathrm{Z}}^2) \;=\; 0.02804 \pm 0.00065\,, \tag{8.2}$$

as used in Chapter 2 for the extraction of the Z resonance parameters. Based on the same analysis technique but including new measurements of the hadronic cross-section at low energies, in particular the precise measurements of the BES collaboration in the range 2 GeV $< \sqrt{s} <$ 5 GeV [203] as well as measurements by the CMD-2 and KLOE experiments below that energy in $\pi^+\pi^-$ production [204, 205], the uncertainty is much reduced [59]:

$$\Delta\alpha_{\mathrm{had}}^{(5)}(m_{\mathrm{Z}}^2) \;=\; 0.02758 \pm 0.00035\,, \tag{8.3}$$

leading to $\Delta\alpha(m_{\mathrm{Z}}^2) = 0.05901 \pm 0.00035$. During the course of the last few years, more theory-driven determinations of $\Delta\alpha_{\mathrm{had}}^{(5)}(m_{\mathrm{Z}}^2)$ have appeared [206, 207], which employ perturbative QCD to calculate the hadronic cross-section in the continuum region at low $\sqrt{s}$, outside the region populated by the hadronic resonances. Since the theoretical uncertainty on the predicted cross-section is assumed to be smaller than that of the experimental measurements, a reduced error on $\Delta\alpha_{\mathrm{had}}^{(5)}(m_{\mathrm{Z}}^2)$ is achieved, for example [207]:

$$\Delta\alpha_{\mathrm{had}}^{(5)}(m_{\mathrm{Z}}^2) \;=\; 0.02749 \pm 0.00012\,, \tag{8.4}$$

which also takes the new results from BES into account. All updated evaluations of $\Delta\alpha^{(5)}_{\rm had}(m^2_{\rm Z})$ are consistent with, but lower than, the previous evaluation of Equation 8.2. In the following analyses, the experiment-driven value of $\Delta\alpha^{(5)}_{\rm had}(m^2_{\rm Z})$ as given in Equation 8.3 will be used, on the same footing as any other experimental measurement with its associated uncertainty.

8.3 Additional Measurements

Obviously, a wealth of measurements are performed in particle physics experiments elsewhere, using various particle beams and targets. The results of these experiments are crucial to explore the predictive power of the SM in as large a breadth as possible. Of all these measurements, those which have a high sensitivity to the five SM input parameters introduced above are particularly interesting here.

The additional results considered in some of the SM analyses presented in the following are the mass of the top quark and the mass and the total width of the W boson. In addition, the SM analyses are used to obtain predictions for electroweak observables measured in reactions at low momentum transfer, $Q^2 \ll m^2_{\rm Z}$, namely those measuring parity violation effects in atomic transitions, in polarised Møller scattering and in neutrino-nucleon scattering. These results are sensitive to different types of new-physics effects than the Z-pole observables. However, since the precision of these results is insufficient to provide additional power in determining the five SM input parameters, they are not included in our fits, but used to test their compatibility with the SM predictions based on the high-Q^2 fits. Predictions of the observables within the SM framework are reported in Appendix G.

8.3.1 Mass of the Top Quark

In 1995, the top quark was discovered in proton-antiproton interactions recorded at the Tevatron collider by the experiments CDF [208] and DØ [209]. Both experiments measure its mass directly, exploiting various decay chains. The published results from CDF [210] and DØ [211] obtained from data collected in Run-I (1992-1996) are combined taking correlated uncertainties into account. The Tevatron Run-I world average value for the pole mass of the top quark is: $m_{\rm t} = 178.0 \pm 4.3$ GeV [212]. Improved direct measurements of $m_{\rm t}$ are expected from the currently ongoing Run-II of the Tevatron.

8.3.2 Mass and Width of the W Boson

Initially, the mass of the W boson was measured in proton-antiproton collisions, first by the experiments UA1 [213] and UA2 [214] at the SPS collider, which discovered the W and Z bosons, and subsequently with much higher precision by the experiments CDF [215] and DØ [216] at the Tevatron. Also the total width of the W boson, $\Gamma_{\rm W}$, is measured by the Tevatron experiments CDF [217] and DØ [218]. The results based on the data collected during Run-I of the Tevatron are final and are combined taking correlated systematic uncertainties into account. The combined results are [219]: $m_{\rm W} = 80.452 \pm 0.059$ GeV and $\Gamma_{\rm W} = 2.102 \pm 0.106$ GeV with an overall correlated error of -0.033 GeV or a correlation coefficient of -0.174 between mass and width. Improved direct measurements of $m_{\rm W}$ and $\Gamma_{\rm W}$ are expected from the currently ongoing Run-II of the Tevatron.

The LEP experiments ALEPH, DELPHI, L3 and OPAL also measure the W-boson mass and width directly in the process $\rm e^+e^- \to W^+W^-$, after the centre-of-mass energy of the LEP

accelerator was more than doubled (LEP-II). Combining all published [220] and *preliminary* LEP-II measurements, the LEP-II results are [221]: $m_{\rm W} = 80.412 \pm 0.042$ GeV and $\Gamma_{\rm W} = 2.150 \pm 0.091$ GeV.

The results obtained at hadron and lepton colliders are in very good agreement with each other. Combining the independent sets of results leads to *preliminary* direct determinations of the W-boson mass and width with high accuracy: $m_{\rm W} = 80.425 \pm 0.034$ GeV and $\Gamma_{\rm W} = 2.133 \pm 0.069$ GeV with a correlation coefficient of -0.067 between mass and width. As for the Z boson, the mass and width of the W boson quoted here are defined according to a Breit-Wigner denominator with s-dependent width, $|s - m_{\rm W}^2 + is\Gamma_{\rm W}/m_{\rm W}|$.

8.3.3 Measurements at Low Momentum Transfer

Combinations of effective coupling constants are also measured in low-Q^2 processes, $Q^2 \ll m_{\rm Z}^2$. However, owing to the running of effective coupling constants with Q^2, the couplings measured in low-Q^2 reactions are different from those measured at the Z pole, $Q^2 = m_{\rm Z}^2$. This running has to be accounted for before comparisons can be made.

Parity Violation in Atoms

The measurement of parity violation in atomic transitions determines the weak charge of the atomic nucleus as probed by the shell electron, $Q_{\rm W}(Z,N) = -2[(2Z+N)C_{\rm 1u} + (Z+2N)C_{\rm 1d}]$ for a nucleus with Z protons and N neutrons. The weak charges $C_{\rm 1q}$ of up and down quarks as seen by the electron through the parity-violating t-channel γ/Z exchange are expressed in terms of effective vector and axial-vector coupling constants, $C_{\rm 1q} = 2g_{\rm Ae}g_{\rm Vq}$ for $Q^2 \to 0$.

Precise measurements of $Q_{\rm W}$ are performed for cesium [222, 223], while less precise results are available for thallium [224, 225]. In recent years, certain aspects in nuclear many-body perturbation theory and QED radiative corrections needed in the experimental analyses have been investigated, see Reference 226 for a review. The newly corrected experimental results for cesium is: $Q_{\rm W}({\rm Cs}) = -72.74 \pm 0.46$ [226]. This result is now in good agreement with the SM calculation [227] included in TOPAZ0 and ZFITTER.

Parity Violation in Møller Scattering

The measurement of parity violation in fixed-target Møller scattering, $\rm e^-e^-$, with beam polarisation, determines the weak charge of the electron, $Q_{\rm W}({\rm e}) = -4g_{\rm Ae}g_{\rm Ve}$. The experiment E-158 at SLAC has published its final measurement [228, 229], performed at an average momentum transfer of $Q^2 = 0.026$ GeV^2. In terms of the weak mixing angle the result is: $\sin^2\theta_{\rm eff}(Q^2) = 0.2397 \pm 0.0013$ or $\sin^2\theta_{\overline{\rm MS}}(m_{\rm Z}) = 0.2330 \pm 0.0015$ using the SM running of the electroweak mixing angle with Q^2. Adding 0.00029 [84] to $\sin^2\theta_{\overline{\rm MS}}(m_{\rm Z})$ yields the effective electroweak mixing angle, $\sin^2\theta_{\rm eff}^{\rm lept}$.

Parity Violation in Neutrino-Nucleon Scattering

The measurement of the neutrino-nucleon neutral-to-charged current cross-section ratio also determines a combination of effective coupling constants. In the ideal case of an iso-scalar target and using both a ν_μ and $\bar\nu_\mu$ beam, the Paschos-Wolfenstein relations hold [230]: $R_\pm \equiv (\sigma_{NC}(\nu) \pm \sigma_{NC}(\bar\nu))/(\sigma_{CC}(\nu) \pm \sigma_{CC}(\bar\nu)) = g^2_{\nu{\rm Lud}} \pm g^2_{\nu{\rm Rud}}$, where $g^2_{\nu{\rm Lud}} = 4g^2_{{\rm L}\nu}(g^2_{\rm Lu} + g^2_{\rm Ld}) = [1/2 - \sin^4\theta_{\rm eff} + (5/9)\sin^4\theta_{\rm eff}]\rho_\nu\rho_{\rm ud}$ and $g^2_{\nu{\rm Rud}} = 4g^2_{{\rm L}\nu}(g^2_{\rm Ru} + g^2_{\rm Rd}) = (5/9)\sin^4\theta_{\rm eff}\rho_\nu\rho_{\rm ud}$. Historically,

the result is often quoted in terms of the on-shell electroweak mixing angle, adding small electroweak radiative corrections and assuming the SM values of the ρ_f parameters for light quarks and neutrinos.

Using both muon neutrino and muon anti-neutrino beams, the NuTeV collaboration has published by far the most precise result in neutrino-nucleon scattering [231], obtained at an average $Q^2 \simeq 20$ GeV^2. Based on an analysis mainly exploiting R_-, the results for the effective couplings defined above are: $g^2_{\nu\mathrm{Lud}} = 0.30005 \pm 0.00137$ and $g^2_{\nu\mathrm{Rud}} = 0.03076 \pm 0.00110$, with a correlation of -0.017. While the result on $g_{\nu\mathrm{Rud}}$ agrees with the SM expectation, the result on $g_{\nu\mathrm{Lud}}$, measured nearly eight times more precisely, shows a deficit with respect to the expectation at the level of 3.0 standard deviations. Possible large theoretical uncertainties in the area of radiative corrections and QCD effects affecting this measurement are discussed in References 232, 233, 234, 235, 236.

Assuming the SM value of $\sin^2\theta_W$, the result corresponds to a deficit of $(1.2 \pm 0.4)\%$ in either ρ_ν or ρ_{ud} [237]. Recall that the neutrino coupling ρ_ν as derived from Γ_{inv} measured at LEP and discussed in Chapter 7 shows a deficit of $(0.5 \pm 0.3)\%$.

Assuming the SM value of the ρ_f parameters for light quarks and neutrinos, the result converts to: $\sin^2\theta_W \equiv 1 - m^2_W/m^2_Z = 0.2277 \pm 0.0016 - 0.00022\frac{m_t^2 - (175\ \mathrm{GeV})^2}{(50\ \mathrm{GeV})^2} + 0.00032 \ln\frac{m_H}{150\ \mathrm{GeV}}$ [231], where the residual dependence of the result on the SM electroweak radiative corrections is explicitly parametrised. Using m_Z from LEP-I, Table 2.13, and ignoring the small m_t and m_H dependence, the $\sin^2\theta_W$ result corresponds to a W-boson mass of $m_W = 80.136 \pm 0.084$ GeV. This value differs from the direct measurement of m_W discussed above by 3.2 standard deviations.

8.4 Parametric and Theoretical Uncertainties

Since the interesting electroweak radiative corrections involving top-quark and Higgs-boson masses are typically on the order of 1% or less at the Z pole, all other effects must be controlled at the per-mille level in order to extract quantitatively these interesting SM effects and the parameters governing them. The precision with which the pseudo-observables can be calculated within the framework of the SM is determined by both theoretical uncertainties and by the manner in which the pseudo-observables depend on the five SM input parameters. When a pseudo-observable depends on several SM parameters, some of which are only poorly determined, the resulting parametric uncertainty can become significant. Due to their importance in determining the precision with which the five SM input parameters can be measured, these parameter dependencies and theoretical uncertainties are discussed in the following.

8.4.1 Parameter Dependence

The fact that the pseudo-observables depend on the five SM input parameters is of course essential for allowing these parameters to be extracted from the data. For determining the interesting SM input parameters, namely the mass of the top quark and the mass of the Higgs boson, a large parametric dependence, or sensitivity, is advantageous, while dependence on the other SM input parameters, in particular the hadronic vacuum polarisation, should be small, in order to limit the resulting parametric uncertainties. Since all five SM input parameters are determined in parallel, these intertwined dependencies are properly accounted for automatically by the analysis procedure discussed in Section 8.5.

Source	δ	$\Gamma_{\rm Z}$ [MeV]	$\sigma^0_{\rm had}$ [nb]	R^0_ℓ	$R^0_{\rm b}$	ρ_ℓ	$\sin^2\theta^{\rm lept}_{\rm eff}$	$m_{\rm W}$ [MeV]
$\Delta\alpha^{(5)}_{\rm had}(m^2_{\rm Z})$	0.00035	0.3	0.001	0.002	0.00001	—	0.00012	6
$\alpha_{\rm S}(m^2_{\rm Z})$	0.003	1.6	0.015	0.020	—	—	0.00001	2
$m_{\rm Z}$	2.1 MeV	0.2	0.002	—	—	—	0.00002	3
$m_{\rm t}$	4.3 GeV	1.0	0.003	0.002	0.00016	0.0004	0.00014	26
$\log_{10}(m_{\rm H}/{\rm GeV})$	0.2	1.3	0.001	0.004	0.00002	0.0003	0.00022	28
Theory		0.1	0.001	0.001	0.00002	—	0.00005	4
Experiment		2.3	0.037	0.025	0.00065	0.0010	0.00016	34

Table 8.1: Uncertainties on the theoretical calculations of selected Z-pole observables and $m_{\rm W}$. Top: parametric uncertainties caused by the five SM input parameters. For each observable, the change is shown when varying the SM input parameter listed in the first column by the amount δ listed in the second column, around the following central values: $\Delta\alpha^{(5)}_{\rm had}(m^2_{\rm Z}) = 0.02758$, $\alpha_{\rm S}(m^2_{\rm Z}) = 0.118$, $m_{\rm Z} = 91.1875$ GeV, $m_{\rm t} = 178$ GeV, $m_{\rm H} = 150$ GeV. Where no number is listed, the effect is smaller than half a unit in the number of digits quoted. Bottom: theoretical uncertainties due to missing higher-order corrections estimated through variation of calculational schemes implemented in ZFITTER (half of full range of values). For comparison, the uncertainties on the experimental measurements are shown in the last row.

In general, the pseudo-observables fall into three groups. First, there are the pseudo-observables which are also SM input parameters, namely the mass of the Z boson, the hadronic vacuum polarisation, and the mass of the top quark. Second, there are the pseudo-observables which have, compared to their experimental uncertainties, very little dependence on the five SM input parameters, such as $\sigma^0_{\rm had}$ or the quark left-right forward-backward asymmetries determining the quark asymmetry parameter $\mathcal{A}_{\rm q}$. Nevertheless they test the SM independent of radiative corrections in terms of its static properties, such as the number of fermion generations or the quantum numbers for weak isospin and electric charge assigned to the fundamental fermions. Third, there are the pseudo-observables which are highly sensitive to electroweak radiative corrections, such as partial widths and the various asymmetries. They determine the ρ parameter and the effective electroweak mixing angle as discussed in the previous chapter.

Numerical results for parametric uncertainties of several selected pseudo-observables are reported in Table 8.1. Direct quantitative comparisons of the interesting SM top-quark and Higgs-boson mass sensitivities of the observables are shown in Figures 8.1 and 8.2; where the sensitivities are quantified as the partial derivative of the SM calculation of the observable with respect to $m_{\rm t}$ or $\log_{10}(m_{\rm H}/{\rm GeV})$, relative to the total measurement error of the observable and multiplied by the uncertainty δ in $m_{\rm t}$ or $\log_{10}(m_{\rm H}/{\rm GeV})$ as listed in Table 8.1, so that they are dimensionless and thus comparable in terms of the ratios of the standard deviations of observable and SM input parameter. For measured observables which are also SM input parameters, their scaled sensitivity is unity with respect to themselves, and vanishes with respect to the other SM input parameters. However, through correlations in multi-parameter fits, measurements of SM input parameters do influence the values and errors of all SM input parameters extracted from fits to the data set, including the mass of the Higgs boson.

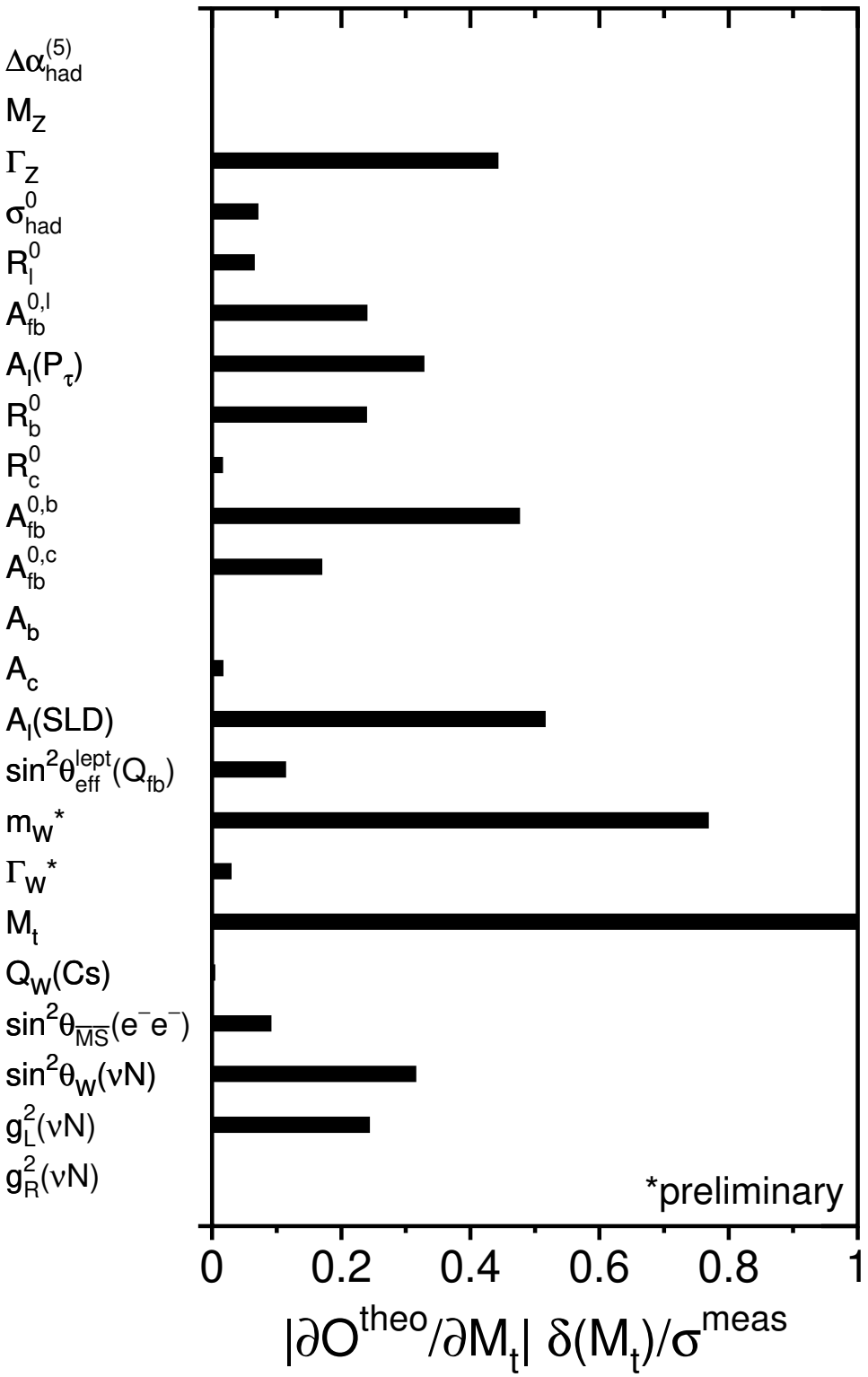

Figure 8.1: Sensitivity of each pseudo-observable to the mass of the top quark, defined as the partial derivative of the SM calculation of the observable with respect to $m_{\rm t}$, relative to the total measurement error σ on the pseudo-observable, and multiplied by the ± 4.3 GeV uncertainty δ in the Tevatron Run-I measurement of $m_{\rm t}$. The other SM input parameters are kept fixed at values $\Delta\alpha^{(5)}_{\rm had}(m^2_{\rm Z}) = 0.02758$, $\alpha_{\rm S}(m^2_{\rm Z}) = 0.118$, $m_{\rm Z} = 91.1875$ GeV, and $m_{\rm H} = 150$ GeV. The direct measurements of $m_{\rm W}$ and $\Gamma_{\rm W}$ used here are preliminary.

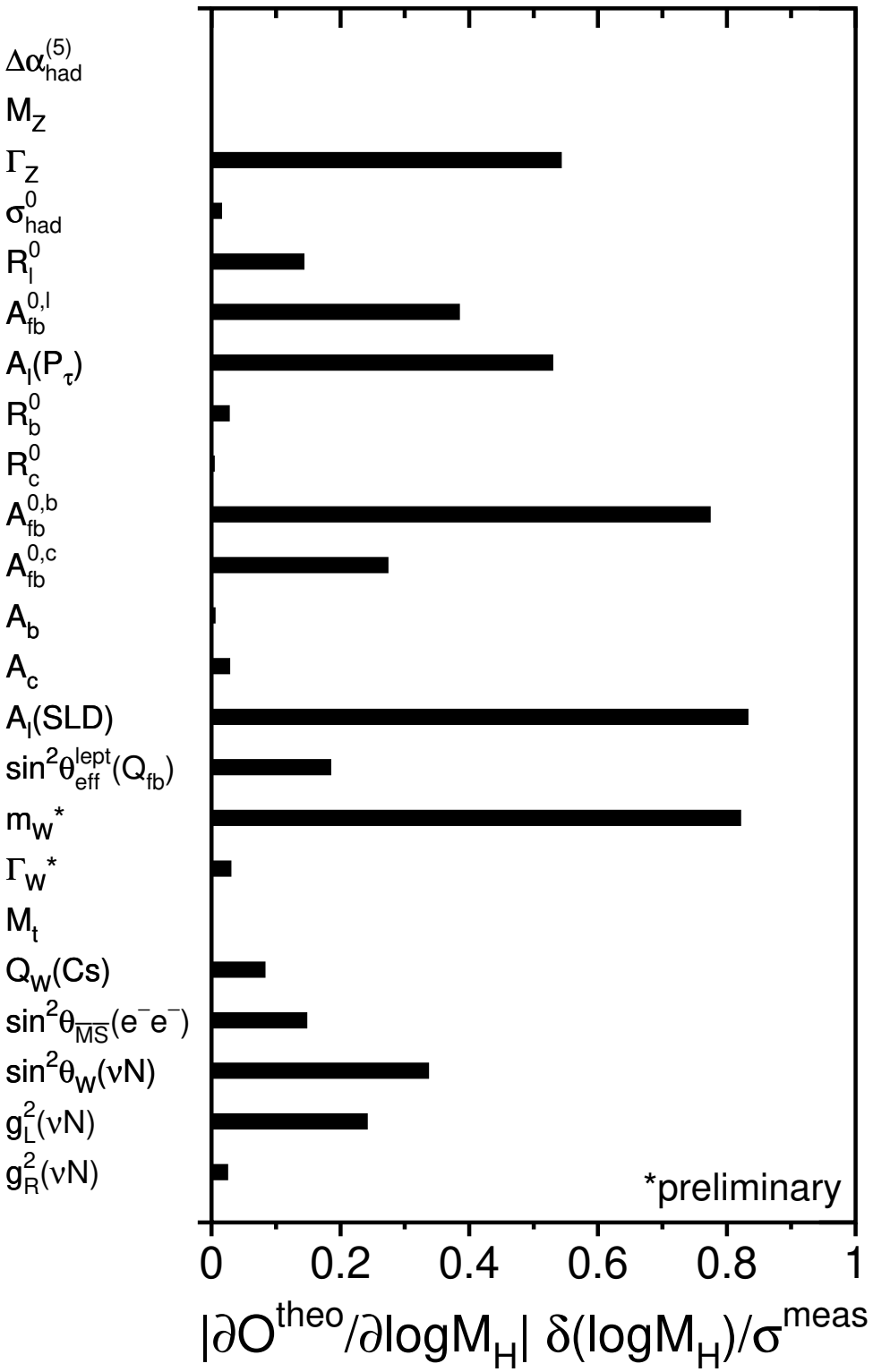

Figure 8.2: Sensitivity of each pseudo-observable to the mass of the Higgs boson, defined as the partial derivative of the SM calculation of the observable with respect to $\log_{10}(m_{\rm H}/{\rm GeV})$, relative to the total measurement error σ on the pseudo-observable, and multiplied by the ± 0.2 uncertainty δ in $\log_{10}(m_{\rm H}/{\rm GeV})$ (see Tables 8.1 and 8.3). The other SM input parameters are kept fixed at values $\Delta\alpha^{(5)}_{\rm had}(m^2_{\rm Z}) = 0.02758$, $\alpha_{\rm S}(m^2_{\rm Z}) = 0.118$, $m_{\rm Z} = 91.1875$ GeV, and $m_{\rm t} = 178$ GeV. The direct measurements of $m_{\rm W}$ and $\Gamma_{\rm W}$ used here are preliminary.

Relative to their measurement accuracy, four pseudo-observables are particularly sensitive to the masses of the interesting SM particles, the top quark or the Higgs boson, while at the same time are largely independent of QCD effects. These pseudo-observables are R_{b}^{0}, $\Gamma_{\ell\ell}$, $\sin^2\theta_{\mathrm{eff}}^{\mathrm{lept}}$ and m_{W}. Each of these measurements imposes a constraint on the size of electroweak radiative corrections, which is graphically shown in Figure 8.3 as a band in the $(m_{\mathrm{H}}, m_{\mathrm{t}})$ plane. Significant non-linearities occur in these constraints over the allowed m_{H} range.

Owing to the top-dependent vertex corrections as shown in Figure 1.10, the quantity R_{b} is sensitive to m_{t}, while as a ratio of hadronic decay widths it is largely insensitive to the other four SM input parameters, including the mass of the Higgs boson, as shown in Figure 7.8. Within the SM framework, the measurement of R_{b}^{0} therefore provides particularly unambiguous information on m_{t}. If R_{b}^{0} had been measured smaller (i.e., its band shifted upwards in Figure 8.3) by a standard deviation, the indirect constraints on m_{t} and m_{H} would both move toward higher values, along the almost parallel and overlapping bands of the $\Gamma_{\ell\ell}$, $\sin^2\theta_{\mathrm{eff}}^{\mathrm{lept}}$ and m_{W} constraints.

The $\Gamma_{\ell\ell}$ band shown in Figure 8.3 implies that the preferred m_{t} exhibits a broad minimum around $m_{\mathrm{H}} \approx 50$ GeV. In combination with the R_{b}^{0} band preferring an even lower value of m_{t}, this results in an indirect determination of m_{t} which is remarkably stable against variations in $\sin^2\theta_{\mathrm{eff}}^{\mathrm{lept}}$. In contrast with the enhanced stability of the m_{t} determination, the favoured value of m_{H} is very sensitive to $\sin^2\theta_{\mathrm{eff}}^{\mathrm{lept}}$. It should also be noted that, of all the bands, only $\sin^2\theta_{\mathrm{eff}}^{\mathrm{lept}}$ is sensitive to the value of $\Delta\alpha_{\mathrm{had}}^{(5)}(m_{\mathrm{Z}}^2)$, as indicated by the arrow in Figure 8.3.

The effects of ZH production, or real Higgsstrahlung, are ignored here, as well as in all results quoted in this paper. They are negligible for $m_{\mathrm{H}} > 50$ GeV. For $m_{\mathrm{H}} < 50$ GeV, the rise of m_{t} with decreasing m_{H} predicted by the $\Gamma_{\ell\ell}$ constraint band would be somewhat suppressed, due to the fact that most, but not all, ZH events where the Z decays to leptons would have been classed as contributing to Γ_{had} rather than $\Gamma_{\ell\ell}$. Based on a detailed analysis [29] it is concluded that, apart from the determination of α_{S}, Higgsstrahlung would not appreciably shift the results of the SM analyses presented in Section 8.6.

The dependence of all pseudo-observables on the mass of the Higgs boson within the framework of the SM is visualised in Figures 8.4 to 8.7, comparing the experimental result with the value of the observable calculated within the framework of the minimal SM as a function of the Higgs-boson mass. Non-linear effects, as already observed in Figure 8.3, are clearly visible.

For the quantity $\sin^2\theta_{\mathrm{eff}}^{\mathrm{lept}}$ determined in various asymmetry measurements, it has already been shown in Figure 7.6 that the parametric uncertainty on the SM prediction arising from $\Delta\alpha_{\mathrm{had}}^{(5)}(m_{\mathrm{Z}}^2)$ is non-negligible compared to the experimental uncertainty of the average. As a consequence, the uncertainty on the hadronic vacuum polarisation is one of the limiting factors in the extraction of the mass of the Higgs boson. This situation underlines the importance of further improved determinations of the hadronic vacuum polarisation through measurements of the hadronic cross-section in electron-positron annihilations at low centre-of-mass energies. Compared to $\sin^2\theta_{\mathrm{eff}}^{\mathrm{lept}}$, the W-boson mass is relatively less sensitive to $\Delta\alpha_{\mathrm{had}}^{(5)}(m_{\mathrm{Z}}^2)$ than to m_{t} and m_{H}, making m_{W}, measured at the Tevatron and at LEP-II, an ideal observable to further reduce the error on the prediction of the Higgs-boson mass.

8.4.2 Theoretical Uncertainties

Theoretical uncertainties in radiative corrections and the calculation of pseudo-observables arise due to the fact that the perturbative expansion is known and calculated only up to a finite order. Many theorists perform the various complicated calculations of radiative corrections. In order to make this work accessible to experimentalists in a consistent way, the relevant calculations

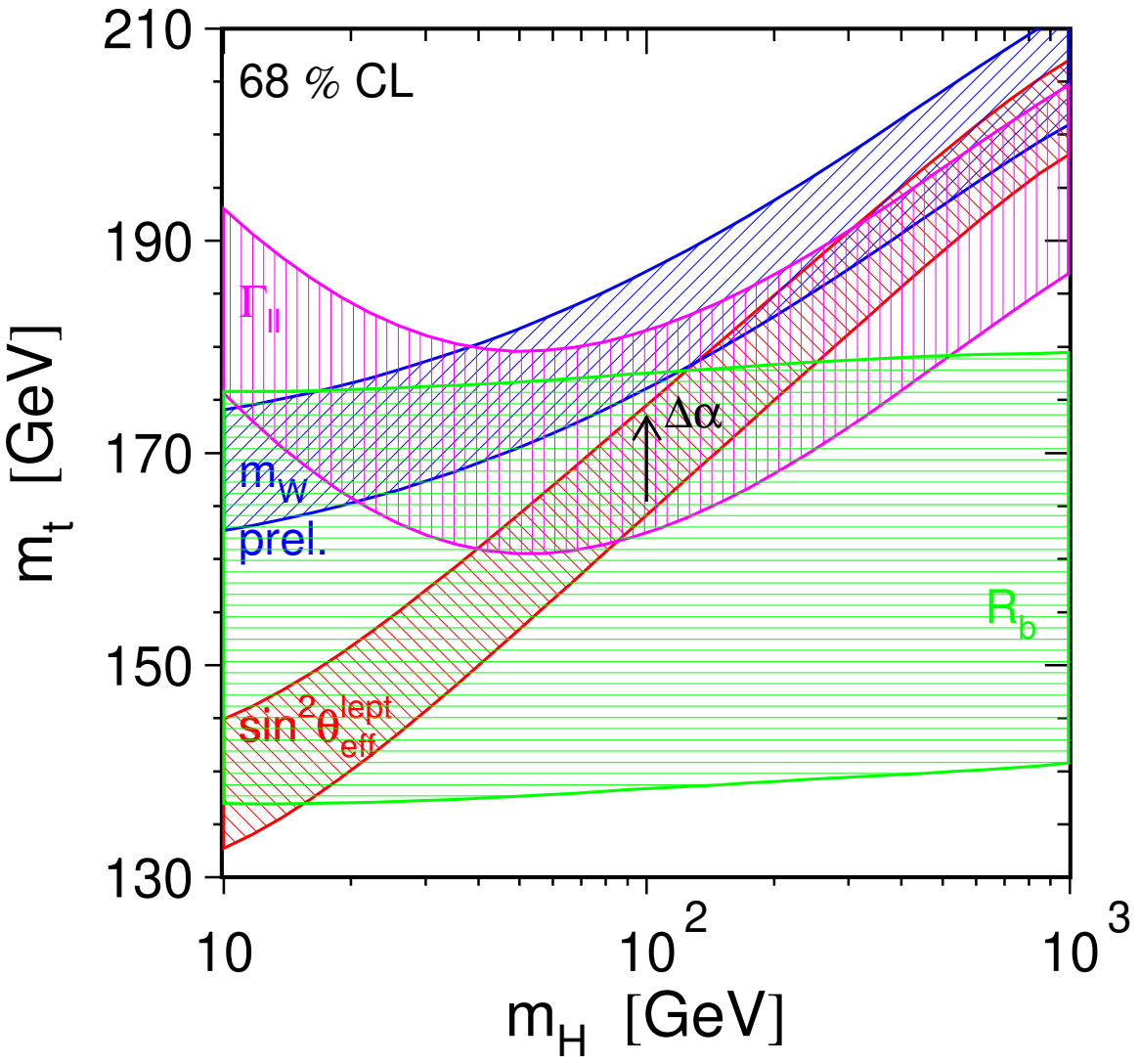

Figure 8.3: Constraints on m_{t} and m_{H} from measurements of R^0_{b}, $\Gamma_{\ell\ell}$, $\sin^2\theta^{\mathrm{lept}}_{\mathrm{eff}}$ and m_{W}. Each band gives the $\pm1\sigma$ constraint from the indicated measurement. The parametric uncertainty due to the uncertainty in the hadronic vacuum polarisation, $\Delta\alpha^{(5)}_{\mathrm{had}}(m^2_{\mathrm{Z}}) = 0.02758 \pm 0.00035$, is not included in the width of these bands as it is small except for the $\sin^2\theta^{\mathrm{lept}}_{\mathrm{eff}}$ band, where the $\pm1\sigma$ uncertainty is indicated by the arrow labeled $\Delta\alpha$. The direct measurement of m_{W} used here is preliminary.

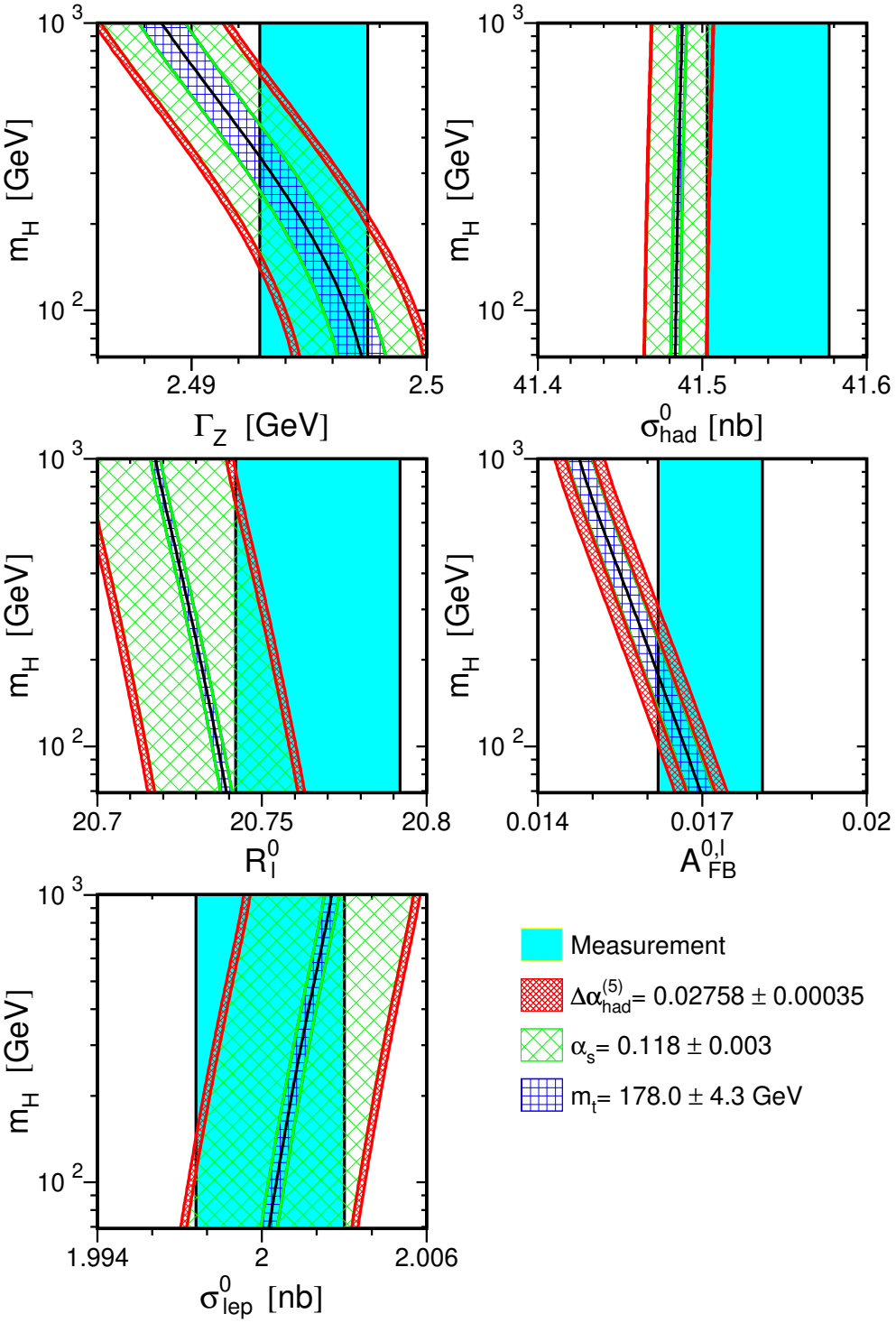

Figure 8.4: Comparison of the LEP combined measurements of $\Gamma_{\rm Z}$, $\sigma^0_{\rm had}$, R^0_ℓ, $A^{0,\ell}_{\rm FB}$ and $\sigma^0_{\rm lep}$ with the SM prediction as a function of the mass of the Higgs boson. The measurement with its uncertainty is shown as the vertical band. The width of the SM band arises due to the uncertainties in $\Delta\alpha^{(5)}_{\rm had}(m^2_{\rm Z})$, $\alpha_{\rm S}(m^2_{\rm Z})$ and $m_{\rm t}$ in the ranges indicated. The total width of the band is the linear sum of these uncertainties.

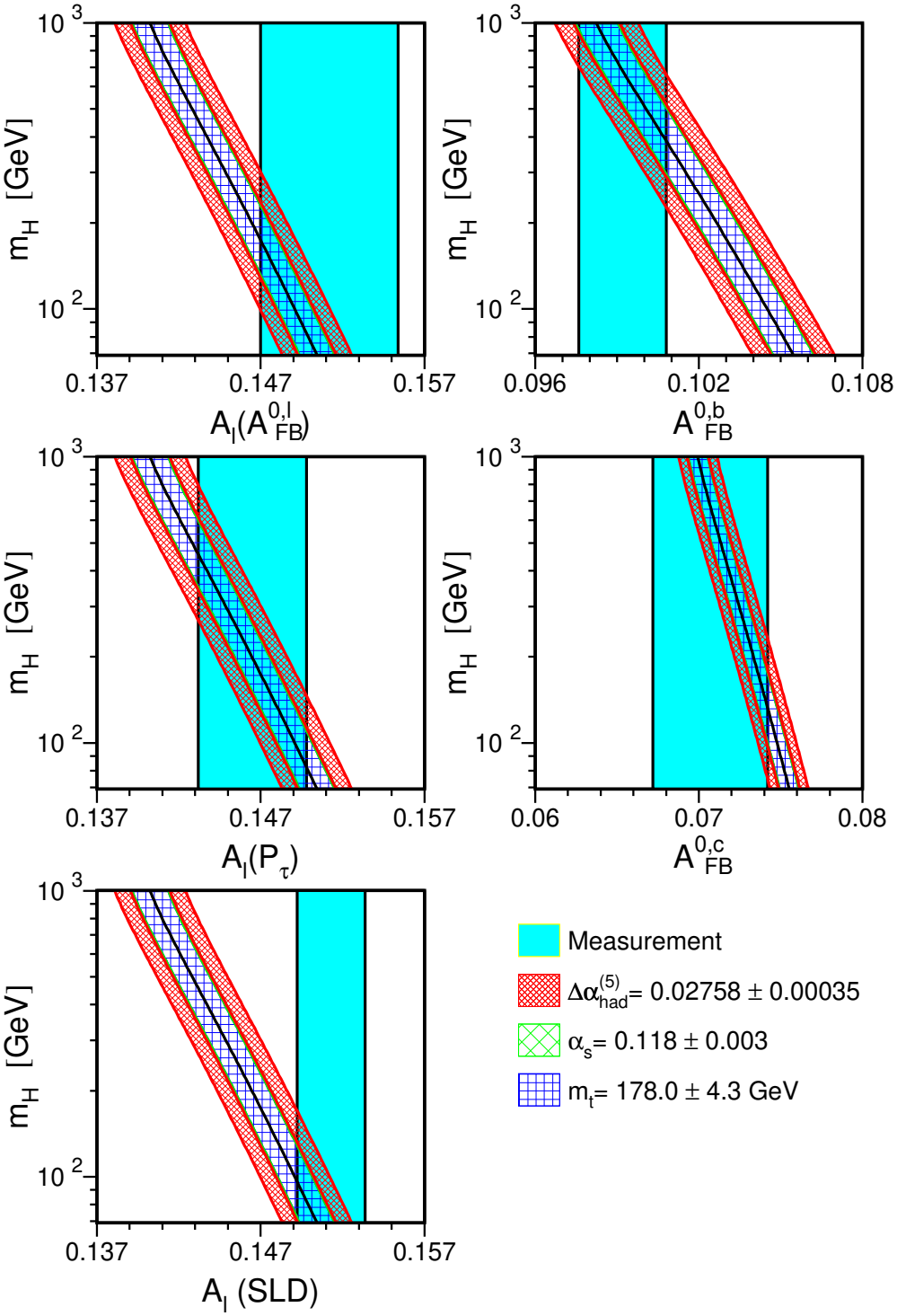

Figure 8.5: Comparison of the LEP/SLD combined measurements of $\mathcal{A}_\ell(A_{\rm FB}^{0,\ell})$, $\mathcal{A}_\ell(P_\tau)$, $\mathcal{A}_\ell$(SLD), $A_{\rm FB}^{0,\rm b}$ and $A_{\rm FB}^{0,\rm c}$ with the SM prediction as a function of the mass of the Higgs boson. The measurement with its uncertainty is shown as the vertical band. The width of the SM band arises due to the uncertainties in $\Delta\alpha_{\rm had}^{(5)}(m_{\rm Z}^2)$, $\alpha_{\rm S}(m_{\rm Z}^2)$ and $m_{\rm t}$ in the ranges indicated. The total width of the band is the linear sum of these uncertainties.

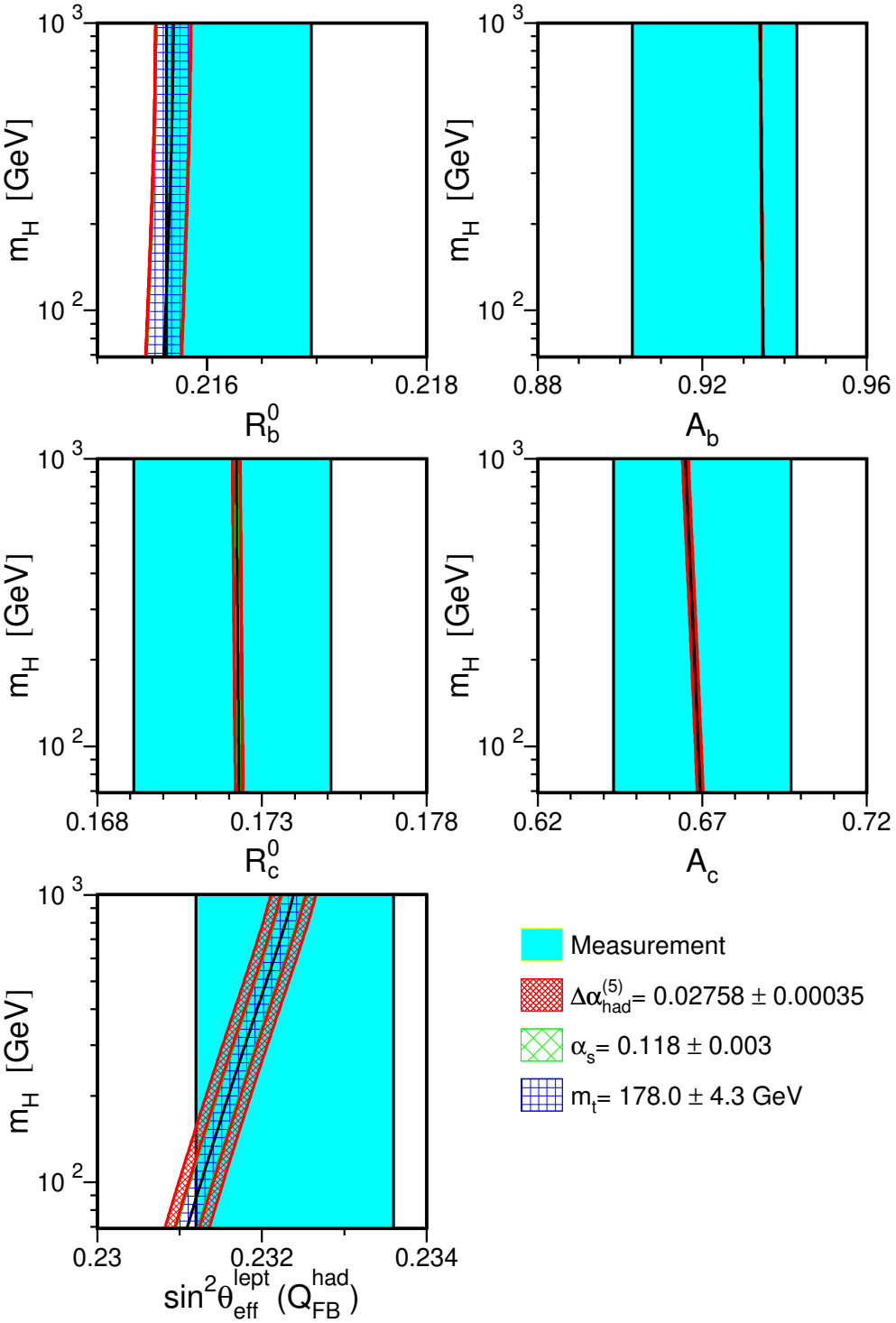

Figure 8.6: Comparison of the LEP/SLD combined measurements of R_{b}^0, R_{c}^0, $\mathcal{A}_{\mathrm{b}}$, $\mathcal{A}_{\mathrm{c}}$ and $\sin^2\theta_{\mathrm{eff}}^{\mathrm{lept}}(Q_{\mathrm{FB}}^{\mathrm{had}})$ with the SM prediction as a function of the mass of the Higgs boson. The measurement with its uncertainty is shown as the vertical band. The width of the SM band arises due to the uncertainties in $\Delta\alpha_{\mathrm{had}}^{(5)}(m_{\mathrm{Z}}^2)$, $\alpha_{\mathrm{S}}(m_{\mathrm{Z}}^2)$ and m_{t} in the ranges indicated. The total width of the band is the linear sum of these uncertainties.

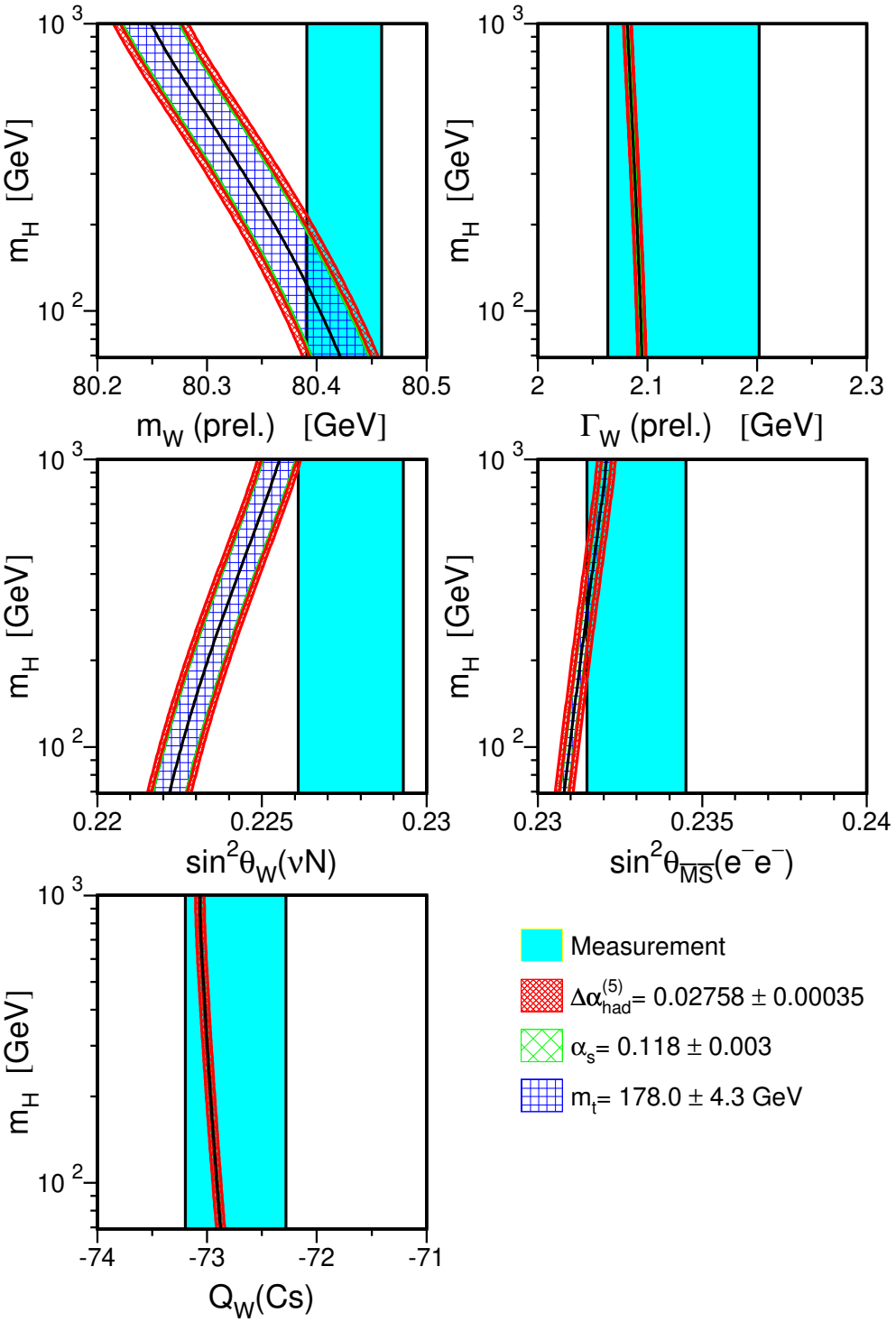

Figure 8.7: Comparison of the combined measurements of m_{W} and Γ_{W}, and the results from low Q^2 processes $\sin^2\theta_{\mathrm{W}}$ (νN), $\sin^2\theta_{\overline{\mathrm{MS}}}(m_{\mathrm{Z}})$ ($\mathrm{e^-e^-}$) and Q_{W} (APV) with the SM prediction as a function of the mass of the Higgs boson. The measurement with its uncertainty is shown as the vertical band. The width of the SM band arises due to the uncertainties in $\Delta\alpha^{(5)}_{\mathrm{had}}(m^2_{\mathrm{Z}})$, $\alpha_{\mathrm{S}}(m^2_{\mathrm{Z}})$ and m_{t} in the ranges indicated. The total width of the band is the linear sum of these uncertainties. The direct measurements of m_{W} and Γ_{W} used here are preliminary.

are incorporated in computer programs such as TOPAZ0 [30], using the general minimal subtraction renormalisation scheme, and ZFITTER [31], using the on-mass-shell renormalisation scheme. For the realistic observables, the measured cross-sections and asymmetries, the following corrections are included in TOPAZ0 and ZFITTER: up to $\mathcal{O}(\alpha^2)$ and leading $\mathcal{O}(\alpha^3)$ for initial-state QED radiation including pairs, $\mathcal{O}(\alpha)$ for final-state QED radiation and QED initial-final state interference, $\mathcal{O}(\alpha_S^3)$ for final-state QCD radiation and $\mathcal{O}(\alpha\alpha_S)$ for mixed QED/QCD final-state radiation. These corrections are needed to extract the pseudo-observables discussed in this report from the realistic observables. For the calculation of the expectation for the extracted pseudo-observables discussed in this report, the final-state corrections listed above are also available for the Z decay widths. Furthermore, complete one-loop electroweak radiative corrections, re-summed leading one-loop corrections and two-loop corrections up to $\mathcal{O}(\alpha\alpha_S, \alpha\alpha_S^2, G_F^2 m_t^4, G_F^2 m_t^2 m_Z^2, G_F m_t^2 \alpha_S, G_F m_t^2 \alpha_S^2)$ are included. Overviews and summaries of radiative corrections in Z-pole physics are given in References 238, 239, 32, which should be consulted for references to the original calculations.

Missing higher-order electroweak, strong and mixed corrections cause the calculation of any observable to be incomplete and thus approximate. Ambiguities also arise due to the choice of renormalisation schemes, re-summation schemes, momentum-transfer scales in loop corrections, and schemes to implement the factorisation of various corrections. These ambiguities reflect and are of the same order as the missing higher-order corrections. The uncertainty on the predicted observables due to these effects is thus estimated by comparing results obtained using different calculations performed to equivalent order [239, 240, 75, 241, 242]. Recent developments in the calculation of electroweak radiative corrections include the complete two-loop corrections for the mass of the W boson [243], leading three-loop top-quark contributions to the ρ parameter [244], and fermionic two-loop corrections for the effective electroweak mixing angle [245]. The remaining theoretical uncertainties are estimated to be ± 4 MeV in m_W [243] and $\pm 4.9 \cdot 10^{-5}$ in $\sin^2\theta_{\rm eff}^{\rm lept}$ [245], respectively.

The recent calculations and their associated theoretical uncertainties are implemented in ZFITTER 6.42 [31] and used here.[2] Numerical results for theoretical uncertainties calculated with ZFITTER are reported in Table 8.1 for several pseudo-observables. The uncertainties due to missing higher-orders are in general small compared to the leading parametric uncertainties, with the exception of the effective electroweak mixing angle. The latter uncertainty dominates all other theoretical uncertainties in global SM analyses.

QCD Uncertainties

The largest QCD correction in the calculation of Z-pole observables arises through the final-state QCD radiation factor in quark-pair production (Equation 1.37), modifying the decay width of the Z into hadrons, $\Gamma_{\rm had}$, and thus also the Z-pole observables $\Gamma_{\rm tot}$, R_ℓ^0, $\sigma_{\rm had}^0$ and $\sigma_{\rm lep}^0$, which depend trivially on $\Gamma_{\rm had}$. The quark asymmetries also require significant QCD corrections. The theoretical uncertainty in the calculation of the observables related to $\Gamma_{\rm had}$ due to unknown higher-order QCD effects, and conversely in the $\alpha_S(m_Z^2)$ values extracted from measurements of these quantities, is a subject of current discussion. Estimates of the corresponding theoretical uncertainty on $\alpha_S(m_Z^2)$ extracted from these observables vary from

[2] The default flags of ZFITTER 6.42 are used, except for setting `AMT4=6` to access these latest electroweak radiative corrections and setting `ALEM=2` to take into account the externally supplied value of $\Delta\alpha_{\rm had}^{(5)}(m_Z^2)$. The effects of the theoretical uncertainties in the calculations of m_W and $\sin^2\theta_{\rm eff}^{\rm lept}$ are simulated by changing the ZFITTER flags `DMWW` and `DSWW` from their default value of `0` to `±1`.

0.0005 to 0.003 [246, 247, 248, 249, 250], a range which spans the uncertainty on $\alpha_S(m_Z^2)$ caused by the experimental errors on the measured hadronic Z-pole observables.

Virtual quark loops with additional gluon exchange induce QCD corrections to the propagators, which introduce an additional, but much smaller α_S dependence in the calculation of each Z-pole observable, mainly through ρ_f and κ_f. These two-loop $\mathcal{O}(\alpha\alpha_S)$ corrections are small but known to leading order only, hence smaller but non-negligible additional theoretical uncertainties on the prediction of any Z-pole observable arise.

This has several consequences: The extracted value of $\alpha_S(m_Z^2)$ is mainly given by the dependence of the hadronic Z-pole observables on the final-state QCD radiation factor. As it is the very same final-state QCD correction factor entering the calculation of all hadronic Z-pole observables, most theoretical QCD uncertainties are fully correlated and affect the extracted $\alpha_S(m_Z^2)$ value independent of which observable is used. Because of this strong correlation, the extracted values of the other SM input parameters are largely insensitive to the theoretical uncertainty due to unknown higher-order QCD effects, as in the fit any such bias is effectively absorbed in the fit value of $\alpha_S(m_Z^2)$.[3]

8.5 Analysis Procedure

In order to determine the five relevant SM input parameters a χ^2 minimisation is performed using the program MINUIT [251]. The χ^2 is calculated as usual by comparing the measurements of Z-pole and other observables, their errors and correlations including those discussed in Chapter 7.1, with the predictions calculated in the framework of the SM. The results combined in the previous chapters under the hypothesis of lepton universality, which is inherent to the SM, are used for measurements of leptonic Z-pole observables. All are reported in Table 8.4. The predictions are calculated as a function of the five SM input parameters by the program ZFITTER, while TOPAZ0 and ZFITTER are used to calculate theoretical uncertainties. Both programs include all relevant electroweak radiative corrections. All five SM input parameters are allowed to vary in the fit, so that parametric uncertainties are correctly treated and propagated.

This analysis procedure tests quantitatively how well the SM is able to describe the complete set of all measurements with just one value for each of the five SM input parameters. For interpreting the adequacy of this description, however, the large contribution to the χ^2 arising from the asymmetry measurements as discussed in the previous chapter has to be taken into account.

In addition, the mass of the only particle of the SM which remains without significant direct experimental evidence, the mass of the Higgs boson, will be constrained. For this determination, the additional measurements presented in Section 8.3, such as the direct measurements of m_W and m_t at LEP-II and the Tevatron, are also included, in order to obtain the best precision.

In the case of those observables which are SM input parameters and thus fit parameters, such as m_Z, $\Delta\alpha^{(5)}_{had}(m_Z^2)$ and m_t, special care is needed when evaluating the performance of various measurements in constraining the fitted mass of the Higgs boson. As in general all measurements carry information about all SM input parameters, a shift of such a measurement by one standard deviation does not lead to a shift of the fitted Higgs-boson mass given by the

[3] Note that this theoretical uncertainty would have to be known quantitatively and included explicitly if external measurements of $\alpha_S(m_Z^2)$ were included in the analyses. For the SM analyses presented here, however, this is not necessary as external constraints on $\alpha_S(m_Z^2)$, even without any uncertainty, would not lead to reduced uncertainties on the other SM input parameters.

corresponding fitted correlation coefficient. As for all other measurements, a fit to the new set of measurements has to be performed.

8.5.1 Treatment of Systematic Uncertainties

As discussed in detail in the previous chapters, the experimental measurements have associated uncertainties which are of both statistical and systematic nature. Both sources are assumed to be and are treated as Gaussian errors corresponding to a symmetric interval around the central value with 68% probability content. While this is a valid model for statistical and many systematic errors, some systematic uncertainties are derived from discrete tests, e.g., performing a Monte Carlo test with and without a certain option affecting the event generation and detector simulation. For errors of this type, a flat, box-like probability distribution, or any other, could also be applicable. For the analyses presented in the following, studies show that the central values of the fitted parameters are affected only slightly by the particular choice of the probability density function for such uncertainties. A somewhat larger effect is seen for the fitted uncertainty of the fitted parameters. Since a box of size $\pm\sigma$ has a spread of $\pm\sigma/\sqrt{3}$, the uncertainties of the fitted parameters would decrease if such a model were to be applied to these less tractable errors. Thus the results presented below are considered conservative.

Theoretical uncertainties due to missing higher order corrections as discussed above are typically implemented by offering various choices or options in the programs TOPAZ0 and ZFITTER when calculating radiative corrections. As these choices correspond to discrete options (flags), they cannot be varied during a fit. Rather, the analysis is repeated with different flag settings. The change in the five extracted SM input parameters is taken as an estimate of the theoretical uncertainty for the option studied. The flags are varied one by one and the fits are repeated. The maximum deviation of any given flag change is taken as the theoretical uncertainty, thus avoiding double counting due to correlated variations governed by different flags. Since this uncertainty is usually much smaller than the uncertainty arising from the experimental uncertainties in the measured Z-pole observables (Table 8.1), it is not included in the results presented in the following. By far the largest electroweak theoretical uncertainty affecting the determination of the five SM input parameters, mainly the mass of the Higgs boson, is that of the effective electroweak mixing angle.

8.6 Standard Model Analyses

8.6.1 Z-Pole Results

Based on the electroweak observables measured at LEP-I and by SLD, and presented before, a fit is performed to the hadronic vacuum polarisation and the 14 Z-pole observables derived under the assumption of lepton universality, in order to determine the five input parameters of the SM. The result is reported in Table 8.2. A χ^2/dof of 16.0/10 is obtained, corresponding to a probability of 9.9%. The largest contribution to the χ^2 arises from the asymmetry measurements as discussed in Section 7.3.5. The SM describes the complete set of measurements with a unique set of values for the five SM input parameters.

Tests show that the inclusion of a direct measurement of $\alpha_S(m_Z^2)$, or even fixing $\alpha_S(m_Z^2)$, results in negligible improvements in the determination of the other SM input parameters, since correlation coefficients between $\alpha_S(m_Z^2)$ and all other parameters are small. Similarly, the cross-section scale, which depends directly on the normalization of the luminosity measurement,

Parameter	Value	Correlations				
		$\Delta\alpha^{(5)}_{\rm had}(m^2_{\rm Z})$	$\alpha_{\rm S}(m^2_{\rm Z})$	$m_{\rm Z}$	$m_{\rm t}$	$\log_{10}(m_{\rm H}/{\rm GeV})$
$\Delta\alpha^{(5)}_{\rm had}(m^2_{\rm Z})$	0.02759 ± 0.00035	1.00				
$\alpha_{\rm S}(m^2_{\rm Z})$	0.1190 ± 0.0027	-0.04	1.00			
$m_{\rm Z}$ [GeV]	91.1874 ± 0.0021	-0.01	-0.03	1.00		
$m_{\rm t}$ [GeV]	$173\pm^{13}_{10}$	-0.03	0.19	-0.07	1.00	
$\log_{10}(m_{\rm H}/{\rm GeV})$	$2.05\pm^{0.43}_{0.34}$	-0.29	0.25	-0.02	0.89	1.00
$m_{\rm H}$ [GeV]	$111\pm^{190}_{60}$	-0.29	0.25	-0.02	0.89	1.00

Table 8.2: Results for the five SM input parameters derived from a fit to the Z-pole results and $\Delta\alpha^{(5)}_{\rm had}(m^2_{\rm Z})$. The fit has a χ^2/dof of 16.0/10, corresponding to a probability of 9.9%. See Section 8.4 for a discussion of the theoretical uncertainties not included here. The results on $m_{\rm H}$, obtained by exponentiating the fit results on $\log_{10}(m_{\rm H}/{\rm GeV})$, are also shown.

decouples from other SM input parameters. The fit results are rather stable except for a small shift in $\alpha_{\rm S}(m^2_{\rm Z})$ when the measurement containing the cross-section normalisation, $\sigma^0_{\rm had}$, is dropped from the input measurements.

Discussion

The Z-pole data alone are not able to improve significantly on the determination of $\Delta\alpha^{(5)}_{\rm had}(m^2_{\rm Z})$ compared to the direct determination presented in Section 8.2. The strong coupling constant, $\alpha_{\rm S}(m^2_{\rm Z})$, mainly determined by the leptonic pole cross-section $\sigma^0_{\rm lep} = \sigma^0_{\rm had}/R^0_\ell$ as discussed in Sections 7.2 and 26 and shown in Figure 8.4, is one of the most precise determinations of this quantity and in good agreement with other determinations [249] and the world average [84], but theoretical issues currently obscure the appropriate theoretical uncertainty to assign in its interpretation, as discussed in Section 8.4.2. A dedicated analysis following the detailed prescription given in Reference 250 yields a theoretical uncertainty of 0.0010 on $\alpha_{\rm S}(m^2_{\rm Z})$ extracted from this set of Z-pole measurements.

The role of the mass of the Z boson is now changed from that of a model-independent parameter, unrelated to the other pseudo-observables except for defining the pole position in the extraction of the pole observables, to that of a fundamental input parameter of the SM affecting the calculation of all pseudo-observables. Because of its high precision with respect to the other measurements, the uncertainty on $m_{\rm Z}$ remains unchanged.

The pole mass of the top quark is predicted with an accuracy of about 12 GeV. This precise prediction for a fundamental particle of the SM not directly accessible at the Z pole emphasises clearly the predictive power of the SM as well as the precision of the experimental results.

Despite the logarithmic dependence of the electroweak radiative corrections on the mass of the Higgs boson, its value is nevertheless predicted within a factor of about 2. The value obtained shows the self-consistency of the SM analysis presented here, as such an analysis would be inconsistent and invalid for resulting Higgs-boson masses too small, as discussed in Section 1.5.4, or close to or larger than 1 TeV. The large correlation coefficient of $m_{\rm H}$ with $m_{\rm t}$ shows that the precision of the $m_{\rm H}$ prediction will significantly improve when the direct measurement of $m_{\rm t}$ is included, as will be shown in Section 8.6.3.

Having determined the five SM input parameters as given in Table 8.2, the parameters discussed in Section 1.4 are then predicted to be:

$$\begin{aligned}
\sin^2\theta_{\mathrm{W}} &= 0.22331 \pm 0.00062 & & \\
\sin^2\theta^{\mathrm{lept}}_{\mathrm{eff}} &= 0.23149 \pm 0.00016 & \kappa_\ell &= 1.0366 \pm 0.0025 \\
\sin^2\theta^{\mathrm{b}}_{\mathrm{eff}} &= 0.23293 \pm^{0.00031}_{0.00025} & \kappa_{\mathrm{b}} &= 1.0431 \pm 0.0036 \\
\rho_\ell &= 1.00509 \pm^{0.00067}_{0.00081} & -\Delta r_{\mathrm{w}} &= 0.0242 \pm 0.0021 \\
\rho_{\mathrm{b}} &= 0.99426 \pm^{0.00079}_{0.00164} & \Delta r &= 0.0363 \pm 0.0019
\end{aligned} \tag{8.5}$$

The quantities presented here are obtained from the same data set. Hence they are correlated with the five SM input parameters and cannot be used independently. Predictions of many more observables within the SM framework are reported in Appendix G.

Besides the hadronic vacuum polarisation $\Delta\alpha^{(5)}_{\mathrm{had}}(m^2_{\mathrm{Z}})$, only results from the Z-pole measurements, whose precision will not be improved in the near future, are used up to this point. The impact of the precision measurements of m_{t}, m_{W} and Γ_{W}, as discussed in Sections 8.3.1 and 8.3.2, is considered in the following. Note that these results are expected to benefit from new measurements in the near future.

8.6.2 The Mass of the Top Quark and of the W Boson

The above indirect constraint on the pole mass of the top quark, $m_{\mathrm{t}} = 173^{+13}_{-10}$ GeV (Table 8.2), can be compared with the result of the direct measurement of m_{t} at Run-I of the Tevatron, $m_{\mathrm{t}} = 178.0 \pm 4.3$ GeV [212]. The indirect determination is in good agreement with the direct measurement. It is impressive to note that even before the discovery of the top-quark in 1995, the then available set of electroweak precision data allowed the mass of the top quark to be predicted correctly as verified by its direct measurement obtained later, see Section 1.6.

The accuracy of the indirect constraint on m_{t} is improved by including the combined results on the W boson mass and width measured at Run-I of the Tevatron and at LEP-II as presented in Section 8.3.2:

$$m_{\mathrm{t}} = 181^{+12}_{-9}\ \mathrm{GeV}\,. \tag{8.6}$$

It can therefore be seen that the direct measurement of the top-quark mass is nearly three times as accurate as its indirect determination within the framework of the SM. The different determinations of m_{t} are compared in Figure 8.8.

Based on the results listed in Table 8.2, the prediction for the mass of the W boson is:

$$m_{\mathrm{W}} = 80.363 \pm 0.032\ \mathrm{GeV}\,, \tag{8.7}$$

which is in agreement at the level of 1.3 standard deviations with the combined direct measurement of $m_{\mathrm{W}} = 80.425 \pm 0.034$ GeV as presented in Section 8.3.2.

The accuracy of the m_{W} prediction is improved when the direct measurement of the top-quark mass from Run-I of the Tevatron is included:

$$m_{\mathrm{W}} = 80.373 \pm 0.023\ \mathrm{GeV}\,. \tag{8.8}$$

The indirect SM constraint on m_{W} is therefore seen to be more precise than the current direct measurements. For a stringent test of the SM, the mass of the W boson should thus be measured directly to an accuracy of 20 MeV or better. The different determinations of m_{W} are compared in Figure 8.9, also showing the NuTeV result when interpreted as a measurement of m_{W}.

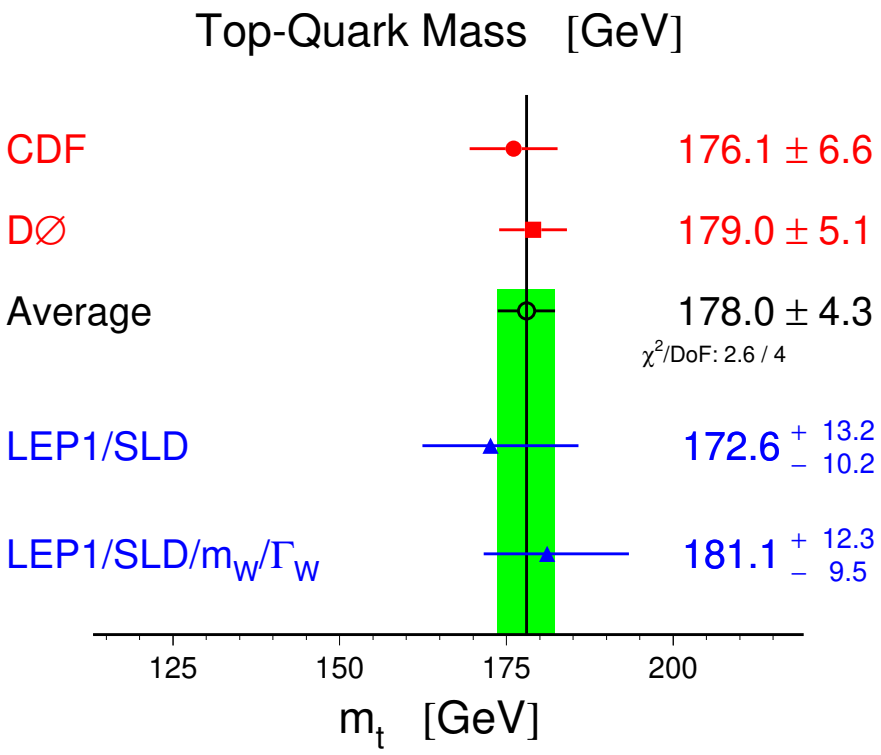

Figure 8.8: Results on the mass of the top quark. The direct measurements of m_{t} at Run-I of the Tevatron (top) are compared with the indirect determinations (bottom).

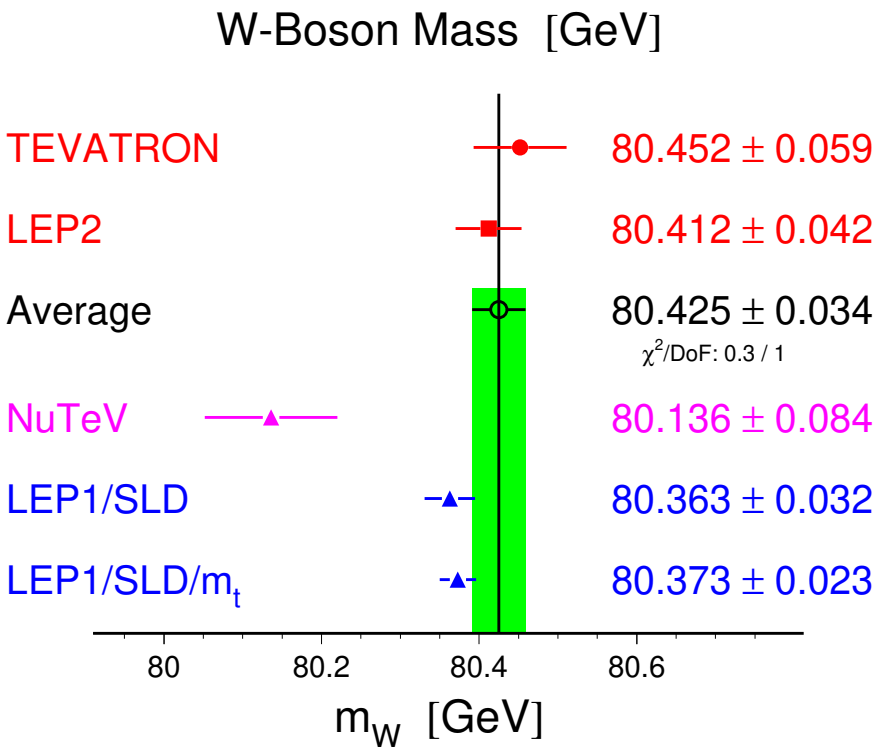

Figure 8.9: Results on the mass of the W boson, m_{W}. The direct measurements of m_{W} at LEP-II (preliminary) and at Run-I of the Tevatron (top) are compared with the indirect determinations (bottom). The NuTeV result interpreted in terms of m_{W} is shown separately.

8.6.3 The Mass of the Higgs Boson

The comparison between the indirect constraints and the direct measurements of $m_{\rm t}$ and $m_{\rm W}$ in the $(m_{\rm t}, m_{\rm W})$ plane is shown in Figure 8.10. The observed agreement is a crucial test of the SM. Since the SM is so successful in predicting the values of $m_{\rm W}$ and $m_{\rm t}$, this type of analysis is now extended to predict the mass of the Higgs boson. As seen in the figure, both contours prefer low values for the mass of the Higgs boson.

In order to obtain the most stringent constraint on the mass of the SM Higgs boson, the analysis is performed using the hadronic vacuum polarisation, the 14 Z-pole results, as well as the three additional results measured in high-Q^2 interactions as discussed in Section 8.3, namely $m_{\rm t}$, $m_{\rm W}$ and $\Gamma_{\rm W}$, for a total of 18 input measurements. The relative importance of including the direct measurements of $m_{\rm t}$ and $m_{\rm W}$ in constraining $m_{\rm H}$ is shown in Figure 8.11. At the current level of experimental precision, the direct measurement of $m_{\rm t}$ is more important. A measurement of $m_{\rm W}$ with increased precision, however, will become very valuable, especially in conjunction with an improved $m_{\rm t}$ measurement.

The results are shown in Table 8.3. A χ^2/dof of 18.3/13 is obtained, corresponding to a probability of 15%. The largest contribution to the χ^2 is again caused by the asymmetry measurements as discussed in Section 7.3.5. Thus also the complete set of measurements is accommodated by a single set of values for the five SM input parameters.

Compared to the results shown in Table 8.2, very good agreement is observed. The relative uncertainty on $m_{\rm H}$ decreases by about a half, mainly due to the inclusion of the direct measurements of $m_{\rm t}$ and $m_{\rm W}$. A change of the measured top-quark mass by one standard deviation, 4.3 GeV, changes the fitted Higgs-boson mass by about 30%, or 0.12 in $\log_{10}(m_{\rm H}/{\rm GeV})$. The importance of the external $\Delta\alpha^{(5)}_{\rm had}(m^2_{\rm Z}) = 0.02758 \pm 0.00035$ determination for the constraint on $m_{\rm H}$ is shown in Figure 8.12. Without the external $\Delta\alpha^{(5)}_{\rm had}(m^2_{\rm Z})$ constraint, the fit results are $\Delta\alpha^{(5)}_{\rm had}(m^2_{\rm Z}) = 0.0298^{+0.0010}_{-0.0017}$ and $m_{\rm H} = 29^{+77}_{-15}$ GeV, with a correlation of -0.88 between these two fit results.

The $\Delta\chi^2(m_{\rm H}) = \chi^2_{min}(m_{\rm H}) - \chi^2_{\rm min}$ curve is shown in Figure 8.13. The effect of the theoretical uncertainties in the SM calculations due to missing higher-order corrections as discussed in Section 8.4 is shown by the thickness of the shaded curve. Including these errors, the one-sided 95% CL upper limit on $\log_{10}(m_{\rm H}/{\rm GeV})$, given at $\Delta\chi^2 = 2.7$, is:

$$\log_{10}(m_{\rm H}/{\rm GeV}) \;<\; 2.455 \quad \text{or} \quad m_{\rm H} \;<\; 285 \text{ GeV}\,, \tag{8.9}$$

assuming a prior probability density flat in $\log_{10}(m_{\rm H}/{\rm GeV})$.[4] In case the theory-driven $\Delta\alpha^{(5)}_{\rm had}(m^2_{\rm Z})$ determination of Equation 8.4 is used, the central value of $m_{\rm H}$ increases while the uncertainty on $m_{\rm H}$ is reduced so that the upper limit changes only slightly. These results are clearly consistent with the 95% confidence level lower limit on $m_{\rm H}$ of 114.4 GeV based on the direct search performed at LEP-II [39].[5]

[4] Integrating the one-dimensional probability density function instead of taking $\Delta\chi^2 = 2.7$, the upper limit at 95% confidence level is 280 GeV. In case a prior probability density flat in $m_{\rm H}$ is assumed, the upper limit at 95% confidence level, calculated by integration, increases to 337 GeV.

[5] The direct search limit can be taken into account as follows: since the electroweak precision observables are sensitive to $\log_{10}(m_{\rm H}/{\rm GeV})$, and the direct search exclusion significance rises steeply with decreasing mass, the direct search limit essentially constitutes a cut off in $\log_{10}(m_{\rm H}/{\rm GeV})$. Renormalising the probability content of the region $m_{\rm H} > 114$ GeV to 100%, with zero probability for $m_{\rm H} < 114$ GeV, the 95% confidence level upper limit on the mass of the Higgs boson becomes: $\log_{10}(m_{\rm H}/{\rm GeV}) < 2.485$ ($m_{\rm H} < 306$ GeV) for a prior probability density flat in $\log_{10}(m_{\rm H}/{\rm GeV})$, or $m_{\rm H} < 353$ GeV for a prior probability density flat in $m_{\rm H}$. For the calculation of both cases, the one-dimensional probability density is integrated.

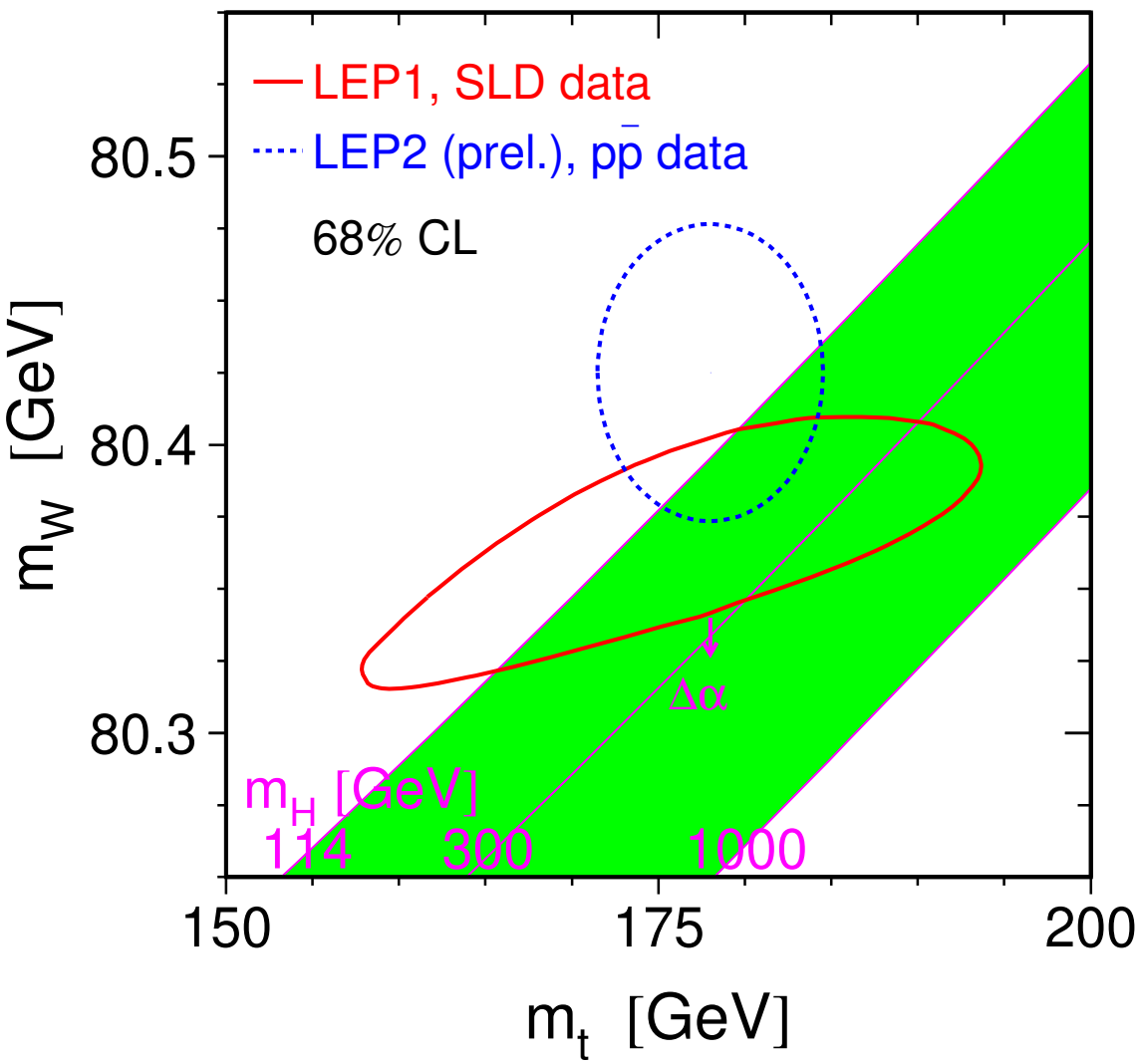

Figure 8.10: Contour curves of 68% probability in the $(m_{\mathrm{t}}, m_{\mathrm{W}})$ plane. The shaded band shows the SM prediction based on the value for G_{F} for various values of the Higgs-boson mass and fixed $\Delta\alpha^{(5)}_{\mathrm{had}}(m^2_{\mathrm{Z}})$; varying the hadronic vacuum polarisation by $\Delta\alpha^{(5)}_{\mathrm{had}}(m^2_{\mathrm{Z}}) = 0.02758 \pm 0.00035$ yields an additional uncertainty on the SM prediction shown by the arrow labeled $\Delta\alpha$. The direct measurement of m_{W} used here is preliminary.

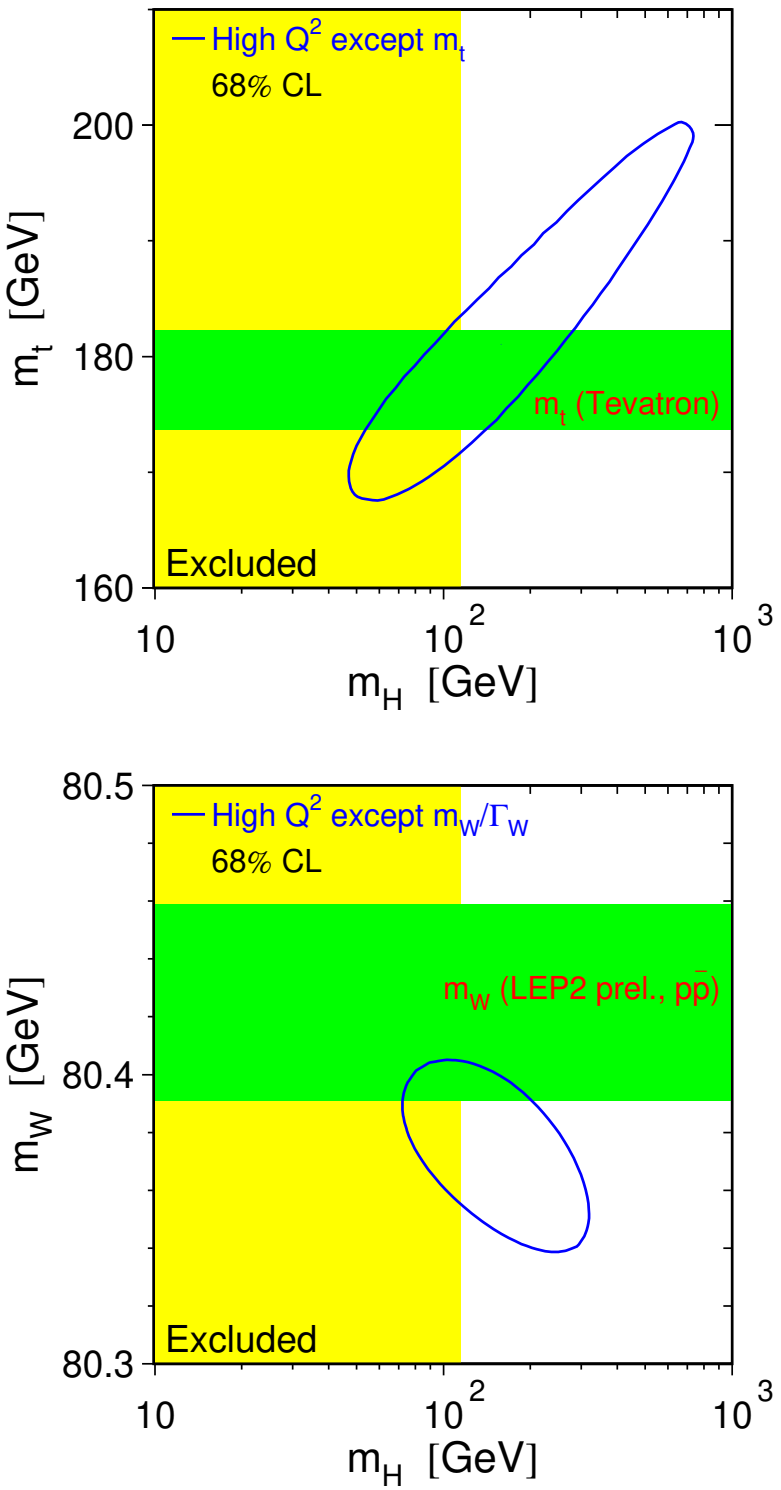

Figure 8.11: Contour curves of 68% probability in (top) the $(m_{\rm t}, m_{\rm H})$ plane and (bottom) the $(m_{\rm W}, m_{\rm H})$ plane, based on all 18 measurements except the direct measurement of $m_{\rm t}$ and the direct measurements of $m_{\rm W}$ and $\Gamma_{\rm W}$, respectively. The direct measurements of these excluded observables are shown as the horizontal bands of width ± 1 standard deviation. The vertical band shows the 95% confidence level exclusion limit on $m_{\rm H}$ of 114.4 GeV derived from the direct search at LEP-II [39]. The direct measurements of $m_{\rm W}$ and $\Gamma_{\rm W}$ used here are preliminary.

Parameter	Value	Correlations				
		$\Delta\alpha^{(5)}_{\rm had}(m_{\rm Z}^2)$	$\alpha_{\rm S}(m_{\rm Z}^2)$	$m_{\rm Z}$	$m_{\rm t}$	$\log_{10}(m_{\rm H}/{\rm GeV})$
$\Delta\alpha^{(5)}_{\rm had}(m_{\rm Z}^2)$	0.02767 ± 0.00034	1.00				
$\alpha_{\rm S}(m_{\rm Z}^2)$	0.1188 ± 0.0027	-0.02	1.00			
$m_{\rm Z}$ [GeV]	91.1874 ± 0.0021	-0.01	-0.02	1.00		
$m_{\rm t}$ [GeV]	178.5 ± 3.9	-0.05	0.11	-0.03	1.00	
$\log_{10}(m_{\rm H}/{\rm GeV})$	2.11 ± 0.20	-0.46	0.18	0.06	0.67	1.00
$m_{\rm H}$ [GeV]	129^{+74}_{-49}	-0.46	0.18	0.06	0.67	1.00

Table 8.3: Results for the five SM input parameters derived from a fit to the Z-pole results and $\Delta\alpha^{(5)}_{\rm had}(m_{\rm Z}^2)$, plus $m_{\rm t}$, $m_{\rm W}$, and $\Gamma_{\rm W}$ from Tevatron Run-I and LEP-II. The fit has a χ^2/dof of 18.3/13, corresponding to a probability of 15%. See Section 8.4 for a discussion of the theoretical uncertainties not included here. The results on $m_{\rm H}$, obtained by exponentiating the fit results on $\log_{10}(m_{\rm H}/{\rm GeV})$, are also shown. The direct measurements of $m_{\rm W}$ and $\Gamma_{\rm W}$ used here are preliminary.

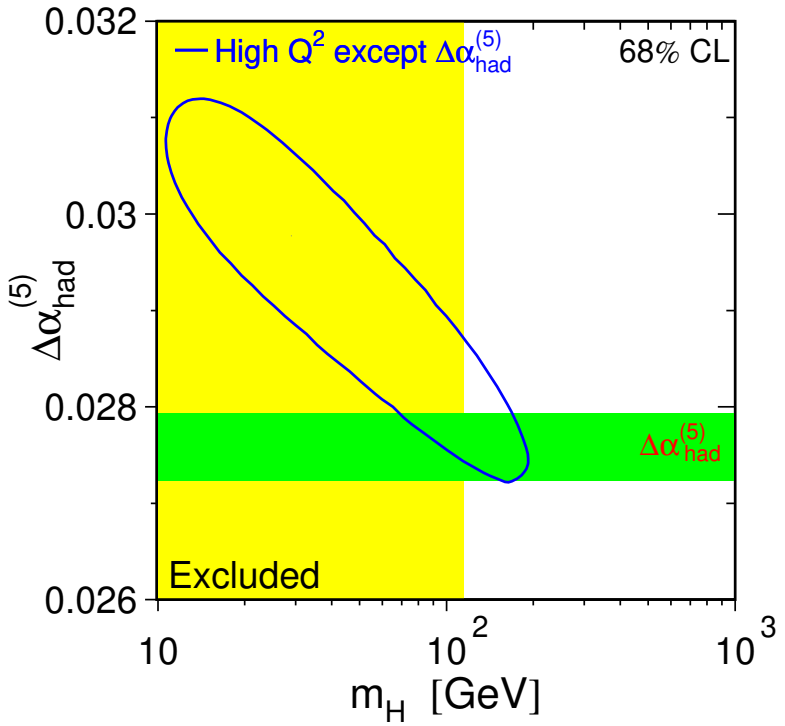

Figure 8.12: Contour curve of 68% probability in the $(\Delta\alpha^{(5)}_{\rm had}(m_{\rm Z}^2), m_{\rm H})$ plane, based on all 18 measurements except the constraint on $\Delta\alpha^{(5)}_{\rm had}(m_{\rm Z}^2)$. The direct measurements of the excluded observable is shown as the horizontal bands of width ±1 standard deviation. The vertical band shows the 95% confidence level exclusion limit on $m_{\rm H}$ of 114.4 GeV derived from the direct search at LEP-II [39]. The direct measurements of $m_{\rm W}$ and $\Gamma_{\rm W}$ used here are preliminary.

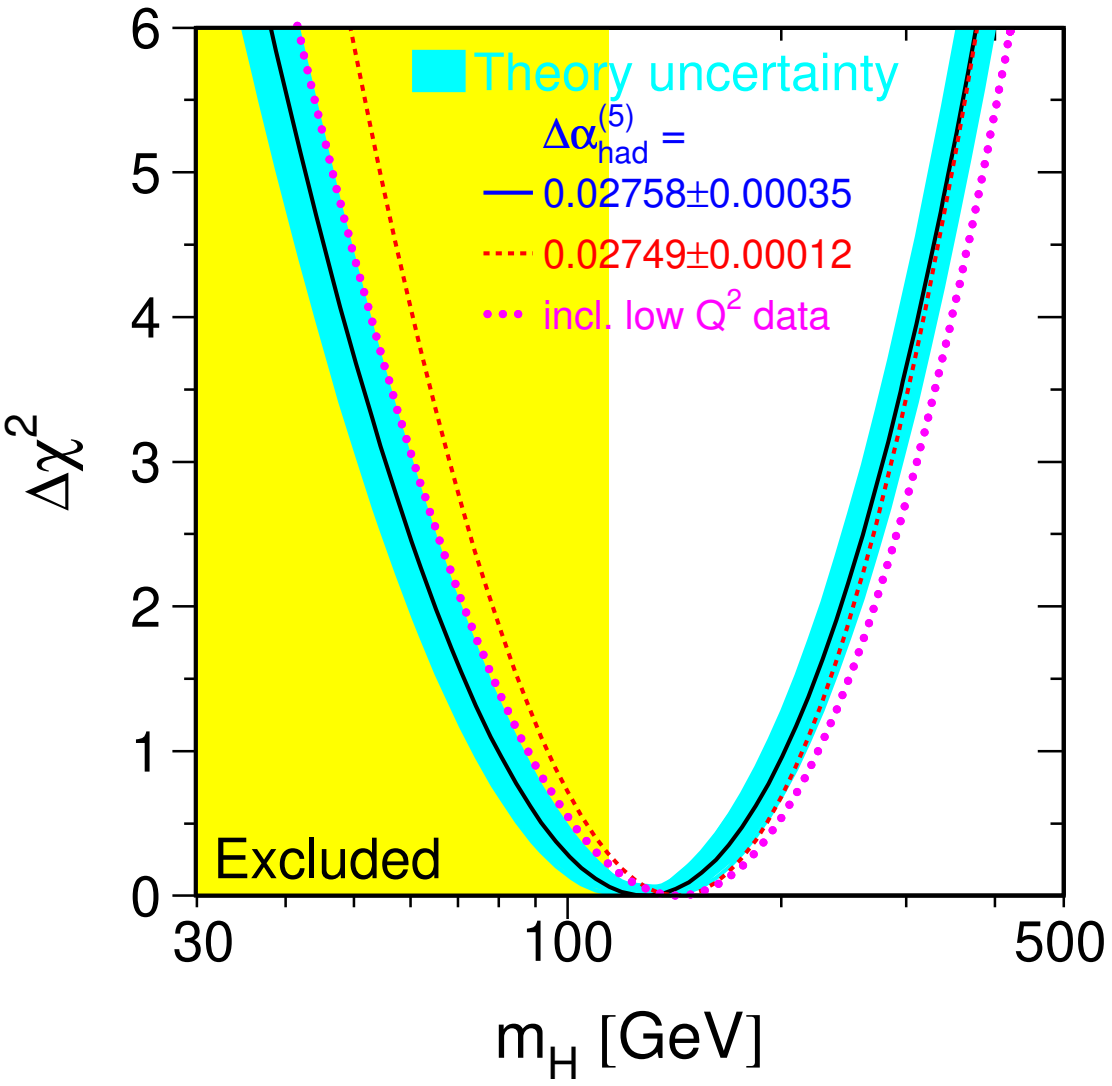

Figure 8.13: $\Delta\chi^2(m_{\rm H}) = \chi^2_{min}(m_{\rm H}) - \chi^2_{\rm min}$ as a function of $m_{\rm H}$. The line is the result of the fit using all 18 results. The associated band represents the estimate of the theoretical uncertainty due to missing higher-order corrections as discussed in Section 8.4. The vertical band shows the 95% confidence level exclusion limit on $m_{\rm H}$ of 114.4 GeV derived from the direct search at LEP-II [39]. The dashed curve is the result obtained using the theory-driven $\Delta\alpha^{(5)}_{\rm had}(m^2_{\rm Z})$ determination of Equation 8.4. The direct measurements of $m_{\rm W}$ and $\Gamma_{\rm W}$ used here are preliminary.

The lower limit on the mass of the SM Higgs boson from LEP-II is derived from the non-observation of direct Higgs production. Similarly, the upper mass limit given above arises from the observation of radiative corrections that can be largely attributed to the presence of a heavy top quark. The inferred radiative corrections are not significantly different from those expected when the Higgs mass is at the electroweak scale, where the contributions to radiative corrections from the Higgs boson are relatively small.

8.7 Discussion

The global χ^2/dof of the SM fit is 18.3/13, corresponding to a probability of 15%. Predictions for the individual measurements entering this analysis and the resulting pulls contributing to the global χ^2 are reported in Table 8.4. Predictions of many other observables within the SM framework are reported in Appendix G. The pulls of the measurements are also shown in Figure 8.14. Here, the pull is defined as the difference between the measured and the predicted value, in units of the measurement uncertainty, calculated for the values of the five SM input parameters in the minimum of the χ^2.

The largest contribution to the overall χ^2, 2.8 standard deviations, has already been discussed in Section 7.3.1, namely the b-quark forward-backward asymmetry measured at LEP-I. Two other measurements, the hadronic pole cross-section $\sigma^0_{\rm had}$ and the left-right asymmetry measured by SLD, dominating $\mathcal{A}_\ell$(SLD), cause pulls of 1.6 standard deviations. The pulls of all other measurements are about one standard deviation or less.

Compared to the uncertainty of the measurements, $\sigma^0_{\rm had}$ exhibits only a weak dependence on any of the five SM input parameters. The principal dependence of this quantity is on the number of light neutrino generations, which is constant and equal to three in the SM. The exclusion of $\sigma^0_{\rm had}$ affects the five fitted SM input parameters only slightly.

The constraint on the Higgs-boson mass arising from each pseudo-observable is shown in Figure 8.15. The corresponding Higgs-boson mass is obtained from a five-parameter SM fit to the observable, constraining $\Delta\alpha^{(5)}_{\rm had}(m^2_{\rm Z}) = 0.02758 \pm 0.00035$, $\alpha_{\rm S}(m^2_{\rm Z}) = 0.118 \pm 0.003$, $m_{\rm Z} = 91.1875 \pm 0.0021$ GeV and Tevatron Run-I $m_{\rm t} = 178.0 \pm 4.3$ GeV. The region of very low Higgs-boson masses is approximate, since in that region the effect of the ZH four-fermion process may become non-negligible, see Section 1.5.4.

As far as the mass of the Higgs boson is concerned, $A^{0,\,\rm b}_{\rm FB}$ and $\mathcal{A}_\ell$(SLD), both determining $\sin^2\theta^{\rm lept}_{\rm eff}$, exhibit a high sensitivity, but prefer a high and a low $m_{\rm H}$ value, respectively, as shown in Figure 8.15. Within the SM analysis, other observables also prefer low values for $m_{\rm H}$, such as the other leptonic asymmetry measurements as well as the combined measurement of the mass of the W boson. Therefore the pull of the $A^{0,\,\rm b}_{\rm FB}$ measurement is enlarged compared to the $\sin^2\theta^{\rm lept}_{\rm eff}$ combination discussed in Section 7.3.4, while the pull of $\mathcal{A}_\ell$(SLD) is reduced.

Because of these considerations, it is interesting to repeat the SM analysis,

- excluding $\mathcal{A}_\ell$(SLD):

$$m_{\rm H} = 175^{+99}_{-66}\ \text{GeV} \quad \text{and} \quad \chi^2/\text{dof} = 14.6/12\ (27\%)\,; \tag{8.10}$$

- excluding $A^{0,\,\rm b}_{\rm FB}$(LEP):

$$m_{\rm H} = \ \ 76^{+54}_{-33}\ \text{GeV} \quad \text{and} \quad \chi^2/\text{dof} = \ \ 9.7/12\ (64\%)\,; \tag{8.11}$$

	Measurement with Total Error	Systematic Error	Standard Model High-Q^2 Fit	Pull
$\Delta\alpha^{(5)}_{\rm had}(m^2_{\rm Z})$ [59]	0.02758 ± 0.00035	0.00034	0.02767 ± 0.00035	0.3
$m_{\rm Z}$ [GeV]	91.1875 ± 0.0021	[(a)] 0.0017	91.1874 ± 0.0021	0.1
$\Gamma_{\rm Z}$ [GeV]	2.4952 ± 0.0023	[(a)] 0.0012	2.4965 ± 0.0015	0.6
$\sigma^0_{\rm had}$ [nb]	41.540 ± 0.037	[(a)] 0.028	41.481 ± 0.014	1.6
R^0_ℓ	20.767 ± 0.025	[(a)] 0.007	20.739 ± 0.018	1.1
$A^{0,\ell}_{\rm FB}$	0.0171 ± 0.0010	[(a)] 0.0003	0.01642 ± 0.00024	0.8
+ correlation matrix Table 2.13				
$\mathcal{A}_\ell$ (P_τ)	0.1465 ± 0.0033	0.0015	0.1480 ± 0.0011	0.5
$\mathcal{A}_\ell$ (SLD)	0.1513 ± 0.0021	0.0011	0.1480 ± 0.0011	1.6
$R^0_{\rm b}$	0.21629 ± 0.00066	0.00050	0.21562 ± 0.00013	1.0
$R^0_{\rm c}$	0.1721 ± 0.0030	0.0019	0.1723 ± 0.0001	0.1
$A^{0,{\rm b}}_{\rm FB}$	0.0992 ± 0.0016	0.0007	0.1037 ± 0.0008	2.8
$A^{0,{\rm c}}_{\rm FB}$	0.0707 ± 0.0035	0.0017	0.0742 ± 0.0006	1.0
$\mathcal{A}_{\rm b}$	0.923 ± 0.020	0.013	0.9346 ± 0.0001	0.6
$\mathcal{A}_{\rm c}$	0.670 ± 0.027	0.015	0.6683 ± 0.0005	0.1
+ correlation matrix Table 5.11				
$\sin^2\theta^{\rm lept}_{\rm eff}$ ($Q^{\rm had}_{\rm FB}$)	0.2324 ± 0.0012	0.0010	0.23140 ± 0.00014	0.8
$m_{\rm t}$ [GeV] (Run-I [212])	178.0 ± 4.3	3.3	178.5 ± 3.9	0.1
$m_{\rm W}$ [GeV]	80.425 ± 0.034		80.389 ± 0.019	1.1
$\Gamma_{\rm W}$ [GeV]	2.133 ± 0.069		2.093 ± 0.002	0.6
+ correlation given in Section 8.3.2				

Table 8.4: Summary of measurements included in the analyses of the five SM input parameters. The top 15 results are included in the Z-pole and the high-Q^2 fit, while the bottom three results are only used in the high-Q^2 fit. The total errors in column 2 include the systematic errors listed in column 3. Although the systematic errors include both correlated and uncorrelated sources, the determination of the systematic part of each error is approximate. The SM results in column 4 and the pulls (absolute value of the difference between measurement and fit in units of the total measurement error, see Figure 8.14) in column 5 are derived from the SM analysis of all 18 results, including also the correlations between results presented in Chapter 7.1. The direct measurements of $m_{\rm W}$ and $\Gamma_{\rm W}$ used here are preliminary.
[(a)] Only common systematic errors are indicated.

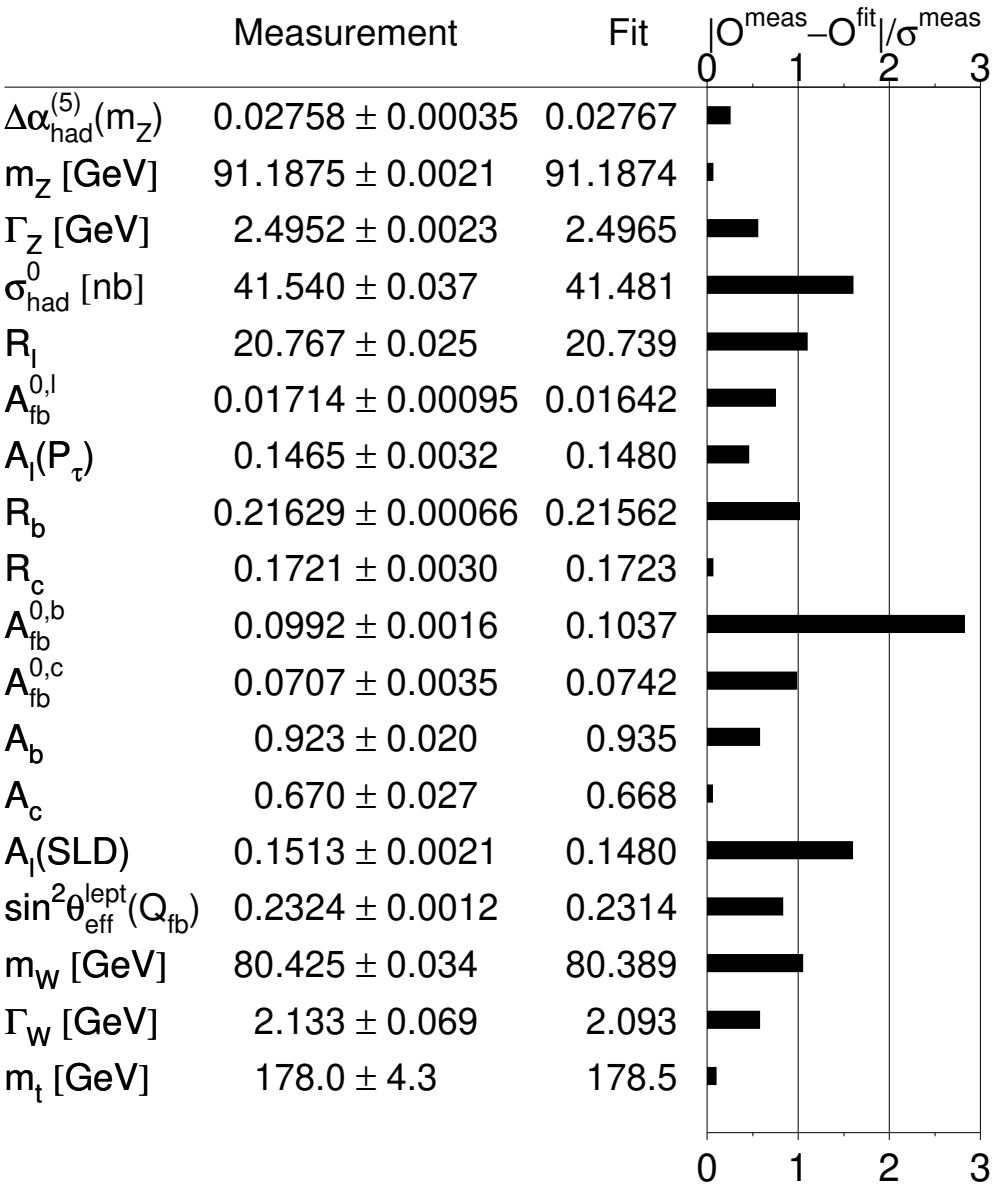

Figure 8.14: Comparison of the measurements with the expectation of the SM, calculated for the five SM input parameter values in the minimum of the global χ^2 of the fit. Also shown is the pull of each measurement, where pull is defined as the difference of measurement and expectation in units of the measurement uncertainty. The direct measurements of m_{W} and Γ_{W} used here are preliminary.

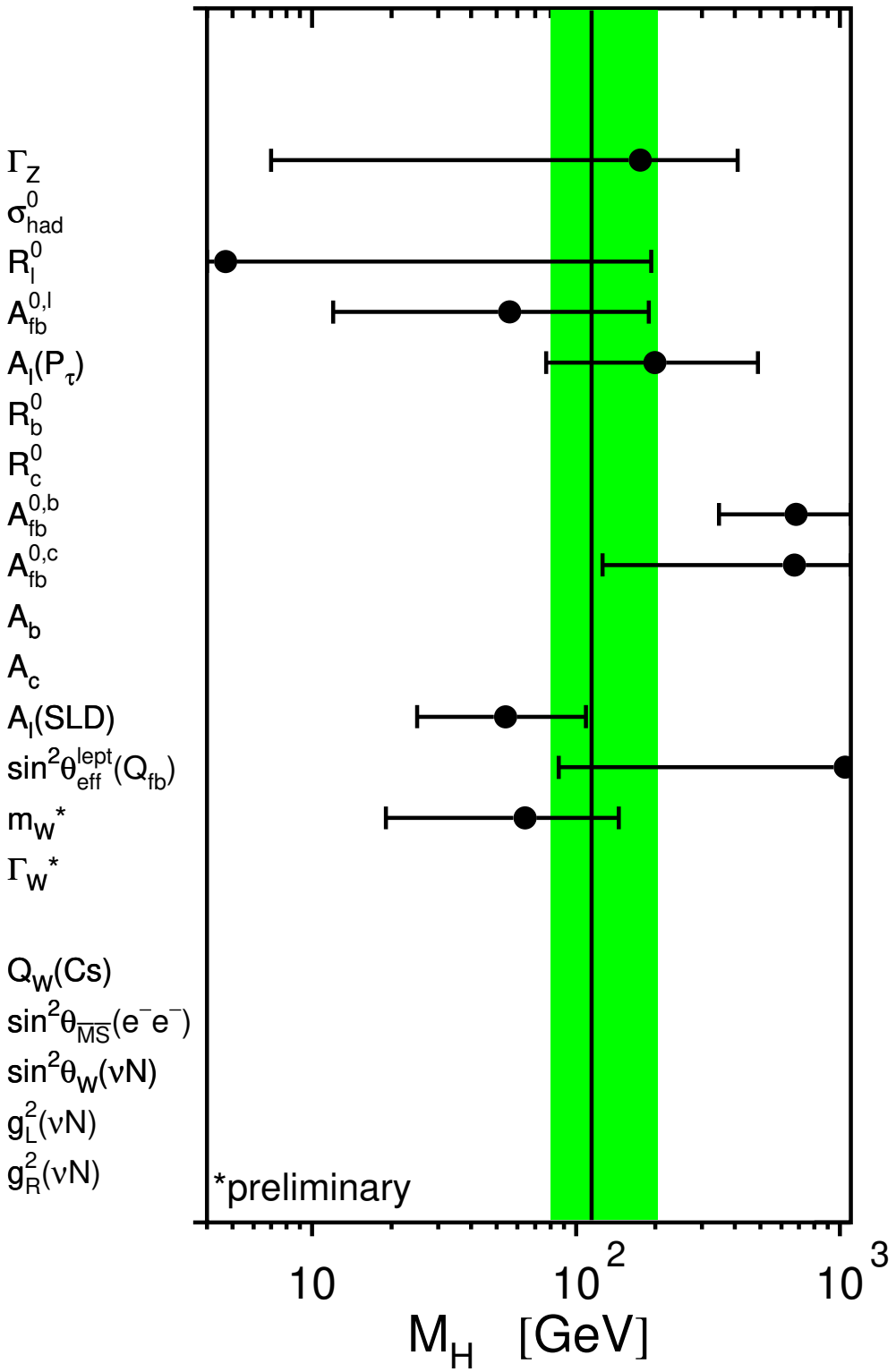

Figure 8.15: Constraints on the mass of the Higgs boson from each pseudo-observable. The Higgs-boson mass and its 68% CL uncertainty is obtained from a five-parameter SM fit to the observable, constraining $\Delta\alpha^{(5)}_{\rm had}(m^2_{\rm Z}) = 0.02758 \pm 0.00035$, $\alpha_{\rm S}(m^2_{\rm Z}) = 0.118 \pm 0.003$, $m_{\rm Z} = 91.1875 \pm 0.0021$ GeV and Tevatron Run-I $m_{\rm t} = 178.0 \pm 4.3$ GeV. Only significant constraints are shown. Because of these four common constraints the resulting Higgs-boson mass values cannot be combined. The shaded band denotes the overall constraint on the mass of the Higgs boson derived from all pseudo-observables reported in Table 8.3. The direct measurements of $m_{\rm W}$ and $\Gamma_{\rm W}$ used in that analysis are preliminary.

- excluding both $\mathcal{A}_\ell$(SLD) and $A_{\rm FB}^{0,\,\rm b}$(LEP):

$$m_{\rm H} = 103^{+76}_{-48}\ {\rm GeV} \quad \text{and} \quad \chi^2/{\rm dof} = \ 8.7/11\ (65\%)\,. \tag{8.12}$$

The largest changes in the results are observed in $\log_{10}(m_{\rm H}/{\rm GeV})$ for the second case, removing $A_{\rm FB}^{0,\,\rm b}$(LEP), as expected when removing this measurement with the largest pull and highly sensitive to $m_{\rm H}$. Given the size of the experimental errors on the b-quark couplings compared to the size of their radiative corrections as expected in the SM, a potential explanation in terms of new physics phenomena would require modifications of the right-handed b-quark coupling at the level of the Born-term values, as already discussed in Section 7.3.5.

The extracted constraints on the five input parameters of the SM can be used to calculate predictions for other measured electroweak observables. As an example, the atomic parity violation parameter of cesium $Q_{\rm W}$(Cs), the electroweak mixing angle $\sin^2\theta_{\overline{\rm MS}}(m_{\rm Z})$ measured in polarised Møller scattering, and the results from neutrino-nucleon scattering on $g^2_{\nu{\rm Lud}}$ and $g^2_{\nu{\rm Rud}}$ by the NuTeV experiment, all discussed in Section 8.3.3, are considered. The measurements and predictions are compared in Table 8.5. While good agreement is found for $Q_{\rm W}$(Cs), $\sin^2\theta_{\overline{\rm MS}}(m_{\rm Z})$ and $g^2_{\nu{\rm Rud}}$, the result on the left-handed coupling $g^2_{\nu{\rm Lud}}$, measured nearly eight times more precisely than the right-handed coupling $g^2_{\nu{\rm Rud}}$, and its prediction show a discrepancy at the level of 3.0 standard deviations. When the four measurements are included in the fit input, the five fitted SM input parameters changed by less than 10% of their error except for the Higgs-boson mass: $\log_{10}(m_{\rm H}/{\rm GeV})$ increases by 0.04 corresponding to an increase of 11% in $m_{\rm H}$, while the χ^2/dof increases to 28.9/17, corresponding to a probability of only 3.5%.

In the data collected at LEP in the year 2000, the last year of LEP-II operation, tantalising hints for the production of the Higgs boson were found [39]. However, combining all data of all four LEP experiments, the observation, compared to the expected background, corresponds to a significance of about 1.7 standard deviations only, at a mass of about 115 GeV [39]. New data is needed to confirm or exclude this indication and its interpretation. Such a value for $m_{\rm H}$ is in good agreement with the above values predicted within the SM based on the analysis of precision electroweak observables.

	Measurement with Total Error	Standard Model High-Q^2 Fit	Pull
APV [226]			
$Q_{\mathrm{W}}(\mathrm{Cs})$	-72.74 ± 0.46	-72.942 ± 0.037	0.4
Møller [229]			
$\sin^2\theta_{\overline{\mathrm{MS}}}(m_{\mathrm{Z}})$	0.2330 ± 0.0015	0.23111 ± 0.00014	1.3
νN [231]			
$g^2_{\nu\mathrm{Lud}}$	0.30005 ± 0.00137	0.30415 ± 0.00023	3.0
$g^2_{\nu\mathrm{Rud}}$	0.03076 ± 0.00110	0.03014 ± 0.00003	0.6

Table 8.5: Summary of predictions for results obtained in low-Q^2 processes described in Section 8.3.3, derived from the fit to all high-Q^2 data. Good agreement is observed except for the νN result on $g^2_{\nu\mathrm{Lud}}$ measured by the NuTeV experiment. The direct measurements of m_{W} and Γ_{W} used in the high-Q^2 fit are preliminary.

Chapter 9

Summary and Conclusions

The four LEP experiments ALEPH, DELPHI, L3 and OPAL and the SLD experiment at the SLC perform measurements in electron-positron collisions at centre-of-mass energies corresponding to the mass of the Z boson. Accumulating about 18 million Z decays with excellent detectors, the measurements are of unprecedented accuracy in high-energy particle physics. In particular, the pair-production of charged leptons and heavy quarks as well as inclusive hadron production are analysed by measuring production cross-sections and various cross-section asymmetries. These measurements are presented in Chapters 2 to 6 .

The measurements are used to determine the mass of the Z boson, its decay widths and its couplings to the various fermion species, for example:

$$\begin{aligned} m_{\mathrm{Z}} &= 91.1875 \pm 0.0021 \text{ GeV} \\ \Gamma_{\mathrm{Z}} &= 2.4952 \pm 0.0023 \text{ GeV} \\ \rho_{\ell} &= 1.0050 \pm 0.0010 \\ \sin^2\theta^{\mathrm{lept}}_{\mathrm{eff}} &= 0.23153 \pm 0.00016 \,. \end{aligned}$$

The number of light neutrino species is determined to be 2.9840 ± 0.0082, in good agreement with expectations based on the three observed generations of fundamental fermions. In general, the uncertainties on the measured parameters have been reduced by two to three orders of magnitude with respect to the experimental results available before the startup of SLC and LEP.

In addition, the large and diverse set of precise measurements allows many relations inspired by the Standard Model to be stringently tested (Chapter 7) and the free parameters of the model to be tightly constrained (Chapter 8). Lepton universality of the neutral weak current is established at the per-mille level. The masses of W boson and top quarks are predicted to be: $m_{\mathrm{W}} = 80.363 \pm 0.032$ GeV and $m_{\mathrm{t}} = 173^{+13}_{-10}$ GeV, agreeing well with the direct measurements of these quantities, successfully testing the Standard Model at the level of its radiative corrections.

While most measurements are well accommodated, the various measurements of forward-backward and polarised asymmetries, when interpreted in terms of a single quantity, the leptonic effective electroweak mixing angle, show a dispersion larger than expected with a χ^2/dof of 11.8/5, corresponding to a probability of 3.7%, for the average value shown above. Within the Standard-Model framework, the large χ^2/dof is mainly caused by the measurement of the forward-backward asymmetry in $\mathrm{b\overline{b}}$ production, discussed in Chapter 8. This could be explained by new physics, for example, modifying the right-handed b-quark coupling, or simply by a fluctuation. Further improvements on the precision of Z-pole observables could come from a linear collider taking data at the Z-pole.

Including the direct measurements of m_{t} and m_{W}, the mass of the Standard-Model Higgs boson is predicted with a relative uncertainty of about 50% and found to be less than 285 GeV at 95% confidence level. These results are in good agreement with the lower limit of 114 GeV at 95% confidence level obtained from direct searches at LEP-II. Overall, the SM is verified to be a good theory up to the 100 GeV scale. The data impose very tight constraints on any new physics beyond the SM. Any extended theory must be consistent with the SM or one or more Higgs doublet models such as super-symmetry.

Analysing results measured in low-Q^2 interactions, the largest deviation with respect to the expectation, at the level of three standard deviations, is found for the left-handed neutrino-quark effective coupling combination, as measured in neutrino-nucleon scattering by the NuTeV collaboration. Note that this measurement and the forward-backward asymmetry in $\mathrm{b\overline{b}}$ production measured at LEP are completely independent experimentally, are of different precision, and are extracted from different processes involving different fermion species, at greatly differing scales of momentum transfer. The constraints on the Standard-Model parameters are rather stable when the NuTeV measurement is included in the determination of Standard-Model parameters, while this is not the case when the measurement of the forward-backward asymmetry in $\mathrm{b\overline{b}}$ production is removed.

In the next years, improvements to three other important electroweak observables will become available, namely the masses of the top quark and of the W boson, and the hadronic vacuum polarisation. Assuming future world-average uncertainties of 2 GeV on m_{t}, 25 MeV on m_{W}, and 0.00010 on $\Delta\alpha^{(5)}_{\mathrm{had}}(m^2_{\mathrm{Z}})$, the mass of the Higgs boson can be predicted with a relative uncertainty of about 30%. The direct observation of Higgs-boson production would eventually allow its mass to be measured at the GeV level, allowing another crucial test of the Standard Model through a comparison of the direct and indirect results.

Appendix A

Author Lists

The ALEPH, DELPHI, L3, OPAL and SLD Collaborations have provided the inputs for the combined results presented in this Report. The LEP Electroweak Working Group and the SLD Heavy Flavour and Electroweak Groups have performed the combinations. The Working Groups consist of members of the five Collaborations. The lists of authors from the Collaborations follow.

A.1 The ALEPH Collaboration

S. Schael,[1] R. Barate,[2] R. Brunelière,[2] D. Buskulic,[2] I. De Bonis,[2] D. Decamp,[2] P. Ghez,[2] C. Goy,[2] S. Jézéquel,[2] J.-P. Lees,[2] A. Lucotte,[2] F. Martin,[2] E. Merle,[2] M.-N. Minard,[2] J.-Y. Nief,[2] P. Odier,[2] B. Pietrzyk,[2] B. Trocmé,[2] S. Bravo,[3] M.P. Casado,[3] M. Chmeissani,[3] P. Comas,[3] J.M. Crespo,[3] E. Fernandez,[3] M. Fernandez-Bosman,[3] Ll. Garrido,[3,a15] E. Grauges,[3] A. Juste,[3] M. Martinez,[3] G. Merino,[3] R. Miquel,[3] Ll.M. Mir,[3] S. Orteu,[3] A. Pacheco,[3] I.C. Park,[3] J. Perlas,[3] I. Riu,[3] H. Ruiz,[3] F. Sanchez,[3] A. Colaleo,[4] D. Creanza,[4] N. De Filippis,[4] M. de Palma,[4] G. Iaselli,[4] G. Maggi,[4] M. Maggi,[4] S. Nuzzo,[4] A. Ranieri,[4] G. Raso,[4,a24] F. Ruggieri,[4] G. Selvaggi,[4] L. Silvestris,[4] P. Tempesta,[4] A. Tricomi,[4,a3] G. Zito,[4] X. Huang,[5] J. Lin,[5] Q. Ouyang,[5] T. Wang,[5] Y. Xie,[5] R. Xu,[5] S. Xue,[5] J. Zhang,[5] L. Zhang,[5] W. Zhao,[5] D. Abbaneo,[6] A. Bazarko,[6] U. Becker,[6] G. Boix,[6,a33] F. Bird,[6] E. Blucher,[6] B. Bonvicini,[6] P. Bright-Thomas,[6] T. Barklow,[6,a26] O. Buchmüller,[6,a26] M. Cattaneo,[6] F. Cerutti,[6] V. Ciulli,[6] B. Clerbaux,[6,a23] H. Drevermann,[6] R.W. Forty,[6] M. Frank,[6] T.C. Greening,[6] R. Hagelberg,[6] A.W. Halley,[6] F. Gianotti,[6] M. Girone,[6] J.B. Hansen,[6] J. Harvey,[6] R. Jacobsen,[6] D.E. Hutchcroft,[6,a30] P. Janot,[6] B. Jost,[6] J. Knobloch,[6] M. Kado,[6,a2] I. Lehraus,[6] P. Lazeyras,[6] P. Maley,[6] P. Mato,[6] J. May,[6] A. Moutoussi,[6] M. Pepe-Altarelli,[6] F. Ranjard,[6] L. Rolandi,[6] D. Schlatter,[6] B. Schmitt,[6] O. Schneider,[6] W. Tejessy,[6] F. Teubert,[6] I.R. Tomalin,[6] E. Tournefier,[6] R. Veenhof,[6] A. Valassi,[6] W. Wiedenmann,[6] A.E. Wright,[6] Z. Ajaltouni,[7] F. Badaud,[7] G. Chazelle,[7] O. Deschamps,[7] S. Dessagne,[7] A. Falvard,[7,a20] C. Ferdi,[7] D. Fayolle,[7] P. Gay,[7] C. Guicheney,[7] P. Henrard,[7] J. Jousset,[7] B. Michel,[7] S. Monteil,[7] J.C. Montret,[7] D. Pallin,[7] J.M. Pascolo,[7] P. Perret,[7] F. Podlyski,[7] H. Bertelsen,[8] T. Fernley,[8] J.D. Hansen,[8] J.R. Hansen,[8] P.H. Hansen,[8] A.C. Kraan,[8] A. Lindahl,[8] R. Mollerud,[8] B.S. Nilsson,[8] B. Rensch,[8] A. Waananen,[8] G. Daskalakis,[9] A. Kyriakis,[9] C. Markou,[9] E. Simopoulou,[9] I. Siotis,[9] A. Vayaki,[9] K. Zachariadou,[9] A. Blondel,[10,a12] G. Bonneaud,[10] J.-C. Brient,[10] F. Machefert,[10] A. Rougé,[10] M. Rumpf,[10] M. Swynghedauw,[10] R. Tanaka,[10] M. Verderi,[10] H. Videau,[10] V. Ciulli,[11] E. Focardi,[11] G. Parrini,[11] K. Zachariadou,[11] M. Corden,[12] C. Georgiopoulos,[12] A. Antonelli,[13] M. Antonelli,[13] G. Bencivenni,[13] G. Bologna,[13,a34] F. Bossi,[13] P. Campana,[13] G. Capon,[13] F. Cerutti,[13] V. Chiarella,[13] G. Felici,[13] P. Laurelli,[13] G. Mannocchi,[13,a5] G.P. Murtas,[13] L. Passalacqua,[13] P. Picchi,[13] P. Colrain,[14] I. ten Have,[14] I.S. Hughes,[14] J. Kennedy,[14] I.G. Knowles,[14] J.G. Lynch,[14] W.T. Morton,[14] P. Negus,[14] V. O'Shea,[14] C. Raine,[14] P. Reeves,[14] J.M. Scarr,[14] K. Smith,[14] A.S. Thompson,[14] R.M. Turnbull,[14] S. Wasserbaech,[15] O. Buchmüller,[16] R. Cavanaugh,[16,a4] S. Dhamotharan,[16,a21] C. Geweniger,[16] P. Hanke,[16] G. Hansper,[16] V. Hepp,[16] E.E. Kluge,[16] A. Putzer,[16] J. Sommer,[16] H. Stenzel,[16] K. Tittel,[16] W. Werner,[16] M. Wunsch,[16,a19] R. Beuselinck,[17] D.M. Binnie,[17] W. Cameron,[17] G. Davies,[17] P.J. Dornan,[17] S. Goodsir,[17] N. Marinelli,[17] E.B Martin,[17] J. Nash,[17] J. Nowell,[17] S.A. Rutherford,[17] J.K. Sedgbeer,[17] J.C. Thompson,[17,a14] R. White,[17] M.D. Williams,[17] V.M. Ghete,[18] P. Girtler,[18] E. Kneringer,[18] D. Kuhn,[18] G. Rudolph,[18] E. Bouhova-Thacker,[19] C.K. Bowdery,[19] P.G. Buck,[19] D.P. Clarke,[19] G. Ellis,[19] A.J. Finch,[19] F. Foster,[19] G. Hughes,[19] R.W.L. Jones,[19] N.R. Keemer,[19] M.R. Pearson,[19] N.A. Robertson,[19] T. Sloan,[19] M. Smizanska,[19] S.W. Snow,[19] M.I. Williams,[19] O. van der Aa,[20] C. Delaere,[20,a28] G.Leibenguth,[20,a31] V. Lemaitre,[20,a29] L.A.T. Bauerdick,[21] U. Blumenschein,[21] P. van Gemmeren,[21] I. Giehl,[21] F. Hölldorfer,[21] K. Jakobs,[21] M. Kasemann,[21] F. Kayser,[21] K. Kleinknecht,[21] A.-S. Müller,[21] G. Quast,[21] B. Renk,[21] E. Rohne,[21] H.-G. Sander,[21] S. Schmeling,[21] H. Wachsmuth,[21] R. Wanke,[21] C. Zeitnitz,[21] T. Ziegler,[21] J.J. Aubert,[22] C. Benchouk,[22] A. Bonissent,[22] J. Carr,[22] P. Coyle,[22] C. Curtil,[22] A. Ealet,[22] F. Etienne,[22] D. Fouchez,[22] F. Motsch,[22] P. Payre,[22] D. Rousseau,[22] A. Tilquin,[22] M. Talby,[22] M.Thulasidas,[22] M. Aleppo,[23] M. Antonelli,[23] F. Ragusa,[23] V. Büscher,[24] A. David,[24] H. Dietl,[24,a32] G. Ganis,[24,a27] K. Hüttmann,[24] G. Lütjens,[24] C. Mannert,[24] W. Männer,[24,a32] H.-G. Moser,[24] R. Settles,[24]

H. Seywerd,[24] H. Stenzel,[24] M. Villegas,[24] W. Wiedenmann,[24] G. Wolf,[24] P. Azzurri,[25] J. Boucrot,[25] O. Callot,[25] S. Chen,[25] A. Cordier,[25] M. Davier,[25] L. Duflot,[25] J.-F. Grivaz,[25] Ph. Heusse,[25] A. Jacholkowska,[25,a6] F. Le Diberder,[25] J. Lefrançois,[25] A.M. Mutz,[25] M.H. Schune,[25] L. Serin,[25] J.-J. Veillet,[25] I. Videau,[25] D. Zerwas,[25] P. Azzurri,[26] G. Bagliesi,[26] S. Bettarini,[26] T. Boccali,[26] C. Bozzi,[26] G. Calderini,[26] R. Dell'Orso,[26] R. Fantechi,[26] I. Ferrante,[26] F. Fidecaro,[26] L. Foà,[26] A. Giammanco,[26] A. Giassi,[26] A. Gregorio,[26] F. Ligabue,[26] A. Lusiani,[26] P.S. Marrocchesi,[26] A. Messineo,[26] F. Palla,[26] G. Rizzo,[26] G. Sanguinetti,[26] A. Sciabà,[26] G. Sguazzoni,[26] P. Spagnolo,[26] J. Steinberger,[26] R. Tenchini,[26] A. Venturi,[26] C. Vannini,[26] A. Venturi,[26] P.G. Verdini,[26] O. Awunor,[27] G.A. Blair,[27] G. Cowan,[27] A. Garcia-Bellido,[27] M.G. Green,[27] T. Medcalf,[27] A. Misiejuk,[27] J.A. Strong,[27] P. Teixeira-Dias,[27] D.R. Botterill,[28] R.W. Clifft,[28] T.R. Edgecock,[28] M. Edwards,[28] S.J. Haywood,[28] P.R. Norton,[28] I.R. Tomalin,[28] J.J. Ward,[28] B. Bloch-Devaux,[29] D. Boumediene,[29] P. Colas,[29] S. Emery,[29] B. Fabbro,[29] W. Kozanecki,[29] E. Lançon,[29] M.-C. Lemaire,[29] E. Locci,[29] P. Perez,[29] J. Rander,[29] J.F. Renardy,[29] A. Roussarie,[29] J.P. Schuller,[29] J. Schwindling,[29] B. Tuchming,[29] B. Vallage,[29] S.N. Black,[30] J.H. Dann,[30] H.Y. Kim,[30] N. Konstantinidis,[30] A.M. Litke,[30] M.A. McNeil,[30] G. Taylor,[30] C.N. Booth,[31] S. Cartwright,[31] F. Combley,[31,a25] P.N. Hodgson,[31] M. Lehto,[31] L.F. Thompson,[31] K. Affholderbach,[32] E. Barberio,[32] A. Böhrer,[32] S. Brandt,[32] H. Burkhardt,[32] E. Feigl,[32] C. Grupen,[32] J. Hess,[32] G. Lutters,[32] H. Meinhard,[32] J. Minguet-Rodriguez,[32] L. Mirabito,[32] A. Misiejuk,[32] E. Neugebauer,[32] A. Ngac,[32] G. Prange,[32] F. Rivera,[32] P. Saraiva,[32] U. Schäfer,[32] U. Sieler,[32] L. Smolik,[32] F. Stephan,[32] H. Trier,[32] M. Apollonio,[33] C. Borean,[33] L. Bosisio,[33] R. Della Marina,[33] G. Giannini,[33] B. Gobbo,[33] G. Musolino,[33] L. Pitis,[33] H. He,[34] H. Kim,[34] J. Putz,[34] J. Rothberg,[34] S.R. Armstrong,[35] L. Bellantoni,[35] K. Berkelman,[35] D. Cinabro,[35] J.S. Conway,[35] K. Cranmer,[35] P. Elmer,[35] Z. Feng,[35] D.P.S. Ferguson,[35] Y. Gao,[35,a13] S. González,[35] J. Grahl,[35] J.L. Harton,[35] O.J. Hayes,[35] H. Hu,[35] S. Jin,[35] R.P. Johnson,[35] J. Kile,[35] P.A. McNamara III,[35] J. Nielsen,[35] W. Orejudos,[35] Y.B. Pan,[35] Y. Saadi,[35] I.J. Scott,[35] V. Sharma,[35] A.M. Walsh,[35] J. Walsh,[35] J. Wear,[35] J.H. von Wimmersperg-Toeller,[35] W. Wiedenmann,[35] J. Wu,[35] S.L. Wu,[35] X. Wu,[35] J.M. Yamartino,[35] G. Zobernig,[35] G. Dissertori.[36]

[1] Physikalisches Institut der RWTH-Aachen, D-52056 Aachen, Germany
[2] Laboratoire de Physique des Particules (LAPP), IN^{2}P^3-CNRS, F-74019 Annecy-le-Vieux Cedex, France
[3] Institut de Física d'Altes Energies, Universitat Autònoma de Barcelona, E-08193 Bellaterra (Barcelona), Spain[a7]
[4] Dipartimento di Fisica, INFN Sezione di Bari, I-70126 Bari, Italy
[5] Institute of High Energy Physics, Academia Sinica, Beijing, The People's Republic of China[a8]
[6] European Laboratory for Particle Physics (CERN), CH-1211 Geneva 23, Switzerland
[7] Laboratoire de Physique Corpusculaire, Université Blaise Pascal, IN^{2}P^3-CNRS, Clermont-Ferrand, F-63177 Aubière, France
[8] Niels Bohr Institute, 2100 Copenhagen, DK-Denmark[a9]
[9] Nuclear Research Center Demokritos (NRCD), GR-15310 Attiki, Greece
[10] Laoratoire Leprince-Ringuet, Ecole Polytechnique, IN^{2}P^3-CNRS, F-91128 Palaiseau Cedex, France
[11] Dipartimento di Fisica, Università di Firenze, INFN Sezione di Firenze, I-50125 Firenze, Italy
[12] Supercomputer Computations Research Institute, Florida State University, Tallahasee, FL-32306-4052, USA
[13] Laboratori Nazionali dell'INFN (LNF-INFN), I-00044 Frascati, Italy

[14] Department of Physics and Astronomy, University of Glasgow, Glasgow G12 8QQ,United Kingdom[a10]
[15] Utah Valley State College, Orem, UT 84058, U.S.A.
[16] Kirchhoff-Institut für Physik, Universität Heidelberg, D-69120 Heidelberg, Germany[a16]
[17] Department of Physics, Imperial College, London SW7 2BZ, United Kingdom[a10]
[18] Institut für Experimentalphysik, Universität Innsbruck, A-6020 Innsbruck, Austria[a18]
[19] Department of Physics, University of Lancaster, Lancaster LA1 4YB, United Kingdom[a10]
[20] Institut de Physique Nucléaire, Département de Physique, Université Catholique de Louvain, 1348 Louvain-la-Neuve, Belgium
[21] Institut für Physik, Universität Mainz, D-55099 Mainz, Germany[a16]
[22] Centre de Physique des Particules de Marseille, Univ Méditerranée, IN^2P^3-CNRS, F-13288 Marseille, France
[23] Dipartimento di Fisica, Università di Milano e INFN Sezione di Milano, I-20133 Milano, Italy.
[24] Max-Planck-Institut für Physik, Werner-Heisenberg-Institut, D-80805 München, Germany[a16]
[25] Laboratoire de l'Accélérateur Linéaire, Université de Paris-Sud, IN^2P^3-CNRS, F-91898 Orsay Cedex, France
[26] Dipartimento di Fisica dell'Università, INFN Sezione di Pisa, e Scuola Normale Superiore, I-56010 Pisa, Italy
[27] Department of Physics, Royal Holloway & Bedford New College, University of London, Egham, Surrey TW20 OEX, United Kingdom[a10]
[28] Particle Physics Dept., Rutherford Appleton Laboratory, Chilton, Didcot, Oxon OX11 OQX, United Kingdom[a10]
[29] CEA, DAPNIA/Service de Physique des Particules, CE-Saclay, F-91191 Gif-sur-Yvette Cedex, France[a17]
[30] Institute for Particle Physics, University of California at Santa Cruz, Santa Cruz, CA 95064, USA[a22]
[31] Department of Physics, University of Sheffield, Sheffield S3 7RH, United Kingdom[a10]
[32] Fachbereich Physik, Universität Siegen, D-57068 Siegen, Germany[a16]
[33] Dipartimento di Fisica, Università di Trieste e INFN Sezione di Trieste, I-34127 Trieste, Italy
[34] Experimental Elementary Particle Physics, University of Washington, Seattle, WA 98195 U.S.A.
[35] Department of Physics, University of Wisconsin, Madison, WI 53706, USA[a11]
[36] Institute for Particle Physics, ETH Hönggerberg, 8093 Zürich, Switzerland.

[a1] Also at CERN, 1211 Geneva 23, Switzerland.
[a2] Now at Fermilab, PO Box 500, MS 352, Batavia, IL 60510, USA
[a3] Also at Dipartimento di Fisica di Catania and INFN Sezione di Catania, 95129 Catania, Italy.
[a4] Now at University of Florida, Department of Physics, Gainesville, Florida 32611-8440, USA
[a5] Also IFSI sezione di Torino, INAF, Italy.
[a6] Also at Groupe d'Astroparticules de Montpellier, Université de Montpellier II, 34095, Montpellier, France.

[a7] Supported by CICYT, Spain.
[a8] Supported by the National Science Foundation of China.
[a9] Supported by the Danish Natural Science Research Council.
[a10] Supported by the UK Particle Physics and Astronomy Research Council.
[a11] Supported by the US Department of Energy, grant DE-FG0295-ER40896.
[a12] Now at Departement de Physique Corpusculaire, Université de Genève, 1211 Genève 4, Switzerland.
[a13] Also at Department of Physics, Tsinghua University, Beijing, The People's Republic of China.
[a14] Supported by the Leverhulme Trust.
[a15] Permanent address: Universitat de Barcelona, 08208 Barcelona, Spain.
[a16] Supported by Bundesministerium für Bildung und Forschung, Germany.
[a17] Supported by the Direction des Sciences de la Matière, C.E.A.
[a18] Supported by the Austrian Ministry for Science and Transport.
[a19] Now at SAP AG, 69185 Walldorf, Germany
[a20] Now at Groupe d' Astroparticules de Montpellier, Université de Montpellier II, 34095 Montpellier, France.
[a21] Now at BNP Paribas, 60325 Frankfurt am Mainz, Germany
[a22] Supported by the US Department of Energy, grant DE-FG03-92ER40689.
[a23] Now at Institut Inter-universitaire des hautes Energies (IIHE), CP 230, Université Libre de Bruxelles, 1050 Bruxelles, Belgique
[a24] Now at Dipartimento di Fisica e Tecnologie Relative, Università di Palermo, Palermo, Italy.
[a25] Deceased.
[a26] Now at SLAC, Stanford, CA 94309, U.S.A
[a27] Now at CERN, 1211 Geneva 23, Switzerland
[a28] Research Fellow of the Belgium FNRS
[a29] Research Associate of the Belgium FNRS
[a30] Now at Liverpool University, Liverpool L69 7ZE, United Kingdom
[a31] Supported by the Federal Office for Scientific, Technical and Cultural Affairs through the Interuniversity Attraction Pole P5/27
[a32] Now at Henryk Niewodniczanski Institute of Nuclear Physics, Polish Academy of Sciences, Cracow, Poland
[a33] Supported by the Commission of the European Communities, contract ERBFMBICT982894
[a34] Also Istituto di Fisica Generale, Università di Torino, 10125 Torino, Italy

A.2 The DELPHI Collaboration

J. Abdallah,[26] P. Abreu,[23] W. Adam,[55] T. Adye,[40] P. Adzic,[12] I. Ajinenko,[46] T. Albrecht,[18] T. Alderweireld,[2] G.D. Alekseev,[17] R. Alemany-Fernandez,[9] T. Allmendinger,[18] P.P. Allport,[24] S. Almehed,[27] U. Amaldi,[31] N. Amapane,[49] S. Amato,[52] E. Anashkin,[39] E.G. Anassontzis,[3] P. Andersson,[48] A. Andreazza,[30] S. Andringa,[23] N. Anjos,[23] P. Antilogus,[26] W.-D. Apel,[18] Y. Arnoud,[15] S. Ask,[27] B. Asman,[48] J.E. Augustin,[26] A. Augustinus,[9] P. Baillon,[9] A. Ballestrero,[50] P. Bambade,[21] F. Barao,[23] G. Barbiellini,[51] R. Barbier,[28] D. Bardin,[17] G. Barker,[18] A. Baroncelli,[42] M. Battaglia,[9] M. Baubillier,[26] K.-H. Becks,[57] M. Begalli,[6] A. Behrmann,[57] P. Beilliere,[8] Yu. Belokopytov,[9] K. Belous,[46] E. Ben-Haim,[21] N. Benekos,[35] A. Benvenuti,[5] C. Berat,[15] M. Berggren,[26] L. Berntzon,[48] D. Bertini,[28] D. Bertrand,[2] M. Besancon,[43] N. Besson,[43] F. Bianchi,[49] M. Bigi,[49] M.S. Bilenky,[17] M.-A. Bizouard,[21] D. Bloch,[10] M. Blom,[34] M. Bluj,[56] M. Bonesini,[31] W. Bonivento,[30] M. Boonekamp,[43] P.S.L. Booth†,[24] A.W. Borgland,[4] G. Borisov,[22] C. Bosio,[45] O. Botner,[53] E. Boudinov,[34] B. Bouquet,[21] C. Bourdarios,[21] T.J.V. Bowcock,[24] I. Boyko,[17] I. Bozovic,[12] M. Bozzo,[14] M. Bracko,[47] P. Branchini,[42] T. Brenke,[57] R. Brenner,[53] E. Brodet,[38] P. Bruckman,[19] J.M. Brunet,[8] L. Bugge,[36] T. Buran,[36] T. Burgsmueller,[57] B. Buschbeck,[55] P. Buschmann,[57] S. Cabrera,[54] M. Caccia,[30] M. Calvi,[31] A.J. Camacho Rozas,[44] T. Camporesi,[9] V. Canale,[41] M. Canepa,[14] F. Carena,[9] L. Carroll,[24] C. Caso,[14] M.V. Castillo Gimenez,[54] N. Castro,[23] A. Cattai,[9] F. Cavallo,[5] Ch. Cerruti,[10] V. Chabaud,[9] M. Chapkin,[46] Ph. Charpentier,[9] L. Chaussard,[28] P. Checchia,[39] G.A. Chelkov,[17] M. Chen,[2] R. Chierici,[9] P. Chliapnikov,[46] P. Chochula,[7] V. Chorowicz,[28] J. Chudoba,[9] S.U. Chung,[9] K. Cieslik,[19] P. Collins,[9] M. Colomer,[54] R. Contri,[14] E. Cortina,[54] G. Cosme,[21] F. Cossutti,[51] M.J. Costa,[54] J.-H. Cowell,[24] H.B. Crawley,[1] D. Crennell,[40] S. Crepe,[15] G. Crosetti,[14] J. Cuevas,[37] S. Czellar,[16] J. D'Hondt,[2] B. Dalmagne,[21] J. Dalmau,[48] G. Damgaard,[32] M. Davenport,[9] T. da Silva,[52] W. Da Silva,[26] A. Deghorain,[2] G. Della Ricca,[51] P. Delpierre,[29] N. Demaria,[9] A. De Angelis,[51] W. De Boer,[18] S. de Brabandere,[2] C. De Clercq,[2] B. De Lotto,[51] N. De Maria,[49] A. De Min,[39] L. de Paula,[52] H. Dijkstra,[9] L. Di Ciaccio,[41] A. Di Diodato,[41] A. Di Simone,[42] A. Djannati,[8] J. Dolbeau,[8] K. Doroba,[56] M. Dracos,[10] J. Drees,[57] K.-A. Drees,[57] M. Dris,[35] A. Duperrin,[28] J.-D. Durand,[9] R. Ehret,[18] G. Eigen,[4] T. Ekelof,[53] G. Ekspong,[48] M. Ellert,[53] M. Elsing,[9] J.-P. Engel,[10] B. Erzen,[47] M.C. Espirito Santo,[23] E. Falk,[27] G. Fanourakis,[12] D. Fassouliotis,[12,3] J. Fayot,[26] M. Feindt,[18] A. Fenyuk,[46] J. Fernandez,[44] P. Ferrari,[30] A. Ferrer,[54] E. Ferrer-Ribas,[21] F. Ferro,[14] S. Fichet,[26] A. Firestone,[1] P.-A. Fischer,[9] U. Flagmeyer,[57] H. Foeth,[9] E. Fokitis,[35] F. Fontanelli,[14] B. Franek,[40] A.G. Frodesen,[4] R. Fruhwirth,[55] F. Fulda-Quenzer,[21] J. Fuster,[54] A. Galloni,[24] D. Gamba,[49] S. Gamblin,[21] M. Gandelman,[52] C. Garcia,[54] J. Garcia,[44] C. Gaspar,[9] M. Gaspar,[52] U. Gasparini,[39] Ph. Gavillet,[9] E. Gazis,[35] D. Gele,[10] J.-P. Gerber,[10] L. Gerdyukov,[46] N. Ghodbane,[28] I. Gil,[54] F. Glege,[57] R. Gokieli,[9,56] B. Golob,[47] G. Gomez-Ceballos,[44] P. Goncalves,[23] I. Gonzalez Caballero,[44] G. Gopal,[40] L. Gorn,[1] M. Gorski,[56] Yu. Gouz,[46] V. Gracco,[14] J. Grahl,[1] E. Graziani,[42] C. Green,[24] A. Grefrath,[57] H.-J. Grimm,[18] P. Gris,[43] G. Grosdidier,[21] K. Grzelak,[56] M. Gunther,[53] J. Guy,[40] C. Haag,[18] F. Hahn,[9] S. Hahn,[57] S. Haider,[9] A. Hallgren,[53] K. Hamacher,[57] K. Hamilton,[38] J. Hansen,[36] F.J. Harris,[38] S. Haug,[36] F. Hauler,[18] V. Hedberg,[27] S. Heising,[18] M. Hennecke,[18] R. Henriques,[23] J.J. Hernandez,[54] P. Herquet,[2] H. Herr†,[9] T.L. Hessing,[38] J.-M. Heuser,[57] E. Higon,[54] J. Hoffman,[56] S.-O. Holmgren,[48] P.J. Holt,[9] D. Holthuizen,[34] S. Hoorelbeke,[2] M.A. Houlden,[24] J. Hrubec,[55] M. Huber,[18] K. Huet,[2] G.J. Hughes,[24] K. Hultqvist,[48] J.N. Jackson,[24] R. Jacobsson,[9] P. Jalocha,[9] R. Janik,[7] Ch. Jarlskog,[27] G. Jarlskog,[27] P. Jarry,[43] B. Jean-Marie,[21] D. Jeans,[38] E.K. Johansson,[48] P.D. Johansson,[48] P. Jonsson,[28] C. Joram,[9] P. Juillot,[10] L. Jungermann,[18] F. Kapusta,[26] K. Karafasoulis,[12] S. Katsanevas,[28] E. Katsoufis,[35] R. Keranen,[18] G. Kernel,[47] B.P. Kersevan,[9,47]

U. Kerzel,[18] B.A. Khomenko,[17] N.N. Khovanski,[17] A. Kiiskinen,[16] B.T. King,[24] A. Kinvig,[24]
N.J. Kjaer,[9] O. Klapp,[57] H. Klein,[9] P. Kluit,[34] D. Knoblauch,[18] P. Kokkinias,[12]
A. Konopliannikov,[46] M. Koratzinos,[9] V. Kostioukhine,[46] C. Kourkoumelis,[3] O. Kouznetsov,[17]
M. Krammer,[55] C. Kreuter,[9] E. Kriznic,[47] J. Krstic,[12] Z. Krumstein,[17] P. Kubinec,[7]
W. Kucewicz,[19] M. Kucharczyk,[19] J. Kurowska,[56] K. Kurvinen,[16] J. Lamsa,[1] L. Lanceri,[51]
D.W. Lane,[1] P. Langefeld,[57] V. Lapin†,[46] J.-P. Laugier,[43] R. Lauhakangas,[16] G. Leder,[55]
F. Ledroit,[15] V. Lefebure,[2] L. Leinonen,[48] A. Leisos,[12] R. Leitner,[33] J. Lemonne,[2] G. Lenzen,[57]
V. Lepeltier,[21] T. Lesiak,[19] M. Lethuillier,[43] J. Libby,[38] W. Liebig,[57] D. Liko,[55] A. Lipniacka,[48]
I. Lippi,[39] B. Loerstad,[27] M. Lokajicek,[13] J.G. Loken,[38] J.H. Lopes,[52] J.M. Lopez,[37]
R. Lopez-Fernandez,[15] D. Loukas,[12] P. Lutz,[43] L. Lyons,[38] J. MacNaughton,[55] J.R. Mahon,[6]
A. Maio,[23] A. Malek,[57] T.G.M. Malmgren,[48] S. Maltezos,[35] V. Malychev,[17] F. Mandl,[55] J. Marco,[44]
R. Marco,[44] B. Marechal,[52] M. Margoni,[39] J.-C. Marin,[9] C. Mariotti,[9] A. Markou,[12]
C. Martinez-Rivero,[44] F. Martinez-Vidal,[54] S. Marti i Garcia,[9] J. Masik,[13]
N. Mastroyiannopoulos,[12] F. Matorras,[44] C. Matteuzzi,[31] G. Matthiae,[41] J. Mazik,[33]
F. Mazzucato,[39] M. Mazzucato,[39] M. Mc Cubbin,[24] R. Mc Kay,[1] R. Mc Nulty,[24] G. Mc Pherson,[24]
C. Meroni,[30] W.T. Meyer,[1] A. Miagkov,[46] E. Migliore,[49] L. Mirabito,[28] W. Mitaroff,[55]
U. Mjoernmark,[27] T. Moa,[48] M. Moch,[18] R. Moeller,[32] K. Moenig,[9,11] R. Monge,[14] J. Montenegro,[34]
D. Moraes,[52] X. Moreau,[26] S. Moreno,[23] P. Morettini,[14] G. Morton,[38] U. Mueller,[57] K. Muenich,[57]
M. Mulders,[34] C. Mulet-Marquis,[15] L. Mundim,[6] R. Muresan,[27] W. Murray,[40] B. Muryn,[20]
G. Myatt,[38] T. Myklebust,[36] F. Naraghi,[15] M. Nassiakou,[12] F. Navarria,[5] S. Navas,[54]
K. Nawrocki,[56] P. Negri,[31] N. Neufeld,[9] W. Neumann,[57] N. Neumeister,[55] R. Nicolaidou,[43]
B.S. Nielsen,[32] M. Nieuwenhuizen,[34] P. Niezurawski,[56] V. Nikolaenko,[10] M. Nikolenko,[17,10]
V. Nomokonov,[16] A. Normand,[24] A. Nygren,[27] A. Oblakowska-Mucha,[20] V. Obraztsov,[46]
A. Olshevski,[17] A. Onofre,[23] R. Orava,[16] G. Orazi,[10] K. Osterberg,[16] A. Ouraou,[43] A. Oyanguren,[54]
P. Paganini,[21] M. Paganoni,[31] S. Paiano,[5] R. Pain,[26] R. Paiva,[23] J.P. Palacios,[24] H. Palka,[19]
Th.D. Papadopoulou,[35] K. Papageorgiou,[12] L. Pape,[9] C. Parkes,[25] F. Parodi,[14] U. Parzefall,[9]
A. Passeri,[42] O. Passon,[57] T. Pavel,[27] M. Pegoraro,[39] L. Peralta,[23] V. Perepelitsa,[54] M. Pernicka,[55]
A. Perrotta,[5] C. Petridou,[51] A. Petrolini,[14] H.T. Phillips,[40] G. Piana,[14] J. Piedra,[44] L. Pieri,[42]
F. Pierre,[43] M. Pimenta,[23] E. Piotto,[9] T. Podobnik,[47] V. Poireau,[9] M.E. Pol,[6] G. Polok,[19]
E. Polycarpo,[52] P. Poropat†,[51] V. Pozdniakov,[17] P. Privitera,[41] N. Pukhaeva,[2,17] A. Pullia,[31]
D. Radojicic,[38] S. Ragazzi,[31] H. Rahmani,[35] D. Rakoczy,[55] J. Rames,[13] L. Ramler,[18] P.N. Ratoff,[22]
A. Read,[36] P. Rebecchi,[9] N.G. Redaelli,[31] M. Regler,[55] J. Rehn,[18] D. Reid,[34] R. Reinhardt,[57]
P. Renton,[38] L.K. Resvanis,[3] F. Richard,[21] J. Ridky,[13] G. Rinaudo,[49] I. Ripp-Baudot,[10]
M. Rivero,[44] D. Rodriguez,[44] O. Rohne,[36] A. Romero,[49] P. Ronchese,[39] E.I. Rosenberg,[1]
P. Rosinsky,[7] P. Roudeau,[21] T. Rovelli,[5] Ch. Royon,[43] V. Ruhlmann-Kleider,[43] A. Ruiz,[44]
D. Ryabtchikov,[46] H. Saarikko,[16] Y. Sacquin,[43] A. Sadovsky,[17] G. Sajot,[15] L. Salmi,[16] J. Salt,[54]
D. Sampsonidis,[12] M. Sannino,[14] A. Savoy-Navarro,[26] T. Scheidle,[18] H. Schneider,[18]
Ph. Schwemling,[26] B. Schwering,[57,58] U. Schwickerath,[9] M.A.E. Schyns,[57] F. Scuri,[51] P. Seager,[22]
Y. Sedykh,[17] A. Segar†,[38] N. Seibert,[18] R. Sekulin,[40] R.C. Shellard,[6] A. Sheridan,[24] M. Siebel,[57]
R. Silvestre,[43] L. Simard,[43] F. Simonetto,[39] A. Sisakian,[17] T.B. Skaali,[36] G. Smadja,[28]
N. Smirnov,[46] O. Smirnova,[27] G.R. Smith,[40] A. Sokolov,[46] A. Sopczak,[22] R. Sosnowski,[56]
T. Spassov,[9] E. Spiriti,[42] P. Sponholz,[57] S. Squarcia,[14] D. Stampfer,[55] C. Stanescu,[42] S. Stanic,[47]
M. Stanitzki,[18] S. Stapnes,[36] K. Stevenson,[38] A. Stocchi,[21] J. Strauss,[55] R. Strub,[10] B. Stugu,[4]
M. Szczekowski,[56] M. Szeptycka,[56] T. Szumlak,[20] T. Tabarelli,[31] A.C. Taffard,[24] F. Tegenfeldt,[53]
F. Terranova,[31] J. Thomas,[38] A. Tilquin,[29] J. Timmermans,[34] N. Tinti,[5] L. Tkatchev,[17] M. Tobin,[24]
T. Todorov,[10] S. Todorovova,[13] D.Z. Toet,[34] A. Tomaradze,[2] B. Tome,[23] A. Tonazzo,[31]
L. Tortora,[42] P. Tortosa,[54] G. Transtromer,[27] P. Travnicek,[13] D. Treille,[9] G. Tristram,[8]

M. Trochimczuk,[56] A. Trombini,[21] C. Troncon,[30] A. Tsirou,[9] M.-L. Turluer,[43] I.A. Tyapkin,[17] P. Tyapkin,[17] S. Tzamarias,[12] O. Ullaland,[9] V. Uvarov,[46] G. Valenti,[5] E. Vallazza,[51] C. Vander Velde,[2] G.W. Van Apeldoorn,[34] P. Van Dam,[34] W. Van den Boeck,[2] W.K. Van Doninck,[2] J. Van Eldik,[9] A. Van Lysebetten,[2] N. van Remortel,[2] I. Van Vulpen,[9] N. Vassilopoulos,[38] G. Vegni,[30] F. Veloso,[23] L. Ventura,[39] W. Venus,[40] F. Verbeure†,[2] P. Verdier,[28] M. Verlato,[39] L.S. Vertogradov,[17] V. Verzi,[41] D. Vilanova,[43] L. Vitale,[51] E. Vlasov,[46] A.S. Vodopyanov,[17] C. Vollmer,[18] G. Voulgaris,[3] V. Vrba,[13] H. Wahlen,[57] C. Walck,[48] A.J. Washbrook,[24] C. Weiser,[18] A.M. Wetherell†,[9] D. Wicke,[9] J. Wickens,[2] G. Wilkinson,[38] M. Winter,[10] M. Witek,[19] T. Wlodek,[21] G. Wolf,[9] J. Yi,[1] O. Yushchenko,[46] A. Zaitsev,[46] A. Zalewska,[19] P. Zalewski,[56] D. Zavrtanik,[47] E. Zevgolatakos†,[12] V. Zhuravlov,[17] N.I. Zimin,[17] A. Zintchenko,[17] Ph. Zoller,[10] G.C. Zucchelli,[48] G. Zumerle,[39] M. Zupan.[12]

[1] Department of Physics and Astronomy, Iowa State University, Ames IA 50011-3160, USA

[2] Physics Department, Universiteit Antwerpen, Universiteitsplein 1, B-2610 Antwerpen, Belgium
and IIHE, ULB-VUB, Pleinlaan 2, B-1050 Brussels, Belgium
and Faculté des Sciences, Univ. de l'Etat Mons, Av. Maistriau 19, B-7000 Mons, Belgium

[3] Physics Laboratory, University of Athens, Solonos Str. 104, GR-10680 Athens, Greece

[4] Department of Physics, University of Bergen, Allégaten 55, NO-5007 Bergen, Norway

[5] Dipartimento di Fisica, Università di Bologna and INFN, Via Irnerio 46, IT-40126 Bologna, Italy

[6] Centro Brasileiro de Pesquisas Físicas, rua Xavier Sigaud 150, BR-22290 Rio de Janeiro, Brazil
and Depto. de Física, Pont. Univ. Católica, C.P. 38071 BR-22453 Rio de Janeiro, Brazil
and Inst. de Física, Univ. Estadual do Rio de Janeiro, rua São Francisco Xavier 524, Rio de Janeiro, Brazil

[7] Comenius University, Faculty of Mathematics and Physics, Mlynska Dolina, SK-84215 Bratislava, Slovakia

[8] Collège de France, Lab. de Physique Corpusculaire, IN2P3-CNRS, FR-75231 Paris Cedex 05, France

[9] CERN, CH-1211 Geneva 23, Switzerland

[10] Institut de Recherches Subatomiques, IN2P3 - CNRS/ULP - BP20, FR-67037 Strasbourg Cedex, France

[11] Now at DESY-Zeuthen, Platanenallee 6, D-15735 Zeuthen, Germany

[12] Institute of Nuclear Physics, N.C.S.R. Demokritos, P.O. Box 60228, GR-15310 Athens, Greece

[13] FZU, Inst. of Phys. of the C.A.S. High Energy Physics Division, Na Slovance 2, CZ-180 40, Praha 8, Czech Republic

[14] Dipartimento di Fisica, Università di Genova and INFN, Via Dodecaneso 33, IT-16146 Genova, Italy

[15] Institut des Sciences Nucléaires, IN2P3-CNRS, Université de Grenoble 1, FR-38026 Grenoble Cedex, France

[16] Helsinki Institute of Physics and Department of Physical Sciences, P.O. Box 64, FIN-00014 University of Helsinki, Finland

[17] Joint Institute for Nuclear Research, Dubna, Head Post Office, P.O. Box 79, RU-101 000 Moscow, Russian Federation
[18] Institut für Experimentelle Kernphysik, Universität Karlsruhe, Postfach 6980, DE-76128 Karlsruhe, Germany
[19] Institute of Nuclear Physics PAN,Ul. Radzikowskiego 152, PL-31142 Krakow, Poland
[20] Faculty of Physics and Nuclear Techniques, University of Mining and Metallurgy, PL-30055 Krakow, Poland
[21] Université de Paris-Sud, Lab. de l'Accélérateur Linéaire, IN2P3-CNRS, Bât. 200, FR-91405 Orsay Cedex, France
[22] School of Physics and Chemistry, University of Lancaster, Lancaster LA1 4YB, UK
[23] LIP, IST, FCUL - Av. Elias Garcia, 14-1^{o}, PT-1000 Lisboa Codex, Portugal
[24] Department of Physics, University of Liverpool, P.O. Box 147, Liverpool L69 3BX, UK
[25] Dept. of Physics and Astronomy, Kelvin Building, University of Glasgow, Glasgow G12 8QQ
[26] LPNHE, IN2P3-CNRS, Univ. Paris VI et VII, Tour 33 (RdC), 4 place Jussieu, FR-75252 Paris Cedex 05, France
[27] Department of Physics, University of Lund, Sölvegatan 14, SE-223 63 Lund, Sweden
[28] Université Claude Bernard de Lyon, IPNL, IN2P3-CNRS, FR-69622 Villeurbanne Cedex, France
[29] Univ. d'Aix - Marseille II - CPP, IN2P3-CNRS, FR-13288 Marseille Cedex 09, France
[30] Dipartimento di Fisica, Università di Milano and INFN-MILANO, Via Celoria 16, IT-20133 Milan, Italy
[31] Dipartimento di Fisica, Univ. di Milano-Bicocca and INFN-MILANO, Piazza della Scienza 2, IT-20126 Milan, Italy
[32] Niels Bohr Institute, Blegdamsvej 17, DK-2100 Copenhagen Ø, Denmark
[33] IPNP of MFF, Charles Univ., Areal MFF, V Holesovickach 2, CZ-180 00, Praha 8, Czech Republic
[34] NIKHEF, Postbus 41882, NL-1009 DB Amsterdam, The Netherlands
[35] National Technical University, Physics Department, Zografou Campus, GR-15773 Athens, Greece
[36] Physics Department, University of Oslo, Blindern, NO-0316 Oslo, Norway
[37] Dpto. Fisica, Univ. Oviedo, Avda. Calvo Sotelo s/n, ES-33007 Oviedo, Spain
[38] Department of Physics, University of Oxford, Keble Road, Oxford OX1 3RH, UK
[39] Dipartimento di Fisica, Università di Padova and INFN, Via Marzolo 8, IT-35131 Padua, Italy
[40] Rutherford Appleton Laboratory, Chilton, Didcot OX11 OQX, UK
[41] Dipartimento di Fisica, Università di Roma II and INFN, Tor Vergata, IT-00173 Rome, Italy
[42] Dipartimento di Fisica, Università di Roma III and INFN, Via della Vasca Navale 84, IT-00146 Rome, Italy
[43] DAPNIA/Service de Physique des Particules, CEA-Saclay, FR-91191 Gif-sur-Yvette Cedex, France
[44] Instituto de Fisica de Cantabria (CSIC-UC), Avda. los Castros s/n, ES-39006 Santander, Spain
[45] Dipartimento di Fisica, Università degli Studi di Roma La Sapienza, Piazzale Aldo Moro 2, IT-00185 Rome, Italy

[46] Inst. for High Energy Physics, Serpukov P.O. Box 35, Protvino, (Moscow Region), Russian Federation
[47] J. Stefan Institute, Jamova 39, SI-1000 Ljubljana, Slovenia and Laboratory for Astroparticle Physics,
and Nova Gorica Polytechnic, Kostanjeviska 16a, SI-5000 Nova Gorica, Slovenia,
and Department of Physics, University of Ljubljana, SI-1000 Ljubljana, Slovenia
[48] Fysikum, Stockholm University, Box 6730, SE-113 85 Stockholm, Sweden
[49] Dipartimento di Fisica Sperimentale, Università di Torino and INFN, Via P. Giuria 1, IT-10125 Turin, Italy
[50] INFN,Sezione di Torino, and Dipartimento di Fisica Teorica, Università di Torino, Via P. Giuria 1, IT-10125 Turin, Italy
[51] Dipartimento di Fisica, Università di Trieste and INFN, Via A. Valerio 2, IT-34127 Trieste, Italy
and Istituto di Fisica, Università di Udine, IT-33100 Udine, Italy
[52] Univ. Federal do Rio de Janeiro, C.P. 68528 Cidade Univ., Ilha do Fundão BR-21945-970 Rio de Janeiro, Brazil
[53] Department of Radiation Sciences, University of Uppsala, P.O. Box 535, SE-751 21 Uppsala, Sweden
[54] IFIC, Valencia-CSIC, and D.F.A.M.N., U. de Valencia, Avda. Dr. Moliner 50, ES-46100 Burjassot (Valencia), Spain
[55] Institut für Hochenergiephysik, Österr. Akad. d. Wissensch., Nikolsdorfergasse 18, AT-1050 Vienna, Austria
[56] Inst. Nuclear Studies and University of Warsaw, Ul. Hoza 69, PL-00681 Warsaw, Poland
[57] Fachbereich Physik, University of Wuppertal, Postfach 100 127, DE-42097 Wuppertal, Germany
[58] Now at I.Physikalisches Institut, RWTH Aachen, Sommerfeldstrasse 14, DE-52056 Aachen, Germany
† Deceased

A.3 The L3 Collaboration

M. Acciarri,[29] P. Achard,[18] O. Adriani,[16] M. Aguilar-Benitez,[27] J. Alcaraz,[27] G. Alemanni,[23] J. Allaby,[10] A. Aloisio,[32] M.G. Alviggi,[32] G. Ambrosi,[18] H. Anderhub,[15] V.P. Andreev,[25,38] T. Angelescu,[7] F. Anselmo,[6] A. Arefiev,[31] T. Azemoon,[28] T. Aziz,[50] P. Bagnaia,[44] A. Bajo,[27] G. Baksay,[17] L. Baksay,[17] A. Balandras,[22] S.V. Baldew,[34] R.C. Ball,[28] S. Banerjee,[50] Sw. Banerjee,[22] A. Barczyk,[15,41] R. Barillère,[10] L. Barone,[44] P. Bartalini,[23] M. Basile,[6] N. Batalova,[42] R. Battiston,[37] A. Bay,[23] F. Becattini,[16] U. Becker,[30] F. Behner,[15] L. Bellucci,[16] R. Berbeco,[28] J. Berdugo,[27] P. Berges,[30] B. Bertucci,[37] B.L. Betev,[15] S. Bhattacharya,[50] M. Biasini,[37] M. Biglietti,[32] A. Biland,[15] J.J. Blaising,[22] S.C. Blyth,[11] G.J. Bobbink,[34] A. Böhm,[1] L. Boldizsar,[8] B. Borgia,[44] S. Bottai,[16] D. Bourilkov,[15] M. Bourquin,[18] S. Braccini,[18] J.G. Branson,[52] V. Brigljevic,[15] F. Brochu,[22] I.C. Brock,[11] A. Buffini,[16] A. Buijs,[53] J.D. Burger,[30] W.J. Burger,[37] A. Button,[28] X.D. Cai,[30] M. Campanelli,[15] M. Capell,[30] G. Cara Romeo,[6] G. Carlino,[32] A. Cartacci,[16] J. Casaus,[27] G. Castellini,[16] F. Cavallari,[44] N. Cavallo,[39] C. Cecchi,[37] M. Cerrada,[27] F. Cesaroni,[24] M. Chamizo,[18] Y.H. Chang,[49] U.K. Chaturvedi,[54] M. Chemarin,[26] A. Chen,[49] G. Chen,[4] G.M. Chen,[4] H.F. Chen,[20] H.S. Chen,[4] G. Chiefari,[32] L. Cifarelli,[45] F. Cindolo,[6] C. Civinini,[16] I. Clare,[30] R. Clare,[43] G. Coignet,[22] A.P. Colijn,[34] N. Colino,[27] S. Costantini,[44] F. Cotorobai,[7] B. Cozzoni,[6] B. de la Cruz,[27] A. Csilling,[8] S. Cucciarelli,[37] T.S. Dai,[30] J.A. van Dalen,[35] R. D'Alessandro,[16] R. de Asmundis,[32] J. Debreczeni,[8] P. Déglon,[18] A. Degré,[22] K. Dehmelt,[17] K. Deiters,[41] D. della Volpe,[32] E. Delmeire,[18] P. Denes,[40] F. DeNotaristefani,[44] A. De Salvo,[15] M. Diemoz,[44] M. Dierckxsens,[34] D. van Dierendonck,[34] F. Di Lodovico,[15] C. Dionisi,[44] M. Dittmar,[15] A. Dominguez,[52] A. Doria,[32] M.T. Dova,[33,♯] D. Duchesneau,[22] D. Dufournaud,[22] M. Duda,[1] P. Duinker,[34] I. Duran,[46] S. Dutta,[50] B. Echenard,[18] A. Eline,[10] A. El Hage,[1] H. El Mamouni,[26] A. Engler,[11] F.J. Eppling,[30] F.C. Erné,[34] P. Extermann,[18] M. Fabre,[41] R. Faccini,[44] M.A. Falagan,[27] S. Falciano,[44] A. Favara,[9] J. Fay,[26] O. Fedin,[38] M. Felcini,[15] T. Ferguson,[11] F. Ferroni,[44] H. Fesefeldt,[1] E. Fiandrini,[37] J.H. Field,[18] F. Filthaut,[35] P.H. Fisher,[30] W. Fisher,[40] I. Fisk,[52] G. Forconi,[30] L. Fredj,[18] K. Freudenreich,[15] C. Furetta,[29] Yu. Galaktionov,[31,30] S.N. Ganguli,[50] P. Garcia-Abia,[27] M. Gataullin,[9] S.S. Gau,[33] S. Gentile,[44] N. Gheordanescu,[7] S. Giagu,[44] Z.F. Gong,[20] G. Grenier,[26] O. Grimm,[15] M.W. Gruenewald,[14] M. Guida,[45] R. van Gulik,[34] V.K. Gupta,[40] A. Gurtu,[50] L.J. Gutay,[42] D. Haas,[3] A. Hasan,[12] D. Hatzifotiadou,[6] T. Hebbeker,[1] A. Hervé,[10] P. Hidas,[8] J. Hirschfelder,[11] H. Hofer,[15] M. Hohlmann,[17] G. Holzner,[15] H. Hoorani,[11] S.R. Hou,[49] I. Iashvili,[55] V. Innocente,[10] B.N. Jin,[4] P. Jindal,[36] L.W. Jones,[28] P. de Jong,[34] I. Josa-Mutuberría,[27] R.A. Khan,[54] M. Kaur,[36] M.N. Kienzle-Focacci,[18] D. Kim,[44] J.K. Kim,[21] J. Kirkby,[10] D. Kiss,[8] W. Kittel,[35] A. Klimentov,[30,31] A.C. König,[35] E. Koffeman,[34] M. Kopal,[42] A. Kopp,[55] V. Koutsenko,[30,31] M. Kräber,[15] R.W. Kraemer,[11] W. Krenz,[1] A. Krüger,[55] H. Kuijten,[35] A. Kunin,[30] P. Ladron de Guevara,[27] I. Laktineh,[26] G. Landi,[16] K. Lassila-Perini,[15] M. Lebeau,[10] A. Lebedev,[30] P. Lebrun,[26] P. Lecomte,[15] P. Lecoq,[10] P. Le Coultre,[15] H.J. Lee,[5] J.M. Le Goff,[10] R. Leiste,[55] E. Leonardi,[44] M. Levtchenko,[29] P. Levtchenko,[38] C. Li,[20] S. Likhoded,[55] C.H. Lin,[49] W.T. Lin,[49] F.L. Linde,[34] L. Lista,[32] Z.A. Liu,[4] W. Lohmann,[55] E. Longo,[44] Y.S. Lu,[4] W. Lu,[9] K. Lübelsmeyer,[1] C. Luci,[44] D. Luckey,[30] L. Luminari,[44] L. Lugnier,[26] W. Lustermann,[15] W.G. Ma,[20] M. Maity,[50] L. Malgeri,[10] A. Malinin,[31] C. Maña,[27] D. Mangeol,[35] J. Mans,[40] P. Marchesini,[15] G. Marian,[13] J.P. Martin,[26] F. Marzano,[44] G.G.G. Massaro,[34] K. Mazumdar,[50] R.R. McNeil,[25] S. Mele,[10,32] L. Merola,[32] M. Merk,[11] M. Meschini,[16] W.J. Metzger,[35] M. von der Mey,[1] A. Mihul,[7] H. Milcent,[10] G. Mirabelli,[44] J. Mnich,[1] G.B. Mohanty,[50] P. Molnar,[5] B. Monteleoni,[16,†] T. Moulik,[50] G.S. Muanza,[26] F. Muheim,[18] A.J.M. Muijs,[34] B. Musicar,[52] M. Musy,[44] S. Nagy,[13] S. Natale,[18] M. Napolitano,[32] F. Nessi-Tedaldi,[15] H. Newman,[9] T. Niessen,[1] A. Nisati,[44] T. Novak,[35] H. Nowak,[55] R. Ofierzynski,[15] G. Organtini,[44] A. Oulianov,[31] I. Pal,[42] C. Palomares,[27] D. Pandoulas,[1] S. Paoletti,[44,10] A. Paoloni,[44]

P. Paolucci[32] R. Paramatti[44] H.K. Park[11] I.H. Park[21] G. Pascale[44] G. Passaleva[16] S. Patricelli[32] T. Paul[33] M. Pauluzzi[37] C. Paus[30] F. Pauss[15] D. Peach[10] M. Pedace[44] S. Pensotti[29] D. Perret-Gallix[22] B. Petersen[35] D. Piccolo[32] F. Pierella[6] M. Pieri[16] M. Pioppi[37] P.A. Piroué[40] E. Pistolesi[29] V. Plyaskin[31] M. Pohl[18] V. Pojidaev[16] H. Postema[30] J. Pothier[10] N. Produit[18] D.O. Prokofiev[42] D. Prokofiev[38] J. Quartieri[45] G. Rahal-Callot[15] M.A. Rahaman[50] P. Raics[13] N. Raja[50] R. Ramelli[15] P.G. Rancoita[29] R. Ranieri[16] A. Raspereza[55] P. Razis[12] D. Ren[15] M. Rescigno[44] S. Reucroft[33] T. van Rhee[53] S. Riemann[55] K. Riles[28] A. Robohm[15] J. Rodin[2] B.P. Roe[28] L. Romero[27] A. Rosca[55] C. Rosemann[1] C. Rosenbleck[1] S. Rosier-Lees[22] S. Roth[1] J.A. Rubio[10] G. Ruggiero[16] D. Ruschmeier[5] H. Rykaczewski[15] A. Sakharov[15] S. Saremi[25] S. Sarkar[44] J. Salicio[10] E. Sanchez[27] M.P. Sanders[35] M.E. Sarakinos[47] C. Schäfer[10] V. Schegelsky[38] S. Schmidt-Kaerst[1] D. Schmitz[1] H. Schopper[19] D.J. Schotanus[35] G. Schwering[1] C. Sciacca[32] D. Sciarrino[18] A. Seganti[6] L. Servoli[37] S. Shevchenko[9] N. Shivarov[48] V. Shoutko[30] E. Shumilov[31] A. Shvorob[9] T. Siedenburg[1] D. Son[21] B. Smith[11] C. Souga[26] P. Spillantini[16] M. Steuer[30] D.P. Stickland[40] A. Stone[25] H. Stone[40,†] B. Stoyanov[48] A. Straessner[18] K. Sudhakar[50] G. Sultanov[48] L.Z. Sun[20] S. Sushkov[1] H. Suter[15] J.D. Swain[33] Z. Szillasi[17,¶] T. Sztaricskai[2,¶] X.W. Tang[4] P. Tarjan[13] L. Tauscher[3] L. Taylor[33] B. Tellili[26] D. Teyssier[26] C. Timmermans[35] S.C.C. Ting[30] S.M. Ting[30] S.C. Tonwar[50] J. Tóth[8] C. Tully[40] K.L. Tung[4] Y. Uchida[30] J. Ulbricht[15] U. Uwer[10] E. Valente[44] R.T. Van de Walle[35] R. Vasquez[42] V. Veszpremi[17] G. Vesztergombi[8] I. Vetlitsky[31] D. Vicinanza[45] G. Viertel[15] S. Villa[43] M. Vivargent[22] S. Vlachos[3] I. Vodopianov[17] H. Vogel[11] H. Vogt[55] I. Vorobiev[11,31] A.A. Vorobyov[38] A. Vorvolakos[12] M. Wadhwa[3] W. Wallraff[1] Q. Wang[35] X.L. Wang[20] Z.M. Wang[20] A. Weber[1] M. Weber[10] P. Wienemann[1] H. Wilkens[35] S.X. Wu[30] S. Wynhoff[40] L. Xia[9] Z.Z. Xu[20] J. Yamamoto[28] B.Z. Yang[20] C.G. Yang[4] H.J. Yang[28] M. Yang[4] J.B. Ye[20] S.C. Yeh[51] J.M. You[11] An. Zalite[38] Yu. Zalite[38] Z.P. Zhang[20] J.Zhao[20] G.Y. Zhu[4] R.Y. Zhu[9] H.L. Zhuang[4] A. Zichichi[6,10,54] G. Zilizi[2,¶] B. Zimmermann[15] M. Zöller[1]

[1] III. Physikalisches Institut, RWTH, D-52056 Aachen, Germany§
[2] University of Alabama, Tuscaloosa, AL 35486, USA
[3] Institute of Physics, University of Basel, CH-4056 Basel, Switzerland
[4] Institute of High Energy Physics, IHEP, 100039 Beijing, China△
[5] Humboldt University, D-10099 Berlin, FRG§
[6] University of Bologna and INFN-Sezione di Bologna, I-40126 Bologna, Italy
[7] Institute of Atomic Physics and University of Bucharest, R-76900 Bucharest, Romania
[8] Central Research Institute for Physics of the Hungarian Academy of Sciences, H-1525 Budapest 114, Hungary‡
[9] California Institute of Technology, Pasadena, CA 91125, USA
[10] European Laboratory for Particle Physics, CERN, CH-1211 Geneva 23, Switzerland
[11] Carnegie Mellon University, Pittsburgh, PA 15213, USA
[12] Department of Physics, University of Cyprus, Nicosia, Cyprus
[13] KLTE-ATOMKI, H-4010 Debrecen, Hungary¶
[14] UCD School of Physics, University College Dublin, Belfield, Dublin 4, Ireland
[15] Eidgenössische Technische Hochschule, ETH Zürich, CH-8093 Zürich, Switzerland
[16] INFN Sezione di Firenze and University of Florence, I-50125 Florence, Italy
[17] Florida Institute of Technology, Melbourne, FL 32901, USA
[18] University of Geneva, CH-1211 Geneva 4, Switzerland
[19] University of Hamburg, D-22761 Hamburg, Germany
[20] Chinese University of Science and Technology, USTC, Hefei, Anhui 230 029, China△

[21] The Center for High Energy Physics, Kyungpook National University, 702-701 Taegu, Republic of Korea
[22] Laboratoire d'Annecy-le-Vieux de Physique des Particules, LAPP,IN2P3-CNRS, BP 110, F-74941 Annecy-le-Vieux CEDEX, France
[23] University of Lausanne, CH-1015 Lausanne, Switzerland
[24] INFN-Sezione di Lecce and Universitá Degli Studi di Lecce, I-73100 Lecce, Italy
[25] Louisiana State University, Baton Rouge, LA 70803, USA
[26] Institut de Physique Nucléaire de Lyon, IN2P3-CNRS,Université Claude Bernard, F-69622 Villeurbanne, France
[27] Centro de Investigaciones Energéticas, Medioambientales y Tecnológicas, CIEMAT, E-28040 Madrid, Spain♭
[28] University of Michigan, Ann Arbor, MI 48109, USA
[29] INFN-Sezione di Milano, I-20133 Milan, Italy
[30] Massachusetts Institute of Technology, Cambridge, MA 02139, USA
[31] Institute of Theoretical and Experimental Physics, ITEP, Moscow, Russia
[32] INFN-Sezione di Napoli and University of Naples, I-80125 Naples, Italy
[33] Northeastern University, Boston, MA 02115, USA
[34] National Institute for High Energy Physics, NIKHEF, and University of Amsterdam, NL-1009 DB Amsterdam, The Netherlands
[35] Radboud University and NIKHEF, NL-6525 ED Nijmegen, The Netherlands
[36] Panjab University, Chandigarh 160 014, India
[37] INFN-Sezione di Perugia and Università Degli Studi di Perugia, I-06100 Perugia, Italy
[38] Nuclear Physics Institute, St. Petersburg, Russia
[39] INFN-Sezione di Napoli and University of Potenza, I-85100 Potenza, Italy
[40] Princeton University, Princeton, NJ 08544, USA
[41] Paul Scherrer Institut, PSI, CH-5232 Villigen, Switzerland
[42] Purdue University, West Lafayette, IN 47907, USA
[43] University of Californa, Riverside, CA 92521, USA
[44] INFN-Sezione di Roma and University of Rome, "La Sapienza", I-00185 Rome, Italy
[45] University and INFN, Salerno, I-84100 Salerno, Italy
[46] Dept. de Fisica de Particulas Elementales, Univ. de Santiago, E-15706 Santiago de Compostela, Spain
[47] SEFT, Research Institute for High Energy Physics, P.O. Box 9, SF-00014 Helsinki, Finland
[48] Bulgarian Academy of Sciences, Central Lab. of Mechatronics and Instrumentation, BU-1113 Sofia, Bulgaria
[49] National Central University, Chung-Li, Taiwan, China
[50] Tata Institute of Fundamental Research, Mumbai (Bombay) 400 005, India
[51] Department of Physics, National Tsing Hua University, Taiwan, China
[52] University of California, San Diego, CA 92093, USA
[53] Utrecht University and NIKHEF, NL-3584 CB Utrecht, The Netherlands
[54] World Laboratory, FBLJA Project, CH-1211 Geneva 23, Switzerland
[55] DESY, D-15738 Zeuthen, Germany

§ Supported by the German Bundesministerium für Bildung, Wissenschaft, Forschung und Technologie.
‡ Supported by the Hungarian OTKA fund under contract numbers T019181, F023259

and T037350.
¶ Also supported by the Hungarian OTKA fund under contract number T026178.
♭ Supported also by the Comisión Interministerial de Ciencia y Tecnología.
♯ Also supported by CONICET and Universidad Nacional de La Plata, CC 67, 1900 La Plata, Argentina.
△ Supported by the National Natural Science Foundation of China.

A.4 The OPAL Collaboration

G. Abbiendi,[5] P.D. Acton,[8] C. Ainsley,[10] P.F. Åkesson,[6] G. Alexander,[33] J. Allison,[20] P.P. Allport,[10] N. Altekamp,[10] P. Amaral,[13] K. Ametewee,[8] G. Anagnostou,[4] K.J. Anderson,[13] S. Anderson,[19] S. Arcelli,[21] J.C. Armitage,[26] S. Asai,[34] S.F. Ashby,[4] P. Ashton,[20] A. Astbury,[36] D. Axen,[7] G. Azuelos,[22,as] G.A. Bahan,[20] I. Bailey,[36] J.T.M. Baines,[20] A.H. Ball,[12] J. Banks,[20] E. Barberio,[12,af] T. Barillari,[23] G.J. Barker,[29] R.J. Barlow,[20] S. Barnett,[20] R. Bartoldus,[6] R.J. Batley,[10] G. Beaudoin,[22] P. Bechtle,[15] J. Bechtluft,[1] A. Beck,[33] J. Becker,[17] C. Beeston,[20] T. Behnke,[15] A.N. Bell,[4] K.W. Bell,[31] P.J. Bell,[4] G. Bella,[33] A. Bellerive,[26] G. Benelli,[30] S. Bentvelsen,[12] P. Berlich,[17] S. Bethke,[23] O. Biebel,[24] U. Binder,[17] V. Blobel,[12] I.J. Bloodworth,[4] J.E. Bloomer,[4] P. Bock,[18] B. Boden,[6] J. Böhme,[1,ai] O. Boeriu,[17] D. Bonacorsi,[5] H.M. Bosch,[18] S. Bougerolle,[7] M. Boutemeur,[24,ab] B.T. Bouwens,[19] B.B. Brabson,[19] S. Braibant,[5] H. Breuker,[12] P. Bright-Thomas,[4] L. Brigliadori,[5] R.M. Brown,[31] R. Brun,[12] R. Bürgin,[17] K. Buesser,[15] A. Buijs,[12] H.J. Burckhart,[12] C. Burgard,[15] J. Cammin,[6] S. Campana,[30] P. Capiluppi,[5] R.K. Carnegie,[26] B. Caron,[2] A.A. Carter,[29] J.R. Carter,[10] C.Y. Chang,[21] C. Charlesworth,[26] D.G. Charlton,[4] J.T.M. Chrin,[20] D. Chrisman,[30] S.L. Chu,[30] C. Ciocca,[5] P.E.L. Clarke,[35] E. Clay,[35] J.C. Clayton,[4] I. Cohen,[33] W.J. Collins,[10] J.E. Conboy,[35] O.C. Cooke,[12] M. Cooper,[32] M. Couch,[4] J. Couchman,[35] M. Coupland,[3] E. do Couto e Silva,[19] R.L. Coxe,[13] A. Csilling,[9] M. Cuffiani,[5] S. Dado,[32] C. Dallapiccola,[21,ae] G.M. Dallavalle,[5] S. Dallison,[20] C. Darling,[16] S. De Jong,[19,aj] A. De Roeck,[12] E.A. De Wolf,[12,b] P. Debu,[11] H. Deng,[21] M.M. Deninno,[5] P. Dervan,[35] K. Desch,[15] A. Dieckmann,[18] B. Dienes,[14] M. Dittmar,[30,aw] M.S. Dixit,[27,e] M. Donkers,[26] M. Doucet,[22] J. Dubbert,[24] J.E. Duboscq,[12] E. Duchovni,[37] G. Duckeck,[24] I.P. Duerdoth,[20] D.J.P. Dumas,[26] G. Eckerlin,[18] J.E.G. Edwards,[20] P.A. Elcombe,[10] P.G. Estabrooks,[26] E. Etzion,[33] H.G. Evans,[13,h] M. Evans,[29] F. Fabbri,[5] M. Fanti,[5] P. Fath,[18] L. Feld,[17] P. Ferrari,[12] F. Fiedler,[24] M. Fierro,[5] M. Fincke-Keeler,[36] H.M. Fischer,[6] I. Fleck,[17] R. Folman,[37] D.G. Fong,[21] M. Ford,[20] M. Foucher,[21] A. Frey,[12] A. Fürtjes,[12] H. Fukui,[34] C. Fukunaga,[34,bb] D.I. Futyan,[20] P. Gagnon,[19] A. Gaidot,[11] O. Ganel,[37] J.W. Gary,[30] J. Gascon,[22,ab] S.M. Gascon-Shotkin,[21,ab] G. Gaycken,[15] N.I. Geddes,[31] C. Geich-Gimbel,[6] S.W. Gensler,[13] F.X. Gentit,[11] T. Geralis,[31] G. Giacomelli,[5] P. Giacomelli,[5] R. Giacomelli,[5] V. Gibson,[10] W.R. Gibson,[29] J.D. Gillies,[31] D.M. Gingrich,[2,as] M. Giunta,[30] D. Glenzinski,[13,q] J. Goldberg,[32] M.J. Goodrick,[10] W. Gorn,[30] K. Graham,[36] C. Grandi,[5] F.C. Grant,[10] E. Gross,[37] J. Grunhaus,[33] M. Gruwé,[15] P.O. Günther,[6] A. Gupta,[13] J. Hagemann,[15] C. Hajdu,[9] M. Hamann,[15] G.G. Hanson,[30] M. Hansroul,[12] M. Hapke,[29] K. Harder,[15] A. Harel,[32] C.K. Hargrove,[27,e] M. Harin-Dirac,[30] P.F. Harrison,[29] P.A. Hart,[13] C. Hartmann,[6] P.M. Hattersley,[4] M. Hauschild,[12] C.M. Hawkes,[4] R. Hawkings,[12] E. Heflin,[30] R.J. Hemingway,[26] C. Hensel,[15] G. Herten,[17] R.D. Heuer,[15] M.D. Hildreth,[12,ak] J.C. Hill,[10] S.J. Hillier,[4] T. Hilse,[17] D.A. Hinshaw,[22] C. Ho,[30] J. Hoare,[10] J.D. Hobbs,[12] P.R. Hobson,[8] D. Hochman,[37] A. Hocker,[13] K. Hoffman,[13] B. Holl,[12] R.J. Homer,[4] A.K. Honma,[12] D. Horváth,[9,j] K.R. Hossain,[2] S.R. Hou,[21] R. Howard,[7] C.P. Howarth,[35] P. Hüntemeyer,[15] R.E. Hughes-Jones,[20] R. Humbert,[17] D.E. Hutchcroft,[10] P. Igo-Kemenes,[18] H. Ihssen,[18] D.C. Imrie,[8] M.R. Ingram,[20] K. Ishii,[34,w] F.R. Jacob,[31] A.C. Janissen,[26] A. Jawahery,[21] P.W. Jeffreys,[31] H. Jeremie,[22] M. Jimack,[4] M. Jobes,[4,†] A. Joly,[22] C.R. Jones,[10] G. Jones,[20] M. Jones,[26,ay] R.W.L. Jones,[12] U. Jost,[18] P. Jovanovic,[4] C. Jui,[30] T.R. Junk,[26,t] N. Kanaya,[36] J. Kanzaki,[34,w] G. Karapetian,[22] D. Karlen,[36] V. Kartvelishvili,[20] K. Kawagoe,[34] T. Kawamoto,[34] R.K. Keeler,[36] R.G. Kellogg,[21] B.W. Kennedy,[31] D.H. Kim,[25] B.J. King,[12] J. Kirk,[12,am] K. Klein,[18,a] C. Kleinwort,[12] D.E. Klem,[28,az] A. Klier,[37] S. Kluth,[23] T. Kobayashi,[34] M. Kobel,[6] L. Köpke,[12] D.S. Koetke,[26] T.P. Kokott,[6] S. Komamiya,[34] L. Kormos,[36] R.V. Kowalewski,[36] T. Krämer,[15] J.F. Kral,[12] T. Kress,[30] H. Kreutzmann,[6] P. Krieger,[26,aq] J. von Krogh,[18] J. Kroll,[13] D. Krop,[19] K. Kruger,[12]

T. Kuhl,[15] M. Kupper,[37] M. Kuwano,[34] P. Kyberd,[29] G.D. Lafferty,[20] H. Lafoux,[11] R. Lahmann,[21,p] W.P. Lai,[25] F. Lamarche,[22] H. Landsman,[32] D. Lanske,[1] W.J. Larson,[30] J. Lauber,[35] S.R. Lautenschlager,[16] I. Lawson,[36] J.G. Layter,[30] D. Lazic,[32,c] P. Le Du,[11] P. Leblanc,[22] A.M. Lee,[16] E. Lefebvre,[22] M.H. Lehto,[35] A. Leins,[24] D. Lellouch,[37] P. Lennert,[18] C. Leroy,[22] L. Lessard,[22] J. Letts,[an] S. Levegrün,[6] L. Levinson,[37] C. Lewis,[35] R. Liebisch,[18] J. Lillich,[17] C. Littlewood,[10] A.W. Lloyd,[4] S.L. Lloyd,[29] F.K. Loebinger,[20] G.D. Long,[36] J.M. Lorah,[21] B. Lorazo,[22] M.J. Losty,[27,ar] X.C. Lou,[19] J. Lu,[7,ar] A. Ludwig,[6] J. Ludwig,[17] A. Luig,[17] A. Macchiolo,[22] A. Macpherson,[2,g] W. Mader,[6,u] P. Mättig,[av] A. Malik,[11] M. Mannelli,[12] S. Marcellini,[5] T.E. Marchant,[20] G. Maringer,[6] C. Markus,[6] A.J. Martin,[29] J.P. Martin,[22] G. Martinez,[21,r] G. Masetti,[5] T. Mashimo,[34] W. Matthews,[8] U. Maur,[6] W.J. McDonald,[2] R.F. McGowan,[20] J. McKenna,[7] E.A. Mckigney,[35] T.J. McMahon,[4] A.I. McNab,[29] J.R. McNutt,[8] A.C. McPherson,[26] R.A. McPherson,[36] F. Meijers,[12] P. Mendez-Lorenzo,[24] W. Menges,[15] S. Menke,[6,ah] D. Menszner,[18] F.S. Merritt,[13] H. Mes,[26,as] J. Meyer,[15] N. Meyer,[15] A. Michelini,[5] R.P. Middleton,[31] S. Mihara,[34] G. Mikenberg,[37] J. Mildenberger,[26,ar] D.J. Miller,[35] C. Milstene,[33] R. Mir,[37] S. Moed,[32] W. Mohr,[17] C. Moisan,[22] A. Montanari,[5] T. Mori,[34] M. Morii,[34,bc] M.W. Moss,[20] T. Mouthuy,[19,ad] U. Müller,[6] P.G. Murphy,[20] A. Mutter,[17] K. Nagai,[29] I. Nakamura,[34,w] H. Nanjo,[34] H.A. Neal,[38] B. Nellen,[6] H.H. Nguyen,[13] B. Nijjhar,[20] R. Nisius,[23] M. Nozaki,[34] F.G. Oakham,[27,e] F. Odorici,[5] M. Ogg,[26] H.O. Ogren,[19] A. Oh,[12] H. Oh,[30] A. Okpara,[18] N.J. Oldershaw,[20] T. Omori,[34,x] S.W. O'Neale,[4,†] B.P. O'Neill,[30] C.J. Oram,[36,as] M.J. Oreglia,[13] S. Orito,[34,†] C. Pahl,[23] J. Pálinkás,[14,k] F. Palmonari,[5] J.P. Pansart,[11] B. Panzer-Steindel,[12] P. Paschievici,[37] G. Pásztor,[30,d] J.R. Pater,[20] G.N. Patrick,[31] S.J. Pawley,[20] N. Paz-Jaoshvili,[33] M.J. Pearce,[4] S. Petzold,[15] P. Pfeifenschneider,[1,ah] P. Pfister,[17] J.E. Pilcher,[13] J. Pinfold,[2] D. Pitman,[36] D.E. Plane,[12] P. Poffenberger,[36] B. Poli,[5] J. Polok,[12] O. Pooth,[1] A. Posthaus,[6] A. Pouladdej,[26] L.A. del Pozo,[12] E. Prebys,[12] T.W. Pritchard,[29] M. Przybycień,[12,i] H. Przysiezniak,[2] A. Quadt,[6] G. Quast,[12,z]. K. Rabbertz,[12,v] B. Raith,[6] M.W. Redmond,[13] D.L. Rees,[4] C. Rembser,[12] P. Renkel,[37] G.E. Richards,[20] H. Rick,[30] D. Rigby,[4] K. Riles,[30,ag] S.A. Robins,[29] D. Robinson,[12] N. Rodning,[2,†] A. Rollnik,[6] J.M. Roney,[36] A. Rooke,[35] E. Ros,[12] S. Rosati,[6] K. Roscoe,[20] S. Rossberg,[17] A.M. Rossi,[5] M. Rosvick,[36] P. Routenburg,[2] Y. Rozen,[32] K. Runge,[17] O. Runolfsson,[12] U. Ruppel,[1] D.R. Rust,[19] R. Rylko,[8] K. Sachs,[26] T. Saeki,[34,w] O. Sahr,[24] S. Sanghera,[26] E.K.G. Sarkisyan,[12,ac] M. Sasaki,[34] C. Sbarra,[36] A.D. Schaile,[24] O. Schaile,[24] W. Schappert,[26] F. Scharf,[6] P. Scharff-Hansen,[12] P. Schenk,[30] J. Schieck,[23] B. Schmitt,[12] H. von der Schmitt,[18,ah] S. Schmitt,[18] T. Schörner-Sadenius,[12,m] S. Schreiber,[6] M. Schröder,[12] P. Schütz,[6] H.C. Schultz-Coulon,[17] M. Schulz,[12] M. Schumacher,[6] J. Schwarz,[17] C. Schwick,[12] J. Schwiening,[6] W.G. Scott,[31] M. Settles,[19] R. Seuster,[1,au] T.G. Shears,[12,aa] B.C. Shen,[30] C.H. Shepherd-Themistocleous,[10,am] P. Sherwood,[35] R. Shypit,[7] A. Simon,[6] P. Singh,[29] G.P. Siroli,[5] A. Sittler,[15] A. Skillman,[35] A. Skuja,[21] A.M. Smith,[12] T.J. Smith,[36,f] G.A. Snow,[21,†] R. Sobie,[36] S. Söldner-Rembold,[20] S. Spagnolo,[31] F. Spano,[13] R.W. Springer,[2,at] M. Sproston,[31] A. Stahl,[6,n] M. Starks,[19] M. Steiert,[18] K. Stephens,[20] J. Steuerer,[15] H.E. Stier,[17,†] B. Stockhausen,[6] K. Stoll,[17] R. Ströhmer,[24] D. Strom,[25] F. Strumia,[12] L. Stumpf,[36] B. Surrow,[12] P. Szymanski,[31] R. Tafirout,[22] H. Takeda,[34] T. Takeshita,[34,ao] S.D. Talbot,[4] S. Tanaka,[34] P. Taras,[22] S. Tarem,[32] M. Tasevsky,[12,al] R.J. Taylor,[35] M. Tecchio,[12,ag] P. Teixeira-Dias,[18] N. Tesch,[6] R. Teuscher,[13] N.J. Thackray,[4] M. Thiergen,[17] J. Thomas,[35] M.A. Thomson,[10] E. von Törne,[6] E. Torrence,[25] S. Towers,[26] D. Toya,[34] Z. Trócsányi,[14,l] P. Tran,[30] G. Transtromer,[8,ap] T. Trefzger,[24] N.J. Tresilian,[20] I. Trigger,[12] M. Tscheulin,[17] T. Tsukamoto,[34,†] E. Tsur,[33] A.S. Turcot,[13] M.F. Turner-Watson,[4] G. Tysarczyk-Niemeyer,[18] I. Ueda,[34] B. Ujvári,[14,l] P. Utzat,[18] B. Vachon,[36] D. Van den plas,[22] R. Van Kooten,[19] G.J. VanDalen,[30,o] P. Vannerem,[17] G. Vasseur,[11] R. Vértesi,[14,l] M. Verzocchi,[21] P. Vikas,[22] M. Vincter,[36,e] C.J. Virtue,[28,ba]

E.H. Vokurka,[20] C.F. Vollmer,[24] H. Voss,[12,y] J. Vossebeld,[12,aa] F. Wäckerle,[17] A. Wagner,[15] D.L. Wagner,[13] C. Wahl,[17] J.P. Walker,[4] D. Waller,[26] C.P. Ward,[10] D.R. Ward,[10] J.J. Ward,[35] P.M. Watkins,[4] A.T. Watson,[4] N.K. Watson,[4] M. Weber,[18] P. Weber,[26] S. Weisz,[12] P.S. Wells,[12] T. Wengler,[12] N. Wermes,[6] D. Wetterling,[18] M. Weymann,[12] M.A. Whalley,[4] J.S. White,[26] B. Wilkens,[17] J.A. Wilson,[4] G.W. Wilson [20,ax] I. Wingerter,[12] V-H. Winterer,[17] T. Wlodek,[37] G. Wolf,[37] N.C. Wood,[20] S. Wotton,[10] T.R. Wyatt,[20] R. Yaari,[37] S. Yamashita,[34] Y. Yang,[30,s] A. Yeaman,[29] G. Yekutieli,[37] M. Yurko,[22] V. Zacek,[22] I. Zacharov,[12] D. Zer-Zion,[30] W. Zeuner,[12,m] L. Zivkovic,[37] G.T. Zorn.[21,†]

[1] Technische Hochschule Aachen, III Physikalisches Institut, Sommerfeldstrasse 26-28, D-52056 Aachen, Germany
[2] University of Alberta, Department of Physics, Edmonton AB T6G 2J1, Canada
[3] Birkbeck College, London, WC1E 7HV, UK
[4] School of Physics and Astronomy, University of Birmingham, Birmingham B15 2TT, UK
[5] Dipartimento di Fisica dell' Università di Bologna and INFN, I-40126 Bologna, Italy
[6] Physikalisches Institut, Universität Bonn, D-53115 Bonn, Germany
[7] University of British Columbia, Department of Physics, Vancouver BC V6T 1Z1, Canada
[8] Brunel University, Uxbridge, Middlesex UB8 3PH, UK
[9] Research Institute for Particle and Nuclear Physics, H-1525 Budapest, P O Box 49, Hungary
[10] Cavendish Laboratory, Cambridge CB3 0HE, UK
[11] CEA, DAPNIA/SPP, CE-Saclay, F-91191 Gif-sur-Yvette, France
[12] CERN, European Organisation for Nuclear Research, CH-1211 Geneva 23, Switzerland
[13] Enrico Fermi Institute and Department of Physics, University of Chicago, Chicago IL 60637, USA
[14] Institute of Nuclear Research, H-4001 Debrecen, P O Box 51, Hungary
[15] Universität Hamburg/DESY, II Institut für Experimental Physik, Notkestrasse 85, D-22607 Hamburg, Germany
[16] Duke University, Department of Physics, Durham, NC 27708-0305, USA
[17] Fakultät für Physik, Albert Ludwigs Universität, D-79104 Freiburg, Germany
[18] Physikalisches Institut, Universität Heidelberg, D-69120 Heidelberg, Germany
[19] Indiana University, Department of Physics, Swain Hall West 117, Bloomington IN 47405, USA
[20] Department of Physics, Schuster Laboratory, The University, Manchester M13 9PL, UK
[21] Department of Physics, University of Maryland, College Park, MD 20742, USA
[22] Laboratoire de Physique Nucléaire, Université de Montréal, Montréal, Quebec H3C 3J7, Canada
[23] Max-Planck-Institute für Physik, Föhring Ring 6, 80805 München, Germany
[24] University Ludwigs-Maximilians-Universität München, Sektion Physik, Am Coulombwall 1, D-85748 Garching, Germany
[25] University of Oregon, Department of Physics, Eugene OR 97403, USA
[26] Ottawa-Carleton Institute for Physics, Department of Physics, Carleton University, Ottawa, Ontario K1S 5B6, Canada
[27] Centre for Research in Particle Physics, Carleton University, Ottawa, Ontario K1S 5B6, Canada
[28] National Research Council of Canada, Herzberg Institute of Astrophysics, Ottawa, Ontario K1A 0R6, Canada

[29] Queen Mary and Westfield College, University of London, London E1 4NS, UK
[30] Department of Physics, University of California, Riverside CA 92521, USA
[31] CLRC Rutherford Appleton Laboratory, Chilton, Didcot, Oxfordshire OX11 0QX, UK
[32] Department of Physics, Technion-Israel Institute of Technology, Haifa 32000, Israel
[33] Department of Physics and Astronomy, Tel Aviv University, Tel Aviv 69978, Israel
[34] International Centre for Elementary Particle Physics and Department of Physics, University of Tokyo, Tokyo 113-0033, and Kobe University, Kobe 657-8501, Japan
[35] University College London, London WC1E 6BT, UK
[36] University of Victoria, Department of Physics, P O Box 3055, Victoria BC V8W 3P6, Canada
[37] Particle Physics Department, Weizmann Institute of Science, Rehovot 76100, Israel
[38] Yale University, Department of Physics, New Haven, CT 06520, USA

[a] now at RWTH Aachen, Germany
[b] now at University of Antwerpen, Physics Department,B-2610 Antwerpen, Belgium
[c] now at Boston University, Boston, USA
[d] and Research Institute for Particle and Nuclear Physics, Budapest, Hungary
[e] now at Department of Physics, Carleton University, Ottawa, ON, K1S 5B6, Canada
[f] now at CERN, 1211 Geneva 23, Switzerland
[g] and CERN, PH Department, 1211 Geneva 23, Switzerland
[h] now at Columbia University, New York, New York, USA
[i] now at University of Mining and Metallurgy, Cracow, Poland
[j] and Institute of Nuclear Research, Debrecen, Hungary
[k] and Department of Experimental Physics, Lajos Kossuth University, Debrecen, Hungary
[l] and Department of Experimental Physics, University of Debrecen, Hungary
[m] now at DESY, Notkestrasse 85, D-22607 Hamburg, Germany
[n] now at DESY Zeuthen, Platanenallee 6, D-15738 Zeuthen, Germany
[o] now at Embry-Riddle Aeronautical University, Prescott, Arizona 86301, USA
[p] now at Friedrich-Alexander-Universität Erlangen-Nürnberg, 91054 Erlangen, Germany
[q] now at Fermi National Accelerator Laboratory, Batavia, Illinois, USA
[r] now at Florida International University, Miami, Florida, USA
[s] on leave from Research Institute for Computer Peripherals, Hangzhou, China
[t] now at Dept. Physics, University of Illinois at Urbana-Champaign, USA
[u] now at University of Iowa, Dept of Physics and Astronomy, Iowa, USA
[v] now at IEKP Universität Karlsruhe, Germany
[w] now at High Energy Accelerator Research Organisation (KEK), Tsukuba, Ibaraki, Japan
[x] and High Energy Accelerator Research Organisation (KEK), Tsukuba, Ibaraki, Japan
[y] now at IPHE Université de Lausanne, CH-1015 Lausanne, Switzerland
[z] now at Institut für Experimentelle Kernphysik, Universität Karlsruhe, Karlsruhe, Germany
[aa] now at University of Liverpool, Dept of Physics, Liverpool L69 3BX, UK
[ab] now at IPNL, Université Claude Bernard Lyon-1, Villeurbanne, France
[ac] and Manchester University Manchester, M13 9PL, Manchester, UK
[ad] now at CPP Marseille, Faculté des Sciences de Luminy, Marseille, France
[ae] now at University of Massachusetts, Amherst, Massachusetts 01003-4525 USA
[af] now at The University of Melbourne, Victoria, Australia
[ag] now at The University of Michigan, Ann Arbor, Michigan, USA

[ah] now at MPI für Physik, 80805 München, Germany
[ai] and MPI für Physik, 80805 München, Germany
[aj] now at IMAPP, Radboud University Nijmegen, Toernooiveld 1, 6525 ED Nijmegen, The Netherlands
[ak] now at University of Notre Dame, Notre Dame, Indiana 46556-5670 USA
[al] now at Institute of Physics, Academy of Sciences of the Czech Republic, Prague, Czech Republic
[am] now at CLRC Rutherford Appleton Laboratory, Chilton, Didcot, Oxfordshire OX11 0QX, UK
[an] now at University of California, San Diego, USA
[ao] and Shinshu University, Matsumoto 390, Japan
[ap] now at Royal Institute of Technology, Stockholm, Sweden
[aq] now at University of Toronto, Dept of Physics, Toronto, Canada
[ar] now at TRIUMF, Vancouver V6T 2A3, Canada
[as] and at TRIUMF, Vancouver V6T 2A3, Canada
[at] now at The University of Utah, Salt Lake City, Utah, USA
[au] now at University of Victoria, Department of Physics, Victoria BC V8W 3P6, Canada
[av] now at Bergische Universität, Wuppertal, Germany
[aw] now at Eidgenossische Technische Hochschule Zurich (ETH), Zurich, Switzerland
[ax] now at University of Kansas, Dept of Physics and Astronomy, Lawrence, KS 66045, USA
[ay] now at Purdue University, West Lafayette, IN 47907, USA
[az] now at Lawrence Livermore National Lab, California, USA
[ba] now at Laurentian University, Ontario, Canada
[bb] now at Tokyo Metropolitan University, Tokyo, Japan
[bc] now at Harvard university, Cambridge, MA, USA
[†] deceased

In addition to the support staff at our own institutions we are pleased to acknowledge the
Department of Energy, USA,
National Science Foundation, USA,
Particle Physics and Astronomy Research Council, UK,
Natural Sciences and Engineering Research Council, Canada,
Israel Science Foundation, administered by the Israel Academy of Science and Humanities,
Benoziyo Center for High Energy Physics,
Japanese Ministry of Education, Culture, Sports, Science and Technology (MEXT) and a grant under the MEXT International Science Research Program,
Japanese Society for the Promotion of Science (JSPS),
German Israeli Bi-national Science Foundation (GIF),
Bundesministerium für Bildung und Forschung, Germany,
National Research Council of Canada,
Hungarian Foundation for Scientific Research, OTKA T-038240, and T-042864,
The NWO/NATO Fund for Scientific Research, the Netherlands.

A.5 The SLD Collaboration

Kenji Abe,[20] Koya Abe,[32] T. Abe,[28] I. Abt,[13] P.D. Acton,[3] I. Adam,[28] G. Agnew,[3] T. Akagi,[28] H. Akimoto,[28] N.J. Allen,[3] W.W. Ash,[28†] D. Aston,[28] N. Bacchetta,[23] K.G. Baird,[16] C. Baltay,[38] H.R. Band,[37] M.B. Barakat,[38] G.J. Baranko,[8] O. Bardon,[18] T.L. Barklow,[28] G.L. Bashindzhagian,[19] R. Battiston,[24] J.M. Bauer,[17] A.O. Bazarko,[9] A. Bean,[28] G. Bellodi,[22] R. Ben-David,[38] A.C. Benvenuti,[4] R. Berger,[28] M. Biasini,[24] T. Bienz,[28] G.M. Bilei,[24] D. Bisello,[23] G. Blaylock,[16] J.R. Bogart,[28] B. Bolen,[17] T. Bolton,[9] G.R. Bower,[28] J.E. Brau,[21] M. Breidenbach,[28] W.M. Bugg,[31] D. Burke,[28] T.H. Burnett,[36] P.N. Burrows,[22] W. Busza,[18] A. Calcaterra,[12] D.O. Caldwell,[33] B. Camanzi,[26] M. Carpinelli,[25] J. Carr,[8] R. Cassell,[28] R. Castaldi,[25] A. Castro,[23] M. Cavalli-Sforza,[34] G.B. Chadwick,[28] A. Chou,[28] E. Church,[36] R. Claus,[28] H.O. Cohn,[31] J.A. Coller,[5] M.R. Convery,[28] V. Cook,[36] R. Cotton,[3] R.F. Cowan,[18] P.A. Coyle,[34] D.G. Coyne,[34] G. Crawford,[28] A. D'Oliveira,[7] C.J.S. Damerell,[26] M. Daoudi,[28] S. Dasu,[37] N. de Groot,[26] R. de Sangro,[12] P. De Simone,[12] S. De Simone,[12] R. Dell'Orso,[25] P.J. Dervan,[3] M. Dima,[10] D.N. Dong,[18] M. Doser,[28] P.Y.C. Du,[31] R. Dubois,[28] J.E. Duboscq,[33] G. Eigen,[6] B.I. Eisenstein,[13] R. Elia,[28] E. Erdos,[8] I. Erofeeva,[19] V. Eschenburg,[17] E. Etzion,[37] S. Fahey,[8] D. Falciai,[12] C. Fan,[8] J.P. Fernandez,[34] M.J. Fero,[18] K. Flood,[16] R. Frey,[21] J.I. Friedman,[18] K. Furuno,[21] E.L. Garwin,[28] T. Gillman,[26] G. Gladding,[13] S. Gonzalez,[18] G.D. Hallewell,[28] E.L. Hart,[31] J.L. Harton,[10] A. Hasan,[3] Y. Hasegawa,[32] K. Hasuko,[32] S. Hedges,[5] S.S. Hertzbach,[16] M.D. Hildreth,[28] D.G. Hitlin,[6] A. Honma,[28] J. S. Huber,[21] M.E. Huffer,[28] E.W. Hughes,[28] X. Huynh,[28] H. Hwang,[21] M. Iwasaki,[21] Y. Iwasaki,[32] J.M. Izen,[13] D.J. Jackson,[26] P. Jacques,[27] J.A. Jaros,[28] Z.Y. Jiang,[28] A.S. Johnson,[28] J.R. Johnson,[37] R.A. Johnson,[7] T. Junk,[28] R. Kajikawa,[20] M. Kalelkar,[27] Y.A. Kamyshkov,[31] H.J. Kang,[27] I. Karliner,[13] H. Kawahara,[28] M.H. Kelsey,[28] H.W. Kendall,[18†] Y.D. Kim,[29] M. King,[28] R. King,[28] R.R. Kofler,[16] N.M. Krishna,[28] Y. Kwon,[28] J.F. Labs,[28] R.S. Kroeger,[17] M. Langston,[21] A. Lath,[18] J.A. Lauber,[8] D.W.G. Leith,[28] V. Lia,[18] C. Lin,[16] M.X. Liu,[34] M. Loreti,[23] A. Lu,[33] H.L. Lynch,[28] J. Ma,[36] G. Mancinelli,[27] S. Manly,[38] G. Mantovani,[24] T.W. Markiewicz,[28] T. Maruyama,[28] H. Masuda,[28] E. Mazzucato,[11] J.F. McGowan,[13] A.K. McKemey,[3] B.T. Meadows,[7] R. Messner,[28] P.M. Mockett,[36] K.C. Moffeit,[28] T.B. Moore,[38] M. Morii,[28] B. Mours,[28] D. Muller,[28] G. Mueller,[28] V. Murzin,[19] T. Nagamine,[32] S. Narita,[32] U. Nauenberg,[8] H. Neal,[38] G. Nesom,[22] M. Nussbaum,[7†] Y. Ohnishi,[20] N. Oishi,[20] D. Onoprienko,[31] L.S. Osborne,[18] R.S. Panvini,[35†] C.H. Park,[30] H. Park,[21] T.J. Pavel,[28] I. Peruzzi,[12] L. Pescara,[23] M. Piccolo,[12] L. Piemontese,[11] E. Pieroni,[25] K.T. Pitts,[21] R.J. Plano,[27] R. Prepost,[37] C.Y. Prescott,[28] G. Punkar,[33] J. Quigley,[18] B.N. Ratcliff,[28] K. Reeves,[28] T.W. Reeves,[35] J. Reidy,[17] P.L. Reinertsen,[34] P.E. Rensing,[28] L.S. Rochester,[28] J.E. Rothberg,[36] P.C. Rowson,[28] J.J. Russell,[28] O.H. Saxton,[28] T. Schalk,[34] R.H. Schindler,[28] U. Schneekloth,[18] B.A. Schumm,[34] J. Schwiening,[28] A. Seiden,[34] S. Sen,[38] V.V. Serbo,[28] L. Servoli,[24] M.H. Shaevitz,[9] J.T. Shank,[5] G. Shapiro,[15†] D.J. Sherden,[28] K.D. Shmakov,[31] C. Simopoulos,[28] N.B. Sinev,[21] S.R. Smith,[28] M.B. Smy,[10] J.A. Snyder,[38] M.D. Sokoloff,[7] H. Staengle,[10] A. Stahl,[28] P. Stamer,[27] H. Steiner,[15] R. Steiner,[1] M.G. Strauss,[16] D. Su,[28] F. Suekane,[32] A. Sugiyama,[20] A. Suzuki,[20] S. Suzuki,[20] M. Swartz,[14] A. Szumilo,[36] T. Takahashi,[28] F.E. Taylor,[18] J.J. Thaler,[13] J. Thom,[28] E. Torrence,[18] A.I. Trandafir,[16] J.D. Turk,[38] T. Usher,[28] J. Va'vra,[28] C. Vannini,[25] E. Vella,[36] J.P. Venuti,[35] R. Verdier,[18] P.G. Verdini,[25] D.L. Wagner,[8] S.R. Wagner,[8] A.P. Waite,[28] S. Walston,[21] J. Wang,[28] S.J. Watts,[3] A.W. Weidemann,[31] E.R. Weiss,[36] J.S. Whitaker,[5] S.L. White,[31] F.J. Wickens,[26] D.A. Williams,[34] D.C. Williams,[34] S.H. Williams,[28] S. Willocq,[16] R.J. Wilson,[10] W.J. Wisniewski,[28] J.L. Wittlin,[16] M. Woods,[28] G.B. Word,[27] T.R. Wright,[37] J. Wyss,[23] R.K. Yamamoto,[18] J.M. Yamartino,[18] X.Q. Yang,[21] J. Yashima,[32] S.J. Yellin,[33] C.C. Young,[28] H. Yuta.[2] G. Zapalac,[37] R.W. Zdarko,[28] C. Zeitlin,[21] J. Zhou.[21]

[1] Adelphi University, Garden City, New York, 11530,
[2] Aomori University, Aomori, 030 Japan,
[3] Brunel University, Uxbridge, Middlesex, UB8 3PH United Kingdom,
[4] INFN Sezione di Bologna, I-40126, Bologna, Italy,
[5] Boston University, Boston, Massachusetts 02215,
[6] California Institute of Technology, Pasadena, California, 91125,
[7] University of Cincinnati, Cincinnati, Ohio, 45221,
[8] University of Colorado, Boulder, Colorado 80309,
[10] Colorado State University, Ft. Collins, Colorado 80523,
[11] INFN Sezione di Ferrara and Universita di Ferrara, I-44100 Ferrara, Italy,
[12] INFN Laboratori Nazionali di Frascati, I-00044 Frascati, Italy,
[13] University of Illinois, Urbana, Illinois, 61801,
[14] Johns Hopkins University, Baltimore, Maryland 21218-2686,
[15] Lawrence Berkeley National Laboratory, University of California, Berkeley, California 94720,
[16] University of Massachusetts, Amherst, Massachusetts 01003,
[17] University of Mississippi, University, Mississippi 38677,
[18] Massachusetts Institute of Technology, Cambridge, Massachusetts 02139,
[19] Institute of Nuclear Physics, Moscow State University, 119899 Moscow, Russia,
[20] Nagoya University, Chikusa-ku, Nagoya, 464 Japan,
[21] University of Oregon, Eugene, Oregon 97403,
[22] Oxford University, Oxford, OX1 3RH, United Kingdom,
[23] INFN Sezione di Padova and Universita di Padova, I-35100 Padova, Italy,
[24] INFN Sezione di Perugia and Universita di Perugia, I-06100 Perugia, Italy,
[25] INFN Sezione di Pisa and Universita di Pisa, I-56100 Pisa, Italy,
[26] Rutherford Appleton Laboratory, Chilton, Didcot, Oxon OX11 0QX United Kingdom,
[27] Rutgers University, Piscataway, New Jersey 08855,
[28] Stanford Linear Accelerator Center, Stanford University, Stanford, California 94309,
[29] Sogang University, Seoul, Korea,
[30] Soongsil University, Seoul, Korea 156-743,
[31] University of Tennessee, Knoxville, Tennessee 37996,
[32] Tohoku University, Sendai, 980 Japan,
[33] University of California at Santa Barbara, Santa Barbara, California 93106,
[34] University of California at Santa Cruz, Santa Cruz, California 95064,
[35] Vanderbilt University, Nashville,Tennessee 37235,
[36] University of Washington, Seattle, Washington 98105,
[37] University of Wisconsin, Madison,Wisconsin 53706,
[38] Yale University, New Haven, Connecticut 06511.
[†] Deceased.

This work was supported by the U.S. Department of Energy and National Science Foundation, the UK Particle Physics and Astronomy Research Council, the Istituto Nazionale di Fisica Nucleare of Italy and the Japan-US Cooperative Research Project on High Energy Physics.

Appendix B

Heavy-Flavour Fit including Off-Peak Asymmetries

The full 18 parameter fit to the LEP and SLD data including the off-peak asymmetries gave the following results:

$$
\begin{aligned}
R_{\mathrm{b}}^{0} &= 0.21628 \pm 0.00066 \\
R_{\mathrm{c}}^{0} &= 0.1722 \pm 0.0031 \\
A_{\mathrm{FB}}^{\mathrm{b\overline{b}}}(-2) &= 0.0560 \pm 0.0066 \\
A_{\mathrm{FB}}^{\mathrm{c\overline{c}}}(-2) &= -0.018 \pm 0.013 \\
A_{\mathrm{FB}}^{\mathrm{b\overline{b}}}(\mathrm{pk}) &= 0.0982 \pm 0.0017 \\
A_{\mathrm{FB}}^{\mathrm{c\overline{c}}}(\mathrm{pk}) &= 0.0635 \pm 0.0036 \\
A_{\mathrm{FB}}^{\mathrm{b\overline{b}}}(+2) &= 0.1125 \pm 0.0055 \\
A_{\mathrm{FB}}^{\mathrm{c\overline{c}}}(+2) &= 0.125 \pm 0.011 \\
\mathcal{A}_{\mathrm{b}} &= 0.924 \pm 0.020 \\
\mathcal{A}_{\mathrm{c}} &= 0.669 \pm 0.027 \\
B(\mathrm{b} \to \ell^{-}) &= 0.1070 \pm 0.0022 \\
B(\mathrm{b} \to \mathrm{c} \to \ell^{+}) &= 0.0802 \pm 0.0018 \\
B(\mathrm{c} \to \ell^{+}) &= 0.0971 \pm 0.0032 \\
\overline{\chi} &= 0.1250 \pm 0.0039 \\
f(\mathrm{D}^{+}) &= 0.235 \pm 0.016 \\
f(\mathrm{D_s}) &= 0.126 \pm 0.026 \\
f(\mathrm{c_{baryon}}) &= 0.092 \pm 0.022 \\
P(\mathrm{c} \to \mathrm{D}^{*+} \to \pi^{+}\mathrm{D}^{0}) &= 0.1622 \pm 0.0048
\end{aligned}
$$

with a χ^2/d.o.f. of $48/(105-18)$. The corresponding correlation matrix is given in Table B.1. The energies for the peak-2, peak and peak$+2$ results are respectively 89.55 GeV, 91.26 GeV and 92.94 GeV. Note that the asymmetry results shown here are not the pole asymmetries.

	1) $R_{\rm b}$	2) $R_{\rm c}$	3) $A_{\rm FB}^{\rm b\overline{b}}$ (−2)	4) $A_{\rm FB}^{\rm c\overline{c}}$ (−2)	5) $A_{\rm FB}^{\rm b\overline{b}}$ (pk)	6) $A_{\rm FB}^{\rm c\overline{c}}$ (pk)	7) $A_{\rm FB}^{\rm b\overline{b}}$ (+2)	8) $A_{\rm FB}^{\rm c\overline{c}}$ (+2)	9) $\mathcal{A}_{\rm b}$	10) $\mathcal{A}_{\rm c}$	11) B (1)	12) B (2)	13) B (3)	14) $\overline{\chi}$	15) $f(\mathrm{D}^+)$	16) $f(\mathrm{D_s})$	17) $f(c_{bar.})$	18) P
1)	1.00																	
2)	−0.18	1.00																
3)	−0.02	0.01	1.00															
4)	0.00	0.01	0.13	1.00														
5)	−0.10	0.03	0.03	0.01	1.00													
6)	0.07	−0.06	0.00	0.02	0.15	1.00												
7)	−0.04	0.01	0.01	0.01	0.08	0.02	1.00											
8)	0.03	−0.04	0.00	0.01	0.02	0.15	0.13	1.00										
9)	−0.08	0.04	0.01	0.00	0.06	−0.02	0.02	−0.01	1.00									
10)	0.04	−0.06	0.00	0.00	0.01	0.04	0.00	0.02	0.11	1.00								
11)	−0.08	0.05	0.00	0.01	0.00	0.18	0.00	0.07	−0.02	0.02	1.00							
12)	−0.03	−0.01	0.00	−0.02	−0.05	−0.23	−0.03	−0.08	0.02	−0.04	−0.24	1.00						
13)	−0.01	−0.29	0.00	0.02	0.00	−0.21	0.00	−0.14	0.03	−0.02	0.00	0.10	1.00					
14)	0.00	0.02	0.01	0.02	0.11	0.08	0.03	0.02	0.06	0.00	0.29	−0.23	0.16	1.00				
15)	−0.15	−0.10	0.00	0.00	0.01	−0.03	0.01	−0.02	0.00	0.00	0.04	0.02	0.00	0.02	1.00			
16)	−0.03	0.13	0.00	0.00	0.00	−0.02	0.00	−0.01	0.00	0.00	0.01	0.00	−0.01	−0.01	−0.40	1.00		
17)	0.11	0.17	0.00	0.00	−0.01	0.04	0.00	0.02	0.00	0.00	−0.02	−0.01	−0.02	0.00	−0.24	−0.49	1.00	
18)	0.13	−0.43	0.00	0.00	−0.02	0.04	−0.01	0.02	−0.02	0.02	−0.01	0.01	0.13	0.00	0.08	−0.06	−0.14	1.00

Table B.1: The correlation matrix for the set of the 18 heavy flavour parameters. $B(1)$, $B(2)$ and $B(3)$ denote $B(\mathrm{b} \to \ell^-)$, $B(\mathrm{b} \to \mathrm{c} \to \ell^+)$ and $B(\mathrm{c} \to \ell^+)$ respectively, P denotes $P(\mathrm{c} \to \mathrm{D}^{*+} \to \pi^+ \mathrm{D}^0)$.

Appendix C

The Measurements used in the Heavy Flavour Averages

In Tables C.1 to C.20 the results used in the combination are listed. In each case an indication of the dataset used and the type of analysis is given. The values of centre-of-mass energy are given where relevant. In each table, following the number quoted in the referenced publication, the corrected value of each measurement is given. For these values all external input parameters as detailed in Section 5.6 are used. In addition all other fit parameters that affect the measurement in question via explicit dependencies or correlations with simultaneous measurements are fixed to the results of the LEP/SLD combination. The corrected value is followed by the statistical error, the internal systematic, the systematic error common to more than one measurement, the effect of a $\pm 1\sigma$ change in all the other averaged parameters on the value used in the average for this measurement, the total systematic error, and the total error.

Contributions to the common systematic error quoted here are from any physics source that is potentially common between the different experiments. Detector systematics that are common between different analyses of the same experiment are considered internal.

	ALEPH	DELPHI	L3	OPAL	SLD
	92-95 [135]	92-95 [127]	94-95 [124]	92-95 [125]	93-98 [133]
Published R_{b}^{0}	0.2159	0.21634	0.2174	0.2178	0.2159
Corrected R_{b}^{0}	0.2158	0.21643	0.2166	0.2176	0.2158
Statistical	0.0009	0.00067	0.0013	0.0011	0.0009
Internal Systematic	0.0007	0.00038	0.0014	0.0009	0.0005
Common Systematic	0.0006	0.00039	0.0018	0.0008	0.0005
Other Param. Sys.	0.0001	0.00014	0.0010	0.0004	0.0002
Total Systematic	0.0009	0.00056	0.0025	0.0012	0.0008
Total Error	0.0013	0.00087	0.0028	0.0017	0.0012

Table C.1: The measurements of R_{b}^{0}. All measurements use a lifetime tag enhanced by other features like invariant mass cuts or high p_T leptons.

	ALEPH			DELPHI		OPAL		SLD
	91-95 D-meson [136]	91-95 c-count (result) [131]	92-95 lepton [136]	92-95 c-count (result) [137]	92-95 D-meson (result) [132, 137]	91-94 c-count (result) [138]	90-95 D-meson (result) [130]	93-97 D-meson [133]
Published R_c^0	0.169	0.174	0.168	0.169	0.161	0.167	0.180	0.1744
Corrected R_c^0	0.168	0.174	0.169	0.169	0.161	0.164	0.177	0.1741
Statistical	0.008	0.005	0.006	0.005	0.010	0.012	0.010	0.0031
Internal Systematic	0.008	0.006	0.004	0.005	0.006	0.013	0.010	0.0010
Common Systematic	0.003	0.009	0.004	0.008	0.006	0.010	0.006	0.0016
Other Param. Sys.	0.000	0.000	0.005	0.000	0.001	0.000	0.000	0.0004
Total Systematic	0.008	0.011	0.008	0.009	0.009	0.016	0.012	0.0020
Total Error	0.012	0.012	0.010	0.010	0.014	0.020	0.015	0.0037

Table C.2: The measurements of R_c^0. "c-count" denotes the determination of R_c^0 from the sum of production rates of weakly decaying charmed hadrons. "D-meson" denotes any single/double tag analysis using exclusive and/or inclusive D meson reconstruction. The columns with the mention "(result)" are not directly used in the global average, only the corresponding measurements ($P(c \to D^{*+} \to \pi^+ D^0)$, $R_c f(D^+)$, $R_c f(D_s)$, $R_c f(\Lambda_c^+)$, $R_c f(D^0)$ and $R_c P(c \to D^{*+} \to \pi^+ D^0)$ see tables C.15-C.20) are included.

	ALEPH				DELPHI			L3	OPAL		
	91-95 lepton [141]	91-95 lepton [141]	91-95 lepton [141]	91-95 jet [142]	91-95 lepton [143]	92-95 D-meson [150]	92-00 multi [148]	90-95 lepton [144]	91-00 jet [147]	90-00 lepton [145]	90-95 D-meson [151]
$\sqrt{s}$ (GeV)	88.38	89.38	90.21	89.47	89.434	89.434	89.449	89.50	89.50	89.51	89.49
Published $A_{\rm FB}^{\rm b\overline{b}}(-2)$	-13.1	5.5	-0.4	4.4	6.7	5.7	6.3	6.1	5.8	4.7	-9.
Corrected $A_{\rm FB}^{\rm b\overline{b}}(-2)$	5.2			4.6	6.4	4.8	6.6	6.3	6.0	5.2	-5.
Statistical	1.8			1.2	2.2	7.3	1.4	2.9	1.5	1.8	10.
Internal Systematic	0.1			0.0	0.2	0.7	0.2	0.3	0.1	0.1	2.
Common Systematic	0.1			0.0	0.1	0.2	0.0	0.2	0.0	0.1	1.
Other Param. Sys.	0.1			0.1	0.2	0.8	0.0	0.1	0.1	0.2	1.
Total Systematic	0.2			0.1	0.3	1.0	0.2	0.4	0.1	0.2	2.
Total Error	1.8			1.2	2.2	7.4	1.4	3.0	1.5	1.8	11.

Table C.3: The measurements of $A_{\rm FB}^{\rm b\overline{b}}(-2)$. The "Corrected" values are quoted at $\sqrt{s} = 89.55\,\text{GeV}$. All numbers are given in %.

	ALEPH				DELPHI		OPAL	
	91-95 lepton [141]	91-95 lepton [141]	91-95 lepton [141]	91-95 D-meson [149]	91-95 lepton [143]	92-95 D-meson [150]	90-00 lepton [145]	90-95 D-meson [151]
$\sqrt{s}$ (GeV)	88.38	89.38	90.21	89.37	89.434	89.434	89.51	89.49
Published $A_{\rm FB}^{\rm c\overline{c}}(-2)$	-12.4	-2.3	-0.3	-1.0	3.1	-5.0	-6.8	3.9
Corrected $A_{\rm FB}^{\rm c\overline{c}}(-2)$	-1.5			0.2	3.5	-4.4	-6.2	2.5
Statistical	2.4			4.3	3.4	3.6	2.5	4.9
Internal Systematic	0.2			0.9	0.4	0.3	0.9	0.8
Common Systematic	0.1			0.1	0.1	0.1	0.1	0.3
Other Param. Sys.	0.1			0.2	0.2	0.1	0.3	0.1
Total Systematic	0.2			0.9	0.4	0.4	0.9	0.8
Total Error	2.4			4.4	3.5	3.6	2.7	5.0

Table C.4: The measurements of $A_{\rm FB}^{\rm c\overline{c}}(-2)$. The "Corrected" values are quoted at $\sqrt{s} = 89.55\,\text{GeV}$. All numbers are given in %.

	ALEPH		DELPHI			L3		OPAL		
	91-95 lepton [141]	91-95 jet [142]	91-95 lepton [143]	92-95 D-meson [150]	92-00 multi [148]	91-95 jet [146]	90-95 lepton [144]	91-00 jet [147]	90-00 lepton [145]	90-95 D-meson [151]
$\sqrt{s}$ (GeV)	91.21	91.23	91.26	91.235	91.231	91.24	91.26	91.26	91.25	91.24
Published $A_{\rm FB}^{\rm b\overline{b}}$(pk)	9.52	10.00	10.04	7.6	9.58	9.3	9.80	9.77	9.72	9.4
Corrected $A_{\rm FB}^{\rm b\overline{b}}$(pk)	9.98	10.03	10.15	7.9	9.67	9.3	9.66	9.71	9.77	9.7
Statistical	0.40	0.27	0.55	1.9	0.32	1.0	0.65	0.36	0.40	2.6
Internal Systematic	0.07	0.10	0.17	0.5	0.15	0.5	0.27	0.15	0.07	2.1
Common Systematic	0.10	0.02	0.16	0.6	0.04	0.2	0.16	0.08	0.13	0.3
Other Param. Sys.	0.12	0.05	0.10	0.2	0.03	0.1	0.12	0.05	0.10	0.2
Total Systematic	0.17	0.12	0.25	0.8	0.15	0.6	0.33	0.18	0.18	2.1
Total Error	0.44	0.29	0.60	2.1	0.35	1.2	0.73	0.40	0.44	3.4

Table C.5: The measurements of $A_{\rm FB}^{\rm b\overline{b}}$(pk). The "Corrected" values are quoted at $\sqrt{s} = 91.26\,\text{GeV}$. All numbers are given in %.

	ALEPH		DELPHI		L3	OPAL	
	91-95 lepton [141]	91-95 D-meson [149]	91-95 lepton [143]	92-95 D-meson [150]	90-95 lepton [144]	90-00 lepton [145]	90-95 D-meson [151]
$\sqrt{s}$ (GeV)	91.21	91.22	91.26	91.235	91.24	91.25	91.24
Published $A_{\rm FB}^{\rm c\bar{c}}$(pk)	6.45	6.3	6.3	6.59	7.8	5.68	6.3
Corrected $A_{\rm FB}^{\rm c\bar{c}}$(pk)	6.62	6.3	6.2	6.49	8.2	5.70	6.5
Statistical	0.56	0.9	0.9	0.93	3.0	0.54	1.2
Internal Systematic	0.24	0.2	0.5	0.26	1.7	0.19	0.5
Common Systematic	0.22	0.2	0.2	0.07	0.6	0.22	0.3
Other Param. Sys.	0.20	0.0	0.2	0.03	0.7	0.20	0.0
Total Systematic	0.38	0.3	0.6	0.27	1.9	0.36	0.6
Total Error	0.68	0.9	1.1	0.97	3.6	0.65	1.3

Table C.6: The measurements of $A_{\rm FB}^{\rm c\bar{c}}$(pk). The "Corrected" values are quoted at $\sqrt{s} = 91.26\,\text{GeV}$. All numbers are given in %.

	ALEPH				DELPHI			L3	OPAL		
	91-95 lepton [141]	91-95 lepton [141]	91-95 lepton [141]	91-95 jet [142]	91-95 lepton [143]	92-95 D-meson [150]	92-00 multi [148]	90-95 lepton [144]	91-00 jet [147]	90-00 lepton [145]	90-95 D-meson [151]
$\sqrt{s}$ (GeV)	92.05	92.94	93.90	92.95	92.990	92.990	92.990	93.10	92.91	92.95	92.95
Published $A_{\rm FB}^{\rm b\overline{b}}(+2)$	11.1	10.4	13.8	11.72	11.2	8.8	10.4	13.7	12.2	10.3	-2.1
Corrected $A_{\rm FB}^{\rm b\overline{b}}(+2)$	11.1			11.69	11.4	8.6	10.4	13.7	12.2	10.1	-0.2
Statistical	1.4			0.98	1.8	6.2	1.2	2.4	1.2	1.5	8.7
Internal Systematic	0.2			0.11	0.1	0.9	0.3	0.3	0.2	0.1	2.0
Common Systematic	0.2			0.02	0.1	0.5	0.0	0.2	0.1	0.2	1.2
Other Param. Sys.	0.2			0.12	0.2	0.5	0.0	0.1	0.1	0.2	0.7
Total Systematic	0.3			0.16	0.3	1.1	0.3	0.4	0.2	0.3	2.4
Total Error	1.5			0.99	1.8	6.3	1.2	2.4	1.3	1.5	9.0

Table C.7: The measurements of $A_{\rm FB}^{\rm b\overline{b}}(+2)$. The "Corrected" values are quoted at $\sqrt{s} = 92.94\,\text{GeV}$. All numbers are given in %.

	ALEPH				DELPHI		OPAL	
	91-95 lepton [141]	91-95 lepton [141]	91-95 lepton [141]	91-95 D-meson [149]	91-95 lepton [143]	92-95 D-meson [150]	90-00 lepton [145]	90-95 D-meson [151]
$\sqrt{s}$ (GeV)	92.05	92.94	93.90	92.96	92.990	92.990	92.95	92.95
Published $A_{\mathrm{FB}}^{\mathrm{c\bar{c}}}(+2)$	10.6	11.9	12.1	11.0	11.0	11.8	14.6	15.8
Corrected $A_{\mathrm{FB}}^{\mathrm{c\bar{c}}}(+2)$		11.9		10.9	10.9	11.4	14.9	14.6
Statistical		2.0		3.3	2.8	3.1	2.0	4.0
Internal Systematic		0.3		0.7	0.4	0.5	0.5	0.7
Common Systematic		0.3		0.1	0.2	0.1	0.2	0.5
Other Param. Sys.		0.3		0.2	0.3	0.1	0.4	0.1
Total Systematic		0.6		0.7	0.6	0.6	0.7	0.9
Total Error		2.1		3.4	2.8	3.1	2.1	4.1

Table C.8: The measurements of $A_{\mathrm{FB}}^{\mathrm{c\bar{c}}}(+2)$. The "Corrected" values are quoted at $\sqrt{s} = 92.94\,\mathrm{GeV}$. All numbers are given in %.

	SLD			
	93-98 lepton [152]	93-98 jet [154]	94-95 $K^{\pm}$ [156]	96-98 K+vertex [155]
$\sqrt{s}$ (GeV)	91.28	91.28	91.28	91.28
Published $\mathcal{A}_{\rm b}$	0.919	0.907	0.86	0.919
Corrected $\mathcal{A}_{\rm b}$	0.939	0.907	0.86	0.917
Statistical	0.030	0.020	0.09	0.018
Internal Systematic	0.018	0.023	0.10	0.017
Common Systematic	0.009	0.003	0.01	0.003
Other Param. Sys.	0.011	0.001	0.00	0.002
Total Systematic	0.023	0.024	0.10	0.017
Total Error	0.037	0.031	0.13	0.025

Table C.9: The measurements of $\mathcal{A}_{\rm b}$.

	SLD		
	93-98 lepton [152]	93-98 D-meson [153]	96-98 K+vertex [155]
$\sqrt{s}$ (GeV)	91.28	91.28	91.28
Published $\mathcal{A}_{\rm c}$	0.583	0.688	0.673
Corrected $\mathcal{A}_{\rm c}$	0.587	0.689	0.674
Statistical	0.055	0.035	0.029
Internal Systematic	0.045	0.020	0.023
Common Systematic	0.022	0.004	0.002
Other Param. Sys.	0.017	0.001	0.002
Total Systematic	0.053	0.021	0.023
Total Error	0.076	0.041	0.037

Table C.10: The measurements of $\mathcal{A}_{\rm c}$.

	ALEPH	DELPHI	L3		OPAL	
	91-95 multi [157]	94-95 multi [158]	94-95 multi [124]	92 multi [159]	92-95 multi [160]	92-95 multi [160]
Published $B(\mathrm{b} \to \ell^-)$	10.70	10.70	10.16	10.68	10.78	10.96
Corrected $B(\mathrm{b} \to \ell^-)$	10.74	10.70	10.26	10.82	10.86	
Statistical	0.10	0.14	0.09	0.11	0.09	
Internal Systematic	0.15	0.14	0.16	0.36	0.21	
Common Systematic	0.23	0.43	0.31	0.22	0.19	
Other Param. Sys.	0.03	0.07	0.03	0.09	0.02	
Total Systematic	0.28	0.45	0.35	0.43	0.29	
Total Error	0.29	0.48	0.36	0.45	0.30	

Table C.11: The measurements of $B(\mathrm{b} \to \ell^-)$. All numbers are given in %.

	ALEPH	DELPHI	OPAL	
	91-95 multi [157]	94-95 multi [158]	92-95 multi [160]	92-95 multi [160]
Published $B(\mathrm{b} \to \mathrm{c} \to \ell^+)$	8.18	7.98	8.37	8.17
Corrected $B(\mathrm{b} \to \mathrm{c} \to \ell^+)$	8.11	7.98	8.42	
Statistical	0.15	0.22	0.15	
Internal Systematic	0.18	0.16	0.22	
Common Systematic	0.15	0.22	0.32	
Other Param. Sys.	0.05	0.04	0.04	
Total Systematic	0.24	0.27	0.39	
Total Error	0.29	0.35	0.42	

Table C.12: The measurements of $B(\mathrm{b} \to \mathrm{c} \to \ell^+)$. All numbers are given in %.

	DELPHI	OPAL
	92-95 D+lepton [132]	90-95 D+lepton [139]
Published $B(\mathrm{c} \to \ell^+)$	9.58	9.5
Corrected $B(\mathrm{c} \to \ell^+)$	9.67	9.6
Statistical	0.42	0.6
Internal Systematic	0.24	0.5
Common Systematic	0.13	0.4
Other Param. Sys.	0.01	0.0
Total Systematic	0.27	0.7
Total Error	0.50	0.9

Table C.13: The measurements of $B(\mathrm{c} \to \ell^+)$. All numbers are given in %.

	ALEPH	DELPHI	L3	OPAL
	91-95 multi [141]	94-95 multi [158]	90-95 lepton [144]	90-00 lepton [145]
Published $\overline{\chi}$	0.1196	0.127	0.1192	0.1312
Corrected $\overline{\chi}$	0.1199	0.127	0.1199	0.1318
Statistical	0.0049	0.013	0.0066	0.0046
Internal Systematic	0.0021	0.005	0.0023	0.0015
Common Systematic	0.0040	0.003	0.0026	0.0037
Other Param. Sys.	0.0012	0.001	0.0016	0.0016
Total Systematic	0.0047	0.006	0.0038	0.0043
Total Error	0.0068	0.014	0.0076	0.0063

Table C.14: The measurements of $\overline{\chi}$.

	DELPHI	OPAL
	92-95 D-meson [132]	90-95 D-meson [130]
Published $P(\mathrm{c} \to \mathrm{D}^{*+} \to \pi^+\mathrm{D}^0)$	0.174	0.1516
Corrected $P(\mathrm{c} \to \mathrm{D}^{*+} \to \pi^+\mathrm{D}^0)$	0.174	0.1546
Statistical	0.010	0.0038
Internal Systematic	0.004	0.0045
Common Systematic	0.001	0.0050
Other Param. Sys.	0.000	0.0021
Total Systematic	0.004	0.0070
Total Error	0.011	0.0080

Table C.15: The measurements of $P(\mathrm{c} \to \mathrm{D}^{*+} \to \pi^+\mathrm{D}^0)$.

	ALEPH	DELPHI	OPAL
	91-95 c-count [131]	92-95 c-count [137]	91-94 c-count [138]
Published $R_\mathrm{c} f(\mathrm{D}^+)$	0.0409	0.0384	0.0393
Corrected $R_\mathrm{c} f(\mathrm{D}^+)$	0.0402	0.0386	0.0386
Statistical	0.0014	0.0014	0.0056
Internal Systematic	0.0012	0.0012	0.0026
Common Systematic	0.0029	0.0025	0.0028
Other Param. Sys.	0.0012	0.0008	0.0015
Total Systematic	0.0033	0.0029	0.0041
Total Error	0.0036	0.0032	0.0069

Table C.16: The measurements of $R_\mathrm{c} f(\mathrm{D}^+)$.

	ALEPH	DELPHI	OPAL
	91-95 c-count [131]	92-95 c-count [137]	91-94 c-count [138]
Published $R_c f(D_s)$	0.0199	0.0213	0.0161
Corrected $R_c f(D_s)$	0.0206	0.0213	0.0158
Statistical	0.0036	0.0018	0.0048
Internal Systematic	0.0011	0.0009	0.0007
Common Systematic	0.0047	0.0048	0.0037
Other Param. Sys.	0.0003	0.0004	0.0006
Total Systematic	0.0048	0.0049	0.0038
Total Error	0.0060	0.0052	0.0061

Table C.17: The measurements of $R_c f(D_s)$.

	ALEPH	DELPHI	OPAL
	91-95 c-count [131]	92-95 c-count [137]	91-94 c-count [138]
Published $R_c f(c_{baryon})$	0.0169	0.0170	0.0107
Corrected $R_c f(c_{baryon})$	0.0155	0.0170	0.0089
Statistical	0.0017	0.0040	0.0065
Internal Systematic	0.0005	0.0014	0.0008
Common Systematic	0.0038	0.0040	0.0028
Other Param. Sys.	0.0004	0.0004	0.0005
Total Systematic	0.0039	0.0043	0.0030
Total Error	0.0042	0.0058	0.0072

Table C.18: The measurements of $R_c f(c_{baryon})$.

	ALEPH	DELPHI	OPAL
	91-95 c-count [131]	92-95 c-count [137]	91-94 c-count [138]
Published $R_c f(D^0)$	0.0961	0.0927	0.1013
Corrected $R_c f(D^0)$	0.0966	0.0929	0.1027
Statistical	0.0031	0.0027	0.0080
Internal Systematic	0.0036	0.0026	0.0033
Common Systematic	0.0042	0.0024	0.0038
Other Param. Sys.	0.0018	0.0019	0.0016
Total Systematic	0.0058	0.0040	0.0053
Total Error	0.0066	0.0048	0.0095

Table C.19: The measurements of $R_c f(D^0)$.

	DELPHI	OPAL
	92-95 D-meson [137]	90-95 D-meson [130]
Published $R_{\mathrm{c}}P(\mathrm{c} \to \mathrm{D}^{*+} \to \pi^{+}\mathrm{D}^{0})$	0.0283	0.0272
Corrected $R_{\mathrm{c}}P(\mathrm{c} \to \mathrm{D}^{*+} \to \pi^{+}\mathrm{D}^{0})$	0.0284	0.0271
Statistical	0.0007	0.0005
Internal Systematic	0.0008	0.0008
Common Systematic	0.0006	0.0010
Other Param. Sys.	0.0009	0.0001
Total Systematic	0.0013	0.0013
Total Error	0.0015	0.0014

Table C.20: The measurements of $R_{\mathrm{c}}P(\mathrm{c} \to \mathrm{D}^{*+} \to \pi^{+}\mathrm{D}^{0})$.

Appendix D

Limits on Non-Standard Z Decays

Numerical limits on possible contributions to Z final states from sources beyond the Standard Model (SM) are obtained by taking the difference between the widths in Table 7.1 or the branching fractions of Table 7.2, and the corresponding SM predictions, as is shown in Table D.1.

Decays of Z-Bosons into non-SM particles with observable final states identical to the SM ones would result in different selection efficiencies, and therefore these limits must be treated with care. Extra contributions to the total width or to the invisible width, however, are safe in this respect.

In order to calculate the upper limit for such contributions, parametric errors on the SM prediction are added in quadrature to the experimental errors. The unknown value of the Higgs boson mass is taken into account by choosing its value within the range of 114 GeV [39] to 1000 GeV such that the SM prediction is minimal, *i.e.*, either $m_{\mathrm{H}} = 114$ GeV for the leptonic branching fractions or $m_{\mathrm{H}} = 1000$ GeV for all other quantities listed in the first column of Table D.1. The values assumed for m_{t} and $\alpha(m_{\mathrm{Z}}^2)$ are those of Table 8.4, while for $\alpha_{\mathrm{S}}(m_{\mathrm{Z}}^2)$ a value with an enlarged error of 0.118 ± 0.003 is chosen. The best description of the Z-pole results is obtained by using the value derived from the full SM fit of Table 8.3, but this value of $\alpha_{\mathrm{S}}(m_{\mathrm{Z}}^2)$ would be affected by contributions from physics beyond the SM to hadronic Z decays and can therefore not be used here. The enlarged error takes into account the uncertainties involved when applying an external value of $\alpha_{\mathrm{S}}(m_{\mathrm{Z}}^2)$ to hadronic Z decays, as is discussed in Section 26. Clearly the derived limits on Z decays involving hadrons depend on the choice of $\alpha_{\mathrm{S}}(m_{\mathrm{Z}}^2)$, while limits on extra contributions to the leptonic widths are almost insensitive to it. All branching fractions, however, depend on the choice of $\alpha_{\mathrm{S}}(m_{\mathrm{Z}}^2)$, due to the their strong correlations arising from constraining their sum to be equal to unity.

The 95% CL upper limits on extra, non-SM contributions to the Z widths and branching fractions derived in the way described above are summarised in Table D.1; these limits are of Bayesian type assuming zero probability below the minimal SM prediction and a uniform prior probability above.

Z-decay to:	$\Delta\Gamma_x$ [MeV]	min. $\Gamma_{\rm SM}$ [MeV]	ΔB_x [%]	min. $B_{\rm SM}$ [%]
Without Lepton Universality				
$f\bar{f}$	11.4	2488.7 $\pm$1.9	—	—
$q\bar{q}$	14.6	1736.6 $\pm$1.8	0.35	69.777 $\pm$0.021
e^+e^-	0.32	83.82$\pm$0.04	0.0075	3.3664$\pm$0.0023
$\mu^+\mu^-$	0.49	83.82$\pm$0.04	0.014	3.3664$\pm$0.0023
$\tau^+\tau^-$	0.82	83.63$\pm$0.04	0.025	3.3588$\pm$0.0023
$b\bar{b}$	5.3	374.6 $\pm$0.4	0.17	15.051 $\pm$0.012
$c\bar{c}$	11.4	299.1 $\pm$0.4	0.43	12.017 $\pm$0.008
inv	3.1	500.9 $\pm$0.2	0.11	20.104 $\pm$0.014
With Lepton Universality				
$f\bar{f}$	11.4	2488.7 $\pm$1.9	—	—
$q\bar{q}$	12.2	1736.6 $\pm$1.8	0.23	69.777 $\pm$0.021
$e^+e^- + \mu^+\mu^- + \tau^+\tau^-$	0.97	251.27$\pm$0.12	0.018	10.0916$\pm$0.0069
$b\bar{b}$	4.8	374.6 $\pm$0.4	0.15	15.051 $\pm$0.012
$c\bar{c}$	11.0	299.1 $\pm$0.4	0.42	12.017 $\pm$0.008
inv	2.0	500.9 $\pm$0.2	0.062	20.104 $\pm$0.014

Table D.1: 95% CL limits on non-SM contributions to the Z widths ($\Delta\Gamma_x$, second column) and branching fractions (ΔB_x, fourth column) derived from the results of Tables 7.1 and 7.2. The minimal SM predictions for the widths and branching fractions with their parametric uncertainties arising from the errors in $m_{\rm t}$, $\alpha_{\rm S}(m_{\rm Z}^2)$ and $\alpha(m_{\rm Z}^2)$ are shown in the third and fifth columns, respectively. Note that there are correlations among the experimental and theoretical errors, and therefore the limits must not be used simultaneously.

Appendix E

Tests of Electroweak Radiative Corrections

E.1 Parametrisations

As discussed in Section 1.4, the expected structure of electroweak radiative corrections in the Standard Model (SM) shows contributions quadratic in the fermion masses and only logarithmic in the Higgs-boson mass. It has been studied how the small Higgs-mass dependence can be disentangled from the large top-quark mass dependence. For this purpose, four new effective parameters, ϵ_1, ϵ_2, ϵ_3 and ϵ_b are introduced [252]. They are defined such that they vanish in the approximation when only effects due to pure QED and QCD are taken into account. In terms of the auxiliary quantities $\sin^2\theta_0$, defined in Equation 7.13, and $\Delta\kappa'$, relating $\sin^2\theta_{\rm eff}^{\rm lept}$ to $\sin^2\theta_0$ analogously to Equation 1.15:

$$\sin^2\theta_{\rm eff}^{\rm lept} = (1+\Delta\kappa')\sin^2\theta_0\,, \tag{E.1}$$

the ϵ parameters are given by:

$$\epsilon_1 = \Delta\rho \tag{E.2}$$

$$\epsilon_2 = \cos^2\theta_0\Delta\rho + \frac{\sin^2\theta_0}{\cos^2\theta_0-\sin^2\theta_0}\Delta r_{\rm w} - 2\sin^2\theta_0\Delta\kappa' \tag{E.3}$$

$$\epsilon_3 = \cos^2\theta_0\Delta\rho + (\cos^2\theta_0-\sin^2\theta_0)\Delta\kappa' \tag{E.4}$$

$$\epsilon_b = \frac{1}{2}\Delta\rho_b\,. \tag{E.5}$$

Within the SM the leading contributions in terms of $m_{\rm t}$ and $m_{\rm H}$ are:

$$\epsilon_1 = \frac{3G_{\rm F}m_{\rm t}^2}{8\sqrt{2}\pi^2} - \frac{3G_{\rm F}m_{\rm W}^2}{4\sqrt{2}\pi^2}\tan^2\theta_{\rm W}\ln\frac{m_{\rm H}}{m_{\rm Z}} + \ldots \tag{E.6}$$

$$\epsilon_2 = -\frac{G_{\rm F}m_{\rm W}^2}{2\sqrt{2}\pi^2}\ln\frac{m_{\rm t}}{m_{\rm Z}} + \ldots \tag{E.7}$$

$$\epsilon_3 = \frac{G_{\rm F}m_{\rm W}^2}{12\sqrt{2}\pi^2}\ln\frac{m_{\rm H}}{m_{\rm Z}} - \frac{G_{\rm F}m_{\rm W}^2}{6\sqrt{2}\pi^2}\ln\frac{m_{\rm t}}{m_{\rm Z}} + \ldots \tag{E.8}$$

$$\epsilon_b = -\frac{G_{\rm F}m_{\rm t}^2}{4\sqrt{2}\pi^2} + \ldots\,. \tag{E.9}$$

Note that comparing to the equations given in Section 1.4, the argument of the natural logarithm is $m_{\rm H}/m_{\rm Z}$ rather than $m_{\rm H}/m_{\rm W}$. The difference is of subleading order.

The ϵ parameters separate electroweak radiative corrections in quadratic m_{t} effects and logarithmic m_{H} effects. Such a rearrangement is also useful in the search for new physics effects in precision measurements. Another commonly used description is based on the so-called STU parameters [253], extended by an additional parameter, γ_b, for the b-quark sector [117]. Approximate linear relations between these two sets of parameters exist:

$$S \simeq +\epsilon_3 \frac{4\sin^2\theta_0}{\alpha(m_{\mathrm{Z}}^2)} - c_S \tag{E.10}$$

$$T \simeq \epsilon_1 \frac{1}{\alpha(m_{\mathrm{Z}}^2)} - c_T \tag{E.11}$$

$$U \simeq -\epsilon_2 \frac{4\sin^2\theta_0}{\alpha(m_{\mathrm{Z}}^2)} - c_U \tag{E.12}$$

$$\gamma_b \simeq 2.29\epsilon_b - c_\gamma\,. \tag{E.13}$$

In the literature, these parameters are in fact defined as shifts relative to a fixed set of SM values c_i, $i = S, T, U, \gamma$, so that $S = T = U = \gamma_b = 0$ at that point. Thus these parameters measure deviations from the electroweak radiative corrections expected in the SM, in particular new physics effects in oblique electroweak corrections, *i.e.*, those entering through vacuum polarisation diagrams. For numerical results presented in the following, we use as the fixed subtraction point the values corresponding to: $\Delta\alpha^{(5)}_{\mathrm{had}}(m_{\mathrm{Z}}^2) = 0.02758$, $\alpha_{\mathrm{S}}(m_{\mathrm{Z}}^2) = 0.118$, $m_{\mathrm{Z}} = 91.1875$ GeV, $m_{\mathrm{t}} = 175$ GeV, $m_{\mathrm{H}} = 150$ GeV. Predictions of these parameters within the SM framework are reported in Appendix G.

E.2 Results

The formulae listed above and in Chapter 1 are combined to express the measured quantities in terms of the ϵ or STU parameters, and the latter are then determined as usual in a χ^2-fit to the measurements. In both analyses, the largest contribution to the χ^2 arises from the asymmetry measurements as discussed in Section 7.3.3. Note that the experimental results on light quark flavours presented in Appendix F are not used.

The Z-pole measurements performed by SLD and at LEP-I constrain the parameters ϵ_1 (T), ϵ_3 (S) and ϵ_b (γ_b). Given these, the measurements of the W-boson mass or of the on-shell electroweak mixing angle are solely determining ϵ_2 (U). The other additional measurements discussed in Section 8.3 are not included here as they can be expressed in terms of neither the ϵ nor the STU parameters without additional assumptions. Because of its explicit m_{t} and m_{H} dependence, the measurement of $\sin^2\theta_{\mathrm{W}}$ by NuTeV cannot be included.

The results of the fit of all ϵ parameters to all LEP and SLD results including the measurements of the W-boson mass are reported in Table E.1, and are shown as a contour curve in the (ϵ_3, ϵ_1) plane in Figure E.1. All ϵ parameters are significantly different from zero, in particular the case for ϵ_2 determined by the W-boson mass, showing again that genuine electroweak radiative corrections beyond the running of α and α_{S} are observed. The allowed region in ϵ-parameter space overlaps with the region expected in the SM for a light Higgs boson. Despite the $\mathcal{A}_{\mathrm{b}}$ result discussed before, the extracted value for ϵ_b agrees with the SM expectation because of the strong constraint given by the R^0_{b} result.

The results of the fit of the STU parameters to the same data set are shown in Table E.2. The constraint $U = 0$ is imposed, as the mass and width of the W boson is the only measurement sensitive to U and models with deviations in U constitute a more severe deviation from the

Parameter	Value	Correlations						
		$\Delta\alpha^{(5)}_{\rm had}(m^2_{\rm Z})$	$\alpha_{\rm S}(m^2_{\rm Z})$	$m_{\rm Z}$	ϵ_1	ϵ_2	ϵ_3	ϵ_b
$\Delta\alpha^{(5)}_{\rm had}(m^2_{\rm Z})$	0.02758±0.00035	1.00						
$\alpha_{\rm S}(m^2_{\rm Z})$	0.1185±0.0039	0.00	1.00					
$m_{\rm Z}$ [GeV]	91.1873±0.0021	0.00	0.02	1.00				
ϵ_1	+0.0054±0.0010	0.00	−0.37	−0.11	1.00			
ϵ_2	−0.0089±0.0012	0.06	−0.25	−0.03	0.60	1.00		
ϵ_3	+0.00534±0.00094	−0.31	−0.28	−0.06	0.86	0.40	1.00	
ϵ_b	−0.0050±0.0016	0.00	−0.63	0.00	0.00	−0.01	0.02	1.00

Table E.1: Results on the ϵ parameters including their correlations derived from a fit to all LEP-I and SLD measurements and including the combined preliminary measurement of the W-boson mass. The χ^2/dof has a value of 15.7/9, corresponding to a probability of 7.2%.

Parameter	Value	Correlations					
		$\Delta\alpha^{(5)}_{\rm had}(m^2_{\rm Z})$	$\alpha_{\rm S}(m^2_{\rm Z})$	$m_{\rm Z}$	S	T	γ_b
$\Delta\alpha^{(5)}_{\rm had}(m^2_{\rm Z})$	0.02760±0.00035	1.00					
$\alpha_{\rm S}(m^2_{\rm Z})$	0.1174±0.0038	0.02	1.00				
$m_{\rm Z}$ [GeV]	91.1872±0.0021	0.00	0.01	1.00			
S	+0.07±0.10	−0.36	−0.20	−0.05	1.00		
T	+0.13±0.10	−0.05	−0.28	−0.11	0.85	1.00	
γ_b	+0.0014±0.0038	0.00	−0.66	0.00	0.02	0.01	1.00

Table E.2: Results on the $STU\gamma_b$ parameters including their correlations derived from a fit to all LEP-I and SLD measurements and including the combined preliminary measurement of the W-boson mass. The parameter U is fixed to 0. The χ^2/dof has a value of 17.1/10, corresponding to a probability of 7.2%.

SM symmetry framework than implied by S and T. In the (T, S) plane, the overall result as well as bands corresponding to the most precise measurements are shown in Figure E.2. The STU analyses show that there are no large unexpected electroweak radiative corrections, as the values of the STU parameters are in agreement with zero.

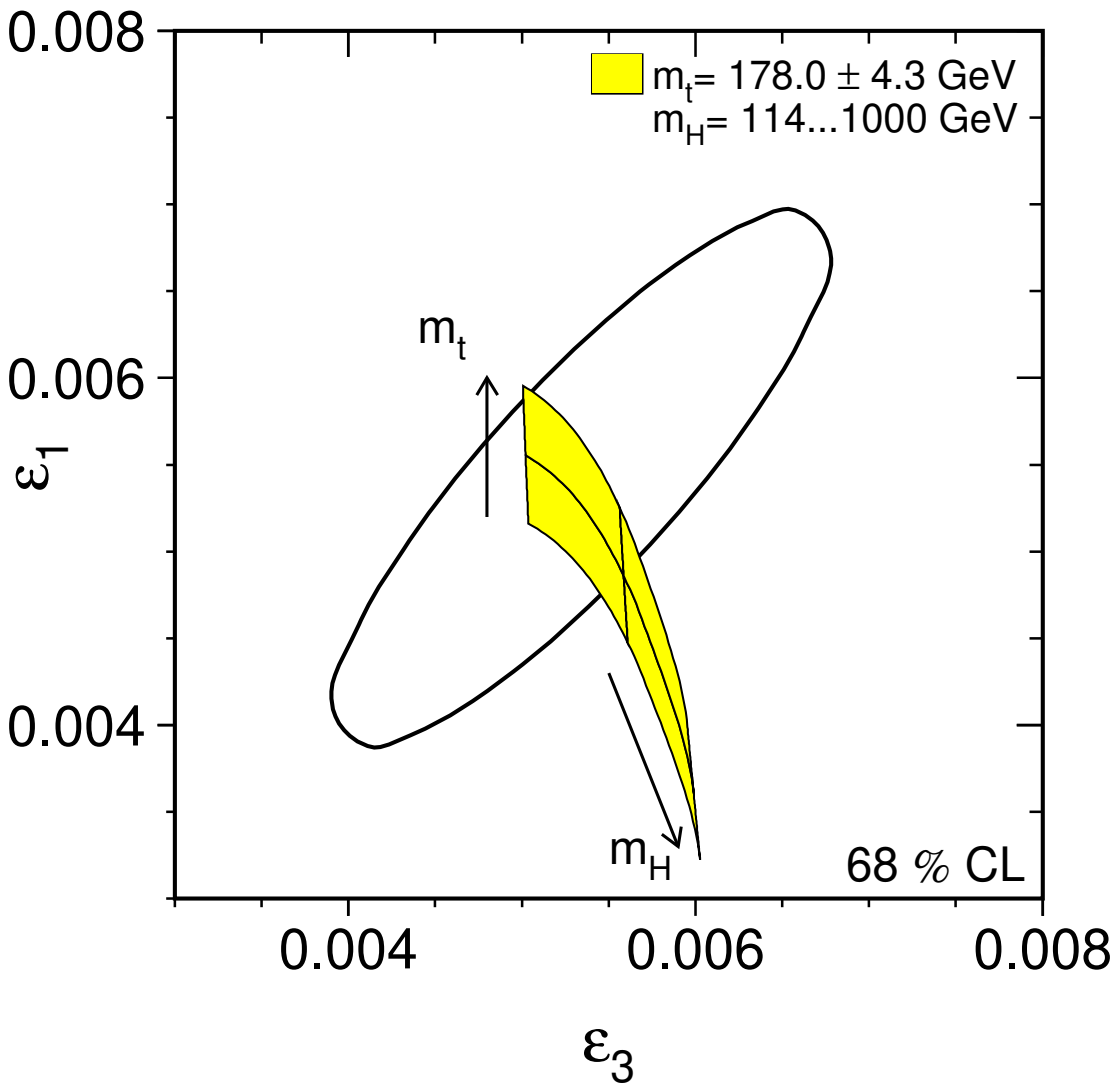

Figure E.1: Contour curve of 68% probability in the (ϵ_3, ϵ_1) plane. The shaded region shows the predictions within the SM for $m_{\rm t} = 178.0 \pm 4.3$ GeV (Tevatron Run-I) and $m_{\rm H} = 300^{+700}_{-186}$ GeV, for a fixed hadronic vacuum polarisation of $\Delta\alpha^{(5)}_{\rm had}(m_{\rm Z}^2) = 0.02758$. The direct measurement of $m_{\rm W}$ used here is preliminary.

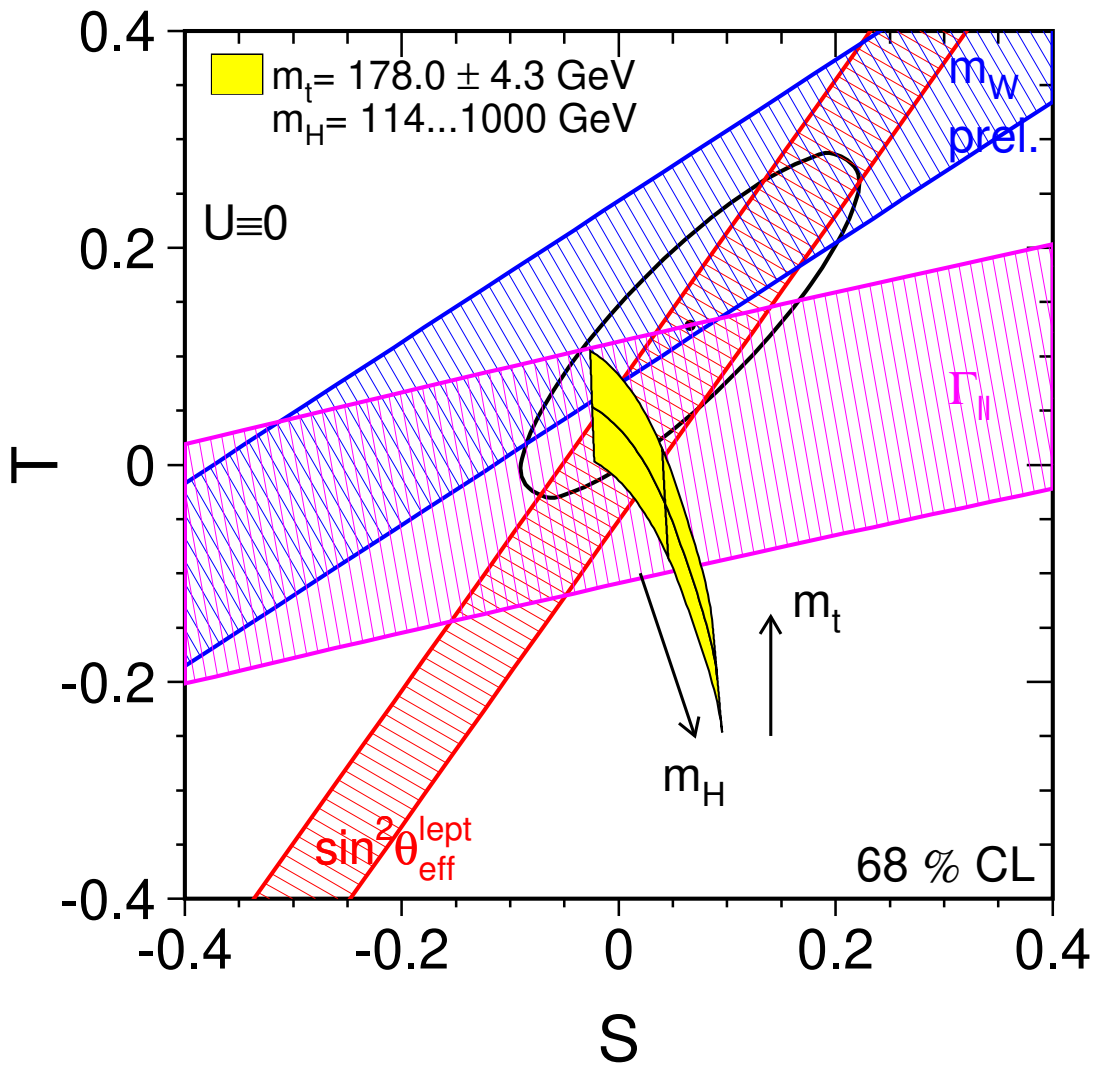

Figure E.2: Contour curve of 68% probability in the (T, S) plane. Also shown are ± 1 standard deviation bands corresponding to the measurements of $\Gamma_{\ell\ell}$, m_{W} and $\sin^2\theta_{\mathrm{eff}}^{\mathrm{lept}}$. The shaded region shows the predictions within the SM for $m_{\mathrm{t}} = 178.0 \pm 4.3$ GeV (Tevatron Run-I) and $m_{\mathrm{H}} = 300^{+700}_{-186}$ GeV, for a fixed hadronic vacuum polarisation of $\Delta\alpha^{(5)}_{\mathrm{had}}(m^2_{\mathrm{Z}}) = 0.02758$. The SM reference point at which all STU parameters vanish is chosen to be: $\Delta\alpha^{(5)}_{\mathrm{had}}(m^2_{\mathrm{Z}}) = 0.02758$, $\alpha_{\mathrm{S}}(m^2_{\mathrm{Z}}) = 0.118$, $m_{\mathrm{Z}} = 91.1875$ GeV, $m_{\mathrm{t}} = 175$ GeV, $m_{\mathrm{H}} = 150$ GeV. The constraint $U = 0$ is always applied. The direct measurement of m_{W} used here is preliminary.

Appendix F

Results using Light Flavour Hadronic Events

Measurements using tagged samples of specific light flavour quarks (up, down or strange) are summarised here, together with information on the partial widths of the Z to up-type and down-type quarks in hadronic Z decays inferred from the observed rate of direct photon production. With some extra assumptions, these results are then used to make checks of light flavour couplings.

F.1 Asymmetry Measurements

The first measurement of the strange quark forward-backward asymmetry was made by DELPHI [254], using 1992 data, and identifying strange quark events from kaons in the Ring Imaging Cherenkov detectors (RICH). The measurement was then updated with the full 1992-1995 data set [255]. The Barrel RICH covers $40^\circ < \theta < 140^\circ$, and was used for the full dataset. The Forward RICH covers $15^\circ < \theta < 35^\circ$ plus $145^\circ < \theta < 165^\circ$, and was used for the 1994–1995 data. Kaons with momenta between 10 and 24 GeV are selected in the RICH detectors, with an average identification efficiency of 53% (42%) in the Barrel (Forward) region. At least two photoelectrons had to be identified in the ring, and the angle of the ring with respect to the track direction had to be consistent with the theoretical expectation for kaons within 2.5 standard deviations, and at least 2 standard deviations away from the pion expectation. The distribution of Cherenkov angle as a function of momentum is shown in Figure F.1. The quark direction is taken to be the event thrust axis, signed according to the charge of the identified kaon. The strange fraction of the sample selected by the kaon tag is 43%. For events in the barrel region, which overlap with the micro-vertex acceptance, bottom and charm quark events are removed by a requirement on the event b-tagging probability, which increases the strange fraction to 55% and reduces the dependence of the result on modelling kaon production in heavy quark decays.

The asymmetry of the selected event sample is a linear combination of five quark forward-backward asymmetries, weighted by the fraction of that flavour and a flavour dependent charge dilution factor, as in Equation 5.13. The asymmetry of the selected sample is estimated by a χ^2 fit to the asymmetry in bins of $\cos\theta$ of the event thrust axis, signed by the charge of the kaon. The sample asymmetry is corrected for background, dominated by misidentified pions. This correction depends on the polar angle of the kaon candidate. The s-quark asymmetry is then evaluated, taking into account the fraction of each quark flavour in the kaon-tagged sample,

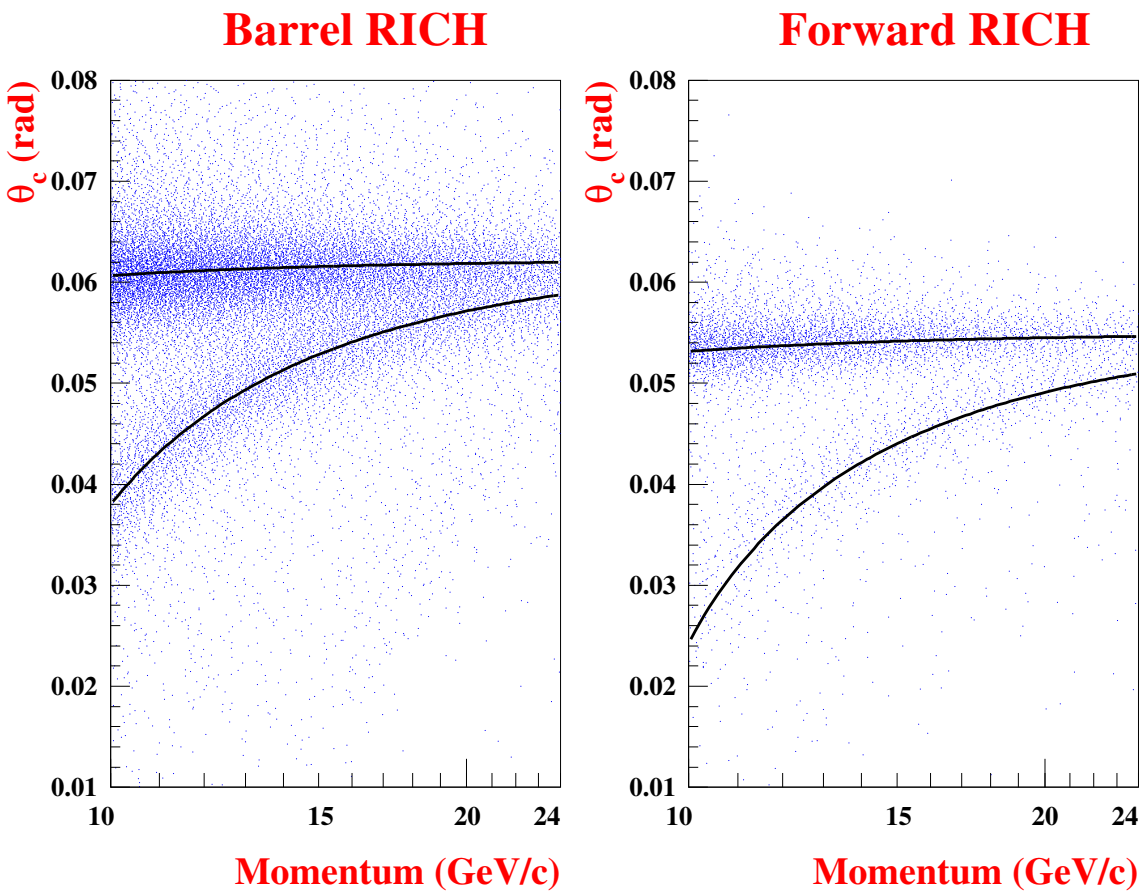

Figure F.1: For a sample of tracks in DELPHI 1994 data, the reconstructed average Cherenkov angle in the gaseous radiator of (left) the barrel RICH and (right) the forward RICH as a function of the particle momentum. The two solid lines show the Cherenkov angle for the pion (upper) and kaon (lower) hypotheses.

and the probability that the charge is correctly tagged for each flavour. Corrections for QED radiation and QCD effects are also made. The analysis is somewhat model dependent, in that it assumes the Standard Model (SM) prediction for production fractions for each flavour, and for non-strange asymmetries, taken either from ZFITTER [31] or from LEP combined measurements. The analysis also relies on the Monte Carlo simulation to compute the efficiencies and dilutions for each flavour. However, the explicit dependence on the other flavour asymmetries can be included in the result, which is:

$$\begin{aligned} A_{\rm FB}^{0,\rm s} &= 0.1008 \pm 0.0113 \pm 0.0036 - 0.0210(A_{\rm FB}^{0,\rm c} - 0.0709)/0.0709 \\ &\quad +0.0121(A_{\rm FB}^{0,\rm d} - 0.1031)/0.1031 + 0.0115(A_{\rm FB}^{0,\rm u} - 0.0736)/0.0736\,, \end{aligned} \tag{F.1}$$

where the first error is statistical and the second systematic. The dependence on the b-quark forward-backward asymmetry is a factor 10 smaller and has been neglected. The quoted systematic error in the original publication of 0.0040 included an uncertainty for the measured c-quark asymmetry, which is replaced by the explicit dependence here.

OPAL [256] has also measured light quark asymmetries, using the full 1990-1995 data-set, and high-momentum stable particles as a tag for light flavour events. Their approach is quite different from that of DELPHI, aiming for the minimum model dependence. The tag method uses the fact that the leading particle in a jet tends to carry the quantum numbers of the primary quark, and that the decay of c- and b-hadrons does not usually yield very high momentum stable particles. Identified $\pi^{\pm}$, $\mathrm{K}^{\pm}$, $\mathrm{p}(\overline{\mathrm{p}})$, $\mathrm{K}^0_{\mathrm{S}}$ or $\Lambda(\overline{\Lambda})$ hadrons with momentum, p_h, satisfying $2p_h/\sqrt{s} > 0.5$ are selected. Charged protons, pions and kaons are identified from the $\mathrm{d}E/\mathrm{d}x$ measured in the OPAL jet chamber, while $\mathrm{K}^0_{\mathrm{S}}$ and $\Lambda(\overline{\Lambda})$ are selected by reconstructing their decay vertex and mass cuts. Only events where the polar angle of the thrust axis satisfies $|\cos\theta| < 0.8$ are considered, and after all selection cuts about 110 thousand tagged hemispheres are retained out of 4.3 million events. The purities range from 89.5% for pions to 59% for protons.

With the 5 different tags, the analysis uses a system of 5 single and 15 double tag equations to derive the light flavour composition of the tagged hemispheres directly from data (see Section 5 for a description of the double tag method). The unknowns are the 15 η^h_{q}, the fractions of hemispheres of flavour q tagged by hadron h, and the three light flavour partial widths R_{q}, plus one hemisphere correlation coefficient which is assumed to be the same for all tagging hadrons and flavours. The small heavy quark fractions are measured from data from a b-tagged sample for b-quarks, and from Monte Carlo simulation using measured uncertainties on their properties for c-quark events. To solve the system of equations, it is then also assumed that $R_{\mathrm{d}} = R_{\mathrm{s}} \equiv R_{\mathrm{d,s}}$, and that a few hadronisation symmetries are valid, for example $\eta^{\pi^{\pm}}_{\mathrm{d}} = \eta^{\pi^{\pm}}_{\mathrm{u}}$. In order to measure the forward-backward asymmetry, the charge tagging probabilities are also measured from the double tagged events, and it is assumed that $A^{0,\,\mathrm{d}}_{\mathrm{FB}} = A^{0,\,\mathrm{s}}_{\mathrm{FB}} \equiv A^{0,\,\mathrm{d,s}}_{\mathrm{FB}}$.

The OPAL results are

$$A^{0,\,\mathrm{d,s}}_{\mathrm{FB}} = 0.072 \pm 0.035 \pm 0.011 - 0.0119(A^{0,\,\mathrm{c}}_{\mathrm{FB}} - 0.0722)/0.0722\,, \tag{F.2}$$

$$A^{0,\,\mathrm{u}}_{\mathrm{FB}} = 0.044 \pm 0.067 \pm 0.018 - 0.0334(A^{0,\,\mathrm{c}}_{\mathrm{FB}} - 0.0722)/0.0722\,. \tag{F.3}$$

The correlation between the two results is +91%. The correlation is positive because although the quark asymmetries have the same sign, the up and down-type quarks have opposite charge. The asymmetry for a given tag particle is therefore of opposite sign if the leading particle includes an up-type quark compared to a down-type quark. These pole asymmetries include corrections of +0.004 which have been applied to the measured $A^{\mathrm{s\overline{s}},\mathrm{d\overline{d}}}_{\mathrm{FB}}$ and $A^{\mathrm{u\overline{u}}}_{\mathrm{FB}}$ to account for QCD and ISR effects. The dependence on the c-quark forward-backward asymmetry has been quoted explicitly, and the results have negligible dependence on other SM parameters. Correlated systematic uncertainties with other measurements are also very small.

SLD have published a measurement of the strange quark coupling parameter, $\mathcal{A}_{\mathrm{s}}$, from the left-right forward-backward asymmetry of events tagged by the presence in each hemisphere of a high momentum $\mathrm{K}^{\pm}$ or $\mathrm{K}^0_{\mathrm{S}}$ [257]. The measurement uses the full sample of 550,000 Z decays recorded in 1993–1998. Charged kaons with momentum above 9 GeV are identified by the Cherenkov Ring Imaging Detector (CRID), with efficiency (purity) of 48% (91.5%). Neutral kaons with momentum above 5 GeV are reconstructed from the decay $\mathrm{K}^0_{\mathrm{S}} \to \pi^+\pi^-$ with an efficiency (purity) of 24% (90.7%). Background from kaons from heavy flavour events is suppressed by identifying B and D decay vertices. Requiring a strange tag in both hemispheres further suppresses the $\mathrm{u\overline{u}}$+$\mathrm{d\overline{d}}$ events. The thrust axis is used to estimate the s-quark production angle, with the charge identified from a $\mathrm{K}^{\pm}$ in one hemisphere, which must be opposite to either a $\mathrm{K}^{\mp}$ or a $\mathrm{K}^0_{\mathrm{S}}$. For the two tagging cases, 1290 and 1580 events are selected, with $\mathrm{s\overline{s}}$ purities of 73% and 60% respectively. The corresponding analysing powers are 0.95 and 0.70,

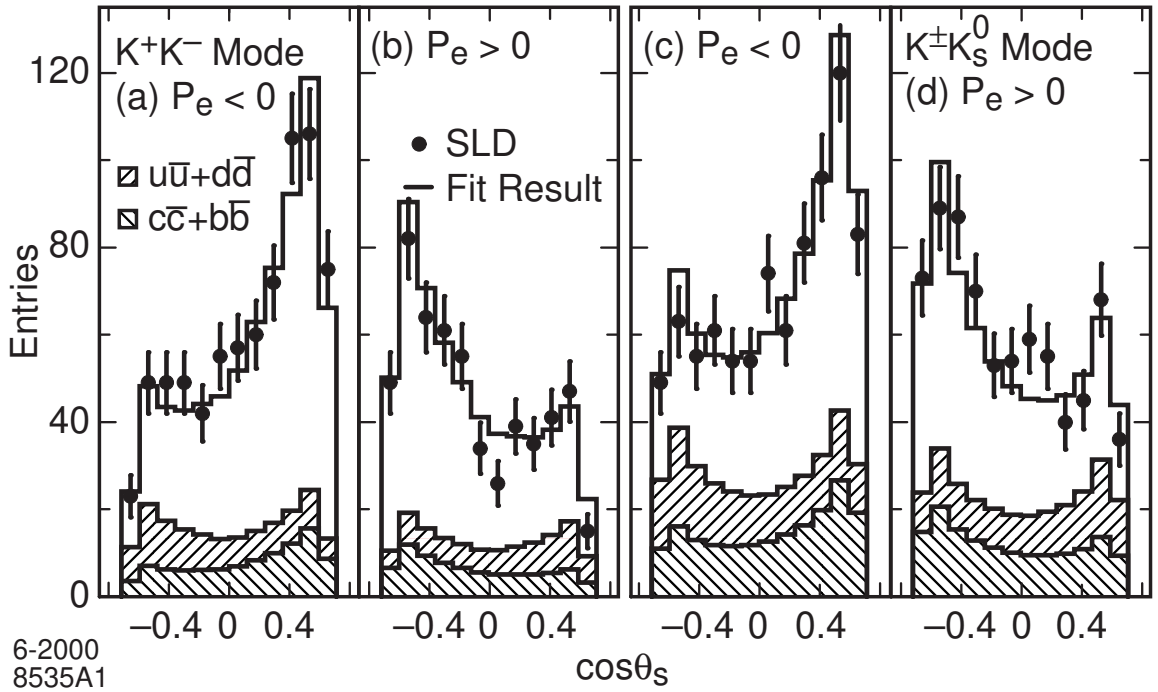

Figure F.2: Measured s-quark polar angle distributions (dots) for selected SLD events in the (a),(b) K^+K^- and (c),(d) $K^\pm K^0_S$ modes, produced with (a),(c) left- and (b),(d) right-polarised electron beams. The histograms represent the result of a simultaneous fit to the four distributions, and the upper (lower) hatched areas indicate the estimated $u\bar{u}+d\bar{d}$ ($c\bar{c}+b\bar{b}$) backgrounds.

where analysing power is defined as $(N_r - N_w)/(N_r + N_w)$, and N_r (N_w) is the number of events where the thrust axis was signed correctly (incorrectly). The asymmetry is derived from a simultaneous maximum likelihood fit to the distributions shown in Figure F.2, taking into account contributions from each flavour. As in the case of the OPAL measurement, this analysis is designed to be self-calibrating as much as possible. The analysing powers and the $u\bar{u} + d\bar{d}$ backgrounds are constrained from the data, by examining the relative rates of single and multi-tagged hemispheres.

The result of the fit is

$$\begin{aligned}\mathcal{A}_s &= 0.895 \pm 0.066 \pm 0.062 - 0.1258(\mathcal{A}_c - 0.641)/0.641 \\ &\quad +0.0275(\mathcal{A}_d - 0.935)/0.935 + 0.0558(\mathcal{A}_u - 0.666)/0.666 \\ &\quad +0.0150(R_c - 0.1735)/0.1735 + 0.2291((R_u + R_d)/R_s - 1.780)/1.780\,, \end{aligned} \qquad \text{(F.4)}$$

where the dependence on other electroweak parameters is given explicitly. The dependences on $\mathcal{A}_b$ and R_b are negligible. Due to strong correlations, the dependence on the light quark partial widths is given in terms of $(R_u + R_d)/R_s$ as a convenient approximation.

Common systematic uncertainties between any of these light quark results and the measurements in the heavy flavour sector, for example from QCD corrections, or the SLC electron beam polarisation, can safely be neglected for all these results, since the total statistical and systematic errors are relatively much larger. Correlations between the light-quark results are also small, in particular because the OPAL and SLD results rely on data to constrain systematic uncertainties.

F.2 Partial Width Measurements

The OPAL analysis described above [256], using 1990-1995 data, and high-momentum stable particles as a light-flavour tag, also gives measurements of the ratios:

$$\frac{R_{\mathrm{u}}}{R_{\mathrm{d}}+R_{\mathrm{u}}+R_{\mathrm{s}}} \;=\; 1-\frac{2R_{\mathrm{d,s}}}{R_{\mathrm{d}}+R_{\mathrm{u}}+R_{\mathrm{s}}} \;=\; 0.258\pm0.031\pm0.032\,, \tag{F.5}$$

where $R_{\mathrm{d,s}} = R_{\mathrm{d}} = R_{\mathrm{s}}$.

In addition, DELPHI [258], L3 [259] and OPAL [260] have used the rate of hadronic events with identified direct photons, interpreted as final-state radiation from quarks, to access effective couplings defined as:

$$c_{\mathrm{u}} \;=\; 4\,(g^2_{\mathrm{Vu}}+g^2_{\mathrm{Au}}+g^2_{\mathrm{Vc}}+g^2_{\mathrm{Ac}})/2 \tag{F.6}$$

$$c_{\mathrm{d}} \;=\; 4\,(g^2_{\mathrm{Vd}}+g^2_{\mathrm{Ad}}+g^2_{\mathrm{Vs}}+g^2_{\mathrm{As}}+g^2_{\mathrm{Vb}}+g^2_{\mathrm{Ab}})/3\,, \tag{F.7}$$

which are proportional to the up-type or down-type partial widths. The measured quantity is the partial width of hadronic events with an isolated photon, which is given by

$$\Gamma(\mathrm{Z}\to\gamma+\mathrm{jets})(y_{\mathrm{cut}}) \;=\; \frac{h}{9}\frac{\alpha}{2\pi}F(y_{\mathrm{cut}})S_{\mathrm{qq}\gamma}\,, \tag{F.8}$$

where $h = 3G_{\mathrm{F}}m^3_{\mathrm{Z}}/24\pi\sqrt{2}$, $F(y_{\mathrm{cut}})$ expresses the theoretical matrix element calculation for the rate of $\mathrm{qq}\gamma$ events as a function of the jet resolution parameter y_{cut}, and $S_{\mathrm{qq}\gamma}$ is a function of the effective couplings. The matrix elements are known to $\mathcal{O}(\alpha\alpha_{\mathrm{S}})$. The values of α_{S} used to evaluate the matrix elements and their uncertainty partly reflect the lack of a higher order calculation. (see for example [261]). The couplings contribute as:

$$S_{\mathrm{qq}\gamma} \;=\; 8c_{\mathrm{u}}+(3-\epsilon)c_{\mathrm{d}}\,. \tag{F.9}$$

This reflects the relative strengths of the up and down-type quark couplings to the photon. The quantity ϵ takes into account the b-quark mass, and is also expected to depend on the jet resolution as discussed below. The analyses combine this with the total hadronic width of the Z, which can be expressed as

$$\Gamma_{\mathrm{had}} \;=\; h\left[1+\frac{\alpha_{\mathrm{S}}}{\pi}+1.41\left(\frac{\alpha_{\mathrm{S}}}{\pi}\right)^2-12.8\left(\frac{\alpha_{\mathrm{S}}}{\pi}\right)^3\right]S_{\mathrm{qq}}\,, \tag{F.10}$$

and

$$S_{\mathrm{qq}} \;=\; 2c_{\mathrm{u}}+3c_{\mathrm{d}}\,. \tag{F.11}$$

In this case the QCD correction is known to third order in α_{S}. The Equations F.9 and F.11 can be solved to give the effective couplings, c_{u} and c_{d}. In this paper we find a LEP combined value for $S_{\mathrm{qq}\gamma}$ and use this in the following section with all the other Z lineshape information to investigate quark couplings. Although ALEPH have also investigated prompt photon production [262], the collaboration chose not to interpret these QCD studies in terms of electroweak couplings.

Experimentally, the photon is identified in hadronic events as an isolated calorimeter cluster, with no associated track. DELPHI and OPAL use shower shape variables to reduce the background from light neutral meson decays such as $\pi^0\to\gamma\gamma$. The other dominant background is from initial-state radiation. This is reduced by restricting the analysis to the central region of the detector. The event samples and the photon selection criteria are outlined in Table F.1.

	DELPHI	L3	OPAL
Data set:			
Years	1991–93	1990–91	1990–95
Multihadron events	1.5 M	320 k	3.0 M
Photon selection:			
θ_γ in range	$25 - 155^\circ$	$45 - 135^\circ$	$\lvert\cos\theta_\gamma\rvert < 0.72$
E_γ satisfies	> 5.5 GeV	> 5.0 GeV	> 7.0 GeV
Isolation half angle	$20^\circ, E > 500$ MeV	$15^\circ, E > 500$ MeV	$0.235\text{rad}, E > 500$ MeV
Jet scheme:	Durham, $y_{\rm cut} = 0.02$	JADE, $y_{\rm cut} = 0.05$	JADE, $y_{\rm cut} = 0.08$
Photon–jet	same	γ 20° from jet	same

Table F.1: Comparison of direct photon analyses. The jet finding schemes and resolution parameters are those chosen for the central value of the electroweak couplings by each experiment.

The particles in the event excluding the photon are grouped into jets using some jet resolution parameter $y_{\rm cut}$. The jet finding is then extended to include the photon using the same jet resolution parameter (DELPHI, OPAL), and the event is only retained if the photon is not merged with a jet. In the case of L3, an angular separation between the photon and the jets is required. The rate of isolated photons therefore depends on the jet resolution parameter that has been chosen. The rate as a function of $y_{\rm cut}$ is used in various QCD studies, but one working point is chosen for the calculation of electroweak parameters of relevance here. The rates are corrected for detector and fragmentation effects, and for the geometric acceptance. When compared with the predictions of matrix element calculations they yield a measurement of $S_{\rm qq\gamma}$.

The correction to account for the b-quark mass was estimated by L3 to be $\epsilon = 0.2 \pm 0.1$. However this correction should depend on the effective mass of the photon-jet system. No correction was used by OPAL, while DELPHI adopted the same correction as L3. However, in the OPAL and DELPHI analyses, the effective mass of the photon-jet system is constrained to be about an order of magnitude larger than for L3, and the relative impact of the b-quark mass should be much smaller. For this reason, the correction has been used here for the L3 result only.

The published values for $S_{\rm qq\gamma}$ with the error categories chosen by the three experiments are as follows: for DELPHI,

$$S_{\rm qq\gamma} \;=\; 11.71 \pm 0.43 \pm 0.78 \pm 0.50 \pm 0.25^{+1.07}_{-1.78}\,, \tag{F.12}$$

where the errors account for statistics, experimental effects, theory, $\alpha_{\rm S}$ and the y_{cut} range respectively; for L3

$$S_{\rm qq\gamma} \;=\; 11.88 \pm 1.17 \pm 0.09 \pm 0.63\,, \tag{F.13}$$

where the errors represent statistical and experimental effects, hadronisation and variations of the photon-jet collinearity cut; and for OPAL,

$$S_{\rm qq\gamma} \;=\; 13.74 \pm 0.30 \pm 0.27^{+0.12}_{-0.04}\,, \tag{F.14}$$

where the the first error is statistical, the second is systematic and the third comes from the uncertainty in evaluating the matrix element $F(y_{\rm cut})$.

The OPAL result uses more data, and controls the experimental uncertainties by fitting the distribution of the shower shape variable for the rate of neutral hadrons misidentified as photons. This result dominates the average. The OPAL uncertainties due to hadronisation or fragmentation, $\alpha_{\rm S}^{(1)}$ and theory amount to 0.25. The uncertainty in the DELPHI and L3 measurements due to these effects are estimated to be 0.60. These uncertainties are treated as fully correlated. An additional common uncertainty of 0.36 due to possible common experimental effects is estimated for DELPHI and L3. These common uncertainties are used to calculate the off-diagonal terms in the covariance matrix relating the three measurements of $S_{\rm qq\gamma}$, which are combined using a χ^2 fit based on the heavy-flavour averaging procedure. The average is very insensitive to variations in the assumptions about correlated uncertainties. The value of ϵ was set equal to zero for the DELPHI and OPAL results, and constrained to $\epsilon = 0.2 \pm 0.1$ for the L3 result. The average value of $S^0_{\rm qq\gamma} \equiv 8c_{\rm u} + 3c_{\rm d}$ was then found to be:

$$S^0_{\rm qq\gamma} \;\equiv\; 8c_{\rm u} + 3c_{\rm d} \;=\; 13.67 \pm 0.42\,. \tag{F.15}$$

This result is uncorrelated with the Z width, and is used in the following section to infer information on quark couplings.

F.3 Comparison with Standard Model Expectations

The SM analysis presented in Table 8.4 predicts the following values for the observables discussed above:

$$A^{0,\,\rm s}_{\rm FB} \;=\; A^{0,\,\rm d}_{\rm FB} \;=\; 0.1039 \pm 0.0008 \tag{F.16}$$

$$A^{0,\,\rm u}_{\rm FB} \;=\; 0.0742 \pm 0.0006 \tag{F.17}$$

$$\mathcal{A}_{\rm s} \;=\; 0.9357 \pm 0.0001 \tag{F.18}$$

$$\frac{R_{\rm u}}{R_{\rm d} + R_{\rm u} + R_{\rm s}} \;=\; 0.2816 \pm 0.0001 \tag{F.19}$$

$$S^0_{\rm qq\gamma} \;=\; 13.677 \pm 0.005\;\;. \tag{F.20}$$

The agreement is good.

F.4 Z Boson Properties and Effective Couplings

The properties of the Z boson and effective couplings of the neutral weak current are now determined for all five quark flavours. In contrast to the procedure adopted in Chapter 7, the hadronic partial width is no longer an independent parameter but is calculated as:

$$\Gamma_{\rm had} \;=\; \Gamma_{\rm d\overline{d}} + \Gamma_{\rm u\overline{u}} + \Gamma_{\rm s\overline{s}} + \Gamma_{\rm c\overline{c}} + \Gamma_{\rm b\overline{b}}\,. \tag{F.21}$$

Since there are not sufficiently many different light-quark flavour pseudo-observables measured to disentangle u, d and s quarks completely, an assumption is made in the extraction of pseudo-observables such as partial widths or effective coupling constants for light quarks: quark universality is imposed for the two down-type light-quark flavours, so that s $\equiv$ d for all pseudo-observables relating to s and d quarks.

As reported in the previous sections, the experimental results on pseudo-observables for light quarks depend explicitly on the values of pseudo-observables for other quark flavours. In

order to treat these dependencies correctly, the global analyses presented in Sections 7.2 and 7.3 are extended to include and treat light quark flavours. For simplicity, the cross-section ratios R_{q} for light quarks u, d and s are interpreted directly as ratios of partial widths, R^0_{q}; this is justified as the difference $R_{\mathrm{q}} - R^0_{\mathrm{q}}$ is negligible relative to the experimental uncertainties of the light quark measurements.

F.4.1 Z-Boson Decay Widths and Branching Fractions

Following the analysis in Section 7.2 and including the ratio of partial widths $R^0_{\mathrm{u}}/(R^0_{\mathrm{d}} + R^0_{\mathrm{u}} + R^0_{\mathrm{s}}) = \Gamma_{\mathrm{u\overline{u}}}/(\Gamma_{\mathrm{d\overline{d}}} + \Gamma_{\mathrm{u\overline{u}}} + \Gamma_{\mathrm{s\overline{s}}})$, Equation F.5, the partial Z decay widths and branching fractions for all five quark flavours are determined. The results for the heavy quark flavours b and c are nearly unchanged from those shown in Tables 7.1 and 7.2, and are not repeated here. The results for the light quark flavours are reported in Tables F.2 and F.3 for partial Z decay widths and Z branching fractions, respectively. The strong anti-correlation between the light-quark partial widths and between their branching fractions arises through Equation F.21 from the precisely measured b, c and inclusive hadronic partial Z decay widths.

Parameter	Value	Correlations	
	[MeV]	$\Gamma_{\mathrm{s\overline{s}}} = \Gamma_{\mathrm{d\overline{d}}}$	$\Gamma_{\mathrm{u\overline{u}}}$
$\Gamma_{\mathrm{s\overline{s}}} = \Gamma_{\mathrm{d\overline{d}}}$	396±24	1.00	
$\Gamma_{\mathrm{u\overline{u}}}$	275±48	−0.99	1.00

Table F.2: Partial Z decay widths and error correlation coefficients for light quarks.

Parameter	Value	Correlations	
	[%]	$B(\mathrm{Z} \to \mathrm{s\overline{s}}) = B(\mathrm{Z} \to \mathrm{d\overline{d}})$	$B(\mathrm{Z} \to \mathrm{u\overline{u}})$
$B(\mathrm{Z} \to \mathrm{s\overline{s}}) = B(\mathrm{Z} \to \mathrm{d\overline{d}})$	15.9±1.0	1.00	
$B(\mathrm{Z} \to \mathrm{u\overline{u}})$	11.0±1.9	−0.99	1.00

Table F.3: Z branching fractions and error correlation coefficients for light quarks.

In order to test quark universality in Z decays quantitatively, the ratios of the quark partial widths or equivalently the ratio of the quark branching fractions are calculated for up-type quarks and for down-type quarks. The results are:

$$\frac{\Gamma_{\mathrm{d\overline{d}}}}{\Gamma_{\mathrm{b\overline{b}}}} = \frac{B(\mathrm{Z} \to \mathrm{d\overline{d}})}{B(\mathrm{Z} \to \mathrm{b\overline{b}})} = 1.049 \pm 0.064 \tag{F.22}$$

$$\frac{\Gamma_{\mathrm{u\overline{u}}}}{\Gamma_{\mathrm{c\overline{c}}}} = \frac{B(\mathrm{Z} \to \mathrm{u\overline{u}})}{B(\mathrm{Z} \to \mathrm{c\overline{c}})} = 0.92 \pm 0.16 \ , \tag{F.23}$$

with a correlation of −0.98. In both cases, good agreement with unity is observed. Assuming quark universality, quark mass effects and SM b-specific vertex corrections are expected to decrease $\Gamma_{\mathrm{b\overline{b}}}$ and $B(\mathrm{Z} \to \mathrm{b\overline{b}})$ by about 1.9% relative to the light down-type quark flavour d; this is also shown in Figure 7.8.

F.4.2 Effective Couplings of the Neutral Weak Current

In addition to the measurement of the partial width ratio, Equation F.5, by including the four measurements of the various light quark asymmetries, Equations F.1 to F.4, and the measurement of $S^0_{\mathrm{qq}\gamma}$, Equation F.15, the analyses presented in Section 7.3 are extended to determine effective couplings of all five quark flavours. The results for the heavy quark flavours b and c are nearly unchanged from those shown in Tables 7.6, 7.9 and 7.11, and are not repeated here. The asymmetry parameters $\mathcal{A}_{\mathrm{s}} = \mathcal{A}_{\mathrm{d}}$ and $\mathcal{A}_{\mathrm{u}}$, derived from the various asymmetry measurements, are listed in Table F.4. The flavour-dependent effective coupling constants as well as the ρ_{q} parameters and the effective electroweak mixing angles $\sin^2\theta^{\mathrm{q}}_{\mathrm{eff}}$ for light quarks are reported in Tables F.5 and F.6, respectively. Good agreement with the SM expectation is observed in all cases.

The results on the effective coupling constants are also shown graphically in Figure F.3. Note that the lepton and heavy-quark regions are expanded in Figures 7.3 and 7.4. Since the energy dependence of the forward-backward asymmetry of light quarks is not measured, the ambiguity $g_{\mathrm{Vq}} \leftrightarrow g_{\mathrm{Aq}}$ arises for the light quarks, corresponding to a mirror symmetry of the contour curves in the $(g_{\mathrm{Vq}}, g_{\mathrm{Aq}})$ plane along the diagonal $g_{\mathrm{Vq}} = g_{\mathrm{Aq}}$. Each light quark contour includes and connects both regions since the light-quark measurements are not precise enough to exclude $g_{\mathrm{Vq}} = g_{\mathrm{Aq}}$ with sufficient significance. In addition, since $\mathcal{A}_{\mathrm{q}}$ determines only the relative sign between g_{Vq} and g_{Aq}, there is also an inversion symmetry about the origin, $(g_{\mathrm{Vq}}, g_{\mathrm{Aq}}) \leftrightarrow (-g_{\mathrm{Vq}}, -g_{\mathrm{Aq}})$, of the contour curves for light quarks. The corresponding mirror solutions are not shown in Figure F.3. Effective couplings for u and d quarks are also measured in electron-proton collisions at HERA [263] and in proton-antiproton collisions at the Tevatron [264], albeit less precisely.

The leptonic effective electroweak mixing angle determined from the four light-quark asymmetry measurements is:

$$\sin^2\theta^{\mathrm{lept}}_{\mathrm{eff}} \;=\; 0.2320 \pm 0.0021\,, \tag{F.24}$$

dominated by DELPHI measurement of $A^{0,\mathrm{s}}_{\mathrm{FB}}$, Equation F.1, where the combination has a χ^2/dof of 1.5/3, corresponding to a probability of 68%. For the determination of $\sin^2\theta^{\mathrm{lept}}_{\mathrm{eff}}$, the parametric dependence of the SLD $\mathcal{A}_{\mathrm{s}}$ result, Equation F.4, on the value of the light-quark partial width ratio $(R_{\mathrm{u}} + R_{\mathrm{d}})/R_{\mathrm{s}}$ is neglected. This result is in good agreement with all the determinations of this quantity presented in Section 7.3.4.

Parameter	Value	Correlations	
		$\mathcal{A}_s = \mathcal{A}_d$	$\mathcal{A}_u$
$\mathcal{A}_s = \mathcal{A}_d$	0.902±0.087	1.00	
$\mathcal{A}_u$	0.82±0.32	0.61	1.00

Table F.4: Results on the asymmetry parameters $\mathcal{A}_q$ for light quarks. Note that since $\mathcal{A}_f = 2r/(1+r^2)$ with $r = g_{Vf}/g_{Af}$, values $|\mathcal{A}_f| > 1$ are unphysical. The combination has a χ^2/dof of 4.9/5, corresponding to a probability of 43%.

Parameter	Value	Correlations			
		$g_{As} = g_{Ad}$	g_{Au}	$g_{Vs} = g_{Vd}$	g_{Vu}
$g_{As} = g_{Ad}$	$-0.52\pm^{0.05}_{0.03}$	1.00			
g_{Au}	$+0.47\pm^{0.05}_{0.33}$	−0.43	1.00		
$g_{Vs} = g_{Vd}$	$-0.33\pm^{0.05}_{0.07}$	−0.92	0.59	1.00	
g_{Vu}	$+0.24\pm^{0.28}_{0.11}$	0.61	−0.91	−0.61	1.00
Parameter	Value	Correlations			
		$g_{Ls} = g_{Ld}$	g_{Lu}	$g_{Rs} = g_{Rd}$	g_{Ru}
$g_{Ls} = g_{Ld}$	−0.423±0.012	1.00			
g_{Lu}	+0.356±0.035	−0.13	1.00		
$g_{Rs} = g_{Rd}$	$+0.10\ \pm^{0.04}_{0.06}$	0.72	−0.59	1.00	
g_{Ru}	$-0.11\ \pm^{0.30}_{0.07}$	−0.51	+0.84	−0.60	1.00

Table F.5: Results on the effective coupling constants g_{Aq} and g_{Vq} as well as g_{Lq} and g_{Rq} for light quarks. Because of the non-parabolic nature of the χ^2 being minimised, the above error matrices are approximate. The combination has a χ^2/dof of 5.4/7, corresponding to a probability of 62%.

Parameter	Value	Correlations			
		$\rho_s = \rho_d$	ρ_u	$\sin^2\theta^s_{eff} = \sin^2\theta^d_{eff}$	$\sin^2\theta^u_{eff}$
$\rho_s = \rho_d$	$1.09\pm^{0.12}_{0.21}$	1.00			
ρ_u	$0.88\pm^{0.20}_{0.37}$	0.42	1.00		
$\sin^2\theta^s_{eff} = \sin^2\theta^d_{eff}$	$0.28\pm^{0.08}_{0.16}$	0.96	0.55	1.00	
$\sin^2\theta^u_{eff}$	$0.18\pm^{0.09}_{0.18}$	0.58	0.94	0.61	1.00

Table F.6: Results on the ρ_q parameter and the effective electroweak mixing angle $\sin^2\theta^q_{eff}$ for light quarks. Because of the non-parabolic nature of the χ^2 being minimised as a function of ρ_q and $\sin^2\theta^q_{eff}$, the above error matrix is approximate. Note that $\sin^2\theta^u_{eff} \geq 0$ has to be enforced as a boundary condition in the calculation of the errors. The combination has a χ^2/dof of 5.4/7, corresponding to a probability of 62%.

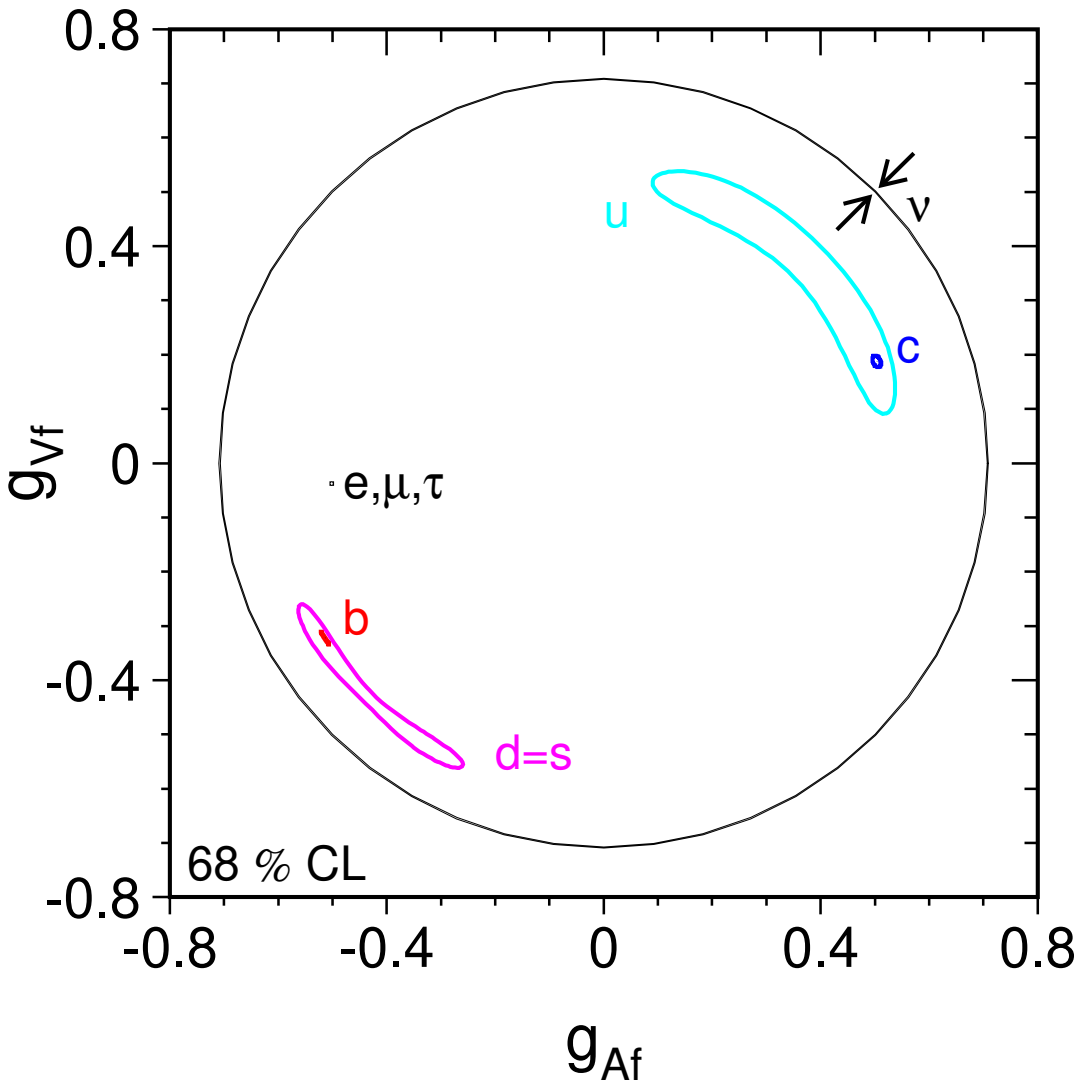

Figure F.3: Comparison of the effective vector and axial-vector coupling constants for fermions. For the light-quark contours (u and d=s), a second solution exists, mirroring the contour curves at the origin. The allowed area for neutrinos, assuming three generations of neutrinos with identical vector couplings and identical axial-vector couplings, is bounded by circles centred at the origin since the invisible partial width constrains the sum of the squares of the effective couplings only.

Appendix G

Standard Model Predictions

Constraints on the free parameters of the Standard Model (SM) derived from the precision electroweak measurements are discussed in Chapter 8. Based on these analyses, SM predictions for all pseudo-observables are calculated and reported in Tables G.1 to G.7. Two sets are calculated, for the Z-pole SM analysis shown in Table 8.2 as well as for the high-Q^2 SM analysis shown in Table 8.3. The improvements in the accuracy of many predictions is clearly visible. Note that all predictions are derived from the same sets of observables, hence they are correlated with the five SM input parameters and cannot be used independently.

The uncertainties quoted on the SM predictions include only the parametric uncertainties arising from the fit to the set of measurements, hence do not take additional theoretical uncertainties (Section 8.4.2) or phase-space uncertainties arising from uncertainties in the masses of fermions other than the top quark into account.

Observable	Standard Model Z-pole Fit	Standard Model High-Q^2 Fit
$\Delta\alpha^{(5)}_{\rm had}(m_{\rm Z})$	0.02759 ± 0.00035	0.02767 ± 0.00034
$\alpha_{\rm S}(m_{\rm Z})$	0.1190 ± 0.0028	0.1188 ± 0.0027
$m_{\rm Z}$ [GeV]	91.1874 ± 0.0021	91.1874 ± 0.0021
$m_{\rm t}$ [GeV]	$173 \pm ^{13}_{10}$	178.5 ± 3.9
$m_{\rm H}$ [GeV]	$111 \pm ^{190}_{60}$	$129 \pm ^{74}_{49}$
$\log_{10}(m_{\rm H}/{\rm GeV})$	$2.05 \pm ^{0.43}_{0.34}$	2.11 ± 0.20
$m_{\rm W}$ [GeV]	80.363 ± 0.032	80.389 ± 0.019
$\sin^2\overline{\theta}^{\overline{\rm MS}}_{\rm W}$	0.23120 ± 0.00016	0.23111 ± 0.00014
$\sin^2\theta_{\rm W}$	0.22331 ± 0.00062	0.22281 ± 0.00036
Δr	0.0363 ± 0.0019	0.0348 ± 0.0011
$\Delta {\rm r}_{\rm w}$	-0.0242 ± 0.0021	-0.0259 ± 0.0013

Table G.1: SM predictions for pseudo-observables derived from the Z-pole and the high-Q^2 SM fits. The matrices of correlation coefficients for the five SM input parameters are shown in Tables 8.2 and 8.3, respectively.

Observable	Standard Model Z-pole Fit	Standard Model High-Q^2 Fit
$\Gamma^{\mathrm{W}}_{\mathrm{tot}}$ [GeV]	2.0910 ± 0.0029	2.0930 ± 0.0017
$\Gamma^{\mathrm{W}}_{\mathrm{had}}$ [GeV]	1.4119 ± 0.0022	1.4132 ± 0.0014
$\Gamma^{\mathrm{W}}_{\mathrm{e}\nu}$ [GeV]	0.22636 ± 0.00028	0.22659 ± 0.00015
$\Gamma^{\mathrm{W}}_{\mu\nu}$ [GeV]	0.22636 ± 0.00028	0.22659 ± 0.00015
$\Gamma^{\mathrm{W}}_{\tau\nu}$ [GeV]	0.22636 ± 0.00028	0.22659 ± 0.00015
$\Gamma^{\mathrm{Z}}_{\mathrm{tot}}$ [GeV]	2.4956 ± 0.0019	2.4965 ± 0.0015
$\Gamma^{\mathrm{Z}}_{\mathrm{had}}$ [GeV]	1.7423 ± 0.0016	1.7427 ± 0.0015
$\Gamma^{\mathrm{Z}}_{\mathrm{ee}}$ [GeV]	$0.083987 \pm ^{0.000058}_{0.000068}$	0.084031 ± 0.000027
$\Gamma^{\mathrm{Z}}_{\mu\mu}$ [GeV]	$0.083986 \pm ^{0.000058}_{0.000068}$	0.084030 ± 0.000027
$\Gamma^{\mathrm{Z}}_{\tau\tau}$ [GeV]	$0.083796 \pm ^{0.000058}_{0.000067}$	0.083840 ± 0.000026
$\Gamma^{\mathrm{Z}}_{\mathrm{dd}}$ [GeV]	0.38299 ± 0.00036	0.38317 ± 0.00026
$\Gamma^{\mathrm{Z}}_{\mathrm{ss}}$ [GeV]	0.38299 ± 0.00036	0.38317 ± 0.00026
$\Gamma^{\mathrm{Z}}_{\mathrm{bb}}$ [GeV]	$0.37602 \pm ^{0.00054}_{0.00074}$	0.37577 ± 0.00037
$\Gamma^{\mathrm{Z}}_{\mathrm{uu}}$ [GeV]	0.30016 ± 0.00046	0.30035 ± 0.00035
$\Gamma^{\mathrm{Z}}_{\mathrm{cc}}$ [GeV]	0.30010 ± 0.00047	0.30028 ± 0.00036
$\Gamma^{\mathrm{Z}}_{\mathrm{inv}}$ [GeV]	$0.50162 \pm ^{0.00034}_{0.00040}$	0.50185 ± 0.00014
$\Gamma^{\mathrm{Z}}_{\mathrm{inv}}/\Gamma^{\mathrm{Z}}_{\ell}$	5.97258 ± 0.00057	5.97227 ± 0.00050
$\Gamma^{\mathrm{Z}}_{\ell}/\Gamma^{\mathrm{Z}}_{\nu}$	0.502296 ± 0.000048	0.502322 ± 0.000042
$\Gamma^{\mathrm{Z}}_{\nu}/\Gamma^{\mathrm{Z}}_{\ell}$	1.99086 ± 0.00019	1.99076 ± 0.00017
$B(\mathrm{W} \to \mathrm{had})$	0.67523 ± 0.00019	0.67522 ± 0.00019
$B(\mathrm{W} \to \mathrm{e}\nu)$	0.108255 ± 0.000065	0.108260 ± 0.000063
$B(\mathrm{W} \to \mu\nu)$	0.108255 ± 0.000065	0.108260 ± 0.000063
$B(\mathrm{W} \to \tau\nu)$	0.108255 ± 0.000065	0.108260 ± 0.000063
$B(\mathrm{Z} \to \mathrm{had})$	0.69812 ± 0.00019	0.69807 ± 0.00018
$B(\mathrm{Z} \to \mathrm{ee})$	0.033653 ± 0.000022	0.033659 ± 0.000020
$B(\mathrm{Z} \to \mu\mu)$	0.033653 ± 0.000022	0.033659 ± 0.000020
$B(\mathrm{Z} \to \tau\tau)$	0.033577 ± 0.000022	0.033583 ± 0.000020
$B(\mathrm{Z} \to \mathrm{dd})$	$0.153464 \pm ^{0.000042}_{0.000030}$	0.153484 ± 0.000014
$B(\mathrm{Z} \to \mathrm{ss})$	$0.153464 \pm ^{0.000042}_{0.000030}$	0.153484 ± 0.000014
$B(\mathrm{Z} \to \mathrm{bb})$	$0.15067 \pm ^{0.00025}_{0.00033}$	0.15052 ± 0.00010
$B(\mathrm{Z} \to \mathrm{uu})$	$0.120273 \pm ^{0.000110}_{0.000087}$	0.120307 ± 0.000069
$B(\mathrm{Z} \to \mathrm{cc})$	$0.120248 \pm ^{0.000113}_{0.000091}$	0.120282 ± 0.000073
$B(\mathrm{Z} \to \mathrm{inv})$	0.20100 ± 0.00013	0.20102 ± 0.00012

Table G.2: SM predictions for pseudo-observables derived from the Z-pole and the high-Q^2 SM fits.

Observable	Standard Model Z-pole Fit	Standard Model High-Q^2 Fit
$g_{\mathrm{A}\nu}$	$0.50199 \pm {}^{0.00017}_{0.00020}$	0.502112 ± 0.000069
g_{Ae}	$-0.50127 \pm {}^{0.00020}_{0.00017}$	-0.501389 ± 0.000068
$g_{\mathrm{A}\mu}$	$-0.50127 \pm {}^{0.00020}_{0.00017}$	-0.501389 ± 0.000068
$g_{\mathrm{A}\tau}$	$-0.50127 \pm {}^{0.00020}_{0.00017}$	-0.501389 ± 0.000068
g_{Ad}	$-0.50168 \pm {}^{0.00020}_{0.00017}$	-0.501803 ± 0.000068
g_{As}	$-0.50168 \pm {}^{0.00020}_{0.00017}$	-0.501803 ± 0.000068
g_{Ab}	$-0.49856 \pm {}^{0.00041}_{0.00020}$	$-0.49844 \pm {}^{0.00013}_{0.00010}$
g_{Au}	$0.50144 \pm {}^{0.00017}_{0.00020}$	0.501562 ± 0.000068
g_{Ac}	$0.50144 \pm {}^{0.00017}_{0.00020}$	0.501562 ± 0.000068
$g_{\mathrm{V}\nu}$	$0.50199 \pm {}^{0.00017}_{0.00020}$	0.502112 ± 0.000069
g_{Ve}	-0.03712 ± 0.00032	-0.03730 ± 0.00028
$g_{\mathrm{V}\mu}$	-0.03712 ± 0.00032	-0.03730 ± 0.00028
$g_{\mathrm{V}\tau}$	-0.03712 ± 0.00032	-0.03730 ± 0.00028
g_{Vd}	-0.34699 ± 0.00017	-0.34714 ± 0.00012
g_{Vs}	-0.34699 ± 0.00017	-0.34714 ± 0.00012
g_{Vb}	$-0.34372 \pm {}^{0.00049}_{0.00028}$	$-0.34360 \pm {}^{0.00018}_{0.00016}$
g_{Vu}	0.19204 ± 0.00023	0.19221 ± 0.00020
g_{Vc}	0.19204 ± 0.00023	0.19221 ± 0.00020
$g_{\mathrm{L}\nu}$	$0.50199 \pm {}^{0.00017}_{0.00020}$	0.502112 ± 0.000069
g_{Le}	-0.26919 ± 0.00020	-0.26935 ± 0.00016
$g_{\mathrm{L}\mu}$	-0.26919 ± 0.00020	-0.26935 ± 0.00016
$g_{\mathrm{L}\tau}$	-0.26919 ± 0.00020	-0.26935 ± 0.00016
g_{Ld}	$-0.42434 \pm {}^{0.00018}_{0.00016}$	-0.424470 ± 0.000087
g_{Ls}	$-0.42434 \pm {}^{0.00018}_{0.00016}$	-0.424470 ± 0.000087
g_{Lb}	$-0.42114 \pm {}^{0.00045}_{0.00024}$	$-0.42102 \pm {}^{0.00015}_{0.00013}$
g_{Lu}	0.34674 ± 0.00017	0.34688 ± 0.00012
g_{Lc}	0.34674 ± 0.00017	0.34688 ± 0.00012
g_{Re}	$0.23208 \pm {}^{0.00016}_{0.00018}$	0.23204 ± 0.00013
$g_{\mathrm{R}\mu}$	$0.23208 \pm {}^{0.00016}_{0.00018}$	0.23204 ± 0.00013
$g_{\mathrm{R}\tau}$	$0.23208 \pm {}^{0.00016}_{0.00018}$	0.23204 ± 0.00013
g_{Rd}	$0.077345 \pm {}^{0.000053}_{0.000061}$	0.077333 ± 0.000044
g_{Rs}	$0.077345 \pm {}^{0.000053}_{0.000061}$	0.077333 ± 0.000044
g_{Rb}	$0.077420 \pm {}^{0.000052}_{0.000061}$	0.077417 ± 0.000040
g_{Ru}	-0.15470 ± 0.00011	-0.154677 ± 0.000087
g_{Rc}	-0.15470 ± 0.00011	-0.154677 ± 0.000087

Table G.3: SM predictions for pseudo-observables derived from the Z-pole and the high-Q^2 SM fits.

Observable	Standard Model Z-pole Fit	Standard Model High-Q^2 Fit
$\mathcal{A}_{\mathrm{e}}$	0.1473 ± 0.0012	0.1480 ± 0.0011
$\mathcal{A}_{\mu}$	0.1473 ± 0.0012	0.1480 ± 0.0011
$\mathcal{A}_{\tau}$	0.1473 ± 0.0012	0.1480 ± 0.0011
$\mathcal{A}_{\mathrm{d}}$	0.93569 ± 0.00010	0.935748 ± 0.000088
$\mathcal{A}_{\mathrm{s}}$	0.93569 ± 0.00010	0.935748 ± 0.000088
$\mathcal{A}_{\mathrm{b}}$	$0.93462 \pm {}^{0.00016}_{0.00020}$	0.934588 ± 0.000100
$\mathcal{A}_{\mathrm{u}}$	0.66798 ± 0.00055	0.66829 ± 0.00048
$\mathcal{A}_{\mathrm{c}}$	0.66798 ± 0.00055	0.66829 ± 0.00048
$\mathcal{P}_{\mathrm{e}}^{\tau}$	0.1473 ± 0.0012	0.1480 ± 0.0011
$\mathcal{P}_{\tau}^{\tau}$	0.1473 ± 0.0012	0.1480 ± 0.0011
$\sigma_{\mathrm{had}}^{0}$ [nb]	41.476 ± 0.015	41.481 ± 0.014
σ_{e}^{0} [nb]	1.9994 ± 0.0026	2.0001 ± 0.0024
σ_{μ}^{0} [nb]	1.9993 ± 0.0026	2.0001 ± 0.0024
σ_{τ}^{0} [nb]	1.9948 ± 0.0026	1.9956 ± 0.0024
R_{e}^{0}	20.744 ± 0.019	20.739 ± 0.018
R_{μ}^{0}	20.745 ± 0.019	20.740 ± 0.018
R_{τ}^{0}	20.792 ± 0.019	20.786 ± 0.018
R_{d}^{0}	$0.219824 \pm {}^{0.000093}_{0.000082}$	0.219868 ± 0.000055
R_{s}^{0}	$0.219824 \pm {}^{0.000093}_{0.000082}$	0.219868 ± 0.000055
R_{b}^{0}	$0.21583 \pm {}^{0.00033}_{0.00045}$	0.21562 ± 0.00013
R_{u}^{0}	$0.17228 \pm {}^{0.00015}_{0.00011}$	0.172341 ± 0.000063
R_{c}^{0}	$0.17225 \pm {}^{0.00016}_{0.00012}$	0.172305 ± 0.000068
$A_{\mathrm{FB}}^{0,\mathrm{e}}$	0.01627 ± 0.00027	0.01642 ± 0.00024
$A_{\mathrm{FB}}^{0,\mu}$	0.01627 ± 0.00027	0.01642 ± 0.00024
$A_{\mathrm{FB}}^{0,\tau}$	0.01627 ± 0.00027	0.01642 ± 0.00024
$A_{\mathrm{FB}}^{0,\mathrm{d}}$	0.10335 ± 0.00088	0.10385 ± 0.00078
$A_{\mathrm{FB}}^{0,\mathrm{s}}$	0.10335 ± 0.00088	0.10385 ± 0.00078
$A_{\mathrm{FB}}^{0,\mathrm{b}}$	0.10324 ± 0.00088	0.10373 ± 0.00077
$A_{\mathrm{FB}}^{0,\mathrm{u}}$	0.07378 ± 0.00068	0.07417 ± 0.00060
$A_{\mathrm{FB}}^{0,\mathrm{c}}$	0.07378 ± 0.00068	0.07417 ± 0.00060

Table G.4: SM predictions for pseudo-observables derived from the Z-pole and the high-Q^2 SM fits.

Observable	Standard Model Z-pole Fit	Standard Model High-Q^2 Fit
ρ_ν	$1.00799 \pm {}^{0.00068}_{0.00081}$	1.00847 ± 0.00028
ρ_e	$1.00509 \pm {}^{0.00067}_{0.00081}$	1.00556 ± 0.00027
ρ_μ	$1.00509 \pm {}^{0.00067}_{0.00081}$	1.00556 ± 0.00027
ρ_τ	$1.00509 \pm {}^{0.00067}_{0.00081}$	1.00556 ± 0.00027
ρ_d	$1.00675 \pm {}^{0.00067}_{0.00081}$	1.00723 ± 0.00027
ρ_s	$1.00675 \pm {}^{0.00067}_{0.00081}$	1.00723 ± 0.00027
ρ_b	$0.99426 \pm {}^{0.00079}_{0.00164}$	$0.99376 \pm {}^{0.00040}_{0.00052}$
ρ_u	$1.00578 \pm {}^{0.00067}_{0.00081}$	1.00626 ± 0.00027
ρ_c	$1.00578 \pm {}^{0.00067}_{0.00081}$	1.00626 ± 0.00027
$\sin^2\theta^\nu_\mathrm{eff}$	0.23111 ± 0.00016	0.23102 ± 0.00014
$\sin^2\theta^\mathrm{e}_\mathrm{eff}$	0.23149 ± 0.00016	0.23140 ± 0.00014
$\sin^2\theta^\mu_\mathrm{eff}$	0.23149 ± 0.00016	0.23140 ± 0.00014
$\sin^2\theta^\tau_\mathrm{eff}$	0.23149 ± 0.00016	0.23140 ± 0.00014
$\sin^2\theta^\mathrm{d}_\mathrm{eff}$	0.23126 ± 0.00016	0.23117 ± 0.00014
$\sin^2\theta^\mathrm{s}_\mathrm{eff}$	0.23126 ± 0.00016	0.23117 ± 0.00014
$\sin^2\theta^\mathrm{b}_\mathrm{eff}$	$0.23293 \pm {}^{0.00031}_{0.00025}$	0.23298 ± 0.00016
$\sin^2\theta^\mathrm{u}_\mathrm{eff}$	0.23138 ± 0.00016	0.23129 ± 0.00014
$\sin^2\theta^\mathrm{c}_\mathrm{eff}$	0.23138 ± 0.00016	0.23129 ± 0.00014
κ_ν	1.0349 ± 0.0026	1.0368 ± 0.0012
κ_e	1.0366 ± 0.0026	1.0385 ± 0.0012
κ_μ	1.0366 ± 0.0026	1.0385 ± 0.0012
κ_τ	1.0366 ± 0.0026	1.0385 ± 0.0012
κ_d	1.0356 ± 0.0026	1.0375 ± 0.0012
κ_s	1.0356 ± 0.0026	1.0375 ± 0.0012
κ_b	1.0431 ± 0.0036	1.0456 ± 0.0015
κ_u	1.0361 ± 0.0026	1.0381 ± 0.0012
κ_c	1.0361 ± 0.0026	1.0381 ± 0.0012

Table G.5: SM predictions for pseudo-observables derived from the Z-pole and the high-Q^2 SM fits.

Observable	Standard Model Z-pole Fit	Standard Model High-Q^2 Fit
ϵ_1	$0.00506 \pm {}^{0.00066}_{0.00080}$	0.00553 ± 0.00027
ϵ_2	$-0.00746 \pm {}^{0.00018}_{0.00021}$	-0.007612 ± 0.000100
ϵ_3	$0.00502 \pm {}^{0.00053}_{0.00076}$	$0.00511 \pm {}^{0.00027}_{0.00039}$
ϵ_b	$-0.00540 \pm {}^{0.00079}_{0.00108}$	-0.00588 ± 0.00032
$S + c_S$	$0.598 \pm {}^{0.064}_{0.090}$	$0.608 \pm {}^{0.032}_{0.046}$
$T + c_T$	$0.653 \pm {}^{0.085}_{0.103}$	0.713 ± 0.035
$U + c_U$	$0.889 \pm {}^{0.026}_{0.022}$	$0.907 \pm {}^{0.013}_{0.011}$
$\gamma_b + c_{\gamma_b}$	$-0.0124 \pm {}^{0.0018}_{0.0025}$	-0.01347 ± 0.00073
S	$-0.025 \pm {}^{0.064}_{0.090}$	$-0.014 \pm {}^{0.032}_{0.046}$
T	$-0.010 \pm {}^{0.085}_{0.103}$	0.051 ± 0.035
U	$-0.001 \pm {}^{0.026}_{0.022}$	$0.017 \pm {}^{0.013}_{0.011}$
γ_b	$0.0005 \pm {}^{0.0018}_{0.0025}$	-0.00066 ± 0.00073
$\Gamma^\mathrm{Z}_\mu/\Gamma^\mathrm{Z}_\mathrm{e}$	$0.99999198984 \pm 0.00000000084$	$0.99999199026 \pm 0.00000000075$
$\Gamma^\mathrm{Z}_\tau/\Gamma^\mathrm{Z}_\mathrm{e}$	$0.99773494 \pm 0.00000024$	$0.99773506 \pm 0.00000021$
$\Gamma^\mathrm{Z}_\mathrm{d}/\Gamma^\mathrm{Z}_\mathrm{b}$	$1.0185 \pm {}^{0.0025}_{0.0019}$	1.01971 ± 0.00077
$\Gamma^\mathrm{Z}_\mathrm{s}/\Gamma^\mathrm{Z}_\mathrm{b}$	$1.0185 \pm {}^{0.0025}_{0.0019}$	1.01971 ± 0.00077
$\Gamma^\mathrm{Z}_\mathrm{u}/\Gamma^\mathrm{Z}_\mathrm{c}$	1.000205 ± 0.000036	1.000207 ± 0.000035
$g_\mathrm{Ad}/g_\mathrm{Ab}$	$1.00626 \pm {}^{0.00110}_{0.00080}$	1.00675 ± 0.00032
$g_\mathrm{As}/g_\mathrm{Ab}$	$1.00626 \pm {}^{0.00110}_{0.00080}$	1.00675 ± 0.00032
$g_\mathrm{Vd}/g_\mathrm{Vb}$	$1.0095 \pm {}^{0.0016}_{0.0012}$	1.01028 ± 0.00048
$g_\mathrm{Vs}/g_\mathrm{Vb}$	$1.0095 \pm {}^{0.0016}_{0.0012}$	1.01028 ± 0.00048
$\overline{m}_\mathrm{Z}$ [GeV]	91.1532 ± 0.0021	91.1532 ± 0.0021
$\overline{\Gamma}^\mathrm{Z}_\mathrm{tot}$ [GeV]	2.4947 ± 0.0019	2.4956 ± 0.0015

Table G.6: SM predictions for pseudo-observables derived from the Z-pole and the high-Q^2 SM fits.

Observable	Standard Model Z-pole Fit	Standard Model High-Q^2 Fit
$C_{1\mathrm{u}}$	-0.18883 ± 0.00024	-0.18902 ± 0.00018
$C_{1\mathrm{d}}$	$0.34105 \pm {}^{0.00030}_{0.00027}$	0.34126 ± 0.00013
$C_{2\mathrm{u}}$	-0.03751 ± 0.00027	-0.03762 ± 0.00023
$C_{2\mathrm{d}}$	0.02351 ± 0.00025	0.02358 ± 0.00021
$Q_{\mathrm{W}}(\mathrm{Cs})$	$-72.926 \pm {}^{0.065}_{0.072}$	-72.942 ± 0.037
$Q_{\mathrm{W}}(\mathrm{Tl})$	-116.40 ± 0.11	-116.432 ± 0.056
$Q_{\mathrm{W}}(\mathrm{Pb})$	$-118.30 \pm {}^{0.10}_{0.12}$	-118.332 ± 0.057
$Q_{\mathrm{W}}(\mathrm{Bi})$	$-119.22 \pm {}^{0.10}_{0.12}$	-119.246 ± 0.057
$g^2_{\nu\mathrm{Lud}}$	0.30381 ± 0.00043	0.30415 ± 0.00022
$g^2_{\nu\mathrm{Rud}}$	0.030126 ± 0.000057	0.030142 ± 0.000031
S_{qq}	6.7502 ± 0.0030	$6.7526 \pm {}^{0.0021}_{0.0024}$
$S_{qq\gamma}$	13.6700 ± 0.0085	13.6768 ± 0.0052
$\Gamma^{\mathrm{Z}}_{\mathrm{u}}/\Gamma^{\mathrm{Z}}_{\mathrm{u+d+s}}$	$0.28154 \pm {}^{0.00014}_{0.00012}$	0.28157 ± 0.00010
$\Gamma^{\mathrm{Z}}_{\mathrm{d}}/\Gamma^{\mathrm{Z}}_{\mathrm{u+d+s}}$	$0.359231 \pm {}^{0.000058}_{0.000069}$	0.359216 ± 0.000052

Table G.7: SM predictions for pseudo-observables derived from the Z-pole and the high-Q^2 SM fits.

Bibliography

[1] Gargamelle Neutrino Collaboration, F. J. Hasert *et al.*, Phys. Lett. **B46** (1973) 138.

[2] UA1 Collaboration, G. Arnison *et al.*, Phys. Lett. **B122** (1983) 103;
UA2 Collaboration, M. Banner *et al.*, Phys. Lett. **B122** (1983) 476.

[3] UA1 Collaboration, G. Arnison *et al.*, Phys. Lett. **B126** (1983) 398;
UA2 Collaboration, P. Bagnaia *et al.*, Phys. Lett. **B129** (1983) 130.

[4] S. L. Glashow, Nucl. Phys. **22** (1961) 579;
S. Weinberg, Phys. Rev. Lett. **19** (1967) 1264;
A. Salam, Weak and Electromagnetic Interactions, p. 367, in Elementary Particle Theory, Proceedings of the 1968 Nobel Symposium, ed. N. Svartholm, (Almquist and Wiksells, Stockholm, 1968);
M. Veltman, Nucl. Phys. **B7** (1968) 637;
G. 't Hooft, Nucl. Phys. **B35** (1971) 167;
G. 't Hooft and M. Veltman, Nucl. Phys. **B44** (1972) 189;
G. 't Hooft and M. Veltman, Nucl. Phys. **B50** (1972) 318.

[5] *LEP DESIGN REPORT: VOL. 2. THE LEP MAIN RING*, Internal report, CERN, 1984, *LEP Design Report*, CERN-LEP/84-01 , June 1984;
The main features of LEP have been reviewed by:;
S. Myers and E. Picasso, Contemp. Phys. **31** (1990) 387–403;
D. Brandt *et al.*, Rept. Prog. Phys. **63** (2000) 939–1000,
A useful retrospective view of the accelerator is presented in:;
R. Assmann, M. Lamont, and S. Myers, Nucl. Phys. Proc. Suppl. **109B** (2002) 17–31.

[6] *SLAC LINEAR COLLIDER CONCEPTUAL DESIGN REPORT*, Internal report, SLAC, 1980, *SLAC Linear Collider Conceptual Design Report*, SLAC-R-229 , June 1980.

[7] ALEPH Collaboration, D. Decamp *et al.*, Nucl. Instrum. Meth. **A294** (1990) 121–178;
ALEPH Collaboration, D. Buskulic *et al.*, Nucl. Instrum. Meth. **A360** (1995) 481–506.

[8] DELPHI Collaboration, P. Aarnio *et al.*, Nucl. Instrum. Meth. **A303** (1991) 233–276;
DELPHI Collaboration, P. Abreu *et al.*, Nucl. Instrum. Meth. **A378** (1996) 57–100.

[9] L3 Collaboration, B. Adeva *et al.*, Nucl. Instrum. Meth. **A289** (1990) 35–102;
M. Acciarri *et al.*, Nucl. Instrum. Meth. **A351** (1994) 300–312;
M. Chemarin *et al.*, Nucl. Instrum. Meth. **A349** (1994) 345–355;
A. Adam *et al.*, Nucl. Instrum. Meth. **A383** (1996) 342–366.

[10] OPAL Collaboration, K. Ahmet *et al.*, Nucl. Instrum. Meth. **A305** (1991) 275–319;
OPAL Collaboration, P. P. Allport *et al.*, Nucl. Instrum. Meth. **A324** (1993) 34–52;
OPAL Collaboration, P. P. Allport *et al.*, Nucl. Instrum. Meth. **A346** (1994) 476–495;
OPAL Collaboration, B. E. Anderson *et al.*, IEEE Trans. Nucl. Sci. **41** (1994) 845–852.

[11] Mark-II Collaboration, G. S. Abrams *et al.*, Phys. Rev. Lett. **63** (1989) 724.

[12] SLD Collaboration, M. J. Fero *et al.*, Nucl. Instrum. Meth. **A367** (1995) 111;
SLD Collaboration, D. Axen *et al.*, Nucl. Instrum. Meth. **A328** (1993) 472;
SLD Collaboration, K. Abe *et al.*, Nucl. Instrum. Meth. **A343** (1994) 74;
SLD Collaboration, S. C. Berridge *et al.*, IEEE Trans. Nucl. Sci. **39** (1992) 1242.

[13] SLD Collaboration, K. Abe *et al.*, Nucl. Instrum. Meth. **A400** (1997) 287;
SLD Collaboration, A. C. Benvenuti *et al.*, Nucl. Instrum. Meth. **A276** (1989) 94.

[14] Working Group on LEP Energy (L. Arnaudon *et al.*), Phys. Lett. **B307** (1993) 187–193;
Working Group on LEP Energy, L. Arnaudon *et al.*, *The Energy Calibration of LEP in 1992*, Preprint CERN SL/93-21 (DI), CERN, 1993;
Working Group on LEP Energy (R. Assmann *et al.*), Z. Phys. **C66** (1995) 567–582.

[15] R. Assmann *et al.*, Eur. Phys. J. **C6** (1999) 187–223.

[16] A. A. Sokolov and I. M. Ternov, Phys. Dokl. **8** (1964) 1203–1205.

[17] T. Sjostrand, Comput. Phys. Commun. **82** (1994) 74–90, (JETSET).

[18] G. Marchesini *et al.*, Comput. Phys. Commun. **67** (1992) 465–508, (HERWIG).

[19] L. Lonnblad, Comput. Phys. Commun. **71** (1992) 15–31, (ARIADNE).

[20] S. Jadach, B.F.L. Ward and Z. Wąs, Comput. Phys. Commun. **79** (1994) 503, (KORALZ 4.0).

[21] S. Jadach, B.F.L. Ward and Z. Wąs, Comput. Phys. Commun. **130** (2000) 260, (KK Monte Carlo).

[22] F.A. Berends, R. Kleiss and W. Hollik, Nucl. Phys. **B304** (1988) 712, (BABAMC).

[23] S. Jadach, W. Placzek, E. Richter-Wąs, B.F.L. Ward and Z. Wąs, Comput. Phys. Commun. **102** (1997) 229, (BHLUMI 4.04).

[24] R. Brun *et al.*, *GEANT3*, Preprint CERN DD/EE/84-1, CERN, 1987, details of its implementation may be found in the individual detector references, [7, 8, 9, 10].

[25] D. A. Ross and M. J. G. Veltman, Nucl. Phys. **B95** (1975) 135;
M. J. G. Veltman, Nucl. Phys. **B123** (1977) 89.

[26] D. A. Ross and J. C. Taylor, Nucl. Phys. **B51** (1973) 125–144;
A. Sirlin, Phys. Rev. **D22** (1980) 971–981.

[27] G. Burgers and F. Jegerlehner, in *Z Physics At Lep 1. Proceedings, Workshop, Geneva, Switzerland, September 4-5, 1989. Vol. 1: Standard Physics*, CERN 89-08, ed. G. Altarelli, R. Kleiss, and C. Verzegnassi, (CERN, Geneva, Switzerland, 1989), p. 55.

[28] F. Jegerlehner, in *Testing the Standard Model - TASI-90*, proceedings: Theoretical Advanced Study Institute in Elementary Particle Physics, Boulder, Colo., Jun 3-27, 1990, ed. M. Cvetic and P. Langacker, (World Scientific, Singapore, 1991), p. 916.

[29] T. Kawamoto and R. G. Kellogg, Phys. Rev. **D69** (2004) 113008.

[30] G. Montagna *et al.*, Nucl. Phys. **B401** (1993) 3–66;
G. Montagna *et al.*, Comput. Phys. Commun. **76** (1993) 328–360;
G. Montagna *et al.*, Comput. Phys. Commun. **93** (1996) 120–126;
G. Montagna *et al.*, Comput. Phys. Commun. **117** (1999) 278–289, updated to include initial state pair radiation (G. Passarino, priv. comm.).

[31] D. Y. Bardin *et al.*, Z. Phys. **C44** (1989) 493;
D. Y. Bardin *et al.*, Comput. Phys. Commun. **59** (1990) 303–312;
D. Y. Bardin *et al.*, Nucl. Phys. **B351** (1991) 1–48;
D. Y. Bardin *et al.*, Phys. Lett. **B255** (1991) 290–296;
D. Y. Bardin *et al.*, *ZFITTER: An Analytical program for fermion pair production in* e^+e^- *annihilation*, Eprint arXiv:hep-ph/9412201, 1992;
D. Y. Bardin *et al.*, Comput. Phys. Commun. **133** (2001) 229–395, updated with results from [57];
Two Fermion Working Group Collaboration, M. Kobel *et al.*, *Two-fermion production in electron positron collisions*, Eprint hep-ph/0007180, 2000;
A. B. Arbuzov *et al.*, *ZFITTER: a semi-analytical program for fermion pair production in e+e- annihilation, from version 6.21 to version 6.42*, Eprint hep-ph/0507146, 2005.

[32] D. Bardin and G. Passarino, The standard model in the making: Precision study of the electroweak interactions, (Clarendon, Oxford, UK, 1999).

[33] F. Berends *et al.*, in *Z Physics At Lep 1. Proceedings, Workshop, Geneva, Switzerland, September 4-5, 1989. Vol. 1: Standard Physics*, CERN 89-08, ed. G. Altarelli, R. Kleiss, and C. Verzegnassi, (CERN, Geneva, Switzerland, 1989), p. 89.

[34] P. A. Grassi, B. A. Kniehl, and A. Sirlin, Phys. Rev. Lett. **86** (2001) 389–392;
A. Sirlin, Phys. Lett. **B267** (1991) 240–242;
A. Sirlin, Phys. Rev. Lett. **67** (1991) 2127–2130.

[35] K. Chetyrkin *et al.*, in *Reports of the working group on precision calculations for the Z resonance*, CERN 95-03, ed. D. Bardin, W. Hollik, and G. Passarino, (CERN, Geneva, Switzerland, 1995), p. 175.

[36] A. Czarnecki and J. H. Kuhn, Phys. Rev. Lett. **77** (1996) 3955–3958;
R. Harlander, T. Seidensticker, and M. Steinhauser, Phys. Lett. **B426** (1998) 125–132.

[37] A. Blondel *et al.*, Nucl. Phys. **B304** (1988) 438.

[38] M. Böhm and W. Hollik, in *Z Physics At Lep 1. Proceedings, Workshop, Geneva, Switzerland, September 4-5, 1989. Vol. 1: Standard Physics*, CERN 89-08, ed. G. Altarelli, R. Kleiss, and C. Verzegnassi, (CERN, Geneva, Switzerland, 1989), pp. 203–234.

[39] ALEPH, DELPHI, L3, and OPAL Collaboration, Phys. Lett. **B565** (2003) 61–75.

[40] L. Lyons, D. Gibaut, and P. Clifford, Nucl. Instrum. Meth. **A270** (1988) 110;
A. Valassi, Nucl. Instrum. Meth. **A500** (2003) 391–405.

[41] ALEPH Collaboration, D. Decamp *et al.*, Z. Phys. **C48** (1990) 365–392;
ALEPH Collaboration, D. Decamp *et al.*, Z. Phys. **C53** (1992) 1–20;
ALEPH Collaboration, D. Buskulic *et al.*, Z. Phys. **C60** (1993) 71–82;
ALEPH Collaboration, D. Buskulic *et al.*, Z. Phys. **C62** (1994) 539–550;
ALEPH Collaboration, R. Barate *et al.*, Eur. Phys. J. **C14** (2000) 1–50.

[42] DELPHI Collaboration, P. Abreu *et al.*, Nucl. Phys. **B367** (1991) 511–574;
DELPHI Collaboration, P. Abreu *et al.*, Nucl. Phys. **B417** (1994) 3–57;
DELPHI Collaboration, P. Abreu *et al.*, Nucl. Phys. **B418** (1994) 403–427;
DELPHI Collaboration, P. Abreu *et al.*, Eur. Phys. J. **C16** (2000) 371–405.

[43] L3 Collaboration, B. Adeva *et al.*, Z. Phys. **C51** (1991) 179–204;
L3 Collaboration, O. Adriani *et al.*, Phys. Rept. **236** (1993) 1–146;
L3 Collaboration, M. Acciarri *et al.*, Z. Phys. **C62** (1994) 551–576;
L3 Collaboration, M. Acciarri *et al.*, Eur. Phys. J. **C16** (2000) 1–40.

[44] OPAL Collaboration, G. Alexander *et al.*, Z. Phys. **C52** (1991) 175–208;
OPAL Collaboration, P. D. Acton *et al.*, Z. Phys. **C58** (1993) 219–238;
OPAL Collaboration, R. Akers *et al.*, Z. Phys. **C61** (1994) 19–34;
OPAL Collaboration, G. Abbiendi *et al.*, Eur. Phys. J. **C19** (2001) 587–651.

[45] OPAL Collaboration, J. Allison *et al.*, Nucl. Instrum. Meth. **A317** (1992) 47–74.

[46] J. H. Field and T. Riemann, Comput. Phys. Commun. **94** (1996) 53–87, (BHAGENE3).

[47] S. Jadach, W. Placzek, and B. F. L. Ward, Phys. Lett. **B390** (1997) 298–308.

[48] H. Anlauf *et al.*, Comput. Phys. Commun. **79** (1994) 466–486, (UNIBAB).

[49] J. Hilgart, R. Kleiss and F. Le Diberder, Comput. Phys. Commun. **75** (1993) 191, (FERMISV).

[50] J. Fujimoto *et al.*, Comput. Phys. Commun. **100** (1997) 128–156, (GRC4f).

[51] For the ALEPH Collaboration, D. Bederede *et al.*, Nucl. Instrum. Meth. **A365** (1995) 117–134;
For the L3 Collaboration, I. C. Brock *et al.*, Nucl. Instrum. Meth. **A381** (1996) 236–266;
OPAL Collaboration, G. Abbiendi *et al.*, Eur. Phys. J. **C14** (2000) 373–425.

[52] W. Beenakker, F.A. Berends and S.C. van der Marck, Nucl. Phys. **B349** (1991) 323–368, (ALIBABA).

[53] LEP Polarization Collaboration, L. Arnaudon *et al.*, Phys. Lett. **B284** (1992) 431–439.

[54] L. Arnaudon *et al.*, Z. Phys. **C66** (1995) 45–62.

[55] L. Knudsen *et al.*, Phys. Lett. **B270** (1991) 97–104.

[56] M. Placidi and R. Rossmanith, Nucl. Instr. Meth. **A274** (1989) 79.

[57] A. B. Arbuzov, JHEP **07** (2001) 043.

[58] S. Eidelman and F. Jegerlehner, Z. Phys. **C67** (1995) 585–602.

[59] H. Burkhardt and B. Pietrzyk, Phys. Rev. **D72** (2005) 057501.

[60] W. Beenakker and G. Passarino, Phys. Lett. **B425** (1998) 199.

[61] W. Beenakker and G. Passarino, private communication.

[62] B. F. L. Ward *et al.*, Phys. Lett. **B450** (1999) 262–266.

[63] G. Montagna *et al.*, Nucl. Phys. **B547** (1999) 39–59;
G. Montagna *et al.*, Phys. Lett. **B459** (1999) 649–652.

[64] F.A. Berends, W.L. van Neerven and G.J.H. Burgers, Nucl. Phys. **B297** (1988) 429, erratum: B304 (1988) 921.

[65] E. A. Kuraev and V. S. Fadin, Sov. J. Nucl. Phys. **41** (1985) 466–472.

[66] G. Montagna, O. Nicrosini and F. Piccinini, Phys. Lett. **B406** (1997) 243–248.

[67] M. Skrzypek, Acta Phys. Polon. **B23** (1992) 135.

[68] S. Jadach, M. Skrzypek and B.F.L. Ward, Phys. Lett. **B257** (1991) 173–178.

[69] D.R. Yennie, S.C. Frautschi and H. Suura, Ann. Phys. **13** (1961) 379–452.

[70] S. Jadach, M. Skrzypek and B. Pietrzyk, Phys. Lett. **B456** (1999) 77.

[71] M. Martinez *et al.*, Z. Phys. **C49** (1991) 645–656;
M. Martinez and F. Teubert, Z. Phys. **C65** (1995) 267–276, updated with results summarized in [70] and [239].

[72] S. Jadach, B. Pietrzyk, E. Tournefier, B.F.L. Ward and Z. Wąs, Phys. Lett. **B465** (1999) 254.

[73] B.A. Kniehl, M. Krawczyk, J.H. Kühn and R.G. Stuart, Phys. Lett. **B209** (1988) 337.

[74] S. Jadach, M. Skrzypek and M. Martinez, Phys. Lett. **B280** (1992) 129–136.

[75] D. Y. Bardin, M. Grünewald, and G. Passarino, *Precision calculation project report*, Eprint arXiv:hep-ph/9902452, 1999.

[76] A. Leike, T. Riemann, and J. Rose, Phys. Lett. **B273** (1991) 513–518;
T. Riemann, Phys. Lett. **B293** (1992) 451–456;
S. Kirsch and T. Riemann, Comp. Phys. Commun. **88** (1995) 89–108.

[77] L3 Collaboration, O. Adriani *et al.*, Phys. Rept. **236** (1993) 1–146;
L3 Collaboration, M. Acciarri *et al.*, Eur. Phys. J. **C16** (2000) 1–40;
OPAL Collaboration, G. Abbiendi *et al.*, Eur. Phys. J. **C19** (2001) 587–651.

[78] TOPAZ Collaboration, K. Miyabayashi *et al.*, Phys. Lett. **B347** (1995) 171.

[79] VENUS Collaboration, K. Yusa *et al.*, Phys. Lett. **B447** (1999) 167.

[80] ALEPH Collaboration, D. Busculic *et al.*, Z.Phys. **C 71** (1996) 179.

[81] DELPHI Collaboration, P. Abreu *et al.*, Eur. Phys. J. **C11** (1999) 383–407.

[82] L3 Collaboration, O. Adriani *et al.*, Phys. Lett. **B315** (1993) 494–502;
L3 Collaboration, M. Acciarri *et al.*, Phys. Lett. **B479** (2000) 101–117;
L3 Collaboration, M. Acciarri *et al.*, Phys. Lett. **B489** (2000) 93–101.

[83] OPAL Collaboration, K. Ackerstaff *et al.*, Eur. Phys. J. **C2** (1998) 441–472.

[84] Particle Data Group Collaboration, S. Eidelman *et al.*, Phys. Lett. **B592** (2004) 1.

[85] SLD Collaboration, K. Abe *et al.*, Phys. Rev. Lett. **70** (1993) 2515–2520;
SLD Collaboration, K. Abe *et al.*, Phys. Rev. Lett. **73** (1994) 25–29;
SLD Collaboration, K. Abe *et al.*, Phys. Rev. Lett. **78** (1997) 2075–2079;
SLD Collaboration, K. Abe *et al.*, Phys. Rev. Lett. **84** (2000) 5945–5949.

[86] T. Maruyama *et al.*, Phys. Rev. **B46** (1992) 4261–4264;
T. Maruyama *et al.*, Phys. Rev. Lett. **66** (1991) 2376–2379;
T. Nakanishi *et al.*, Phys. Lett. **A158** (1991) 345–349.

[87] T. Limberg, P. Emma, and R. Rossmanith, *The North Arc of the SLC as a spin rotator*, Internal Report SLAC-PUB-6210, SLAC, 1993, Presented at 1993 Particle Accelerator Conference (PAC 93), Washington, DC, 17-20 May 1993;
R. C. King, A precise measurement of the left-right asymmetry of Z boson production at the SLAC linear collider, Ph.D. thesis, Stanford Univ., Sep 1994, SLAC-0452, pp.40-46.

[88] F. W. Lipps and H. A. Tolhoek, Physica **20** (1954) 85–98.

[89] A. Lath, A Precise measurement of the left-right cross-section asymmetry in Z boson production, Ph.D. thesis, Mass. Inst. of Tech., Sep 1994, SLAC-0454, pp.93-96.

[90] W. R. Nelson, H. Hirayama, and D. W. O. Rogers, *THE EGS4 CODE SYSTEM*, Internal Report SLAC-0265, SLAC, Dec 1985.

[91] E. C. Torrence, Search for anomalous couplings in the decay of polarized Z bosons to tau lepton pairs, Ph.D. thesis, Mass. Inst. of Tech., Jun 1997, SLAC-R-0509, pp.191-214.

[92] R. C. Field *et al.*, IEEE Trans. Nucl. Sci. **45** (1998) 670–675.

[93] S. C. Berridge *et al.*, *A quartz fiber / tungsten calorimeter for the Compton polarimeter at SLAC*, Internal Report SLAC-REPRINT-1998-024, SLAC, 1998, Prepared for 13th International Symposium on High-Energy Spin Physics (SPIN 98), Protvino, Russia, 8-12 Sep 1998;
D. V. Onoprienko, Precise measurement of the left-right asymmetry in Z boson production by e^+e^- collisions: Electron beam polarization measurement with the quartz fiber calorimeter, Ph.D. thesis, SLAC and Tennessee U., Aug 2000, SLAC-R-556, pp.53-100.

[94] M. L. Swartz, Phys. Rev. **D58** (1998) 014010.

[95] M. E. Levi *et al.*, *Precision Synchrotron Radiation Detectors*, Internal Report SLAC-PUB-4921, SLAC, 1989, Presented at IEEE Particle Accelerator Conf., Chicago, Ill., Mar 20-23, 1989;
J. Kent *et al.*, *Precision Measurements of the SLC Beam Energy*, Internal Report SLAC-PUB-4922, SLAC, 1989, Presented at IEEE Particle Accelerator Conf., Chicago, Ill., Mar 20-23, 1989.

[96] D. V. Onoprienko, Precise measurement of the left-right asymmetry in Z boson production by e^+e^- collisions: Electron beam polarization measurement with the quartz fiber calorimeter, Ph.D. thesis, SLAC and Tennessee U., Aug 2000, SLAC-R-556, pp.25-31.

[97] R. J. Ben-David, The First measurement of the left-right cross-section asymmetry in Z boson production, Ph.D. thesis, Yale Univ., May 1994, UMI-94-33702, pp.69-92.

[98] H. Park, A Measurement of the left-right cross-section asymmetry in Z production with polarized e^+e^- collisions, Ph.D. thesis, Oregon Univ., Dec 1993, SLAC-435, pp.61-95, 130-150.

[99] R. D. Elia, Measurement of the left-right asymmetry in Z boson production by electron - positron collisions, Ph.D. thesis, Stanford Univ., Apr 1993, SLAC-0429, pp.123-126.

[100] M. Swartz *et al.*, Nucl. Instrum. Meth. **A363** (1995) 526–537.

[101] G. Mulhollan *et al.*, *A derivative standard for polarimeter calibration*, Internal Report SLAC-PUB-7325, SLAC, 1995, Talk given at 16th IEEE Particle Accelerator Conference (PAC 95) and International Conference on High-energy Accelerators (IUPAP), Dallas, Texas, 1-5 May 1995.

[102] H. R. Band, P. C. Rowson, and T. R. Wright, *The Positron Polarization (POSPOL) Experiments: T-419*, Internal Report SLD-note 268, SLD, 2000, http://www-sldnt.slac.stanford.edu/sldbb/SLDNotes/sld-note%20268.pdf.

[103] SLD Collaboration, K. Abe *et al.*, Phys. Rev. Lett. **86** (2001) 1162–1166.

[104] SLD Collaboration, K. Abe *et al.*, Phys. Rev. Lett. **79** (1997) 804–808.

[105] M. Martinez and R. Miquel, Z. Phys. **C53** (1992) 115–126.

[106] P. H. Eberhard *et al.*, in *Z Physics At Lep 1. Proceedings, Workshop, Geneva, Switzerland, September 4-5, 1989. Vol. 1: Standard Physics*, CERN 89-08, ed. G. Altarelli, R. Kleiss, and C. Verzegnassi, (CERN, Geneva, Switzerland, 1989), pp. 235–265.

[107] K. Hagiwara, A. D. Martin, and D. Zeppenfeld, Phys. Lett. **B235** (1990) 198–202.

[108] M. Davier *et al.*, Phys. Lett. **B306** (1993) 411–417.

[109] Y.-S. Tsai, Phys. Rev. **D4** (1971) 2821, [Erratum-ibid. D **13** (1976) 771].

[110] ALEPH Collaboration, A. Heister *et al.*, Eur. Phys. J. **C20** (2001) 401–430;
ALEPH Collaboration, D. Buskulic *et al.*, Z. Phys. **C69** (1996) 183–194;
ALEPH Collaboration, D. Buskulic *et al.*, Z. Phys. **C59** (1993) 369–386;
ALEPH Collaboration, D. Decamp *et al.*, Phys. Lett. **B265** (1991) 430–444.

[111] DELPHI Collaboration, P. Abreu *et al.*, Eur. Phys. J. **C14** (2000) 585–611;
DELPHI Collaboration, P. Abreu *et al.*, Z. Phys. **C67** (1995) 183–202.

[112] L3 Collaboration, M. Acciarri *et al.*, Phys. Lett. **B429** (1998) 387–398;
L3 Collaboration, M. Acciarri *et al.*, Phys. Lett. **B341** (1994) 245–256;
L3 Collaboration, O. Adriani *et al.*, Phys. Lett. **B294** (1992) 466–478.

[113] OPAL Collaboration, G. Abbiendi *et al.*, Eur. Phys. J. **C21** (2001) 1–21;
OPAL Collaboration, G. Alexander *et al.*, Z. Phys. **C72** (1996) 365–375;
OPAL Collaboration, R. Akers *et al.*, Z. Phys. **C65** (1995) 1–16;
OPAL Collaboration, G. Alexander *et al.*, Phys. Lett. **B266** (1991) 201–217.

[114] J. Smith, J. A. M. Vermaseren, and J. G. Grammer, Phys. Rev. **D15** (1977) 3280.

[115] F. A. Berends, P. H. Daverveldt, and R. Kleiss, Phys. Lett. **B148** (1984) 489.

[116] F. A. Berends, P. H. Daverveldt, and R. Kleiss, Nucl. Phys. **B253** (1985) 441.

[117] Particle Data Group Collaboration, C. Caso *et al.*, Eur. Phys. J. **C3** (1998) 1–794.

[118] Particle Data Group Collaboration, D. E. Groom *et al.*, Eur. Phys. J. **C15** (2000) 1–878.

[119] S. Jadach, J. H. Kuhn, and Z. Wąs, Comput. Phys. Commun. **64** (1990) 275–299, (TAUOLA);
S. Jadach *et al.*, Comput. Phys. Commun. **76** (1993) 361–380, (TAUOLA: Version 2.4).

[120] E. Barbiero, B. van Eijk, and Z. Wąs, Comput. Phys. Commun. **66** (1991) 115, CERN-TH 7033/93, (PHOTOS).

[121] R. Decker and M. Finkemeier, Phys. Rev. **D48** (1993) 4203.

[122] M. Finkemeier, Radiative corrections to the decay $\tau \to \pi\nu$, Ph.D. thesis, University of Karlsruhe, Feb 1994.

[123] ALEPH Collaboration, D. Buskulic *et al.*, Phys. Lett. **B313** (1993) 535–548.

[124] L3 Collaboration, M. Acciarri *et al.*, Eur. Phys. J. **C13** (2000) 47–61.

[125] OPAL Collaboration, G. Abbiendi *et al.*, Eur. Phys. J. **C8** (1999) 217–239.

[126] D. J. Jackson, Nucl. Instrum. Meth. **A388** (1997) 247–253.

[127] DELPHI Collaboration, P. Abreu *et al.*, Eur. Phys. J. **C10** (1999) 415–442.

[128] DELPHI Collaboration, J. Abdallah *et al.*, Eur. Phys. J. **C32** (2004) 185–208.

[129] ALEPH Collaboration, R. Barate *et al.*, Phys. Lett. **B401** (1997) 150–162.

[130] OPAL Collaboration, K. Ackerstaff *et al.*, Eur. Phys. J. **C1** (1998) 439–459.

[131] ALEPH Collaboration, R. Barate *et al.*, Eur. Phys. J. **C16** (2000) 597–611.

[132] DELPHI Collaboration, P. Abreu *et al.*, Eur. Phys. J. **C12** (2000) 209–224.

[133] SLD Collaboration, K. Abe *et al.*, Phys. Rev. **D71** (2005) 112004.

[134] P. Billoir *et al.*, Nucl. Instrum. Meth. **A360** (1995) 532–558.

[135] ALEPH Collaboration, R. Barate *et al.*, Phys. Lett. **B401** (1997) 163–175.

[136] ALEPH Collaboration, R. Barate *et al.*, Eur. Phys. J. **C4** (1998) 557–570.

[137] DELPHI Collaboration, P. Abreu *et al.*, Eur. Phys. J. **C12** (2000) 225–241.

[138] OPAL Collaboration, G. Alexander *et al.*, Z. Phys. **C72** (1996) 1–16.

[139] OPAL Collaboration, G. Abbiendi *et al.*, Eur. Phys. J. **C8** (1999) 573–584.

[140] LEP Heavy Flavor Working Group Collaboration, D. Abbaneo *et al.*, Eur. Phys. J. **C4** (1998) 185–191.

[141] ALEPH Collaboration, A. Heister *et al.*, Eur. Phys. J. **C24** (2002) 177–191.

[142] ALEPH Collaboration, A. Heister *et al.*, Eur. Phys. J. **C22** (2001) 201–215.

[143] DELPHI Collaboration, P. Abreu *et al.*, Z. Phys. **C65** (1995) 569–586;
DELPHI Collaboration, J. Abdallah *et al.*, Eur. Phys. J. **C34** (2004) 109–125.

[144] L3 Collaboration, O. Adriani *et al.*, Phys. Lett. **B292** (1992) 454–462;
L3 Collaboration, M. Acciarri *et al.*, Phys. Lett. **B448** (1999) 152–162.

[145] OPAL Collaboration, G. Abbiendi *et al.*, Phys. Lett. **B577** (2003) 18–36.

[146] L3 Collaboration, M. Acciarri *et al.*, Phys. Lett. **B439** (1998) 225–236.

[147] OPAL Collaboration, G. Abbiendi *et al.*, Phys. Lett. **B546** (2002) 29–47.

[148] DELPHI Collaboration, J. Abdallah *et al.*, Eur. Phys. J. **C40** (2005) 1–25.

[149] ALEPH Collaboration, R. Barate *et al.*, Phys. Lett. **B434** (1998) 415–425.

[150] DELPHI Collaboration, P. Abreu *et al.*, Eur. Phys. J. **C10** (1999) 219–237.

[151] OPAL Collaboration, G. Alexander *et al.*, Z. Phys. **C73** (1997) 379–395.

[152] SLD Collaboration, K. Abe *et al.*, Phys. Rev. Lett. **88** (2002) 151801;
SLD Collaboration, K. Abe *et al.*, Phys. Rev. Lett. **83** (1999) 3384–3389.

[153] SLD Collaboration, K. Abe *et al.*, Phys. Rev. **D63** (2001) 032005.

[154] SLD Collaboration, K. Abe *et al.*, Phys. Rev. Lett. **81** (1998) 942–946;
SLD Collaboration, K. Abe *et al.*, Phys. Rev. Lett. **90** (2003) 141804.

[155] SLD Collaboration, K. Abe *et al.*, Phys. Rev. Lett. **94** (2005) 091801.

[156] SLD Collaboration, K. Abe *et al.*, Phys. Rev. Lett. **83** (1999) 1902–1907.

[157] ALEPH Collaboration, A. Heister *et al.*, Eur. Phys. J. **C22** (2002) 613–626.

[158] DELPHI Collaboration, P. Abreu *et al.*, Eur. Phys. J. **C20** (2001) 455–478.

[159] L3 Collaboration, M. Acciarri *et al.*, Z. Phys. **C71** (1996) 379–390.

[160] OPAL Collaboration, G. Abbiendi *et al.*, Eur. Phys. J. **C13** (2000) 225–240.

[161] C. Peterson *et al.*, Phys. Rev. **D27** (1983) 105.

[162] ALEPH Collaboration, D. Buskulic *et al.*, Phys. Lett. **B357** (1995) 699–714.

[163] ALEPH Collaboration, D. Buskulic *et al.*, Z. Phys. **C62** (1994) 179–198.

[164] DELPHI Collaboration, P. Abreu *et al.*, Z. Phys. **C66** (1995) 323–340.

[165] OPAL Collaboration, G. Alexander *et al.*, Phys. Lett. **B364** (1995) 93–106.

[166] OPAL Collaboration, R. Akers *et al.*, Z. Phys. **C60** (1993) 199–216.

[167] P. D. B. Collins and T. P. Spiller, J. Phys. **G11** (1985) 1289.

[168] V. G. Kartvelishvili, A. K. Likhoded, and V. A. Petrov, Phys. Lett. **B78** (1978) 615.

[169] ALEPH Collaboration, D. Buskulic *et al.*, Z. Phys. **C62** (1994) 1–14.

[170] DELPHI Collaboration, P. Abreu *et al.*, Z. Phys. **C59** (1993) 533, erratum: Z. Phys. C65 (1995) 709.

[171] OPAL Collaboration, R. Akers *et al.*, Z. Phys. **C67** (1995) 27–44.

[172] ALEPH Collaboration, R. Barate *et al.*, Phys. Lett. **B434** (1998) 437–450;
DELPHI Collaboration, P. Abreu *et al.*, Phys. Lett. **B405** (1997) 202–214;
DELPHI Collaboration, P. Abreu *et al.*, Phys. Lett. **B462** (1999) 425–439;
OPAL Collaboration, G. Abbiendi *et al.*, Eur. Phys. J. **C18** (2001) 447–460;
SLD Collaboration, K. Abe *et al.*, Phys. Lett. **B507** (2001) 61–69.

[173] L3 Collaboration, M. Acciarri *et al.*, Phys. Lett. **B476** (2000) 243–255.

[174] OPAL Collaboration, G. Abbiendi *et al.*, Eur. Phys. J. **C13** (2000) 1–13.

[175] A. Giammanco, in Gluon splitting into heavy flavours at the Z peak. Proceedings, 12th International Workshop, DIS 2004, Strbske Pleso, Slovakia, April 14-18, 2004. Vol. 1 + 2, ed. D. Bruncko, J. Ferencei, and P. Strizenec, (Inst. Exp. Phys. SAS, Kosice, Slovak Republic, 2004), pp. 783–786.

[176] DELPHI Collaboration, P. Abreu *et al.*, Phys. Lett. **B425** (1998) 399–412;
L3 Collaboration, M. Acciarri *et al.*, Phys. Lett. **B416** (1998) 220–232;
OPAL Collaboration, R. Akers *et al.*, Z. Phys. **C61** (1994) 209–222.

[177] MARK-III Collaboration, D. Coffman *et al.*, Phys. Lett. **B263** (1991) 135–140.

[178] CLEO Collaboration, D. E. Jaffe *et al.*, Phys. Rev. **D62** (2000) 072005.

[179] CLEO Collaboration, S. Henderson *et al.*, Phys. Rev. **D45** (1992) 2212–2231.

[180] G. Altarelli *et al.*, Nucl. Phys. **B208** (1982) 365.

[181] N. Isgur *et al.*, Phys. Rev. **D39** (1989) 799.

[182] DELCO Collaboration, W. Bacino *et al.*, Phys. Rev. Lett. **43** (1979) 1073.

[183] MARK-III Collaboration, R. M. Baltrusaitis *et al.*, Phys. Rev. Lett. **54** (1985) 1976.

[184] ALEPH, DELPHI, L3, OPAL Collaboration, The LEP collaborations, Nucl. Instrum. Meth. **A378** (1996) 101–115.

[185] CLEO Collaboration, D. Bortoletto *et al.*, Phys. Rev. **D45** (1992) 21–35.

[186] CLEO Collaboration, T. E. Coan *et al.*, Phys. Rev. Lett. **80** (1998) 1150–1155;
CLEO Collaboration, D. Gibaut *et al.*, Phys. Rev. **D53** (1996) 4734–4746;
CLEO Collaboration, R. Ammar *et al.*, Phys. Rev. **D55** (1997) 13–18.

[187] ALEPH Collaboration, R. Barate *et al.*, Eur. Phys. J. **C4** (1998) 387–407.

[188] ALEPH Collaboration, R. Barate *et al.*, Eur. Phys. J. **C19** (2001) 213–227;
DELPHI Collaboration, P. Abreu *et al.*, Phys. Lett. **B496** (2000) 43–58;
L3 Collaboration, M. Acciarri *et al.*, Phys. Lett. **B332** (1994) 201–208;
L3 Collaboration, M. Acciarri *et al.*, Z. Phys. **C71** (1996) 379–390.

[189] P. Nason and C. Oleari, Phys. Lett. **B407** (1997) 57–60.

[190] G. Altarelli and B. Lampe, Nucl. Phys. **B391** (1993) 3–22.

[191] V. Ravindran and W. L. van Neerven, Phys. Lett. **B445** (1998) 214–222.

[192] S. Catani and M. H. Seymour, JHEP **9907** (1999) 023.

[193] A. Freitas and K. Mönig, Eur. Phys. J. **C40** (2005) 493–496.

[194] ALEPH Collaboration, D. Buskulic *et al.*, Z. Phys. **C71** (1996) 357–378.

[195] DELPHI Collaboration, P. Abreu *et al.*, Phys. Lett. **B277** (1992) 371–382.

[196] OPAL Collaboration, P. D. Acton *et al.*, Phys. Lett. **B294** (1992) 436–450.

[197] ALEPH Collaboration, D. Buskulic *et al.*, Phys. Lett. **B388** (1996) 419–430;
L3 Collaboration, M. Acciarri *et al.*, Phys. Lett. **B450** (1999) 281–293;
OPAL Collaboration, G. Abbiendi *et al.*, Phys. Lett. **B544** (2002) 259–273.

[198] ALEPH Collaboration, R. Barate *et al.*, Eur. Phys. J. **C12** (2000) 183–207;
DELPHI Collaboration, P. Abreu *et al.*, Phys. Lett. **B485** (2000) 45–61;
L3 Collaboration, O. Adriani *et al.*, Phys. Lett. **B306** (1993) 187–196;
OPAL Collaboration, G. Abbiendi *et al.*, Eur. Phys. J. **C33** (2004) 173–212.

[199] U. Amaldi *et al.*, Phys. Rev. **D36** (1987) 1385.

[200] T. van Ritbergen and R. G. Stuart, Phys. Rev. Lett. **82** (1999) 488–491;
T. van Ritbergen and R. G. Stuart, Nucl. Phys. **B564** (2000) 343–390;
M. Steinhauser and T. Seidensticker, Phys. Lett. **B467** (1999) 271–278.

[201] M. Steinhauser, Phys. Lett. **B429** (1998) 158–161.

[202] H. Burkhardt and B. Pietrzyk, Phys. Lett. **B356** (1995) 398–403.

[203] BES Collaboration, J. Z. Bai *et al.*, Phys. Rev. Lett. **88** (2002) 101802.

[204] CMD-2 Collaboration, R. R. Akhmetshin *et al.*, Phys. Lett. **B578** (2004) 285–289.

[205] KLOE Collaboration, A. Aloisio *et al.*, Phys. Lett. **B606** (2005) 12–24.

[206] M. L. Swartz, Phys. Rev. **D53** (1996) 5268–5282;
A. D. Martin and D. Zeppenfeld, Phys. Lett. **B345** (1995) 558–563;
R. Alemany, M. Davier, and A. Hocker, Eur. Phys. J. **C2** (1998) 123–135;
M. Davier and A. Hocker, Phys. Lett. **B419** (1998) 419–431;
J. H. Kuhn and M. Steinhauser, Phys. Lett. **B437** (1998) 425–431;
F. Jegerlehner, in Proceedings, 4th International Symposium, RADCOR'98, ed. J. Sola, (World Scientific, Singapore, Sep 1999), p. 75;
J. Erler, Phys. Rev. **D59** (1999) 054008;
A. D. Martin, J. Outhwaite, and M. G. Ryskin, Phys. Lett. **B492** (2000) 69–73;
J. F. de Troconiz and F. J. Yndurain, Phys. Rev. **D65** (2002) 093002;
K. Hagiwara *et al.*, Phys. Rev. **D69** (2004) 093003.

[207] J. F. de Troconiz and F. J. Yndurain, Phys. Rev. **D71** (2005) 073008.

[208] CDF Collaboration, F. Abe *et al.*, Phys. Rev. Lett. **73** (1994) 225–231;
CDF Collaboration, F. Abe *et al.*, Phys. Rev. Lett. **74** (1995) 2626–2631.

[209] DØ Collaboration, S. Abachi *et al.*, Phys. Rev. Lett. **74** (1995) 2632–2637.

[210] CDF Collaboration, F. Abe *et al.*, Phys. Rev. Lett. **80** (1998) 2779–2784;
CDF Collaboration, F. Abe *et al.*, Phys. Rev. Lett. **82** (1999) 271–276;
CDF Collaboration, F. Abe *et al.*, Erratum: Phys. Rev. Lett. **82** (1999) 2808–2809;
CDF Collaboration, F. Abe *et al.*, Phys. Rev. Lett. **80** (1998) 2767–2772;
CDF Collaboration, T. Affolder *et al.*, Phys. Rev. **D63** (2001) 032003;
CDF Collaboration, F. Abe *et al.*, Phys. Rev. Lett. **79** (1997) 1992–1997.

[211] DØ Collaboration, B. Abbott *et al.*, Phys. Rev. Lett. **80** (1998) 2063–2068;
DØ Collaboration, B. Abbott *et al.*, Phys. Rev. **D60** (1999) 052001;
DØ Collaboration, S. Abachi *et al.*, Phys. Rev. Lett. **79** (1997) 1197–1202;
DØ Collaboration, B. Abbott *et al.*, Phys. Rev. **D58** (1998) 052001;
DØ Collaboration, V. M. Abazov *et al.*, Nature **429** (2004) 638–642;
DØ Collaboration, V. M. Abazov *et al.*, *New measurement of the top quark mass in lepton + jets t anti-t events at DØ*, Eprint hep-ex/0407005, 2004;
DØ Collaboration, V. M. Abazov *et al.*, Phys. Lett. **B606** (2005) 25–33.

[212] The CDF and DØ Collaborations, and the Tevatron Electroweak Working Group, *Combination of CDF and DØ results on the top-quark mass*, Eprint hep-ex/0404010, 2004.

[213] UA1 Collaboration, C. Albajar *et al.*, Z. Phys. **C44** (1989) 15.

[214] UA2 Collaboration, J. Alitti *et al.*, Phys. Lett. **B276** (1992) 354–364.

[215] CDF Collaboration, T. Affolder *et al.*, Phys. Rev. **D64** (2001) 52001–39;
CDF Collaboration, F. Abe *et al.*, Phys. Rev. Lett. **75** (1995) 11–16;
CDF Collaboration, F. Abe *et al.*, Phys. Rev. **D52** (1995) 4784–4827;
CDF Collaboration, F. Abe *et al.*, Phys. Rev. Lett. **65** (1990) 2243–2246;
CDF Collaboration, F. Abe *et al.*, Phys. Rev. **D43** (1991) 2070–2093.

[216] DØ Collaboration, B. Abbott *et al.*, Phys. Rev. Lett. **80** (1998) 3008;
DØ Collaboration, B. Abbott *et al.*, Phys. Rev. Lett. **84** (2000) 222–227;
DØ Collaboration, V. M. Abazov *et al.*, Phys. Rev. **D66** (2002) 012001;
DØ Collaboration, B. Abbott *et al.*, Phys. Rev. **D62** (2000) 092006.

[217] CDF Collaboration, T. Affolder *et al.*, Phys. Rev. Lett. **85** (2000) 3347–3352.

[218] DØ Collaboration, V. M. Abazov *et al.*, Phys. Rev. **D66** (2002) 032008.

[219] The CDF Collaboration, the DØ Collaboration, and the Tevatron Electroweak Working Group, Phys. Rev. **D70** (2004) 092008.

[220] ALEPH Collaboration, R. Barate *et al.*, Eur. Phys. J. **C17** (2000) 241–261;
DELPHI Collaboration, P. Abreu *et al.*, Phys. Lett. **B511** (2001) 159–177;
L3 Collaboration, M. Acciarri *et al.*, Phys. Lett. **B454** (1999) 386–398;
OPAL Collaboration, G. Abbiendi *et al.*, Phys. Lett. **B507** (2001) 29–46.

[221] The LEP Collaborations ALEPH, DELPHI, L3, OPAL, the LEP Electroweak Working Group, and the SLD Electroweak and Heavy Flavour Groups, *A combination of preliminary electroweak measurements and constraints on the standard model*, Eprint hep-ex/0412015, CERN, 2004.

[222] C. S. Wood *et al.*, Science **275** (1997) 1759.

[223] S. C. Bennett and C. E. Wieman, Phys. Rev. Lett. **82** (1999) 2484–2487.

[224] N. H. Edwards *et al.*, Phys. Rev. Lett. **74** (1995) 2654–2657.

[225] P. A. Vetter *et al.*, Phys. Rev. Lett. **74** (1995) 2658–2661.

[226] J. S. M. Ginges and V. V. Flambaum, Phys. Rept. **397** (2004) 63–154.

[227] D. Y. Bardin *et al.*, Eur. Phys. J. **C22** (2001) 99–104.

[228] SLAC E158 Collaboration, P. Anthony *et al.*, Phys. Rev. Lett. **92** (2004) 181602.

[229] SLAC E158 Collaboration, P. L. Anthony *et al.*, Phys. Rev. Lett. **95** (2005) 081601.

[230] E. A. Paschos and L. Wolfenstein, Phys. Rev. **D7** (1973) 91–95.

[231] NuTeV Collaboration, G. P. Zeller *et al.*, Phys. Rev. Lett. **88** (2002) 091802, erratum: 90 (2003) 239902.

[232] NuTeV Collaboration, G. P. Zeller *et al.*, Phys. Rev. **D65** (2002) 111103.

[233] K. S. McFarland and S.-O. Moch, *Conventional physics explanations for the NuTeV* $\sin^2\theta_{\rm W}$, Eprint hep-ph/0306052, 2003.

[234] F. Olness *et al.*, Eur. Phys. J. **C40** (2005) 145–156.

[235] S. Kretzer *et al.*, Phys. Rev. Lett. **93** (2004) 041802.

[236] A. D. Martin *et al.*, Eur. Phys. J. **C39** (2005) 155–161.

[237] K. S. McFarland *et al.*, Nucl. Phys. Proc. Suppl. **112** (2002) 226–233.

[238] Ed. G. Altarelli, R. Kleiss, and C. Verzegnassi, *Z Physics At Lep 1. Proceedings, Workshop, Geneva, Switzerland, September 4-5, 1989. Vol. 1: Standard Physics*, (CERN, Geneva, Switzerland, 1989), Yellow Report CERN 89-08.

[239] D. Bardin *et al.*, in *Reports of the working group on precision calculations for the Z resonance*, CERN 95-03, ed. D. Bardin, W. Hollik, and G. Passarino, (CERN, Geneva, Switzerland, 1995), pp. 7–162.

[240] D. Y. Bardin and G. Passarino, *Upgrading of precision calculations for electroweak observables*, Eprint hep-ph/9803425, 1998.

[241] U. Baur *et al.*, eConf **C010630** (2001) P122, hep-ph/0111314.

[242] The Snowmass Working Group on Precision Electroweak Measurements, eConf **C010630** (2001) P1WG1, hep-ph/0202001.

[243] M. Awramik *et al.*, Phys. Rev. **D69** (2004) 053006.

[244] M. Faisst *et al.*, Nucl. Phys. **B665** (2003) 649–662.

[245] M. Awramik *et al.*, Phys. Rev. Lett. **93** (2004) 201805.

[246] K. G. Chetyrkin, J. H. Kuhn, and A. Kwiatkowski, Phys. Rept. **277** (1996) 189–281.

[247] D. E. Soper and L. R. Surguladze, Phys. Rev. **D54** (1996) 4566–4577.

[248] S. Bethke, J. Phys. **G26** (2000) R27.

[249] S. Bethke, Nucl. Phys. Proc. Suppl. **135** (2004) 345–352.

[250] H. Stenzel, JHEP **07** (2005) 0132.

[251] F. James and M. Roos, Comp. Phys. Commun. **10** (1975) 343.

[252] G. Altarelli and R. Barbieri, Phys. Lett. **B253** (1991) 161–167;
G. Altarelli, R. Barbieri, and S. Jadach, Nucl. Phys. **B369** (1992) 3–32;
G. Altarelli, R. Barbieri, and S. Jadach, Nucl. Phys. **B376** (1992) 444;
G. Altarelli, R. Barbieri, and F. Caravaglios, Nucl. Phys. **B405** (1993) 3–23;
G. Altarelli, R. Barbieri, and F. Caravaglios, Phys. Lett. **B314** (1993) 357–363;
G. Altarelli, R. Barbieri, and F. Caravaglios, Phys. Lett. **B349** (1995) 145–154;
G. Altarelli, R. Barbieri, and F. Caravaglios, Int. J. Mod. Phys. **A13** (1998) 1031.

[253] M. E. Peskin and T. Takeuchi, Phys. Rev. Lett. **65** (1990) 964–967;
M. E. Peskin and T. Takeuchi, Phys. Rev. **D46** (1992) 381–409.

[254] DELPHI Collaboration, P. Abreu *et al.*, Z. Phys. **C67** (1995) 1–14.

[255] DELPHI Collaboration, P. Abreu *et al.*, Eur. Phys. J. **C14** (2000) 613–631.

[256] OPAL Collaboration, K. Ackerstaff *et al.*, Z. Phys. **C76** (1997) 387–400.

[257] SLD Collaboration, K. Abe *et al.*, Phys. Rev. Lett. **85** (2000) 5059–5063.

[258] DELPHI Collaboration, P. Abreu *et al.*, Z. Phys. **C69** (1995) 1–14.

[259] L3 Collaboration, O. Adriani *et al.*, Phys. Lett. **B301** (1993) 136–144.

[260] OPAL Collaboration, G. Abbiendi *et al.*, Phys. Lett. **B586** (2004) 167–182.

[261] OPAL Collaboration, P. D. Acton *et al.*, Z. Phys. **C58** (1993) 405–418.

[262] ALEPH Collaboration, D. Buskulic *et al.*, Z. Phys. **C57** (1993) 17–36.

[263] H1 Collaboration, A. Aktas *et al.*, *A determination of electroweak parameters at HERA*, Eprint hep-ex/0507080, 2005, accepted for publication in Physics Letters B.

[264] CDF Collaboration, D. Acosta *et al.*, Phys. Rev. **D71** (2005) 052002.